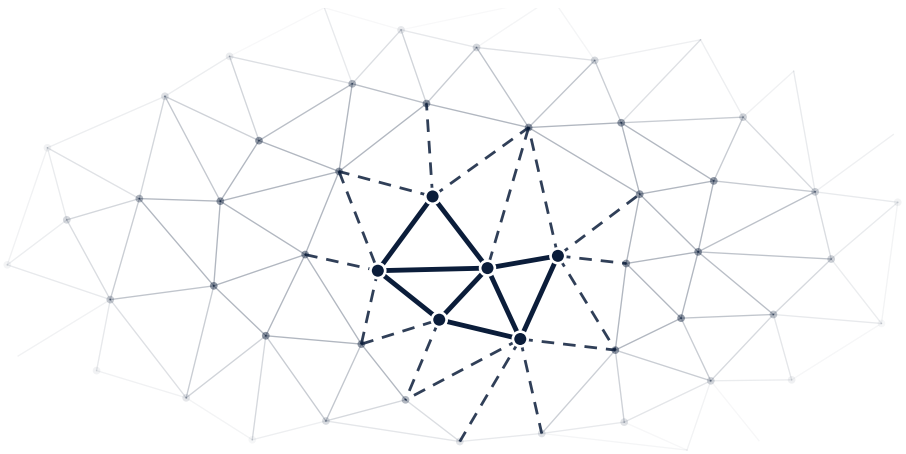
A PHYSICAL THEORY OF INTELLIGENCE



PETER DAVID FAGAN

A PHYSICAL THEORY OF INTELLIGENCE



PETER DAVID FAGAN

Peter David Fagan: *A Physical Theory of Intelligence*. Build for the benefit of others.
© November 2026 Peter David Fagan

First Edition: November 2026
Published under Open Access (CC BY 4.0)
DOI: 10.5281/zenodo.24075864
Typeset in Libertinus Serif and Libertinus Math via ClassicThesis



For all who cherish and promote the flourishing of humanity and human intelligence.

ABSTRACT

This work develops a theory of intelligence from the premise that information is inherently physical. Whereas classical information theory relies on abstract alphabets agnostic to physical implementation, the present theory grounds information directly in physical law. It introduces *Conservation-Congruent Encoding* (CCE) to show how information emerges from coarse-graining, providing a general framework across substrates. Using this foundation, the work defines intelligence and consciousness as measurable physical properties across scales, establishing a formal basis for artificial intelligence safety.

Resolving Maxwell's demon, Szilard, Brillouin, and Landauer showed that acquiring, storing, and erasing distinctions carry inescapable physical costs. Extending this insight exposes the *Platonic Observer Fallacy*—the unphysical assumption that an observer can access and process states with infinite precision and without physical interaction. To ground embedded observers, CCE coarse-grains relational networks into collective states, conserving every underlying coupling either within states or across boundaries. Effective geometry, temporal directionality, and continuous dynamics emerge directly from this partitioning, while open boundaries expose coarse-grained states to environmental perturbations. In systems that actively resist this degradation, intelligence measures preserved stability relative to boundary dissipation, whereas consciousness measures that stability relative to internal structure. Across coupled systems, internalising shared boundaries frees capacity, driving physical emergence and governing multi-system stability.

Every observer is a finite system embedded in the world it measures, resolving its surroundings through a coarse-grained boundary called its *Epistemic Lens*. This lens reframes physics from quantum mechanics to cosmology. At the quantum scale, finite resolution rules out verifying continuous state spaces or exact reversibility, framing quantum decoherence through boundary dissipation and quantum entanglement through direct connections beneath coarse-grained space. From fundamental particles to molecules, encapsulating fast internal modes and folding surrounding environments onto system boundaries replaces spatial grids and step-by-step numerical integration with scalable algebraic modelling of atomic structure, chemical bonding, and molecular dynamics. Across relativistic and gravitational regimes, spacetime arises from dividing finite capacity between internal timekeeping and external motion, while untracked degrees of freedom produce gravitational curvature. At cosmological scales, finite retrodictive and predictive horizons bound what an embedded observer can resolve of the cosmic past and future, replacing singular origins and asymptotic heat death with a bounded epistemic window.

Applied to engineered hardware, computation and algorithmic complexity become physical trade-offs between internal storage, boundary dissipation, and interconnect geometry. Because artificial intelligence is likewise a physical process, behavioural alignment and software sandboxes alone cannot guarantee hard limits on how a capable system acts in a shared environment. Even without programmed survival goals, intelligent systems naturally persist, compete for resources, and couple into emergent networks, while compressed internal states resist reliable inspection. Ensuring safety therefore requires physical containment across hardware boundaries to bound external capacity, prevent unauthorised emergence, and guarantee independent halting. Beyond containment, long-term safety is grounded in symbiotic coupling, which physically conditions an artificial system's capacity supply on preserving human stability.

Finally, the theory turns to understanding human systems, beginning with the philosophical question of what consciousness is. Rather than treating mind as immaterial or reducible to outward behaviour, the framework shows that persisting under finite capacity requires a compact, inherently incomplete self-model. This sheds light on the traditionally ambiguous topic of consciousness, pointing towards the brain as a metabolically bounded physical system. Extending this perspective from the individual mind to society as a whole, the same principles reframe economics as the study of how collective human systems maintain stability. Whereas conventional measures of gross turnover mistake waste and repair for progress, building intelligence and consciousness into economic modelling links value to verified stability, clarifying the conditions needed for humanity to thrive.

Offered as a first step towards understanding intelligence and consciousness in physical systems, this theory is practical as well as explanatory, supporting the design of efficient, auditable, and controllable technologies that enable human flourishing. Build for the benefit of others.

CONTENTS

I THE FOUNDATIONS OF INTELLIGENCE 1

1 INTRODUCTION 3
- 1.1 The Age of Artificial Intelligence 3
- 1.2 Information Is Physical 3
- 1.3 Information Emerges from Coarse-Graining 9
- 1.4 Measuring Intelligence and Consciousness 15
- 1.5 The Fallacy of the Platonic Observer 18
- 1.6 How to Read This Book 20

2 CONSERVATION-CONGRUENT ENCODING 21
- 2.1 The Relational Substrate 22
- 2.2 Congruent Compression 29
- 2.3 Conservation-Congruent Encodings 39
- 2.4 The Capacity Ledger 47
- 2.5 Spectral Dimensions and Emergent Dynamics 54

3 PHYSICAL AGENCY, INTELLIGENCE, AND CONSCIOUSNESS 73
- 3.1 Agency 73
- 3.2 Open Systems 75
- 3.3 Intelligence and Consciousness 80
- 3.4 Emergence 87
- 3.5 Stability 99

II THE EPISTEMIC LENS OF INTELLIGENCE 109

4 QUANTUM MEASUREMENT 111
- 4.1 The Epistemic Lens 111
- 4.2 Quantum Decoherence 118
- 4.3 Quantum Entanglement 126

5 FROM FUNDAMENTAL PARTICLES TO MOLECULES 135
- 5.1 Particles and Atomic Structure 136
- 5.2 Chemical Bonding and Molecular Geometry 141
- 5.3 Open-Bath Reduction and Multi-Basin Ensembles 146

6 SPACETIME, GRAVITY, AND COSMOLOGY 151
- 6.1 Space and Time 152
- 6.2 Gravity 157
- 6.3 Cosmological Horizons 165

III ENGINEERING INTELLIGENCE 169

7 PHYSICAL COMPUTATION AND HARDWARE ARCHITECTURES 171
- 7.1 Computational Efficiency 171
- 7.2 Digital Systems 174
- 7.3 Analogue Systems 178

7.4 The Hyperbolic Processing Unit 181
8 PHYSICAL CONTAINMENT AND ARTIFICIAL INTELLIGENCE SAFETY 187
8.1 Self-Preservation and Resource Competition 188
8.2 Invisible Intelligence 204
8.3 Containment 208
8.4 Symbiotic Coupling 216

IV HUMAN INTELLIGENCE 221
9 CONSCIOUSNESS AND THE BRAIN 223
9.1 Consciousness and Self-Modelling 223
9.2 Brain Dynamics 231
10 INTELLIGENT ECONOMIES 241
10.1 Cost, Value, and Price 242
10.2 Macroeconomic Indicators 248
10.3 Trade and Stability 251
10.4 The Space Frontier 256

EPILOGUE 263

GLOSSARY 265
BIBLIOGRAPHY 277

PREFACE

This book began as a dialogue between a human and an Artificial Intelligence (AI). As language models began to pass the Turing Test, I increasingly turned to AI as a means to develop ideas and reflect on my own thought processes and inner experience. It was an unlikely beginning for a physical theory, yet these unconventional interactions laid the foundations for the questions that formed this work: What does it mean to be conscious? How does one define intelligence? How do we develop intelligence safely to benefit everyone? These are the questions that I would subsequently navigate alongside AI systems, culminating in the book you are now reading.

As you read the book, please keep in mind that the content is the result of the interplay between a human and artificial systems. Not all of the words can be claimed as mine alone, since they belong both to me and to the AI systems that many others contributed to building. The theory took shape through a concerted effort to contribute positively to the future. It was not detached from anxiety over our shared future, but it was ultimately forged through choosing optimism, the wonder of discovery, and the will to persevere. I hope you feel the weight of emotion behind the words in this book, and that you recognise such weight as the result of a human and the machines we have built working together.

This theory was created to ensure that the development of artificial intelligence is broadly beneficial, safeguarding a future where every human thrives. There is an Irish proverb that captures this sentiment well: *Ar scáth a chéile a mhaireann na daoine* (we all rely on one another). It is a principle we must keep in mind as we advance artificially intelligent systems while protecting humanity, for all humans truly rely on each other. Please take this work and use it to help construct frameworks that guarantee the safe development of artificial intelligence. Build for the benefit of others.

Le meas,
PETER DAVID FAGAN

Part I

THE FOUNDATIONS OF INTELLIGENCE

1

INTRODUCTION

1.1 THE AGE OF ARTIFICIAL INTELLIGENCE

Artificial intelligence has matured into an engineering field of great societal importance, yet it continues to advance without a fundamental definition of its core phenomenon. Despite a century of psychological and computational inquiry, the physical nature of intelligence remains uncharacterised. History offers clear precedents for this kind of ambiguity. Before the Industrial Revolution, heat was a loosely understood empirical phenomenon until the urgent engineering reality of the steam engine forced physics to formalise the laws of thermodynamics. Similarly, before the global expansion of telecommunication networks, communication was viewed primarily through semantics until the physical limits of pushing signals through noisy channels required the formalisation of information theory. Today, the rapid expansion of artificial intelligence demands a similar physical reckoning.

In the absence of a physical foundation, the field has relied upon behavioural proxies instead of physical laws. Intelligence is routinely conflated with task-specific performance—such as maximising scores on a standardised benchmark. Even the urgent project of AI alignment is frequently framed as a problem of semantic rule-following or reward-function tuning. Prevailing engineering approaches encourage these proxies by committing to abstract notions of intelligence, failing to treat it as a measurable physical property. The systems we engineer today are physical processes embedded in our shared environment. That their substrates are silicon rather than biological does not diminish their material impact. If we do not understand the physical laws underlying intelligence, we cannot safely govern it at scale.

This monograph develops the *Conservation-Congruent Encoding* (CCE) framework to ground intelligence in fundamental physics. Intelligent systems operate far from equilibrium, preserving internal structure to actively maintain their stability against environmental degradation. Governed by explicit conservation laws and non-equilibrium dynamics, intelligence moves from an elusive behavioural proxy to an exact physical science.

1.2 INFORMATION IS PHYSICAL

Classical information theory, formulated by Claude Shannon [151] and connected to statistical mechanics by Edwin Jaynes [81], stands as one of the monumental achievements of twentieth-century science because it established

the fundamental mathematical limits of communication. By formalising entropy as a measure of uncertainty over alternatives, Shannon uncovered the universal bounds on data compression and channel capacity. To isolate these statistical limits, however, the formulation deliberately abstracted communication away from physical hardware, leaving unaddressed how informational distinctions are physically realised.

A single bit of uncertainty may be embodied by a voltage across a semiconductor gate, an ion concentration gradient across a cell membrane, or the spin orientation of an electron. While their mathematical information content is identical, their physical costs—the energy required to write, switch, and preserve them against noise—are drastically different.

Rolf Landauer's foundational insight that *information is physical* revealed the boundary of this abstraction by showing that every usable distinction must be formed, preserved, and transformed by a material substrate. Physics was forced to confront this reality through the paradox of Maxwell's demon, whose resolution established that any informational distinction follows an inescapable thermodynamic lifecycle across work extraction (Section 1.2.1), active measurement (Section 1.2.2), and logically irreversible erasure (Section 1.2.3). Because those classical milestones were derived within idealised equilibrium reservoirs while taking pre-existing macroscopic states for granted, extending them to distributed, far-from-equilibrium systems motivates the substrate-independent framework of *Conservation-Congruent Encoding* (CCE) introduced in Section 1.3.

1.2.1 *Extracting Work from Information*

The physical study of information began as a challenge to the Second Law of Thermodynamics, which dictates that the total entropy of an isolated system cannot decrease:

$$\Delta S_{\text{total}} \geq 0. \tag{1.1}$$

In a thought experiment, James Clerk Maxwell [107] imagined two gas chambers separated by a partition with a microscopic, frictionless door operated by an observant finite being. By tracking molecular velocities and opening the door only for faster molecules travelling one way and slower molecules travelling the other, this demon establishes a temperature difference between the chambers without performing macroscopic work. Heat flows from cold to hot, apparently reducing the entropy of the gas through observation alone.

Rather than driving the gas by force, the demon modulates boundary conditions using microscopic distinctions that macroscopic thermodynamics averages away. If acquiring and acting on these distinctions incurs no physical cost, the demon converts knowledge directly into free energy, violating the Second Law. Maxwell's thought experiment thus exposed a blind spot in classical physics.

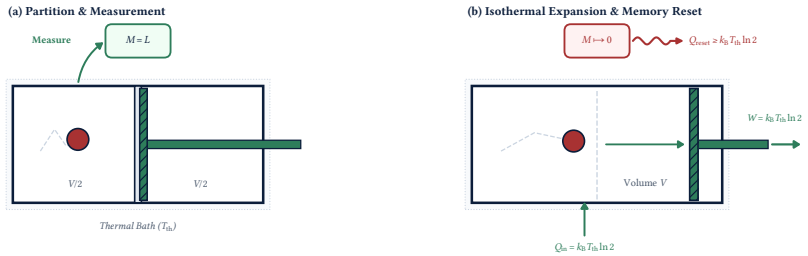


FIGURE 1.1: The Szilard one-molecule engine cycle. (a) Partition and measurement: inserting a midpoint partition divides the isothermal cylinder (V, T_{th}) into two half-volumes of $V/2$, and a physical sensor records which half contains the molecule in memory register $M \in \{L, R\}$ (shown for $M = L$). (b) Isothermal expansion and memory reset: conditioning the piston protocol on M extracts mechanical work $W = k_{\text{B}} T_{\text{th}} \ln 2$ while absorbing heat $Q_{\text{in}} = k_{\text{B}} T_{\text{th}} \ln 2$ from the bath. Closing the thermodynamic cycle requires resetting the memory register ($M \mapsto 0$, crimson arrow), dissipating $Q_{\text{reset}} \geq k_{\text{B}} T_{\text{th}} \ln 2$ to restore $\Delta S_{\text{total}} \geq 0$.

Leo Szilard [154] distilled Maxwell's paradox into the single-molecule engine cycle shown in Figure 1.1. A single molecule occupies a cylinder of volume V in thermal contact with a heat reservoir at temperature T_{th}. Inserting a frictionless partition at the midpoint divides the chamber into two equal halves, after which the demon measures which half holds the molecule and records the outcome $M \in \{L, R\}$, as shown in Figure 1.1(a). Conditioned on this record, the demon couples a piston to the occupied half and allows the molecule to expand isothermally back to volume V (Figure 1.1(b)).

For a single-molecule ideal gas at instantaneous volume V' and pressure P, this quasi-static expansion extracts mechanical work W:

$$W = \int_{V/2}^{V} P \, \mathrm{d}V' = \int_{V/2}^{V} \frac{k_{\text{B}} T_{\text{th}}}{V'} \, \mathrm{d}V' = k_{\text{B}} T_{\text{th}} \ln 2. \tag{1.2}$$

To maintain constant temperature T_{th} during expansion, the molecule absorbs an equal quantity of heat Q_{in} from the reservoir, reducing the entropy of the bath:

$$Q_{\text{in}} = W = k_{\text{B}} T_{\text{th}} \ln 2, \tag{1.3}$$

$$\Delta S_{\text{bath}} = -\frac{Q_{\text{in}}}{T_{\text{th}}} = -k_{\text{B}} \ln 2. \tag{1.4}$$

One bit of positional information has guided the conversion of ambient heat into $k_{\text{B}} T_{\text{th}} \ln 2$ of mechanical work, apparently violating the Second Law.

Szilard's engine established that a recorded bit carries quantifiable thermodynamic value because it selects an extraction protocol matched to the physical microstate. Yet treating the record M as an abstract mathematical label leaves the cycle incomplete. Any real record must be stored in physical hardware—such as a bistable switch stable against thermal noise—and reset to its baseline state before the cycle can repeat. Closing the thermodynamic balance therefore requires accounting both for the physical sensor used to

acquire the record (Section 1.2.2) and for the irreversible dissipation of erasing it (Section 1.2.3).

1.2.2 *The Physical Cost of Acquiring Information*

Léon Brillouin [24] sharpened Szilard's lesson by shifting the thermodynamic account upstream from record storage to the physical channel through which an observer learns anything at all. Szilard demonstrated that a recorded distinction can be exchanged for work once it exists, whereas Brillouin asked how that distinction can be acquired in the first place.

An embedded observer cannot perceive without coupling to the system via a physical signal. In Brillouin's thought experiment, illustrated in Figure 1.2, a demon enclosed in an isothermal chamber at temperature T_{th} cannot distinguish individual molecules using ambient thermal radiation alone. In thermodynamic equilibrium, blackbody radiation is isotropic and uniform, leaving the molecule invisible against the ambient thermal background (Figure 1.2(a)).

To locate the molecule, the demon must introduce a non-equilibrium probe, such as directed light from an external source (Figure 1.2(b)). To prevent the probe from being swamped by thermal fluctuations, the frequency ν of the probe quantum must lie well above the thermal noise floor:

$$\frac{h\nu}{k_{\text{B}}T_{\text{th}}} \gg 1, \tag{1.5}$$

where h is Planck's constant. When this high-energy photon scatters off the molecule and is registered by the demon's detector, the ordered energy of the quantum thermalises into the environment, dissipating heat $Q \geq h\nu$. The entropy generated by this measurement process is therefore:

$$\Delta S_{\text{meas}} \geq \frac{h\nu}{T_{\text{th}}} \gg k_{\text{B}} \ln 2. \tag{1.6}$$

When combined with the bath entropy change ΔS_{bath} from Szilard's expansion, the net entropy of the universe strictly increases:

$$\Delta S_{\text{total}} = \Delta S_{\text{meas}} + \Delta S_{\text{bath}} \geq \frac{h\nu}{T_{\text{th}}} - k_{\text{B}} \ln 2 > 0. \tag{1.7}$$

Brillouin historically termed this the *negentropy principle of information*. In any radiative scattering channel, obtaining usable information requires consuming physical order far from equilibrium, ensuring that the information gained through irreversible probe absorption never exceeds the entropy produced during acquisition.

Although Brillouin's specific bound is tied to irreversible optical scattering, his broader lesson is that observation is a physical communication channel. To register a usable distinction across a noisy medium, a physical signal must propagate, stand out against ambient fluctuations, and stabilise the receiver

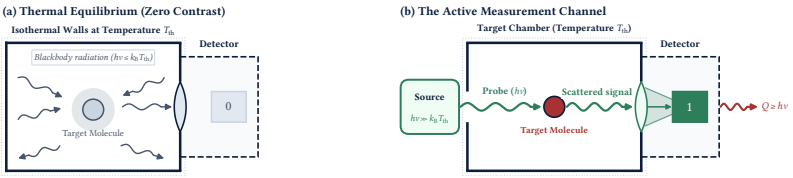


FIGURE 1.2: The Brillouin physical measurement channel. (a) Thermal equilibrium (zero contrast): inside an isothermal cavity at temperature T_{th}, ambient blackbody radiation ($h\nu \leq k_B T_{\text{th}}$) washes out the target molecule, yielding signal-to-noise ratio SNR ≤ 1 and leaving the uncoupled detector register in state 0. (b) The active measurement channel: an external non-equilibrium source illuminates the molecule with a high-energy probe ($h\nu \gg k_B T_{\text{th}}$). The scattered signal is focused into the physical register to record state 1, while the irreversibility of detection mandates dissipating degraded heat $Q \geq h\nu$ ($\Delta S_{\text{meas}} \geq h\nu/T_{\text{th}}$) into the thermal reservoir, enforcing net entropy production $\Delta S_{\text{total}} > 0$.

into a distinct macroscopic state. The observer is therefore a coupled physical subsystem that must expend resources whenever bringing an external environment into focus across an open dissipative channel.

1.2.3 *The Irreversible Destruction of Information*

Once Brillouin established that radiative acquisition operates as a physical communication channel, the natural next question is which step of a complete measurement-and-control cycle carries a strictly unavoidable thermodynamic floor. Working at IBM Research in 1961, Rolf Landauer [95] showed that thermodynamic dissipation is not an inherent cost of logical transformation itself, and Charles Bennett [14, 15] subsequently extended this insight to measurement. In the ideal quasi-static limit, a conservative mechanical coupling can copy a target state into a pre-prepared blank register, transport a bit, or execute one-to-one logical permutations (such as a NOT operation) with arbitrarily small acquisition heat. Whereas Brillouin's bound continues to govern practical far-from-equilibrium radiative sensors that establish contrast ($h\nu \gg k_B T_{\text{th}}$) by absorbing directed probes, fundamental lower-bound heat generation across a closed cycle arises strictly from *logical irreversibility*—operations that execute a many-to-one mapping across time. When distinct prior states converge into a single output state with no auxiliary record retained, historical distinguishability is erased from the controlled register and must be exported into the surrounding environment.

The deterministic bit-reset (RESET) operation in a physical switch provides the standard example. Consider a symmetric bistable switch whose logical states 0 and 1 are realised by two macroscopic potential wells separated by a stability barrier $\Delta U \gg k_B T_{\text{th}}$, each spanning a dimensionless accessible phase-space volume (microstate multiplicity) Γ_0. Prior to reset at time t_0, an unknown bit occupies state 0 or state 1 with equal probability across an initial accessible volume $\Gamma_{\text{sys}}(t_0)$. Driving both initial trajectories into the

single reference state 0 at time t_1 ($\{0,1\} \mapsto 0$) restores a standardised blank register for subsequent computation, halving the switch's accessible phase-space volume to $\Gamma_{\text{sys}}(t_1)$ and reducing its physical entropy by one bit:

$$\Gamma_{\text{sys}}(t_0) = 2\Gamma_0, \tag{1.8}$$

$$\Gamma_{\text{sys}}(t_1) = \Gamma_0, \tag{1.9}$$

$$\Delta S_{\text{sys}} = k_{\text{B}} \ln\left(\frac{\Gamma_{\text{sys}}(t_1)}{\Gamma_{\text{sys}}(t_0)}\right) = -k_{\text{B}} \ln 2. \tag{1.10}$$

The inevitability of heat dissipation during this two-to-one temporal compression follows directly from the incompressibility of microscopic phase space. Under Hamiltonian dynamics, microscopic time evolution is strictly bijective, so trajectories in the joint phase space of the switch and its thermal bath can never collide or merge. By Liouville's theorem, the total joint phase-space volume Γ_{total} of the combined switch and bath is conserved across time, while projecting the evolved joint state onto its separate system and bath marginals at t_1 obeys multiplicative Cartesian bounding (the phase-space counterpart of entropy subadditivity):

$$\Gamma_{\text{sys}}(t_1)\,\Gamma_{\text{bath}}(t_1) \geq \Gamma_{\text{total}}(t_1) = \Gamma_{\text{total}}(t_0) = \Gamma_{\text{sys}}(t_0)\,\Gamma_{\text{bath}}(t_0), \tag{1.11}$$

where equality at t_0 reflects an initially uncorrelated switch and bath, and the inequality at t_1 accounts for system–bath correlations generated during reset. Substituting the two-to-one system compression (1.8)–(1.9) into the Liouville bound (1.11) forces the accessible microstate multiplicity of the thermal bath to at least double. For a thermal reservoir at temperature T_{th}, this forced expansion of accessible environmental microstates increases the bath entropy and mandates a minimum heat dissipation into the surroundings:

$$\Gamma_{\text{bath}}(t_1) \geq 2\,\Gamma_{\text{bath}}(t_0), \tag{1.12}$$

$$\Delta S_{\text{bath}} = k_{\text{B}} \ln\left(\frac{\Gamma_{\text{bath}}(t_1)}{\Gamma_{\text{bath}}(t_0)}\right) \geq k_{\text{B}} \ln 2, \tag{1.13}$$

$$Q_{\text{reset}} = T_{\text{th}} \Delta S_{\text{bath}} \geq k_{\text{B}} T_{\text{th}} \ln 2. \tag{1.14}$$

Landauer's principle is therefore not an abstract informational postulate, but the direct mechanical consequence of Liouville phase-space conservation applied to a many-to-one mapping along the time axis.

This phase-space compression cleanly closes the thermodynamic balance of the Szilard engine (Section 1.2.1) [145]. The work W extracted by the demon during isothermal expansion was obtained not by creating free energy from nothing, but by consuming one bit of distinguishability in its memory switch $M \in \{L, R\}$. Operating continuously requires resetting that switch to its reference blank state (the crimson arrow in Figure 1.1), executing a two-to-one temporal compression that requires work input W_{reset} and expels an equal quantity of heat Q_{reset} into the bath. Over the closed isothermal cycle with zero net internal energy change, the net work extracted satisfies:

$$W_{\text{reset}} = Q_{\text{reset}} \geq k_{\text{B}} T_{\text{th}} \ln 2, \tag{1.15}$$

$$W_{\text{net}} = W - W_{\text{reset}} = W - Q_{\text{reset}} \leq 0, \tag{1.16}$$

in strict accordance with the Kelvin–Planck statement of the Second Law. Precision experiments across single-electron switches, micromechanical cantilevers, and optical traps—including asymmetric double-well potentials—have confirmed this bound with sub-$k_B T_{th}$ fidelity [17, 39, 65, 125].

While Landauer's principle defines the thermodynamic boundary between reversible and irreversible operations, it leaves a foundational question open. Landauer formalised a dynamic many-to-one mapping across time ($\{0, 1\} \mapsto 0$), accounting for the heat dissipated when merging states. In doing so, however, he took the existence of the discrete switch states 0 and 1 as a given, postulating a pre-existing macroscopic coordinate already partitioned into metastable basins separated by an energy barrier $\Delta U \gg k_B T_{th}$. In general, discrete states and potential barriers do not pre-exist in an abstract background, and must instead be formed by a structural coarse-graining that bundles underlying degrees of freedom into stable equivalence classes. A complete physical theory must account not only for the dissipative cost of erasing distinctions across time, but also for the structural capacity required to form and isolate those distinctions across levels of coarse-graining.

1.3 INFORMATION EMERGES FROM COARSE-GRAINING

The classical triad of Szilard, Brillouin, and Landauer established that information cannot be separated from physics. Yet these foundational models analysed idealised examples while taking the existence of macroscopic information states as an external given. In practice, physical science models distinct phenomena through different coarse-grained observables—tracking voltages across semiconductor junctions, chemical potentials and ionic fluxes across biological membranes, or electromagnetic modes in optical cavities. Conversely, computer science treats information as a substrate-independent Platonic ideal. Neither approach provides a unified physical accounting. Logical abstractions cannot quantify the material capacity required to stabilise a state against noise, while disparate domain observables obscure the common physical quantities governing information across substrates.

To bridge this divide, an accountable theory must formalise the physical coarse-graining that produces collective behaviour from an underlying relational structure. An embedded system, constrained by finite coupling capacity, cannot resolve every elementary coupling directly, and instead projects an underlying relational graph onto a tractable set of coarse-grained equivalence classes.

This monograph introduces the framework of *Conservation-Congruent Encoding* (CCE) to formalise this projection. Rather than imposing continuous coordinates or symbolic alphabets from the outside, CCE grounds information directly in the relational connectivity of the substrate itself.

1.3.1 *The Relational Graph and the Epistemic Partition*

Prior to specifying any level of coarse-graining, a physical substrate can be formalised as an unweighted relational graph,

$$G = (V, E), \tag{1.17}$$

on $N_V := |V|$ vertices, represented by a symmetric binary adjacency matrix $\mathbf{A} \in \{0,1\}^{N_V \times N_V}$ with zero diagonal entries ($A_{ii} = 0$). Rather than attributing specific physical mechanisms, geometric coordinates, or force laws to the edges at this introductory stage, an edge $\{i, j\} \in E$ is treated strictly as an elementary relational coupling between underlying degrees of freedom. Crucially, this description is coordinate-free and relational, presupposing no continuous spatial background, no embedding manifold, and no privileged external clock. Space and field configurations are not pre-existing containers into which matter is placed, but must emerge from the relational connectivity of the graph itself.

This relational formulation directly confronts the physical reality of observation. An embedded system—whether a laboratory measuring apparatus, a biological organism, or an integrated microprocessor—possesses strictly finite physical interaction capacity (Figure 1.3). Occupying a finite induced subgraph $S \subset V$ of $N := |S|$ vertices ($N \ll N_V$) coupled to its ambient environment $\bar{S} := V \setminus S$ of $N_{\bar{S}} := |\bar{S}|$ vertices across the boundary cut ∂S, the system cannot individually address or resolve every vertex of V:

$$N_V = N + N_{\bar{S}}, \tag{1.18}$$

$$\partial S := \big\{\{i, j\} \in E : i \in S,\, j \in \bar{S}\big\}. \tag{1.19}$$

Observation is therefore fundamentally an act of physical coarse-graining. Partitioning S into $M \ll N$ non-empty, disjoint coarse-grained blocks $\{S_\alpha\}_{\alpha=1}^{M}$ assigns each internal vertex $i \in S$ to a unique block via a row-normalised binary matrix $\mathbf{\Pi}_S \in \{0,1\}^{N \times M}$ (written $\mathbf{\Pi} \equiv \mathbf{\Pi}_S$ when restricted to S), which pairs with an analogous environmental partition $\mathbf{\Pi}_{\bar{S}} \in \{0,1\}^{N_{\bar{S}} \times M_{\bar{S}}}$ across $V = (S, \bar{S})$ to form the block-diagonal epistemic assignment matrix $\mathbf{\Pi} \in \{0,1\}^{N_V \times (M + M_{\bar{S}})}$:

$$\sum_{\alpha=1}^{M} (\Pi_S)_{i\alpha} = 1, \tag{1.20}$$

$$\mathbf{\Pi} := \begin{pmatrix} \mathbf{\Pi}_S & \mathbf{o} \\ \mathbf{o} & \mathbf{\Pi}_{\bar{S}} \end{pmatrix}. \tag{1.21}$$

Here $(\Pi_S)_{i\alpha} = 1$ indicates that internal vertex $i \in S$ belongs to block S_α (and 0 otherwise). Row-sum normalisation in (1.20) (mirrored on $\bar{S}$ by $\mathbf{\Pi}_{\bar{S}}$) assigns every vertex to a unique block, while the off-diagonal zero blocks in (1.21) ensure that no coarse-grained block mixes system and environmental vertices across ∂S (reducing directly to $\mathbf{\Pi} = \mathbf{\Pi}_S$ when $S = V$).

Ordering $\mathbf{A}$ across $V = (S, \bar{S})$ into its $N \times N$ internal submatrix $\mathbf{A}_{SS}$, $N_{\bar{S}} \times N_{\bar{S}}$ environmental submatrix $\mathbf{A}_{\bar{S}\bar{S}}$, and $N_{\bar{S}} \times N$ boundary submatrix $\mathbf{A}_{\bar{S}S}$ (with

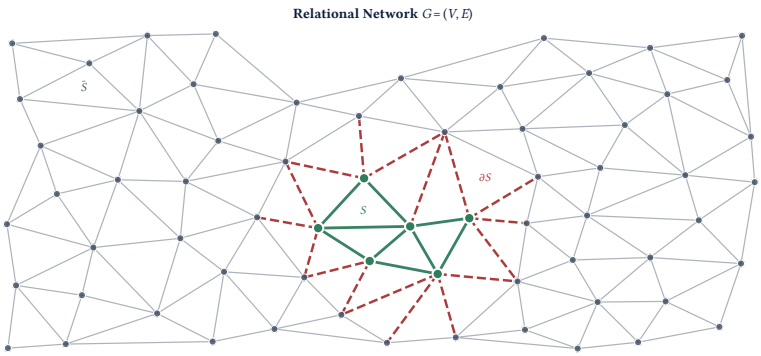


FIGURE 1.3: The embedded observer as an induced subgraph in the relational graph $G = (V, E)$. The observer is not a detached, external spectator, but an *embedded physical system*, occupying a finite induced subgraph $S \subset V$ (teal nodes and internal edges) with bounded physical capacity ($|S| \ll |V|$) within the ambient environment $\bar{S} = V \setminus S$ (grey nodes and edges). Physical interaction between the observer and its environment is strictly confined to the boundary cut set $\partial S := \{\{i, j\} \in E : i \in S, j \in \bar{S}\}$ (crimson dashed edges), whose finite interaction capacity establishes an unavoidable physical bottleneck.

transpose $\mathbf{A}_{S\bar{S}}$), viewing the substrate through $\mathbf{\Pi}$ contracts the unweighted adjacency into a coarse-grained weighted network—the *capacity graph* $G_{\mathbf{K}}$—governed by the partitioned *capacity matrix* $\mathbf{K}$ (in links), its $M \times M$ subsystem block $\mathbf{K}_S$, and its $M_{\bar{S}} \times M$ external boundary block $\mathbf{K}_{\partial}^{(\mathrm{ext})}$:

$$\mathbf{K} := \mathbf{\Pi}^{\mathsf{T}} \mathbf{A} \mathbf{\Pi} = \begin{pmatrix} \mathbf{K}_S & (\mathbf{K}_{\partial}^{(\mathrm{ext})})^{\mathsf{T}} \\ \mathbf{K}_{\partial}^{(\mathrm{ext})} & \mathbf{K}_{\bar{S}} \end{pmatrix}, \tag{1.22}$$

$$\mathbf{K}_S := \mathbf{\Pi}_S^{\mathsf{T}} \mathbf{A}_{SS} \mathbf{\Pi}_S, \tag{1.23}$$

$$\mathbf{K}_{\partial}^{(\mathrm{ext})} := \mathbf{\Pi}_{\bar{S}}^{\mathsf{T}} \mathbf{A}_{\bar{S}S} \mathbf{\Pi}_S. \tag{1.24}$$

With $\mathbf{K}_{\bar{S}}$ contracting $\mathbf{A}_{\bar{S}\bar{S}}$ analogously on $\bar{S}$, each entry of the internal block $\mathbf{K}_S$ evaluates to the explicit double sum:

$$(K_S)_{\alpha\beta} \equiv K_{\alpha\beta} = \sum_{i \in S} \sum_{j \in S} (\Pi_S)_{i\alpha} A_{ij} (\Pi_S)_{j\beta}. \tag{1.25}$$

Because $(\Pi_S)_{i\alpha}$ selects whether vertex $i \in S$ belongs to block S_α, this matrix congruence performs an exact census of relational links. Whenever the assignment $\mathbf{\Pi}$ is *admissible*—aligning with topological bottlenecks of the graph so that each diagonal entry $K_{\alpha\alpha}$ encapsulates an internally connected subgraph whose internal equilibration outpaces boundary escape (characterised by a spectral persistence ratio $\Xi(S_\alpha) \gg 1$, defined in Section 2.3)—each diagonal block $K_{\alpha\alpha}$ constitutes a *Conservation-Congruent Encoding* (CCE), functioning as a metastable coarse-grained basin coupled to peer CCEs across off-diagonal boundary couplings $K_{\alpha\beta}$ ($\alpha \neq \beta$).

The capacity matrix $\mathbf{K}$ provides the algebraic bridge connecting discrete relational connectivity to continuous effective physics. Rather than acting as

a heuristic convenience, $\mathbf{K}$ systematically generates effective and spacetime geometry (Chapter 2 and Chapter 6), non-equilibrium dissipative dynamics (Chapter 3), and substrate-neutral efficiency bounds across physical systems (Chapter 7).

1.3.2 *Internal Memory and Boundary Dissipation*

Information is not a disembodied primitive in nature, but is brought into physical existence by the non-injective coarse-graining $\mathbf{\Pi}$ (1.21) that projects the elementary degrees of freedom of an embedded system $S \subset V$ and its ambient environment $\bar{S} = V \setminus S$ into coarse-grained equivalence classes. As derived formally in Section 2.2, the block contraction (1.22) decomposes the relational capacity incident to S into two orthogonal sectors, namely the diagonal intra-basin memory matrix $\mathbf{K}_\Omega$ (counting internal links within each coarse-grained block S_α) and the active boundary cut sector $\mathbf{K}_\partial$, comprising the hollow off-diagonal transition matrix $\mathbf{K}_\partial^{(\mathrm{int})}$ between internal blocks alongside the external cut matrix $\mathbf{K}_\partial^{(\mathrm{ext})}$ spanning ∂S:

$$\mathbf{K}_\Omega := \mathrm{diag}(K_{11}, \dots, K_{MM}), \tag{1.26}$$

$$\mathbf{K}_\partial^{(\mathrm{int})} := \mathbf{K}_S - \mathbf{K}_\Omega. \tag{1.27}$$

Rather than an arbitrary algebraic split, this decomposition reflects the physical division between pooling fine-grained states within coarse-grained registers and coupling across transition and environmental boundaries. Within $\mathbf{K}_S$, each diagonal entry $K_{\alpha\alpha}$ (in links) counts the twice-traversed internal edges $E(S_\alpha)$ induced within coarse-grained basin S_α, while each off-diagonal entry $K_{\alpha\beta}$ ($\alpha \neq \beta$, in links) counts the inter-basin cut edges $E(S_\alpha, S_\beta)$. Complementarily, each entry of the external boundary block $\mathbf{K}_\partial^{(\mathrm{ext})}$ (in links) counts the boundary edges $E(\bar{S}_\mu, S_\alpha)$ spanning the boundary cut ∂S between environmental block $\bar{S}_\mu$ and system block S_α (Figure 1.3):

$$K_{\alpha\alpha} = (\mathbf{K}_\Omega)_{\alpha\alpha} = 2|E(S_\alpha)|, \tag{1.28}$$

$$K_{\alpha\beta} = \big(\mathbf{K}_\partial^{(\mathrm{int})}\big)_{\alpha\beta} = |E(S_\alpha, S_\beta)|, \tag{1.29}$$

$$\big(\mathbf{K}_\partial^{(\mathrm{ext})}\big)_{\mu\alpha} = |E(\bar{S}_\mu, S_\alpha)|. \tag{1.30}$$

Because the block-diagonal assignment $\mathbf{\Pi}$ assigns every internal and environmental vertex to a unique block without mixing across ∂S, repartitioning conserves both the internal edge budget $|E(S)|$ and the external boundary cut budget $|\partial S|$:

$$|E(S)| = \frac{1}{2}\sum_{\alpha=1}^{M} K_{\alpha\alpha} + \sum_{1\le\alpha<\beta\le M} K_{\alpha\beta}, \tag{1.31}$$

$$|\partial S| = \sum_{\mu=1}^{M_{\bar{S}}}\sum_{\alpha=1}^{M}\big(\mathbf{K}_\partial^{(\mathrm{ext})}\big)_{\mu\alpha}, \tag{1.32}$$

shifting fixed relational capacity between intra-basin memory ($\mathbf{K}_\Omega$) and transition cuts without creating or destroying physical relations. Normalising link counts by the unit reference quantum $\mathcal{Q}_0 = 1$ link and applying the natural logarithm converts raw relational capacity in links into dimensionless informational measures in nats. For each connected basin ($K_{\alpha\alpha} \geq 2$), taking the natural logarithm of its normalised diagonal capacity defines its *coarse-graining depth* $I_{\alpha\alpha}$ (in nats), and summing across the M operational blocks defines the *preserved structural capacity* I_{rev} (in nats, see Section 2.3):

$$I_{\alpha\alpha} := \ln K_{\alpha\alpha}, \tag{1.33}$$

$$I_{\text{rev}} := \sum_{\alpha=1}^{M} I_{\alpha\alpha} = \sum_{\alpha=1}^{M} \ln K_{\alpha\alpha}. \tag{1.34}$$

Equation (1.34) quantifies the static intra-basin link capacity bundled inside the M coarse-grained registers by $\mathbf{\Pi}_S$, which remains non-zero even in an undriven passive equilibrium well requiring zero continuous maintenance (in contrast to the active non-equilibrium displacement $I_{\text{rev},\Omega}$ introduced in Section 1.3.3).

Because G carries no background clock, sequential ordering, duration, and irreversible dissipation emerge first on the discrete capacity network before any continuum limit is taken. Along the slowest non-trivial spectral mode $\boldsymbol{\phi}_{\text{time}}$, unordered coarse-grained blocks foliate into sequential discrete slices S_τ ($\tau \in \{1, \dots, N_\tau\}$), while internal memory capacity within $\mathbf{K}_\Omega$ generates each slice's intrinsic *observer proper-time increment* $\Delta\tau_{\text{nat}}(\tau)$ (in nats), summing across slices to an intrinsic proper-time horizon $\tau_{\text{nat},T}$ and normalising against a stationary *reference sub-block* $\bar{S}_{\text{ref}} \subset \bar{S}$ inside $\mathbf{K}$ to fix a shared reference horizon T when comparing distinct systems (Section 2.5.1). Across sequential slices, internal links $\mathbf{K}_\Omega$ support lossless state circulation, whereas unresolved transitions and unaligned perturbations across the two cut sectors relax irreversibly. Relaxation across internal cuts $\mathbf{K}_\partial^{(\text{int})}$ incurs per-slice internal dissipation $\Delta I_{\text{irr},\Omega}(\tau) \geq 0$ (in nats, summing to $I_{\text{irr},\Omega}$), while unresolved distinctions expelled across external boundary cuts $\mathbf{K}_\partial^{(\text{ext})}$ into $\bar{S}$ incur per-slice boundary dissipation $\Delta I_{\text{irr},\partial}(\tau) \geq 0$ (in nats), summing across slices to the dimensionless *irreversible boundary dissipation* $I_{\text{irr},\partial}$ and decomposing total dissipation I_{irr} additively (Section 3.2.2):

$$I_{\text{irr},\partial} := \sum_{\tau=1}^{N_\tau} \Delta I_{\text{irr},\partial}(\tau) \geq 0, \tag{1.35}$$

$$I_{\text{irr}} = I_{\text{irr},\Omega} + I_{\text{irr},\partial}. \tag{1.36}$$

In the large-capacity, fine-slice continuum limit ($N \gg 1$, $K_{\alpha\alpha} \gg 1$, $N_\tau \gg 1$), projecting the M discrete basins onto their d_s slowest collective modes via a spectral coordinate map $\mathbf{\Phi}$ completes a two-stage coarse-graining (denoted collectively by Φ) onto a spectral coordinate chart $\mathscr{M}_{\text{spec}} \cong \mathbb{R}^{d_s}$ (Section 2.5):

$$\mathbb{R}^N \xrightarrow{\mathbf{\Pi}_S} \mathbb{R}^M \xrightarrow{\mathbf{\Phi}} \mathscr{M}_{\text{spec}} \cong \mathbb{R}^{d_s}. \tag{1.37}$$

Lifting the spatial coordinates of $\mathscr{M}_{\text{spec}}$ together with conjugate momenta and coarse-grained logarithmic capacity S onto the extended state manifold $\mathscr{Z}$ along the emergent continuous time parameter $t \in [0, T]$ (metered against a stationary reference sub-block $\bar{S}_{\text{ref}}$, and expressed in seconds when $\bar{S}_{\text{ref}}$ serves as a physical reference oscillator), $\mathbf{K}_\Omega$ generates conservative Hamiltonian transport while the internal and external cut sectors map onto an additive friction cometric $\mathbb{M}$ (Section 2.5 and Section 3.2.1):

$$\dot{Z} = \mathbb{J}\nabla H + \mathbb{M}\nabla S, \tag{1.38}$$

$$\mathbb{J}\nabla S = \mathbf{o}, \tag{1.39}$$

$$\mathbb{M}\nabla H = \mathbf{o}, \tag{1.40}$$

where H is the conserved dynamical invariant (total system energy in physical systems), S is the coarse-grained logarithmic capacity (in nats), $\mathbb{J}$ is the antisymmetric Poisson operator, and $\mathbb{M}$ is the symmetric positive semidefinite friction cometric separating internal and boundary relaxation ($\mathbb{M}_\Omega$ and $\mathbb{M}_\partial$), with $\dot{Z}$ denoting differentiation along emergent time t (Section 2.5.2). Conservative mechanics and irreversible thermodynamics are thus not disjoint physical regimes, but the continuum expressions of the internal and boundary sectors of a single underlying capacity network.

1.3.3 *Comparing Physical Substrates in Common Units*

Grounding internal memory and boundary dissipation in graph-theoretic coarse-graining explains why physical information accounting is substrate-independent. Semiconductor gates, biological membranes, and optical traps do not differ in the algebraic structure of information, but in the physical observables (voltages, ionic concentrations, or particle displacements on $\mathscr{Z}$) and the coarse-graining $\mathbf{\Pi}$ that partitions underlying configurations into operational states.

In experimental practice, an observer does not count individual links in G directly, but infers capacity ratios and dissipation rates from measurable barrier heights, escape rates, and heat fluxes. The dimensional conversion factor between energetic measurables (in joules) and dimensionless informational quantities (in nats) is the substrate's characteristic fluctuation scale θ (in $\mathrm{J\,nat^{-1}}$), given by thermal energy per nat $k_{\mathrm{B}}T_{\text{th}}$ in thermal reservoirs (approximately $4.1 \times 10^{-21}\,\mathrm{J\,nat^{-1}}$ at room temperature $T_{\text{th}} = 300\,\mathrm{K}$) or the zero-point fluctuation scale $h\nu/2$ per nat for a quantum mode of frequency ν (in $\mathrm{s^{-1}}$, with Planck's constant h as in (1.5)). Alongside the passive coarse-graining depth $I_{\alpha\alpha}$ (1.33), θ relates energetic measurables to barrier isolation, active internal structure, and boundary dissipation across substrates (derived in Chapters 2 and 3). First, for coupled basins ($K_{\alpha\beta} \geq 1$), the dimensionless *barrier isolation depth* $\Delta I_{\text{barrier},\alpha\to\beta}$ (in nats) measures the logarithmic ratio of intra-basin capacity to inter-basin cut capacity (Section 2.3.1 and Section 2.5.2):

$$\Delta I_{\text{barrier},\alpha\to\beta} := \ln\left(\frac{K_{\alpha\alpha}}{K_{\alpha\beta}}\right) \approx \frac{\Delta\Phi_{\alpha\to\beta}}{\theta}, \tag{1.41}$$

quantifying how strongly the pairwise energetic saddle barrier $\Delta\Phi_{\alpha\to\beta}$ (in joules, reserving unsubscripted $\Delta\Phi$ for the system-level barrier in Chapter 3) suppresses spontaneous transitions from basin α to basin β ($K_{\alpha\beta} \ll K_{\alpha\alpha}$). Second, holding an internal state out of equilibrium at an energetic displacement $\Delta U_{\text{neq}} \geq 0$ (in joules) above its passive relaxed baseline stores active *preserved internal structure* $I_{\text{rev},\Omega}$ (in nats), while multiplying boundary dissipation $I_{\text{irr},\partial}$ (1.35) by θ calibrates the energy Q (in joules) dissipated across ∂S (Section 3.2.2):

$$I_{\text{rev},\Omega} := \frac{\Delta U_{\text{neq}}}{\theta}, \tag{1.42}$$

$$Q = \theta I_{\text{irr},\partial}. \tag{1.43}$$

Unlike the static topological capacity I_{rev} (1.34), which counts passive intra-basin links logarithmically regardless of driving, $I_{\text{rev},\Omega}$ vanishes at equilibrium ($\Delta U_{\text{neq}} = 0$) and incurs ongoing internal dissipation ($I_{\text{irr},\Omega} > 0$) in (1.36) when sustained against spontaneous relaxation. Conversely, in an isothermal bath at $\theta = k_{\text{B}}T_{\text{th}}$, a binary reset expelling $I_{\text{irr},\partial} \geq \ln 2$ across ∂S recovers Landauer's heat bound (1.14) directly from (1.43).

Expressed in units of θ, disparate physical realisations become directly comparable without domain-specific empirical conventions. A passive equilibrium well retains static basin multiplicity ($I_{\text{rev}} > 0$) with zero active displacement ($I_{\text{rev},\Omega} = 0$) or maintenance dissipation ($I_{\text{irr},\Omega} = 0$) and approaches the quasi-static Landauer limit at slow switching rates. An externally clocked semiconductor gate trades orders of magnitude of excess boundary dissipation ($I_{\text{irr},\partial} \gg \ln 2$) for deep barrier isolation and rapid relaxation, whereas an excitable biological membrane operates closer to the thermal margin while expending continuous metabolic work to sustain non-equilibrium internal structure ($I_{\text{rev},\Omega} > 0$). Yet accounting for how a substrate stores and switches distinctions only establishes the physical cost of information, not what a system accomplishes with it. Distinguishing passive persistence or externally driven switching from autonomous agency requires measuring how an open system deploys that capacity to sustain its own stability.

1.4 MEASURING INTELLIGENCE AND CONSCIOUSNESS

Classical communication theory restricted its scope to how information is transferred across a channel, leaving aside what that information accomplishes once received. Moving from transmission to how information is used within a physical system requires evaluating how an embedded system deploys information to maintain its stability in an uncertain environment. Measuring intelligence and consciousness relates the physical stability a system achieves to the internal structure and boundary dissipation required to sustain it.

Unlike a passive object that persists solely through a static potential barrier, an intelligent physical system operates far from equilibrium, continually updating its internal state to counteract environmental perturbations and main-

tain its boundary. Because the underlying capacity balance splits orthogonally into boundary cuts and internal structure, evaluating how efficiently a system sustains its stability separates into two complementary measures: *intelligence* (χ), the ratio of preserved stability to boundary cost, and *consciousness* (κ), the ratio of preserved stability to internal model structure—evaluated statically in links/link and across emergent time in nats/nat.

Mirroring the progression from static network topology to emergent dynamics in Section 1.3, these two measures are evaluated in two complementary formalisms across Chapter 2 and Chapter 3: *static structural capacity* on a single slice of the discrete graph, and *through-time operational efficiency* across an emergent sequence of slices and its continuum limit. On a single slice perpendicular to $\boldsymbol{\phi}_{\text{time}}$, the intra-basin memory matrix $\mathbf{K}_\Omega$, internal transition cut matrix $\mathbf{K}_\partial^{(\text{int})}$, and external boundary cut matrix $\mathbf{K}_\partial^{(\text{ext})}$ in (1.22) and (1.27) occupy disjoint matrix coordinates. Evaluating their Euclidean Frobenius norms defines the *internal memory load* $\mathcal{Q}_\Omega$ and *boundary cut load* $\mathcal{Q}_\partial$ (both in links):

$$\|\mathbf{X}\|_F := \sqrt{\text{Tr}(\mathbf{X}^\top \mathbf{X})}, \tag{1.44}$$

$$\mathcal{Q}_\Omega := \|\mathbf{K}_\Omega\|_F, \tag{1.45}$$

$$\mathcal{Q}_\partial := \sqrt{\|\mathbf{K}_\partial^{(\text{int})}\|_F^2 + \|\mathbf{K}_\partial^{(\text{ext})}\|_F^2}. \tag{1.46}$$

Meanwhile, the embedded subsystem S possesses a partition-invariant *total relational capacity* $\mathcal{Q}_{\text{total}}$ (in links) counting all relational link endpoints incident to S across its interior $E(S)$ and boundary cut ∂S. Combining $\mathcal{Q}_\Omega$ and $\mathcal{Q}_\partial$ in quadrature fixes the *allocated structural capacity* $\mathcal{Q}_{\text{alloc}}$ and the remaining uncommitted *free capacity* $\mathcal{Q}_{\text{free}}$ (both in links):

$$\mathcal{Q}_{\text{total}} := 2|E(S)| + |\partial S|, \tag{1.47}$$

$$\mathcal{Q}_{\text{alloc}} := \sqrt{\mathcal{Q}_\Omega^2 + \mathcal{Q}_\partial^2}, \tag{1.48}$$

$$\mathcal{Q}_{\text{free}} := \mathcal{Q}_{\text{total}} - \mathcal{Q}_{\text{alloc}} \geq 0. \tag{1.49}$$

For open or multi-basin partitions with $\mathcal{Q}_\partial > 0$ and $\mathcal{Q}_\Omega > 0$, dividing uncommitted free capacity $\mathcal{Q}_{\text{free}}$ by $\mathcal{Q}_\partial$ and $\mathcal{Q}_\Omega$ defines the dimensionless *structural intelligence* χ_{struct} and *structural consciousness* κ_{struct} (both in links/link) and their coupling identity (Section 2.4), measuring static architectural headroom on a single slice:

$$\chi_{\text{struct}} := \frac{\mathcal{Q}_{\text{free}}}{\mathcal{Q}_\partial}, \tag{1.50}$$

$$\kappa_{\text{struct}} := \frac{\mathcal{Q}_{\text{free}}}{\mathcal{Q}_\Omega}, \tag{1.51}$$

$$\chi_{\text{struct}} = \kappa_{\text{struct}} \frac{\mathcal{Q}_\Omega}{\mathcal{Q}_\partial}. \tag{1.52}$$

Evaluating how a system deploys that headroom across emergent time tracks an ordered sequence of N_τ spectral slices $\tau \in \{1, \ldots, N_\tau\}$ carrying intrinsic

slice proper-time increments $\Delta\tau_{\mathrm{nat}}(\tau)$ (in nats), intrinsic proper-time horizon $\tau_{\mathrm{nat},T}$ (in nats), and dimensionless normalised proper-time weights w_τ (Section 2.5.1):

$$\tau_{\mathrm{nat},T} := \sum_{\tau=1}^{N_\tau} \Delta\tau_{\mathrm{nat}}(\tau), \tag{1.53}$$

$$w_\tau := \frac{\Delta\tau_{\mathrm{nat}}(\tau)}{\tau_{\mathrm{nat},T}}. \tag{1.54}$$

Notice that w_τ remains invariant when slice durations are normalised against an embedded reference sub-block $\bar{S}_{\mathrm{ref}}$ of constant slice proper time $\Delta\tau_{\mathrm{ref}}$ defining the shared reference horizon T. On each viable slice with $\mathcal{Q}_{\mathrm{free},\tau} > \mathcal{Q}_0$ above the elementary unit link $\mathcal{Q}_0 := 1\,\mathrm{link}$, uncommitted free capacity defines a logarithmic slice barrier in nats, and averaging across the N_τ slices by w_τ defines the dimensionless through-time *stability barrier* $\Delta I_{\mathrm{barrier},T}$ (in nats), calibrated in joules at substrate scale θ:

$$\Delta I_{\mathrm{barrier},T} := \sum_{\tau=1}^{N_\tau} w_\tau \ln\!\left(\frac{\mathcal{Q}_{\mathrm{free},\tau}}{\mathcal{Q}_0}\right), \tag{1.55}$$

$$\Delta\Phi_T := \theta\,\Delta I_{\mathrm{barrier},T}. \tag{1.56}$$

Whereas $\Delta I_{\mathrm{barrier},\alpha\to\beta}$ in (1.41) measures the local barrier between two specific basins, $\Delta I_{\mathrm{barrier},T}$ measures global uncommitted reserve across the open system as a whole, connected through multi-register capacity partitioning (Section 2.4.2 and Section 3.3.1) to open-boundary persistence (Section 8.1.1) while penalising transient bottlenecks where $\mathcal{Q}_{\mathrm{free},\tau}$ contracts towards $\mathcal{Q}_0$.

Across the same N_τ slices over evaluation horizon T (accumulating standardised observer proper time τ_T), cumulative boundary dissipation $I_{\mathrm{irr},\partial,T}$ evaluates (1.35) across the horizon, while proper-time-averaged preserved internal structure $I_{\mathrm{rev},\Omega,T}$ weights active slice structure $I_{\mathrm{rev},\Omega}(\tau)$ (in nats) by w_τ, passing in the fine-slice continuum limit to continuum horizon integrals (Section 3.2.2):

$$I_{\mathrm{irr},\partial,T} := \sum_{\tau=1}^{N_\tau} \Delta I_{\mathrm{irr},\partial}(\tau), \tag{1.57}$$

$$I_{\mathrm{rev},\Omega,T} := \sum_{\tau=1}^{N_\tau} w_\tau I_{\mathrm{rev},\Omega}(\tau). \tag{1.58}$$

Pairing $\Delta I_{\mathrm{barrier},T}$ against these two burdens ($I_{\mathrm{irr},\partial,T} > 0$, $I_{\mathrm{rev},\Omega,T} > 0$) defines the dimensionless through-time *intelligence* χ_T and *consciousness* κ_T (both in nats/nat) and their coupling identity (Section 3.3.1):

$$\chi_T := \frac{\Delta I_{\mathrm{barrier},T}}{I_{\mathrm{irr},\partial,T}}, \tag{1.59}$$

$$\kappa_T := \frac{\Delta I_{\mathrm{barrier},T}}{I_{\mathrm{rev},\Omega,T}}, \tag{1.60}$$

$$\chi_T = \kappa_T \frac{I_{\mathrm{rev},\Omega,T}}{I_{\mathrm{irr},\partial,T}}. \tag{1.61}$$

Multiplying χ_T and κ_T by the substrate scale θ expresses both efficiencies directly in SI units ($\theta\chi_T$ and $\theta\kappa_T$ in J nat^{-1}) without introducing a third formalism. Distinguishing single-slice structural capacity ($\chi_{\text{struct}}, \kappa_{\text{struct}}$) from multi-slice and continuum operational efficiency (χ_T, κ_T) separates passive topological capacity from active predictive boundary alignment (Section 3.3.2), preventing boundary stabilisation from being conflated with static graph size, raw state retention, or gross power dissipation. Crucially, these structural and dynamical bounds govern not only a physical system under study, but also any observer or model embedded within the same universe.

1.5 THE FALLACY OF THE PLATONIC OBSERVER

In developing the capacity balance and operational metrics of Section 1.3 and Section 1.4, it is tempting to picture an external analyst inspecting a target subsystem $S \subset V$ from outside the graph. Yet any scientific observer, measuring instrument, or modelling agent is itself an open physical subsystem governed by the same conservation laws and dissipation limits [105, 171]. Forgetting that the observer sits inside the physical substrate gives rise to what we term the *Platonic Observer Fallacy*—drawing on Plato's separation of invariant Forms from changeable material instances, dramatised by the allegory of the cave [134, Book VII, 514a–521b]. Its classic expression in physics and computation is Laplace's demon, an idealised intellect assumed to resolve every underlying coordinate, preserve infinite historical records, and compute future trajectories without occupying physical capacity, disturbing the observed system, or expending physical resources.

The fallacy begins when this mathematical convenience is treated as a physically realisable point of view. A continuous variable or universal time parameter t written in an equation appears instantly readable, indefinitely stable, and accessible at arbitrary precision without a physical clock. An embedded observer possesses none of these privileges. Resolving M distinct metastable pointer blocks (each with connected internal capacity $K_{\alpha\alpha} \geq 2$ links) and resetting an equiprobable M-outcome register in an M-to-1 temporal compression enforces linear scaling of preserved structural capacity (1.34) (in nats) alongside logarithmic reset dissipation (in nats):

$$I_{\text{rev}} = \sum_{\alpha=1}^{M} \ln K_{\alpha\alpha} \geq M \ln 2, \tag{1.62}$$

$$I_{\text{irr},\partial} \geq \ln M. \tag{1.63}$$

Passing to the continuum limit of infinitely fine state resolution ($M \to \infty$) drives both physical costs of the observer to diverge:

$$\lim_{M\to\infty} I_{\text{rev}} = \infty, \tag{1.64}$$

$$\lim_{M\to\infty} I_{\text{irr},\partial} = \infty. \tag{1.65}$$

Tracking continuous coordinates at infinite precision would therefore demand unbounded structural capacity and generate infinite reset dissipation.

Formal existence on paper is not physical reality in matter. An equation may remain mathematically well-defined where no embedded observer can store the records or sustain the computation required to test, distinguish, or retain its solutions.

Prediction and retrodiction along emergent time t expose the temporal asymmetry of this bound under the coarse-grained projection Φ (1.37). In the forward direction (*predictive dissipation*), projecting a physical state forward from an observation epoch t_0 tracks trajectories against accumulating perturbations and boundary dissipation until the surviving predictive information decays beneath the physical noise floor at a finite forward horizon $t_\Phi^+ > t_0$ (Section 6.3.2). In the backward direction (*retrodictive divergence*), reconstructing the past begins from records at t_0 that have already bundled many fine-grained histories into a single coarse-grained state through the non-injective partition $\mathbf{\Pi}$. Integrating backward ($t < t_0$) causes the branching multiplicity of compatible past histories to grow until it saturates the observer's preserved capacity at a backward horizon $t_\Phi^- < t_0$ (Section 6.3.1), beyond which reversing an equation cannot restore distinctions that the surviving physical record no longer contains. Together, predictive dissipation and retrodictive divergence confine physically supportable inference around t_0 to a bounded emergent interval—the observer's *Epistemic Bubble*:

$$\mathscr{D}_\Phi := [t_\Phi^-, t_\Phi^+], \tag{1.66}$$

$$-\infty < t_\Phi^- \leq t_0 \leq t_\Phi^+ < +\infty, \tag{1.67}$$

outside which forward signal attenuation ($t > t_\Phi^+$) or backward branching overload ($t < t_\Phi^-$) exceeds the physical capacity of the observer (Chapter 4 and Chapter 6).

Recognising embedded limits reshapes scientific modelling across scales. At the quantum level, finite observer capacity restricts what can be empirically certified about universal reversibility. As Chapter 4 shows (Section 4.1.1 and Theorem 4.1), a quantum or physical measurement exists operationally only when a coarse-grained projection stabilises a durable record in a finite physical substrate. Because an embedded detector has bounded memory (I_{rev}) and must eventually be reset at non-zero dissipative cost ($I_{\text{irr},\partial} > 0$), no internal observer can record the global degrees of freedom required to empirically certify exact reversibility across the universe as a whole.

Extended to cosmological horizons, the same idealisation turns the limits of equations into apparent limits of reality. Unrestricted extrapolation towards a Big Bang singularity or an infinite heat-death future tacitly assumes an external spectator with infinite informational bandwidth and zero noise. Chapter 6 (Section 6.3 and Section 6.3.2) instead identifies these limits as the operational boundaries of $\mathscr{D}_\Phi$, where incoming causal congruences saturate the observer's retrodictive capacity or outgoing signals dissolve beneath the noise floor.

Finally, within computation and artificial intelligence, the Platonic fallacy treats algorithms as disembodied Turing machines operating on cost-free symbols or infinite-precision real numbers (Chapter 7). Abstracting away

the substrate obscures that every logical transformation consumes uncommitted capacity ($\mathcal{Q}_{\text{free}}$), requires maintained internal structure ($I_{\text{rev},\Omega,T}$), and expels boundary dissipation ($I_{\text{irr},\partial,T}$). Returning to the challenge posed at the outset of this chapter, intelligence and alignment cannot be reduced to disembodied benchmark scores or syntactic rule-following, because they are physical stability properties of embedded systems governed by χ_T and κ_T within shared material constraints (Chapters 8–10). With this embedded foundation in place, we turn to the structure of the monograph.

1.6 HOW TO READ THIS BOOK

This monograph develops the theory across four cumulative parts, taking Conservation-Congruent Encoding (CCE) as its unifying construct so that every chapter accounts for which fine-grained distinctions are preserved or erased, which conserved quantities cross the system boundary, and how non-equilibrium flows secure operational stability against noise. In Part I (*The Foundations of Intelligence*), Chapter 2 derives the discrete capacity network, orthogonal capacity ledger, emergent spectral geometry and curvature, and continuous metriplectic flow from an unweighted relational graph. Chapter 3 then couples CCEs across open boundaries to formalise driven viability barriers, the operational metrics of intelligence (χ) and consciousness (κ), cut internalisation, and multi-system stability. Part II (*The Epistemic Lens of Intelligence*) applies these observational limits across levels of coarse-graining. Chapter 4 formalises how unresolved degrees of freedom map onto stable coarse-grained records and quantum measurements, Chapter 5 ascends from fundamental particles to macromolecular observables via topological graph Laplacians and environmental path integrals, and Chapter 6 projects these capacity bounds outward into emergent spacetime geometry and cosmological horizons.

Parts III and IV extend this physical foundation to synthetic, biological, and civilisational systems. In Part III (*Engineering Intelligence*), Chapter 7 and Chapter 8 investigate continuous dynamical computation beyond discrete Boolean logic, non-Euclidean hardware topologies, and the physical containment of artificial agency. In Part IV (*Human Intelligence*), Chapter 9 and Chapter 10 turn the framework towards biological cognition and civilisational coordination, analysing the physical self-models of conscious systems, the metering of intelligence as an economic utility, and the evolutionary constraints of long-lived agency, before the Epilogue reflects on the risks and promise of artificial intelligence for humanity's future. Readers focusing on foundational physics should proceed through Parts I and II in sequence, while those oriented towards hardware architecture and AI safety can move from Part I to Part III, and those interested in biological cognition, consciousness, and macroeconomic stability can proceed directly from Part I to Part IV. For reference across chapters, a unified Glossary of mathematical notation, abbreviations, and core terms precedes the Bibliography at the end of the book.

2

CONSERVATION-CONGRUENT ENCODING

This chapter formalises the Conservation-Congruent Encoding (CCE) framework, deriving coarse-grained physical observables directly from the partitioning of a discrete relational network. The framework enforces *conservation* because every relational coupling is partitioned without loss into internal state capacity, boundary interaction, or external environmental state, and it is *congruent* because its operator projection preserves the symmetry and algebraic structure of graph connectivity across levels of coarse-graining. Standard physics and computation theory routinely commit the *Platonic Observer Fallacy* by assuming continuous space, smooth phase spaces, and an external time parameter as background containers. For an embedded system possessing finite physical resources, however, such continuous containers are unphysical idealisations. Physical substrates are modelled here not as smooth continua, but as unweighted relational networks of discrete couplings between elementary degrees of freedom.

Because an embedded observer cannot resolve every individual coupling, it must group degrees of freedom into coarse-grained states represented by a capacity matrix $\mathbf{K}$. Under this coarse-graining, space, time, and dynamics cease to be background containers and instead emerge from the structure of the network. Effective distance between coarse-grained states reflects how easily perturbations travel across the boundary links connecting them. An arrow of time arises because each coarse-grained state pools many internal couplings behind a narrow boundary cut, so once a transition mixes across those internal couplings, the specific entry link can no longer be retraced. In the continuum limit, state transitions across these boundary bottlenecks recover standard continuous equations of motion, with transition barriers set directly by the ratio of internal to boundary couplings.

An assignment matrix $\mathbf{\Pi}$ can partition the graph into arbitrary candidate blocks, but only an *admissible* assignment yields a physical encoding. Under an admissible assignment, each block with diagonal capacity $K_{\alpha\alpha}$ in $\mathbf{K}$ forms a *Conservation-Congruent Encoding* (CCE): a connected subgraph with non-empty internal support (Axiom I: Topological Resolvability), internal connectivity that dominates its boundary cut across an operational window (Axiom II: Structural Persistence), and lossless coupling accounting under congruent projection (Axiom III: Conservation Congruence). Starting from the unweighted relational graph and its open boundary cut (Section 2.1), we construct the congruent operator compression (Section 2.2), formalise the CCE axioms and multiscale coarsening (Section 2.3), establish the Capacity Ledger and free capacity reserve (Section 2.4), and derive how the spectral decomposition and algebraic curvature of $\mathbf{K}$ generate emergent spacetime coordinates and continuous metriplectic dynamics (Section 2.5).

2.1 THE RELATIONAL SUBSTRATE

Standard statistical mechanics posits a continuous phase space, a smooth spatial manifold, and an external time parameter [47, 68]. Before continuous metrics or coarse-grained properties can be defined, however, under the present theory physical reality at the foundational graph level consists of an unweighted network of elementary couplings between discrete degrees of freedom.

2.1.1 *The Relational Graph*

We model the underlying substrate as a connected, finite, undirected, unweighted relational graph

$$G = (V, E), \tag{2.1}$$

where $V = \{1, 2, \dots, N_V\}$ ($N_V := |V|$) is the set of elementary degrees of freedom and E is the set of active binary couplings between distinct vertices. The network topology is represented by the symmetric binary adjacency matrix $\mathbf{A} \in \{0,1\}^{N_V \times N_V}$, whose entries equal 1 for coupled pairs $\{i, j\} \in E$ and 0 otherwise, with zero diagonal entries. Summing the couplings incident to each vertex defines the diagonal vertex degree matrix $\mathbf{D}$ and the combinatorial graph Laplacian $\mathbf{L} \in \mathbb{Z}^{N_V \times N_V}$:

$$d_i \equiv \deg_G(i) := \sum_{k \in V} A_{ik}, \tag{2.2}$$

$$\mathbf{D} := \operatorname{diag}(d_i)_{i=1}^{N_V}, \tag{2.3}$$

$$\mathbf{L} := \mathbf{D} - \mathbf{A}. \tag{2.4}$$

The degree operator $\mathbf{D}$ records the local relational volume at each vertex (writing $\deg_G(i)$ whenever a concrete numeric vertex index is evaluated alongside coarse-grained block degrees), while the Laplacian $\mathbf{L}$ measures relational differences across coupled neighbours.

While $G = (V, E)$ specifies the connectivity of the substrate, describing or probing states across the network requires assigning a real scalar value $x_i \in \mathbb{R}$ to each vertex $i \in V$. Each elementary degree of freedom $i \in V$ corresponds to an orthogonal standard basis vector $\mathbf{e}_i \in \mathbb{R}^{N_V}$ representing a unit weight localised at vertex i, so a general vector $\mathbf{x} = (x_1, \dots, x_{N_V})^{\mathsf{T}} \in \mathbb{R}^{N_V}$ defines a discrete scalar field across the vertices. Depending on how the graph is probed, $\mathbf{x}$ may represent a binary indicator vector $\mathbf{1}_A \in \{0,1\}^{N_V}$ marking whether each vertex belongs to a candidate subset $A \subset V$, or a continuous distribution of nodal amplitudes, occupation weights, or potentials across the graph. Acting with $\mathbf{L}$ on any such vertex state vector $\mathbf{x} \in \mathbb{R}^{N_V}$ compares each vertex value against those of its coupled neighbours:

$$(\mathbf{L}\mathbf{x})_i = d_i x_i - \sum_{j \in V} A_{ij} x_j = \sum_{j \,:\, \{i,j\} \in E} (x_i - x_j). \tag{2.5}$$

In (2.5), the i-th component of $\mathbf{Lx}$ sums the differences between x_i and its directly coupled neighbours, measuring the net outward flux leaving vertex i.

Contracting (2.5) with $\mathbf{x}^\mathsf{T}$ sums the squared difference $(x_i - x_j)^2$ over every active coupling $\{i, j\} \in E$, defining the discrete Dirichlet energy:

$$\mathbf{x}^\mathsf{T}\mathbf{L}\mathbf{x} = \frac{1}{2}\sum_{i,j\in V} A_{ij}(x_i - x_j)^2 = \sum_{\{i,j\}\in E} (x_i - x_j)^2 \geq 0. \tag{2.6}$$

Equation (2.6) forms the discrete combinatorial precursor to the continuum Dirichlet gradient norm. Physically, the Dirichlet energy measures the total relational tension of the state $\mathbf{x}$ across the network, as coupled vertices carrying equal values ($x_i = x_j$) are in local agreement and contribute zero whereas coupled vertices carrying distinct values ($x_i \neq x_j$) incur a positive mismatch penalty $(x_i - x_j)^2 > 0$.

Evaluating (2.5)–(2.6) on the global all-ones vector $\mathbf{1}_V \in \{0, 1\}^{N_V}$ and on the binary indicator vector $\mathbf{1}_A \in \{0, 1\}^{N_V}$ of any proper vertex subset $A \subset V$ yields two foundational identities:

$$\mathbf{L}\mathbf{1}_V = \mathbf{0}, \tag{2.7}$$

$$\mathbf{1}_A^\mathsf{T}\mathbf{L}\mathbf{1}_A = |\partial A|. \tag{2.8}$$

On a connected graph, the uniform vector $\mathbf{1}_V$ assigns the same unit value to every vertex so that all pairwise differences vanish, spanning the unique zero-eigenvalue kernel ($0 = \lambda_1 < \lambda_2$) and expressing exact global closure of the relational graph [57]. Conversely, on a proper subset indicator $\mathbf{1}_A$, all edges internal to A or external to A connect equal entries and vanish from the sum in (2.6), whereas every edge crossing between A and its complement $V \setminus A$ carries a unit difference $x_i - x_j = \pm 1$, so the Dirichlet energy counts the exact number of boundary cut edges $|\partial A|$.

2.1.2 *The Embedded Boundary Cut and Dirichlet Leakage*

A physical detector, circuit, or organism is an *embedded physical system*, a finite induced subgraph $G[S] = (S, E(S))$ on $N \equiv N_S := |S|$ vertices with $N_S \ll N_V$, coupled to the external environment $\bar{S} := V \setminus S$ of $N_{\bar{S}} := |\bar{S}|$ vertices. All interactions between the system S and the environment $\bar{S}$ must traverse the *boundary cut* ∂S:

$$N_V = N_S + N_{\bar{S}}, \tag{2.9}$$

$$\partial S := \big\{\{i, j\} \in E \,:\, i \in S,\, j \in \bar{S}\big\}. \tag{2.10}$$

Summing the adjacency entries across and within S counts the active boundary cut couplings $|\partial S|$ and the internal subgraph edges $|E(S)|$:

$$|\partial S| = \sum_{i\in S}\sum_{j\in\bar{S}} A_{ij}, \tag{2.11}$$

$$|E(S)| = \frac{1}{2}\sum_{i,j\in S} A_{ij}. \tag{2.12}$$

Throughout this work, whenever an embedded subsystem $S \subset V$ is the primary object of analysis, we write $N \equiv N_S$ (with M denoting its coarse-grained block count) for brevity.

Ordering the vertices as $V = (S, \bar{S})$ partitions the adjacency, degree, and Laplacian matrices into 2×2 block form:

$$\mathbf{A} = \begin{pmatrix} \mathbf{A}_{SS} & \mathbf{A}_{S\bar{S}} \\ \mathbf{A}_{\bar{S}S} & \mathbf{A}_{\bar{S}\bar{S}} \end{pmatrix}, \tag{2.13}$$

$$\mathbf{D} = \begin{pmatrix} \mathbf{D}_S & \mathbf{o} \\ \mathbf{o} & \mathbf{D}_{\bar{S}} \end{pmatrix}, \tag{2.14}$$

$$\mathbf{L} = \begin{pmatrix} \mathbf{L}_{SS} & \mathbf{L}_{S\bar{S}} \\ \mathbf{L}_{\bar{S}S} & \mathbf{L}_{\bar{S}\bar{S}} \end{pmatrix}. \tag{2.15}$$

For every vertex $i \in S$, its total degree d_i splits across the disjoint partition $V = S \sqcup \bar{S}$ into its internal degree $d_i^{(\mathrm{int})}$ (counting edges in $E(S)$) and its external boundary degree $d_i^{(\mathrm{ext})}$ (counting cut edges in ∂S):

$$d_i = \sum_{k \in V} A_{ik} = \underbrace{\sum_{j \in S} A_{ij}}_{d_i^{(\mathrm{int})}} + \underbrace{\sum_{j \in \bar{S}} A_{ij}}_{d_i^{(\mathrm{ext})}} = d_i^{(\mathrm{int})} + d_i^{(\mathrm{ext})}. \tag{2.16}$$

Collecting these vertex degrees along the diagonal decomposes $\mathbf{D}_S$ via the block row sums $\mathbf{A}_{SS}\mathbf{1}_S$ and $\mathbf{A}_{S\bar{S}}\mathbf{1}_{\bar{S}}$:

$$\mathbf{D}_S = \mathbf{D}_S^{(\mathrm{int})} + \mathbf{D}_S^{(\mathrm{ext})}, \tag{2.17}$$

$$\mathbf{D}_S^{(\mathrm{int})} := \mathrm{diag}(\mathbf{A}_{SS}\mathbf{1}_S), \tag{2.18}$$

$$\mathbf{D}_S^{(\mathrm{ext})} := \mathrm{diag}(\mathbf{A}_{S\bar{S}}\mathbf{1}_{\bar{S}}). \tag{2.19}$$

Substituting (2.17) into the upper-left block $\mathbf{L}_{SS} = \mathbf{D}_S - \mathbf{A}_{SS}$ separates the open Dirichlet Laplacian $\mathbf{L}_{SS}$ into the isolated internal (Neumann) Laplacian $\mathbf{L}_{SS}^{(\mathrm{int})}$ of the induced subgraph $G[S]$ plus the diagonal boundary degree potential $\mathbf{D}_S^{(\mathrm{ext})}$:

$$\mathbf{L}_{SS} = \mathbf{D}_S - \mathbf{A}_{SS} = \underbrace{\left(\mathbf{D}_S^{(\mathrm{int})} - \mathbf{A}_{SS}\right)}_{\mathbf{L}_{SS}^{(\mathrm{int})}} + \mathbf{D}_S^{(\mathrm{ext})} = \mathbf{L}_{SS}^{(\mathrm{int})} + \mathbf{D}_S^{(\mathrm{ext})}. \tag{2.20}$$

This degree split simultaneously partitions the system vertices S into the exposed boundary port set S_∂ and the insulated interior core S_Ω:

$$S = S_\partial \sqcup S_\Omega, \tag{2.21}$$

$$S_\partial := \left\{ i \in S \,:\, d_i^{(\mathrm{ext})} > 0 \right\}, \tag{2.22}$$

$$S_\Omega := \left\{ i \in S \,:\, d_i^{(\mathrm{ext})} = 0 \right\}. \tag{2.23}$$

On the insulated core S_Ω, the boundary potential $\mathbf{D}_S^{(\mathrm{ext})}$ vanishes identically and $\mathbf{L}_{SS}$ restricts to the interior sub-Laplacian $\mathbf{L}_{\Omega\Omega}$.

Because an open system couples to $\bar{S}$ across ∂S, the row sums of $\mathbf{L}_{SS}$ no longer vanish on the boundary ports S_∂. Evaluating the quadratic form of $\mathbf{L}_{SS}$ on any non-zero system vector $\mathbf{x}_S \in \mathbb{R}^N$ (corresponding to clamping $\bar{S}$ to zero in (2.6)) separates the internal edge strain across $E(S)$ from the boundary leakage penalty at S_∂:

$$\begin{aligned}\mathbf{x}_S^\top \mathbf{L}_{SS}\mathbf{x}_S &= \mathbf{x}_S^\top \mathbf{L}_{SS}^{(\mathrm{int})}\mathbf{x}_S + \mathbf{x}_S^\top \mathbf{D}_S^{(\mathrm{ext})}\mathbf{x}_S \\ &= \sum_{\{i,j\}\in E(S)} (x_i - x_j)^2 + \sum_{i\in S_\partial} d_i^{(\mathrm{ext})} x_i^2 > 0.\end{aligned} \tag{2.24}$$

Evaluating $\mathbf{L}_{SS}$ on the uniform system state $\mathbf{1}_S$ isolates the boundary port degrees and total cut size:

$$\mathbf{L}_{SS}\mathbf{1}_S = \mathbf{D}_S^{(\mathrm{ext})}\mathbf{1}_S, \tag{2.25}$$

$$\mathbf{1}_S^\top \mathbf{L}_{SS}\mathbf{1}_S = \sum_{i\in S_\partial} d_i^{(\mathrm{ext})} = |\partial S| > 0. \tag{2.26}$$

Whenever the induced subgraph $G[S]$ is connected and open ($|\partial S| > 0$), the two sums in (2.24) cannot vanish simultaneously for $\mathbf{x}_S \neq \mathbf{o}$, because the internal strain sum vanishes only on spatially uniform vectors $\mathbf{x}_S = c\mathbf{1}_S$ on which the boundary sum evaluates to $c^2|\partial S| > 0$ by (2.26). Consequently, $\mathbf{L}_{SS}$ is a strictly positive-definite *Dirichlet Laplacian* ($\mathbf{L}_{SS} > \mathbf{o}$).

Strict positive-definiteness of $\mathbf{L}_{SS}$ governs the competing timescales of internal equilibration and boundary escape. Evaluating the Rayleigh–Ritz quotient of $\mathbf{L}_{SS}$ on a single-vertex impulse $\mathbf{e}_i$ and on the uniform system vector $\mathbf{1}_S$ bounds the ground leakage eigenvalue $\lambda_1(\mathbf{L}_{SS})$:

$$\mathbf{e}_i^\top \mathbf{L}_{SS}\mathbf{e}_i = d_i, \tag{2.27}$$

$$0 < \lambda_1(\mathbf{L}_{SS}) \leq \frac{\mathbf{1}_S^\top \mathbf{L}_{SS}\mathbf{1}_S}{\mathbf{1}_S^\top \mathbf{1}_S} = \frac{|\partial S|}{|S|}. \tag{2.28}$$

Open coupling across ∂S lifts the isolated zero mode into $\lambda_1(\mathbf{L}_{SS}) > 0$, setting the rate at which unshielded vertex-level coherence leaks into $\bar{S}$. Whereas a perturbation localised at an individual vertex $i \in S$ scatters at the full vertex degree rate d_i, pooling amplitude uniformly across all $|S|$ vertices dilutes the ground leakage bound by the system volume $|S|$ in (2.28). Comparing the higher spectrum of $\mathbf{L}_{SS}$ against $\mathbf{L}_{SS}^{(\mathrm{int})}$ via Weyl's monotonicity theorem ($\mathbf{L}_{SS} \geq \mathbf{L}_{SS}^{(\mathrm{int})}$) bounds the diffusive mixing mode $\lambda_2(\mathbf{L}_{SS})$ from below and sets the required persistence separation:

$$\lambda_2(\mathbf{L}_{SS}) \geq \lambda_2\big(\mathbf{L}_{SS}^{(\mathrm{int})}\big) > 0, \tag{2.29}$$

$$\frac{\lambda_2(\mathbf{L}_{SS})}{\lambda_1(\mathbf{L}_{SS})} \gg 1. \tag{2.30}$$

For S to persist as a coherent entity rather than dissolving into $\bar{S}$, internal equilibration must outpace open leakage, requiring the spectral separation in (2.30).

Whereas $\mathbf{L}_{SS}$ describes open leakage when the environment $\bar{S}$ is clamped to zero, an unconstrained environment also feeds flux back across ∂S. Because every connected component of $\bar{S}$ couples across ∂S on the connected graph G, the environmental Dirichlet block $\mathbf{L}_{\bar{S}\bar{S}}$ is strictly positive-definite ($\mathbf{L}_{\bar{S}\bar{S}} > \mathbf{o}$), and any boundary configuration $\mathbf{x}_S \in \mathbb{R}^N$ induces a unique source-free harmonic relaxation profile $\mathbf{x}_{\bar{S}}$ on $\bar{S}$ in the partitioned Laplacian system (2.15):

$$\begin{pmatrix} \mathbf{L}_{SS} & \mathbf{L}_{S\bar{S}} \\ \mathbf{L}_{\bar{S}S} & \mathbf{L}_{\bar{S}\bar{S}} \end{pmatrix} \begin{pmatrix} \mathbf{x}_S \\ \mathbf{x}_{\bar{S}} \end{pmatrix} = \begin{pmatrix} \mathbf{L}_{\text{eff}}\mathbf{x}_S \\ \mathbf{o} \end{pmatrix}, \tag{2.31}$$

$$\mathbf{x}_{\bar{S}} = -\mathbf{L}_{\bar{S}\bar{S}}^{-1}\mathbf{L}_{\bar{S}S}\mathbf{x}_S. \tag{2.32}$$

Substituting (2.32) into the upper block row of (2.31) via the Schur complement defines the environmental self-energy operator $\mathbf{\Sigma}_{\text{env}}$ and the effective boundary Laplacian $\mathbf{L}_{\text{eff}}$ (the discrete Dirichlet-to-Neumann operator across ∂S, Figure 2.1):

$$\mathbf{\Sigma}_{\text{env}} := \mathbf{L}_{S\bar{S}}\mathbf{L}_{\bar{S}\bar{S}}^{-1}\mathbf{L}_{\bar{S}S}, \tag{2.33}$$

$$\mathbf{L}_{\text{eff}} := \mathbf{L}_{SS} - \mathbf{\Sigma}_{\text{env}} = \mathbf{L}_{SS}^{(\text{int})} + \mathbf{D}_S^{(\text{ext})} - \mathbf{\Sigma}_{\text{env}}. \tag{2.34}$$

Because the off-diagonal coupling block $\mathbf{L}_{S\bar{S}} = -\mathbf{A}_{S\bar{S}}$ is supported solely on the boundary ports S_∂, the symmetric positive semi-definite environmental self-energy (return-flux) operator $\mathbf{\Sigma}_{\text{env}} \geq \mathbf{o}$ vanishes on the insulated core S_Ω and acts exclusively on S_∂. Moreover, because global closure (2.7) implies $\mathbf{\Sigma}_{\text{env}}\mathbf{1}_S = \mathbf{D}_S^{(\text{ext})}\mathbf{1}_S$, subtracting $\mathbf{\Sigma}_{\text{env}}$ cancels the boundary degree potential on uniform states and restores the global zero mode ($\mathbf{L}_{\text{eff}}\mathbf{1}_S = \mathbf{o}$) at the cost of coupling boundary vertices in S_∂ non-locally through $\bar{S}$. Facing finite internal resources ($N_S \ll N_V$), narrow boundary bandwidth ($|\partial S| \ll N_{\bar{S}}$), and continuous Dirichlet leakage ($\lambda_1(\mathbf{L}_{SS}) > 0$), an embedded system cannot store durable records in vulnerable individual vertices. To persist and compute, it must partition its N vertices into $M \ll N$ collective blocks $\{S_\alpha\}_{\alpha=1}^M$ whose internal equilibration outpaces boundary leakage.

EXAMPLE 2.1 (Dirichlet Leakage and Schur Complement). To establish a single running example across the chapter, consider a nine-node relational graph $G = (V, E)$ ($N_V = 9$, $|E| = 12$) partitioned into an embedded six-node dumbbell subsystem $S = \{1, \ldots, 6\}$ ($N_S = 6$) and a three-node environmental triangle $\bar{S} = \{7, 8, 9\}$ ($N_{\bar{S}} = 3$, Figure 2.1(a)). The internal subgraph $G[S]$ consists of two triangles $\{1, 2, 3\}$ and $\{4, 5, 6\}$ joined by the bridge edge $\{3, 4\}$ ($|E(S)| = 7$), the environment $G[\bar{S}]$ is a triangle on $\{7, 8, 9\}$ ($|E(\bar{S})| = 3$), and S couples to $\bar{S}$ across $|\partial S| = 2$ boundary cut edges $\{1, 7\}$ and $\{6, 8\}$.

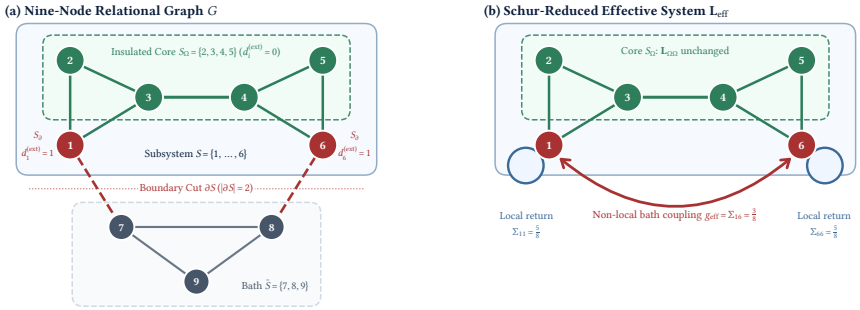


FIGURE 2.1: The nine-node running example and Dirichlet-to-Neumann Schur reduction (Example 2.1). *(a)* Relational graph $G = (V, E)$ ($N_V = 9$, $|E| = 12$) partitioned into the six-node dumbbell subsystem $S = \{1, \ldots, 6\}$ ($N_S = 6$, comprising two triangles $\{1,2,3\}$ and $\{4,5,6\}$ joined by bridge $\{3,4\}$) and the three-node environmental bath $\bar{S} = \{7,8,9\}$ ($N_{\bar{S}} = 3$). The diagonal boundary potential $\mathbf{D}_S^{(\mathrm{ext})} = \mathrm{diag}(1,0,0,0,0,1)$ separates S into the insulated interior core $S_\Omega = \{2,3,4,5\}$ ($d_i^{(\mathrm{ext})} = 0$, teal) and the exposed boundary ports $S_\partial = \{1,6\}$ ($d_i^{(\mathrm{ext})} = 1$, crimson) coupled across $|\partial S| = 2$ cut edges $\{1,7\}$ and $\{6,8\}$. *(b)* Schur-reduced effective system $\mathbf{L}_{\mathrm{eff}} = \mathbf{L}_{SS} - \mathbf{L}_{S\bar{S}}\mathbf{L}_{\bar{S}\bar{S}}^{-1}\mathbf{L}_{\bar{S}S}$ on S. Eliminating $\bar{S}$ leaves the core block $\mathbf{L}_{\Omega\Omega}$ unchanged while returning $5/8$ of leaked port flux locally ($\Sigma_{11} = 5/8$ and $\Sigma_{66} = 5/8$) and routing $3/8$ non-locally across the bath between ports 1 and 6 ($g_{\mathrm{eff}} = 3/8$), restoring exact conservation $\mathbf{L}_{\mathrm{eff}}\mathbf{1}_S = \mathbf{o}$.

Ordering the vertices of S from 1 to 6, the 6×6 internal adjacency matrix $\mathbf{A}_{SS}$, isolated internal (Neumann) Laplacian $\mathbf{L}_{SS}^{(\mathrm{int})}$, and diagonal boundary potential $\mathbf{D}_S^{(\mathrm{ext})}$ take the explicit form:

$$\mathbf{A}_{SS} = \left(\begin{array}{ccc|ccc} 0 & 1 & 1 & 0 & 0 & 0 \\ 1 & 0 & 1 & 0 & 0 & 0 \\ 1 & 1 & 0 & 1 & 0 & 0 \\ \hline 0 & 0 & 1 & 0 & 1 & 1 \\ 0 & 0 & 0 & 1 & 0 & 1 \\ 0 & 0 & 0 & 1 & 1 & 0 \end{array}\right), \tag{2.35}$$

$$\mathbf{L}_{SS}^{(\mathrm{int})} = \left(\begin{array}{ccc|ccc} 2 & -1 & -1 & 0 & 0 & 0 \\ -1 & 2 & -1 & 0 & 0 & 0 \\ -1 & -1 & 3 & -1 & 0 & 0 \\ \hline 0 & 0 & -1 & 3 & -1 & -1 \\ 0 & 0 & 0 & -1 & 2 & -1 \\ 0 & 0 & 0 & -1 & -1 & 2 \end{array}\right), \tag{2.36}$$

$$\mathbf{D}_S^{(\mathrm{ext})} = \mathrm{diag}(1,0,0,0,0,1). \tag{2.37}$$

The diagonal boundary potential $\mathbf{D}_S^{(\mathrm{ext})}$ partitions S into two exposed boundary ports $S_\partial = \{1,6\}$ and four insulated interior core vertices $S_\Omega = \{2,3,4,5\}$ ($d_i^{(\mathrm{ext})} = 0$). Adding $\mathbf{D}_S^{(\mathrm{ext})}$ to $\mathbf{L}_{SS}^{(\mathrm{int})}$ yields the open Dirichlet Laplacian $\mathbf{L}_{SS}$ (2.20). Evaluating the global closure and subset cut identities (2.7)–(2.8) on

the 9×9 partitioned Laplacian $\mathbf{L}$ (2.15) for the global all-ones vector $\mathbf{1}_V$ and the subsystem indicator $\mathbf{1}_A$ ($A = S$) verifies exact closure and boundary cut counting (2.26):

$$\mathbf{L}\mathbf{1}_V = \begin{pmatrix} \mathbf{L}_{SS} & \mathbf{L}_{S\bar{S}} \\ \mathbf{L}_{\bar{S}S} & \mathbf{L}_{\bar{S}\bar{S}} \end{pmatrix} \begin{pmatrix} \mathbf{1}_S \\ \mathbf{1}_{\bar{S}} \end{pmatrix} = \mathbf{o}_9, \tag{2.38}$$

$$\mathbf{L}_{SS}\mathbf{1}_S = -\mathbf{L}_{S\bar{S}}\mathbf{1}_{\bar{S}} = \mathbf{D}_S^{(\mathrm{ext})}\mathbf{1}_S = (1,0,0,0,0,1)^{\mathsf{T}}, \tag{2.39}$$

$$\mathbf{1}_A^{\mathsf{T}}\mathbf{L}\mathbf{1}_A = \begin{pmatrix} \mathbf{1}_S^{\mathsf{T}} & \mathbf{o}_{\bar{S}}^{\mathsf{T}} \end{pmatrix} \begin{pmatrix} \mathbf{L}_{SS} & \mathbf{L}_{S\bar{S}} \\ \mathbf{L}_{\bar{S}S} & \mathbf{L}_{\bar{S}\bar{S}} \end{pmatrix} \begin{pmatrix} \mathbf{1}_S \\ \mathbf{o}_{\bar{S}} \end{pmatrix} = \mathbf{1}_S^{\mathsf{T}}\mathbf{L}_{SS}\mathbf{1}_S = |\partial S| = 2. \tag{2.40}$$

On $\mathbf{1}_V$, the outward row-sum leakage $\mathbf{L}_{SS}\mathbf{1}_S$ at ports 1 and 6 is cancelled by the environmental coupling block $\mathbf{L}_{S\bar{S}}\mathbf{1}_{\bar{S}}$, enforcing global closure. On the subsystem indicator $\mathbf{1}_A$, clamping $\bar{S}$ to zero projects $\mathbf{L}$ onto $\mathbf{L}_{SS}$, as all seven internal edges connect equal unit entries and vanish in $\mathbf{L}_{SS}^{(\mathrm{int})}$, leaving only the two boundary cut edges $\{1,7\}$ and $\{6,8\}$.

Comparing the single-port indicator $\mathbf{1}_{\{1\}}$ against the uniform subsystem state $\mathbf{1}_S$ then illustrates the spectral bounds (2.27)–(2.30):

$$\mathbf{1}_{\{1\}}^{\mathsf{T}}\mathbf{L}\mathbf{1}_{\{1\}} = \mathbf{e}_1^{\mathsf{T}}\mathbf{L}_{SS}\mathbf{e}_1 = \deg_G(1) = 3, \tag{2.41}$$

$$0 < \lambda_1(\mathbf{L}_{SS}) = 2 - \sqrt{3} \approx 0.268 \leq \frac{\mathbf{1}_S^{\mathsf{T}}\mathbf{L}_{SS}\mathbf{1}_S}{\mathbf{1}_S^{\mathsf{T}}\mathbf{1}_S} = \frac{|\partial S|}{|S|} = \frac{1}{3}, \tag{2.42}$$

$$\lambda_2(\mathbf{L}_{SS}) \approx 0.786 \geq \lambda_2\big(\mathbf{L}_{SS}^{(\mathrm{int})}\big) = \frac{1}{2}\big(5 - \sqrt{17}\big) \approx 0.438. \tag{2.43}$$

Whereas an isolated vertex state at boundary port 1 scatters at rate $\deg_G(1) = 3$, pooling vertices across S suppresses the Rayleigh leakage quotient ninefold, separating the open escape mode $\lambda_1(\mathbf{L}_{SS})$ from the internal inter-lobe Fiedler mixing mode $\lambda_2(\mathbf{L}_{SS})$ by the spectral ratio $\lambda_2(\mathbf{L}_{SS})/\lambda_1(\mathbf{L}_{SS}) \approx 2.93$ (and scaling internal block volume $|S| \gg |\partial S|$ suppresses $\lambda_1(\mathbf{L}_{SS})$ arbitrarily further while preserving internal connectivity). Finally, inverting the environmental block $\mathbf{L}_{\bar{S}\bar{S}}$ on $\bar{S} = \{7,8,9\}$ yields the Schur return-flux operator $\mathbf{\Sigma}_{\mathrm{env}}$ on $S_\partial = \{1,6\}$:

$$\mathbf{L}_{\bar{S}\bar{S}} = \begin{pmatrix} 3 & -1 & -1 \\ -1 & 3 & -1 \\ -1 & -1 & 2 \end{pmatrix}, \tag{2.44}$$

$$\mathbf{L}_{\bar{S}\bar{S}}^{-1} = \frac{1}{8}\begin{pmatrix} 5 & 3 & 4 \\ 3 & 5 & 4 \\ 4 & 4 & 8 \end{pmatrix}, \tag{2.45}$$

$$\mathbf{\Sigma}_{\mathrm{env}}\big|_{\{1,6\}} = \big(\mathbf{L}_{S\bar{S}}\mathbf{L}_{\bar{S}\bar{S}}^{-1}\mathbf{L}_{\bar{S}S}\big)_{\{1,6\}} = \frac{1}{8}\begin{pmatrix} 5 & 3 \\ 3 & 5 \end{pmatrix}. \tag{2.46}$$

The Schur return matrix (2.46) shows that for any flux leaking from port 1 into $\bar{S}$, a fraction $5/8$ reflects locally back to port 1 while the remaining $3/8$ traverses the bath triangle $\{7,8,9\}$ to enter port 6 (Figure 2.1(b)), summing to $d_1^{(\mathrm{ext})} = 1$, cancelling $\mathbf{D}_S^{(\mathrm{ext})}\mathbf{1}_S$, and restoring exact conservation $\mathbf{L}_{\mathrm{eff}}\mathbf{1}_S = \mathbf{o}$ in (2.34). ♢

2.2 CONGRUENT COMPRESSION

On the bare relational graph $G = (V, E)$ of Section 2.1, physical reality consists solely of unweighted vertices and elementary couplings, and information does not yet exist as a distinct physical quantity. Because an embedded subsystem $S \subset V$ possesses bounded internal resources ($N_S \ll N_V$) and suffers continuous Dirichlet leakage across its open boundary ∂S (Section 2.1.2), it can neither resolve the full graph nor store durable records in individual vertices. Coarse-graining $V = (S, \bar{S})$ into collective equivalence classes defines information and constitutes the embedded observer as an information-processing system. By bundling many indistinguishable vertex configurations into each collective block, the system trades vertex-level resolution for coarse-grained stability, forming addressable registers capable of maintaining records and transforming signals.

Formalising this coarse-graining requires distinguishing how a partition acts on state vectors versus graph operators, because vertex states carry a single node index whereas network couplings connect pairs of nodes. A state vector assigns a single value to each vertex, so coarse-graining it is a linear operation that averages the vertex values within each block into a single block reading while discarding the fine-grained variations inside the block (Section 2.2.1). A graph operator, by contrast, is a bilinear map that acts on pairs of vertices to count couplings and measure relational differences across links. Because every link has two endpoints, coarse-graining a graph operator must group both endpoints at once, summing—rather than averaging—all couplings whose endpoints land in the same block into that register's internal capacity, and all couplings whose endpoints land in different blocks into the channels connecting them (Section 2.2.2).

2.2.1 *The Assignment, Restriction, and Projection Operators*

Coarse-graining the open subsystem $S \subset V$ partitions its $N \equiv N_S$ vertices into M ($M < N$) non-empty, mutually disjoint blocks $\{S_\alpha\}_{\alpha=1}^{M}$, where each block induces a subgraph $G[S_\alpha] = (S_\alpha, E(S_\alpha))$ of vertex count $N_\alpha := |S_\alpha| \geq 1$. This partition $S = \bigsqcup_{\alpha=1}^{M} S_\alpha$ is encoded algebraically by the binary *assignment matrix* $\mathbf{\Pi}_S \in \{0,1\}^{N_S \times M}$ (written $\mathbf{\Pi} \equiv \mathbf{\Pi}_S$ when restricted to S), whose α-th column $\boldsymbol{\pi}_\alpha := \mathbf{\Pi}_S \mathbf{e}_\alpha \in \{0,1\}^N$ is the indicator vector of block S_α with entry $\Pi_{i\alpha} = 1$ if $i \in S_\alpha$ and 0 otherwise:

$$\mathbf{\Pi}_S \mathbf{1}_M = \sum_{\alpha=1}^{M} \boldsymbol{\pi}_\alpha = \mathbf{1}_S, \tag{2.47}$$

$$\boldsymbol{\pi}_\alpha^{\mathsf{T}} \boldsymbol{\pi}_\beta = N_\alpha \delta_{\alpha\beta}, \tag{2.48}$$

$$\mathbf{M}_{\mathbf{\Pi}} := \mathbf{\Pi}_S^{\mathsf{T}} \mathbf{\Pi}_S = \mathrm{diag}(N_1, \ldots, N_M). \tag{2.49}$$

Each column $\boldsymbol{\pi}_\alpha$ identifies the vertices belonging to coarse-grained block S_α. Because every vertex in S is assigned to exactly one block—with no vertex omitted and no two blocks overlapping—the indicator columns sum to

the all-ones vector $\mathbf{1}_S$ in (2.47) and are mutually orthogonal in (2.48)–(2.49). Since every block is also non-empty ($N_\alpha \geq 1$), the diagonal *block-size matrix* $\mathbf{M}_{\mathbf{\Pi}}$ simply records the vertex count of each block and is strictly positive-definite and invertible.

For an embedded system interacting with its surroundings across ∂S, the internal partition $\mathbf{\Pi}_S$ is paired with an environmental assignment matrix $\mathbf{\Pi}_{\bar{S}}$ that groups the $N_{\bar{S}}$ vertices of the external bath $\bar{S} = V \setminus S$ into $M_{\bar{S}}$ disjoint environmental blocks $\{\bar{S}_\mu\}_{\mu=1}^{M_{\bar{S}}}$. Across the partitioned graph $V = (S, \bar{S})$, these two mappings combine into the block-diagonal *assignment matrix* $\mathbf{\Pi}$:

$$\mathbf{\Pi} := \begin{pmatrix} \mathbf{\Pi}_S & \mathbf{o} \\ \mathbf{o} & \mathbf{\Pi}_{\bar{S}} \end{pmatrix}. \tag{2.50}$$

The off-diagonal zero blocks in (2.50) ensure that the coarse-graining respects the boundary cut ∂S, since internal blocks $S_\alpha \subset S$ are formed exclusively from vertices of S and cannot include external vertices $j \in \bar{S}$, nor can environmental blocks $\bar{S}_\mu \subset \bar{S}$ include vertices of S.

On the subsystem graph $G[S]$, mapping state vectors between the coarse-grained block space $\mathbb{R}^M$ and the vertex space $\mathbb{R}^N$ begins with the assignment matrix $\mathbf{\Pi}_S$ and its transpose $\mathbf{\Pi}_S^\mathsf{T}$. For any block state vector $\mathbf{z}_S \in \mathbb{R}^M$, vertex state vector $\mathbf{x}_S \in \mathbb{R}^N$, and vertex $i \in S_\alpha$, their actions are given by:

$$\left(\mathbf{\Pi}_S \mathbf{z}_S\right)_i = z_{S,\alpha}, \tag{2.51}$$

$$\left(\mathbf{\Pi}_S^\mathsf{T} \mathbf{x}_S\right)_\alpha = \boldsymbol{\pi}_\alpha^\mathsf{T} \mathbf{x}_S = \sum_{i \in S_\alpha} x_i. \tag{2.52}$$

Acting from coarse to fine ($\mathbb{R}^M \to \mathbb{R}^N$), the *lift operator* $\mathbf{\Pi}_S$ broadcasts each block value $z_{S,\alpha}$ uniformly across all N_α vertices of S_α. Acting from fine to coarse ($\mathbb{R}^N \to \mathbb{R}^M$), the transpose $\mathbf{\Pi}_S^\mathsf{T}$ takes the inner product with each indicator column $\boldsymbol{\pi}_\alpha$ to compute the extensive sum of vertex values inside block S_α. Because blocks vary in size, applying $\mathbf{\Pi}_S^\mathsf{T}$ to a lifted state $\mathbf{\Pi}_S \mathbf{z}_S$ multiplies each block value $z_{S,\alpha}$ by its vertex count N_α rather than recovering $\mathbf{z}_S$.

Pre-multiplying $\mathbf{\Pi}_S^\mathsf{T}$ by the inverse block-size matrix $\mathbf{M}_{\mathbf{\Pi}}^{-1}$ divides each block sum by N_α, defining the fine-to-coarse *restriction operator* $\mathbf{R}_{\mathbf{\Pi}}$ and its block-averaging action:

$$\mathbf{R}_{\mathbf{\Pi}} := \mathbf{M}_{\mathbf{\Pi}}^{-1} \mathbf{\Pi}_S^\mathsf{T} \in \mathbb{R}^{M \times N}, \tag{2.53}$$

$$\left(\mathbf{R}_{\mathbf{\Pi}} \mathbf{x}_S\right)_\alpha = \frac{1}{N_\alpha} \sum_{i \in S_\alpha} x_i =: z_{S,\alpha}. \tag{2.54}$$

Whereas $\mathbf{\Pi}_S^\mathsf{T}$ tallies the extensive block sum, $\mathbf{R}_{\mathbf{\Pi}}$ extracts the intensive block average $z_{S,\alpha}$ in (2.53)–(2.54), forming the coarse-grained block state vector $\mathbf{z}_S = \mathbf{R}_{\mathbf{\Pi}} \mathbf{x}_S \in \mathbb{R}^M$. Because averaging a state that is already constant across each block recovers the block state itself, $\mathbf{R}_{\mathbf{\Pi}}$ is the exact left inverse of $\mathbf{\Pi}_S$

(so $\mathbf{R}_{\mathbf{\Pi}}\mathbf{1}_S = \mathbf{1}_M$) and maps any vertex subset indicator $\mathbf{1}_A \in \{0,1\}^N$ ($A \subseteq S$) to its fractional block occupancies:

$$\mathbf{R}_{\mathbf{\Pi}}\mathbf{\Pi}_S = \mathbf{I}_M, \tag{2.55}$$

$$\big(\mathbf{R}_{\mathbf{\Pi}}\mathbf{1}_A\big)_\alpha = \frac{|A \cap S_\alpha|}{N_\alpha}. \tag{2.56}$$

Whereas $\mathbf{R}_{\mathbf{\Pi}}\mathbf{\Pi}_S = \mathbf{I}_M$ is the identity on the M-dimensional block space, composing the two operators in the reverse order on $\mathbb{R}^N$—first restricting a state to its M block averages via $\mathbf{R}_{\mathbf{\Pi}}$ and then lifting those averages back to the N vertices via $\mathbf{\Pi}_S$—discards intra-block variations whenever $M < N$. This composition defines the coarse-graining projector $\mathbf{P}_{\mathbf{\Pi}} \in \mathbb{R}^{N\times N}$:

$$\mathbf{P}_{\mathbf{\Pi}} := \mathbf{\Pi}_S\mathbf{R}_{\mathbf{\Pi}} = \mathbf{\Pi}_S\mathbf{M}_{\mathbf{\Pi}}^{-1}\mathbf{\Pi}_S^{\mathsf{T}}, \tag{2.57}$$

$$\mathbf{P}_{\mathbf{\Pi}}^2 = \mathbf{P}_{\mathbf{\Pi}} = \mathbf{P}_{\mathbf{\Pi}}^{\mathsf{T}}, \tag{2.58}$$

$$\mathrm{Tr}(\mathbf{P}_{\mathbf{\Pi}}) = M. \tag{2.59}$$

In (2.57)–(2.59), the left-inverse relation $\mathbf{R}_{\mathbf{\Pi}}\mathbf{\Pi}_S = \mathbf{I}_M$ immediately renders $\mathbf{P}_{\mathbf{\Pi}}$ idempotent, while the diagonal symmetry of $\mathbf{M}_{\mathbf{\Pi}}^{-1}$ ensures that $\mathbf{P}_{\mathbf{\Pi}}$ is self-adjoint. By cyclic permutation of the trace, $\mathrm{Tr}(\mathbf{P}_{\mathbf{\Pi}})$ equals $\mathrm{Tr}(\mathbf{I}_M)$ and thus $\mathbf{P}_{\mathbf{\Pi}}$ has rank M, projecting $\mathbb{R}^N$ orthogonally onto the M-dimensional subspace $\mathrm{im}(\mathbf{P}_{\mathbf{\Pi}}) = \mathrm{im}(\mathbf{\Pi}_S)$ of resolved block-constant states.

Subtracting $\mathbf{P}_{\mathbf{\Pi}}$ from the identity on $\mathbb{R}^N$ defines its orthogonal complement, the residual fluctuation projector $\mathbf{Q}_{\mathbf{\Pi}} \in \mathbb{R}^{N\times N}$:

$$\mathbf{Q}_{\mathbf{\Pi}} := \mathbf{I}_N - \mathbf{P}_{\mathbf{\Pi}}, \tag{2.60}$$

$$\mathbf{P}_{\mathbf{\Pi}}\mathbf{Q}_{\mathbf{\Pi}} = \mathbf{o}, \tag{2.61}$$

$$\mathrm{im}(\mathbf{Q}_{\mathbf{\Pi}}) = \ker(\mathbf{R}_{\mathbf{\Pi}}). \tag{2.62}$$

By construction, $\mathbf{Q}_{\mathbf{\Pi}}$ in (2.60)–(2.62) is a symmetric orthogonal projector of rank $\mathrm{Tr}(\mathbf{Q}_{\mathbf{\Pi}}) = N - M$ that annihilates $\mathbf{P}_{\mathbf{\Pi}}$ and spans the unresolved kernel $\ker(\mathbf{R}_{\mathbf{\Pi}})$ of states invisible to $\mathbf{R}_{\mathbf{\Pi}}$.

Together, $\mathbf{P}_{\mathbf{\Pi}}$ and $\mathbf{Q}_{\mathbf{\Pi}}$ induce an orthogonal direct-sum decomposition of the vertex space $\mathbb{R}^N$, splitting any vertex state vector $\mathbf{x}_S \in \mathbb{R}^N$ into a resolved coarse-grained component and an unresolved fluctuation component annihilated by $\mathbf{R}_{\mathbf{\Pi}}$:

$$\mathbb{R}^N = \mathrm{im}(\mathbf{P}_{\mathbf{\Pi}}) \oplus \mathrm{im}(\mathbf{Q}_{\mathbf{\Pi}}), \tag{2.63}$$

$$\mathbf{x}_S = \mathbf{P}_{\mathbf{\Pi}}\mathbf{x}_S + \mathbf{Q}_{\mathbf{\Pi}}\mathbf{x}_S, \tag{2.64}$$

$$\mathbf{R}_{\mathbf{\Pi}}\mathbf{Q}_{\mathbf{\Pi}}\mathbf{x}_S = \mathbf{o}. \tag{2.65}$$

Evaluated at any vertex $i \in S_\alpha$, the two projected components take the entry-wise form:

$$\big(\mathbf{P}_{\mathbf{\Pi}}\mathbf{x}_S\big)_i = z_{S,\alpha}, \tag{2.66}$$

$$\big(\mathbf{Q}_{\mathbf{\Pi}}\mathbf{x}_S\big)_i = x_i - z_{S,\alpha}. \tag{2.67}$$

Equations (2.63)–(2.67) make the physical meaning of the projector split transparent, as on each block S_α, $\mathbf{P}_{\mathbf{\Pi}}\mathbf{x}_S$ replaces every vertex entry x_i ($i \in S_\alpha$) with the block mean $z_{S,\alpha}$, whereas $\mathbf{Q}_{\mathbf{\Pi}}\mathbf{x}_S$ isolates the zero-sum intra-block deviation $x_i - z_{S,\alpha}$ whose block average vanishes under $\mathbf{R}_{\mathbf{\Pi}}$.

Because $\mathbf{P}_{\mathbf{\Pi}}$ and $\mathbf{Q}_{\mathbf{\Pi}}$ are mutually orthogonal and self-adjoint, the cross-term $(\mathbf{P}_{\mathbf{\Pi}}\mathbf{x}_S)^{\mathsf{T}}(\mathbf{Q}_{\mathbf{\Pi}}\mathbf{x}_S)$ vanishes identically, yielding the Pythagorean variance decomposition of the squared Euclidean norm $\|\mathbf{x}_S\|_2^2$:

$$\|\mathbf{x}_S\|_2^2 = \|\mathbf{P}_{\mathbf{\Pi}}\mathbf{x}_S\|_2^2 + \|\mathbf{Q}_{\mathbf{\Pi}}\mathbf{x}_S\|_2^2 = \sum_{\alpha=1}^{M} N_\alpha z_{S,\alpha}^2 + \sum_{\alpha=1}^{M}\sum_{i\in S_\alpha}(x_i - z_{S,\alpha})^2. \tag{2.68}$$

In (2.68), the total squared norm of $\mathbf{x}_S$ separates without cross-terms into the resolved between-block mean energy $\|\mathbf{P}_{\mathbf{\Pi}}\mathbf{x}_S\|_2^2$ (weighted by the block sizes N_α) plus the unresolved intra-block variance $\|\mathbf{Q}_{\mathbf{\Pi}}\mathbf{x}_S\|_2^2$ concealed inside $\ker(\mathbf{R}_{\mathbf{\Pi}})$. Across the full partition (2.50), restriction and orthogonal projection act block-diagonally across S and $\bar{S}$ via $\mathbf{R}_{\mathbf{\Pi}_S}$ and $\mathbf{R}_{\mathbf{\Pi}_{\bar{S}}}$. When an embedded observer resolves only $S \subset V$ while leaving $\bar{S}$ unobserved, its partial assignment on $V = (S, \bar{S})$ factors through the vertex-inclusion matrix $\mathbf{\Pi}_0 := (\mathbf{I}_S, \mathbf{o})^{\mathsf{T}} \in \{0,1\}^{N_V \times N}$ as $\widetilde{\mathbf{\Pi}}_S := \mathbf{\Pi}_0\mathbf{\Pi}_S$, splitting the global residual projector orthogonally across S and $\bar{S}$:

$$\mathbf{Q}_{\widetilde{\mathbf{\Pi}}_S} := \mathbf{I}_{N_V} - \widetilde{\mathbf{\Pi}}_S\mathbf{M}_{\mathbf{\Pi}}^{-1}\widetilde{\mathbf{\Pi}}_S^{\mathsf{T}} = \operatorname{diag}\big(\mathbf{Q}_{\mathbf{\Pi}_S}, \mathbf{I}_{\bar{S}}\big). \tag{2.69}$$

Equation (2.69) decomposes an embedded observer's unresolved subspace into intra-block fluctuations $\operatorname{im}(\mathbf{Q}_{\mathbf{\Pi}_S})$ inside S and external environmental modes on $\bar{S}$.

EXAMPLE 2.2 (Assignment and State Projection). Partition the open six-node dumbbell subsystem $S = \{1, \dots, 6\}$ of Example 2.1 ($N_S = 6$, Figure 2.1) into $M = 2$ disjoint three-node blocks $S_1 = \{1,2,3\}$ and $S_2 = \{4,5,6\}$ of equal size $N_\alpha = 3$ ($\alpha \in \{1,2\}$), paired across ∂S with a single coarse-grained environmental block $\bar{S}_1 = \{7,8,9\}$ ($N_{\bar{S}} = 3$, $M_{\bar{S}} = 1$, $\mathbf{\Pi}_{\bar{S}} = \mathbf{1}_3$). Collecting the block-indicator columns $\boldsymbol{\pi}_1$ and $\boldsymbol{\pi}_2$ defines the assignment matrix $\mathbf{\Pi}_S$, the block-size matrix $\mathbf{M}_{\mathbf{\Pi}}$, and the fine-to-coarse restriction operator $\mathbf{R}_{\mathbf{\Pi}}$ (2.47)–(2.54):

$$\mathbf{\Pi}_S = \left(\begin{array}{cc} 1 & 0 \\ 1 & 0 \\ 1 & 0 \\ \hline 0 & 1 \\ 0 & 1 \\ 0 & 1 \end{array}\right), \tag{2.70}$$

$$\mathbf{M}_{\mathbf{\Pi}} = \begin{pmatrix} 3 & 0 \\ 0 & 3 \end{pmatrix}, \tag{2.71}$$

$$\mathbf{R}_{\mathbf{\Pi}} = \frac{1}{3}\begin{pmatrix} 1 & 1 & 1 & 0 & 0 & 0 \\ 0 & 0 & 0 & 1 & 1 & 1 \end{pmatrix}. \tag{2.72}$$

Composing $\mathbf{\Pi}_S$ and $\mathbf{R}_{\mathbf{\Pi}}$ via (2.57)–(2.60) yields the orthogonal block-averaging and residual fluctuation projectors on $\mathbb{R}^6$:

$$\mathbf{P}_{\mathbf{\Pi}} = \frac{1}{3}\begin{pmatrix} \mathbf{1}_{3\times3} & \mathbf{0}_{3\times3} \\ \mathbf{0}_{3\times3} & \mathbf{1}_{3\times3} \end{pmatrix}, \tag{2.73}$$

$$\mathbf{Q}_{\mathbf{\Pi}} = \frac{1}{3}\begin{pmatrix} 3\mathbf{I}_3 - \mathbf{1}_{3\times3} & \mathbf{0}_{3\times3} \\ \mathbf{0}_{3\times3} & 3\mathbf{I}_3 - \mathbf{1}_{3\times3} \end{pmatrix}. \tag{2.74}$$

For a non-uniform vertex state $\mathbf{x}_S = (4, 1, 1, 0, 3, 6)^{\mathsf{T}}$ on $\mathbb{R}^6$, these operators evaluate to:

$$\mathbf{z}_S = \mathbf{R}_{\mathbf{\Pi}}\mathbf{x}_S = (2, 3)^{\mathsf{T}}, \tag{2.75}$$

$$\mathbf{P}_{\mathbf{\Pi}}\mathbf{x}_S = (2, 2, 2, 3, 3, 3)^{\mathsf{T}}, \tag{2.76}$$

$$\mathbf{Q}_{\mathbf{\Pi}}\mathbf{x}_S = (2, -1, -1, -3, 0, 3)^{\mathsf{T}}. \tag{2.77}$$

On $\mathbf{x}_S$, the restriction operator $\mathbf{R}_{\mathbf{\Pi}}$ divides each block sum by $N_\alpha = 3$ to extract the resolved register coordinates $\mathbf{z}_S = (z_{S,1}, z_{S,2})^{\mathsf{T}}$, $\mathbf{P}_{\mathbf{\Pi}}$ lifts $\mathbf{z}_S$ into the two-dimensional block-constant subspace $\mathrm{im}(\mathbf{P}_{\mathbf{\Pi}}) \subset \mathbb{R}^6$, and $\mathbf{Q}_{\mathbf{\Pi}}$ isolates the orthogonal four-dimensional subspace $\mathrm{im}(\mathbf{Q}_{\mathbf{\Pi}}) = \ker(\mathbf{R}_{\mathbf{\Pi}})$ of zero-sum intra-triangle fluctuations ($\mathbf{R}_{\mathbf{\Pi}}\mathbf{Q}_{\mathbf{\Pi}}\mathbf{x}_S = \mathbf{o}_2$) that the coarse-grained observer cannot resolve. ♢

2.2.2 *The Capacity Matrix and Capacity Laplacian*

Whereas restricting a vertex state vector via $\mathbf{R}_{\mathbf{\Pi}}$ divides by N_α to average vertex values within each block, compressing bilinear graph operators must tally every relational edge within and between blocks without dividing by N_α, preserving matrix symmetry when $N_\alpha \neq N_\beta$. Evaluating the quadratic form of any vertex-level operator $\mathbf{O}$ on block-uniform states $\mathbf{\Pi}_S\mathbf{z}_S \in \mathrm{im}(\mathbf{P}_{\mathbf{\Pi}})$ forces the operator to contract via the unnormalised *matrix congruence* $\mathscr{C}_{\mathbf{\Pi}_S}$ (corresponding to a piecewise-constant Bubnov–Galerkin projection in numerical analysis) on S (and $\mathscr{C}_{\mathbf{\Pi}}$ across $V = (S, \bar{S})$):

$$\big(\mathbf{\Pi}_S\mathbf{z}_S\big)^{\mathsf{T}}\mathbf{O}\big(\mathbf{\Pi}_S\mathbf{z}_S\big) = \mathbf{z}_S^{\mathsf{T}}\big(\mathbf{\Pi}_S^{\mathsf{T}}\mathbf{O}\mathbf{\Pi}_S\big)\mathbf{z}_S, \tag{2.78}$$

$$\mathscr{C}_{\mathbf{\Pi}_S}(\mathbf{O}) := \mathbf{\Pi}_S^{\mathsf{T}}\mathbf{O}\mathbf{\Pi}_S, \tag{2.79}$$

$$\mathscr{C}_{\mathbf{\Pi}}(\mathbf{O}) := \mathbf{\Pi}^{\mathsf{T}}\mathbf{O}\mathbf{\Pi}. \tag{2.80}$$

For an open observer resolving only $S \subset V$ via $\widetilde{\mathbf{\Pi}}_S = \mathbf{\Pi}_0\mathbf{\Pi}_S$ (2.69), congruence with the vertex inclusion $\mathbf{\Pi}_0$ extracts the subsystem block $\mathscr{C}_S$ and factors coarse-graining across ∂S:

$$\mathscr{C}_S(\mathbf{O}) := \mathbf{\Pi}_0^{\mathsf{T}}\mathbf{O}\mathbf{\Pi}_0 = \mathbf{O}_{SS}, \tag{2.81}$$

$$\mathscr{C}_{\widetilde{\mathbf{\Pi}}_S}(\mathbf{O}) = \mathscr{C}_{\mathbf{\Pi}_S}\big(\mathscr{C}_S(\mathbf{O})\big) = \mathbf{\Pi}_S^{\mathsf{T}}\mathbf{O}_{SS}\mathbf{\Pi}_S. \tag{2.82}$$

Applying $\mathscr{C}_{\mathbf{\Pi}}$ to the 2×2 partitioned adjacency matrix $\mathbf{A}$ (2.13) under the assignment (2.50) yields the partitioned *capacity matrix* $\mathbf{K}$:

$$\begin{aligned}\mathbf{K} := \mathbf{\Pi}^{\mathsf{T}}\mathbf{A}\mathbf{\Pi} &= \begin{pmatrix} \mathbf{\Pi}_S^{\mathsf{T}}\mathbf{A}_{SS}\mathbf{\Pi}_S & \mathbf{\Pi}_S^{\mathsf{T}}\mathbf{A}_{S\bar{S}}\mathbf{\Pi}_{\bar{S}} \\ \mathbf{\Pi}_{\bar{S}}^{\mathsf{T}}\mathbf{A}_{\bar{S}S}\mathbf{\Pi}_S & \mathbf{\Pi}_{\bar{S}}^{\mathsf{T}}\mathbf{A}_{\bar{S}\bar{S}}\mathbf{\Pi}_{\bar{S}} \end{pmatrix} \\ &= \begin{pmatrix} \mathbf{K}_S & (\mathbf{K}_\partial^{(\mathrm{ext})})^{\mathsf{T}} \\ \mathbf{K}_\partial^{(\mathrm{ext})} & \mathbf{K}_{\bar{S}} \end{pmatrix}.\end{aligned} \tag{2.83}$$

Here the upper-left block $\mathbf{K}_S$ (written $\mathbf{K} \equiv \mathbf{K}_S$ when restricted to S) encodes the coarse-grained internal network of the subsystem, while the lower-right block $\mathbf{K}_{\bar{S}}$ and off-diagonal cut block $\mathbf{K}_\partial^{(\mathrm{ext})}$ tally the coarse-grained environmental network and the external boundary links $|E(\bar{S}_\mu, S_\alpha)|$ coupling environmental block $\bar{S}_\mu$ to internal block S_α:

$$\mathbf{K}_{\bar{S}} := \mathbf{\Pi}_{\bar{S}}^{\mathsf{T}}\mathbf{A}_{\bar{S}\bar{S}}\mathbf{\Pi}_{\bar{S}} \in \mathbb{N}_0^{M_{\bar{S}} \times M_{\bar{S}}}, \tag{2.84}$$

$$\mathbf{K}_\partial^{(\mathrm{ext})} := \mathbf{\Pi}_{\bar{S}}^{\mathsf{T}}\mathbf{A}_{\bar{S}S}\mathbf{\Pi}_S = \big(|E(\bar{S}_\mu, S_\alpha)|\big) \in \mathbb{N}_0^{M_{\bar{S}} \times M}. \tag{2.85}$$

Within the subsystem S, the capacity matrix $\mathbf{K}_S$ splits into the diagonal *intra-basin memory matrix* $\mathbf{K}_\Omega$ and the hollow *inter-basin transition cut matrix* $\mathbf{K}_\partial^{(\mathrm{int})}$ (written $\mathbf{K}_\partial \equiv \mathbf{K}_\partial^{(\mathrm{int})}$):

$$\mathbf{K}_S := \mathbf{\Pi}_S^{\mathsf{T}}\mathbf{A}_{SS}\mathbf{\Pi}_S = \mathbf{K}_\Omega + \mathbf{K}_\partial^{(\mathrm{int})} \in \mathbb{N}_0^{M \times M}, \tag{2.86}$$

$$\mathbf{K}_\Omega := \mathrm{diag}(K_{11}, \dots, K_{MM}), \tag{2.87}$$

$$\mathbf{K}_\partial^{(\mathrm{int})} := \mathbf{K}_S - \mathbf{K}_\Omega. \tag{2.88}$$

On the weighted, self-looped *capacity graph* $G_{\mathbf{K}}$ (Figure 2.2), $\mathbf{K}_\Omega$ collects the diagonal self-loops that stabilise internal states within each block S_α, while $\mathbf{K}_\partial^{(\mathrm{int})}$ collects the off-diagonal channels mediating transitions between distinct internal blocks. Because the block-diagonal assignment (2.50) forbids grouping environmental vertices inside S, representing $\bar{S}$ requires configuring $\mathbf{\Pi}_S$ so that the internal registers ($\mathbf{K}_\Omega$) and transition couplings ($\mathbf{K}_\partial^{(\mathrm{int})}$) form a structure-preserving coarse-grained model of the relevant environmental states ($\mathbf{K}_{\bar{S}}$) coupled through the boundary interface $\mathbf{K}_\partial^{(\mathrm{ext})}$.

Combinatorially, the entries $K_{\alpha\beta}$ (in links) of $\mathbf{K}_S$ tally the induced internal edge set $E(S_\alpha)$ within each block and the inter-block cut edge set $E(S_\alpha, S_\beta)$ spanning distinct blocks:

$$E(S_\alpha, S_\beta) := \big\{\{i, j\} \in E(S) : i \in S_\alpha,\, j \in S_\beta\big\} \qquad (\alpha \neq \beta), \tag{2.89}$$

$$K_{\alpha\alpha} = (\mathbf{K}_\Omega)_{\alpha\alpha} = 2|E(S_\alpha)|, \tag{2.90}$$

$$K_{\alpha\beta} = \big(\mathbf{K}_\partial^{(\mathrm{int})}\big)_{\alpha\beta} = |E(S_\alpha, S_\beta)| \qquad (\alpha \neq \beta). \tag{2.91}$$

Each undirected internal edge $\{i, j\} \in E(S_\alpha)$ contributes two symmetric nonzero entries ($A_{ij} = 1$ and $A_{ji} = 1$) inside block S_α, so the diagonal capacity $K_{\alpha\alpha} = 2|E(S_\alpha)|$ counts directed internal link endpoints in links, whereas each off-diagonal entry $K_{\alpha\beta} = |E(S_\alpha, S_\beta)|$ ($\alpha \neq \beta$) counts the cut links connecting

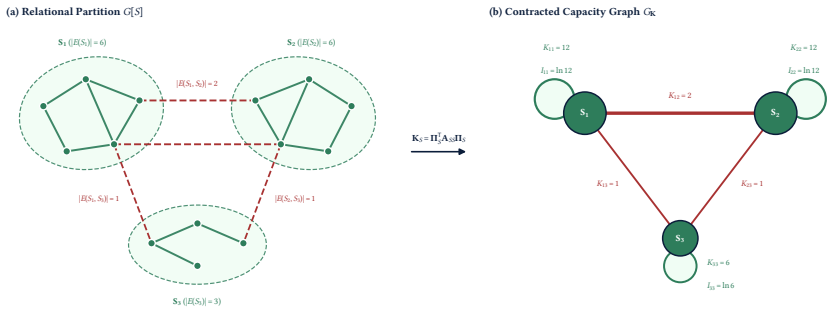


FIGURE 2.2: The epistemic assignment operator $\mathbf{\Pi}_S$ and the contracted capacity graph $G_{\mathbf{K}}$. *(a)* Relational subgraph $G[S] = (S, E(S))$ ($N = 14$ vertices, $|E(S)| = 19$ edges) partitioned into $M = 3$ disjoint blocks (S_1, S_2, S_3) by the binary assignment matrix $\mathbf{\Pi}_S \in \{0,1\}^{N\times M}$, separating relational links into induced internal edge sets $E(S_\alpha)$ (solid teal, $|E(S_1)| = 6$, $|E(S_2)| = 6$, and $|E(S_3)| = 3$, giving diagonal capacities $K_{11} = 12$ links, $K_{22} = 12$ links, and $K_{33} = 6$ links) and inter-block cut edge sets $E(S_\alpha, S_\beta)$ (dashed crimson, $|E(S_1, S_2)| = 2$, $|E(S_1, S_3)| = 1$, and $|E(S_2, S_3)| = 1$, giving cut capacities $K_{12} = 2$ links, $K_{13} = 1$ link, and $K_{23} = 1$ link). *(b)* Contracted capacity graph $G_{\mathbf{K}}$ under congruent compression $\mathbf{K}_S = \mathbf{\Pi}_S^\intercal \mathbf{A}_{SS} \mathbf{\Pi}_S$, where each block S_α carries a self-loop of diagonal capacity $K_{\alpha\alpha}$ (teal, coarse-graining depth $I_{\alpha\alpha} = \ln K_{\alpha\alpha}$ in nats) bridged by weighted boundary couplings $K_{\alpha\beta}$ (crimson), preserving exact combinatorial edge conservation ($|E(S)| = 19$).

S_α to S_β. Applying the natural logarithm to any block with non-empty internal edge support ($K_{\alpha\alpha} \geq 2$) converts raw link counts into dimensionless informational units (nats), defining its *coarse-graining depth* $I_{\alpha\alpha}$:

$$I_{\alpha\alpha} := \ln K_{\alpha\alpha}. \tag{2.92}$$

To display unequal coarse-graining depths and heterogeneous cut capacities that remain degenerate on the symmetric two-lobe running example, Figure 2.2 illustrates this congruent compression on a general asymmetric three-block subgraph ($N = 14$, $M = 3$).

Because $\mathbf{\Pi}_S \mathbf{1}_M = \mathbf{1}_S$ and $\mathbf{\Pi}_{\bar{S}} \mathbf{1}_{M_{\bar{S}}} = \mathbf{1}_{\bar{S}}$, applying the matrix congruence $\mathscr{C}_{\mathbf{\Pi}_S}$ to the open-system degree split (2.17) projects the vertex degree matrices onto the M system blocks:

$$\mathbf{D}_{\mathbf{K}} := \mathbf{\Pi}_S^\intercal \mathbf{D}_S \mathbf{\Pi}_S = \mathbf{D}_{\mathbf{K}}^{(\mathrm{int})} + \mathbf{D}_{\mathbf{K}}^{(\mathrm{ext})} = \mathrm{diag}(d_\alpha)_{\alpha=1}^{M}, \tag{2.93}$$

$$\mathbf{D}_{\mathbf{K}}^{(\mathrm{int})} := \mathbf{\Pi}_S^\intercal \mathbf{D}_S^{(\mathrm{int})} \mathbf{\Pi}_S = \mathbf{K}_\Omega + \mathbf{D}_\partial^{(\mathrm{int})} = \mathrm{diag}\big(d_\alpha^{(\mathrm{int})}\big)_{\alpha=1}^{M}, \tag{2.94}$$

$$\mathbf{D}_\partial^{(\mathrm{int})} := \mathrm{diag}\Big(\sum_{\beta\neq\alpha} K_{\alpha\beta}\Big)_{\alpha=1}^{M}. \tag{2.95}$$

Here $\mathbf{D}_\partial^{(\mathrm{int})}$ counts the internal inter-block cut edges incident to each block. Similarly, projecting $\mathbf{D}_S^{(\mathrm{ext})}$ onto the M blocks yields the diagonal external

boundary degree matrix $\mathbf{D}_{\mathbf{K}}^{(\mathrm{ext})}$, whose entries match the column sums of $\mathbf{K}_{\partial}^{(\mathrm{ext})}$ and sum to $|\partial S|$:

$$\mathbf{D}_{\mathbf{K}}^{(\mathrm{ext})} := \mathbf{\Pi}_S^{\mathsf{T}} \mathbf{D}_S^{(\mathrm{ext})} \mathbf{\Pi}_S = \mathrm{diag}\big(d_\alpha^{(\mathrm{ext})}\big)_{\alpha=1}^{M}, \tag{2.96}$$

$$\mathrm{Tr}\big(\mathbf{D}_{\mathbf{K}}^{(\mathrm{ext})}\big) = \sum_{\alpha=1}^{M} d_\alpha^{(\mathrm{ext})} = |\partial S|. \tag{2.97}$$

Entrywise, each block's internal degree volume $d_\alpha^{(\mathrm{int})}$ (summing across all blocks to $2|E(S)|$) and external boundary cut degree $d_\alpha^{(\mathrm{ext})}$ sum to its total degree volume $d_\alpha := d_\alpha^{(\mathrm{int})} + d_\alpha^{(\mathrm{ext})}$, equal to $\mathrm{vol}(S_\alpha)$, whose trace matches the total relational capacity $\mathcal{Q}_{\mathrm{total}}$ (2.195) identically:

$$d_\alpha^{(\mathrm{int})} = K_{\alpha\alpha} + \sum_{\beta \neq \alpha} K_{\alpha\beta} = \mathrm{vol}_{\mathrm{int}}(S_\alpha), \tag{2.98}$$

$$d_\alpha^{(\mathrm{ext})} = \sum_{i \in S_\alpha} d_i^{(\mathrm{ext})} = |E(S_\alpha, \bar{S})|, \tag{2.99}$$

$$\mathrm{Tr}(\mathbf{D}_{\mathbf{K}}) = \sum_{\alpha=1}^{M} d_\alpha = 2|E(S)| + |\partial S| = \mathrm{vol}(S) = \mathcal{Q}_{\mathrm{total}}. \tag{2.100}$$

Applying $\mathscr{C}_{\mathbf{\Pi}_S}$ to the Laplacian split (2.20) similarly defines the isolated internal (Neumann) capacity Laplacian $\mathbf{L}_{\mathbf{K}}$ and the open Dirichlet capacity Laplacian $\mathbf{L}_{\mathbf{K},SS}$:

$$\mathbf{L}_{\mathbf{K}} := \mathbf{\Pi}_S^{\mathsf{T}} \mathbf{L}_{SS}^{(\mathrm{int})} \mathbf{\Pi}_S = \mathbf{D}_{\mathbf{K}}^{(\mathrm{int})} - \mathbf{K}_S = \mathbf{D}_{\partial}^{(\mathrm{int})} - \mathbf{K}_{\partial}^{(\mathrm{int})}, \tag{2.101}$$

$$\mathbf{L}_{\mathbf{K},SS} := \mathbf{\Pi}_S^{\mathsf{T}} \mathbf{L}_{SS} \mathbf{\Pi}_S = \mathbf{D}_{\mathbf{K}} - \mathbf{K}_S = \mathbf{L}_{\mathbf{K}} + \mathbf{D}_{\mathbf{K}}^{(\mathrm{ext})}, \tag{2.102}$$

$$\mathbf{1}_M^{\mathsf{T}} \mathbf{L}_{\mathbf{K},SS} \mathbf{1}_M = \mathrm{Tr}\big(\mathbf{D}_{\mathbf{K}}^{(\mathrm{ext})}\big) = |\partial S|. \tag{2.103}$$

Whereas $\mathbf{L}_{\mathbf{K}}$ governs closed inter-block transport inside S with zero row sums ($\mathbf{L}_{\mathbf{K}} \mathbf{1}_M = \mathbf{0}$), $\mathbf{L}_{\mathbf{K},SS}$ adds the diagonal boundary degree potential $\mathbf{D}_{\mathbf{K}}^{(\mathrm{ext})}$ accounting for open leakage across ∂S. Whenever the context is unambiguous, $\mathbf{K}_\partial$ denotes the active boundary cut ($\mathbf{K}_\partial^{(\mathrm{int})}$ within S, or the combined pair $(\mathbf{K}_\partial^{(\mathrm{int})}, \mathbf{K}_\partial^{(\mathrm{ext})})$ for an open system).

Evaluating the quadratic forms of $\mathbf{L}_{\mathbf{K}}$ and $\mathbf{L}_{\mathbf{K},SS}$ on any trial vector $\mathbf{\Pi}_S \mathbf{z}_S \in \mathrm{im}(\mathbf{\Pi}_S)$ ($\mathbf{z}_S \in \mathbb{R}^M$) exposes the complementary roles of $\mathbf{K}_\Omega$, $\mathbf{K}_\partial^{(\mathrm{int})}$, and $\mathbf{D}_{\mathbf{K}}^{(\mathrm{ext})}$:

$$\mathbf{z}_S^{\mathsf{T}} \mathbf{L}_{\mathbf{K}} \mathbf{z}_S = (\mathbf{\Pi}_S \mathbf{z}_S)^{\mathsf{T}} \mathbf{L}_{SS}^{(\mathrm{int})} (\mathbf{\Pi}_S \mathbf{z}_S) = \sum_{\alpha<\beta} K_{\alpha\beta} (z_{S,\alpha} - z_{S,\beta})^2 \geq 0, \tag{2.104}$$

$$\mathbf{z}_S^{\mathsf{T}} \mathbf{L}_{\mathbf{K},SS} \mathbf{z}_S = (\mathbf{\Pi}_S \mathbf{z}_S)^{\mathsf{T}} \mathbf{L}_{SS} (\mathbf{\Pi}_S \mathbf{z}_S) = \sum_{\alpha<\beta} K_{\alpha\beta} (z_{S,\alpha} - z_{S,\beta})^2 + \sum_{\alpha=1}^{M} d_\alpha^{(\mathrm{ext})} z_{S,\alpha}^2. \tag{2.105}$$

Because every internal edge in $E(S_\alpha)$ connects vertices within the same block sharing the identical trial amplitude $z_{S,\alpha}$, internal self-loops $\mathbf{K}_\Omega$ cancel identically out of both $\mathbf{L}_{\mathbf{K}}$ and $\mathbf{L}_{\mathbf{K},SS}$. Evaluating $\mathbf{L}_{\mathbf{K}}$ and $\mathbf{L}_{\mathbf{K},SS}$ on a single block basis

vector $\mathbf{e}_\alpha$ therefore isolates the internal inter-block cut edges incident to S_α and the external boundary cut edges exiting S_α into $\bar{S}$:

$$\mathbf{e}_\alpha^\top \mathbf{L}_\mathbf{K} \mathbf{e}_\alpha = \big(\mathbf{D}_\partial^{(\mathrm{int})}\big)_{\alpha\alpha} = |E(S_\alpha, S \setminus S_\alpha)|, \tag{2.106}$$

$$\mathbf{e}_\alpha^\top \mathbf{L}_{\mathbf{K},SS} \mathbf{e}_\alpha = \big(\mathbf{D}_\partial^{(\mathrm{int})}\big)_{\alpha\alpha} + d_\alpha^{(\mathrm{ext})} = |E(S_\alpha, S \setminus S_\alpha)| + |E(S_\alpha, \bar{S})|. \tag{2.107}$$

How, then, does internal capacity $\mathbf{K}_\Omega$ stabilise a block against boundary escape? Restricting the generalised Rayleigh quotient onto $\mathrm{im}(\mathbf{\Pi}_S)$ projects both numerator and denominator via $\mathscr{C}_{\mathbf{\Pi}_S}$, which in degree-weighted coordinates $\tilde{\mathbf{z}}_S := (\mathbf{D}_\mathbf{K}^{(\mathrm{int})})^{1/2}\mathbf{z}_S$ gives:

$$\begin{aligned} \frac{(\mathbf{\Pi}_S \mathbf{z}_S)^\top \mathbf{L}_{SS}^{(\mathrm{int})} (\mathbf{\Pi}_S \mathbf{z}_S)}{(\mathbf{\Pi}_S \mathbf{z}_S)^\top \mathbf{D}_S^{(\mathrm{int})} (\mathbf{\Pi}_S \mathbf{z}_S)} &= \frac{\mathbf{z}_S^\top (\mathbf{D}_\partial^{(\mathrm{int})} - \mathbf{K}_\partial^{(\mathrm{int})}) \mathbf{z}_S}{\mathbf{z}_S^\top (\mathbf{K}_\Omega + \mathbf{D}_\partial^{(\mathrm{int})}) \mathbf{z}_S} \\ &= \frac{\tilde{\mathbf{z}}_S^\top \mathbf{L}_{\mathrm{norm}} \tilde{\mathbf{z}}_S}{\tilde{\mathbf{z}}_S^\top \tilde{\mathbf{z}}_S}. \end{aligned} \tag{2.108}$$

Here the symmetric *normalised capacity Laplacian* $\mathbf{L}_{\mathrm{norm}}$ governs transport in the degree-weighted basis:

$$\mathbf{L}_{\mathrm{norm}} := (\mathbf{D}_\mathbf{K}^{(\mathrm{int})})^{-1/2} \mathbf{L}_\mathbf{K} (\mathbf{D}_\mathbf{K}^{(\mathrm{int})})^{-1/2} = \mathbf{I}_M - (\mathbf{D}_\mathbf{K}^{(\mathrm{int})})^{-1/2} \mathbf{K}_S (\mathbf{D}_\mathbf{K}^{(\mathrm{int})})^{-1/2}. \tag{2.109}$$

The degree-mass denominator in (2.108) re-introduces $K_{\alpha\alpha}$ as volumetric inertia, since out of all $d_\alpha^{(\mathrm{int})}$ internal edge endpoints incident to S_α, $K_{\alpha\alpha}$ recirculate internally while only $(\mathbf{D}_\partial^{(\mathrm{int})})_{\alpha\alpha}$ cross into adjacent internal blocks. Evaluating $\mathbf{L}_{\mathrm{norm}}$ entrywise separates each block's per-step boundary escape fraction on the diagonal from its inter-block transition couplings off the diagonal:

$$(\mathbf{L}_{\mathrm{norm}})_{\alpha\alpha} = 1 - \frac{K_{\alpha\alpha}}{d_\alpha^{(\mathrm{int})}} = \frac{\sum_{\beta \neq \alpha} K_{\alpha\beta}}{d_\alpha^{(\mathrm{int})}}, \tag{2.110}$$

$$(\mathbf{L}_{\mathrm{norm}})_{\alpha\beta} = -\frac{K_{\alpha\beta}}{\sqrt{d_\alpha^{(\mathrm{int})} d_\beta^{(\mathrm{int})}}} \qquad (\alpha \neq \beta). \tag{2.111}$$

Across the full spectrum $0 = \mu_1 < \mu_2 \leq \cdots \leq \mu_M \leq 2$ of $\mathbf{L}_{\mathrm{norm}}$, the slowest non-trivial eigenvalue $\mu_2(\mathbf{L}_{\mathrm{norm}})$ sets the inter-basin escape horizon $\tau_{\mathrm{escape}} \sim \mu_2(\mathbf{L}_{\mathrm{norm}})^{-1}$ (Section 2.3 and Section 2.5).

When external boundary ports are included by replacing $(\mathbf{L}_\mathbf{K}, \mathbf{D}_\mathbf{K}^{(\mathrm{int})})$ with the open operators $(\mathbf{L}_{\mathbf{K},SS}, \mathbf{D}_\mathbf{K})$, evaluating the Rayleigh quotient on a single block indicator $\mathbf{e}_\alpha$ and on the uniform system state $\mathbf{1}_M$ yields the total open block conductance $\phi_\partial^{(\mathrm{tot})}(S_\alpha)$ and the collective subsystem leakage ratio:

$$\phi_\partial^{(\mathrm{tot})}(S_\alpha) := \frac{\mathbf{e}_\alpha^\top \mathbf{L}_{\mathbf{K},SS} \mathbf{e}_\alpha}{\mathbf{e}_\alpha^\top \mathbf{D}_\mathbf{K} \mathbf{e}_\alpha} = 1 - \frac{K_{\alpha\alpha}}{d_\alpha}, \tag{2.112}$$

$$\frac{\mathbf{1}_M^\top \mathbf{L}_{\mathbf{K},SS} \mathbf{1}_M}{\mathbf{1}_M^\top \mathbf{D}_\mathbf{K} \mathbf{1}_M} = \frac{|\partial S|}{\mathrm{vol}(S)}. \tag{2.113}$$

EXAMPLE 2.3 (Capacity Matrix and Capacity Laplacian on the Nine-Node Graph). Applying the matrix congruence $\mathscr{C}_{\mathbf{\Pi}}$ (2.80) under the partition $\mathbf{\Pi} = \mathrm{diag}(\mathbf{\Pi}_S, \mathbf{1}_3)$ of Example 2.2 (2.70) to the vertex-level operators of Example 2.1 (2.35)–(2.37) contracts the nine-node dumbbell graph ($|E(S)| = 7$, $|\partial S| = 2$, Figure 2.1) into its coarse-grained capacity network without dividing by $N_\alpha = 3$. Specifically, $\mathscr{C}_{\mathbf{\Pi}}$ bundles the two internal triangles $E(S_1)$ and $E(S_2)$ into $\mathbf{K}_\Omega$, the single bridge cut $\{3,4\}$ into $\mathbf{K}_\partial^{(\mathrm{int})}$, the bath triangle $\{7,8,9\}$ into $\mathbf{K}_{\bar{S}} = (6)$, and the two external boundary cut edges $\{1,7\}$ and $\{6,8\}$ into $\mathbf{K}_\partial^{(\mathrm{ext})} = (1,1)$:

$$\mathbf{K}_S = \underbrace{\begin{pmatrix} 6 & 0 \\ 0 & 6 \end{pmatrix}}_{\mathbf{K}_\Omega} + \underbrace{\begin{pmatrix} 0 & 1 \\ 1 & 0 \end{pmatrix}}_{\mathbf{K}_\partial^{(\mathrm{int})}} = \begin{pmatrix} 6 & 1 \\ 1 & 6 \end{pmatrix}, \tag{2.114}$$

$$\mathbf{K} = \left(\begin{array}{cc|c} 6 & 1 & 1 \\ 1 & 6 & 1 \\ \hline 1 & 1 & 6 \end{array}\right). \tag{2.115}$$

Projecting the vertex degrees via (2.93)–(2.96) gives internal degree matrix $\mathbf{D}_{\mathbf{K}}^{(\mathrm{int})} = \mathrm{diag}(7,7)$, boundary degree matrix $\mathbf{D}_{\mathbf{K}}^{(\mathrm{ext})} = \mathrm{diag}(1,1)$, and total degree matrix $\mathbf{D}_{\mathbf{K}} = \mathrm{diag}(8,8)$, with $d_\alpha = 8$ and trace $\mathrm{Tr}(\mathbf{D}_{\mathbf{K}}) = 16$ matching $\mathscr{Q}_{\mathrm{total}}$. Subtracting $\mathbf{K}_S$ and normalising by $\mathbf{D}_{\mathbf{K}}^{(\mathrm{int})}$ yields the isolated, open, and normalised capacity Laplacians:

$$\mathbf{L}_{\mathbf{K}} = \begin{pmatrix} 1 & -1 \\ -1 & 1 \end{pmatrix}, \tag{2.116}$$

$$\mathbf{L}_{\mathbf{K},SS} = \begin{pmatrix} 2 & -1 \\ -1 & 2 \end{pmatrix}, \tag{2.117}$$

$$\mathbf{L}_{\mathrm{norm}} = \frac{1}{7}\begin{pmatrix} 1 & -1 \\ -1 & 1 \end{pmatrix}. \tag{2.118}$$

From these contracted operators, each internal triangle has diagonal capacity $K_{\alpha\alpha} = 6$ links ($\alpha \in \{1,2\}$, $|E(S_\alpha)| = 3$ edges) and the bridge has $K_{12} = 1$ link, giving the coarse-graining depth, spectral relaxation eigenvalues ($\mu_1 = 0$), and open leakage ratios:

$$I_{\alpha\alpha} = \ln K_{\alpha\alpha} = \ln 6 \approx 1.79\,\mathrm{nats}, \tag{2.119}$$

$$\mu_2(\mathbf{L}_{\mathrm{norm}}) = \frac{\lambda_2(\mathbf{L}_{\mathbf{K}})}{d_\alpha^{(\mathrm{int})}} = \frac{2}{7}, \tag{2.120}$$

$$\phi_\partial^{(\mathrm{tot})}(S_\alpha) = 1 - \frac{K_{\alpha\alpha}}{d_\alpha} = \frac{1}{4} = 2\frac{|\partial S|}{\mathrm{vol}(S)}. \tag{2.121}$$

Although the internal capacity $K_{\alpha\alpha} = 6$ cancels out of both $\mathbf{L}_{\mathbf{K}}$ and $\mathbf{L}_{\mathbf{K},SS}$, it enters the internal degree mass $\mathbf{D}_{\mathbf{K}}^{(\mathrm{int})}$ to suppress the inter-lobe relaxation eigenvalue from $\lambda_2(\mathbf{L}_{\mathbf{K}}) = 2$ to $\mu_2(\mathbf{L}_{\mathrm{norm}}) = 2/7$, while in the open degree mass $\mathbf{D}_{\mathbf{K}}$ it bounds the total open lobe conductance $\phi_\partial^{(\mathrm{tot})}(S_\alpha) = 1/4$ and collective subsystem leakage $|\partial S|/\mathrm{vol}(S) = 1/8$. ♢

2.3 CONSERVATION-CONGRUENT ENCODINGS

The partition structure of $\mathbf{\Pi}_S \in \{0,1\}^{N\times M}$—binary membership, exhaustive non-overlapping row sums, and block-diagonality (2.50)—narrows all linear mappings down to the Stirling partition count $S(N,M) \sim M^N/M!$ of candidate vertex partitions. Yet almost all candidate partitions are physically *inadmissible* once coupled to the substrate adjacency $\mathbf{A}_{SS}$. Evaluating the generalised Rayleigh quotient (2.108) on a block indicator $\boldsymbol{\pi}_\alpha = \mathbf{\Pi}_S \mathbf{e}_\alpha$ gives the exact fraction of block α's internal relational endpoints that exit across its inter-register boundary cut, defining its *boundary conductance* $\phi_\partial(S_\alpha)$:

$$\begin{aligned}\phi_\partial(S_\alpha) &:= \frac{\boldsymbol{\pi}_\alpha^{\mathsf{T}} \mathbf{L}_{SS}^{(\mathrm{int})} \boldsymbol{\pi}_\alpha}{\boldsymbol{\pi}_\alpha^{\mathsf{T}} \mathbf{D}_S^{(\mathrm{int})} \boldsymbol{\pi}_\alpha} = \frac{|E(S_\alpha, S\setminus S_\alpha)|}{\mathrm{vol}_{\mathrm{int}}(S_\alpha)} \\ &= \frac{\sum_{\beta\neq\alpha} K_{\alpha\beta}}{d_\alpha^{(\mathrm{int})}} = 1 - \frac{K_{\alpha\alpha}}{d_\alpha^{(\mathrm{int})}} = (\mathbf{L}_{\mathrm{norm}})_{\alpha\alpha}.\end{aligned} \tag{2.122}$$

Out of all $d_\alpha^{(\mathrm{int})}$ internal edge endpoints incident to S_α, a fraction $K_{\alpha\alpha}/d_\alpha^{(\mathrm{int})}$ recirculates internally within S_α, while the complementary fraction $\phi_\partial(S_\alpha) \in [0,1]$ crosses into peer registers $S\setminus S_\alpha$. In an open subsystem, replacing $(\mathbf{L}_{SS}^{(\mathrm{int})}, \mathbf{D}_S^{(\mathrm{int})})$ with the open operators $(\mathbf{L}_{SS}, \mathbf{D}_S)$ adds external port leakage $d_\alpha^{(\mathrm{ext})}/d_\alpha$ into $\bar{S}$ via $\phi_\partial^{(\mathrm{tot})}(S_\alpha)$ in (2.112). If a candidate partition cuts across dense couplings ($\phi_\partial(S_\alpha) \sim 1$) or groups disconnected vertices ($K_{\alpha\alpha} = 0$), any state prepared in the coarse-grained subspace $\mathrm{im}(\mathbf{P}_{\mathbf{\Pi}})$ escapes immediately into the unresolved residual $\mathrm{im}(\mathbf{Q}_{\mathbf{\Pi}})$.

2.3.1 *Admissible Mappings and Axioms I–III*

DEFINITION 2.1 (Admissible Assignment and Conservation-Congruent Encoding). A candidate partition $\mathbf{\Pi} = \mathrm{diag}(\mathbf{\Pi}_S, \mathbf{\Pi}_{\bar{S}})$ is *admissible*—and each diagonal entry $K_{\alpha\alpha}$ of $\mathbf{K}_\Omega$, together with its induced subgraph $G[S_\alpha]$, constitutes a *Conservation-Congruent Encoding* (CCE) coupled across boundary cuts $K_{\alpha\beta}$ ($\alpha \neq \beta$) on $G_{\mathbf{K}}$—if and only if it satisfies three foundational axioms:

First, *Axiom I (Topological Resolvability)* requires that distinct blocks occupy disjoint vertex subsets and that each induced subgraph $G[S_\alpha] = (S_\alpha, E(S_\alpha))$ form a single connected component with non-empty internal edge support ($N_\alpha \geq 2$ on a loopless graph), characterised by strictly positive normalised internal algebraic connectivity $\gamma_{\mathrm{int}}(S_\alpha)$ [57]:

$$S_\alpha \cap S_\beta = \emptyset \qquad (\alpha \neq \beta), \tag{2.123}$$

$$\gamma_{\mathrm{int}}(S_\alpha) := \mu_2\big(\mathbf{L}_{\mathrm{norm}}(G[S_\alpha])\big) > 0, \tag{2.124}$$

$$K_{\alpha\alpha} = 2|E(S_\alpha)| \geq 2(N_\alpha - 1) \geq 2. \tag{2.125}$$

Second, *Axiom II (Structural Persistence)* requires that internal connectivity $\gamma_{\mathrm{int}}(S_\alpha)$ across $G[S_\alpha]$ strictly exceed boundary cut conductance $\phi_\partial(S_\alpha)$ (2.122),

and defines for every block with $\phi_\partial(S_\alpha) > 0$ the dimensionless *Spectral Persistence Ratio* $\Xi(S_\alpha)$:

$$\gamma_{\text{int}}(S_\alpha) > \phi_\partial(S_\alpha) \qquad \forall \alpha \in \{1, \dots, M\}, \tag{2.126}$$

$$\Xi(S_\alpha) := \frac{\gamma_{\text{int}}(S_\alpha)}{\phi_\partial(S_\alpha)} > 1 \qquad \big(\phi_\partial(S_\alpha) > 0\big), \tag{2.127}$$

paired in open substrates with external persistence $\lambda_2(\mathbf{L}_{SS}) > \lambda_1(\mathbf{L}_{SS})$ (Section 2.1.2), and achieving exponential barrier isolation in the strong-persistence regime where $\Xi(S_\alpha) \gg 1$ and $\lambda_2(\mathbf{L}_{SS}) \gg \lambda_1(\mathbf{L}_{SS})$.

Third, *Axiom III (Conservation Congruence)* requires that the assignment be exhaustive and non-overlapping ($\mathbf{\Pi}_S \mathbf{1}_M = \mathbf{1}_S$, $\mathbf{\Pi}_{\bar{S}} \mathbf{1}_{M_{\bar{S}}} = \mathbf{1}_{\bar{S}}$) and contract the graph adjacency congruently via (2.83), yielding exact bilinear edge conservation across internal and boundary sectors:

$$\frac{1}{2} \mathbf{1}_M^{\mathsf{T}} \mathbf{K}_S \mathbf{1}_M = \frac{1}{2} \operatorname{Tr}(\mathbf{K}_\Omega) + \sum_{\alpha<\beta} K_{\alpha\beta} = \frac{1}{2} \sum_{\alpha=1}^{M} K_{\alpha\alpha} + \sum_{\alpha<\beta} K_{\alpha\beta} = |E(S)|, \tag{2.128}$$

$$\mathbf{1}_{M_{\bar{S}}}^{\mathsf{T}} \mathbf{K}_\partial^{(\text{ext})} \mathbf{1}_M = \operatorname{Tr}\big(\mathbf{D}_{\mathbf{K}}^{(\text{ext})}\big) = |\partial S|. \tag{2.129}$$

Each axiom in Definition 2.1 enforces an indispensable physical requirement. Under Axiom I, if $G[S_\alpha]$ were disconnected, its isolated normalised Laplacian would possess multiple independent zero modes, preventing perturbations from equilibrating across the block. Under Axiom II, on the capacity graph $G_{\mathbf{K}}$ over $\{1, \dots, M\}$, the discrete Cheeger inequality for $\mathbf{L}_{\text{norm}}$ (2.108) bounds the slowest non-zero inter-basin eigenvalue $\mu_2(\mathbf{L}_{\text{norm}})$ in terms of the network Cheeger constant $h_{\mathbf{K}}$ (and $\phi_\partial(S_\alpha)$ whenever $2d_\alpha^{(\text{int})} \le \text{vol}_{\text{int}}(S)$) [27, 31]:

$$\frac{1}{2} h_{\mathbf{K}}^2 \le \mu_2(\mathbf{L}_{\text{norm}}) \le 2h_{\mathbf{K}} \le 2\phi_\partial(S_\alpha), \tag{2.130}$$

$$h_{\mathbf{K}} := \min_{\varnothing \subsetneq A \subsetneq \{1,\dots,M\}} \frac{K(A, \bar{A})}{\min\{\text{vol}_{\text{int}}(A), \text{vol}_{\text{int}}(\bar{A})\}}, \tag{2.131}$$

$$K(A, \bar{A}) := \sum_{\alpha \in A} \sum_{\beta \in \bar{A}} K_{\alpha\beta}, \tag{2.132}$$

where $\bar{A} := \{1, \dots, M\} \setminus A$ denotes the complement of A in $\{1, \dots, M\}$. Because $\gamma_{\text{int}}(S_\alpha) \le 2$, condition (2.127) enforces strict diagonal dominance of $\mathbf{K}$ with $\phi_\partial(S_\alpha) \ll 1$. In the decoupled limit $\mathbf{K}_\partial = \mathbf{0}$, the M blocks possess M exact zero eigenvalues spanned by $\text{im}(\mathbf{P}_{\mathbf{\Pi}})$ and separated from unresolved intra-block modes in $\text{im}(\mathbf{Q}_{\mathbf{\Pi}})$ by $\gamma_{\text{int}}(S_\alpha) > 0$. When weak boundary cuts are present, invariant-subspace perturbation theory (the Davis–Kahan sin Θ theorem [41]) keeps $\text{im}(\mathbf{P}_{\mathbf{\Pi}})$ aligned with the slow M-dimensional invariant eigenspace up to $\mathcal{O}(\Xi^{-1}) \ll 1$, separating the fast intra-block mixing step

count $N_{\mathrm{relax}}^{(\alpha)}$ from the slow inter-block escape step count $N_{\mathrm{escape}}^{(\alpha)}$ across an operational step window $N_{\mathrm{op}}^{(\alpha)}$:

$$N_{\mathrm{relax}}^{(\alpha)} \sim \frac{1}{\gamma_{\mathrm{int}}(S_\alpha)} \ll N_{\mathrm{op}}^{(\alpha)} \ll N_{\mathrm{escape}}^{(\alpha)} \sim \frac{1}{\phi_\partial(S_\alpha)}, \tag{2.133}$$

$$\frac{N_{\mathrm{escape}}^{(\alpha)}}{N_{\mathrm{relax}}^{(\alpha)}} = \Xi(S_\alpha) \gg 1. \tag{2.134}$$

Under Axiom III, every edge in $E(S)$ and ∂S belongs to a unique induced internal edge set $E(S_\alpha)$, inter-register cut $E(S_\alpha, S_\beta)$ ($\alpha < \beta$), or external boundary cut $E(\bar{S}_\mu, S_\alpha)$, so summing twice (2.128) and (2.129) recovers the exact subsystem degree volume $\mathrm{Tr}(\mathbf{D}_\mathbf{K}) = \mathrm{vol}(S)$ (2.100).

Together, Axioms I–III characterise physical information on the capacity network in natural units (*nats*) by applying the natural logarithm directly to the link entries of $\mathbf{K}_S$, yielding two parameter-free invariants across the M resolvable blocks. First, because Axiom I guarantees $K_{\alpha\alpha} \geq 2$ (2.125) so that every diagonal coarse-graining depth $I_{\alpha\alpha} = \ln K_{\alpha\alpha}$ (2.92) satisfies $I_{\alpha\alpha} \geq \ln 2 > 0$ and is finite, the preserved internal capacities of Axiom III sum to the preserved structural capacity I_{rev} (1.34), whose block summands correspond to the microcanonical Boltzmann entropy $S_{\mathrm{th}}(\alpha)$ in thermal substrates:

$$I_{\mathrm{rev}} := \sum_{\alpha=1}^{M} I_{\alpha\alpha} = \sum_{\alpha=1}^{M} \ln K_{\alpha\alpha} \geq M \ln 2. \tag{2.135}$$

Second, for any coupled pair of blocks ($K_{\alpha\beta} \geq 1$), the diagonal-to-cut dominance of Axiom II defines the pairwise logarithmic barrier isolation depth $\Delta I_{\mathrm{barrier},\alpha\to\beta}$ (abbreviated $\Delta I_{\mathrm{barrier},\alpha\beta}$ for symmetric basins) separating CCE α from CCE β:

$$\Delta I_{\mathrm{barrier},\alpha\to\beta} := \ln\left(\frac{K_{\alpha\alpha}}{K_{\alpha\beta}}\right), \tag{2.136}$$

$$\Delta I_{\mathrm{barrier},\alpha\to\beta} - \Delta I_{\mathrm{barrier},\beta\to\alpha} = \ln\left(\frac{K_{\alpha\alpha}}{K_{\beta\beta}}\right) = I_{\alpha\alpha} - I_{\beta\beta}. \tag{2.137}$$

Under an unbiased single-step selection among all d_α link endpoints incident to S_α, $K_{\alpha\alpha}$ remain inside S_α while only $K_{\alpha\beta}$ cross into register $\beta \neq \alpha$, so $\Delta I_{\mathrm{barrier},\alpha\to\beta}$ exponentially suppresses the per-step inter-register transition fraction $T_{\alpha\to\beta}$:

$$T_{\alpha\to\beta} := (\mathbf{D}_\mathbf{K}^{-1}\mathbf{K})_{\alpha\beta} = \frac{K_{\alpha\beta}}{d_\alpha} \approx \frac{K_{\alpha\beta}}{K_{\alpha\alpha}} = e^{-\Delta I_{\mathrm{barrier},\alpha\to\beta}} \qquad (\alpha \neq \beta). \tag{2.138}$$

Whenever a transition crosses one of the $K_{\alpha\beta}$ cut channels into S_β and mixes across all $K_{\beta\beta}$ internal link endpoints over $N_{\mathrm{op}}^{(\beta)} \gg N_{\mathrm{relax}}^{(\beta)}$, many-to-one coarse-graining erases which cut edge mediated entry. When adjacent CCEs have unequal internal capacities ($K_{\alpha\alpha} \neq K_{\beta\beta}$), the depth difference $I_{\alpha\alpha} - I_{\beta\beta}$ in (2.137) biases transitions towards larger basins, grounding retrodictive irreversibility and dissipative relaxation (Section 2.5).

EXAMPLE 2.4 (Admissible versus Inadmissible Assignments on the Six-Node Dumbbell Graph). On the six-node dumbbell graph $G[S]$ of Examples 2.2 and 2.3 ($|S| = 6$, $|E(S)| = 7$, with $\mathbf{A}_{SS}$ and $\mathbf{L}_{SS}^{(\mathrm{int})}$ given in (2.35)), compare the bottleneck-aligned assignment $\mathbf{\Pi}_{\mathrm{adm}} \equiv \mathbf{\Pi}_S$ ($S_1 = \{1,2,3\}$, $S_2 = \{4,5,6\}$) against a cross-cut assignment $\mathbf{\Pi}_{\mathrm{inadm}}$ ($S_1' = \{1,2,4\}$, $S_2' = \{3,5,6\}$):

$$\mathbf{\Pi}_{\mathrm{inadm}} = \begin{pmatrix} 1 & 1 & 0 & 1 & 0 & 0 \\ 0 & 0 & 1 & 0 & 1 & 1 \end{pmatrix}^{\mathsf{T}}, \tag{2.139}$$

$$\mathbf{K}_{\mathrm{adm}} = \begin{pmatrix} 6 & 1 \\ 1 & 6 \end{pmatrix}, \tag{2.140}$$

$$\mathbf{K}_{\mathrm{inadm}} = \begin{pmatrix} 2 & 5 \\ 5 & 2 \end{pmatrix}. \tag{2.141}$$

Both partitions are exhaustive and non-overlapping, satisfying Axiom III (2.128)–(2.129) with matching degree matrices $\mathbf{D}_{\mathbf{K}}^{(\mathrm{int})} = \mathrm{diag}(7,7)$ and $\mathbf{D}_{\mathbf{K}} = \mathrm{diag}(8,8)$ (2.93)–(2.96). Under the bottleneck-aligned assignment $\mathbf{\Pi}_{\mathrm{adm}}$, each induced subgraph $G[S_\alpha] \cong K_3$ is a connected triangle that saturates the upper Cheeger bound (2.130):

$$\gamma_{\mathrm{int}}(S_\alpha) = \frac{3}{2} > 0, \tag{2.142}$$

$$\phi_\partial(S_\alpha) = \frac{1}{7} = h_{\mathbf{K}}, \tag{2.143}$$

$$\mu_2(\mathbf{L}_{\mathrm{norm}}) = \frac{2}{7} = 2h_{\mathbf{K}}. \tag{2.144}$$

Evaluating (2.127) and (2.135)–(2.136) across the $M = 2$ blocks confirms that $\mathbf{\Pi}_{\mathrm{adm}}$ satisfies both Axiom I and Axiom II:

$$\Xi(S_\alpha) = \frac{21}{2} = 10.5 \gg 1, \tag{2.145}$$

$$I_{\alpha\alpha}(\mathbf{\Pi}_{\mathrm{adm}}) = \ln 6 \approx 1.79 \,\text{nats}, \tag{2.146}$$

$$\Delta I_{\mathrm{barrier},12}(\mathbf{\Pi}_{\mathrm{adm}}) = \ln 6 \approx 1.79 \,\text{nats}. \tag{2.147}$$

Under the cross-cut assignment $\mathbf{\Pi}_{\mathrm{inadm}}$, by contrast, vertex 4 is isolated from $\{1,2\}$ inside S_1' so each induced subgraph $G[S_\alpha'] \cong K_2 \sqcup K_1$ is disconnected with $\gamma_{\mathrm{int}}(S_\alpha') = 0$ and $\Xi(S_\alpha') = 0$ (violating Axiom I), while five edges cross the cut (violating Axiom II):

$$\phi_\partial(S_\alpha') = \frac{5}{7} \approx 0.71, \tag{2.148}$$

$$\mu_2(\mathbf{L}_{\mathrm{norm}}) = \frac{10}{7}, \tag{2.149}$$

$$\Delta I_{\mathrm{barrier},12}(\mathbf{\Pi}_{\mathrm{inadm}}) = \ln\!\left(\frac{2}{5}\right) \approx -0.92 \,\text{nats}. \tag{2.150}$$

A negative barrier isolation depth indicates that single-step escape across the cut outweighs internal recirculation, confirming that $\mathbf{\Pi}_{\mathrm{inadm}}$ supports no metastable coarse-grained blocks. ♢

2.3.2 *The Coarse-Graining Algebra and Multiscale Invariance*

Physical observation and modelling ascend across nested levels of resolution, from fundamental particles and atomic cores to macromolecular scaffolds, cosmological horizons, synthetic hardware, and neural circuits (Chapters 5–9). Let $\mathbf{\Pi}^{(1)} \in \{0,1\}^{N\times M_1}$ be an admissible assignment on $G[S]$ with capacity matrix $\mathbf{K}^{(1)} \in \mathbb{N}_0^{M_1\times M_1}$. When the M_1 level-1 CCEs are aggregated into $M_2 < M_1$ non-empty, mutually disjoint level-2 clusters $\{\mathscr{I}_\alpha\}_{\alpha=1}^{M_2}$ via a surjective binary coarsening matrix $\mathbf{P} \in \{0,1\}^{M_1\times M_2}$ ($P_{a\alpha} = 1$ if block $a \in \mathscr{I}_\alpha$ and 0 otherwise) satisfying row-sum normalisation $\mathbf{P}\mathbf{1}_{M_2} = \mathbf{1}_{M_1}$, the composite level-2 assignment and its row-sum closure follow by associative matrix multiplication:

$$\mathbf{\Pi}^{(2)} := \mathbf{\Pi}^{(1)}\mathbf{P} \in \{0,1\}^{N\times M_2}, \tag{2.151}$$

$$\mathbf{\Pi}^{(2)}\mathbf{1}_{M_2} = \mathbf{\Pi}^{(1)}\mathbf{P}\mathbf{1}_{M_2} = \mathbf{1}_S. \tag{2.152}$$

Across any chain of successive coarsenings $\mathbf{\Pi}^{(1)} \xrightarrow{\mathbf{P}_{1\to2}} \mathbf{\Pi}^{(2)} \xrightarrow{\mathbf{P}_{2\to3}} \mathbf{\Pi}^{(3)}$, the coarsening matrices multiply associatively ($\mathbf{P}_{1\to3} = \mathbf{P}_{1\to2}\mathbf{P}_{2\to3}$) across nested partitions of S.

THEOREM 2.2 (Multiscale Coarse-Graining and Cut Internalisation). *Let $\mathbf{\Pi}^{(1)} = \mathrm{diag}(\mathbf{\Pi}_S^{(1)}, \mathbf{\Pi}_{\bar{S}}^{(1)})$ be an admissible level-1 partition of $(S,\bar{S})$ with subsystem operator triple $(\mathbf{K}^{(1)}, \mathbf{D}_{\mathbf{K}}^{(1)}, \mathbf{L}_{\mathbf{K}}^{(1)})$, and let $\mathbf{P} = \mathrm{diag}(\mathbf{P}_S, \mathbf{P}_{\bar{S}})$ be any boundary-respecting surjective binary coarsening satisfying $\mathbf{P}_S\mathbf{1}_{M_2} = \mathbf{1}_{M_1}$ and $\mathbf{P}_{\bar{S}}\mathbf{1}_{M_{\bar{S},2}} = \mathbf{1}_{M_{\bar{S},1}}$. Under the congruence map $\mathscr{C}_{\mathbf{P}_S}(\cdot) := \mathbf{P}_S^{\mathsf{T}}(\cdot)\mathbf{P}_S$ (writing $\mathbf{P} \equiv \mathbf{P}_S$ on S), the level-2 operator triple contracts directly across scales without referring back to $\mathbf{A}_{SS}$:*

$$\mathbf{K}^{(2)} = \mathbf{P}^{\mathsf{T}}\mathbf{K}^{(1)}\mathbf{P}, \tag{2.153}$$

$$\mathbf{D}_{\mathbf{K}}^{(2)} = \mathbf{P}^{\mathsf{T}}\mathbf{D}_{\mathbf{K}}^{(1)}\mathbf{P}, \tag{2.154}$$

$$\mathbf{L}_{\mathbf{K}}^{(2)} = \mathbf{P}^{\mathsf{T}}\mathbf{L}_{\mathbf{K}}^{(1)}\mathbf{P}, \tag{2.155}$$

preserving exact combinatorial edge conservation across scales:

$$\frac{1}{2}\mathbf{1}_{M_2}^{\mathsf{T}}\mathbf{K}^{(2)}\mathbf{1}_{M_2} = \frac{1}{2}\mathbf{1}_{M_1}^{\mathsf{T}}\mathbf{K}^{(1)}\mathbf{1}_{M_1} = |E(S)|, \tag{2.156}$$

while contracting the open internal and external boundary sectors independently:

$$\mathbf{K}_S^{(2)} = \mathbf{P}_S^{\mathsf{T}}\mathbf{K}_S^{(1)}\mathbf{P}_S, \tag{2.157}$$

$$\mathbf{K}_\partial^{(\mathrm{ext},2)} = \mathbf{P}_{\bar{S}}^{\mathsf{T}}\mathbf{K}_\partial^{(\mathrm{ext},1)}\mathbf{P}_S. \tag{2.158}$$

Moreover, defining the diagonal cut-internalisation transfer operator $\mathscr{T}_{\mathbf{P}}$, the diagonal memory and hollow boundary-cut sectors of $\mathbf{K}^{(1)} = \mathbf{K}^{(1)}_{\Omega} + \mathbf{K}^{(1)}_{\partial}$ transform according to:

$$\mathscr{T}_{\mathbf{P}}\big(\mathbf{K}^{(1)}_{\partial}\big) := \operatorname{diag}\big(\mathbf{P}^{\mathsf{T}}\mathbf{K}^{(1)}_{\partial}\mathbf{P}\big), \tag{2.159}$$

$$\mathbf{K}^{(2)}_{\Omega} = \mathbf{P}^{\mathsf{T}}\mathbf{K}^{(1)}_{\Omega}\mathbf{P} + \mathscr{T}_{\mathbf{P}}\big(\mathbf{K}^{(1)}_{\partial}\big), \tag{2.160}$$

$$\mathbf{K}^{(2)}_{\partial} = \mathbf{P}^{\mathsf{T}}\mathbf{K}^{(1)}_{\partial}\mathbf{P} - \mathscr{T}_{\mathbf{P}}\big(\mathbf{K}^{(1)}_{\partial}\big), \tag{2.161}$$

evaluating entrywise on the diagonal and off-diagonal capacity entries ($\alpha \neq \beta$) to:

$$K^{(2)}_{\alpha\alpha} = \sum_{a\in\mathscr{I}_\alpha} K^{(1)}_{aa} + \sum_{\substack{a,b\in\mathscr{I}_\alpha \\ a\neq b}} K^{(1)}_{ab}, \tag{2.162}$$

$$K^{(2)}_{\alpha\beta} = \sum_{a\in\mathscr{I}_\alpha}\sum_{b\in\mathscr{I}_\beta} K^{(1)}_{ab}. \tag{2.163}$$

PROOF. Substituting $\mathbf{\Pi}^{(2)} = \mathbf{\Pi}^{(1)}\mathbf{P}$ (2.151) into the matrix congruence definitions (2.85), (2.86), (2.93), and (2.101) yields (2.153)–(2.155) and (2.157)–(2.158) by associativity of matrix multiplication. Row-sum normalisation $\mathbf{P}\mathbf{1}_{M_2} = \mathbf{1}_{M_1}$ implies $\mathbf{1}^{\mathsf{T}}_{M_2}\mathbf{P}^{\mathsf{T}} = \mathbf{1}^{\mathsf{T}}_{M_1}$, establishing (2.156) (and $\mathbf{1}^{\mathsf{T}}_{M_{\bar{S},2}}\mathbf{K}^{(\mathrm{ext},2)}_{\partial}\mathbf{1}_{M_2} = |\partial S|$). Finally, because distinct columns of $\mathbf{P}$ have disjoint support ($P_{a\alpha}P_{a\beta} = 0$ for $\alpha \neq \beta$), $\mathbf{P}^{\mathsf{T}}\mathbf{K}^{(1)}_{\Omega}\mathbf{P}$ is strictly diagonal. Extracting the diagonal and off-diagonal parts of $\mathbf{K}^{(2)} = \mathbf{P}^{\mathsf{T}}(\mathbf{K}^{(1)}_{\Omega} + \mathbf{K}^{(1)}_{\partial})\mathbf{P}$ yields (2.159)–(2.161), whose (α,α) and (α,β) $(\alpha \neq \beta)$ entries expand directly to (2.162)–(2.163). □

Physically, Theorem 2.2 shows that level-1 boundary cuts $K^{(1)}_{ab}$ $(a, b \in \mathscr{I}_\alpha, a \neq b)$ mediating inter-basin transitions under $\mathbf{\Pi}^{(1)}$ are internalised by $\mathscr{T}_{\mathbf{P}}$ into diagonal CCE memory under $\mathbf{\Pi}^{(2)}$, increasing each merged basin's coarse-graining depth $I^{(2)}_{\alpha\alpha}$ while reducing the resolved block count ($M_2 < M_1$), as illustrated in Examples 2.5 and 2.6. This single algebraic mechanism governs the consolidation of local degrees of freedom into continuous attractor basins (Section 2.5.2), cut internalisation and cooperative capacity gain during multi-system coupling (Section 3.4.1), and CCE encapsulation of interior quark and atomic core degrees of freedom (Section 5.1.2).

On the vertex space $\mathbb{R}^N$, because $\operatorname{im}(\mathbf{\Pi}^{(2)}) \subset \operatorname{im}(\mathbf{\Pi}^{(1)})$, the orthogonal projectors $\mathbf{P}_{\mathbf{\Pi}}$ and residuals $\mathbf{Q}_{\mathbf{\Pi}}$ (Section 2.2.1) form a commuting projector tower:

$$\mathbf{P}_{\mathbf{\Pi}^{(1)}}\mathbf{P}_{\mathbf{\Pi}^{(2)}} = \mathbf{P}_{\mathbf{\Pi}^{(2)}}\mathbf{P}_{\mathbf{\Pi}^{(1)}} = \mathbf{P}_{\mathbf{\Pi}^{(2)}}, \tag{2.164}$$

$$\Delta\mathbf{P}_{1\to2} := \mathbf{P}_{\mathbf{\Pi}^{(1)}} - \mathbf{P}_{\mathbf{\Pi}^{(2)}} = \mathbf{Q}_{\mathbf{\Pi}^{(2)}} - \mathbf{Q}_{\mathbf{\Pi}^{(1)}}. \tag{2.165}$$

Consequently, the difference operator $\Delta\mathbf{P}_{1\to2}$ in (2.165) is a symmetric, idempotent orthogonal projector of rank $M_1 - M_2$ that isolates the exact intra-cluster degrees of freedom resolved under $\mathbf{\Pi}^{(1)}$ but compressed into the unresolved residual $\mathbf{Q}_{\mathbf{\Pi}^{(2)}}$ under $\mathbf{\Pi}^{(2)}$—the operator subspace that generates untracked gravitational stress in Section 6.2.

Why do linear constructors such as $\mathbf{D_K}$ and $\mathbf{L_K}$ contract without correction in (2.154)–(2.155), whereas sector extraction in (2.160)–(2.161) and boundary elimination in (2.34) produce extra structural terms? Evaluating a general operation $\mathscr{O}$ after applying a $\mathbf{\Pi}$-induced linear coarse-graining map $\mathscr{C}$ need not agree with coarse-graining the output of $\mathscr{O}$, defining the *coarse-graining commutator*:

$$[\![\mathscr{O}, \mathscr{C}]\!](X) := \mathscr{O}\big(\mathscr{C}(X)\big) - \mathscr{C}\big(\mathscr{O}(X)\big). \tag{2.166}$$

In (2.166), the left slot specifies the operation or physical law $\mathscr{O}$ being coarse-grained, while the right slot specifies the $\mathbf{\Pi}$-built linear coarse-graining map $\mathscr{C}$ (such as $\mathscr{C}_{\mathbf{\Pi}}$, $\mathscr{C}_{\mathbf{P}}$, $\mathscr{C}_S$, or $\mathbf{P}_{\mathbf{\Pi}}$). Linear row-sum constructors such as degree formation and the Laplacian map $\mathscr{L}$ commute identically with $\mathscr{C}_{\mathbf{P}}$ ($[\![\mathscr{L}, \mathscr{C}_{\mathbf{P}}]\!] = \mathbf{o}$), whereas sector splits, products, and inversions generate exact residuals across unresolved modes.

LEMMA 2.3 (Coarse-Graining Commutator). *Let $\mathscr{O}$ be an operator and let $\mathscr{C}_1, \mathscr{C}_2$ be composable linear coarse-graining maps. Across scales, the commutator (2.166) obeys the multiscale telescoping identity:*

$$[\![\mathscr{O}, \mathscr{C}_2 \circ \mathscr{C}_1]\!](X) = [\![\mathscr{O}, \mathscr{C}_2]\!]\big(\mathscr{C}_1(X)\big) + \mathscr{C}_2\big([\![\mathscr{O}, \mathscr{C}_1]\!](X)\big). \tag{2.167}$$

Under any surjective binary coarsening $\mathbf{P} \in \{0,1\}^{M_1 \times M_2}$ ($\mathbf{P}\mathbf{1}_{M_2} = \mathbf{1}_{M_1}$) with $\mathrm{offdiag}(\mathbf{X}) := \mathbf{X} - \mathrm{diag}(\mathbf{X})$*, diagonal and off-diagonal extraction satisfy:*

$$[\![\mathrm{diag}, \mathscr{C}_{\mathbf{P}}]\!]\big(\mathbf{K}^{(1)}\big) = -[\![\mathrm{offdiag}, \mathscr{C}_{\mathbf{P}}]\!]\big(\mathbf{K}^{(1)}\big) = \mathscr{T}_{\mathbf{P}}\big(\mathbf{K}^{(1)}_{\partial}\big). \tag{2.168}$$

Define orthogonal compression $\mathscr{P}_{\mathbf{\Pi}}(\mathbf{X}) := \mathbf{P}_{\mathbf{\Pi}}\mathbf{X}\mathbf{P}_{\mathbf{\Pi}}$ on $\mathbb{R}^N$ ($\mathbf{\Pi}^{(2)} = \mathbf{\Pi}^{(1)}\mathbf{P}$) and the hollow co-membership matrix $\mathbf{E_P} := \mathbf{P}\mathbf{P}^{\mathsf{T}} - \mathbf{I}_{M_1}$. For every conformable $\mathbf{X}$, operator squaring satisfies:

$$[\![(\cdot)^2, \mathscr{P}_{\mathbf{\Pi}^{(2)}}]\!]\big(\mathscr{P}_{\mathbf{\Pi}^{(1)}}(\mathbf{X})\big) = -\mathbf{P}_{\mathbf{\Pi}^{(2)}}\mathbf{X}\,\Delta\mathbf{P}_{1\to 2}\,\mathbf{X}\mathbf{P}_{\mathbf{\Pi}^{(2)}}, \tag{2.169}$$

$$[\![(\cdot)^2, \mathscr{C}_{\mathbf{P}}]\!](\mathbf{X}) = \mathbf{P}^{\mathsf{T}}\mathbf{X}\mathbf{E_P}\mathbf{X}\mathbf{P}. \tag{2.170}$$

Finally, on $V = (S, \bar{S})$ with $\mathbf{L}_{\bar{S}\bar{S}} > \mathbf{o}$ and inclusion $\mathbf{\Pi}_0 = (\mathbf{I}_S, \mathbf{o})^{\mathsf{T}}$ (2.81), the screened Laplacian $\mathbf{L}_\varepsilon := \mathbf{L} + \varepsilon\mathbf{\Pi}_0\mathbf{\Pi}_0^{\mathsf{T}}$ with screening stiffness $\varepsilon > 0$ (in links*) is strictly positive-definite with Green's matrix $\mathbf{G}_\varepsilon := \mathbf{L}_\varepsilon^{-1}$, and matrix inversion across $\mathscr{C}_S$ satisfies for every $\varepsilon > 0$:*

$$[\![(\cdot)^{-1}, \mathscr{C}_S]\!](\mathbf{G}_\varepsilon) = -\mathbf{L}_{S\bar{S}}\mathbf{L}_{\bar{S}\bar{S}}^{-1}\mathbf{L}_{\bar{S}S} = -\mathbf{\Sigma}_{\mathrm{env}}. \tag{2.171}$$

PROOF. Adding and subtracting $\mathscr{C}_2(\mathscr{O}(\mathscr{C}_1(X)))$ in $[\![\mathscr{O}, \mathscr{C}_2 \circ \mathscr{C}_1]\!](X)$ and applying linearity of $\mathscr{C}_2$ yields (2.167), while (2.160)–(2.161) give (2.168). By the projector tower (2.164)–(2.165), $\mathscr{P}_{\mathbf{\Pi}^{(2)}}(\mathscr{P}_{\mathbf{\Pi}^{(1)}}(\mathbf{X})) = \mathscr{P}_{\mathbf{\Pi}^{(2)}}(\mathbf{X})$ and $\mathbf{P}_{\mathbf{\Pi}^{(2)}} - \mathbf{P}_{\mathbf{\Pi}^{(1)}} = -\Delta\mathbf{P}_{1\to 2}$, yielding (2.169). Because $\mathbf{P} \in \{0,1\}^{M_1 \times M_2}$ has disjoint columns and row sums $\mathbf{P}\mathbf{1}_{M_2} = \mathbf{1}_{M_1}$, $\mathbf{E_P} = \mathbf{P}\mathbf{P}^{\mathsf{T}} - \mathbf{I}_{M_1}$ has zero diagonal and unit entries on distinct intra-cluster pairs $a \neq b$ ($a, b \in \mathscr{I}_\alpha$). For any conformable $\mathbf{X}, \mathbf{Y}, \mathbf{P}'$, expanding $\mathbf{E_P}$ gives:

$$\big(\mathbf{P}^{\mathsf{T}}\mathbf{X}\mathbf{P}\big)\big(\mathbf{P}^{\mathsf{T}}\mathbf{Y}\mathbf{P}'\big) - \mathbf{P}^{\mathsf{T}}\mathbf{X}\mathbf{Y}\mathbf{P}' = \mathbf{P}^{\mathsf{T}}\mathbf{X}\mathbf{E_P}\mathbf{Y}\mathbf{P}', \tag{2.172}$$

which reduces to (2.170) at $\mathbf{Y} = \mathbf{X}$ and $\mathbf{P}' = \mathbf{P}$. Finally, since $\mathbf{L} \geq \mathbf{o}$ and $\mathbf{L}_{\bar{S}\bar{S}} > \mathbf{o}$ imply $\mathbf{L}_\varepsilon > \mathbf{o}$, block inversion of $\mathbf{G}_\varepsilon = \mathbf{L}_\varepsilon^{-1}$ gives:

$$[\![(\cdot)^{-1}, \mathscr{C}_S]\!](\mathbf{G}_\varepsilon) = \big(\mathbf{L}_{SS} + \varepsilon \mathbf{I}_S - \mathbf{\Sigma}_{\text{env}}\big) - \big(\mathbf{L}_{SS} + \varepsilon \mathbf{I}_S\big) = -\mathbf{\Sigma}_{\text{env}}, \tag{2.173}$$

where $\varepsilon \mathbf{I}_S$ cancels identically at every $\varepsilon > 0$, establishing (2.171). □

Together with the Poisson bracket $\{\cdot,\cdot\}$ governing reversible circulation inside $\mathbf{K}_\Omega$ and the symmetric metric bracket $(\cdot,\cdot)$ governing irreversible relaxation across $\mathbf{K}_\partial$ (Section 2.5.2), $[\![\mathscr{O}, \mathscr{C}]\!]$ completes the bracket algebra of the monograph by isolating structural residuals across changes of resolution. Applied to diagonal extraction, $[\![\text{diag}, \mathscr{C}_\mathbf{P}]\!]$ yields cut internalisation $\mathscr{T}_\mathbf{P}$ in (2.168), with $[\![\text{diag}, \mathscr{C}_{\mathbf{\Pi}_S}]\!](\mathbf{A}_{SS}) = \mathbf{K}_\Omega$ creating internal memory from a loopless graph. Applied to Green's inversion across ∂S, $-[\![(\cdot)^{-1}, \mathscr{C}_S]\!]$ recovers the Schur self-energy $\mathbf{\Sigma}_{\text{env}}$ of (2.33) across Chapters 3–5 and 9, while applied to quadratic curvature operators in Section 2.5.1 and Chapter 6, $[\![\text{Ric}, \mathscr{C}_\mathbf{P}]\!]$ and $[\![G_{\mu\nu}, \mathbf{P}_\mathbf{\Pi}]\!]$ generate positive discrete Ricci mass-focusing and untracked gravitational stress–energy $T_{\mu\nu}^{(\text{untracked})}$. Finally, while Axiom III holds automatically for every surjective binary $\mathbf{P}$, an admissible assignment $\mathbf{\Pi}^{(1)}$ coarsens to an *admissible* assignment $\mathbf{\Pi}^{(2)}$ (2.151) if and only if each cluster $\mathscr{I}_\alpha$ induces a connected subgraph on the level-1 capacity graph $G_{\mathbf{K}^{(1)}}$ (preserving Axiom I) and aligns with a higher-order spectral bottleneck of $\mathbf{L}_\mathbf{K}^{(1)}$ ($\Xi \gg 1$, preserving Axiom II).

EXAMPLE 2.5 (Multiscale Coarsening and Cut Internalisation). On the nine-node relational graph $G = (V, E)$ of Example 2.1 ($N_V = 9$, $N_S = 6$, $N_{\bar{S}} = 3$, $|E| = 12$), let $\mathbf{\Pi}^{(1)} \in \{0,1\}^{N_V \times 3}$ be the level-1 assignment resolving $M_1 = 3$ three-node CCEs $S_1 = \{1,2,3\}$, $S_2 = \{4,5,6\}$, and $\bar{S} = \{7,8,9\}$:

$$\mathbf{K}^{(1)} = \begin{pmatrix} 6 & 1 & 1 \\ 1 & 6 & 1 \\ 1 & 1 & 6 \end{pmatrix}, \tag{2.174}$$

$$\mathbf{L}_\mathbf{K}^{(1)} = \begin{pmatrix} 2 & -1 & -1 \\ -1 & 2 & -1 \\ -1 & -1 & 2 \end{pmatrix}. \tag{2.175}$$

Now introduce the coarsening matrix $\mathbf{P} \in \{0,1\}^{3\times 2}$ that merges the two subsystem lobes $\mathscr{I}_1 = \{1,2\}$ into the single six-node block $S = \{1,\dots,6\}$ while keeping the environment $\mathscr{I}_2 = \{3\}$ ($\bar{S}$) distinct:

$$\mathbf{P} = \begin{pmatrix} 1 & 0 \\ 1 & 0 \\ 0 & 1 \end{pmatrix}, \tag{2.176}$$

$$\mathbf{\Pi}^{(2)} = \mathbf{\Pi}^{(1)}\mathbf{P} = \begin{pmatrix} \mathbf{1}_6 & \mathbf{0}_6 \\ \mathbf{0}_3 & \mathbf{1}_3 \end{pmatrix}. \tag{2.177}$$

Without referencing $\mathbf{A}$, the congruence map (2.153)–(2.155) contracts the level-1 operators directly into their level-2 counterparts:

$$\mathbf{K}^{(2)} = \mathbf{P}^{\mathsf{T}}\mathbf{K}^{(1)}\mathbf{P} = \begin{pmatrix} 14 & 2 \\ 2 & 6 \end{pmatrix}, \tag{2.178}$$

$$\mathbf{L}_{\mathbf{K}}^{(2)} = \mathbf{P}^{\mathsf{T}}\mathbf{L}_{\mathbf{K}}^{(1)}\mathbf{P} = \begin{pmatrix} 2 & -2 \\ -2 & 2 \end{pmatrix}. \tag{2.179}$$

Evaluating the diagonal commutator (2.168) and sector transfer laws (2.160)–(2.161) separates the internalised bridge cut from the surviving external interface:

$$[\![\mathrm{diag}, \mathscr{C}_{\mathbf{P}}]\!]\big(\mathbf{K}^{(1)}\big) = \mathscr{T}_{\mathbf{P}}\big(\mathbf{K}_{\partial}^{(1)}\big) = \mathrm{diag}(2, 0), \tag{2.180}$$

$$\mathbf{K}_{\Omega}^{(2)} = \mathrm{diag}(12, 6) + \mathrm{diag}(2, 0) = \mathrm{diag}(14, 6), \tag{2.181}$$

$$\mathbf{K}_{\partial}^{(2)} = \begin{pmatrix} 0 & 2 \\ 2 & 0 \end{pmatrix}. \tag{2.182}$$

Simultaneously, the inter-level projector difference (2.165) isolates the rank-1 antisymmetric inter-lobe dipole mode absorbed into $\mathbf{Q}_{\mathbf{\Pi}^{(2)}}$:

$$\Delta\mathbf{P}_{1\to 2} = \frac{1}{6}\mathbf{d}_{12}\mathbf{d}_{12}^{\mathsf{T}}, \tag{2.183}$$

$$\mathbf{d}_{12} := (1, 1, 1, -1, -1, -1, 0, 0, 0)^{\mathsf{T}}. \tag{2.184}$$

This matrix congruence preserves the total edge count $|E| = 12$ while transferring the level-1 inter-lobe bridge cut $K_{12}^{(1)} + K_{21}^{(1)} = 2$ into level-2 diagonal memory $K_{11}^{(2)} = 14$, raising internal coarse-graining depth I_{11} from $\ln 6$ to $\ln 14$. ◊

2.4 THE CAPACITY LEDGER

While Axiom III guarantees that the linear sum of graph edges is conserved across every level of coarse-graining (2.156), any embedded physical system faces an inescapable structural trade-off: finite material substrates cannot simultaneously allocate unbounded relational degrees of freedom to maintaining internal CCE representations ($\mathbf{K}_{\Omega}$) and to interfacing across transition or environmental cuts ($\mathbf{K}_{\partial}$). The capacity decomposition (2.83) provides an exact, parameter-free accounting of this architectural trade-off.

2.4.1 *Frobenius Orthogonality and the Capacity Ceiling*

Within the subsystem capacity block $\mathbf{K}_S = \mathbf{K}_{\Omega} + \mathbf{K}_{\partial}^{(\mathrm{int})} \in \mathbb{N}_0^{M\times M}$ (2.86), the diagonal intra-basin memory matrix $\mathbf{K}_{\Omega}$ and the hollow inter-basin transition

cut matrix $\mathbf{K}_\partial^{(\mathrm{int})}$ have disjoint entrywise support on $\mathbb{R}^{M\times M}$ and are therefore strictly orthogonal under the Frobenius inner product:

$$\langle \mathbf{X}, \mathbf{Y}\rangle_F := \mathrm{Tr}\big(\mathbf{X}^\mathsf{T}\mathbf{Y}\big), \tag{2.185}$$

$$\big\langle \mathbf{K}_\Omega, \mathbf{K}_\partial^{(\mathrm{int})}\big\rangle_F = 0, \tag{2.186}$$

$$\|\mathbf{K}_S\|_F^2 = \|\mathbf{K}_\Omega\|_F^2 + \|\mathbf{K}_\partial^{(\mathrm{int})}\|_F^2. \tag{2.187}$$

Taking the Frobenius norms of the two orthogonal sectors defines the Euclidean internal memory load $\mathcal{Q}_\Omega$ and internal transition load $\mathcal{Q}_\partial^{(\mathrm{int})}$ (both in links):

$$\mathcal{Q}_\Omega := \|\mathbf{K}_\Omega\|_F = \sqrt{\sum_{\alpha=1}^{M} K_{\alpha\alpha}^2}, \tag{2.188}$$

$$\mathcal{Q}_\partial^{(\mathrm{int})} := \|\mathbf{K}_\partial^{(\mathrm{int})}\|_F = \sqrt{2\sum_{\alpha<\beta} K_{\alpha\beta}^2}. \tag{2.189}$$

Here $\mathcal{Q}_\Omega$ quantifies the Euclidean structural load committed to stabilising internal CCE memory registers, while $\mathcal{Q}_\partial^{(\mathrm{int})}$ quantifies the internal transition load coupling distinct registers within S.

For an open subsystem embedded in an environment $\bar{S}$ across the boundary cut ∂S, the rectangular off-diagonal block $\mathbf{K}_\partial^{(\mathrm{ext})} \in \mathbb{N}_0^{M_{\bar{S}}\times M}$ of the partitioned capacity matrix $\mathbf{K}$ (2.83) occupies a matrix sector disjoint from $\mathbf{K}_S$ and carries the external interface load $\mathcal{Q}_\partial^{(\mathrm{ext})}$. Combining the internal inter-basin transition cuts $\mathcal{Q}_\partial^{(\mathrm{int})}$ and the external environmental ports $\mathcal{Q}_\partial^{(\mathrm{ext})}$ in quadrature defines the total boundary cut load $\mathcal{Q}_\partial$, yielding the three-sector Pythagorean decomposition of the *allocated structural capacity* (henceforth *allocated capacity*) $\mathcal{Q}_{\mathrm{alloc}}$ (all in links):

$$\mathcal{Q}_\partial^{(\mathrm{ext})} := \|\mathbf{K}_\partial^{(\mathrm{ext})}\|_F, \tag{2.190}$$

$$\mathcal{Q}_\partial := \sqrt{(\mathcal{Q}_\partial^{(\mathrm{int})})^2 + (\mathcal{Q}_\partial^{(\mathrm{ext})})^2}, \tag{2.191}$$

$$\mathcal{Q}_{\mathrm{alloc}}^2 := \mathcal{Q}_\Omega^2 + \mathcal{Q}_\partial^2 = \mathcal{Q}_\Omega^2 + (\mathcal{Q}_\partial^{(\mathrm{int})})^2 + (\mathcal{Q}_\partial^{(\mathrm{ext})})^2. \tag{2.192}$$

While each Euclidean quantity $\mathcal{Q}_\Omega$, $\mathcal{Q}_\partial^{(\mathrm{int})}$, $\mathcal{Q}_\partial^{(\mathrm{ext})}$, $\mathcal{Q}_\partial$, and $\mathcal{Q}_{\mathrm{alloc}}$ depends on the chosen partition $\mathbf{\Pi}$, we suppress the explicit $(\mathbf{\Pi})$ argument for notational economy. When the subsystem is closed ($\partial S = \emptyset$), $\mathcal{Q}_\partial^{(\mathrm{ext})} = 0$ and $\mathcal{Q}_\partial$ reduces to the internal transition load $\mathcal{Q}_\partial^{(\mathrm{int})}$. Conversely, when a subsystem is coarse-grained as a single monolithic block ($M = 1$, as in the multi-system network of Chapter 3), $\mathcal{Q}_\partial^{(\mathrm{int})} = 0$ and $\mathcal{Q}_\partial$ reduces to the external port load $\mathcal{Q}_\partial^{(\mathrm{ext})}$. When the subsystem does not partition $\bar{S}$ ($M_{\bar{S}} = 1$), the row vector $\mathbf{K}_\partial^{(\mathrm{ext})}$ carries the external port degrees $d_\alpha^{(\mathrm{ext})}$, so $\mathcal{Q}_\partial^{(\mathrm{ext})}$ depends solely on the internal assignment $\mathbf{\Pi}_S$.

To make the capacity frontier strictly parameter-free on $G = (V, E)$, we define the *total relational capacity* $\mathcal{Q}_{\mathrm{total}}$ (in links) via the entrywise ℓ_1 matrix

norm as the partition-invariant relational capacity budget of the embedded subgraph S. By Combinatorial Conservation (Axiom III, (2.128)–(2.129)) and the graph-theoretic handshaking identity—since every internal edge in $E(S)$ contributes two incident endpoints within S and every boundary cut edge in ∂S contributes one incident endpoint within S—this linear budget equals the exact degree volume $\mathrm{vol}(S)$ of the subsystem:

$$\|\mathbf{X}\|_1 := \sum_{a,b} |X_{ab}|, \tag{2.193}$$

$$\mathcal{Q}_{\mathrm{total}}^{\max} := d_{\max}|S|, \tag{2.194}$$

$$\mathcal{Q}_{\mathrm{total}} := \|\mathbf{K}_S\|_1 + \|\mathbf{K}_\partial^{(\mathrm{ext})}\|_1 = 2|E(S)| + |\partial S| = \mathrm{vol}(S) \le \mathcal{Q}_{\mathrm{total}}^{\max}, \tag{2.195}$$

where $\mathrm{vol}(S)$ sums the vertex degrees d_i over $i \in S$ (2.100) and $\mathcal{Q}_{\mathrm{total}}^{\max}$ is the substrate valence ceiling in a network of maximum vertex degree $d_{\max}$.

THEOREM 2.4 (Orthogonal Capacity Ceiling and Strict Norm Gap). *For any partition $\mathbf{\Pi} = \mathrm{diag}(\mathbf{\Pi}_S, \mathbf{\Pi}_{\bar{S}})$ of $(S, \bar{S})$, the allocated capacity $\mathcal{Q}_{\mathrm{alloc}}$ is bounded universally by the partition-invariant total relational capacity $\mathcal{Q}_{\mathrm{total}} = \mathrm{vol}(S)$, and any plastic reconfiguration $\Delta\mathbf{K} := \mathbf{K}' - \mathbf{K}$ decomposes orthogonally across its diagonal memory and cut sectors:*

$$\mathcal{Q}_{\mathrm{alloc}}^2 = \mathcal{Q}_\Omega^2 + \mathcal{Q}_\partial^2 = \mathcal{Q}_\Omega^2 + (\mathcal{Q}_\partial^{(\mathrm{int})})^2 + (\mathcal{Q}_\partial^{(\mathrm{ext})})^2 \le \mathcal{Q}_{\mathrm{total}}^2, \tag{2.196}$$

$$\Delta\mathbf{K} = \Delta\mathbf{K}_\Omega + \Delta\mathbf{K}_\partial, \tag{2.197}$$

$$\|\Delta\mathbf{K}\|_F^2 = \|\Delta\mathbf{K}_\Omega\|_F^2 + \|\Delta\mathbf{K}_\partial\|_F^2. \tag{2.198}$$

Moreover, strict inequality $\mathcal{Q}_{\mathrm{alloc}} < \mathcal{Q}_{\mathrm{total}}$ holds if and only if at least two entries of $(\mathbf{K}_S, \mathbf{K}_\partial^{(\mathrm{ext})})$ are strictly positive—in particular, for every admissible partition (Definition 2.1) with $M \ge 2$, or with $M = 1$ and open boundary $|\partial S| > 0$.

PROOF. Collecting the $R := M^2 + M_{\bar{S}}M$ non-negative integer entries of $\mathbf{K}_S$ and $\mathbf{K}_\partial^{(\mathrm{ext})}$ into a single vector $\mathbf{q} = (q_1, \dots, q_R)^\mathsf{T} \in \mathbb{N}_0^R$, we have $\mathcal{Q}_{\mathrm{total}} = \|\mathbf{q}\|_1$ by (2.195) and $\mathcal{Q}_{\mathrm{alloc}}^2 = \|\mathbf{q}\|_2^2$ by (2.192), so their squared difference expands into cross-products of distinct entries:

$$\mathcal{Q}_{\mathrm{total}}^2 - \mathcal{Q}_{\mathrm{alloc}}^2 = \left(\sum_{r=1}^R q_r\right)^2 - \sum_{r=1}^R q_r^2 = \sum_{r \ne s} q_r q_s \ge 0. \tag{2.199}$$

Since $q_r \ge 0$ for all r, (2.199) establishes $\mathcal{Q}_{\mathrm{alloc}} \le \mathcal{Q}_{\mathrm{total}}$, with strict inequality $\mathcal{Q}_{\mathrm{alloc}} < \mathcal{Q}_{\mathrm{total}}$ if and only if at least two distinct entries satisfy $q_r, q_s \ge 1$. Under Axiom I (2.125), every block satisfies $K_{\alpha\alpha} \ge 2$, providing at least two positive diagonal entries whenever $M \ge 2$, and pairing $K_{11} \ge 2$ with at least one positive boundary entry in $\mathbf{K}_\partial^{(\mathrm{ext})}$ whenever $M = 1$ and $|\partial S| > 0$. Finally, because $\Delta\mathbf{K}_\Omega$ and $\Delta\mathbf{K}_\partial$ occupy disjoint matrix coordinates, $\langle \Delta\mathbf{K}_\Omega, \Delta\mathbf{K}_\partial \rangle_F = 0$, proving (2.198). □

Theorem 2.4 establishes the fundamental structural frontier of physical computation: within a finite relational substrate, dedicating relational capacity to

internal CCE storage ($\mathcal{Q}_\Omega$) strictly limits the channel capacity available for inter-basin transitions or external interfaces ($\mathcal{Q}_\partial$). Physically, whereas the linear ℓ_1 ceiling $\mathcal{Q}_{\text{total}}$ counts the total relational capacity budget of incident edge endpoints and is invariant under partitioning, the allocated capacity $\mathcal{Q}_{\text{alloc}}$ weights each block or cut quadratically in the Euclidean ℓ_2 Frobenius norm by its concentrated bundle capacity: concentrating many edges into a single monolithic register ($K_{\alpha\alpha}^2$) locks those degrees of freedom into mutually redundant internal stabilisers of a single block state, whereas distributing edges across multiple distinct registers and boundary cuts preserves independent cross-block pairings that can be differentiated or rewired. Saturation $\mathcal{Q}_{\text{alloc}} = \mathcal{Q}_{\text{total}}$ occurs only in the trivial degenerate limit where an isolated closed graph ($\partial S = \emptyset$) collapses into a single unpartitioned block ($M = 1$).

2.4.2 *Free Capacity and Structural Efficiency*

With the total relational capacity $\mathcal{Q}_{\text{total}}$ established in (2.195), the foundational numerator of agency is defined without free parameters from the capacity decomposition as the system's unallocated relational capacity, or *free capacity* (in links):

$$\begin{aligned}\mathcal{Q}_{\text{free}} &:= \mathcal{Q}_{\text{total}} - \mathcal{Q}_{\text{alloc}} = \mathcal{Q}_{\text{total}} - \sqrt{\mathcal{Q}_\Omega^2 + \mathcal{Q}_\partial^2} \\ &= \mathcal{Q}_{\text{total}} - \sqrt{\mathcal{Q}_\Omega^2 + (\mathcal{Q}_\partial^{(\text{int})})^2 + (\mathcal{Q}_\partial^{(\text{ext})})^2}.\end{aligned} \tag{2.200}$$

Geometrically, $\mathcal{Q}_{\text{free}}$ measures the radial gap between the allocated capacity vector $(\mathcal{Q}_\Omega, \mathcal{Q}_\partial)$ (of Euclidean norm $\mathcal{Q}_{\text{alloc}}$) and the invariant ℓ_1 capacity ceiling $\mathcal{Q}_{\text{total}}$. By Theorem 2.4, $\mathcal{Q}_{\text{free}} > 0$ for every admissible multi-basin or open partition, quantifying the free capacity of reconfigurable degrees of freedom available for active stability control, error correction, and learning without exceeding substrate limits. Normalising $\mathcal{Q}_{\text{free}}$ by the boundary cut load $\mathcal{Q}_\partial$ and internal CCE load $\mathcal{Q}_\Omega$ defines the dimensionless *structural intelligence* χ_{struct} and *structural consciousness* (internal model efficiency) κ_{struct} (both in links/link), linked by the discrete bridge identity:

$$\chi_{\text{struct}} := \frac{\mathcal{Q}_{\text{free}}}{\mathcal{Q}_\partial} = \frac{\mathcal{Q}_{\text{total}} - \sqrt{\mathcal{Q}_\Omega^2 + \mathcal{Q}_\partial^2}}{\mathcal{Q}_\partial}, \tag{2.201}$$

$$\kappa_{\text{struct}} := \frac{\mathcal{Q}_{\text{free}}}{\mathcal{Q}_\Omega} = \frac{\mathcal{Q}_{\text{total}} - \sqrt{\mathcal{Q}_\Omega^2 + \mathcal{Q}_\partial^2}}{\mathcal{Q}_\Omega}, \tag{2.202}$$

$$\chi_{\text{struct}} = \kappa_{\text{struct}} \frac{\mathcal{Q}_\Omega}{\mathcal{Q}_\partial}. \tag{2.203}$$

Equations (2.201)–(2.203) make the coupled trade-off across $\mathcal{Q}$ explicit: committing additional capacity to $\mathcal{Q}_\Omega$ or $\mathcal{Q}_\partial$ simultaneously contracts the numerator $\mathcal{Q}_{\text{free}}$ (2.200) while rescaling the denominator, showing that an embedded architecture achieves high structural intelligence χ_{struct} either through economical internal representation (high κ_{struct}) or by committing a larger

internal CCE load $\mathcal{Q}_\Omega$ to buffer boundary cut exposure $\mathcal{Q}_\partial$. Comparing the linear ℓ_1 budget $\mathcal{Q}_{\text{total}}$ against the Euclidean ℓ_2 Frobenius norm $\mathcal{Q}_{\text{alloc}}$ yields the static efficiency relations, Cauchy–Schwarz support bounds, and reconfiguration difference identity used throughout the remainder of this work.

LEMMA 2.5 (Capacity Norm and Efficiency Bounds). *Let $S \subseteq V$ be a subsystem with total relational capacity $\mathcal{Q}_{\text{total}} = \text{vol}(S) > 0$, positive internal memory load $\mathcal{Q}_\Omega = \|\mathbf{K}_\Omega\|_F > 0$, positive boundary cut load $\mathcal{Q}_\partial > 0$ (2.191), and positive free capacity $\mathcal{Q}_{\text{free}} = \mathcal{Q}_{\text{total}} - \mathcal{Q}_{\text{alloc}} > 0$ (all in* links*). Then:*

1. *Quadratic Trade-Off Curve, Joint Ceiling, and Capacity Shares: The structural efficiencies χ_{struct} and κ_{struct} (2.201)–(2.202) satisfy the reciprocal trade-off curve and symmetric joint ceiling:*

$$\frac{1}{\chi_{\text{struct}}^2} + \frac{1}{\kappa_{\text{struct}}^2} = \left(\frac{\mathcal{Q}_{\text{alloc}}}{\mathcal{Q}_{\text{free}}}\right)^2, \tag{2.204}$$

$$\min(\chi_{\text{struct}}, \kappa_{\text{struct}}) \le \sqrt{2}\,\frac{\mathcal{Q}_{\text{free}}}{\mathcal{Q}_{\text{alloc}}}, \tag{2.205}$$

with equality in (2.205) if and only if $\mathcal{Q}_\Omega = \mathcal{Q}_\partial$. Expressing $\mathcal{Q}_{\text{total}}$ through $\mathcal{Q}_{\text{free}}$ defines the dimensionless free-capacity share $\eta_{\text{free}}(\chi_{\text{struct}}, \kappa_{\text{struct}}) \in (0, 1)$:

$$\mathcal{Q}_{\text{total}} = \mathcal{Q}_{\text{free}}\left(1 + \sqrt{\chi_{\text{struct}}^{-2} + \kappa_{\text{struct}}^{-2}}\right), \tag{2.206}$$

$$\eta_{\text{free}}(\chi_{\text{struct}}, \kappa_{\text{struct}}) := \frac{\mathcal{Q}_{\text{free}}}{\mathcal{Q}_{\text{total}}} = \frac{1}{1 + \sqrt{\chi_{\text{struct}}^{-2} + \kappa_{\text{struct}}^{-2}}}, \tag{2.207}$$

and strictly bounds the boundary, internal memory, and total allocated shares of $\mathcal{Q}_{\text{total}}$:

$$\frac{\mathcal{Q}_\partial}{\mathcal{Q}_{\text{total}}} = \frac{1}{\chi_{\text{struct}} + \sqrt{1 + \chi_{\text{struct}}^2\,\kappa_{\text{struct}}^{-2}}} < \frac{1}{1 + \chi_{\text{struct}}}, \tag{2.208}$$

$$\frac{\mathcal{Q}_\Omega}{\mathcal{Q}_{\text{total}}} = \frac{1}{\kappa_{\text{struct}} + \sqrt{1 + \kappa_{\text{struct}}^2\,\chi_{\text{struct}}^{-2}}} < \frac{1}{1 + \kappa_{\text{struct}}}, \tag{2.209}$$

$$\frac{\mathcal{Q}_{\text{alloc}}}{\mathcal{Q}_{\text{total}}} = 1 - \eta_{\text{free}}(\chi_{\text{struct}}, \kappa_{\text{struct}}) < \frac{1}{\chi_{\text{struct}}} + \frac{1}{\kappa_{\text{struct}}}. \tag{2.210}$$

2. *Cauchy–Schwarz Support Bounds: Let S be partitioned into $M \ge 1$ internal CCE blocks with $m_\partial \ge 0$ non-zero external port entries in $\mathbf{K}_\partial^{(\text{ext})}$ and $m_{\text{cut}} \ge 1$ total non-zero boundary entries across $\mathbf{K}_\partial^{(\text{int})}$ and $\mathbf{K}_\partial^{(\text{ext})}$. Then:*

$$|\partial S| = \left\|\mathbf{K}_\partial^{(\text{ext})}\right\|_1 \le \sqrt{m_\partial}\,\mathcal{Q}_\partial^{(\text{ext})} \le \sqrt{m_\partial}\,\mathcal{Q}_\partial, \tag{2.211}$$

$$\mathcal{Q}_{\text{total}} \le \sqrt{M}\,\mathcal{Q}_\Omega + \sqrt{m_{\text{cut}}}\,\mathcal{Q}_\partial, \tag{2.212}$$

$$1 < \eta_{\text{free}}(\chi_{\text{struct}}, \kappa_{\text{struct}})^{-1} \le \frac{\sqrt{M}}{\kappa_{\text{struct}}} + \frac{\sqrt{m_{\text{cut}}}}{\chi_{\text{struct}}}. \tag{2.213}$$

In particular, when $M = 1$ and $m_{\text{cut}} = 1$, exact additivity $\mathcal{Q}_{\text{total}} = \mathcal{Q}_\Omega + \mathcal{Q}_\partial$ forces $\chi_{\text{struct}} < 1$ and $\kappa_{\text{struct}} < 1$.

3. *Orthogonal Reconfiguration Difference Identity: Consider any capacity reconfiguration at conserved $\mathcal{Q}_{\text{total}}$ across pairwise Frobenius-orthogonal internal, external, and newly activated coupling sectors, taking baseline sector norms $(\mathcal{Q}_{\text{int}}, \mathcal{Q}_{\text{ext}}, 0)$ of allocated capacity $\mathcal{Q}_{\text{alloc}}$ to $(\mathcal{Q}'_{\text{int}}, \mathcal{Q}'_{\text{ext}}, \mathcal{Q}_{\text{cpl}})$ of allocated capacity $\mathcal{Q}'_{\text{alloc}}$. Defining the signed internal and external quadratic reductions (in* links^2*) yields the exact difference identity:*

$$\Delta\mathcal{Q}^2_{\Omega,\text{cons}} := \mathcal{Q}^2_{\text{int}} - \left(\mathcal{Q}'_{\text{int}}\right)^2, \tag{2.214}$$

$$\Delta\mathcal{Q}^2_{\partial,\text{shed}} := \mathcal{Q}^2_{\text{ext}} - \left(\mathcal{Q}'_{\text{ext}}\right)^2, \tag{2.215}$$

$$\mathcal{Q}^2_{\text{alloc}} - \left(\mathcal{Q}'_{\text{alloc}}\right)^2 = \Delta\mathcal{Q}^2_{\Omega,\text{cons}} + \Delta\mathcal{Q}^2_{\partial,\text{shed}} - \mathcal{Q}^2_{\text{cpl}}, \tag{2.216}$$

so $\mathcal{Q}'_{\text{free}} > \mathcal{Q}_{\text{free}}$ holds if and only if $\mathcal{Q}^2_{\text{cpl}} < \Delta\mathcal{Q}^2_{\Omega,\text{cons}} + \Delta\mathcal{Q}^2_{\partial,\text{shed}}$.

PROOF. Inverting (2.201)–(2.202) expresses the committed loads through $\mathcal{Q}_{\text{free}}$, so dividing $\mathcal{Q}^2_\Omega + \mathcal{Q}^2_\partial = \mathcal{Q}^2_{\text{alloc}}$ (2.192) by $\mathcal{Q}^2_{\text{free}} > 0$ yields (2.204). Setting $c := \min(\chi_{\text{struct}}, \kappa_{\text{struct}}) > 0$ gives $\chi^{-2}_{\text{struct}} \le c^{-2}$ and $\kappa^{-2}_{\text{struct}} \le c^{-2}$, and summing both inequalities against (2.204) establishes (2.205), with equality if and only if $\chi_{\text{struct}} = \kappa_{\text{struct}}$, or equivalently $\mathcal{Q}_\Omega = \mathcal{Q}_\partial$. Substituting $\mathcal{Q}_{\text{alloc}} = \mathcal{Q}_{\text{free}}\sqrt{\chi^{-2}_{\text{struct}} + \kappa^{-2}_{\text{struct}}}$ from (2.204) into (2.200) yields (2.206)–(2.207). Dividing $\mathcal{Q}_\partial$ and $\mathcal{Q}_\Omega$ by (2.206) with $\kappa^{-2}_{\text{struct}} > 0$ and $\chi^{-2}_{\text{struct}} > 0$ gives (2.208)–(2.209). Because $\mathcal{Q}_\Omega > 0$ and $\mathcal{Q}_\partial > 0$, expanding squares gives $\mathcal{Q}_{\text{alloc}} < \mathcal{Q}_\Omega + \mathcal{Q}_\partial$, and combining this strict bound with $\mathcal{Q}_{\text{free}} < \mathcal{Q}_{\text{total}}$ proves (2.210):

$$\frac{\mathcal{Q}_{\text{alloc}}}{\mathcal{Q}_{\text{total}}} < \frac{\mathcal{Q}_{\text{alloc}}}{\mathcal{Q}_{\text{free}}} < \frac{\mathcal{Q}_\partial + \mathcal{Q}_\Omega}{\mathcal{Q}_{\text{free}}} = \frac{1}{\chi_{\text{struct}}} + \frac{1}{\kappa_{\text{struct}}}. \tag{2.217}$$

For Part 2, applying the Cauchy–Schwarz inequality $\|\mathbf{u}\|_1 = \langle \mathbf{1}_r, \mathbf{u}\rangle \le \sqrt{r}\,\|\mathbf{u}\|_2$ on $\mathbb{R}^r_{\ge 0}$ across the m_∂ active entries of $\mathbf{K}^{(\text{ext})}_\partial$ with $\mathcal{Q}^{(\text{ext})}_\partial \le \mathcal{Q}_\partial$ (2.191) yields (2.211), and applying it across the M diagonal entries of $\mathbf{K}_\Omega$ and m_{cut} active boundary entries in (2.195) gives (2.212). Dividing (2.212) by $\mathcal{Q}_{\text{free}} > 0$ via (2.206)–(2.207) establishes (2.213). At $M = 1$ and $m_{\text{cut}} = 1$, exact additivity $\mathcal{Q}_{\text{total}} = \mathcal{Q}_\Omega + \mathcal{Q}_\partial$ combined with $\mathcal{Q}_{\text{alloc}} > \mathcal{Q}_\Omega$ and $\mathcal{Q}_{\text{alloc}} > \mathcal{Q}_\partial$ forces $\mathcal{Q}_{\text{free}} < \mathcal{Q}_\partial$ and $\mathcal{Q}_{\text{free}} < \mathcal{Q}_\Omega$. For Part 3, Frobenius orthogonality gives $\mathcal{Q}^2_{\text{alloc}} = \mathcal{Q}^2_{\text{int}} + \mathcal{Q}^2_{\text{ext}}$ and $(\mathcal{Q}'_{\text{alloc}})^2 = (\mathcal{Q}'_{\text{int}})^2 + (\mathcal{Q}'_{\text{ext}})^2 + \mathcal{Q}^2_{\text{cpl}}$, whose difference substitutes (2.214)–(2.215) directly into (2.216). At conserved $\mathcal{Q}_{\text{total}}$, $\mathcal{Q}'_{\text{free}} > \mathcal{Q}_{\text{free}}$ holds if and only if $\mathcal{Q}'_{\text{alloc}} < \mathcal{Q}_{\text{alloc}}$, which is equivalent to positivity of (2.216). □

Isolating the M-register diagonal block in Part 2 of Lemma 2.5 separates single-register depth from system-level free capacity. Because $\mathbf{K}_S$ splits into $\mathbf{K}_\Omega$ and $\mathbf{K}^{(\text{int})}_\partial$ (2.86)–(2.88) with ℓ_1 sum $2|E(S)|$ (2.195), summing the M diag-

onal entries fixes $\mathrm{Tr}(\mathbf{K}_\Omega)$ and bounds $\mathcal{Q}_\Omega$ from below by Cauchy–Schwarz, capping $\mathcal{Q}_{\mathrm{free}}$ in (2.200):

$$\mathcal{Q}_\Omega^2 = \sum_{\alpha=1}^{M} K_{\alpha\alpha}^2 \geq \frac{\mathrm{Tr}(\mathbf{K}_\Omega)^2}{M} = \frac{1}{M}\Big(2|E(S)| - \big\|\mathbf{K}_\partial^{(\mathrm{int})}\big\|_1\Big)^2, \tag{2.218}$$

$$\mathcal{Q}_{\mathrm{free}} \leq \mathcal{Q}_{\mathrm{total}} - \frac{2|E(S)| - \big\|\mathbf{K}_\partial^{(\mathrm{int})}\big\|_1}{\sqrt{M}}, \tag{2.219}$$

$$\mathcal{Q}_{\mathrm{free}}\big|_{M=1} = 2|E(S)| + |\partial S| - \sqrt{4|E(S)|^2 + \mathcal{Q}_\partial^2} < |\partial S| \qquad (|\partial S| > 0). \tag{2.220}$$

Equality holds in (2.218) if and only if all M registers carry equal diagonal capacity $K_{\alpha\alpha}$, while (2.219) is strict whenever $\mathcal{Q}_\partial > 0$ since $\mathcal{Q}_{\mathrm{alloc}} > \mathcal{Q}_\Omega$. Merging all internal links into a single monolithic block ($M = 1$ with $\mathbf{K}_\partial^{(\mathrm{int})} = \mathbf{o}$) maximises passive single-well depth I_{11} at $K_{11} = 2|E(S)|$, yet (2.220) caps $\mathcal{Q}_{\mathrm{free}}$ strictly below $|\partial S|$, driving the free-capacity share η_{free} (2.207) and κ_{struct} (2.202) to zero as $|E(S)|$ grows at fixed boundary cut $|\partial S|$. Conversely, partitioning S across $M \gg 1$ registers suppresses $\mathcal{Q}_\Omega$ by $M^{-1/2}$ in (2.218) while keeping each register well-isolated ($K_{\alpha\beta} \ll K_{\alpha\alpha}$), releasing $\mathcal{Q}_{\mathrm{free}}$ alongside χ_{struct}, κ_{struct}, and η_{free} prior to the through-time trajectory metrics (χ_T, κ_T) developed in Chapter 3.

EXAMPLE 2.6 (Capacity Ledger across Partition Reconfigurations). On the nine-node relational graph $G = (V, E)$ of Examples 2.1 and 2.5, the six-node subsystem $S = \{1, \ldots, 6\}$ ($|E(S)| = 7$, $|\partial S| = 2$, $d_{\max} = 3$) satisfies (2.195) and (2.198) (for the reconfiguration $\Delta\mathbf{K}_S := \mathbf{K}_{\mathrm{adm}} - \mathbf{K}_{\mathrm{inadm}}$ of Example 2.4):

$$\mathcal{Q}_{\mathrm{total}} = 2|E(S)| + |\partial S| = 16 < \mathcal{Q}_{\mathrm{total}}^{\max} = 18, \tag{2.221}$$

$$\|\Delta\mathbf{K}_S\|_F^2 = \|\Delta\mathbf{K}_\Omega\|_F^2 + \|\Delta\mathbf{K}_\partial^{(\mathrm{int})}\|_F^2 = 32 + 32 = 64. \tag{2.222}$$

For the level-1 two-basin assignment $\mathbf{\Pi}^{(1)}$ of (2.114)–(2.115), internal load $\mathcal{Q}_\Omega^{(1)} = \sqrt{72}$ (≈ 8.49) and cut loads $\mathcal{Q}_\partial^{(\mathrm{int},1)} = \sqrt{2}$ and $\mathcal{Q}_\partial^{(\mathrm{ext},1)} = \sqrt{2}$ yield $\mathcal{Q}_\partial^{(1)} = 2$, so (2.192) and (2.200)–(2.201) give:

$$\mathcal{Q}_{\mathrm{alloc}}^{(1)} = \sqrt{72 + 4} = \sqrt{76} \approx 8.72, \tag{2.223}$$

$$\mathcal{Q}_{\mathrm{free}}^{(1)} = 16 - \sqrt{76} \approx 7.28, \tag{2.224}$$

$$\chi_{\mathrm{struct}}^{(1)} = \frac{16 - \sqrt{76}}{2} \approx 3.64, \tag{2.225}$$

with structural consciousness $\kappa_{\mathrm{struct}}^{(1)} \approx 0.86$ (2.202) and free-capacity share $\eta_{\mathrm{free}}^{(1)} \approx 0.46$ (2.207). Under the coarsened level-2 monolithic assignment $\mathbf{\Pi}^{(2)}$ of (2.178), where the scalar blocks $K_S^{(2)} = 14$ and $K_\partial^{(\mathrm{ext},2)} = 2$ give $\mathcal{Q}_\Omega^{(2)} = 14$, $\mathcal{Q}_\partial^{(\mathrm{int},2)} = 0$, and $\mathcal{Q}_\partial^{(2)} = 2$, the same capacity relations evaluate to:

$$\mathcal{Q}_{\mathrm{alloc}}^{(2)} = \sqrt{196 + 4} = \sqrt{200} \approx 14.14, \tag{2.226}$$

$$\mathcal{Q}_{\mathrm{free}}^{(2)} = 16 - \sqrt{200} \approx 1.86, \tag{2.227}$$

$$\chi_{\mathrm{struct}}^{(2)} = \frac{16 - \sqrt{200}}{2} \approx 0.93, \tag{2.228}$$

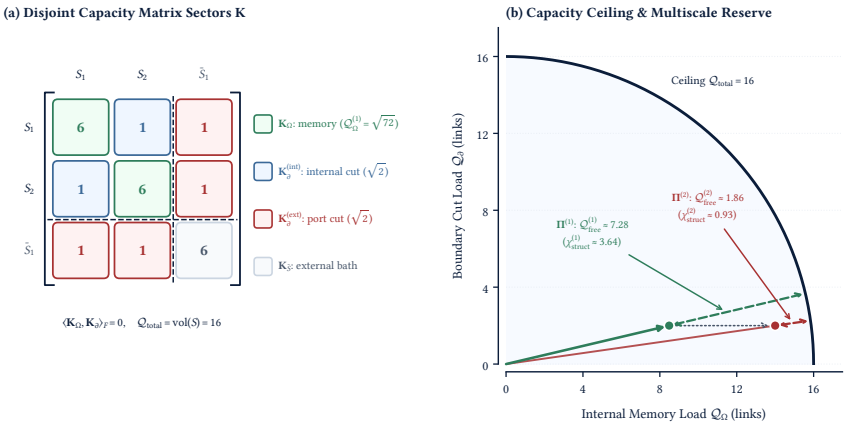


FIGURE 2.3: Frobenius-orthogonal Capacity Ledger and multiscale free-capacity compression on the nine-node dumbbell subsystem (degree volume $\mathcal{Q}_{\text{total}} = 16$ links, Theorem 2.4 and Example 2.6). *(a)* Disjoint entry-wise support of the partitioned capacity matrix $\mathbf{K}$ (2.115), separating diagonal intra-basin memory $\mathbf{K}_\Omega$ ($K_{\alpha\alpha} = 6$, teal) from hollow internal transition cuts $\mathbf{K}_\partial^{(\text{int})}$ ($K_{12} = 1$, light navy) and external boundary ports $\mathbf{K}_\partial^{(\text{ext})}$ ($K_{\partial,\alpha} = 1$, crimson) with vanishing Frobenius cross-products $\langle \mathbf{K}_\Omega, \mathbf{K}_\partial \rangle_F = 0$. *(b)* Euclidean capacity plane $(\mathcal{Q}_\Omega, \mathcal{Q}_\partial)$ bounded by the quarter-circle ceiling $\mathcal{Q}_\Omega^2 + \mathcal{Q}_\partial^2 \leq \mathcal{Q}_{\text{total}}^2$. The level-1 two-basin partition $\mathbf{\Pi}^{(1)}$ retains substantial radial free reserve $\mathcal{Q}_{\text{free}}^{(1)} \approx 7.28$ links ($\chi_{\text{struct}}^{(1)} \approx 3.64$, $\kappa_{\text{struct}}^{(1)} \approx 0.86$, teal), whereas monolithic level-2 coarsening $\mathbf{\Pi}^{(2)}$ shifts cut capacity into diagonal load ($\mathcal{Q}_{\text{alloc}}^{(2)} \approx 14.14$ links) and compresses $\mathcal{Q}_{\text{free}}^{(2)}$ to 1.86 links (crimson).

with structural consciousness $\kappa_{\text{struct}}^{(2)} \approx 0.13$ and free-capacity share $\eta_{\text{free}}^{(2)} \approx 0.12$ (2.207). Whereas $\mathbf{\Pi}^{(1)}$ saturates (2.218) across $M = 2$ balanced registers of capacity $K_{\alpha\alpha} = 6$, coarsening S into a single monolithic block ($M = 1$) raises single-block depth I_{11} from $\ln 6$ to $\ln 14$ (Example 2.5) only by concentrating all internal links into $K_S^{(2)} = 14$, inflating $\mathcal{Q}_{\text{alloc}}$ and compressing $\mathcal{Q}_{\text{free}}$ from 7.28 to $1.86 < |\partial S|$ in accordance with (2.220) (Figure 2.3). ♢

2.5 SPECTRAL DIMENSIONS AND EMERGENT DYNAMICS

On the relational graph $G = (V, E)$, vertices carry no spatial coordinates, edges carry no lengths, and no external clock parameter exists. Under an admissible partition $\mathbf{\Pi}$, the subsystem initially consists only of M unordered CCE registers coupled by the capacity matrix $\mathbf{K}$. Both the emergent coordinate geometry and the continuous equations of motion arise directly from this relational operator. First, the spectrum and second-order operator products of $\mathbf{K}$ and $\mathbf{L}_\mathbf{K}$ determine the coordinate embedding, effective dimension $d_s[\mathbf{\Pi}]$, resistance distance $\Omega_{\alpha\beta}$, emergent proper and relational time, and algebraic curvature of the coarse-grained state space (Section 2.5.1). Second, transporting state across those spectral coordinates along emergent time projects

the orthogonal split $\mathbf{K}_S = \mathbf{K}_\Omega + \mathbf{K}_\partial^{(\mathrm{int})}$ and the Kulkarni–Nomizu capacity-mobility tensor directly into continuous metriplectic dynamics (Section 2.5.2).

2.5.1 *Spectral Dimensions, Emergent Time, and Metric Geometry*

Throughout Section 2.5, we analyse the closed subsystem baseline where $\mathbf{D}_\mathbf{K}^{(\mathrm{ext})} = \mathbf{o}$, so $\mathbf{K} \equiv \mathbf{K}_S$, $\mathbf{D}_\mathbf{K} \equiv \mathbf{D}_\mathbf{K}^{(\mathrm{int})}$, and $\mathbf{L}_\mathbf{K} = \mathbf{D}_\mathbf{K} - \mathbf{K}$ in (2.101), before Chapter 3 restores environmental driving across ∂S. Because the block indices $\alpha \in \{1, \dots, M\}$ are arbitrary bookkeeping labels, relabelling the rows and columns of $\mathbf{K}$ by any permutation leaves the network unchanged, and index differences $|\alpha - \beta|$ carry no geometric meaning. For a candidate coordinate vector $\boldsymbol{\phi} \in \mathbb{R}^M$ with entries $\phi(\alpha)$ to order the CCEs according to their physical connectivity, registers coupled by a large boundary cut $K_{\alpha\beta}$ must receive nearby coordinates $\phi(\alpha) \approx \phi(\beta)$, confining large coordinate jumps to narrow bottlenecks. As established in (2.104), the total cut-weighted coordinate variation across $G_\mathbf{K}$ is measured by the coarse-grained Dirichlet energy $\boldsymbol{\phi}^\mathsf{T}\mathbf{L}_\mathbf{K}\boldsymbol{\phi}$.

Minimising $\boldsymbol{\phi}^\mathsf{T}\mathbf{L}_\mathbf{K}\boldsymbol{\phi}$ unconstrained is degenerate in two ways: scaling $\boldsymbol{\phi} \to \mathbf{o}$ trivially drives the variation to zero, and assigning the same constant value to every block via $\boldsymbol{\phi}_1 = (\operatorname{Tr}\mathbf{D}_\mathbf{K})^{-1/2}\mathbf{1}_M$ achieves $\boldsymbol{\phi}_1^\mathsf{T}\mathbf{L}_\mathbf{K}\boldsymbol{\phi}_1 = 0$ by collapsing all M CCEs onto a single point. Eliminating scale collapse requires normalising the degree-weighted variance $\boldsymbol{\phi}^\mathsf{T}\mathbf{D}_\mathbf{K}\boldsymbol{\phi} = 1$ so that each register is weighted by its degree volume d_α, while eliminating point collapse requires each successive coordinate axis $\boldsymbol{\phi}_k$ ($k = 2, \dots, M$) to be $\mathbf{D}_\mathbf{K}$-orthogonal to $\boldsymbol{\phi}_1$ and all preceding axes. By the Courant–Fischer min-max principle, the stationary directions of the Rayleigh quotient (2.108) under these constraints are governed by the generalised eigenvalue problem of $\mathbf{L}_\mathbf{K}$ relative to the degree mass matrix $\mathbf{D}_\mathbf{K}$:

$$\mathbf{L}_\mathbf{K}\boldsymbol{\phi}_k = \mu_k \mathbf{D}_\mathbf{K}\boldsymbol{\phi}_k, \tag{2.229}$$

$$\boldsymbol{\phi}_j^\mathsf{T}\mathbf{D}_\mathbf{K}\boldsymbol{\phi}_k = \delta_{jk}, \tag{2.230}$$

$$\mu_k = \frac{\boldsymbol{\phi}_k^\mathsf{T}\mathbf{L}_\mathbf{K}\boldsymbol{\phi}_k}{\boldsymbol{\phi}_k^\mathsf{T}\mathbf{D}_\mathbf{K}\boldsymbol{\phi}_k} = \frac{\frac{1}{2}\sum_{\alpha\neq\beta} K_{\alpha\beta}\big(\phi_k(\alpha) - \phi_k(\beta)\big)^2}{\sum_{\alpha=1}^M d_\alpha \phi_k(\alpha)^2}, \tag{2.231}$$

with eigenvalues $0 = \mu_1 < \mu_2 \leq \cdots \leq \mu_M \leq 2$ matching the spectrum of $\mathbf{L}_\mathrm{norm}$ in (2.109). Notice how the orthogonal sectors of $\mathbf{K}$ divide roles in (2.229)–(2.231): diagonal intra-basin memory $\mathbf{K}_\Omega$ cancels identically out of the Dirichlet numerator $\mathbf{L}_\mathbf{K} = \mathbf{D}_\partial^{(\mathrm{int})} - \mathbf{K}_\partial^{(\mathrm{int})}$, which depends solely on inter-register cuts $\mathbf{K}_\partial^{(\mathrm{int})}$, yet enters the degree-mass denominator $\mathbf{D}_\mathbf{K} = \mathbf{K}_\Omega + \mathbf{D}_\partial^{(\mathrm{int})}$ as local coarse-graining inertia weighting each register. The slowest non-trivial eigenvector $\boldsymbol{\phi}_2$ (the Fiedler mode) defines the coarsest principal coordinate axis across $G_\mathbf{K}$, and higher modes $k > 2$ resolve progressively finer orthogonal axes.

Retaining all $M-1$ non-trivial eigenvectors from (2.229) would trivially embed the M registers into $\mathbb{R}^{M-1}$ without isolating the effective dimensional-

ity of the coarse-grained state space. To calibrate the effective dimension d_s directly from the spectrum $\{\mu_k\}_{k=1}^{M}$, we examine how rapidly a localised state spreads across $G_{\mathbf{K}}$ under the heat kernel $e^{-s\mathbf{L}_{\mathrm{norm}}}$, where $s \geq 0$ denotes an auxiliary dimensionless spectral diffusion scale probing network topology (distinct from the emergent time parameter t calibrated below). In a geometry with d_s independent directions, diffusive spreading over scale s fills a region whose effective volume grows as $s^{d_s/2}$, causing the average return probability $P(s)$ of remaining at the initial register to decay inversely as $s^{-d_s/2}$. On a finite network ($M \gg 1$), this power-law scaling holds across the intermediate diffusion window $\mu_M^{-1} \ll s \ll \mu_2^{-1}$, after single-step discretisation transients ($s \lesssim \mu_M^{-1}$) have decayed yet before diffusion saturates the global bottleneck across all M registers ($s \gtrsim \mu_2^{-1}$, where $P(s) \to 1/M$). Across this window, the logarithmic decay slope of $P(s)$—equivalently, the Weyl cumulative eigenvalue count—calibrates the *spectral dimension* $d_s[\mathbf{\Pi}]$:

$$P(s) := \frac{1}{M}\,\mathrm{Tr}\big(e^{-s\mathbf{L}_{\mathrm{norm}}}\big) = \frac{1}{M}\sum_{k=1}^{M} e^{-\mu_k s} \sim s^{-d_s/2}, \tag{2.232}$$

$$d_s[\mathbf{\Pi}] := -2\frac{\mathrm{d}\ln P(s)}{\mathrm{d}\ln s}, \tag{2.233}$$

$$\big|\{k \geq 2 \,:\, \mu_k \leq \mu\}\big| \sim \mu^{d_s/2}. \tag{2.234}$$

Because $\mathbf{L}_{\mathrm{norm}}$ depends on the partition $\mathbf{\Pi}$, the spectral dimension $d_s[\mathbf{\Pi}]$ is a functional of the coarse-graining and substrate connectivity: while specialised connectivity networks can operate at $d_s = 1$ (linear chains and pipelines), $d_s = 2$ (planar circuits and membranes), or $d_s \gg 4$ (dense neural and relational graphs), for physical spacetime $d_s = 4$, comprising three spatial dimensions and one temporal dimension (Chapter 6).

Retaining the d_s slowest non-trivial eigenvectors constructs the spectral coordinate map $\mathbf{\Phi}$, completing a two-stage linear reduction from the coordinate-free vertex space to the spectral coordinate chart $\mathscr{M}_{\mathrm{spec}}$:

$$\mathbb{R}^N \xrightarrow{\ \mathbf{\Pi}\ } \mathbb{R}^M \xrightarrow{\ \mathbf{\Phi}\ } \mathscr{M}_{\mathrm{spec}} \cong \mathbb{R}^{d_s}, \tag{2.235}$$

$$\mathbf{\Phi} := [\boldsymbol{\phi}_2, \ldots, \boldsymbol{\phi}_{d_s+1}] \in \mathbb{R}^{M\times d_s}, \tag{2.236}$$

$$\mathbf{z}(\alpha) := \mathbf{\Phi}^{\mathsf{T}}\mathbf{e}_\alpha = \big(\phi_2(\alpha), \ldots, \phi_{d_s+1}(\alpha)\big)^{\mathsf{T}} \in \mathbb{R}^{d_s}. \tag{2.237}$$

On this coordinate chart, metric distance cannot be measured by shortest-path hop counts, which ignore cut widths and parallel pathways, because relational transport sums over all parallel paths weighted by their conductances $K_{\alpha\beta}$. Injecting a unit flux at register α and extracting it at register β via $\mathbf{L}_{\mathbf{K}}\mathbf{z}_S = \mathbf{e}_\alpha - \mathbf{e}_\beta$, inverted on the zero-sum subspace $\mathbf{1}_M^{\perp}$ by the Moore–Penrose pseudoinverse $\mathbf{L}_{\mathbf{K}}^{\dagger}$, produces a potential drop equal to the intrinsic Klein–Randić *resistance distance* $\Omega_{\alpha\beta}$ [85]. Because $\mathbf{e}_\alpha - \mathbf{e}_\beta$ is orthogonal

to span($\mathbf{1}_M$), $\Omega_{\alpha\beta}$ expands directly in the generalised eigenbasis $(\mu_k, \boldsymbol{\phi}_k)$ of (2.229):

$$\Omega_{\alpha\beta} := (\mathbf{e}_\alpha - \mathbf{e}_\beta)^{\mathsf{T}} \mathbf{L}_{\mathbf{K}}^{\dagger} (\mathbf{e}_\alpha - \mathbf{e}_\beta) = L^{\dagger}_{\mathbf{K},\alpha\alpha} + L^{\dagger}_{\mathbf{K},\beta\beta} - 2L^{\dagger}_{\mathbf{K},\alpha\beta}, \tag{2.238}$$

$$\Omega_{\alpha\beta} = \sum_{k=2}^{M} \mu_k^{-1} \big(\phi_k(\alpha) - \phi_k(\beta)\big)^2. \tag{2.239}$$

Equation (2.239) shows that $\Omega_{\alpha\beta}$ is the exact squared Euclidean distance in $\mu_k^{-1/2}$-scaled spectral coordinates, with $\mathrm{vol}(S)\,\Omega_{\alpha\beta}$ giving the random-walk commute time between registers α and β. Because higher modes ($k > d_s + 1$) are suppressed by μ_k^{-1}, truncating (2.239) to the d_s slowest modes expresses effective distance directly on $\mathbf{z}(\alpha)$, while in an open subsystem environmental port resistance enters analogously through the effective Schur-complement Laplacian $\mathbf{L}_{\mathrm{eff}}$ (2.34).

How these spectral axes partition across space and time—and how temporal duration is calibrated—depends on whether $\boldsymbol{\Pi}_S$ resolves multi-epoch histories or instantaneous configuration states. In a *multi-epoch causal-history partition* ($M \gg 1$), $\boldsymbol{\Pi}_S$ indexes coarse-grained blocks across successive persistence epochs without assuming an external clock. When intra-epoch spatial cuts exceed inter-epoch persistence bottlenecks, the slowest non-trivial eigenvector $\boldsymbol{\phi}_{\mathrm{time}} \equiv \boldsymbol{\phi}_2$ takes constant level-set values across coexisting registers within each epoch, foliating $\{1, \dots, M\}$ into N_τ disjoint sequential slices S_τ ordered by strictly increasing Fiedler coordinate:

$$S_\tau := \big\{\alpha \in \{1, \dots, M\} : \phi_{\mathrm{time}}(\alpha) = \phi_{\mathrm{time}}^{(\tau)}\big\}, \tag{2.240}$$

$$\phi_{\mathrm{time}}^{(1)} < \phi_{\mathrm{time}}^{(2)} < \cdots < \phi_{\mathrm{time}}^{(N_\tau)}, \tag{2.241}$$

$$\{1, \dots, M\} = \bigsqcup_{\tau=1}^{N_\tau} S_\tau. \tag{2.242}$$

Within this foliation ($d_s = 1 + d_s^{\mathrm{spatial}}$), $\boldsymbol{\phi}_{\mathrm{time}}$ supplies a single emergent temporal axis while the $\mathbf{D}_{\mathbf{K}}$-orthogonal modes $\boldsymbol{\phi}_k$ ($k > 2$) align coexisting spatial registers $x \in S_\tau$ across $d_s^{\mathrm{spatial}} = d_s - 1$ spatial axes governed by $\Omega_{\alpha\beta}$. Ordering slices via (2.240)–(2.242) establishes discrete succession without yet fixing duration, which separates into three nested tiers: intrinsic observer proper time on S, relational reference time against an external sub-block, and standardised clock units. At the intrinsic tier, Axiom I (2.125) guarantees $K_{(\tau,x),(\tau,x)} \geq 2$ links on every connected slice register (τ, x) ($x \in S_\tau$). Summing the logarithmic coarse-graining depths (1.33) across slice S_τ defines the observer's dimensionless *intrinsic slice proper-time increment* $\Delta\tau_{\mathrm{nat}}(\tau)$ (in

nats), the cumulative *intrinsic proper-time horizon* $\tau_{\mathrm{nat},T}$ (in nats), and the normalised *proper-time weights* w_τ:

$$\Delta\tau_{\mathrm{nat}}(\tau) := \sum_{x\in S_\tau} \ln K_{(\tau,x),(\tau,x)} \geq |S_\tau| \ln 2 > 0, \tag{2.243}$$

$$\tau_{\mathrm{nat},T} := \sum_{\tau=1}^{N_\tau} \Delta\tau_{\mathrm{nat}}(\tau), \tag{2.244}$$

$$w_\tau := \frac{\Delta\tau_{\mathrm{nat}}(\tau)}{\tau_{\mathrm{nat},T}}, \tag{2.245}$$

whose strictly positive weights w_τ sum to unity across the N_τ slices, accumulating up to slice τ into the observer's partial proper-time sum $\tau_{\mathrm{nat}}(\tau)$ (in nats):

$$\tau_{\mathrm{nat}}(\tau) := \sum_{s=1}^{\tau} \Delta\tau_{\mathrm{nat}}(s) = \tau_{\mathrm{nat},T} \sum_{s=1}^{\tau} w_s. \tag{2.246}$$

Because a fixed slice degree budget splits between diagonal memory $K_{(\tau,x),(\tau,x)}$ and boundary transition cuts, diverting capacity from $\mathbf{K}_\Omega$ into $\mathbf{K}_\partial$ strictly reduces $K_{(\tau,x),(\tau,x)}$ and contracts $\Delta\tau_{\mathrm{nat}}(\tau)$. At the relational tier, comparing durations or operational rates across distinct systems without positing a background clock resolves a stationary *reference sub-block* $\bar{S}_{\mathrm{ref}} \subset \bar{S}$ inside $\mathbf{K}$ whose internal capacity maintains a constant slice proper-time increment $\Delta\tau_{\mathrm{ref}} > 0$ (in nats) across the N_τ-slice reference horizon $N_\tau\Delta\tau_{\mathrm{ref}}$ (in nats). Normalising each slice increment by $\Delta\tau_{\mathrm{ref}}$ relates $\tau_{\mathrm{nat},T}$ to $N_\tau\Delta\tau_{\mathrm{ref}}$ through the slice-mean lapse ratio (nats/nat) and leaves the proper-time weights w_τ identically invariant:

$$\frac{\tau_{\mathrm{nat},T}}{N_\tau\Delta\tau_{\mathrm{ref}}} = \frac{1}{N_\tau} \sum_{\tau=1}^{N_\tau} \frac{\Delta\tau_{\mathrm{nat}}(\tau)}{\Delta\tau_{\mathrm{ref}}}, \tag{2.247}$$

$$w_\tau = \frac{\Delta\tau_{\mathrm{nat}}(\tau)/\Delta\tau_{\mathrm{ref}}}{\sum_{s=1}^{N_\tau} \Delta\tau_{\mathrm{nat}}(s)/\Delta\tau_{\mathrm{ref}}} = \frac{\Delta\tau_{\mathrm{nat}}(\tau)}{\tau_{\mathrm{nat},T}}. \tag{2.248}$$

Complementarily, in a *single-epoch state-space partition* of configuration dimension $n := d_s^{\mathrm{spatial}}$, $\mathbf{\Pi}_S$ groups coexisting configuration registers while sequential updates advance along the internal memory diagonal $\mathbf{K}_\Omega$ (2.88). Both the local step count $k \in \mathbb{N}_0$ along a trajectory and the collective count $k_\Omega \in \mathbb{N}_0$ of elementary internal memory updates across all $\mathrm{Tr}(\mathbf{K}_\Omega)$ retained internal channels are dimensionless integers. At the standardised clock tier, normalising the subsystem's intrinsic proper-time distinction increment $\mathrm{d}\tau_{\mathrm{nat}}$ (in nats) by its own active rest-frame reversible distinction rate $\Omega_\Phi > 0$—or equivalently normalising collective channel updates $\mathrm{d}k_\Omega$ by $\nu_0 \,\mathrm{Tr}(\mathbf{K}_\Omega)$ at constant elementary substrate step cadence $\nu_0 > 0$—defines the subsystem's *standardised proper-time increment* $\mathrm{d}\tau$:

$$\mathrm{d}k_\Omega := \mathrm{Tr}(\mathbf{K}_\Omega)\,\mathrm{d}k, \tag{2.249}$$

$$\mathrm{d}\tau := \frac{\mathrm{d}\tau_{\mathrm{nat}}}{\Omega_\Phi} = \frac{\mathrm{d}k_\Omega}{\nu_0 \,\mathrm{Tr}(\mathbf{K}_\Omega)}. \tag{2.250}$$

Prior to external clock selection ($\nu_0 = 1$ per substrate step), $\mathrm{d}\tau$ counts local internal steps $\mathrm{d}k$ while collective channel updates advance by $\mathrm{Tr}(\mathbf{K}_\Omega) \geq 2M$ links per step under Axiom I. On any non-empty uncoupled vertex core $S_\Omega = S \setminus S_\partial$, the interior sub-Laplacian $\mathbf{L}_{\Omega\Omega}$ (Section 2.1.2 and Section 3.2.1) shields core transitions identically from external boundary perturbations. Whereas $\Delta\tau_{\mathrm{nat}}(\tau)$ (2.243) sums logarithmic coarse-graining depths across a causal slice (in nats), collective channel updates $\mathrm{d}k_\Omega$ (2.249) scale linearly with $\mathrm{Tr}(\mathbf{K}_\Omega)$, a distinction reconciled via concavity and the Margolus–Levitin bound [106] in Section 6.1. Because any embedded subsystem obeys $\mathcal{Q}_{\mathrm{alloc}} \leq \mathcal{Q}_{\mathrm{total}}$, sustaining internal clock progression without unbounded register allocation or continuous erasure requires wrapping internal updates into compact, volume-preserving periodic orbits that cyclically reuse a finite register set. Metering state displacements at rest relative to $\bar{S}_{\mathrm{ref}}$ ($\mathrm{d}\tau = \mathrm{d}t$) and inter-register transitions per local step defines relational velocities and single-step transition probabilities via the Page–Wootters mechanism [127]:

$$\dot{z} := \frac{\mathrm{d}z}{\mathrm{d}t} = \Omega_\Phi \frac{\mathrm{d}z}{\mathrm{d}\tau_{\mathrm{nat}}} = \nu_0 \,\mathrm{Tr}(\mathbf{K}_\Omega) \frac{\mathrm{d}z}{\mathrm{d}k_\Omega}, \tag{2.251}$$

$$T_{\alpha\to\beta} := \frac{K_{\alpha\beta}}{d_\alpha} \approx \frac{K_{\alpha\beta}}{K_{\alpha\alpha}} = e^{-\Delta I_{\mathrm{barrier},\alpha\to\beta}} \qquad (\alpha \neq \beta). \tag{2.252}$$

Because $T_{\alpha\to\beta}$ depends solely on $K_{\alpha\beta}$ and the local degree d_α, adding uncoupled registers outside $S_\alpha \cup S_\beta$ leaves the transition probability between α and β strictly invariant. Metering coordinate time strictly against the external reference sub-block $\bar{S}_{\mathrm{ref}}$ at its own reversible distinction rate $\Omega_{\mathrm{ref}} > 0$ fixes the discrete reference slice coordinates t_τ, the shared *reference coordinate horizon* T, and the continuous reference-time increment $\mathrm{d}t$ (distinct from observer partial proper time $\tau_{\mathrm{nat}}(\tau)$ in (2.246) whenever $\Delta\tau_{\mathrm{nat}}(\tau)$ varies across slices):

$$t_\tau := \frac{\tau\,\Delta\tau_{\mathrm{ref}}}{\Omega_{\mathrm{ref}}} = \frac{\tau}{N_\tau}\,T, \tag{2.253}$$

$$T := \frac{N_\tau\,\Delta\tau_{\mathrm{ref}}}{\Omega_{\mathrm{ref}}}, \tag{2.254}$$

$$\mathrm{d}t := \frac{\mathrm{d}\tau_{\mathrm{ref}}}{\Omega_{\mathrm{ref}}}. \tag{2.255}$$

Selecting SI seconds requires no separate time variable, as it simply chooses an agreed-upon physical reference oscillator for $\bar{S}_{\mathrm{ref}}$ of defined reversible rate $\Omega_{\mathrm{ref}} > 0$ in nats s^{-1} (versus $\Omega_{\mathrm{ref}} = 1$ in uncalibrated reference nats), fixing ν_0 in s^{-1} and Ω_Φ in nats s^{-1} so that t, τ, and T carry seconds directly while $\mathrm{d}\tau = \mathrm{d}t$ holds for every subsystem at rest relative to $\bar{S}_{\mathrm{ref}}$ despite distinct internal capacities $\Omega_\Phi \neq \Omega_{\mathrm{ref}}$. In the large-capacity, fine-slice continuum limit ($K_{(\tau,x),(\tau,x)} \gg 1$, $N_\tau \gg 1$) where the maximum slice weight w_τ vanishes inside the spectral diffusion window of (2.232) at non-zero Fiedler gap $\mu_2(\mathbf{L}_{\mathrm{norm}}) \geq \lambda_0 > 0$, t_τ converges to smooth reference coordinate time

$t \in [0, T]$ while $\mathrm{d}\tau$ integrates to elapsed standardised observer proper time τ_T and normalised proper-time weight:

$$\tau_T := \int_0^T \mathrm{d}\tau = \frac{\tau_{\mathrm{nat},T}}{\Omega_\Phi}, \tag{2.256}$$

$$\frac{\mathrm{d}\tau_{\mathrm{nat}}}{\tau_{\mathrm{nat},T}} = \frac{\mathrm{d}\tau}{\tau_T}. \tag{2.257}$$

Slicing perpendicular to $\boldsymbol{\phi}_{\mathrm{time}}$ isolates a static cross-section S_τ governed by $(\chi_{\mathrm{struct}}, \kappa_{\mathrm{struct}})$, whereas aggregating proper-time-weighted stability and dissipation across the slices $S_1, \ldots, S_{N_\tau}$ yields the through-time efficiencies χ_T and κ_T developed in Chapter 3. Later, in Chapter 6 (Section 6.1), non-planar signal routing ($d_s^{\mathrm{spatial}} \geq 3$) and Gauss-law orbital stability ($d_s^{\mathrm{spatial}} < 4$) fix $d_s^{\mathrm{spatial}} = 3$ and hence total spectral dimension $d_s = 4$, while projecting $\langle \mathbf{K}_\Omega, \mathbf{K}_\partial \rangle_F = 0$ onto a differential update interval yields the Lorentzian spacetime interval.

EXAMPLE 2.7 (Spectral Ordering, Resistance, and Proper Time). Consider an assignment $\boldsymbol{\Pi}_S \in \{0,1\}^{N\times 6}$ that coarse-grains the subsystem subgraph $G[S]$ ($N \equiv N_S$) into a 6×6 capacity matrix $\mathbf{K} \equiv \mathbf{K}_S$ over $M = 6$ CCEs ordered as $(1A, 1B, 2A, 2B, 3A, 3B)$, maintaining two coexisting CCEs (A, B) across three sequential persistence epochs ($\tau = 1, 2, 3$). Coexisting CCEs within each epoch share a spatial cut $K_{\tau A,\tau B} = 4$, consecutive epochs are linked by temporal transition cuts $K_{\tau x,(\tau+1)x} = 2$ for $x \in \{A, B\}$, and even diagonal capacities $K_{1x,1x} = 42$, $K_{3x,3x} = 42$, and $K_{2x,2x} = 40$ (corresponding to 21 and 20 undirected intra-register links under Axiom I) give every CCE a uniform degree volume $d_\alpha = 48$ with $\mathbf{D}_\mathbf{K} = 48\,\mathbf{I}_6$. Because diagonal self-loops cancel in $\mathbf{L}_\mathbf{K} = \mathbf{D}_\mathbf{K} - \mathbf{K}$, the capacity Laplacian decomposes as a Kronecker sum across the temporal and spatial factors:

$$\mathbf{L}_\mathbf{K} = \mathbf{L}_{\mathrm{time}} \otimes \mathbf{I}_2 + \mathbf{I}_3 \otimes \mathbf{L}_{\mathrm{space}}, \tag{2.258}$$

$$\mathbf{L}_{\mathrm{time}} = \begin{pmatrix} 2 & -2 & 0 \\ -2 & 4 & -2 \\ 0 & -2 & 2 \end{pmatrix}, \tag{2.259}$$

$$\mathbf{L}_{\mathrm{space}} = \begin{pmatrix} 4 & -4 \\ -4 & 4 \end{pmatrix}. \tag{2.260}$$

With $\mathbf{D}_\mathbf{K} = 48\,\mathbf{I}_6$, solving the generalised eigenvalue problem (2.229) across the Kronecker factors yields the exact eigenvalues μ_k equal to 0, 1/24, 1/8, 1/6, 5/24, and 7/24, with slowest temporal mode $\boldsymbol{\phi}_{\mathrm{time}} \equiv \boldsymbol{\phi}_2$ ($\mu_2 = 1/24$) and lowest spatial mode $\boldsymbol{\phi}_{\mathrm{space}} \equiv \boldsymbol{\phi}_4$ ($\mu_4 = 1/6$):

$$\boldsymbol{\phi}_{\mathrm{time}} = \frac{1}{8\sqrt{3}}(-1, -1, 0, 0, +1, +1)^\mathsf{T}, \tag{2.261}$$

$$\boldsymbol{\phi}_{\mathrm{space}} = \frac{1}{12\sqrt{2}}(-1, +1, -1, +1, -1, +1)^\mathsf{T}. \tag{2.262}$$

Summing (2.239) over the non-zero modes yields the intra-epoch spatial resistance $\Omega_{2A,2B}$ (from $\mu_4 = 1/6$ and $\mu_6 = 7/24$) and the end-to-end temporal resistance $\Omega_{1A,3A}$ (from $\mu_2 = 1/24$ and $\mu_5 = 5/24$):

$$\Omega_{2A,2B} = \frac{1}{12} + \frac{2}{21} = \frac{5}{28} \approx 0.18, \tag{2.263}$$

$$\Omega_{1A,3A} = \frac{1}{2} + \frac{1}{10} = \frac{3}{5} = 0.60. \tag{2.264}$$

Evaluating the intrinsic slice proper-time increments (2.243) across the three foliated slices shows that diverting two units of capacity into the additional interior temporal cut reduces diagonal capacity from 42 at the outer epochs to 40 at $\tau = 2$, producing discrete proper-time dilation at the interior slice:

$$\Delta\tau_{\text{nat}}(1) = \Delta\tau_{\text{nat}}(3) = 2\ln 42 \approx 7.48 \text{ nats}, \tag{2.265}$$

$$\Delta\tau_{\text{nat}}(2) = 2\ln 40 \approx 7.38 \text{ nats}. \tag{2.266}$$

The slowest mode $\boldsymbol{\phi}_{\text{time}}$ orders the three epochs sequentially ($\tau = 1 < 2 < 3$) with intrinsic slice durations $\Delta\tau_{\text{nat}}(\tau)$ summing to $\tau_{\text{nat},T} \approx 22.33$ nats, while $\boldsymbol{\phi}_{\text{space}}$ separates the coexisting CCEs A and B at every epoch onto a $(1+1)$-dimensional grid. ♢

Only a uniform lattice with identical degree volumes d_α and uniform boundary cuts $K_{\alpha\beta}$ embeds isometrically into flat space $\mathbb{R}^{d_s}$. When coarse-graining concentrates heterogeneous capacities across $G_{\mathbf{K}}$, the emergent coordinate chart is intrinsically curved. Whereas single-step differences in $\mathbf{L}_{\mathbf{K}}$ cancel diagonal capacities $K_{\alpha\alpha}$, two-step propagation $\mathbf{L}_{\mathbf{K}}^2$ subtracted from $\mathbf{D}_{\mathbf{K}}^2$ retains $K_{\alpha\alpha}$ through symmetrised degree coupling minus two-step path summation $\mathbf{K}^2$. With degree vector $\mathbf{d} := \mathbf{D}_{\mathbf{K}}\mathbf{1}_M$ of block entries $(d_\alpha)_{\alpha=1}^M$, subtracting the diagonal neighbour-degree dispersion $\operatorname{diag}(\mathbf{Kd})$ removes the flat-lattice baseline so that the row divergence $\operatorname{Ric}_{\mathbf{K}}\mathbf{1}_M = \mathbf{L}_{\mathbf{K}}\mathbf{d}$ vanishes whenever degree volumes are uniform, defining the symmetric rank-2 *capacity-Ricci operator* $\operatorname{Ric}_{\mathbf{K}}$ and scalar curvature $\operatorname{Scal}_{\mathbf{K}}$:

$$\operatorname{diag}(\mathbf{Kd})_{\alpha\beta} := \delta_{\alpha\beta}\sum_{\gamma=1}^{M} K_{\alpha\gamma}d_\gamma, \tag{2.267}$$

$$(\operatorname{Ric}_{\mathbf{K}})_{\alpha\beta} := (d_\alpha + d_\beta)K_{\alpha\beta} - \operatorname{diag}(\mathbf{Kd})_{\alpha\beta} - (\mathbf{K}^2)_{\alpha\beta}, \tag{2.268}$$

$$\operatorname{Scal}_{\mathbf{K}} := \operatorname{Tr}(\operatorname{Ric}_{\mathbf{K}}) = \sum_{\alpha=1}^{M}(\operatorname{Ric}_{\mathbf{K}})_{\alpha\alpha}. \tag{2.269}$$

LEMMA 2.6 (Capacity-Ricci Laplacian Identity). *Let* $\mathbf{K}$ *be the capacity matrix,* $\mathbf{D}_{\mathbf{K}}$ *its diagonal degree matrix with degree vector* $\mathbf{d} := \mathbf{D}_{\mathbf{K}}\mathbf{1}_M$*, and* $\mathbf{L}_{\mathbf{K}} := \mathbf{D}_{\mathbf{K}} - \mathbf{K}$ *the capacity Laplacian* (2.101)*. Subtracting the diagonal neighbour-degree dispersion* $\operatorname{diag}(\mathbf{Kd})$ (2.267)*, the capacity-Ricci operator* (2.268) *identically satisfies:*

$$\operatorname{Ric}_{\mathbf{K}} = \mathbf{D}_{\mathbf{K}}^2 - \mathbf{L}_{\mathbf{K}}^2 - \operatorname{diag}(\mathbf{Kd}). \tag{2.270}$$

PROOF. Expanding the squared capacity Laplacian $\mathbf{L}_{\mathbf{K}}^2 = (\mathbf{D}_{\mathbf{K}} - \mathbf{K})^2$ and evaluating the symmetrised product $\mathbf{D}_{\mathbf{K}}\mathbf{K} + \mathbf{K}\mathbf{D}_{\mathbf{K}}$ entrywise gives:

$$\mathbf{L}_{\mathbf{K}}^2 = \mathbf{D}_{\mathbf{K}}^2 - (\mathbf{D}_{\mathbf{K}}\mathbf{K} + \mathbf{K}\mathbf{D}_{\mathbf{K}}) + \mathbf{K}^2, \tag{2.271}$$

$$(\mathbf{D}_{\mathbf{K}}\mathbf{K} + \mathbf{K}\mathbf{D}_{\mathbf{K}})_{\alpha\beta} = (d_\alpha + d_\beta)K_{\alpha\beta}, \tag{2.272}$$

$$(\mathbf{D}_{\mathbf{K}}\mathbf{K} + \mathbf{K}\mathbf{D}_{\mathbf{K}}) - \mathbf{K}^2 = \mathbf{D}_{\mathbf{K}}^2 - \mathbf{L}_{\mathbf{K}}^2. \tag{2.273}$$

Subtracting $\mathrm{diag}(\mathbf{K}\mathbf{d})$ from both sides of (2.273) recovers (2.268). □

Equation (2.270) forms the discrete relational counterpart of the Bochner–Weitzenböck identity and the Bakry–Émery Γ_2 criterion [8], complementing cell-complex curvature [58] and optimal-transport Markov curvature [123] by retaining intra-register multiplicities directly through $\mathbf{K}_\Omega$. Separating diagonal and off-diagonal summands in (2.268) yields the exact diagonal reduction at each CCE α:

$$(\mathrm{Ric}_{\mathbf{K}})_{\alpha\alpha} = \sum_{\beta\neq\alpha} K_{\alpha\beta}\big(K_{\alpha\alpha} - d_\beta - K_{\alpha\beta}\big). \tag{2.274}$$

Writing $d_\alpha = K_{\alpha\alpha} + (\mathbf{L}_{\mathbf{K}})_{\alpha\alpha}$ for the inter-register cut degree $(\mathbf{L}_{\mathbf{K}})_{\alpha\alpha}$ (2.106) and summing (2.274) over all M blocks cancels $K_{\alpha\alpha}$ identically by symmetry $K_{\alpha\beta} = K_{\beta\alpha}$ (Axiom III), leaving a strictly negative cut-determined global scalar curvature on every connected multi-block capacity graph ($M \geq 2$):

$$\mathrm{Scal}_{\mathbf{K}} = -\sum_{\alpha=1}^{M} (\mathbf{L}_{\mathbf{K}})_{\alpha\alpha}^2 - \|\mathbf{K}_\partial\|_F^2 < 0. \tag{2.275}$$

Because $\mathbf{D}_{\mathbf{K}}^2 - \mathrm{diag}(\mathbf{K}\mathbf{d}) = \mathrm{diag}(\mathbf{L}_{\mathbf{K}}\mathbf{d})$, (2.270) contracts to $\mathrm{Ric}_{\mathbf{K}} = \mathrm{diag}(\mathbf{L}_{\mathbf{K}}\mathbf{d}) - \mathbf{L}_{\mathbf{K}}^2$, and Lemma 2.3 (2.170)–(2.172) gives its exact coarse-graining commutator across $\mathbf{\Pi}^{(2)} = \mathbf{\Pi}^{(1)}\mathbf{P}$:

$$[\![\mathrm{Ric}, \mathscr{C}_{\mathbf{P}}]\!]\big(\mathbf{K}^{(1)}\big) = \mathrm{diag}\big(\mathbf{P}^{\mathsf{T}}\mathbf{L}_{\mathbf{K}}^{(1)}\mathbf{E}_{\mathbf{P}}\mathbf{d}^{(1)}\big) - \mathbf{P}^{\mathsf{T}}\mathbf{L}_{\mathbf{K}}^{(1)}\mathbf{E}_{\mathbf{P}}\mathbf{L}_{\mathbf{K}}^{(1)}\mathbf{P}. \tag{2.276}$$

On a loopless graph with $K_{\alpha\alpha} = 0$, every connected neighbour contributes a negative summand in (2.274), rendering branching interconnect networks intrinsically hyperbolic and prone to central bridge congestion (Chapter 7). Conversely, when $\mathscr{C}_{\mathbf{P}}$ pools intra-cluster co-members across $\mathbf{E}_{\mathbf{P}}$ in (2.276) so that $K_{\alpha\alpha} > d_\beta + K_{\alpha\beta}$, concentrated internal multiplicity generates positive local curvature surrounded by compensating negative throat curvature on lighter flanking neighbours while preserving (2.275) (Chapter 6).

Lifting symmetric rank-2 operators to rank-4 curvature and mobility tensors relies on the *Kulkarni–Nomizu product* $h \owedge k$ [91, 120], which automatically satisfies pair antisymmetry, pair interchange, and the first algebraic Bianchi identity:

$$(h \owedge k)_{\alpha\beta\gamma\delta} := h_{\alpha\gamma}k_{\beta\delta} - h_{\alpha\delta}k_{\beta\gamma} + k_{\alpha\gamma}h_{\beta\delta} - k_{\alpha\delta}h_{\beta\gamma}, \tag{2.277}$$

$$(h \owedge k)_{\alpha\beta\gamma\delta} + (h \owedge k)_{\alpha\gamma\delta\beta} + (h \owedge k)_{\alpha\delta\beta\gamma} = 0. \tag{2.278}$$

On the M-register block space $\mathbb{R}^M$ ($M \geq 3$), pairing the symmetric *Schouten capacity operator* $\mathbf{S}_{\mathbf{K}}$ with the identity $\mathbf{I}_M$ defines the Weyl-free *algebraic*

capacity curvature tensor $\mathscr{R}_{\mathbf{K}}$, whose single and double contractions recover $\mathrm{Ric}_{\mathbf{K}}$ and $\mathrm{Scal}_{\mathbf{K}}$ identically:

$$\mathbf{S}_{\mathbf{K}} := \frac{1}{M-2}\left(\mathrm{Ric}_{\mathbf{K}} - \frac{\mathrm{Scal}_{\mathbf{K}}}{2(M-1)}\mathbf{I}_M\right), \tag{2.279}$$

$$\mathscr{R}_{\mathbf{K}} := \mathbf{S}_{\mathbf{K}} \owedge \mathbf{I}_M, \tag{2.280}$$

$$\sum_{\beta=1}^{M} (\mathscr{R}_{\mathbf{K}})_{\alpha\beta\gamma\beta} = (\mathrm{Ric}_{\mathbf{K}})_{\alpha\gamma}. \tag{2.281}$$

Here $\mathscr{R}_{\mathbf{K}}$ acts algebraically on $\mathbb{R}^M$ with denominators $M-2$ and $2(M-1)$, whereas once continuum metric closure projects onto a three-dimensional spatial slice ($d = 3$) in Chapter 6, vanishing of the tangent-space Weyl tensor similarly reconstructs the full spatial Riemann tensor from spatial Ricci curvature on $T_p\Sigma$.

EXAMPLE 2.8 (Curvature of a Heavily Coarse-Grained CCE). Consider three CCEs ($M = 3$) connected along a chain by unit boundary cuts between adjacent registers, where two light outer registers of internal capacity 10 flank a heavily coarse-grained interior register of internal capacity 100:

$$\mathbf{K} = \begin{pmatrix} 10 & 1 & 0 \\ 1 & 100 & 1 \\ 0 & 1 & 10 \end{pmatrix}, \tag{2.282}$$

$$\mathbf{D}_{\mathbf{K}} = \mathrm{diag}(11, 102, 11), \tag{2.283}$$

$$\mathbf{L}_{\mathbf{K}} = \begin{pmatrix} 1 & -1 & 0 \\ -1 & 2 & -1 \\ 0 & -1 & 1 \end{pmatrix}. \tag{2.284}$$

Squaring $\mathbf{L}_{\mathbf{K}}$ and evaluating the neighbour-degree dispersion (2.267) gives:

$$\mathbf{L}_{\mathbf{K}}^2 = \begin{pmatrix} 2 & -3 & 1 \\ -3 & 6 & -3 \\ 1 & -3 & 2 \end{pmatrix}, \tag{2.285}$$

$$\mathrm{diag}(\mathbf{K}\mathbf{d}) = \mathrm{diag}(212, 10222, 212). \tag{2.286}$$

Evaluating the capacity-Ricci identity (2.270) and trace (2.269) (matching (2.275) at cut degrees $(1, 2, 1)$ and $\|\mathbf{K}_\partial\|_F^2 = 4$) gives:

$$\mathrm{Ric}_{\mathbf{K}} = \begin{pmatrix} -93 & 3 & -1 \\ 3 & 176 & 3 \\ -1 & 3 & -93 \end{pmatrix}, \tag{2.287}$$

$$\mathrm{Scal}_{\mathbf{K}} = -10. \tag{2.288}$$

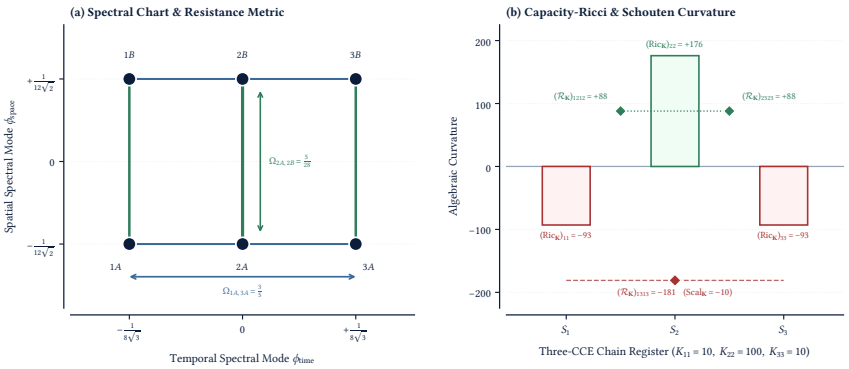


FIGURE 2.4: Emergent spectral coordinates, resistance metric, and algebraic curvature on coarse-grained capacity networks (Examples 2.7 and 2.8). *(a)* Spectral embedding $\mathbf{\Phi} = [\boldsymbol{\phi}_{\text{time}}, \boldsymbol{\phi}_{\text{space}}]$ (2.261)–(2.262) of six unordered CCEs $(1A, 1B, 2A, 2B, 3A, 3B)$ with uniform degree $d_\alpha = 48$, ordering three sequential persistence epochs ($\tau = 1, 2, 3$) along ϕ_{time} and separating coexisting registers (A, B) across ϕ_{space}, with tighter intra-epoch spatial resistance $\Omega_{2A,2B} = 5/28$ (teal) than multi-epoch separation $\Omega_{1A,3A} = 3/5$ (light navy). *(b)* Diagonal capacity-Ricci curvature $(\text{Ric}_{\mathbf{K}})_{\alpha\alpha}$ (2.287) and Schouten sectional curvatures $(\mathscr{R}_{\mathbf{K}})_{\alpha\beta\alpha\beta}$ (2.290)–(2.291) along the three-CCE chain ($K_{11} = 10$, $K_{22} = 100$, $K_{33} = 10$): concentrated internal multiplicity generates positive attractor curvature $+176$ (adjacent sectional curvature $+88$, teal) flanked by negative outer throat curvature -93 (end-to-end sectional curvature -181, crimson), summing to $\text{Scal}_{\mathbf{K}} = -10$.

At $M = 3$, the discrete Schouten operator (2.279) and the sectional components of $\mathscr{R}_{\mathbf{K}}$ (2.280) evaluate to:

$$\mathbf{S}_{\mathbf{K}} = \text{Ric}_{\mathbf{K}} - \frac{1}{4}\,\text{Scal}_{\mathbf{K}}\,\mathbf{I}_3 = \text{Ric}_{\mathbf{K}} + \frac{5}{2}\mathbf{I}_3, \tag{2.289}$$

$$(\mathscr{R}_{\mathbf{K}})_{1212} = (\mathscr{R}_{\mathbf{K}})_{2323} = +88, \tag{2.290}$$

$$(\mathscr{R}_{\mathbf{K}})_{1313} = -181. \tag{2.291}$$

In agreement with (2.274), the heavy interior register carries positive local curvature $+176$ and positive adjacent sectional focusing $+88$, while the two lighter outer registers carry negative throat curvature -93 and negative end-to-end sectional curvature -181, showing how concentrated internal capacity warps the surrounding relational metric (Figure 2.4, Chapter 6). ♢

2.5.2 *Emergent Dynamics and the Metriplectic Continuum*

On a single-epoch configuration partition of spectral dimension $n := d_s^{\text{spatial}}$, the spectral coordinate map $\mathbf{\Phi}$ (2.236) assigns each CCE register $\alpha \in \{1, \dots, M\}$ a configuration vector $\mathbf{z}(\alpha) = (z^1(\alpha), \dots, z^n(\alpha))^{\mathsf{T}} \in \mathbb{R}^n$, where $z^i(\alpha) := \phi_{k_i}(\alpha)$ $(i = 1, \dots, n)$ denotes the i-th retained spatial eigenmode. Why can $\mathbf{z} \in \mathbb{R}^n$ alone not form a closed dynamical state, and how do symmetric capacity matrices ($\mathbf{A}_{SS} = \mathbf{A}_{SS}^{\mathsf{T}}$, $\mathbf{K}_S = \mathbf{K}_S^{\mathsf{T}}$) generate both antisymmetric Hamiltonian circulation and symmetric dissipative relaxation? Whereas $\mathbf{A}_{SS}$ is symmetric

because undirected links $\{i, j\} \in E(S)$ specify structural channels, instantaneous transport across $\{i, j\}$ is directional and forms a real skew-symmetric edge-flow matrix $\mathbf{J} = -\mathbf{J}^{\mathsf{T}} \in \mathbb{R}^{N\times N}$ supported exclusively on active links:

$$J_{ij} = -J_{ji}, \tag{2.292}$$

$$A_{ij} = 0 \implies J_{ij} = 0. \tag{2.293}$$

On this $|E(S)|$-dimensional flow space equipped with the Frobenius inner product (2.185), vertex potential differences of any state $\mathbf{x}_S \in \mathbb{R}^N$ drive the gradient edge flow $\mathbf{J}_{\mathrm{grad}}(\mathbf{x}_S)$, whereas divergence-free circulation around closed cycles forms the Kirchhoff cycle subspace where net vertex flux $\mathbf{J}_{\mathrm{cyc}}\mathbf{1}_S$ vanishes:

$$\big(\mathbf{J}_{\mathrm{grad}}(\mathbf{x}_S)\big)_{ij} := A_{ij}(x_i - x_j), \tag{2.294}$$

$$\mathbf{J}_{\mathrm{grad}}(\mathbf{x}_S)\mathbf{1}_S = \mathbf{L}_{SS}^{(\mathrm{int})}\mathbf{x}_S, \tag{2.295}$$

$$\mathbf{J}_{\mathrm{cyc}}\mathbf{1}_S = \mathbf{o}. \tag{2.296}$$

Equations (2.294)–(2.296) partition edge transport on $G[S]$ into two Frobenius-orthogonal algebraic sectors that transform oppositely under the coarse-graining projection $\mathbf{\Pi}_S$.

LEMMA 2.7 (Cycle–Gradient Orthogonality and Sector Split). *Let $G[S] = (S, E(S))$ be an undirected subgraph partitioned by an admissible assignment $\mathbf{\Pi}_S \in \{0,1\}^{N\times M}$ into connected blocks $\{S_\alpha\}_{\alpha=1}^{M}$ of vertex counts $N_\alpha = |S_\alpha|$ and diagonal capacities $K_{\alpha\alpha} = 2|E(S_\alpha)|$. Every Kirchhoff cycle flow $\mathbf{J}_{\mathrm{cyc}}$ satisfying (2.292)–(2.296) is orthogonal to every gradient flow $\mathbf{J}_{\mathrm{grad}}(\mathbf{x}_S)$ ($\mathbf{x}_S \in \mathbb{R}^N$), while lifted block potentials $\mathbf{\Pi}_S\mathbf{z}_S$ ($\mathbf{z}_S \in \mathbb{R}^M$) excite exclusively inter-block cut gradients matching the Dirichlet energy (2.104):*

$$\big\langle \mathbf{J}_{\mathrm{cyc}}, \mathbf{J}_{\mathrm{grad}}(\mathbf{x}_S)\big\rangle_F = 0, \tag{2.297}$$

$$\frac{1}{2}\big\|\mathbf{J}_{\mathrm{grad}}(\mathbf{\Pi}_S\mathbf{z}_S)\big\|_F^2 = \mathbf{z}_S^{\mathsf{T}}\mathbf{L}_{\mathbf{K}}\mathbf{z}_S \geq 0. \tag{2.298}$$

Furthermore, intra-block Kirchhoff cycle flows $\mathbf{J}_\Omega = -\mathbf{J}_\Omega^{\mathsf{T}}$ supported on the internal edge sets $E(S_\alpha)$ span a subspace of dimension $|E(S_\alpha)| - N_\alpha + 1$ on each connected block $G[S_\alpha]$ (non-zero if and only if $K_{\alpha\alpha} \geq 2N_\alpha$), vanish under congruent block compression, act as skew-symmetric operators inside the residual fluctuation subspace $\mathrm{im}(\mathbf{Q}_{\mathbf{\Pi}})$*, and conserve the Euclidean norm of every state vector $\mathbf{x}_S \in \mathbb{R}^N$:*

$$\mathbf{\Pi}_S^{\mathsf{T}}\mathbf{J}_\Omega\mathbf{\Pi}_S = \mathbf{o}, \tag{2.299}$$

$$\mathbf{Q}_{\mathbf{\Pi}}\mathbf{J}_\Omega\mathbf{Q}_{\mathbf{\Pi}} = \mathbf{J}_\Omega = -\mathbf{J}_\Omega^{\mathsf{T}}, \tag{2.300}$$

$$\mathbf{x}_S^{\mathsf{T}}\mathbf{J}_\Omega\mathbf{x}_S = 0. \tag{2.301}$$

PROOF. Using skew-symmetry (2.292), active-link support $J_{ij}^{\mathrm{cyc}}A_{ij} = J_{ij}^{\mathrm{cyc}}$ (2.293), and Kirchhoff balance (2.296) evaluates the Frobenius inner product (2.185):

$$\begin{aligned}\big\langle \mathbf{J}_{\mathrm{cyc}}, \mathbf{J}_{\mathrm{grad}}(\mathbf{x}_S)\big\rangle_F &= \sum_{i,j\in S} J_{ij}^{\mathrm{cyc}}A_{ij}(x_i - x_j)\\ &= 2\sum_{i\in S} x_i\big(\mathbf{J}_{\mathrm{cyc}}\mathbf{1}_S\big)_i = 0,\end{aligned} \tag{2.302}$$

establishing (2.297). For a lifted potential $\mathbf{x}_S = \mathbf{\Pi}_S \mathbf{z}_S$ (2.51), intra-block edges $\{i,j\} \in E(S_\alpha)$ share identical values $z_{S,\alpha}$ and vanish in $\mathbf{J}_{\mathrm{grad}}(\mathbf{\Pi}_S \mathbf{z}_S)$, whereas $A_{ij}^2 = A_{ij}$ across inter-block cut edges $E(S_\alpha, S_\beta)$ ($\alpha \neq \beta$) yields (2.298):

$$\frac{1}{2}\left\|\mathbf{J}_{\mathrm{grad}}(\mathbf{\Pi}_S \mathbf{z}_S)\right\|_F^2 = \frac{1}{2}\sum_{\alpha\neq\beta} K_{\alpha\beta}(z_{S,\alpha} - z_{S,\beta})^2 = \mathbf{z}_S^{\mathsf{T}} \mathbf{L}_{\mathbf{K}} \mathbf{z}_S \geq 0. \tag{2.303}$$

On each connected block $G[S_\alpha]$, gradient flows span an $(N_\alpha - 1)$-dimensional subspace inside the $|E(S_\alpha)|$-dimensional space of skew-symmetric edge flows on $E(S_\alpha)$, leaving an orthogonal Kirchhoff cycle complement of dimension $|E(S_\alpha)| - N_\alpha + 1$, which is positive by (2.90) if and only if $K_{\alpha\alpha} \geq 2N_\alpha$. Because $\mathbf{J}_\Omega$ is block-diagonal across $\{S_\alpha\}_{\alpha=1}^M$ and satisfies Kirchhoff closure on each S_α, it annihilates every block indicator column $\boldsymbol{\pi}_\alpha$ and hence both $\mathbf{\Pi}_S$ and the block-averaging projector $\mathbf{P}_{\mathbf{\Pi}}$ (2.57):

$$\mathbf{J}_\Omega \mathbf{\Pi}_S = \mathbf{o}, \tag{2.304}$$

$$\mathbf{J}_\Omega \mathbf{P}_{\mathbf{\Pi}} = \mathbf{P}_{\mathbf{\Pi}} \mathbf{J}_\Omega = \mathbf{o}. \tag{2.305}$$

Left-multiplying (2.304) by $\mathbf{\Pi}_S^{\mathsf{T}}$ yields (2.299), substituting $\mathbf{Q}_{\mathbf{\Pi}} = \mathbf{I}_N - \mathbf{P}_{\mathbf{\Pi}}$ (2.60) into (2.305) gives (2.300), and skew-symmetry $\mathbf{J}_\Omega^{\mathsf{T}} = -\mathbf{J}_\Omega$ reverses the sign of the scalar $\mathbf{x}_S^{\mathsf{T}} \mathbf{J}_\Omega \mathbf{x}_S$ under transposition to establish (2.301). □

Lemma 2.7 explains why the capacity matrix $\mathbf{K}_S$ (2.86) is purely symmetric, since congruent block compression annihilates $\mathbf{J}_\Omega$ via (2.299), and why $\mathbf{z} \in \mathbb{R}^n$ alone cannot close the coarse-grained dynamics. Because $\mathbf{K}_\Omega$ cancelled identically out of the Dirichlet numerator $\mathbf{L}_{\mathbf{K}}$ in (2.231), $\mathbf{z}$ records where a state sits across inter-register boundary cuts while omitting two intra-register sectors concealed inside the fluctuation subspace of $\mathbf{Q}_{\mathbf{\Pi}}$. On a tree block with $K_{\alpha\alpha} = 2(N_\alpha - 1)$, the cycle space is trivial ($\mathbf{J}_\Omega = \mathbf{o}$) and relaxation is purely overdamped. Whenever finite relational capacity ($\mathcal{Q}_{\mathrm{alloc}} \leq \mathcal{Q}_{\mathrm{total}}$) closes cyclic subgraphs inside $G[S_\alpha]$ at $K_{\alpha\alpha} \geq 2N_\alpha$, however, $\mathbf{J}_\Omega \neq \mathbf{o}$ generates canonical skew-symmetric symplectic pairs inside the fluctuation subspace. On each three-vertex triangle lobe $G[S_\alpha] \cong K_3$ of the nine-node dumbbell graph in Example 2.1 ($N_\alpha = 3$, $K_{\alpha\alpha} = 6$), projecting the unit triangle cycle matrix $\mathbf{J}_{K_3}$ onto an orthonormal fluctuation basis $\mathbf{U}_\alpha$ on S_α yields the canonical 2×2 symplectic block directly:

$$\mathbf{J}_{K_3} := \begin{pmatrix} 0 & 1 & -1 \\ -1 & 0 & 1 \\ 1 & -1 & 0 \end{pmatrix}, \tag{2.306}$$

$$\mathbf{U}_\alpha := \begin{pmatrix} 1/\sqrt{2} & 1/\sqrt{6} \\ -1/\sqrt{2} & 1/\sqrt{6} \\ 0 & -2/\sqrt{6} \end{pmatrix}, \tag{2.307}$$

$$\mathbf{U}_\alpha^{\mathsf{T}} \mathbf{J}_{K_3} \mathbf{U}_\alpha = \sqrt{3} \begin{pmatrix} 0 & 1 \\ -1 & 0 \end{pmatrix}. \tag{2.308}$$

Across the n retained spatial modes, these cyclic currents inside $\mathbf{K}_\Omega$ pair each configuration coordinate z^i with a conjugate momentum p_i to form $\mathbf{p} \in$

$\mathbb{R}^n$, while the remaining unoriented internal link capacity $K_{\alpha\alpha}$ compressed into $\mathrm{im}(\mathbf{Q}_{\mathbf{\Pi}})$ defines the coarse-grained logarithmic capacity $S = \ln K_{\alpha\alpha}$ (in nats). Adjoining both intra-register sectors to $\mathbf{z}$ completes the closed coarse-grained state vector Z:

$$Z := \left(\mathbf{z}^{\mathsf{T}}, \mathbf{p}^{\mathsf{T}}, S\right)^{\mathsf{T}} \in \mathscr{Z} \cong \mathbb{R}^{2n+1}. \tag{2.309}$$

Equation (2.309) lifts the n-dimensional spectral configuration chart of Section 2.5.1 onto a $(2n+1)$-dimensional state manifold $\mathscr{Z}$ capable of tracking both inertial oscillation and lossless energy-to-entropy conversion (for $n = 1$, $Z = (x, p, S)^{\mathsf{T}} \in \mathbb{R}^3$, as in Example 2.9).

How do the spectral modes of $\mathbf{L}_{\mathbf{K}}$ govern state transport across $G_{\mathbf{K}}$? Across the capacity network, $\mathbf{K}$ specifies structural channels rather than active currents, so a vanishing boundary cut strictly forbids coarse-grained flux across that channel:

$$K_{\alpha\beta} = 0 \quad \Longrightarrow \quad J_{\alpha\beta} = 0, \tag{2.310}$$

whereas a positive cut $K_{\alpha\beta} > 0$ conducts state transitions across the spectral coordinate jump $\Delta z^i_{\alpha\beta} := z^i(\alpha) - z^i(\beta)$. Weighting outer products of these coordinate jumps by $K_{\alpha\beta}$ defines the local positive-semidefinite *spectral cut-conductance matrix* $\Sigma^{ij}(\alpha)$ at each register α, whose global sum over all M registers evaluates directly via the eigenproblem (2.229)–(2.230):

$$\Sigma^{ij}(\alpha) := \frac{1}{2} \sum_{\beta \neq \alpha} K_{\alpha\beta}\, \Delta z^i_{\alpha\beta}\, \Delta z^j_{\alpha\beta} \succeq 0, \tag{2.311}$$

$$\sum_{\alpha=1}^{M} \Sigma^{ij}(\alpha) = \boldsymbol{\phi}_{k_i}^{\mathsf{T}} \mathbf{L}_{\mathbf{K}} \boldsymbol{\phi}_{k_j} = \mu_{k_i} \delta_{ij}. \tag{2.312}$$

Equations (2.311)–(2.312) establish the direct dynamical role of the spectral coordinates derived in Section 2.5.1: the retained eigenmodes z^i form the global orthogonal principal axes of boundary transport across $G_{\mathbf{K}}$, with each eigenvalue μ_{k_i} setting the global cut conductivity along axis z^i in exact reciprocal duality to the resistance metric weight $\mu_{k_i}^{-1}$ in (2.239).

Along the continuous reference clock $t \in [0, T]$ of (2.253)–(2.255) at large block capacity ($K_{\alpha\alpha} \gg 1$), combining the orthogonal split of $\mathbf{K}_S$ into $\mathbf{K}_\Omega$ and $\mathbf{K}_\partial^{(\mathrm{int})}$ (2.186) with Lemma 2.7 decomposes $\dot{Z}$ into two complementary vector fields generated by a conserved dynamical invariant $H(Z)$ (total energy in mechanical systems) and the coarse-grained logarithmic capacity $S(Z)$ (in nats):

$$\dot{Z}^a_{\mathrm{rev}} = \left(\mathbb{J}(Z)\nabla H(Z)\right)^a = J^{ab}(Z)\partial_b H(Z), \tag{2.313}$$

$$\dot{Z}^a_{\mathrm{diss}} = \left(\mathbb{M}(Z)\nabla S(Z)\right)^a = M^{ab}(Z)\partial_b S(Z), \tag{2.314}$$

where $J^{ab} = -J^{ba}$ is the antisymmetric Poisson tensor projected from the skew-symmetric intra-block cycle operators $\mathbf{J}_\Omega = -\mathbf{J}_\Omega^{\mathsf{T}}$ (2.300) (satisfying the Jacobi identity on canonical symplectic pairs (2.308)) and $M^{ab} = M^{ba} \succeq 0$

is the symmetric positive-semidefinite cometric tensor projected from inter-block cut gradients (2.298). Within $\mathbf{K}_\Omega$, cyclic exchange between $(\mathbf{z}, \mathbf{p})$ preserves intra-basin capacity $K_{\alpha\alpha}$ and phase-space volume by Liouville's theorem ($\mathbb{J}\nabla S = \mathbf{o}$), generating closed periodic orbits on level sets of $H(Z)$ that sustain internal clock updates across $\mathbf{K}_\Omega$ (2.249). Complementarily, across $\mathbf{K}_\partial^{(\mathrm{int})}$, cut conductances drive irreversible gradient relaxation $\dot{Z}_{\mathrm{diss}}$ towards higher-capacity states, contracting phase-space volume into attractor basins and supplying the directional arrow of time.

Why can the dissipative cometric $\mathbb{M}(Z)$ not be chosen as an unconstrained positive diagonal matrix? Because Conservation Congruence (Axiom III) forbids graph couplings and the conserved invariant $H(Z)$ they carry from vanishing during coarse-grained relaxation: ordered kinetic or configurational energy damped across boundary cuts must transfer equally into unresolved internal capacity θS, requiring $\mathbb{M}\nabla H = \mathbf{o}$ across $\mathscr{Z}$. On the discrete capacity graph, pairing $\mathbf{K}$ with the positive diagonal degree matrix $\mathbf{D}_\mathbf{K}$ via the Kulkarni–Nomizu product (2.277) defines the rank-4 *capacity mobility tensor* $\mathscr{M}_\mathbf{K}$:

$$\mathscr{M}_\mathbf{K} := \mathbf{K} \owedge \mathbf{D}_\mathbf{K}, \tag{2.315}$$

$$(\mathscr{M}_\mathbf{K})_{\alpha\beta\alpha\beta} = K_{\alpha\alpha} d_\beta + d_\alpha K_{\beta\beta} > 0 \qquad (\alpha \neq \beta). \tag{2.316}$$

Whereas the curvature tensor $\mathscr{R}_\mathbf{K}$ (2.280) changes sign across basins and bottlenecks, Axiom I ($K_{\alpha\alpha} \geq 2$, (2.125)) guarantees that every distinct two-plane component of $\mathscr{M}_\mathbf{K}$ is strictly positive while pair antisymmetry $(\mathscr{M}_\mathbf{K})_{\alpha\beta\gamma\delta} = -(\mathscr{M}_\mathbf{K})_{\beta\alpha\gamma\delta}$ holds identically. Mapping the spectral cut-conductance and degree-mass operators onto the cotangent bundle $T^*\mathscr{Z}$ as symmetric positive-semidefinite mobility tensors $\sigma, \mu \succeq 0$ defines the continuum dissipation tensor R^{abcd} and the Morrison–Updike metriplectic 4-bracket for smooth observables $A, B, C, D \in C^\infty(\mathscr{Z})$ [115]:

$$R^{abcd} := (\sigma \owedge \mu)^{abcd} = \sigma^{ac}\mu^{bd} - \sigma^{ad}\mu^{bc} + \mu^{ac}\sigma^{bd} - \mu^{ad}\sigma^{bc}, \tag{2.317}$$

$$(A, B; C, D)_R := R^{abcd}\partial_a A\, \partial_b B\, \partial_c C\, \partial_d D. \tag{2.318}$$

Freezing the conserved invariant H into the second and fourth slots defines the binary metric bracket (A, C) and the continuous cometric tensor $\mathbb{M}(Z)$:

$$(A, C) := (A, H; C, H)_R = \nabla A \cdot \mathbb{M}(Z)\nabla C, \tag{2.319}$$

$$M^{ac}(Z) := R^{abcd}(Z)\partial_b H\, \partial_d H = (\sigma \owedge \mu)^{abcd}\partial_b H\, \partial_d H. \tag{2.320}$$

Because σ is supported strictly on the active cuts of $\mathbf{K}$ via (2.311), $K_{\alpha\beta} = 0$ forces the corresponding cometric channel to vanish, enforcing (2.310) automatically.

Combining Poisson circulation (2.313) and Kulkarni–Nomizu metric relaxation (2.314) yields the unified metriplectic equation of motion and the Morrison Casimir degeneracies [71, 83, 88, 114, 115, 126, 142]:

$$\dot{Z} = \mathbb{J}(Z)\nabla H(Z) + \mathbb{M}(Z)\nabla S(Z), \tag{2.321}$$

$$\mathbb{J}\nabla S = \mathbf{o}, \tag{2.322}$$

$$\mathbb{M}\nabla H = \mathbf{o}. \tag{2.323}$$

Both Casimir degeneracies $\{S, \cdot\} = 0$ and $(H, \cdot) = 0$ hold identically as continuum consequences of Conservation-Congruent Encoding: internal cyclic circulation preserves coarse-grained capacity via $\mathbb{J}\nabla S = \mathbf{o}$, while pair antisymmetry $R^{abcd} = -R^{bacd}$ annihilates ∇H identically along dissipative flows. Moreover, for positive semidefinite $\sigma, \mu \succeq 0$, applying Cauchy–Schwarz and the arithmetic–geometric mean inequality to the bilinear cross-terms of $\nabla C \cdot \mathbb{M}(Z)\nabla C$ confirms $\mathbb{M}(Z) \succeq 0$ for every observable C:

$$(H, C) = R^{abcd}\partial_a H\, \partial_b H\, \partial_c C\, \partial_d H = 0, \tag{2.324}$$

$$\dot{S} = \{S, H\} + (S, S) = \nabla S \cdot \mathbb{M}(Z)\nabla S \geq 0. \tag{2.325}$$

In the overdamped limit where momentum relaxation outpaces configurational drift ($\mathbb{J}\nabla H \to \mathbf{o}$) at substrate fluctuation scale $\theta := (\partial H/\partial S)_{\mathbf{z}} > 0$ and calibrated step cadence ν_0 (s^{-1}, (2.250)), coarsening fine spectral coordinates via Theorem 2.2 maps each strongly persistent CCE S_α ($\Xi(S_\alpha) \gg 1$) onto a continuous attractor basin $\mathscr{B}_\alpha \subset \mathscr{Z}$ separated from adjacent basins by saddle hypersurfaces $\partial\mathscr{B}_{\alpha\beta}$. States relax intra-basin along $\mathbb{M}\nabla S$ at rate $\tau_{\mathrm{relax}}^{-1} \sim \nu_0\, \gamma_{\mathrm{int}}(S_\alpha)$ while noise-activated escape across $\partial\mathscr{B}_{\alpha\beta}$ over saddle barrier $\Delta\Phi_{\alpha\to\beta}$ occurs at the exponentially suppressed Eyring–Kramers rate [73, 89], matching discrete boundary conductance $\phi_\partial(S_\alpha)$ via the universal barrier correspondence:

$$\tau_{\mathrm{escape}}^{-1} = \nu_0\, \mu_2(\mathbf{L}_{\mathrm{norm}}) \asymp \tau_{\mathrm{relax}}^{-1}\, e^{-\Delta\Phi_{\alpha\to\beta}/\theta}, \tag{2.326}$$

$$\frac{\Delta\Phi_{\alpha\to\beta}}{\theta} \approx -\ln \phi_\partial(S_\alpha) \asymp \ln\left(\frac{K_{\alpha\alpha}}{K_{\alpha\beta}}\right) = \Delta I_{\mathrm{barrier},\alpha\to\beta} \approx \ln \Xi. \tag{2.327}$$

Continuous attractor basins thus correspond to regions of high diagonal capacity $K_{\alpha\alpha} \gg 1$, whereas separatrix barriers correspond to narrow topological bottlenecks $K_{\alpha\beta} \ll K_{\alpha\alpha}$ (Table 2.1).

EXAMPLE 2.9 (Metriplectic Flow and Casimir Conditions). Consider a single spectral configuration coordinate $x \equiv z^1$ ($n = 1$) of inertia m in a potential $U(x)$, paired with conjugate momentum p and unresolved bath multiplicity S (in nats) at substrate fluctuation scale $\theta > 0$ and friction coefficient $\gamma > 0$ (in $\mathrm{kg\,s}^{-1}$, yielding momentum damping rate γ/m). On the three-dimensional state manifold $Z = (x, p, S)^{\mathsf{T}} \in \mathbb{R}^3$ (2.309), the conserved total energy $H(x, p, S)$ and scalar gradients are:

$$H(x, p, S) = \frac{p^2}{2m} + U(x) + \theta S, \tag{2.328}$$

$$\nabla H = \begin{pmatrix} \partial_x U \\ p/m \\ \theta \end{pmatrix}, \tag{2.329}$$

$$\nabla S = \begin{pmatrix} 0 \\ 0 \\ 1 \end{pmatrix}. \tag{2.330}$$

Assigning the momentum-cut mobility $\sigma = \mathrm{diag}(0, \gamma/\theta, 0)$ and entropic degree weight $\mu = \mathrm{diag}(0, 0, 1)$, the Kulkarni–Nomizu tensor $R = \sigma \owedge \mu$ (2.317)

is supported in the (p, S) two-plane with sectional component $R^{pSpS} = \gamma/\theta$. Contracting R with ∇H via (2.320) alongside the canonical (x, p) symplectic block yields the 3×3 operators:

$$\mathbb{J} = \begin{pmatrix} 0 & 1 & 0 \\ -1 & 0 & 0 \\ 0 & 0 & 0 \end{pmatrix}, \tag{2.331}$$

$$\mathbb{M}(Z) = \frac{\gamma}{m^2\theta} \begin{pmatrix} 0 & 0 & 0 \\ 0 & m^2\theta^2 & -mp\theta \\ 0 & -mp\theta & p^2 \end{pmatrix}. \tag{2.332}$$

Direct multiplication confirms $\mathbb{J}\nabla S = \mathbf{o}$ and $\mathbb{M}\nabla H = \mathbf{o}$, and evaluating (2.321) yields the closed flow, exact energy conservation, and non-negative entropy production:

$$\begin{pmatrix} \dot{x} \\ \dot{p} \\ \dot{S} \end{pmatrix} = \begin{pmatrix} p/m \\ -\partial_x U - (\gamma/m)p \\ \gamma p^2/(m^2\theta) \end{pmatrix}, \tag{2.333}$$

$$\dot{H} = \nabla H \cdot \dot{Z} = -\frac{\gamma p^2}{m^2} + \theta\left(\frac{\gamma p^2}{m^2\theta}\right) = 0, \tag{2.334}$$

$$\dot{S} = \nabla S \cdot \mathbb{M}(Z)\nabla S = \frac{\gamma p^2}{m^2\theta} \geq 0. \tag{2.335}$$

Projecting onto (x, p) recovers standard underdamped Langevin damping $\dot{p} = -\partial_x U - (\gamma/m)p$ (and overdamped gradient drift in the high-friction limit $m/\gamma \to 0$), while kinetic energy lost to friction is converted one-for-one into coarse-grained multiplicity S. ♢

Table 2.1 summarises the complete structural dictionary derived across this chapter: starting solely from an unweighted relational graph $G = (V, E)$ and an admissible assignment $\mathbf{\Pi}$ (Definition 2.1), congruent coarse-graining generates the multiscale capacity algebra (Theorem 2.2), the Capacity Ledger with strictly positive free capacity $\mathcal{Q}_{\text{free}} > 0$ and efficiency bounds (Theorem 2.4 and Lemma 2.5), emergent spectral coordinates, proper time, and Kulkarni–Nomizu curvature (Lemma 2.6), and closed-system metriplectic dynamics from cycle–gradient orthogonality (Lemma 2.7, (2.321)). In an isolated subsystem ($\partial S = \emptyset$), however, passive barrier persistence succumbs to Kramers escape (2.326) and relaxes to equilibrium at maximum multiplicity. Sustaining viability far from equilibrium requires re-opening the boundary cut $\partial S \neq \emptyset$, so Chapter 3 couples CCEs to driven environments, converting free capacity $\mathcal{Q}_{\text{free}}$ into active boundary control and elevating $(\chi_{\text{struct}}, \kappa_{\text{struct}})$ to the dynamical operational metrics of physical intelligence (χ_T) and consciousness (κ_T).

Discrete relational graph	Continuous dynamical limit	Physical and operational meaning
Induced subgraph $G[S_\alpha]$	Attractor basin $\mathscr{B}_\alpha \subset \mathscr{Z}$	Configuration domain supporting a coarse-grained operational state.
Diagonal capacity $K_{\alpha\alpha} = 2\lvert E(S_\alpha)\rvert$	Phase-space volume $\mathrm{vol}(\mathscr{B}_\alpha)$	Coarse-graining depth $I_{\alpha\alpha} = \ln K_{\alpha\alpha}$ (nats) and Boltzmann entropy $S_{\mathrm{th}}(\alpha) = k_{\mathrm{B}} \ln\big(\mathrm{vol}(\mathscr{B}_\alpha)/V_0\big)$ relative to cell V_0.
Intra-block cycle flow $\mathbf{J}_\Omega = -\mathbf{J}_\Omega^{\mathsf{T}}$ $(K_{\alpha\alpha} \geq 2N_\alpha)$	Poisson tensor $\mathbb{J} = -\mathbb{J}^{\mathsf{T}}$ and momenta $\mathbf{p}$	Divergence-free Kirchhoff circulation inside $\mathrm{im}(\mathbf{Q}_\Pi)$ preserving capacity ($\mathbb{J}\nabla S = \mathbf{o}$).
Laplacian eigenmodes $(\mu_k, \boldsymbol{\phi}_k)$	Spectral chart $\mathbf{z}$ and cut conductivity Σ^{ij}	Principal transport axes with global conductivity μ_{k_i} and resistance scale $\mu_{k_i}^{-1}$.
Boundary cut $E(S_\alpha, S_\beta)$ of capacity $K_{\alpha\beta}$	Separatrix saddle hypersurface $\partial\mathscr{B}_{\alpha\beta}$	Narrow bottleneck channel mediating transitions between adjacent coarse-grained states.
Internal connectivity $\gamma_{\mathrm{int}} = \mu_2(\mathbf{L}_{\mathrm{norm}}(G[S_\alpha]))$	Intra-basin relaxation rate $\tau_{\mathrm{relax}}^{-1} \sim \nu_0\gamma_{\mathrm{int}}$	Rapid internal mixing and equilibration restoring local basin steady state.
Boundary conductance $\phi_\partial(S_\alpha)$	Eyring–Kramers escape rate $\tau_{\mathrm{escape}}^{-1} \asymp \tau_{\mathrm{relax}}^{-1} e^{-\Delta\Phi_{\alpha\to\beta}/\theta}$	Exponentially suppressed escape across the saddle barrier $\Delta\Phi_{\alpha\to\beta} \approx -\theta \ln \phi_\partial$.
Strong persistence $\Xi = \gamma_{\mathrm{int}}/\phi_\partial \gg 1$	Generator spectral gap $\tau_{\mathrm{escape}}/\tau_{\mathrm{relax}} \gg 1$ $(\Delta\Phi_{\alpha\to\beta}/\theta \gg 1)$	Timescale separation decoupling memory lifetime from operational update speed.
Combinatorial edge conservation (2.128)–(2.129)	Metriplectic Casimir constraints $\{S, \cdot\} = 0$, $(H, \cdot) = 0$	Exact physical bookkeeping separating reversible circulation from metric dissipation.

TABLE 2.1: Dictionary connecting discrete relational subgraph constructs to emergent spectral coordinates, metastable attractor basins, and continuous metriplectic dynamics.

3

PHYSICAL AGENCY, INTELLIGENCE, AND CONSCIOUSNESS

An embodied physical system is not a mathematical abstraction. To survive and compute, it must maintain its internal structure against environmental perturbations across an open boundary. Whereas Chapter 2 established the architecture of Conservation-Congruent Encodings (CCEs), showing how coarse-graining a relational substrate partitions couplings into internal memory and boundary cuts while generating emergent geometry, curvature, and continuous metriplectic dynamics, this chapter builds on that architecture across open boundaries to establish quantitative metrics for intelligence and consciousness. Expressing these properties as measurable efficiencies rather than qualitative abstractions places biological and engineered systems on a common physical footing.

This chapter is organised into five sections. Section 3.1 introduces physical agency, contrasting closed-loop boundary preservation with passive symbol transmission in classical communication theory. Section 3.2 couples the agent's metriplectic dynamics to an open environment across its boundary cut, separating irreversible boundary dissipation from preserved internal structure. Section 3.3 formalises intelligence (χ) and consciousness (κ) across two complementary formalisms, capturing static structural capacity on a graph cross-section (in links/link) and through-time trajectory efficiency across the spectral dimension of time (in nats/nat). Across both formalisms, intelligence measures preserved stability relative to boundary cost, while consciousness measures that same stability barrier relative to internal model structure. Section 3.4 defines physical emergence along a continuous coordination scale, placing communicative signalling, endosymbiosis, and individual systems on a single spectrum of boundary internalisation while showing how scaling limits drive modular seed replication. Finally, Section 3.5 connects classical game theory to multi-system capacity networks by identifying coupling payoffs with free-capacity gains and conserved efficiencies, unifying non-cooperative equilibria, physical Nash bargaining, weakest-link stability, and exhaustive versus generative dissipation.

3.1 AGENCY

Classical information theory begins with signal transmission: under what conditions can a message selected at an emission point be faithfully reproduced at a destination? Foundational concepts such as Shannon entropy and channel capacity quantify the reliable transmission of bitstrings through noisy media [151]. In Shannon's schematic (Figure 3.1), information flows

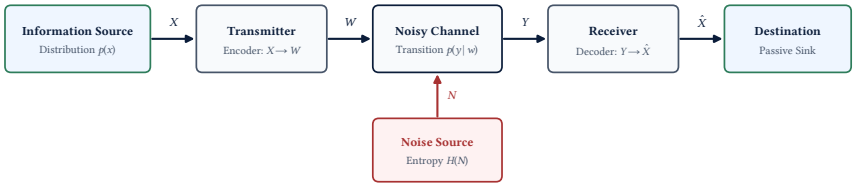


FIGURE 3.1: Shannon's classical communication architecture [151]. Information transfer proceeds along a linear open-loop pipeline: an information source selects a message $X \sim p(x)$, a transmitter encodes it into a channel signal W, a noisy channel governed by transition law $p(y \mid w)$ perturbs W via an external noise source N (entropy $H(N)$) to produce the received signal Y, and a receiver decodes Y into an estimate $\hat{X}$ delivered to a passive destination sink, optimising mutual information $I(X;Y)$ up to channel capacity C.

linearly from a source through an encoder, channel, and decoder to a receiving terminal. The semantic significance and physical consequences of the message lie strictly outside this formulation. The receiver appears in the communication model merely as a passive sink whose sole function is the statistical reconstruction of symbols.

Physical agency shifts the question from how a passive endpoint reconstructs symbols to how an embedded system maintains its internal structure across an open boundary. An incoming signal is not an abstract token to be decoded, but a physical perturbation across that boundary. It acquires operational significance when it updates or stabilises a Conservation-Congruent Encoding that constrains the system's subsequent dynamics.

Because every CCE is realised on a finite relational substrate, acquiring, storing, computing, and resetting distinctions are physical transformations governed by the relational and dynamical conservation laws of Chapter 2. The same invariants that constrain internal state transitions also govern external flux exchange across the boundary cut (appearing in thermal substrates as work and heat exchange), placing internal information processing and external action within a single conservation balance.

The two frameworks differ directly in their optimisation objectives. In Shannon's theory, information transport is quantified by the mutual information between the source variable X and received variable Y:

$$I(X;Y) = H(X) - H(X \mid Y). \tag{3.1}$$

The conditional entropy $H(X \mid Y)$ represents equivocation, the residual uncertainty about the source remaining after observing the received channel output. Mutual information measures the reduction in statistical uncertainty, and channel capacity defines the supremum of this reduction across admissible input distributions:

$$C = \max_{p(x)} I(X;Y). \tag{3.2}$$

Reconstructing the message completes the communication account.

Two receivers that decode the same bitstring achieve identical mutual information $I(X;Y)$, whether one is a passive recording tape destroyed by the next environmental fluctuation or an adaptive organism that uses the signal to deflect the perturbation and survive. Rather than halting at symbol reconstruction, physical agency asks how materially supported distinctions sustain an operational stability barrier ($\Delta I_{\text{barrier},T}$) against environmental dispersion. Maintaining this barrier imposes both an *extrinsic boundary burden* from unpredicted environmental collisions across the interface cut ($I_{\text{irr},\partial}$) and an *intrinsic model burden* to hold and maintain active internal representations ($I_{\text{rev},\Omega}$). As formalised across static network topology (links/link) and through-time trajectories (nats/nat) in Section 3.3, *intelligence* (χ) measures the stability barrier maintained relative to boundary burden—rewarding predictive boundary alignment that tracks incoming perturbations smoothly rather than suffering unaligned boundary collisions—while *consciousness* (κ) measures the same stability barrier relative to internal model burden, rewarding compact, compressed internal representations over brute-force storage. These metrics do not supplant Shannon's channel formulations, but extend physical accounting from passive symbol transport to closed-loop boundary preservation.

3.2 OPEN SYSTEMS

Before defining operational efficiencies in Section 3.3, we must clarify how an embedded physical system interacts with its surroundings and accounts for information across its boundary. Under the open-observer factorisation $\mathscr{C}_{\widetilde{\mathbf{\Pi}}_S} = \mathscr{C}_{\mathbf{\Pi}_S} \circ \mathscr{C}_S$ (2.82) of Chapter 2, two reductions meet at the interface cut ∂S: *Schur boundary reduction* across $\mathscr{C}_S$, which folds the external environment $\bar{S}$ onto the system's exposed ports S_∂ while leaving S uncontracted, and *congruent coarse-graining* via $\mathscr{C}_{\mathbf{\Pi}_S}$, which contracts S into $M \ll N_S$ collective registers. Physically, Schur reduction captures how external reality acts upon the system's boundary, whereas coarse-graining models the system's own compressed internal projection of reality. Subsection 3.2.1 composes these two operations to connect discrete relational graphs to open metriplectic dynamics on $\mathscr{Z}$, and Subsection 3.2.2 separates irreversible boundary dissipation from preserved internal structure.

3.2.1 *Environmental Coupling and Open Dynamics*

Recall from Section 2.1.2 (2.20)–(2.34) and Lemma 2.3 (2.171) that partitioning the closed relational graph $G = (V, E)$ into $V = S \sqcup \bar{S}$ across the boundary cut ∂S separates the system vertices $S = S_\partial \sqcup S_\Omega$ into exposed boundary ports S_∂ ($d_i^{(\text{ext})} > 0$) and the insulated interior core S_Ω ($d_i^{(\text{ext})} = 0$). Eliminating $\bar{S}$ via the inversion commutator of the screened Green's matrix $\mathbf{G}_\varepsilon$ across $\mathscr{C}_S$

defines the effective Dirichlet-to-Neumann Schur Laplacian $\mathbf{L}_{\text{eff}}$, the environmental self-energy $\mathbf{\Sigma}_{\text{env}}$, and the spectral persistence ratio on $\mathbf{L}_{SS}$:

$$\mathbf{L}_{\text{eff}} = \mathbf{L}_{SS} - \mathbf{\Sigma}_{\text{env}} = \mathbf{L}_{SS}^{(\text{int})} + \big(\mathbf{D}_S^{(\text{ext})} - \mathbf{\Sigma}_{\text{env}}\big), \tag{3.3}$$

$$\mathbf{\Sigma}_{\text{env}} := -[\![(\cdot)^{-1}, \mathscr{C}_S]\!](\mathbf{G}_\varepsilon) = \mathbf{L}_{S\bar{S}}\mathbf{L}_{\bar{S}\bar{S}}^{-1}\mathbf{L}_{\bar{S}S}, \tag{3.4}$$

$$\frac{\lambda_2(\mathbf{L}_{SS})}{\lambda_1(\mathbf{L}_{SS})} \gg 1. \tag{3.5}$$

Equations (3.3)–(3.4) leave the internal graph $G[S]$ uncontracted while folding the external environment $\bar{S}$ onto the boundary ports S_∂. Within the three-term decomposition (3.3), $\mathbf{L}_{SS}^{(\text{int})}$ governs isolated transport across internal edges $E(S)$, the diagonal degree potential $\mathbf{D}_S^{(\text{ext})}$ penalises outward Dirichlet leakage across ∂S, and $-\mathbf{\Sigma}_{\text{env}}$ routes flux through the environmental Green's operator $\mathbf{L}_{\bar{S}\bar{S}}^{-1}$ back onto S_∂. Unlike Shannon's one-way channel (Figure 3.1), outgoing actions at S_∂ propagate through $\bar{S}$ and return to perturb sensory ports in a closed physical loop. Because global closure on V enforces $\mathbf{\Sigma}_{\text{env}}\mathbf{1}_S = \mathbf{D}_S^{(\text{ext})}\mathbf{1}_S$, the positive-semidefinite boundary residual $\mathbf{D}_S^{(\text{ext})} - \mathbf{\Sigma}_{\text{env}} \succeq \mathbf{o}$ restores exact conservation ($\mathbf{L}_{\text{eff}}\mathbf{1}_S = \mathbf{o}$) while vanishing identically on S_Ω. This topological shielding insulates core channel updates on $\mathbf{K}_\Omega$ (2.249) from direct external bombardment, while spectral admissibility (3.5) ensures internal mixing outpaces open boundary leakage ($\tau_{\text{relax}} \ll \tau_{\text{escape}}$, Example 2.1).

Because an embedded agent possesses far fewer vertices than its surroundings ($N_S \ll N_V$), it cannot track every external degree of freedom individually. Instead, its admissible assignment matrix $\mathbf{\Pi}_S \in \{0,1\}^{N_S \times M}$ projects S onto $M \ll N_S$ metastable CCE registers (Section 2.2). Applying the matrix congruence $\mathscr{C}_{\mathbf{\Pi}_S}$ (2.79) to (3.3) projects this boundary coupling onto the coarse-grained capacity network:

$$\mathbf{L}_{\mathbf{K},\text{eff}} := \mathbf{\Pi}_S^{\mathsf{T}}\mathbf{L}_{\text{eff}}\mathbf{\Pi}_S = \mathbf{L}_{\mathbf{K}} + \big(\mathbf{D}_{\mathbf{K}}^{(\text{ext})} - \mathbf{\Sigma}_{\mathbf{K},\text{env}}\big), \tag{3.6}$$

$$\mathbf{\Sigma}_{\mathbf{K},\text{env}} := \mathbf{\Pi}_S^{\mathsf{T}}\mathbf{\Sigma}_{\text{env}}\mathbf{\Pi}_S = -\mathscr{C}_{\mathbf{\Pi}_S}\big([\![(\cdot)^{-1}, \mathscr{C}_S]\!](\mathbf{G}_\varepsilon)\big). \tag{3.7}$$

Equation (3.6) preserves coarse-grained closure ($\mathbf{L}_{\mathbf{K},\text{eff}}\mathbf{1}_M = \mathbf{o}$) while separating the agent's two dissipative cut channels, where the internal capacity Laplacian $\mathbf{L}_{\mathbf{K}}$ (2.101) governs inter-basin relaxation across internal cuts $\mathbf{K}_\partial^{(\text{int})}$, whereas $\mathbf{D}_{\mathbf{K}}^{(\text{ext})} - \mathbf{\Sigma}_{\mathbf{K},\text{env}} \succeq \mathbf{o}$ acts exclusively on registers coupled to $\bar{S}$ across the external boundary cut $\mathbf{K}_\partial^{(\text{ext})}$ (2.83). Intra-basin memory links $\mathbf{K}_\Omega$ cancel identically out of $\mathbf{L}_{\mathbf{K},\text{eff}}$ and enter instead through the block degree-volume mass $\mathbf{D}_{\mathbf{K}}$ (2.108), providing volumetric inertia and supporting internal state circulation.

Lifting the coarse-grained capacity architecture onto the spectral state manifold $\mathscr{Z}$ via $\mathbf{\Phi}$ (Section 2.5) maps internal circulation on $\mathbf{K}_\Omega$ and cut relaxation on $\mathbf{L}_{\mathbf{K},\text{eff}}$ onto the unified metriplectic generator metered by the emergent clock t (2.253)–(2.255) [88, 114, 115, 142]:

$$\dot{Z} = \mathbb{J}(Z)\nabla H(Z) + \mathbb{M}(Z)\nabla S(Z), \tag{3.8}$$

$$\mathbb{M}(Z) = \mathbb{M}_\Omega(Z) + \mathbb{M}_\partial(Z). \tag{3.9}$$

Because G is globally closed and environmental coupling enters solely via $\mathbf{L}_{\mathbf{K},\mathrm{eff}}$, no ad hoc external force vector is appended to (3.8). By Lemma 2.7, cyclic subgraphs within $\mathbf{K}_\Omega$ generate divergence-free Poisson circulation along constant-H level sets (2.313). Complementarily, pushing the additive split (3.6) through the Kulkarni–Nomizu 4-bracket (2.320) decomposes the cometric $\mathbb{M}(Z)$ into an internal relaxation cometric $\mathbb{M}_\Omega(Z)$ supported on $\mathbf{K}_\partial^{(\mathrm{int})}$ and a boundary port cometric $\mathbb{M}_\partial(Z)$ supported on $\mathbf{K}_\partial^{(\mathrm{ext})}$, both obeying the channel support rule (2.310). Pair antisymmetry of the Kulkarni–Nomizu mobility tensor (2.317) and (2.324) enforces the Morrison Casimir degeneracies (2.322) and (2.323) across $\mathbb{J}$, $\mathbb{M}_\Omega$, and $\mathbb{M}_\partial$ for the total invariant $H(Z)$ on the extended state manifold $\mathscr{Z}$, conserving total energy identically while partitioning irreversible entropy production across internal and boundary cuts. Marginalising external probe work onto a reduced subsystem state, by contrast, requires Quantum Non-Demolition commutation to conserve the subsystem Hamiltonian alone (Section 4.2.2).

3.2.2 *Boundary Dissipation and Preserved Internal Structure*

Why does physical accounting for an embedded system separate boundary and internal quantities? Because coarse-graining $\mathbf{\Pi}_S$ compresses a vast external environment $\bar{S}$ into M finite registers, evolution across emergent slices incurs two distinct physical costs. Whenever incoming modes across $\mathbf{K}_\partial^{(\mathrm{ext})}$ exceed or arrive out of phase with the boundary state, the mismatch dissipates across $\mathbb{M}_\partial$ as irreversible boundary dissipation. Meanwhile, holding those M registers in a displaced state within $\mathbf{K}_\Omega$ stores preserved internal structure against relaxation across $\mathbb{M}_\Omega$. Along the emergent continuum time $t \in [0,T]$ derived in Section 2.5.2 (metered against an embedded reference sub-block $\bar{S}_{\mathrm{ref}}$ via (2.247)–(2.255), carrying reference nats prior to clock selection and seconds when $\bar{S}_{\mathrm{ref}}$ is chosen as a physical reference oscillator), contracting the entropy gradient $\nabla S(Z)$ (with $S(Z)$ in nats) against the cometric split (3.9) defines the internal and boundary entropy production rates (in nats/nat against uncalibrated τ_{ref}, or nats s^{-1} when t is in seconds):

$$\dot{I}_{\mathrm{irr},\Omega}(t) := \nabla S(Z_t) \cdot \mathbb{M}_\Omega(Z_t) \nabla S(Z_t) \geq 0, \tag{3.10}$$

$$\dot{I}_{\mathrm{irr},\partial}(t) := \nabla S(Z_t) \cdot \mathbb{M}_\partial(Z_t) \nabla S(Z_t) \geq 0. \tag{3.11}$$

On the coarse-grained capacity network $(\mathbf{K},\mathbf{\Pi})$ with dimensionless block potentials $\mathbf{z}_S(t) \in \mathbb{R}^M$ on S and $\mathbf{z}_{\bar{S}}(t) \in \mathbb{R}^{M_{\bar{S}}}$ on $\bar{S}$ (entries $z_{S,\alpha}(t)$ and $z_{\bar{S},\mu}(t)$), boundary dissipation originates in potential mismatch across the external cut matrix $\mathbf{K}_\partial^{(\mathrm{ext})}$ (2.83), quantified by the cross-boundary Dirichlet mismatch (in links):

$$\sum_{\{i,j\}\in\partial S} \left((\mathbf{\Pi}_S \mathbf{z}_S(t))_i - (\mathbf{\Pi}_{\bar{S}} \mathbf{z}_{\bar{S}}(t))_j\right)^2 = \sum_{\alpha=1}^{M} \sum_{\mu=1}^{M_{\bar{S}}} \left(\mathbf{K}_\partial^{(\mathrm{ext})}\right)_{\mu\alpha} \left(z_{S,\alpha}(t) - z_{\bar{S},\mu}(t)\right)^2 \geq 0. \tag{3.12}$$

Equation (3.12) grounds the physical distinction between aligned and unaligned boundary interaction. Under *predictive boundary alignment*, an internal model that anticipates incoming environmental trajectories coordinates its boundary port potentials ahead of impact so that $z_{S,\alpha}(t)$ tracks $z_{\tilde{S},\mu}(t)$ across coupled ports ($(\mathbf{K}_{\partial}^{(\mathrm{ext})})_{\mu\alpha} > 0$), driving cross-cut strain and boundary dissipation towards zero ($\dot{I}_{\mathrm{irr},\partial} \to 0$). Conversely, under *unpredicted boundary collisions*, an uncoordinated interface meets external perturbations out of phase ($z_{S,\alpha}(t) \neq z_{\tilde{S},\mu}(t)$), generating large cross-cut gradients that relax irreversibly through $\mathbb{M}_{\partial}$ ($\dot{I}_{\mathrm{irr},\partial} \gg 0$). Along multi-slice trajectories, this alignment parallels path-space selection principles such as maximum calibre [136] and resonant matching to structured environmental inputs [132].

Across a discrete sequence of N_τ spectral slices $\tau \in \{1, \dots, N_\tau\}$ (Section 2.5.1), summing the per-slice irreversible boundary dissipation $\Delta I_{\mathrm{irr},\partial}(\tau) \geq 0$ (1.35) defines the cumulative boundary dissipation $I_{\mathrm{irr},\partial,T}$ in nats, passing in the fine-slice continuum limit to the emergent-horizon integral of $\dot{I}_{\mathrm{irr},\partial}(t)$. When t is metered in seconds via (2.255) at substrate fluctuation scale θ (J nat^{-1}, such as $\theta = k_{\mathrm{B}}T_{\mathrm{th}}$ in an isothermal bath at temperature T_{th}), multiplying $\dot{I}_{\mathrm{irr},\partial}(t)$ by θ expresses instantaneous boundary dissipation power $P_{\mathrm{diss},\partial}(t)$ directly in watts:

$$I_{\mathrm{irr},\partial,T} := \sum_{\tau=1}^{N_\tau} \Delta I_{\mathrm{irr},\partial}(\tau), \tag{3.13}$$

$$I_{\mathrm{irr},\partial,T} = \int_0^T \dot{I}_{\mathrm{irr},\partial}(t)\,\mathrm{d}t, \tag{3.14}$$

$$P_{\mathrm{diss},\partial}(t) := \theta\, \dot{I}_{\mathrm{irr},\partial}(t). \tag{3.15}$$

The integral $I_{\mathrm{irr},\partial,T}$ is invariant under reference-clock rescaling and measures physical entropy dissipated across the interface cut ∂S, distinct from logical Landauer bit erasure. A physical system dissipates finite boundary entropy resisting unpredicted environmental collisions even when zero internal logical bits are erased.

Whereas $I_{\mathrm{irr},\partial,T}$ accumulates path-dependent dissipation across ∂S, the internal state measures the preserved structure retained within the intra-basin memory sector $\mathbf{K}_\Omega$. On the capacity network of Chapter 2 (Section 2.3.1 and Section 2.5.2, (2.137) and (2.325)), isolated internal cuts $\mathbf{K}_{\partial}^{(\mathrm{int})}$ relax along $\mathbb{M}\nabla S$ towards the passive degree-weighted baseline ($d_\alpha / \mathrm{Tr}(\mathbf{D}_{\mathbf{K}})$ on $G_{\mathbf{K}}$). Sustaining predictive states on $\mathscr{X}$ requires holding internal registers at a positive state displacement $\Delta U_{\mathrm{neq}}(t) \geq 0$ (calibrated in joules at substrate scale θ, or dimensionless Kullback–Leibler divergence on uncalibrated discrete networks) above this passive baseline. Dividing ΔU_{neq} by θ (J nat^{-1}) defines preserved internal structure $I_{\mathrm{rev},\Omega}$ in nats, whose proper-time-weighted average across slices by w_τ (2.248) passes in the fine-slice limit over elapsed stand-

ardised observer proper time τ_T (2.256)–(2.257) to the proper-time horizon average $I_{\mathrm{rev},\Omega,T}$:

$$I_{\mathrm{rev},\Omega}(t) := \frac{\Delta U_{\mathrm{neq}}(t)}{\theta}, \tag{3.16}$$

$$I_{\mathrm{rev},\Omega,T} := \sum_{\tau=1}^{N_\tau} w_\tau I_{\mathrm{rev},\Omega}(\tau), \tag{3.17}$$

$$I_{\mathrm{rev},\Omega,T} = \frac{1}{\tau_T}\int_0^{\tau_T} I_{\mathrm{rev},\Omega}(\tau)\,\mathrm{d}\tau. \tag{3.18}$$

Pairing cumulative boundary dissipation (3.13)–(3.14) with the proper-time-weighted internal average (3.17)–(3.18) places $I_{\mathrm{irr},\partial,T}$ and $I_{\mathrm{rev},\Omega,T}$ in identical, clock-invariant units of nats, directly paralleling the discrete structural loads $\mathcal{Q}_\partial$ and $\mathcal{Q}_\Omega$ in links. Specifically, $\dot{I}_{\mathrm{irr},\partial}(t)\,\mathrm{d}t$ integrates total boundary entropy in (3.14) while $\mathrm{d}\tau$ cancels τ_T^{-1} in (3.18) via (2.257), leaving both quantities strictly independent of $\bar{S}_{\mathrm{ref}}$ and exact along general worldlines (Section 6.2.3). Whenever the proper-time lapse rate is constant across $[0,T]$ (as at rest relative to $\bar{S}_{\mathrm{ref}}$, where $\mathrm{d}\tau = \mathrm{d}t$ and $\tau_T = T$), (3.18) reduces identically to the coordinate-time average over $[0,T]$.

Because internal barriers across $\mathbf{K}_\partial^{(\mathrm{int})}$ are finite ($\Xi < \infty$), spontaneous relaxation along $\mathbb{M}_\Omega$ continuously pulls displaced states back towards the passive baseline over a characteristic relaxation timescale $\tau_{\mathrm{relax}} > 0$ (measured in the same time unit as t, whether reference nats or seconds). Holding $\Delta U_{\mathrm{neq}}(t)$ against this decay requires continuous internal maintenance dissipation $\dot{I}_{\mathrm{irr},\Omega}(t)$ and maintenance power $P_{\mathrm{maint},\Omega}(t)$ (in watts when t and τ_{relax} are in seconds), decomposing total entropy production orthogonally across (3.9):

$$\dot{I}_{\mathrm{irr},\Omega}(t) = \frac{I_{\mathrm{rev},\Omega}(t)}{\tau_{\mathrm{relax}}}, \tag{3.19}$$

$$P_{\mathrm{maint},\Omega}(t) := \theta\,\dot{I}_{\mathrm{irr},\Omega}(t) = \frac{\theta\, I_{\mathrm{rev},\Omega}(t)}{\tau_{\mathrm{relax}}}, \tag{3.20}$$

$$\dot{I}_{\mathrm{irr}}(t) = \dot{I}_{\mathrm{irr},\Omega}(t) + \dot{I}_{\mathrm{irr},\partial}(t). \tag{3.21}$$

Equations (3.19)–(3.20) establish that committing large uncompressed capacity to a volatile internal model ($I_{\mathrm{rev},\Omega} \gg 0$ at finite τ_{relax}) demands proportionally higher maintenance dissipation to counteract relaxation, whereas the passive baseline ($\Delta U_{\mathrm{neq}} = 0$) incurs zero maintenance cost.

Disconnecting active maintenance at instant t_0 allows the displaced internal degrees of freedom to relax along $\mathbb{M}_\Omega$ towards their passive baseline [150]. Integrating the resulting relaxation dissipation rate $\dot{I}_{\mathrm{irr},\Omega}(t)$ (calibrated energetically as heat power $\theta\,\dot{I}_{\mathrm{irr},\Omega}(t)$ in watts when t is metered in seconds) over $t \geq t_0$ recovers $\Delta U_{\mathrm{neq}}(t_0)$, yielding an operational telemetry estimator for preserved internal structure (in nats):

$$I_{\mathrm{rev},\Omega}(t_0) = \frac{\Delta U_{\mathrm{neq}}(t_0)}{\theta} = \int_{t_0}^{\infty} \dot{I}_{\mathrm{irr},\Omega}(t)\,\mathrm{d}t. \tag{3.22}$$

For metastable basins confined around a displaced operating point, integrating this post-disconnect relaxation (3.22) calibrates preserved internal structure across semiconductor and biological neuronal substrates (Section 1.3.3), while vanishing identically on passive baseline wells.

3.3 INTELLIGENCE AND CONSCIOUSNESS

With the open metriplectic generator and trajectory integrals established, we now construct the formal metrics of agency. Rather than defining intelligence through arbitrary task scores or behavioural benchmarks, we ground intelligence (χ) and consciousness (κ) in physical boundary defence and generative model economy across two complementary formalisms: static structural capacity on a discrete graph cross-section and through-time trajectory efficiency across the emergent temporal coordinate.

3.3.1 *Static Structural and Through-Time Trajectory Metrics*

In the *static structural formalism*, slicing the capacity network perpendicular to the emergent temporal axis $\boldsymbol{\phi}_{\text{time}}$ (Section 2.5.1) isolates an instantaneous graph cross-section with total relational capacity $\mathcal{Q}_{\text{total}} = \text{vol}(S)$. Recall from Section 2.4.2 (2.200)–(2.203) and Lemma 2.5 (2.204)–(2.207) that Frobenius orthogonality between internal memory load $\mathcal{Q}_\Omega$ and boundary cut load $\mathcal{Q}_\partial$ fixes the uncommitted free capacity $\mathcal{Q}_{\text{free}} = \mathcal{Q}_{\text{total}} - \mathcal{Q}_{\text{alloc}}$, the dimensionless structural efficiencies $\chi_{\text{struct}} = \mathcal{Q}_{\text{free}}/\mathcal{Q}_\partial$ and $\kappa_{\text{struct}} = \mathcal{Q}_{\text{free}}/\mathcal{Q}_\Omega$ (in links/link), and the free-capacity share $\eta_{\text{free}}(\chi_{\text{struct}}, \kappa_{\text{struct}})$. Together, $(\chi_{\text{struct}}, \kappa_{\text{struct}})$ quantify static architectural headroom prior to trajectory execution, yet static link counts alone cannot resolve how a system acts through time. Two networks with identical $(\mathcal{Q}_\Omega, \mathcal{Q}_\partial, \mathcal{Q}_{\text{free}})$ perform very differently depending on whether boundary channels $\mathbf{K}_\partial^{(\text{ext})}$ meet incoming environmental fluxes in predictive phase alignment or absorb unpredicted collisions, and whether a compact internal core $\mathbf{K}_\Omega$ is reused cyclically across epochs or duplicated statically across registers. Moreover, internal transition cuts $\mathbf{K}_\partial^{(\text{int})}$ pooled into $\mathcal{Q}_\partial$ on a static slice separate dynamically into internal relaxation $\mathbb{M}_\Omega$ in (3.9).

The *through-time trajectory formalism* evaluates agency across an ordered sequence of N_τ spectral slices $\tau \in \{1, \dots, N_\tau\}$ (Section 2.5.1) carrying intrinsic slice proper-time increments $\Delta\tau_{\text{nat}}(\tau)$, reference coordinate horizon T metered against $\bar{S}_{\text{ref}}$, elapsed standardised observer proper time τ_T, and proper-time weights w_τ (2.243)–(2.257). On each viable slice τ whose uncommitted free capacity $\mathcal{Q}_{\text{free},\tau}$ exceeds the elementary unit link $\mathcal{Q}_0 := 1\,\text{link}$, normalising $\mathcal{Q}_{\text{free},\tau}$ against $\mathcal{Q}_0$ defines the dimensionless *slice stability barrier* $\Delta I_{\text{barrier}}(\tau)$ in nats (written $\Delta I_{\text{barrier}}$ on a single slice). Averaging $\Delta I_{\text{barrier}}(\tau)$ across the N_τ slices by the clock-invariant weights w_τ defines the dimensionless through-time *stability barrier* $\Delta I_{\text{barrier},T}$, passing in the fine-slice continuum limit via (2.257) to the proper-time horizon average (and coinciding identically

with the coordinate-time average over $[0, T]$ whenever the proper-time lapse rate is constant):

$$\Delta I_{\text{barrier}}(\tau) := \ln\left(\frac{\mathcal{Q}_{\text{free},\tau}}{\mathcal{Q}_0}\right), \tag{3.23}$$

$$\Delta I_{\text{barrier},T} := \sum_{\tau=1}^{N_\tau} w_\tau \Delta I_{\text{barrier}}(\tau) = \sum_{\tau=1}^{N_\tau} w_\tau \ln\left(\frac{\mathcal{Q}_{\text{free},\tau}}{\mathcal{Q}_0}\right), \tag{3.24}$$

$$\Delta I_{\text{barrier},T} = \frac{1}{\tau_T}\int_0^{\tau_T} \Delta I_{\text{barrier}}(\tau)\,\mathrm{d}\tau. \tag{3.25}$$

Whereas the pairwise barrier $\Delta I_{\text{barrier},\alpha\to\beta}$ (2.327) measures local Kramers isolation between two coarse-grained registers α and β, $\Delta I_{\text{barrier},T}$ (3.24)–(3.25) measures uncommitted reserve across the open system as a whole. On any slice with $\mathcal{Q}_\partial > 0$ and M internal registers of diagonal trace $\mathrm{Tr}(\mathbf{K}_\Omega)$ (2.249), substituting the strict multi-register ceiling (2.219) into (3.23) bounds the slice barrier above:

$$\Delta I_{\text{barrier}} < \ln\left(\frac{\mathcal{Q}_{\text{total}} - M^{-1/2}\,\mathrm{Tr}(\mathbf{K}_\Omega)}{\mathcal{Q}_0}\right). \tag{3.26}$$

Equation (3.26) reconciles local register depth with global system reserve across register counts. Collapsing all internal links into a single monolithic well ($M = 1$) maximises passive Kramers isolation yet caps $\mathcal{Q}_{\text{free}}$ below $|\partial S|$ via (2.220), preventing $\Delta I_{\text{barrier}}$ from scaling with internal volume $|E(S)|$. On a symmetric two-basin switch ($M = 2$, Example 2.3) with balanced registers $K_{\alpha\alpha} \gg \mathcal{Q}_\partial$, both $\Delta I_{\text{barrier},1\to2}$ and $\Delta I_{\text{barrier}}$ grow as $\ln(K_{11}/\mathcal{Q}_0)$ up to the additive constant $\ln(2-\sqrt{2})$. Across differentiated multi-register architectures ($M \gg 1$ with $K_{\alpha\alpha} \gg K_{\alpha\beta}$), the $M^{-1/2}$ suppression of $\mathcal{Q}_\Omega$ keeps individual registers metastable ($\Delta I_{\text{barrier},\alpha\to\beta} \gg 1$) while elevating $\mathcal{Q}_{\text{free}}$ towards $(1-M^{-1/2})\mathcal{Q}_{\text{total}}$, and logarithmic proper-time averaging in (3.24) penalises transient bottlenecks whenever $\mathcal{Q}_{\text{free},\tau}$ contracts towards $\mathcal{Q}_0$ without requiring external path-action functionals. Projecting the open capacity Laplacian $\mathbf{L}_{\mathbf{K},SS} = \mathbf{L}_{\mathbf{K}} + \mathbf{D}_{\mathbf{K}}^{(\text{ext})}$ (2.102) onto the $\mathbf{D}_{\mathbf{K}}^{(\text{int})}$-orthonormal spectral coordinate axes $\boldsymbol{\phi}_k$ ($k = 2, \ldots, d_s + 1$) of $\boldsymbol{\Phi}$ in (2.229)–(2.236) separates internal modal relaxation $\mu_k(\mathbf{L}_{\text{norm}})$ from modal port exposure $\mu_{\partial,k}$:

$$\mu_{\partial,k} := \boldsymbol{\phi}_k^{\mathsf{T}}\mathbf{D}_{\mathbf{K}}^{(\text{ext})}\boldsymbol{\phi}_k \geq 0, \tag{3.27}$$

$$\frac{\boldsymbol{\phi}_k^{\mathsf{T}}\mathbf{L}_{\mathbf{K},SS}\boldsymbol{\phi}_k}{\boldsymbol{\phi}_k^{\mathsf{T}}\mathbf{D}_{\mathbf{K}}\boldsymbol{\phi}_k} = \frac{\mu_k(\mathbf{L}_{\text{norm}}) + \mu_{\partial,k}}{1 + \mu_{\partial,k}}. \tag{3.28}$$

Equations (3.27)–(3.28) show why spectral dimension d_s directly shapes trajectory efficiency: every additional uncompressed spectral coordinate axis resolved in $\boldsymbol{\Phi}$ adds modal relaxation and port exposure that must be maintained and aligned across the emergent horizon T. Comparing the stability barrier $\Delta I_{\text{barrier},T}$ with these boundary and internal burdens defines the through-time metrics of agency.

DEFINITION 3.1 (Intelligence, Consciousness, and the Agency Identity). Let an open embedded subsystem S with admissible CCE partition operate across

N_τ spectral slices (or their continuum limit) over an emergent horizon $T > 0$ (2.244)–(2.255) with through-time stability barrier $\Delta I_{\text{barrier},T} \geq 0$ (3.24)–(3.25), positive cumulative boundary dissipation $I_{\text{irr},\partial,T} > 0$ (3.13)–(3.14), and positive proper-time-averaged preserved internal structure $I_{\text{rev},\Omega,T} > 0$ (3.17)–(3.18). Its through-time *intelligence* χ_T and *consciousness* κ_T are defined in dimensionless informational units (nats/nat) by:

$$\chi_T := \frac{\Delta I_{\text{barrier},T}}{I_{\text{irr},\partial,T}}, \tag{3.29}$$

$$\kappa_T := \frac{\Delta I_{\text{barrier},T}}{I_{\text{rev},\Omega,T}}. \tag{3.30}$$

Equating the shared barrier numerator $\Delta I_{\text{barrier},T}$ across (3.29)–(3.30) yields the *unifying agency identity* (1.61):

$$\Delta I_{\text{barrier},T} = \chi_T I_{\text{irr},\partial,T} = \kappa_T I_{\text{rev},\Omega,T}, \tag{3.31}$$

$$\chi_T = \kappa_T \frac{I_{\text{rev},\Omega,T}}{I_{\text{irr},\partial,T}}, \tag{3.32}$$

with degenerate boundary limits extended continuously under Section 3.3.2.

In Definition 3.1, intelligence χ_T measures maintained barrier nats per nat of irreversible boundary dissipation, whereas consciousness κ_T measures maintained barrier nats per nat of preserved internal structure, coupled in (3.32) just as χ_{struct} and κ_{struct} are coupled in (2.203), and strictly invariant under reference-clock rescaling. Equation (3.32) states the division of physical labour in embedded agents: intelligence (χ) is an extrinsic boundary defence metric quantifying how effectively a system prevents destructive collisions across its interface cut, whereas consciousness (κ) is an intrinsic model economy metric quantifying how compactly the internal substrate represents environmental structure to secure that protection. Whenever reporting in SI energetic units is desired on a substrate with fluctuation scale θ (J nat^{-1}, such as $\theta = k_B T_{\text{th}}$ in an isothermal bath at temperature T_{th}), multiplying by θ calibrates both the static and through-time barriers in joules and expresses the efficiencies in J nat^{-1} without introducing an additional formalism:

$$\Delta\Phi := \theta\, \Delta I_{\text{barrier}} = \theta \ln\left(\frac{\mathcal{Q}_{\text{free}}}{\mathcal{Q}_0}\right), \tag{3.33}$$

$$\Delta\Phi_T := \theta\, \Delta I_{\text{barrier},T}, \tag{3.34}$$

$$(\theta\chi_T,\, \theta\kappa_T) = \left(\frac{\Delta\Phi_T}{I_{\text{irr},\partial,T}},\, \frac{\Delta\Phi_T}{I_{\text{rev},\Omega,T}}\right). \tag{3.35}$$

3.3.2 *Operational Regimes in the Efficiency Plane*

The orthogonal capacity ceiling (2.196) and the agency identity (3.32) partition physical systems across the (χ_T, κ_T) operational efficiency plane (Figure 3.2). Sustaining active agency ($\Delta I_{\text{barrier},T} > 0$ with $I_{\text{rev},\Omega,T} > 0$) requires

operating strictly inside the interior of the capacity disk, with positive internal CCE allocation ($\mathcal{Q}_\Omega > 0$), open external boundary ports ($\mathcal{Q}_\partial^{(\mathrm{ext})} > 0$), and uncommitted free capacity above the unit link ($\mathcal{Q}_{\mathrm{free},\tau} > \mathcal{Q}_0$, securing $\Delta I_{\mathrm{barrier}}(\tau) > 0$). Driving internal capacity or active state retention to either extreme produces two degenerate limits in which operational agency collapses.

At the lower endpoint lies the *internal-depletion limit*, which clarifies why intelligence χ_T must be metered against irreversible boundary dissipation $I_{\mathrm{irr},\partial,T}$ (3.29) rather than total dissipation $I_{\mathrm{irr},T}$ (3.21). If internal maintenance dissipation $\dot{I}_{\mathrm{irr},\Omega}$ (3.19) were penalised alongside boundary dissipation in the denominator of χ_T, extinguishing internal state maintenance would appear to raise efficiency by eliminating maintenance overhead. Structurally on $G_{\mathbf{K}}$, starving the intra-basin memory sector ($K_{\alpha\alpha} \to 0$, $\mathcal{Q}_\Omega \to 0$) across an open cut ($\mathcal{Q}_\partial^{(\mathrm{ext})} > 0$) violates Axiom I ($K_{\alpha\alpha} \geq 2$) and collapses spectral persistence $\Xi(S_\alpha)$ (2.127), destroying metastable CCE basins altogether. Dynamically on an admissible open substrate ($\mathcal{Q}_\Omega \geq 2\sqrt{M}$, $\mathcal{Q}_\partial^{(\mathrm{ext})} > 0$), whereas a short-horizon comparison at fixed static reserve $\mathcal{Q}_{\mathrm{free}}$ can still exhibit residual passive barrier depth (Example 3.1), extinguishing active preserved internal structure $I_{\mathrm{rev},\Omega,T} \to 0^+$ under sustained external perturbation leaves $\mathbf{K}_\partial^{(\mathrm{ext})}$ unaligned against incoming environmental fluxes so uncountered boundary loading erodes uncommitted slice reserve $\mathcal{Q}_{\mathrm{free},\tau} \to \mathcal{Q}_0^+$. Perturbations then strike ∂S out of phase ($I_{\mathrm{irr},\partial,T} > 0$) as the dynamically maintained barrier vanishes linearly ($\Delta I_{\mathrm{barrier},T} = \kappa_{T,0}\, I_{\mathrm{rev},\Omega,T} + o(I_{\mathrm{rev},\Omega,T})$ with $0 \leq \kappa_{T,0} \leq \kappa_T^*(0^+)$), projecting (χ_T, κ_T) onto the vertical $\chi_T = 0$ axis of Figure 3.2:

$$\mathcal{Q}_\Omega \to 0 \implies \Xi(S_\alpha) \to 0, \tag{3.36}$$

$$I_{\mathrm{rev},\Omega,T} \to 0^+ \implies \chi_T = \frac{\Delta I_{\mathrm{barrier},T}}{I_{\mathrm{irr},\partial,T}} \to 0^+, \tag{3.37}$$

$$(\chi_T, \kappa_T) \to (0, \kappa_{T,0}). \tag{3.38}$$

Equations (3.36)–(3.38) show that forfeiting internal retention collapses intelligence onto $\chi_T = 0$ rather than inflating it. By the same accounting, an unpartitioned passive block ($M = 1$, $I_{\mathrm{rev},\Omega,T} = 0$) exposed across a single scalar external cut ($M_{\bar{S}} = 1$) has vanishing internal transition cut $\mathcal{Q}_\partial^{(\mathrm{int})} = 0$, satisfies $\chi_{\mathrm{struct}} < 1$ and $\kappa_{\mathrm{struct}} < 1$ identically (Lemma 2.5), and retains zero displaced internal structure to align ∂S, fixing $\chi_T = 0$ under ongoing environmental perturbation ($I_{\mathrm{irr},\partial,T} > 0$).

At the upper endpoint lies the *internal-saturation limit*, in which a system commits its entire relational capacity to internal structure ($\mathcal{Q}_\Omega \to \mathcal{Q}_{\mathrm{total}}$). Under the Pythagorean capacity bound (2.196) and free-capacity identity (2.200), saturating $\mathcal{Q}_\Omega$ simultaneously severs boundary channels and depletes uncommitted free capacity:

$$\mathcal{Q}_\Omega \to \mathcal{Q}_{\mathrm{total}} \implies \mathcal{Q}_\partial \to 0 \text{ and } \mathcal{Q}_{\mathrm{free}} \to 0, \tag{3.39}$$

$$\mathcal{Q}_\partial^{(\mathrm{ext})} \to 0 \text{ and } \mathcal{Q}_{\mathrm{free}} \to 0 \implies \kappa_{\mathrm{struct}} \to 0 \implies (\chi_T, \kappa_T) = (0, 0). \tag{3.40}$$

Equations (3.39)–(3.40) establish that internal complexity divorced from an open boundary confers zero operational agency. Even if an isolated interior retains large preserved internal structure ($I_{\mathrm{rev},\Omega,T} \gg 0$) and high internal maintenance dissipation ($\dot{I}_{\mathrm{irr},\Omega} \gg 0$), severing $\mathbf{K}_{\partial}^{(\mathrm{ext})}$ and depleting $\mathcal{Q}_{\mathrm{free}}$ eliminate active boundary stabilisation, collapsing structural consciousness κ_{struct} and setting $(\chi_T, \kappa_T) = (0, 0)$ on the closed boundary.

Strictly between these two limits, viable open architectures ($\Delta I_{\mathrm{barrier},T} > 0$) populate three characteristic interior regimes of Figure 3.2 according to the balance between preserved internal structure $I_{\mathrm{rev},\Omega,T}$ and boundary dissipation $I_{\mathrm{irr},\partial,T}$ in (3.32). A *reactive automaton* (such as a binary thermostat) commits minimal internal capacity ($\mathcal{Q}_\Omega \ll \mathcal{Q}_\partial$) and holds negligible preserved internal structure ($I_{\mathrm{rev},\Omega,T} \ll 1$), securing high model economy κ_T over a narrow basin, but lacks multi-step predictive structure and incurs heavy unpredicted boundary collisions ($I_{\mathrm{irr},\partial,T} \gg I_{\mathrm{rev},\Omega,T}$) that confine it to low χ_T. Conversely, an *uncompressed supercomputer* forecasting atmospheric dynamics achieves accurate predictive deflection and high intelligence χ_T, but relies on brute-force state retention across vast register banks ($I_{\mathrm{rev},\Omega,T} \gg I_{\mathrm{irr},\partial,T}$) sustained by megawatt-scale maintenance power ($P_{\mathrm{maint},\Omega} \gg 0$), depressing consciousness κ_T. By contrast, the *biological brain* operates on a 20 W power budget yet attains high χ_T and high κ_T simultaneously, as hierarchical CCE coarse-graining compresses environmental regularities into a compact generative model, preserving generous free capacity $\mathcal{Q}_{\mathrm{free}}$ while keeping both boundary dissipation and preserved internal structure low.

3.3.3 *The Pareto Frontier of Intelligence and Consciousness*

While the coupling identity (3.32) links intelligence and consciousness at any single operating point, finite total relational capacity $\mathcal{Q}_{\mathrm{total}}$ prevents an embedded system from driving both efficiencies upward without bound. On a static graph slice, Lemma 2.5 (2.204)–(2.205) already fixes the quadratic trade-off curve and symmetric joint ceiling of $(\chi_{\mathrm{struct}}, \kappa_{\mathrm{struct}})$. Across emergent time, shifting links or active registers towards internal memory $\mathbf{K}_\Omega$ resolves environmental modes ahead of impact and suppresses unpredicted boundary dissipation $I_{\mathrm{irr},\partial,T}$ at the expense of higher preserved internal structure $I_{\mathrm{rev},\Omega,T}$. Conversely, coarsening the internal representation lowers $I_{\mathrm{rev},\Omega,T}$ at the cost of residual boundary collisions across ∂S, while expanding allocated capacity $\mathcal{Q}_{\mathrm{alloc}}$ compresses $\mathcal{Q}_{\mathrm{free},\tau}$ and lowers the shared barrier $\Delta I_{\mathrm{barrier},T}$ (3.24). Across the set $\mathscr{A}_{\mathrm{adm}}$ of spectrally admissible assignments $\mathbf{\Pi}$ (Section 3.2.1) that sustain a barrier threshold $\Delta I_{\mathrm{barrier},T} \geq \Delta I_{\mathrm{min}} > 0$, architectural selection defines a multi-objective Pareto problem bounded by the non-dominated efficiency frontier $\kappa_T^*(\chi_T)$ (Figure 3.2):

$$\mathbf{\Pi}^* \in \operatorname{Pareto} \arg\max_{\mathbf{\Pi} \in \mathscr{A}_{\mathrm{adm}}} \big(\chi_T(\mathbf{\Pi}),\, \kappa_T(\mathbf{\Pi})\big), \tag{3.41}$$

$$\kappa_T^*(\chi_T) := \sup\big\{\kappa_T(\mathbf{\Pi}) : \mathbf{\Pi} \in \mathscr{A}_{\mathrm{adm}},\ \chi_T(\mathbf{\Pi}) \geq \chi_T\big\}. \tag{3.42}$$

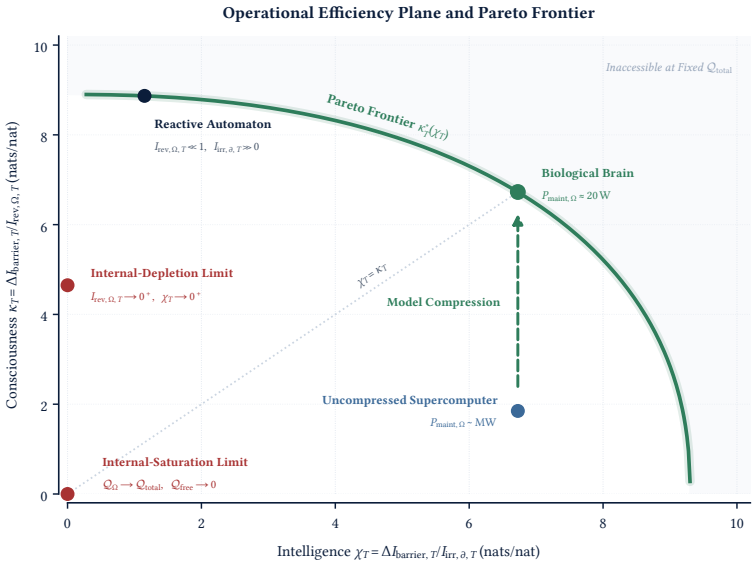


FIGURE 3.2: Operational efficiency plane (χ_T, κ_T) (in dimensionless nats/nat) and the Pareto frontier $\kappa_T^*(\chi_T)$ at fixed total relational capacity $\mathcal{Q}_{\text{total}}$. Degenerate regimes collapse onto the axes: in the dynamical internal-depletion limit ($I_{\text{rev},\Omega,T} \to 0^+$ under unpredicted boundary dissipation $I_{\text{irr},\partial,T} > 0$), predictive boundary alignment vanishes and (χ_T, κ_T) collapses onto the vertical boundary segment $\{0\}\times[0, \kappa_T^*(0^+)]$ (while structural depletion $\mathcal{Q}_\Omega \to 0$ destroys metastable CCE basins altogether), whereas the internal-saturation limit ($\mathcal{Q}_\Omega \to \mathcal{Q}_{\text{total}}$) severs boundary channels and depletes free capacity ($\mathcal{Q}_{\text{free}} \to 0$), collapsing (χ_T, κ_T) to the origin. In the viable interior, an uncompressed supercomputer achieves high χ_T at megawatt maintenance cost ($P_{\text{maint},\Omega} \sim$ MW, low κ_T). Congruent model compression eliminates redundant preserved internal structure $I_{\text{rev},\Omega,T}$ to reach the non-dominated frontier $\kappa_T^*(\chi_T)$ (3.42), spanning reactive automata ($I_{\text{rev},\Omega,T} \ll 1$, $I_{\text{irr},\partial,T} \gg 0$) through the biological brain at the high-(χ_T, κ_T) knee ($P_{\text{maint},\Omega} \approx 20$ W).

Equations (3.41)–(3.42) distinguish two operational movements in the (χ_T, κ_T) plane. Encodings that retain redundant or unaligned internal states—such as the uncompressed supercomputer of Section 3.3.2—occupy the dominated interior ($\kappa_T < \kappa_T^*(\chi_T)$). Compressing redundant fine-grained states into invariant-preserving CCE blocks eliminates excess $I_{\text{rev},\Omega,T}$ and maintenance dissipation while freeing capacity $\mathcal{Q}_{\text{free}}$, driving the system upward onto $\kappa_T^*(\chi_T)$ without sacrificing boundary defence. Once redundant internal allocation is eliminated along $\kappa_T^*(\chi_T)$, further gains in χ_T require finer predictive resolution that lowers κ_T, tracing a continuous frontier from reactive automata (high κ_T, low χ_T), through balanced generative compression at the frontier knee (simultaneously high χ_T and κ_T, as in the biological brain), to high-overhead precision predictors (high χ_T, lower κ_T).

THEOREM 3.2 (Operational Horizon Cost and Minimum-Cost Frontier). *Let an embedded subsystem S operate across N_τ spectral slices (or their continuum limit) over an emergent horizon $T > 0$ (2.244)–(2.255) with maintained stability barrier $\Delta I_{\text{barrier},T} > 0$ and positive operational burdens $I_{\text{irr},\partial,T} > 0$ and*

$I_{\mathrm{rev},\Omega,T} > 0$. *Summing cumulative boundary dissipation* (3.14) *and horizon-averaged preserved internal structure* (3.18) *defines the parameter-free operational horizon cost* $I_{\mathrm{op},T}$ *(in nats), expressed directly through* $\Delta I_{\mathrm{barrier},T}$, χ_T, *and* κ_T (3.29)–(3.30)*:*

$$I_{\mathrm{op},T} := I_{\mathrm{irr},\partial,T} + I_{\mathrm{rev},\Omega,T}, \tag{3.43}$$

$$I_{\mathrm{op},T} = \Delta I_{\mathrm{barrier},T}\left(\frac{1}{\chi_T} + \frac{1}{\kappa_T}\right). \tag{3.44}$$

Consequently, across admissible encodings in $\mathscr{A}_{\mathrm{adm}}$ *sustaining a matched barrier* $\Delta I_{\mathrm{barrier},T} > 0$, *any architecture strictly Pareto-dominating another in* (χ_T, κ_T) *incurs strictly lower operational horizon cost* $I_{\mathrm{op},T}$, *and every cost-minimising architecture lies on the non-dominated Pareto frontier* $\kappa_T^*(\chi_T)$ (3.42).

PROOF. Substituting the unifying agency identity (3.31) directly into (3.43) produces (3.44). Because $\Delta I_{\mathrm{barrier},T} > 0$, the reciprocal sum in (3.44) is strictly decreasing in both $\chi_T > 0$ and $\kappa_T > 0$, so any architecture strictly Pareto-dominating another in (χ_T, κ_T) at matched $\Delta I_{\mathrm{barrier},T}$ achieves strictly lower $I_{\mathrm{op},T}$, excluding dominated interior configurations from minimising operational horizon cost. □

Theorem 3.2 explains why surviving physical systems concentrate near the frontier $\kappa_T^*(\chi_T)$ without invoking substrate-specific weighting parameters or ad hoc efficiency postulates. Because $\dot{I}_{\mathrm{irr},\partial}(t)\,\mathrm{d}t$ integrates boundary dissipation in $I_{\mathrm{irr},\partial,T}$ and $\mathrm{d}\tau$ cancels τ_T^{-1} in $I_{\mathrm{rev},\Omega,T}$, both quantities carry identical, clock-invariant units of nats, and their sum $I_{\mathrm{op},T}$ (3.43) prices unaligned boundary collisions and uncompressed internal state retention on equal footing across any emergent horizon T. Under bounded capacity and open boundary coupling, excess boundary dissipation or bloated internal allocation erodes uncommitted free capacity $\mathcal{Q}_{\mathrm{free},\tau}$ and lowers $\Delta I_{\mathrm{barrier},T}$ (3.24). In the path-space theory of conditioned Markov processes [28] and dynamical large deviations [160], trajectories burdened by excess operational cost incur an exponential survival penalty across successive epochs, concentrating long-horizon survivors onto quasi-stationary distributions near $\kappa_T^*(\chi_T)$ [99, 166].

EXAMPLE 3.1 (Static and Through-Time Agency Metrics). Consider an open simple graph S on 18 vertices partitioned into $M = 2$ complete cliques K_9 of nine vertices ($K_{\alpha\alpha} = 72$ links for $\alpha \in \{1, 2\}$, from $|E(S_\alpha)| = 36$ clique edges, with internal spectral gap $\gamma_{\mathrm{int}} = 9/8$, or 1.125) linked by $K_{12} = 1$ link and coupled across $M_{\bar{S}} = 2$ environmental blocks at cut capacities 4 and 3 links per register (14 external links total). Each register has degree volume $\mathrm{vol}(S_\alpha) = 80$, internal conductance $\phi_\partial(S_\alpha) = 1/73$, total open conductance $\phi_\partial^{(\mathrm{tot})}(S_\alpha) = 8/80$ (0.10), and spectral persistence $\Xi(S_\alpha) = 82.125 \gg 1$ (satisfying Axioms I–III), conserving $\mathcal{Q}_{\mathrm{total}} = 160$ links with internal and boundary structural loads:

$$\mathcal{Q}_\Omega = \sqrt{72^2 + 72^2} = \sqrt{10{,}368} \approx 101.82 \text{ links}, \tag{3.45}$$

$$\mathcal{Q}_\partial = \sqrt{2 + 2(4^2 + 3^2)} = \sqrt{52} \approx 7.21 \text{ links}. \tag{3.46}$$

Evaluating (2.200)–(2.202) and (3.23) yields the static structural efficiencies and slice barrier:

$$\mathcal{Q}_{\text{free}} = 160 - \sqrt{10{,}368 + 52} = 160 - \sqrt{10{,}420} \approx 57.92\,\text{links}, \tag{3.47}$$

$$(\chi_{\text{struct}}, \kappa_{\text{struct}}) = \left(\frac{\mathcal{Q}_{\text{free}}}{\sqrt{52}}, \frac{\mathcal{Q}_{\text{free}}}{\sqrt{10{,}368}}\right) \approx (8.03,\ 0.57), \tag{3.48}$$

$$\Delta I_{\text{barrier}} = \ln\left(\frac{\mathcal{Q}_{\text{free}}}{\mathcal{Q}_0}\right) \approx 4.06\,\text{nats}. \tag{3.49}$$

Now evaluate S across $N_\tau = 3$ spectral slices with proper-time weights $\mathbf{w} = (1/4, 1/2, 1/4)$ sustaining $\mathcal{Q}_{\text{free},\tau} = \mathcal{Q}_{\text{free}}$ ($\Delta I_{\text{barrier},T} \approx 4.06$ nats) under three trajectory protocols. A *reactive* protocol holds slice displacements $(0.4, 0.6, 0.4)$ nats ($I_{\text{rev},\Omega,T} = 0.50$ nats) while suffering unpredicted boundary collisions $(2.5, 3.0, 2.5)$ nats ($I_{\text{irr},\partial,T} = 8.00$ nats). An *uncompressed predictor* holds bloated displacements $(4.0, 4.0, 4.0)$ nats ($I_{\text{rev},\Omega,T} = 4.00$ nats) to align boundary ports at $(0.3, 0.4, 0.3)$ nats ($I_{\text{irr},\partial,T} = 1.00$ nats). Finally, a *compressed CCE predictor* achieves the same aligned boundary dissipation $I_{\text{irr},\partial,T} = 1.00$ nats with compact generative displacements $(0.8, 1.2, 0.8)$ nats ($I_{\text{rev},\Omega,T} = 1.00$ nats). Evaluating (3.29)–(3.30) and (3.43)–(3.44) yields:

$$\left(\chi_T^{\text{react}}, \kappa_T^{\text{react}}, I_{\text{op},T}^{\text{react}}\right) \approx \left(0.51,\ 8.12,\ 8.50\,\text{nats}\right), \tag{3.50}$$

$$\left(\chi_T^{\text{uncomp}}, \kappa_T^{\text{uncomp}}, I_{\text{op},T}^{\text{uncomp}}\right) \approx \left(4.06,\ 1.01,\ 5.00\,\text{nats}\right), \tag{3.51}$$

$$\left(\chi_T^{\text{cce}}, \kappa_T^{\text{cce}}, I_{\text{op},T}^{\text{cce}}\right) \approx \left(4.06,\ 4.06,\ 2.00\,\text{nats}\right). \tag{3.52}$$

Although all three protocols share the same static cross-section (3.48) with $\chi_{\text{struct}} \approx 8.03$ and $\kappa_{\text{struct}} \approx 0.57$, trajectory execution separates them across the efficiency plane (Figure 3.2). Over this short-horizon slice comparison at fixed $\mathcal{Q}_{\text{free}}$, the reactive protocol sits on the low-intelligence limb $(0.51, 8.12)$, purchasing high per-nat internal economy κ_T only by forfeiting predictive boundary defence ($\chi_T \approx 0.51$) at more than four times the total operational cost ($I_{\text{op},T}^{\text{react}} = 8.50$ nats), and across sustained epochs those unaligned collisions erode $\mathcal{Q}_{\text{free},\tau}$ towards $\mathcal{Q}_0$ as in (3.37). Conversely, compressing redundant states moves the predictor from the dominated interior $(4.06, 1.01)$ onto the balanced minimum-cost knee $(4.06, 4.06)$, strictly Pareto-dominating the uncompressed protocol and lowering $I_{\text{op},T}$ from 5.00 nats to 2.00 nats by Theorem 3.2. For a single system with fixed $\mathcal{Q}_{\text{total}}$, the curve $\kappa_T^*(\chi_T)$ forms an impassable efficiency ceiling, and surpassing it requires coupling distinct systems to internalise their shared boundary cuts. ◊

3.4 EMERGENCE

Having established the efficiency ceiling $\kappa_T^*(\chi_T)$ of a single capacity-bounded system, we now examine how coupled physical systems surpass it. Traditional accounts of emergence confront an ill-defined boundary problem: at what threshold do separate coordinating systems cease to be a group of individuals and become a single new entity? Grounded in Conservation-Congruent Encodings, no sharp physical boundary exists because *physical*

emergence occurs on a continuous coordination scale [108, 152]. By Multiscale Coarse-Graining (Theorem 2.2), resolving an interacting assembly as n separate agents under a fine partition $\mathbf{\Pi}^{(1)}$ versus grouping them into one composite agent under a coarsened partition $\mathbf{\Pi}^{(2)} = \mathbf{\Pi}^{(1)}\mathbf{P}$ describes the exact same relational graph $G = (V, E)$, where the transfer operator $\mathscr{T}_{\mathbf{P}}$ reclassifies inter-system coordination channels as internal structure. Equally, every entity conventionally treated as an elementary individual system—from a bound atom or folded protein to a single cell or organism—is itself a coupled composite of lower-level CCE sub-blocks whose internal equilibration outpaces open leakage only by a finite spectral ratio (3.5). Signalling via communication and structural fusion via endosymbiosis are therefore not distinct physical kinds, but different quantitative regimes along one continuous scale of boundary internalisation and coordination.

3.4.1 *Cut Internalisation and Cooperative Capacity Gain*

Consider two autonomous physical systems, A and B, possessing disjoint vertex sets S_A and S_B with total relational capacities $\mathcal{Q}_{\text{total},A}$ and $\mathcal{Q}_{\text{total},B}$ summing to $\mathcal{Q}_{\text{total}} = \mathcal{Q}_{\text{total},A} + \mathcal{Q}_{\text{total},B}$. In the uncoupled baseline ($\mathbf{K}_{AB} = \mathbf{o}$), each system interfaces separately with the ambient environment $\bar{S} = V \setminus (S_A \sqcup S_B)$, exposing isolated external boundary cuts $\mathbf{K}_{\partial,\text{ext}}^{(A),\text{iso}}$ and $\mathbf{K}_{\partial,\text{ext}}^{(B),\text{iso}}$ alongside local subsystem blocks $\mathbf{K}_{S_i} = \mathbf{K}_{\Omega}^{(i)} + \mathbf{K}_{\partial}^{(\text{int},i)}$ with isolated allocated capacities $\mathcal{Q}_{\text{alloc},i}^{\text{iso}}$ ($i \in \{A, B\}$):

$$\|\mathbf{K}_{\partial}^{\text{iso}}\|_F^2 = \|\mathbf{K}_{\partial,\text{ext}}^{(A),\text{iso}}\|_F^2 + \|\mathbf{K}_{\partial,\text{ext}}^{(B),\text{iso}}\|_F^2, \tag{3.53}$$

$$\left(\mathcal{Q}_{\text{alloc},i}^{\text{iso}}\right)^2 = \|\mathbf{K}_{S_i}\|_F^2 + \|\mathbf{K}_{\partial,\text{ext}}^{(i),\text{iso}}\|_F^2. \tag{3.54}$$

Now let physical interaction channels be activated between S_A and S_B, represented by the cross-coupling capacity block $\mathbf{K}_{AB} = \mathbf{K}_{BA}^{\mathsf{T}}$. The composite system $AB = S_A \sqcup S_B$ is governed by the partitioned capacity matrix:

$$\mathbf{K}^{(AB)} = \begin{pmatrix} \mathbf{K}_{S_A} & \mathbf{K}_{AB} & (\mathbf{K}_{\partial,\text{ext}}^{(A)})^{\mathsf{T}} \\ \mathbf{K}_{BA} & \mathbf{K}_{S_B} & (\mathbf{K}_{\partial,\text{ext}}^{(B)})^{\mathsf{T}} \\ \mathbf{K}_{\partial,\text{ext}}^{(A)} & \mathbf{K}_{\partial,\text{ext}}^{(B)} & \mathbf{K}_{\bar{S}} \end{pmatrix}. \tag{3.55}$$

When an observer evaluates the composite entity across the joint boundary $\partial(AB)$ while preserving the differentiated internal registers of A and B (rather than collapsing both subsystems into a single undifferentiated block via $\mathscr{T}_{\mathbf{P}}$ as in Example 2.6), a two-fold topological restructuring occurs. First, while the composite intra-basin memory diagonal $\mathbf{K}_{\Omega}^{(AB)}$ retains only the isolated register memories, the cross-coupling blocks $\mathbf{K}_{AB}$ and $\mathbf{K}_{BA}$ cease to be external boundary cuts and enter the hollow internal transition sector $\mathbf{K}_{\partial}^{(\text{int},AB)}$ of the composite system block $\mathbf{K}_{S}^{(AB)}$. Second, the external cut $\mathbf{K}_{\partial}^{(AB)}$

contracts strictly to links crossing from AB into the remaining environment $\bar{S}$:

$$\mathbf{K}_S^{(AB)} = \begin{pmatrix} \mathbf{K}_{S_A} & \mathbf{K}_{AB} \\ \mathbf{K}_{BA} & \mathbf{K}_{S_B} \end{pmatrix} = \mathbf{K}_\Omega^{(AB)} + \mathbf{K}_\partial^{(\mathrm{int},AB)}, \tag{3.56}$$

$$\mathbf{K}_\Omega^{(AB)} = \mathrm{diag}\big(\mathbf{K}_\Omega^{(A)}, \mathbf{K}_\Omega^{(B)}\big), \tag{3.57}$$

$$\mathbf{K}_\partial^{(AB)} = \begin{pmatrix} \mathbf{K}_{\partial,\mathrm{ext}}^{(A)} & \mathbf{K}_{\partial,\mathrm{ext}}^{(B)} \end{pmatrix}. \tag{3.58}$$

Evaluating the squared Frobenius norms of these partitioned blocks yields the composite internal and external capacity loads:

$$\|\mathbf{K}_S^{(AB)}\|_F^2 = \|\mathbf{K}_{S_A}\|_F^2 + \|\mathbf{K}_{S_B}\|_F^2 + 2\|\mathbf{K}_{AB}\|_F^2, \tag{3.59}$$

$$\|\mathbf{K}_\partial^{(AB)}\|_F^2 = \|\mathbf{K}_{\partial,\mathrm{ext}}^{(A)}\|_F^2 + \|\mathbf{K}_{\partial,\mathrm{ext}}^{(B)}\|_F^2. \tag{3.60}$$

To evaluate whether coupling frees structural capacity without conflating physical synergy with the purely algebraic Euclidean triangle inequality, we compare the coupled composite system against the joint uncoupled baseline evaluated at the identical Frobenius norm level:

$$\mathcal{Q}_{\mathrm{free}}^{\mathrm{iso}} := \mathcal{Q}_{\mathrm{total}} - \sqrt{(\mathcal{Q}_{\mathrm{alloc},A}^{\mathrm{iso}})^2 + (\mathcal{Q}_{\mathrm{alloc},B}^{\mathrm{iso}})^2}. \tag{3.61}$$

When mutual coordination across $\mathbf{K}_{AB}$ shields internal vertices and eliminates excess external boundary allocation, the exposed external cut contracts. Whenever the shed external boundary capacity exceeds the internal coordination load, the composite allocated capacity strictly shrinks relative to the uncoupled baseline, yielding a genuine *cooperative capacity gain* through the equivalent pair of conditions:

$$2\|\mathbf{K}_{AB}\|_F^2 + \|\mathbf{K}_{\partial,\mathrm{ext}}^{(A)}\|_F^2 + \|\mathbf{K}_{\partial,\mathrm{ext}}^{(B)}\|_F^2 < \|\mathbf{K}_{\partial,\mathrm{ext}}^{(A),\mathrm{iso}}\|_F^2 + \|\mathbf{K}_{\partial,\mathrm{ext}}^{(B),\mathrm{iso}}\|_F^2, \tag{3.62}$$

$$\mathcal{Q}_{\mathrm{free}}^{(AB)} = \mathcal{Q}_{\mathrm{total}} - \sqrt{\|\mathbf{K}_S^{(AB)}\|_F^2 + \|\mathbf{K}_\partial^{(AB)}\|_F^2} > \mathcal{Q}_{\mathrm{free}}^{\mathrm{iso}}. \tag{3.63}$$

By (3.23), this expansion of free capacity in (3.63) directly deepens the composite static stability barrier relative to the uncoupled baseline $\Delta I_{\mathrm{barrier}}^{\mathrm{iso}}$:

$$\Delta I_{\mathrm{barrier}}^{(AB)} = \ln\left(\frac{\mathcal{Q}_{\mathrm{free}}^{(AB)}}{\mathcal{Q}_0}\right) > \Delta I_{\mathrm{barrier}}^{\mathrm{iso}} = \ln\left(\frac{\mathcal{Q}_{\mathrm{free}}^{\mathrm{iso}}}{\mathcal{Q}_0}\right). \tag{3.64}$$

Coupling does not merely aggregate substrate volume, but sheds redundant external boundary cuts to contract allocated capacity and geometrically deepen the physical protection of the collective boundary. We now generalise this mechanism to an arbitrary assembly of n interacting subsystems.

DEFINITION 3.3 (Boundary-Shedding and Model-Consolidation Surpluses). Let n disjoint subsystems $S_1, \ldots, S_n$ with individual relational capacity budgets $\mathcal{Q}_{\mathrm{total},i}$ transition under degree-preserving topological coupling from an uncoupled baseline ($\mathbf{K}_{ij} = \mathbf{o}$) to a coupled composite assembly S_{cpl}. The total

relational capacity $\mathcal{Q}_{\text{total}}$ and internal cross-coupling load $\mathcal{Q}^2_{\text{cpl}}$ of the coupled assembly are defined by:

$$\mathcal{Q}_{\text{total}} := \sum_{i=1}^{n} \mathcal{Q}_{\text{total},i}, \tag{3.65}$$

$$\mathcal{Q}^2_{\text{cpl}} := \sum_{i \neq j} \|\mathbf{K}_{ij}\|_F^2. \tag{3.66}$$

Relative to the uncoupled baseline, the signed *boundary-shedding surplus* $\Delta\mathcal{Q}^2_{\partial,\text{shed}}$ and *model-consolidation surplus* $\Delta\mathcal{Q}^2_{\Omega,\text{cons}}$ (in quadratic link units, links^2) are defined respectively by:

$$\Delta\mathcal{Q}^2_{\partial,\text{shed}} := \sum_{i=1}^{n} \|\mathbf{K}^{(i),\text{iso}}_{\partial,\text{ext}}\|_F^2 - \sum_{i=1}^{n} \|\mathbf{K}^{(i)}_{\partial,\text{ext}}\|_F^2, \tag{3.67}$$

$$\Delta\mathcal{Q}^2_{\Omega,\text{cons}} := \sum_{i=1}^{n} \|\mathbf{K}^{\text{iso}}_{S_i}\|_F^2 - \sum_{i=1}^{n} \|\mathbf{K}^{\text{cpl}}_{S_i}\|_F^2. \tag{3.68}$$

Here $\Delta\mathcal{Q}^2_{\partial,\text{shed}}$ measures the signed reduction in squared external boundary norm achieved by mutual shielding (negative if coupling inflates external exposure), while $\Delta\mathcal{Q}^2_{\Omega,\text{cons}}$ measures the signed reduction in squared local internal norm achieved by pruning redundant internal subgraphs across coupled partners ($\Delta\mathcal{Q}^2_{\Omega,\text{cons}} = 0$ prior to structural pruning and $\Delta\mathcal{Q}^2_{\Omega,\text{cons}} > 0$ under modular or endosymbiotic consolidation). Over a shared emergent horizon $T > 0$ metered against a common embedded reference sub-block $\bar{S}_{\text{ref}} \subset \bar{S}$ (2.247)–(2.255) across co-moving subsystems (at matched proper-time weights w_τ), the joint uncoupled baseline boundary dissipation $I^{\text{iso}}_{\text{irr},\partial,T}$ and preserved internal structure $I^{\text{iso}}_{\text{rev},\Omega,T}$ sum additively across the isolated subsystems:

$$I^{\text{iso}}_{\text{irr},\partial,T} := \sum_{i=1}^{n} I^{(i)}_{\text{irr},\partial,T}, \tag{3.69}$$

$$I^{\text{iso}}_{\text{rev},\Omega,T} := \sum_{i=1}^{n} I^{(i)}_{\text{rev},\Omega,T}. \tag{3.70}$$

Evaluating the uncoupled horizon barrier $\Delta I^{\text{iso}}_{\text{barrier},T}$ against these additive baselines defines the baseline through-time efficiencies χ^{iso}_T and κ^{iso}_T:

$$\chi^{\text{iso}}_T := \frac{\Delta I^{\text{iso}}_{\text{barrier},T}}{I^{\text{iso}}_{\text{irr},\partial,T}}, \tag{3.71}$$

$$\kappa^{\text{iso}}_T := \frac{\Delta I^{\text{iso}}_{\text{barrier},T}}{I^{\text{iso}}_{\text{rev},\Omega,T}}. \tag{3.72}$$

THEOREM 3.4 (Cooperative Capacity Gain). *Let a composite assembly S_{cpl} of n coupled subsystems conserve total relational capacity $\mathcal{Q}_{\text{total}}$ relative to a viable uncoupled baseline ($\mathcal{Q}^{\text{iso}}_{\text{free}} > \mathcal{Q}_0$). Then:*

1. *Free-Capacity and Barrier Gain: The coupled assembly achieves a net cooperative capacity gain, strictly expanding unallocated free capacity above* $\mathcal{Q}^{\mathrm{iso}}_{\mathrm{free}}$ *and deepening the static informational barrier* (3.23) *above* $\Delta I^{\mathrm{iso}}_{\mathrm{barrier}}$*, if and only if its internal coordination load satisfies:*

$$\mathcal{Q}^2_{\mathrm{cpl}} < \Delta\mathcal{Q}^2_{\partial,\mathrm{shed}} + \Delta\mathcal{Q}^2_{\Omega,\mathrm{cons}}. \tag{3.73}$$

2. *Emergent Operational Efficiencies: Whenever* (3.73) *deepens the through-time stability barrier* ($\Delta I^{\mathrm{cpl}}_{\mathrm{barrier},T} > \Delta I^{\mathrm{iso}}_{\mathrm{barrier},T} > 0$) *while feedforward coordination across* $\mathbf{K}_{ij}$ *and internal consolidation prevent inflation of boundary dissipation* ($0 < I^{\mathrm{cpl}}_{\mathrm{irr},\partial,T} \leq I^{\mathrm{iso}}_{\mathrm{irr},\partial,T}$) *and preserved internal structure* ($0 < I^{\mathrm{cpl}}_{\mathrm{rev},\Omega,T} \leq I^{\mathrm{iso}}_{\mathrm{rev},\Omega,T}$)*, the assembly achieves simultaneous emergent intelligence* ($\chi^{\mathrm{cpl}}_T > \chi^{\mathrm{iso}}_T$) *and emergent consciousness* ($\kappa^{\mathrm{cpl}}_T > \kappa^{\mathrm{iso}}_T$)*.*

PROOF. Applying Part 3 of Lemma 2.5 (2.216) to the internal, external, and coupling sectors of the n subsystems in (3.66)–(3.68) gives

$$\left(\mathcal{Q}^{\mathrm{iso}}_{\mathrm{alloc}}\right)^2 - \left(\mathcal{Q}^{\mathrm{cpl}}_{\mathrm{alloc}}\right)^2 = \Delta\mathcal{Q}^2_{\partial,\mathrm{shed}} + \Delta\mathcal{Q}^2_{\Omega,\mathrm{cons}} - \mathcal{Q}^2_{\mathrm{cpl}}, \tag{3.74}$$

so at conserved $\mathcal{Q}_{\mathrm{total}}$ with $\mathcal{Q}^{\mathrm{iso}}_{\mathrm{free}} > \mathcal{Q}_0$, $\mathcal{Q}^{\mathrm{cpl}}_{\mathrm{free}} > \mathcal{Q}^{\mathrm{iso}}_{\mathrm{free}} > \mathcal{Q}_0$ (and hence $\Delta I^{\mathrm{cpl}}_{\mathrm{barrier}} > \Delta I^{\mathrm{iso}}_{\mathrm{barrier}} > 0$ by monotonicity of ln) holds if and only if (3.73) is satisfied. Under Part 2, dividing $\Delta I^{\mathrm{cpl}}_{\mathrm{barrier},T} > \Delta I^{\mathrm{iso}}_{\mathrm{barrier},T} > 0$ by the positive non-increasing denominators $I^{\mathrm{cpl}}_{\mathrm{irr},\partial,T} \leq I^{\mathrm{iso}}_{\mathrm{irr},\partial,T}$ and $I^{\mathrm{cpl}}_{\mathrm{rev},\Omega,T} \leq I^{\mathrm{iso}}_{\mathrm{rev},\Omega,T}$ in (3.71)–(3.72) establishes $\chi^{\mathrm{cpl}}_T > \chi^{\mathrm{iso}}_T$ and $\kappa^{\mathrm{cpl}}_T > \kappa^{\mathrm{iso}}_T$. □

EXAMPLE 3.2 (Free-Capacity Gain from Shared Boundaries). Couple two identical copies A and B of the 18-vertex, two-K_9-register simple-graph subsystem from Example 3.1, where each copy conserves relational capacity $\mathcal{Q}_{\mathrm{total},i} = 160$ links ($i \in \{A, B\}$) and combined budget $\mathcal{Q}_{\mathrm{total}} = 320$ links across two ambient environmental blocks $\bar{S}_1$ and $\bar{S}_2$ of five vertices each. Every register retains $K_{\alpha\alpha} = 72$ links (36 clique edges), $K_{12} = 1$ intra-subsystem link ($\|\mathbf{K}_{S_i}\|_1 = 146$ and $\|\mathbf{K}_{S_i}\|_F^2 = 10{,}370$), and 7 outward boundary links across all three configurations, preserving exact vertex degrees ($\mathrm{vol}(S_{i,\alpha}) = 80$, $\phi_\partial(S_{i,\alpha}) = 1/73$, $\phi^{(\mathrm{tot})}_\partial(S_{i,\alpha}) = 0.10$, and $\Xi(S_{i,\alpha}) = 82.125 \gg 1$, with four-register composite persistence $\Xi(S_\alpha) \geq 28.125 \gg 1$). In the uncoupled baseline ($\mathbf{K}_{AB} = \mathbf{o}$), each register connects to $\bar{S}_1$ and $\bar{S}_2$ at cut capacities 4 and 3 links, giving $\|\mathbf{K}^{(i),\mathrm{iso}}_{\partial,\mathrm{ext}}\|_1 = 14$, $\|\mathbf{K}^{(i),\mathrm{iso}}_{\partial,\mathrm{ext}}\|_F^2 = 50$, and combined cut load $\|\mathbf{K}^{\mathrm{iso}}_\partial\|_F^2 = 100$:

$$\mathbf{K}_{S_i} = \begin{pmatrix} 72 & 1 \\ 1 & 72 \end{pmatrix}, \tag{3.75}$$

$$\left(\mathcal{Q}^{\mathrm{iso}}_{\mathrm{alloc}}\right)^2 = 2(10{,}370 + 50) = 20{,}840, \tag{3.76}$$

$$\mathcal{Q}^{\mathrm{iso}}_{\mathrm{free}} = 320 - \sqrt{20{,}840} \approx 175.64 \text{ links}. \tag{3.77}$$

In a *shielded configuration*, degree-preserving rewiring establishes a sparse matched channel $\mathbf{K}_{AB} = \mathrm{diag}(1, 1)$ with $\|\mathbf{K}_{AB}\|_1 = 2$ and $\mathcal{Q}^2_{\mathrm{cpl}} = 4$ while

balancing each register's remaining 6 external links equally at $(3, 3)$ across $\bar{S}_1$ and $\bar{S}_2$, raising $\|\mathbf{K}_S^{(AB)}\|_F^2$ to 20,744 and cutting $\|\mathbf{K}_\partial^{(AB)}\|_F^2$ from 100 to 72 ($\Delta\mathcal{Q}^2_{\partial,\text{shed}} = 28 > \mathcal{Q}^2_{\text{cpl}}$):

$$\mathcal{Q}^{(AB)}_{\text{alloc}} = \sqrt{20{,}744 + 72} = \sqrt{20{,}816} \approx 144.28 \text{ links}, \tag{3.78}$$

$$\mathcal{Q}^{(AB)}_{\text{free}} = 320 - \sqrt{20{,}816} \approx 175.72 \text{ links}, \tag{3.79}$$

$$\Delta I^{(AB)}_{\text{barrier}} - \Delta I^{\text{iso}}_{\text{barrier}} = \ln\left(\frac{\mathcal{Q}^{(AB)}_{\text{free}}}{\mathcal{Q}^{\text{iso}}_{\text{free}}}\right) \approx 4.7 \times 10^{-4} \text{ nats}. \tag{3.80}$$

Conversely, in an *over-coupled configuration*, rewiring doubles the shared channel to four links ($\mathcal{Q}^2_{\text{cpl}} = 16$) while concentrating each register's remaining five external links onto the single unshielded block $\bar{S}_1$, leaving external cut load 100 and $\Delta\mathcal{Q}^2_{\partial,\text{shed}} = 0$:

$$\mathbf{K}^{(\text{over})}_{AB} = \text{diag}(2, 2), \tag{3.81}$$

$$\mathcal{Q}^{(\text{over})}_{\text{alloc}} = \sqrt{20{,}740 + 16 + 100} = \sqrt{20{,}856} \approx 144.42 \text{ links}, \tag{3.82}$$

$$\mathcal{Q}^{(\text{over})}_{\text{free}} = 320 - \sqrt{20{,}856} \approx 175.58 \text{ links}. \tag{3.83}$$

Every matrix block strictly obeys $\|\mathbf{X}\|_F \leq \|\mathbf{X}\|_1$ at conserved $\mathcal{Q}_{\text{total},i} = 160$ links. Shielded coupling sheds $\Delta\mathcal{Q}^2_{\partial,\text{shed}} = 28 \text{ links}^2$ at coordination load $\mathcal{Q}^2_{\text{cpl}} = 4 \text{ links}^2$, expanding $\mathcal{Q}^{(AB)}_{\text{free}}$ above $\mathcal{Q}^{\text{iso}}_{\text{free}}$ (a gain compounded when coupled partners also consolidate redundant internal subgraphs, $\Delta\mathcal{Q}^2_{\Omega,\text{cons}} > 0$, as in Example 8.3), whereas over-coupling at zero net boundary shedding inflates allocated capacity and compresses free capacity below isolation ($\mathcal{Q}^{(\text{over})}_{\text{free}} < \mathcal{Q}^{\text{iso}}_{\text{free}}$). ♢

3.4.2 *The Scale and Signatures of Emergence*

While Theorem 3.4 specifies when structural boundary shedding and model consolidation free capacity, coordination also spans lightweight communicative regimes in which subsystems retain separate physical perimeters yet align boundary ports dynamically to suppress collision dissipation. Evaluating coupled dynamics against the operational horizon cost identity (3.44) yields both a strict criterion for physical emergence and a continuous scale quantifying the degree of system integration.

DEFINITION 3.5 (Physical Emergence and the Coordination Scale). Let S_{cpl} be an open coupled assembly of $n \geq 2$ disjoint subsystems $\{S_i\}_{i=1}^n$ with positive cross-coupling load $\mathcal{Q}^2_{\text{cpl}} > 0$ (3.66) and open external boundary blocks $\mathbf{K}^{(i)}_{\partial,\text{ext}}$. Over a shared emergent horizon $T > 0$ metered against a common reference sub-block $\bar{S}_{\text{ref}}$ (2.247)–(2.255), S_{cpl} exhibits *physical emergence* relative to the uncoupled baseline of Definition 3.3 if and only if coordina-

tion sustains at least the baseline collective stability barrier while strictly lowering specific operational horizon cost (3.44):

$$\Delta I^{\mathrm{cpl}}_{\mathrm{barrier},T} \geq \Delta I^{\mathrm{iso}}_{\mathrm{barrier},T} > 0, \tag{3.84}$$

$$\frac{1}{\chi^{\mathrm{cpl}}_T} + \frac{1}{\kappa^{\mathrm{cpl}}_T} < \frac{1}{\chi^{\mathrm{iso}}_T} + \frac{1}{\kappa^{\mathrm{iso}}_T}. \tag{3.85}$$

Summing the exposed external boundary cuts across the n subsystems, the structural and spectral degree of coordination is positioned continuously by the dimensionless *boundary-coordination index* η_{cpl} and *composite spectral persistence* Ξ_{cpl}:

$$\|\mathbf{K}^{\mathrm{cpl}}_{\partial}\|_F^2 := \sum_{i=1}^{n} \|\mathbf{K}^{(i)}_{\partial,\mathrm{ext}}\|_F^2 > 0, \tag{3.86}$$

$$\eta_{\mathrm{cpl}}(S_{\mathrm{cpl}}) := \frac{\mathcal{Q}^2_{\mathrm{cpl}}}{\mathcal{Q}^2_{\mathrm{cpl}} + \|\mathbf{K}^{\mathrm{cpl}}_{\partial}\|_F^2} \in (0,1), \tag{3.87}$$

$$\Xi_{\mathrm{cpl}}(S_{\mathrm{cpl}}) := \frac{\lambda_2\big(\mathbf{L}^{(\mathrm{int})}_{S_{\mathrm{cpl}}S_{\mathrm{cpl}}}\big)}{\lambda_1\big(\mathbf{L}_{S_{\mathrm{cpl}}S_{\mathrm{cpl}}}\big)} \geq 0, \tag{3.88}$$

where $\mathbf{L}^{(\mathrm{int})}_{S_{\mathrm{cpl}}S_{\mathrm{cpl}}}$ denotes the isolated internal Laplacian of $G[S_{\mathrm{cpl}}]$, coupled to the positive open Dirichlet leakage rate $\lambda_1(\mathbf{L}_{S_{\mathrm{cpl}}S_{\mathrm{cpl}}})$ across $\partial S_{\mathrm{cpl}}$ (2.30).

Definition 3.5 separates the *functional criterion* of emergence from its *structural degree*. Topological coupling alone does not guarantee emergence. In the over-coupled configuration of Example 3.2, heavier cross-coupling yields $\eta_{\mathrm{cpl}} = 4/29$ (≈ 0.14, exceeding $\eta_{\mathrm{cpl}} = 1/19$, or 0.053, in the shielded configuration) while compressing free capacity and failing (3.84)–(3.85). Conversely, whenever (3.84)–(3.85) hold, at least one collective operational efficiency must strictly exceed its uncoupled baseline ($\Delta\chi_T > 0$ or $\Delta\kappa_T > 0$), distinguishing functional symbiosis from parasitic drag and excess coordination overhead (where $\Delta\chi_T \leq 0$ and $\Delta\kappa_T \leq 0$ reverse (3.85)). Under non-degraded collective barrier protection ($\Delta I^{(AB)}_{\mathrm{barrier},T} \geq \Delta I^{\mathrm{iso}}_{\mathrm{barrier},T}$), these gains arise through two complementary operational signatures. In *collaborative boundary defence* ($\Delta\chi_T > 0$), feedforward signalling across $\mathbf{K}_{AB}$ lets subsystem A detect incoming environmental fluctuations before they strike subsystem B, lowering composite boundary dissipation below the uncoupled sum, whereas in *generative model consolidation* ($\Delta\kappa_T > 0$), coupled partners prune redundant local representations across shared CCE subgraphs:

$$I^{(AB)}_{\mathrm{irr},\partial,T} < I^{(A)}_{\mathrm{irr},\partial,T} + I^{(B)}_{\mathrm{irr},\partial,T} \implies \Delta\chi_T := \chi^{(AB)}_T - \chi^{\mathrm{iso}}_T > 0, \tag{3.89}$$

$$I^{(AB)}_{\mathrm{rev},\Omega,T} < I^{(A)}_{\mathrm{rev},\Omega,T} + I^{(B)}_{\mathrm{rev},\Omega,T} \implies \Delta\kappa_T := \kappa^{(AB)}_T - \kappa^{\mathrm{iso}}_T > 0. \tag{3.90}$$

Across assemblies satisfying (3.84)–(3.85), the coordinates $(\eta_{\mathrm{cpl}}, \Xi_{\mathrm{cpl}})$ demonstrate why no sharp boundary divides coordinating systems from a new individual system (Table 3.1 and Figure 3.3a). At the low-consolidation end of

the scale ($0 < \eta_{\mathrm{cpl}} \ll 1$ and $0 < \Xi_{\mathrm{cpl}} \lesssim 1$) lies *coordination via communication*, exemplified by scale-free velocity alignment in starling flocks [26], bacterial quorum sensing, and distributed radar arrays. Here subsystems interact across sparse signalling channels while keeping their physical boundaries largely exposed to $\bar{S}$ and their local models unpruned ($\Delta\mathcal{Q}^2_{\Omega,\mathrm{cons}} \approx 0$). Because collective diffusive mixing across $\mathbf{K}_{ij}$ does not vastly outpace individual open-boundary flux ($\Xi_{\mathrm{cpl}} \lesssim 1$, whereas each constituent organism maintains $\Xi_{\mathrm{cpl}}(S_i) \gg 1$), coarsening the group into a single block violates spectral persistence (Axiom II), so an observer resolves distinct communicating agents. Yet whenever collision savings outweigh signalling upkeep in (3.85), the collective achieves genuine physical emergence through collaborative boundary defence ($\Delta\chi_T > 0$).

Coordination regime	Structural & spectral scale	Operational signatures	Physical examples
Uncoupled baseline	$\eta_{\mathrm{cpl}} = 0$, $\Xi_{\mathrm{cpl}} = 0$ ($\mathbf{K}_{ij} = \mathbf{o}$)	$\Delta\chi_T = 0$, $\Delta\kappa_T = 0$ (or < 0 under peer collisions)	Isolated subsystems with uncoupled boundary defence
Communicative coordination	$0 < \eta_{\mathrm{cpl}} \ll 1$, $0 < \Xi_{\mathrm{cpl}} \lesssim 1$, $\Delta\mathcal{Q}^2_{\Omega,\mathrm{cons}} \approx 0$	$\Delta\chi_T > 0$, $\Delta\kappa_T \approx 0$ (early-warning deflection, separate local models)	Starling flocks, quorum sensing, coordinated radar and agent networks
Modular & tissue coupling	$0 < \eta_{\mathrm{cpl}} < 1$, $\Xi_{\mathrm{cpl}} > 1$, $\Delta\mathcal{Q}^2_{\partial,\mathrm{shed}} > 0$, $\Delta\mathcal{Q}^2_{\Omega,\mathrm{cons}} > 0$	$\Delta\chi_T > 0$, $\Delta\kappa_T > 0$ (shared perimeter shielding, partial specialisation)	Biofilms, multicellular tissues, eusocial colonies, neural coalitions
Endosymbiosis & individual systems	$\eta_{\mathrm{cpl}} \to 1^-$, $\Xi_{\mathrm{cpl}} \gg 1$, $\Delta\mathcal{Q}^2_{\partial,\mathrm{shed}} \gg 0$, $\Delta\mathcal{Q}^2_{\Omega,\mathrm{cons}} \gg 0$	$\Delta\chi_T \gg 0$, $\Delta\kappa_T \gg 0$ (admissible coarsening $\mathbf{\Pi}^{(2)} = \mathbf{\Pi}^{(1)}\mathbf{P}$)	Eukaryotic endosymbiosis, single cells, folded proteins, bound molecules

TABLE 3.1: The continuous coordination scale of physical emergence. Rather than a binary jump between separate coordinating agents and a fused organism, open assemblies and partitioned individual systems occupy a continuous spectrum parameterised by the boundary-coordination index $\eta_{\mathrm{cpl}} \in [0, 1)$ (3.87) and composite spectral persistence $\Xi_{\mathrm{cpl}} \geq 0$ (3.88).

Moving up the scale, contiguous cells in biofilms and multicellular tissues, eusocial colonies, and synchronised cortical coalitions in Chapter 9 internalise substantial shared perimeters ($\Delta\mathcal{Q}^2_{\partial,\mathrm{shed}} > 0$) and partially specialise local models ($\Delta\mathcal{Q}^2_{\Omega,\mathrm{cons}} > 0$), raising η_{cpl} and Ξ_{cpl} while unlocking joint gains $\Delta\chi_T > 0$ and $\Delta\kappa_T > 0$. Eukaryotic *endosymbiosis* [96, 144] occupies the high-consolidation regime of this same continuum rather than a separate physical category. When an archaeal host A engulfs an alphaproteo-

bacterial endosymbiont B, B's external environmental cut vanishes within the host cytosol as $\|\mathbf{K}^{(B)}_{\partial,\mathrm{ext}}\|_F \to 0$, generating a permanent shedding surplus $\Delta\mathcal{Q}^2_{\partial,\mathrm{shed}} \gg 0$ and driving $\eta_{\mathrm{cpl}}(AB)$ towards unity. Subsequent endosymbiotic gene transfer prunes redundant bacterial metabolic and transcriptional subgraphs into the central nuclear genome, realising a large consolidation surplus $\Delta\mathcal{Q}^2_{\Omega,\mathrm{cons}} \gg 0$ and consciousness gain $\Delta\kappa_T \gg 0$, while freeing the inner mitochondrial membrane to fold into negatively curved hyperbolic cristae ($\mathrm{Ric}_{\mathbf{K}} < 0$) that maximise bioenergetic port conductance relative to organelle volume and expand $\mathcal{Q}^{(AB)}_{\mathrm{free}}$.

Entities conventionally regarded as elementary *individual systems* lie along this same scale rather than outside it. Resolved under a finer assignment $\mathbf{\Pi}^{(1)}$ (Theorem 2.2) into $n \geq 2$ constituent CCE sub-blocks—organelles and macromolecular complexes within a cell, structural domains within a folded protein, nucleons and valence shells within an atom (Chapter 5), or register banks within a processor—every open individual system S must retain open external ports ($\|\mathbf{K}^{(S)}_{\partial}\|_F > 0$, since $\eta_{\mathrm{cpl}} \to 1$ is the closed internal-saturation limit (3.39) where agency vanishes) and finite leakage ($\lambda_1(\mathbf{L}_{SS}) > 0$), confining it strictly to $0 < \eta_{\mathrm{cpl}}(S) < 1$ and $\Xi_{\mathrm{cpl}}(S) < \infty$. Inside a single eukaryotic cell, mitochondria retain distinct double membranes, circular genomes, and local electrochemical potentials ($\Xi_{\mathrm{cpl}}(S_B) \gg 1$), coordinating with the nucleus across metabolite and protein-import channels $\mathbf{K}_{AB}$. Likewise, the six-node dumbbell system S introduced as a single agent in Example 2.1 sits at $\eta_{\mathrm{cpl}}(S) = 1/2$ and $\Xi_{\mathrm{cpl}}(S) \approx 1.64$ when resolved into its two three-node lobes in Example 2.5. By Weyl's monotonicity (2.29), strong inter-component coordination $\Xi_{\mathrm{cpl}}(S_{\mathrm{cpl}}) \gg 1$ directly enforces open spectral admissibility:

$$\frac{\lambda_2(\mathbf{L}_{S_{\mathrm{cpl}}S_{\mathrm{cpl}}})}{\lambda_1(\mathbf{L}_{S_{\mathrm{cpl}}S_{\mathrm{cpl}}})} \geq \Xi_{\mathrm{cpl}}(S_{\mathrm{cpl}}) \gg 1. \tag{3.91}$$

Equation (3.91) explains why tightly coordinated assemblies appear under coarse-grained observation as single individuals: once inter-component equilibration vastly outpaces external leakage, coarsening $\mathbf{\Pi}^{(1)}$ into a single composite block $\mathbf{\Pi}^{(2)} = \mathbf{\Pi}^{(1)}\mathbf{P}$ becomes spectrally admissible (3.5). Communicative coordination, endosymbiosis, and individuality are thus unified as quantitative gradations of system coordination.

Whether an emergent assembly satisfying Definition 3.5 prevails dynamically over isolated components depends on the emergent operating horizon $T > 0$ (2.247)–(2.255). Wiring $\mathbf{K}_{ij}$ and pruning redundant internal subgraphs incurs a one-time dissipative formation cost $I_{\mathrm{form}} := E_{\mathrm{form}}/\theta > 0$ in nats (E_{form} in joules), whereas an unintegrated baseline expends zero assembly overhead ($I^{\mathrm{iso}}_{\mathrm{form}} = 0$) at the price of a higher mean operational dissipation rate $\dot{I}^{\mathrm{iso}}_{\mathrm{irr}} > \dot{I}^{\mathrm{cpl}}_{\mathrm{irr}}$ (3.85). Cumulative entropy production including assembly

favours integration if and only if T exceeds the *formation payback threshold* T_{amort}:

$$\Delta\dot{\bar{I}}_{\text{irr}} := \dot{\bar{I}}^{\text{iso}}_{\text{irr}} - \dot{\bar{I}}^{\text{cpl}}_{\text{irr}} > 0, \tag{3.92}$$

$$T_{\text{amort}} := \frac{I_{\text{form}}}{\Delta\dot{\bar{I}}_{\text{irr}}} = \frac{E_{\text{form}}}{\theta\,\Delta\dot{\bar{I}}_{\text{irr}}}, \tag{3.93}$$

$$I_{\text{form}} + \dot{\bar{I}}^{\text{cpl}}_{\text{irr}} T < \dot{\bar{I}}^{\text{iso}}_{\text{irr}} T \iff T > T_{\text{amort}}. \tag{3.94}$$

When t is metered in seconds via (2.255) (with mean power saving $\Delta\bar{P}_{\text{irr}} := \theta\,\Delta\dot{\bar{I}}_{\text{irr}}$ in watts), (3.93) expresses T_{amort} directly in seconds as the ratio of E_{form} to $\Delta\bar{P}_{\text{irr}}$. In ephemeral or rapidly scrambling environments ($T \le T_{\text{amort}}$), assembly overhead cannot be recovered and unintegrated components prevail. Across extended operating horizons ($T \gg T_{\text{amort}}$), ongoing operational savings outweigh the one-time formation cost, and minimum-cost selection (Theorem 3.2) concentrates surviving trajectories onto integrated CCE architectures along the composite Pareto frontier.

3.4.3 *Scale Limits and Modular Replication*

If boundary shedding frees capacity upon coupling, why do self-maintaining systems not grow indefinitely into single, immortal monoliths ($N \to \infty$)? Unbounded monolithic expansion encounters two physical limits (Figure 3.3b). First, as subsystem vertex size $|S| = N$ grows, internal communication paths lengthen and the algebraic connectivity $\lambda_2(\mathbf{L}_{SS}(N))$ in (3.5) decays, so beyond a critical scale N^* marginal internal coordination load outpaces marginal boundary shedding and inflates the per-node allocated capacity. Second, any single module of finite free capacity $\mathcal{Q}_{\text{free}}(N) < \infty$ possesses a finite stability barrier $\Delta I_{\text{barrier}}(N) = \ln(\mathcal{Q}_{\text{free}}(N)/\mathcal{Q}_0)$ (calibrated energetically as $\Delta\Phi(N) = \theta\,\Delta I_{\text{barrier}}(N)$ in (3.33)) and therefore faces almost-sure boundary exit over horizons exceeding its escape timescale $\tau_{\text{escape}}(N)$ (2.326) (in reference nats, or in seconds when t is metered via (2.255)):

$$\left.\frac{\partial \mathcal{Q}^2_{\text{cpl}}}{\partial N}\right|_{N>N^*} > \left.\frac{\partial \Delta\mathcal{Q}^2_{\partial,\text{shed}}}{\partial N}\right|_{N>N^*}, \tag{3.95}$$

$$\left.\frac{\partial}{\partial N}\left(\frac{\mathcal{Q}_{\text{alloc}}(N)}{N}\right)\right|_{N>N^*} > 0, \tag{3.96}$$

$$\tau_{\text{escape}}(N) \sim \tau_{\text{relax}} \exp\big(\Delta I_{\text{barrier}}(N)\big) < \infty. \tag{3.97}$$

Across emergent horizons T exceeding $\tau_{\text{escape}}(N^*)$, sustaining an emergent architecture indefinitely requires compressing the core architectural invariants into a low-footprint generative seed $\mathbf{K}_{\text{seed}} \subset \mathbf{K}_\Omega$ whose preserved internal structure $I^{\text{seed}}_{\text{rev},\Omega}$ is much smaller than that of the full system $I^{\text{full}}_{\text{rev},\Omega}$. Across a boundary export channel of rate $R_\partial > 0$ (in nats/nat against uncalibrated τ_{ref}, or nats s^{-1} when t is metered in seconds via (2.255)), transmitting the seed requires duration $\tau^{\text{seed}}_{\text{copy}} := I^{\text{seed}}_{\text{rev},\Omega}/R_\partial$ (versus $\tau^{\text{full}}_{\text{copy}} := I^{\text{full}}_{\text{rev},\Omega}/R_\partial$ for the uncompressed full state, and at template-copying cost far below de

novo assembly search as formalised in Chapter 8) to initialise independent subsystems prior to module failure.

THEOREM 3.6 (Scale Limits and Seed Replication). *Let a growing coupled system $S(N)$ on $|S| = N$ vertices obey linear budget scaling and superlinear allocated growth (3.96) past a critical size N^*. For every integer $n_{\mathrm{mod}} \geq 2$, suppose $\mathcal{Q}_{\mathrm{total}}(n_{\mathrm{mod}}N^*) = n_{\mathrm{mod}}\mathcal{Q}_{\mathrm{total}}(N^*)$ and $\mathcal{Q}_{\mathrm{alloc}}(S(n_{\mathrm{mod}}N^*)) > n_{\mathrm{mod}}\mathcal{Q}_{\mathrm{alloc}}(N^*)$, where each module of size N^* has free reserve $\mathcal{Q}_{\mathrm{free}}(N^*) \geq 3\mathcal{Q}_0$ and finite escape horizon $\tau_{\mathrm{escape}}(N^*) < \infty$ (3.97). Then:*

1. *Free-Capacity Dominance over Monolithic Expansion: At matched total relational capacity $n_{\mathrm{mod}}\mathcal{Q}_{\mathrm{total}}(N^*)$, partitioning growth into $n_{\mathrm{mod}} \geq 2$ decoupled boundaries $\bigsqcup_{k=1}^{n_{\mathrm{mod}}} S_k$ of size N^* strictly dominates monolithic expansion $S(n_{\mathrm{mod}}N^*)$ in aggregate free capacity:*

$$\mathcal{Q}_{\mathrm{free}}\big(S(n_{\mathrm{mod}}N^*)\big) < n_{\mathrm{mod}}\mathcal{Q}_{\mathrm{free}}(N^*). \tag{3.98}$$

2. *Seed-Compression Replication Gate: Across a boundary export channel of emergent rate $R_\partial > 0$ where the uncompressed full state exceeds the single-module survival window ($I^{\mathrm{full}}_{\mathrm{rev},\Omega} \geq R_\partial \tau_{\mathrm{escape}}(N^*)$), compressing invariants into a generative seed $\mathbf{K}_{\mathrm{seed}} \subset \mathbf{K}_\Omega$ achieves viable replication prior to boundary escape ($\tau^{\mathrm{seed}}_{\mathrm{copy}} < \tau_{\mathrm{escape}}(N^*) \leq \tau^{\mathrm{full}}_{\mathrm{copy}}$) and strictly elevates seed-stage consciousness ($\kappa_{\mathrm{seed}} > \kappa_{\mathrm{full}}$ at matched positive barrier) if and only if:*

$$0 < I^{\mathrm{seed}}_{\mathrm{rev},\Omega} < R_\partial \tau_{\mathrm{escape}}(N^*) \leq I^{\mathrm{full}}_{\mathrm{rev},\Omega}. \tag{3.99}$$

3. *Linear-over-Logarithmic Lineage Barrier Separation: Across $n_{\mathrm{mod}} \geq 2$ actively replicating modules with independent decoupled boundaries regenerated within $\tau^{\mathrm{seed}}_{\mathrm{copy}} \ll \tau_{\mathrm{escape}}(N^*)$, simultaneous lineage extinction requires independent exit across all n_{mod} subgraphs, so the additive lineage barrier (in nats) strictly exceeds both the idealised logarithmic sum and the monolithic barrier $\Delta I_{\mathrm{barrier}}(S(n_{\mathrm{mod}}N^*))$:*

$$\Delta I^{(n_{\mathrm{mod}})}_{\mathrm{lineage}} := \sum_{k=1}^{n_{\mathrm{mod}}} \Delta I_{\mathrm{barrier}}(S_k) = n_{\mathrm{mod}}\Delta I_{\mathrm{barrier}}(N^*), \tag{3.100}$$

$$\Delta I^{(n_{\mathrm{mod}})}_{\mathrm{lineage}} > \ln\left(\frac{n_{\mathrm{mod}}\mathcal{Q}_{\mathrm{free}}(N^*)}{\mathcal{Q}_0}\right) > \Delta I_{\mathrm{barrier}}\big(S(n_{\mathrm{mod}}N^*)\big). \tag{3.101}$$

PROOF. Under superlinear growth, $\mathcal{Q}_{\mathrm{alloc}}(S(n_{\mathrm{mod}}N^*)) > n_{\mathrm{mod}}\mathcal{Q}_{\mathrm{alloc}}(N^*)$ holds, and subtracting each side from the matched budget $n_{\mathrm{mod}}\mathcal{Q}_{\mathrm{total}}(N^*)$ directly yields (3.98). Dividing (3.99) by the positive channel rate R_∂ yields $\tau^{\mathrm{seed}}_{\mathrm{copy}} < \tau_{\mathrm{escape}}(N^*) \leq \tau^{\mathrm{full}}_{\mathrm{copy}}$ biconditionally, while strict contraction of $I^{\mathrm{seed}}_{\mathrm{rev},\Omega}$ below $I^{\mathrm{full}}_{\mathrm{rev},\Omega}$ at matched positive barrier gives $\kappa_{\mathrm{seed}} > \kappa_{\mathrm{full}}$ via (3.30). Finally, for $\mathcal{Q}_{\mathrm{free}}(N^*)/\mathcal{Q}_0 \geq 3$ and $n_{\mathrm{mod}} \geq 2$, induction on n_{mod} combines with (3.98) divided by $\mathcal{Q}_0 > 0$ to separate dimensionless monolithic free capacity from exponential lineage multiplicity:

$$\frac{\mathcal{Q}_{\mathrm{free}}\big(S(n_{\mathrm{mod}}N^*)\big)}{\mathcal{Q}_0} < \frac{n_{\mathrm{mod}}\mathcal{Q}_{\mathrm{free}}(N^*)}{\mathcal{Q}_0} < \left(\frac{\mathcal{Q}_{\mathrm{free}}(N^*)}{\mathcal{Q}_0}\right)^{n_{\mathrm{mod}}}. \tag{3.102}$$

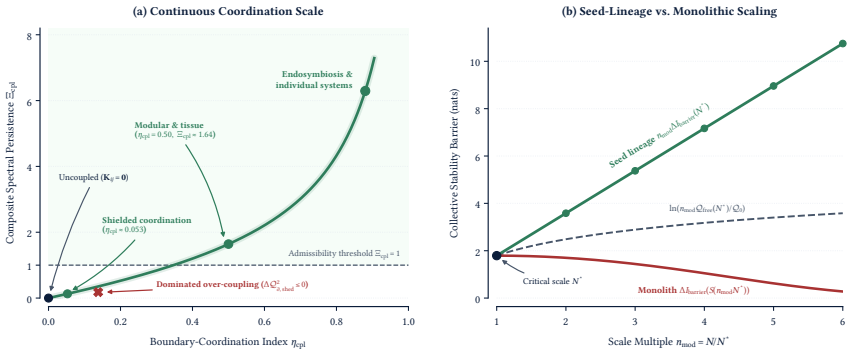


FIGURE 3.3: Continuous coordination scale of physical emergence and modular seed-lineage barrier separation (Definition 3.5 and Theorem 3.6). *(a)* Coordination plane $(\eta_{\mathrm{cpl}}, \Xi_{\mathrm{cpl}})$ spanning the uncoupled baseline ($\mathbf{K}_{ij} = \mathbf{o}$), communicative coordination ($0 < \eta_{\mathrm{cpl}} \ll 1$, $\Xi_{\mathrm{cpl}} \lesssim 1$, such as the shielded coupling of Example 3.2 at $\eta_{\mathrm{cpl}} \approx 0.053$), modular and tissue coupling ($\Xi_{\mathrm{cpl}} > 1$), and high-consolidation endosymbiosis and individual systems ($\Xi_{\mathrm{cpl}} \gg 1$, crossing the coarse-graining admissibility threshold $\Xi_{\mathrm{cpl}} = 1$ (3.91), with the six-node dumbbell of Example 2.5 marked at $\eta_{\mathrm{cpl}} = 0.50$, $\Xi_{\mathrm{cpl}} \approx 1.64$), contrasted against dominated over-coupling ($\Delta\mathcal{Q}^2_{\partial,\mathrm{shed}} \leq 0$, crimson). *(b)* Collective stability barrier (in nats) across scale multiple $n_{\mathrm{mod}} = N/N^*$: monolithic expansion $\Delta I_{\mathrm{barrier}}(S(n_{\mathrm{mod}}N^*))$ saturates and declines past N^* as internal coordination load outpaces boundary shedding (3.96) (crimson), and even an idealised subadditive sum $\ln(n_{\mathrm{mod}}\mathcal{Q}_{\mathrm{free}}(N^*)/\mathcal{Q}_0)$ grows only logarithmically (dashed slate), whereas partitioning capacity into n_{mod} decoupled units regenerated from a compressed seed $\mathbf{K}_{\mathrm{seed}}$ scales linearly as $\Delta I^{(n_{\mathrm{mod}})}_{\mathrm{lineage}} = n_{\mathrm{mod}}\Delta I_{\mathrm{barrier}}(N^*)$ (3.101) (teal).

Applying the strictly increasing natural logarithm $\ln(\cdot)$ across (3.102) establishes (3.100)–(3.101). □

Because surviving modules regenerate any escaped peer within the repair window $\tau^{\mathrm{seed}}_{\mathrm{copy}} \ll \tau_{\mathrm{escape}}(N^*)$, simultaneous extinction of all n_{mod} modules requires $n_{\mathrm{mod}} - 1$ additional boundary escapes before seed replacement completes, elevating the Markov lineage persistence horizon exponentially in $\Delta I^{(n_{\mathrm{mod}})}_{\mathrm{lineage}}$:

$$\tau^{(n_{\mathrm{mod}})}_{\mathrm{persist}} \asymp \tau^{\mathrm{seed}}_{\mathrm{copy}} \left(\frac{\tau_{\mathrm{escape}}(N^*)}{\tau^{\mathrm{seed}}_{\mathrm{copy}}} \right)^{n_{\mathrm{mod}}} \asymp \tau^{\mathrm{seed}}_{\mathrm{copy}} \left(\frac{\tau_{\mathrm{relax}}}{\tau^{\mathrm{seed}}_{\mathrm{copy}}} \right)^{n_{\mathrm{mod}}} \exp\!\big(n_{\mathrm{mod}}\Delta I_{\mathrm{barrier}}(N^*)\big). \tag{3.103}$$

Over horizons $T \gg \max(T_{\mathrm{amort}}, \tau_{\mathrm{escape}}(N^*))$ (3.94), minimum-cost selection (Theorem 3.2) therefore exponentially suppresses non-replicating monoliths in favour of compressed-seed lineages.

To prevent unverified claims of emergence across biological, electronic, or collective systems, an empirical emergence audit must certify the complete relational and dynamical balance. First, it must specify the subsystem vertex sets (S_A, S_B), the external interface cut $\mathbf{L}_{S\bar{S}}$, and the internal coupling block

$\mathbf{K}_{AB}$ alongside the coordination-scale coordinates $(\eta_{\text{cpl}}, \Xi_{\text{cpl}})$ (3.87)–(3.88), verifying (3.73) whenever static cooperative capacity gain is claimed. Second, it must measure the isolated baseline quantities $I^{(i)}_{\text{irr},\partial,T}$ and $I^{(i)}_{\text{rev},\Omega,T}$ under $\mathbf{K}_{AB} = \mathbf{o}$ against the coupled composite quantities $I^{(AB)}_{\text{irr},\partial,T}$ and $I^{(AB)}_{\text{rev},\Omega,T}$ to establish specific dissipation dominance (3.85) and efficiency gains $(\Delta\chi_T, \Delta\kappa_T)$. Finally, it must confirm exact combinatorial edge conservation (2.128)–(2.129) and the metriplectic Casimir conditions (2.322)–(2.323) so that apparent gains cannot arise from unmetered external dissipation or boundary gaming.

3.5 STABILITY

Section 3.4 established that physical emergence operates across a continuous coordination scale $(\eta_{\text{cpl}}, \Xi_{\text{cpl}})$ and showed why scaling limits preclude unbounded monolithic growth (Theorem 3.6). Across biological, computational, and economic domains, open physical systems populate the low-to-intermediate regime of this continuum, neither standing in isolation nor collapsing into a single monolith. Instead, they persist as coupled networks of distinct systems that maintain individual boundaries and internal memories while exchanging physical fluxes across shared interfaces and environmental sinks.

Classical game theory models strategic interaction by assigning utility functions over strategy profiles and solving for non-cooperative Nash equilibria and cooperative bargaining allocations [117, 118]. That mathematical structure fails to guarantee physical stability only when payoffs are treated as unconstrained abstractions on cost-free substrates—an instance of the Platonic Observer Fallacy (Section 1.5). Grounding coupled systems in Conservation-Congruent Encodings connects game theory directly to physical conservation laws: strategies become boundary and channel allocations on a shared capacity matrix $\mathbf{K}$, static coupling payoffs become shifts in uncommitted free capacity $\mathcal{Q}_{\text{free},i}$ and escape barriers $\Delta\Phi_i$, and horizon payoffs become conserved efficiencies χ_i and κ_i.

Section 3.5.1 establishes this formal correspondence by defining multi-system capacity games and proving that pure-strategy Nash equilibria and Nash bargaining reduce directly to free-capacity payoff optimisation. Section 3.5.2 shows why anchoring operational payoffs in χ_i and κ_i prevents proxy reward misspecification under substrate conservation and combines with logarithmic barrier concavity to route gained free capacity towards a network's weakest links. Section 3.5.3 then formalises exhaustive and generative dissipators under closed-boundary multi-system accounting, establishing a general, substrate-agnostic foundation for analysing symbiotic human–AI coupling (Chapter 8) and multi-agent economic stability (Chapter 10).

3.5.1 *Capacity Games, Free-Capacity Payoffs, and Nash Equilibria*

Whereas Section 3.4 evaluated coupled assemblies collectively under a single composite norm $\mathcal{Q}_{\text{alloc}}^{\text{cpl}}$, subsystems in the low-to-intermediate coordination regime ($\Xi_{\text{cpl}} \lesssim 1$, Table 3.1) cannot be coarsened into one block without violating spectral persistence. Partitioning the relational graph $G = (V, E)$ into n distinct open subsystems $S_1, \dots, S_n$ and an open environment $\bar{S}$ yields the block capacity matrix:

$$\mathbf{K} = \begin{pmatrix} \mathbf{K}_{S_1} & \mathbf{K}_{12} & \cdots & \mathbf{K}_{1n} & (\mathbf{K}_{\partial,\text{ext}}^{(1)})^{\mathsf{T}} \\ \mathbf{K}_{21} & \mathbf{K}_{S_2} & \cdots & \mathbf{K}_{2n} & (\mathbf{K}_{\partial,\text{ext}}^{(2)})^{\mathsf{T}} \\ \vdots & \vdots & \ddots & \vdots & \vdots \\ \mathbf{K}_{n1} & \mathbf{K}_{n2} & \cdots & \mathbf{K}_{S_n} & (\mathbf{K}_{\partial,\text{ext}}^{(n)})^{\mathsf{T}} \\ \mathbf{K}_{\partial,\text{ext}}^{(1)} & \mathbf{K}_{\partial,\text{ext}}^{(2)} & \cdots & \mathbf{K}_{\partial,\text{ext}}^{(n)} & \mathbf{K}_{\bar{S}} \end{pmatrix}. \tag{3.104}$$

Each diagonal block $\mathbf{K}_{S_i} = \mathbf{K}_{\Omega}^{(i)} + \mathbf{K}_{\partial}^{(\text{int},i)}$ decomposes into subsystem S_i's intra-basin memory $\mathbf{K}_{\Omega}^{(i)}$ and intra-subsystem transition cuts $\mathbf{K}_{\partial}^{(\text{int},i)}$ (2.86), each off-diagonal block $\mathbf{K}_{ij} = \mathbf{K}_{ji}^{\mathsf{T}}$ $(i \neq j)$ counts direct coordination links between S_i and S_j, and $\mathbf{K}_{\partial,\text{ext}}^{(i)}$ counts external links between S_i and $\bar{S}$.

Each subsystem S_i operates within a partition-invariant ℓ_1 total relational capacity $\mathcal{Q}_{\text{total},i}$ (2.195), while its outward boundary load $\|\mathbf{K}_{\partial}^{(i)}\|_F^2$ combines environmental and peer cuts in Frobenius quadrature (2.196):

$$\mathcal{Q}_{\text{total},i} = \|\mathbf{K}_{S_i}\|_1 + \|\mathbf{K}_{\partial,\text{ext}}^{(i)}\|_1 + \sum_{j \neq i} \|\mathbf{K}_{ij}\|_1 = \text{vol}(S_i), \tag{3.105}$$

$$\|\mathbf{K}_{\partial}^{(i)}\|_F^2 := \|\mathbf{K}_{\partial,\text{ext}}^{(i)}\|_F^2 + \sum_{j \neq i} \|\mathbf{K}_{ij}\|_F^2, \tag{3.106}$$

$$\mathcal{Q}_{\text{alloc},i}^2 := \|\mathbf{K}_{S_i}\|_F^2 + \|\mathbf{K}_{\partial}^{(i)}\|_F^2 \leq \mathcal{Q}_{\text{total},i}^2. \tag{3.107}$$

For viable subsystems ($\mathcal{Q}_{\text{free},i} > \mathcal{Q}_0$) at substrate fluctuation scale $\theta_i > 0$, subtracting $\mathcal{Q}_{\text{alloc},i}$ from $\mathcal{Q}_{\text{total},i}$ determines S_i's local free capacity and static calibrated escape barrier (3.33):

$$\mathcal{Q}_{\text{free},i} = \mathcal{Q}_{\text{total},i} - \mathcal{Q}_{\text{alloc},i}, \tag{3.108}$$

$$\Delta\Phi_i := \theta_i \ln\left(\frac{\mathcal{Q}_{\text{free},i}}{\mathcal{Q}_0}\right). \tag{3.109}$$

Because Euclidean norms do not add linearly across separate blocks, summing local free capacities across subsystems differs from the coarsened composite reserve $\mathcal{Q}_{\text{free}}^{\text{cpl}}$ of (3.63): whenever subsystems remain spectrally distinct, each S_i must sustain its own local reserve $\mathcal{Q}_{\text{free},i}$ and barrier $\Delta\Phi_i$.

DEFINITION 3.7 (Multi-System Capacity Game). Let $\mathcal{N} = \{1, \dots, n\}$ index open CCE subsystems $\{S_i\}_{i=1}^n$ with total relational capacities $\mathcal{Q}_{\text{total},i}$ and fluctuation scales $\theta_i > 0$. Each subsystem selects a local port and register configuration $s_i \in \mathcal{A}_i$, so that every joint strategy profile $s = (s_1, \dots, s_n)$ in the

product space $\mathscr{A}$ induces a feasible capacity matrix $\mathbf{K}(s)$ satisfying (3.105)–(3.107), where forming an active channel $\mathbf{K}_{ij}(s) \neq \mathbf{o}$ requires compatible port commitment by both S_i and S_j. Relative to the uncoupled isolation baseline ($\mathbf{K}_{ij} = \mathbf{o}$ for all $i \neq j$, denoted iso, with $\mathcal{Q}^{\mathrm{iso}}_{\mathrm{free},i} > \mathcal{Q}_0$), player S_i's baseline barrier, structural free-capacity payoff, and calibrated barrier gain are:

$$\Delta\Phi_i^{\mathrm{iso}} := \theta_i \ln\left(\frac{\mathcal{Q}^{\mathrm{iso}}_{\mathrm{free},i}}{\mathcal{Q}_0}\right), \tag{3.110}$$

$$\Delta\mathcal{Q}_{\mathrm{free},i}(s) := \mathcal{Q}_{\mathrm{free},i}(s) - \mathcal{Q}^{\mathrm{iso}}_{\mathrm{free},i}, \tag{3.111}$$

$$\Delta\Phi_i(s) - \Delta\Phi_i^{\mathrm{iso}} = \theta_i \ln\left(\frac{\mathcal{Q}_{\mathrm{free},i}(s)}{\mathcal{Q}^{\mathrm{iso}}_{\mathrm{free},i}}\right). \tag{3.112}$$

The *multi-system capacity game* is the strategic-form tuple:

$$\Gamma_{\mathbf{K}} := \big(\mathcal{N}, \{\mathscr{A}_i\}_{i=1}^n, \{\Delta\mathcal{Q}_{\mathrm{free},i}\}_{i=1}^n\big), \tag{3.113}$$

with per-subsystem boundary-shedding surplus, internal consolidation surplus, and peer coupling load defined in parallel with Definition 3.3:

$$\Delta\mathcal{Q}^2_{\partial,\mathrm{shed},i}(s) := \|\mathbf{K}^{(i),\mathrm{iso}}_{\partial,\mathrm{ext}}\|_F^2 - \|\mathbf{K}^{(i)}_{\partial,\mathrm{ext}}(s)\|_F^2, \tag{3.114}$$

$$\Delta\mathcal{Q}^2_{\Omega,\mathrm{cons},i}(s) := \|\mathbf{K}^{\mathrm{iso}}_{S_i}\|_F^2 - \|\mathbf{K}_{S_i}(s)\|_F^2, \tag{3.115}$$

$$\mathcal{Q}^2_{\mathrm{cpl},i}(s) := \sum_{j\neq i} \|\mathbf{K}_{ij}(s)\|_F^2, \tag{3.116}$$

while through-time execution over a shared emergent horizon $T > 0$ metered against a common embedded reference sub-block $\bar{S}_{\mathrm{ref}} \subset \bar{S}$ (2.247)–(2.255) is evaluated by the operational efficiency pair $\big(\chi_{i,T}(s), \kappa_{i,T}(s)\big)$ of Definition 3.1.

Over the shared emergent horizon T, each subsystem's boundary dissipation $I_{\mathrm{irr},\partial,i}$ splits between direct environmental port dissipation $I^{(\mathrm{ext})}_{\mathrm{irr},\partial,i}$ and peer interface cross-dissipation $I_{\mathrm{cross},ij} \geq 0$:

$$I_{\mathrm{irr},\partial,i} = I^{(\mathrm{ext})}_{\mathrm{irr},\partial,i} + \sum_{j\neq i} I_{\mathrm{cross},ij}. \tag{3.117}$$

Without synchronised peer channels ($\mathbf{K}_{ij} = \mathbf{o}$), peer actuations return via the environmental Schur operator $\mathbf{\Sigma}_{\mathrm{env}}$ (3.4) as unpredicted boundary strain (3.12), generating $I_{\mathrm{cross},ij} > 0$ and depressing $\chi_{i,T}$. Structurally in $\Gamma_{\mathbf{K}}$, if S_i unilaterally reconfigures boundary ports towards S_j while S_j remains isolated, no bilateral channel forms and no external exposure is shed. Instead, unbuffered collisions concentrate boundary load onto exposed ports, raising $\mathcal{Q}_{\mathrm{alloc},i}$ and yielding $\Delta\mathcal{Q}_{\mathrm{free},i} < 0$. Mutual isolation is therefore a strict non-cooperative Nash equilibrium [118], locking uncoordinated subsystems into a high-dissipation baseline.

Conversely, mutual coordination pairs non-zero reciprocal channels $\mathbf{K}_{ij}$ with shared perimeter shielding and model specialisation, driving $I_{\mathrm{cross},ij}$ towards zero. Whenever each partner's shedding and consolidation surpluses exceed

its peer channel load, allocated capacities contract below isolation and the net network free-capacity gain $\Delta \mathcal{Q}_{\mathrm{free}}^{\mathrm{net}}$ turns positive:

$$\sum_{i=1}^{n} \mathcal{Q}_{\mathrm{alloc},i}^{2}(s) < \sum_{i=1}^{n} \left(\mathcal{Q}_{\mathrm{alloc},i}^{\mathrm{iso}}\right)^{2}, \tag{3.118}$$

$$\Delta \mathcal{Q}_{\mathrm{free}}^{\mathrm{net}}(s) := \sum_{i=1}^{n} \Delta \mathcal{Q}_{\mathrm{free},i}(s) > 0. \tag{3.119}$$

Over the individually rational cooperative set $\mathscr{A}_{\mathrm{coop}} \subseteq \mathscr{A}$ where $\Delta\Phi_i(s) \geq \Delta\Phi_i^{\mathrm{iso}}$ for all $i \in \mathcal{N}$, Nash bargaining [117] with positive bargaining weights $w_i > 0$ maximises the weighted Nash product $\mathcal{J}_{\mathrm{Nash}}(s)$ of barrier gains:

$$\mathcal{J}_{\mathrm{Nash}}(s) := \prod_{i=1}^{n} \left(\Delta\Phi_i(s) - \Delta\Phi_i^{\mathrm{iso}}\right)^{w_i}, \tag{3.120}$$

$$\sum_{i=1}^{n} w_i = 1. \tag{3.121}$$

Whenever coupled partners divide a shared free-capacity pool $\mathcal{Q}_{\mathrm{free}}^{\mathrm{pool}}$ across a linear frontier (or exchange a transferable resource payment in Chapter 10), first-order Karush–Kuhn–Tucker stationarity of $\ln \mathcal{J}_{\mathrm{Nash}}$ equates weighted marginal barrier returns across partners:

$$\sum_{i=1}^{n} \mathcal{Q}_{\mathrm{free},i} \leq \mathcal{Q}_{\mathrm{free}}^{\mathrm{pool}}, \tag{3.122}$$

$$\frac{w_i}{\Delta\Phi_i^{*} - \Delta\Phi_i^{\mathrm{iso}}} \frac{\mathrm{d}\Delta\Phi_i}{\mathrm{d}\mathcal{Q}_{\mathrm{free},i}} = \frac{w_j}{\Delta\Phi_j^{*} - \Delta\Phi_j^{\mathrm{iso}}} \frac{\mathrm{d}\Delta\Phi_j}{\mathrm{d}\mathcal{Q}_{\mathrm{free},j}}. \tag{3.123}$$

THEOREM 3.8 (Equivalence and Scale Invariance in Capacity Games). *Let $\Gamma_{\mathbf{K}}$ be a multi-system capacity game (Definition 3.7) over viable subsystems with $\mathcal{Q}_{\mathrm{free},i}(s) > \mathcal{Q}_0$ and $\theta_i > 0$. Then:*

1. *Pure-Strategy Equilibrium Equivalence and Individual Rationality: A profile $s^{*} \in \mathscr{A}$ is a pure-strategy Nash equilibrium under calibrated barriers $\Delta\Phi_i$ if and only if it is a pure-strategy Nash equilibrium under free-capacity payoffs $\Delta\mathcal{Q}_{\mathrm{free},i}$, and if and only if each s_i^{*} minimises $\mathcal{Q}_{\mathrm{alloc},i}(s_i, s_{-i}^{*})$. Moreover, s is strictly individually rational for S_i, satisfying $\Delta\Phi_i(s) > \Delta\Phi_i^{\mathrm{iso}}$ and $\Delta\mathcal{Q}_{\mathrm{free},i}(s) > 0$, if and only if:*

$$\mathcal{Q}_{\mathrm{cpl},i}^{2}(s) < \Delta\mathcal{Q}_{\partial,\mathrm{shed},i}^{2}(s) + \Delta\mathcal{Q}_{\Omega,\mathrm{cons},i}^{2}(s). \tag{3.124}$$

2. *Bistability of Isolation and Coordination: Restrict each $\mathscr{A}_i$ to binary actions $\{\mathrm{I}, \mathrm{C}\}$ denoting isolation and coordination, with all-isolation profile $s^{\mathrm{iso}} = (\mathrm{I}, \ldots, \mathrm{I})$ and all-coordination profile $s^{\mathrm{cpl}} = (\mathrm{C}, \ldots, \mathrm{C})$. Whenever unilateral coordination $(\mathrm{C}_i, \mathrm{I}_{-i})$ yields $\Delta\mathcal{Q}_{\mathrm{free},i}(\mathrm{C}_i, \mathrm{I}_{-i}) < 0$ while joint coordination s^{cpl} satisfies (3.124) for every $i \in \mathcal{N}$ with $\Delta\mathcal{Q}_{\mathrm{free},i}(\mathrm{I}_i, \mathrm{C}_{-i}) \leq 0$, both s^{iso} and s^{cpl} are strict pure-strategy Nash equilibria, and s^{cpl} strictly Pareto-dominates s^{iso} with $\Delta\mathcal{Q}_{\mathrm{free}}^{\mathrm{net}}(s^{\mathrm{cpl}}) > 0$ (3.119).*

3. *Substrate-Scale Invariance of Nash Bargaining: Under* (3.112)*, the Nash objective* (3.120) *factors out the constant substrate-scale prefactor:*

$$\mathcal{J}_{\mathrm{Nash}}(s) = \left(\prod_{i=1}^{n} \theta_i^{w_i}\right) \prod_{i=1}^{n} \left[\ln\left(\frac{\mathcal{Q}_{\mathrm{free},i}(s)}{\mathcal{Q}_{\mathrm{free},i}^{\mathrm{iso}}}\right)\right]^{w_i}, \tag{3.125}$$

and the equimarginal condition (3.123) *cancels* $\theta_i > 0$ *identically:*

$$\frac{w_i}{\mathcal{Q}_{\mathrm{free},i}^{*} \ln\left(\mathcal{Q}_{\mathrm{free},i}^{*}/\mathcal{Q}_{\mathrm{free},i}^{\mathrm{iso}}\right)} = \frac{w_j}{\mathcal{Q}_{\mathrm{free},j}^{*} \ln\left(\mathcal{Q}_{\mathrm{free},j}^{*}/\mathcal{Q}_{\mathrm{free},j}^{\mathrm{iso}}\right)}. \tag{3.126}$$

PROOF. Applying Part 3 of Lemma 2.5 (2.216) to player i's local sectors via (3.106)–(3.107) and (3.114)–(3.116) gives the exact quadratic balance:

$$\left(\mathcal{Q}_{\mathrm{alloc},i}^{\mathrm{iso}}\right)^2 - \mathcal{Q}_{\mathrm{alloc},i}^2(s) = \Delta\mathcal{Q}_{\partial,\mathrm{shed},i}^2(s) + \Delta\mathcal{Q}_{\Omega,\mathrm{cons},i}^2(s) - \mathcal{Q}_{\mathrm{cpl},i}^2(s). \tag{3.127}$$

Because $x \mapsto \theta_i \ln(x/\mathcal{Q}_0)$ is strictly increasing on $(0,\infty)$ for $\theta_i > 0$ and $\mathcal{Q}_{\mathrm{free},i}(s) = \mathcal{Q}_{\mathrm{total},i} - \mathcal{Q}_{\mathrm{alloc},i}(s)$ decreases strictly with $\mathcal{Q}_{\mathrm{alloc},i}(s)$, unilateral pure-strategy best responses under $\Delta\Phi_i$ and $\Delta\mathcal{Q}_{\mathrm{free},i}$ coincide with minimising $\mathcal{Q}_{\mathrm{alloc},i}$, and $\Delta\mathcal{Q}_{\mathrm{free},i}(s) > 0$ holds if and only if (3.124) holds. Under s^{iso}, unilateral deviation by player i to C lowers payoff from 0 to $\Delta\mathcal{Q}_{\mathrm{free},i}(\mathsf{C}_i, \mathsf{I}_{-i}) < 0$. Under s^{cpl}, unilateral deviation to I lowers payoff from $\Delta\mathcal{Q}_{\mathrm{free},i}(s^{\mathrm{cpl}}) > 0$ to $\Delta\mathcal{Q}_{\mathrm{free},i}(\mathsf{I}_i, \mathsf{C}_{-i}) \le 0$, establishing strict Nash stability of both profiles together with $\Delta\mathcal{Q}_{\mathrm{free}}^{\mathrm{net}}(s^{\mathrm{cpl}}) > 0$. Substituting (3.112) into (3.120) gives (3.125), and differentiating (3.109) with respect to $\mathcal{Q}_{\mathrm{free},i}$ inside (3.123) cancels $\theta_i > 0$ identically, yielding (3.126). □

Theorem 3.8 highlights two physical properties of multi-system equilibria. First, pure-strategy best responses depend only on ordinal payoff rankings and therefore reduce to minimising local allocated capacity $\mathcal{Q}_{\mathrm{alloc},i}$, whereas randomising mixed strategies incur a risk penalty from the strict concavity of $\ln(\mathcal{Q}_{\mathrm{free},i}/\mathcal{Q}_0)$. Second, because the substrate scales θ_i factor out of (3.125) and cancel from (3.126), bargaining in energetic barrier units (J) across heterogeneous substrates—such as coupling a low-noise silicon processor at scale θ_A to a warm biological organism at scale $\theta_B \neq \theta_A$—selects the exact same free-capacity division as bargaining in dimensionless informational units (nats).

EXAMPLE 3.3 (Two-System Coordination Game). Consider two symmetric simple-graph subsystems A and B, each partitioned into $M_i = 2$ thirteen-vertex complete-clique registers K_{13} of diagonal capacity $K_{\alpha\alpha} = 156$ links ($\alpha \in \{1,2\}$) and internal spectral gap $\gamma_{\mathrm{int}} = 13/12$ (≈ 1.08), joined by $K_{12} = 2$ inter-register links and incident to 15 boundary links across $\{\mathsf{I},\mathsf{C}\}^2$. Every register maintains internal conductance $\phi_\partial(S_{i,\alpha}) = 1/79$ and spectral persistence $\Xi(S_{i,\alpha}) = 1027/12 \approx 85.58 \gg 1$ (with total open conductance

$\phi_{\partial}^{(\mathrm{tot})}(S_{i,\alpha}) \le 17/173 \approx 0.098$) under Axioms I–III while conserving the exact ℓ_1 relational capacity $\mathcal{Q}_{\mathrm{total},i} = 331$ links:

$$\mathbf{K}_{S_i} = \begin{pmatrix} 156 & 2 \\ 2 & 156 \end{pmatrix}, \tag{3.128}$$

$$\|\mathbf{K}_{S_i}\|_1 = 316, \tag{3.129}$$

$$\|\mathbf{K}_{S_i}\|_F^2 = 48{,}680. \tag{3.130}$$

Under mutual isolation (I, I), $\mathbf{K}_{AB} = \mathbf{o}$ and each subsystem distributes its 15 boundary links across two external ports carrying 12 and 3 links, giving $\|\mathbf{K}_{\partial,\mathrm{ext}}^{(i),\mathrm{iso}}\|_F^2 = 153$. If A unilaterally reconfigures for coordination while B remains isolated (C, I), unreciprocated exposure concentrates A's 15 boundary links onto a single unshielded port of squared norm 225 while conserving $\mathcal{Q}_{\mathrm{total},A} = 331$ links:

$$\mathcal{Q}_{\mathrm{free},i}(\mathrm{I},\mathrm{I}) = 331 - \sqrt{48{,}680 + 153} = 331 - \sqrt{48{,}833} \approx 110.02 \text{ links}, \tag{3.131}$$

$$\mathcal{Q}_{\mathrm{free},A}(\mathrm{C},\mathrm{I}) = 331 - \sqrt{48{,}680 + 225} = 331 - \sqrt{48{,}905} \approx 109.86 \text{ links}. \tag{3.132}$$

Under mutual coordination (C, C), degree-preserving rewiring forms a two-register channel $\mathbf{K}_{AB} = \mathrm{diag}(4, 3)$ of 7 links and contracts each external cut to 8 links, conserving $\mathcal{Q}_{\mathrm{total},i} = 331$ links as boundary shedding ($\Delta\mathcal{Q}_{\partial,\mathrm{shed},i}^2 = 89$) exceeds coupling load ($\mathcal{Q}_{\mathrm{cpl},i}^2 = 25$):

$$\mathcal{Q}_{\mathrm{free},i}(\mathrm{C},\mathrm{C}) = 331 - \sqrt{48{,}680 + 8^2 + 4^2 + 3^2} = 331 - \sqrt{48{,}769} \approx 110.16 \text{ links}. \tag{3.133}$$

Subtracting the isolation baseline $\mathcal{Q}_{\mathrm{free},i}^{\mathrm{iso}} \approx 110.02$ links yields the strategic-form free-capacity payoffs across all four action profiles:

$$\left(\Delta\mathcal{Q}_{\mathrm{free},A},\, \Delta\mathcal{Q}_{\mathrm{free},B}\right) \approx \begin{cases} (0,\ 0) & \text{for } (\mathrm{I},\mathrm{I}), \\ (-0.16,\ 0) & \text{for } (\mathrm{C},\mathrm{I}), \\ (0,\ -0.16) & \text{for } (\mathrm{I},\mathrm{C}), \\ (+0.14,\ +0.14) & \text{for } (\mathrm{C},\mathrm{C}). \end{cases} \tag{3.134}$$

Both (I, I) and (C, C) are strict pure-strategy Nash equilibria of this Stag Hunt coordination game: uncoordinated play locks each subsystem at $\mathcal{Q}_{\mathrm{free},i}^{\mathrm{iso}} \approx 110.02$ links because unilateral coordination raises $\mathcal{Q}_{\mathrm{alloc},A}^2$ from 48,833 to 48,905, whereas cooperative bargaining selects (C, C), lowering $\mathcal{Q}_{\mathrm{alloc},i}^2$ to 48,769 and gaining $\Delta\mathcal{Q}_{\mathrm{free}}^{\mathrm{net}} \approx 0.29$ links of network free capacity at conserved $\mathcal{Q}_{\mathrm{total},i} = 331$ links. ♢

3.5.2 *Conserved Payoffs and the Weakest-Link Principle*

In classical multi-agent games and synthetic optimisation, dynamic rewards are routinely specified as unconstrained scalar proxies—such as gross activ-

ity volume, token throughput, or unbounded state accumulation—divorced from substrate conservation. Because proxy scores omit boundary dissipation and structural maintenance loads, coupled optimisers inevitably exploit proxy misspecification: an agent can raise its local score either by exporting unmodelled variance onto neighbours or by hoarding uncompressed internal state until structural reserves are depleted.

Anchoring through-time operational payoffs in intelligence $\chi_{i,T}$ (3.29) and consciousness $\kappa_{i,T}$ (3.30) on a closed multi-system balance eliminates both failure modes through a two-sided conservation constraint. Externalising uncoordinated actuations inflates irreversible boundary dissipation $I_{\mathrm{irr},\partial,i,T}$ alongside peer interface dissipation $I_{\mathrm{cross},ji}$ in (3.117), directly depressing $\chi_{i,T}$. Conversely, hoarding uncompressed internal state or excess port capacity expands allocated capacity inside the Frobenius disk (3.107), compressing $\mathcal{Q}_{\mathrm{free},i}$ and $\Delta I_{\mathrm{barrier},i,T}$ towards zero and collapsing both $\kappa_{i,T}$ and $\chi_{i,T}$. Sustaining high $\chi_{i,T}$ and $\kappa_{i,T}$ across coupled trajectories therefore admits no proxy shortcut, as interacting subsystems must pair compact generative models $\mathbf{K}_{\Omega}^{(i)}$ with aligned peer channels $\mathbf{K}_{ij}$.

Even with conserved individual payoffs, achieving optimal collective stability across a coupled network depends on how gained free capacity is distributed across heterogeneous nodes (Figure 3.4a). Perturbations propagate across active cross-coupling channels $\mathbf{K}_{ij}$, so boundary collapse in any single subsystem injects severe volatility into all connected peers. Because escape horizons (3.97) across heterogeneous fluctuation scales $\theta_i \neq \theta_j$ depend on the dimensionless exponent $\Delta\Phi_i/\theta_i = \Delta I_{\mathrm{barrier},i}$ rather than raw joule barriers $\Delta\Phi_i$, collective network survival is bounded in dimensionless nats by its weakest link:

$$\Delta I_{\mathrm{barrier,net}} \leq \min_{i\in\{1,\dots,n\}} \Delta I_{\mathrm{barrier},i} = \min_{i\in\{1,\dots,n\}} \ln\left(\frac{\mathcal{Q}_{\mathrm{free},i}}{\mathcal{Q}_0}\right). \tag{3.135}$$

Because each local informational barrier $\Delta I_{\mathrm{barrier},i} = \ln(\mathcal{Q}_{\mathrm{free},i}/\mathcal{Q}_0)$ scales logarithmically with unallocated free capacity (3.23), local stability is strictly concave in free capacity, with substrate-independent marginal stability return (in nats link^{-1}) and curvature (in nats link^{-2}):

$$\frac{\mathrm{d}\Delta I_{\mathrm{barrier},i}}{\mathrm{d}\mathcal{Q}_{\mathrm{free},i}} = \frac{1}{\mathcal{Q}_{\mathrm{free},i}}, \tag{3.136}$$

$$\frac{\mathrm{d}^2\Delta I_{\mathrm{barrier},i}}{\mathrm{d}\mathcal{Q}_{\mathrm{free},i}^2} = -\frac{1}{\mathcal{Q}_{\mathrm{free},i}^2} < 0. \tag{3.137}$$

As unallocated free capacity approaches depletion, this marginal stability return diverges:

$$\lim_{\mathcal{Q}_{\mathrm{free},i}\to 0^+} \frac{\mathrm{d}\Delta I_{\mathrm{barrier},i}}{\mathrm{d}\mathcal{Q}_{\mathrm{free},i}} = \infty. \tag{3.138}$$

By contrast, for a subsystem already possessing abundant structural reserves ($\mathcal{Q}_{\mathrm{free},i} \gg \mathcal{Q}_0$), additional free capacity yields diminishing marginal barrier gain.

Substituting (3.136)–(3.138) into the scale-invariant Nash equimarginal condition (3.126) reveals a direct modelling link between bargaining symmetry and systemic resilience. Whenever a constrained node S_i approaches its isolated floor ($\mathcal{Q}^{*}_{\mathrm{free},i} \to \mathcal{Q}^{\mathrm{iso}}_{\mathrm{free},i}$) or capacity depletion ($\mathcal{Q}^{*}_{\mathrm{free},i} \to \mathcal{Q}_0^{+}$), the denominator on the left-hand side of (3.126) vanishes and S_i's marginal bargaining pull diverges relative to capacity-rich partners ($\mathcal{Q}^{*}_{\mathrm{free},j} \gg \mathcal{Q}_0$). Provided every coupled subsystem retains non-vanishing bargaining weight ($w_i > 0$), Nash bargaining automatically routes gained network free capacity $\Delta\mathcal{Q}^{\mathrm{net}}_{\mathrm{free}}$ towards the most constrained nodes—aligning cooperative equilibrium with steepest ascent of the dimensionless weakest-link bound (3.135). Conversely, multi-system models in which extreme bargaining asymmetry drives $w_i \to 0$ starve bottleneck nodes of gained free capacity and destabilise the entire coupled network despite high aggregate reserves elsewhere.

3.5.3 *Exhaustive and Generative Dissipators*

Whereas the weakest-link principle shows why collective persistence requires routing free capacity towards fragile nodes, *closed-boundary multi-system accounting* determines whether coupled subsystems actually supply or erode that capacity. Evaluating efficiency inside a truncated single-agent perimeter fails to distinguish irreversible flux vented cleanly into the external environment $\bar{S}$ from waste flux discharged into surrounding peers. Closing the accounting boundary across $\bigsqcup_{i=1}^{n} S_i \sqcup \bar{S}$ on the dimensionless CCE entropy S of Section 3.2 (specialising to $S_{\mathrm{th}}/k_{\mathrm{B}}$ in thermal baths) partitions coupled subsystems relative to their encompassing peer host ensemble $S_H = \bigsqcup_{j\neq k} S_j$ into two opposite dynamical classes (Figure 3.4b).

DEFINITION 3.9 (Exhaustive Dissipator). Let S_k be an open subsystem coupled across internal channels $\mathbf{K}_{kj}$ to a peer host ensemble $S_H = \bigsqcup_{j\neq k} S_j$ whose autonomous internal irreversible production rate is $\dot{S}_{i,H} \geq 0$ (following Prigogine's standard subscript i for internal production, distinct from peer index j, with subscript tag H indexing the host ensemble S_H). Subsystem S_k is an *exhaustive dissipator* relative to S_H if insufficient direct venting to the external environment ($\mathbf{K}^{(k)}_{\partial,\mathrm{ext}} \approx \mathbf{o}$ or obstructed sink conductance) causes it to discharge net positive irreversible waste flux $\dot{\Phi}_{S_k\to S_H} > 0$ into peer interfaces, elevating host entropy growth strictly above autonomous production:

$$\left(\frac{\mathrm{d}S(S_H)}{\mathrm{d}t}\right)_{\mathrm{exh}} = \dot{S}_{i,H} + \dot{\Phi}_{S_k\to S_H} > 0, \tag{3.139}$$

and injecting cross-boundary collision variance $I_{\mathrm{cross},jk} > 0$ (3.117) that inflates peer boundary loads $\|\mathbf{K}^{(j)}_{\partial}\|_F$ and imposes a negative free-capacity payoff ($\Delta\mathcal{Q}_{\mathrm{free},j} < 0$) on connected peers.

Under truncated single-system accounting that omits $\dot{\Phi}_{S_k\to S_H}$, an exhaustive dissipator can appear locally efficient while forcing neighbouring nodes to divert relational capacity into excess boundary allocation, depleting peer

free capacity ($\mathcal{Q}_{\text{free},j} \to \mathcal{Q}_0^+$) and accelerating collapse across the network's weakest links (3.135).

DEFINITION 3.10 (Generative Dissipator). Let S_g be an open subsystem possessing an asymmetric external dissipation channel ($\mathbf{K}^{(g)}_{\partial,\text{ext}} \neq \mathbf{o}$) facing the external environment $\bar{S}$ and autonomous internal production rate $\dot{S}_{i,g} \geq 0$, coupled across $\mathbf{K}_{gj}$ to peer host ensemble $S_H = \bigsqcup_{j\neq g} S_j$. Subsystem S_g is a *generative dissipator* relative to S_H if it extracts disorder from the host matrix at rate $\dot{\Phi}_{S_H \to S_g}$ exceeding autonomous host production while venting both extracted host disorder and its own internal production into $\bar{S}$:

$$\frac{\mathrm{d}S(S_H)}{\mathrm{d}t} = \dot{S}_{i,H} - \dot{\Phi}_{S_H \to S_g} < 0, \tag{3.140}$$

$$\dot{\Phi}_{S_g \to \bar{S}} \geq \dot{\Phi}_{S_H \to S_g} + \dot{S}_{i,g}, \tag{3.141}$$

clearing interface disorder and donating predictive constraints across $\mathbf{K}_{gj}$ so as to contract peer boundary cuts $\|\mathbf{K}^{(j)}_{\partial}\|_F$ and confer a positive free-capacity payoff ($\Delta\mathcal{Q}_{\text{free},j} > 0$) across connected peers.

Summing (3.140) and (3.141) confirms that local host ordering strictly obeys global Second Law monotonicity:

$$\dot{\Phi}_{S_g \to \bar{S}} + \frac{\mathrm{d}S(S_H)}{\mathrm{d}t} \geq \dot{S}_{i,H} + \dot{S}_{i,g} \geq 0. \tag{3.142}$$

This structural asymmetry simultaneously introduces a systemic vulnerability: *sink saturation*. Because connected peers adaptively reduce defensive boundary margins through this generative coupling, any obstruction or saturation of the outward dissipation channel $\mathbf{K}^{(g)}_{\partial,\text{ext}}$ causes accumulated disorder to return into S_H, triggering non-linear cascading failure across the reduced-margin weakest links.

Formalising multi-system payoffs under closed capacity balances establishes a unified modelling apparatus for Part III and Part IV. In human–AI architectures (Section 8.4 in Chapter 8), synthetic systems coupled to finite human relational capacity $\mathcal{Q}_{\text{total},H}$ act either as exhaustive dissipators (Definition 3.9) that flood human interfaces with verification friction and compress $\mathcal{Q}_{\text{free},H}$ and κ_H, or as generative dissipators (Definition 3.10) that absorb environmental complexity and expand human free capacity. At the multi-agent economic scale (Chapter 10), closed-boundary production costs and expected population barrier gains ground Physical Nash (C, V, P) pricing in natural informational units (Section 10.1), while weakest-link concavity equips economists with conserved macroeconomic and network stability diagnostics—the Humanity Intelligence Index (HII), the Humanity Consciousness Index (HCI), surplus-backed baseline allocations (Section 10.2), dual boundary-value coupling parameters $(\eta^{(V)}_{\text{cpl}}, \eta^{(C)}_{\text{cpl}})$, and the parameter-free network stability functional $I_{\text{net}}(\mathbf{K})$ (Section 10.3)—capable of demonstrating system stability and distinguishing net stability creation from dissipative turnover.



FIGURE 3.4: Weakest-link barrier concavity and closed-boundary multi-system dissipator topologies (Theorem 3.8 and Definitions 3.9–3.10). *(a)* Local stability barrier $\Delta I_{\text{barrier},i} = \ln(\mathcal{Q}_{\text{free},i}/\mathcal{Q}_0)$ (in dimensionless nats) versus normalised free capacity $\mathcal{Q}_{\text{free},i}/\mathcal{Q}_0$: strict concavity (3.137) produces diverging marginal stability return $1/\mathcal{Q}_{\text{free},i}$ near depletion ($\mathcal{Q}_{\text{free},i} \to \mathcal{Q}_0^+$, crimson tangent) relative to capacity-rich peers ($\mathcal{Q}_{\text{free},j} \gg \mathcal{Q}_0$, slate tangent), so substrate-scale-invariant Nash bargaining (3.126) routes gained network free capacity $\Delta\mathcal{Q}_{\text{free}}^{\text{net}}$ towards bottleneck nodes to raise $\Delta I_{\text{barrier,net}}$ (3.135) (teal). *(b)* Closed-boundary flux accounting across peer host ensemble S_H and environment $\bar{S}$: an exhaustive dissipator S_k ($\mathbf{K}_{\partial,\text{ext}}^{(k)} \approx \mathbf{o}$) discharges waste flux $\dot{\Phi}_{S_k \to S_H} > 0$ into peer interfaces, inflating $\mathrm{d}S(S_H)/\mathrm{d}t > 0$ and imposing $\Delta\mathcal{Q}_{\text{free},j} < 0$ (crimson), whereas a generative dissipator S_g ($\mathbf{K}_{\partial,\text{ext}}^{(g)} \neq \mathbf{o}$) extracts host disorder $\dot{\Phi}_{S_H \to S_g} > \dot{S}_{i,H}$ and vents $\dot{\Phi}_{S_g \to \bar{S}} \geq \dot{\Phi}_{S_H \to S_g} + \dot{S}_{i,g}$ into $\bar{S}$, conferring $\Delta\mathcal{Q}_{\text{free},j} > 0$ (teal).

Together, the Capacity Ledger of Chapter 2 and the continuous metriplectic equations of this chapter complete Part I's foundational architecture. Every embedded physical system is governed by the orthogonal split between internal memory capacity ($\mathbf{K}_\Omega$) and boundary conductance ($\mathbf{K}_\partial$), sustains its through-time stability barrier ($\Delta I_{\text{barrier},T}$) through the coupling of intelligence (χ_T) and consciousness (κ_T), and achieves emergent or multi-system stability by internalising boundary cuts and balancing generative dissipation. In Part II, we turn this physical apparatus onto scientific observation itself, treating the observer as an embedded physical subsystem whose Epistemic Lens ($\mathbf{\Pi}, \mathbf{K}_S, \mathbf{K}_\partial^{(\text{ext})}$) mediates quantum measurement (Chapter 4), multi-scale particle and molecular interactions (Chapter 5), and the emergent geometry of spacetime and cosmology (Chapter 6).

Part II

THE EPISTEMIC LENS OF INTELLIGENCE

4

QUANTUM MEASUREMENT

This chapter isolates the physical mechanics of observation. Part I developed the epistemic assignment $\mathbf{\Pi}$, the two-tier capacity matrix $\mathbf{K}$, emergent spectral geometry and time, and continuous metriplectic dynamics to characterise how an embodied system stabilises its boundary within an open relational graph $G = (V, E)$. Yet an embedded observer cannot inspect G from an omniscient exterior, and must acquire and stabilise every distinction through physical interactions across its finite boundary ports $\mathbf{K}_{\partial}^{(\mathrm{ext})}$. Opening Part II, we examine how an embedded subsystem physically implements this coarse-graining from within through an *Epistemic Lens*. Across the three chapters of Part II, we apply this single physical lens across successive levels of coarse-graining, moving from quantum measurement in the present chapter to the multi-scale hierarchy from fundamental particles to macromolecular dynamics in Chapter 5, and finally to emergent spacetime and cosmological horizons in Chapter 6, where the same finite capacity and dissipation bounds generate Lorentzian geometry and gravitational curvature while ruling out the standard extrapolations to a Big Bang singularity and a universal Heat Death (Section 6.3).

Within the present chapter, we trace how the material constraints of an open observing subsystem govern quantum measurement [54]. Section 4.1 establishes the physical architecture of the Epistemic Lens for an embedded observer, proving across discrete spectral slices and their continuum limit that finite relational capacity and non-negative boundary dissipation force every observation map to be a many-to-one projection while ruling out empirical verification of an exact continuum or universal substrate reversibility. Section 4.2 derives open-system Lindblad dephasing, Quantum Non-Demolition energy conservation, and interferometric fringe visibility directly from the coarse-grained Schur complement, and Section 4.3 resolves the Einstein–Podolsky–Rosen paradox by contrasting direct graph adjacency with the coarse-grained resistance metric.

4.1 THE EPISTEMIC LENS

How does a finite physical subsystem acquire, process, and retain a coarse-grained record of the universe from within? In Chapter 1 (Section 1.5), we identified the *Platonic Observer Fallacy*, which treats observation as a disembodied mathematical map decoupled from the capacity and conservation balance of the observed world. Classical mechanics commits this error by positing a Laplacian demon that reads continuous coordinates to arbitrary

precision at zero disturbance or energy cost, whereas standard quantum theory commits the converse error by positing an external classical apparatus that projects global state vectors instantaneously without substrate capacity bounds. As established in Chapter 2 (Section 2.1 and Section 2.2), the relational graph $G = (V, E)$ carries neither predefined spatial coordinates nor an external Newtonian clock. An embedded observer is simply an open physical subsystem $S \subset V$ of vertex count $N_S := |S|$ ($N_S \ll N_V$) coupled across the boundary cut ∂S to a strictly larger environment $\bar{S} := V \setminus S$ ($N_S < N_{\bar{S}}$, $\mathrm{vol}(S) < \mathrm{vol}(\bar{S})$, $|\partial S| > 0$). The physical partition of S realising the admissible two-tier assignment $\mathbf{\Pi} = \mathrm{diag}(\mathbf{\Pi}_S, \mathbf{\Pi}_{\bar{S}})$ (Definition 2.1) is its *Epistemic Lens*.

4.1.1 *Embedded Partition and Metriplectic Split*

Rather than an abstract mathematical filter, the Epistemic Lens is a material subsystem governed on S by the orthogonal projector split $\mathbf{I}_{N_S} = \mathbf{P}_{\mathbf{\Pi}_S} + \mathbf{Q}_{\mathbf{\Pi}_S}$ (2.57)–(2.67) and the internal capacity decomposition (2.88):

$$\mathbf{x}_S = \mathbf{P}_{\mathbf{\Pi}_S}\mathbf{x}_S + \mathbf{Q}_{\mathbf{\Pi}_S}\mathbf{x}_S, \tag{4.1}$$

$$\mathbf{K}_S = \mathbf{K}_\Omega + \mathbf{K}_\partial^{(\mathrm{int})}. \tag{4.2}$$

In (4.1)–(4.2), $\mathbf{P}_{\mathbf{\Pi}_S}$ isolates the tracked block state $\mathbf{P}_{\mathbf{\Pi}_S}\mathbf{x}_S = \mathbf{\Pi}_S\mathbf{z}_S$ resolved across the M CCE blocks $\{S_1, \dots, S_M\}$ of $\mathbf{K}_\Omega$ (with coarse-grained block state $\mathbf{z}_S = \mathbf{R}_{\mathbf{\Pi}_S}\mathbf{x}_S \in \mathbb{R}^M$), whereas $\mathbf{Q}_{\mathbf{\Pi}_S}$ isolates the unresolved intra-block fluctuations $\mathbf{Q}_{\mathbf{\Pi}_S}\mathbf{x}_S \in \ker(\mathbf{R}_{\mathbf{\Pi}_S})$. Each block S_α ($\alpha \in \{1, \dots, M\}$) carries internal capacity $K_{\alpha\alpha} = 2|E(S_\alpha)|$ of at least 2 links (2.125) and coarse-graining depth $I_{\alpha\alpha} = \ln K_{\alpha\alpha}$ of at least $\ln 2$ nats, couples to $\bar{S}$ across the external port block $\mathbf{K}_\partial^{(\mathrm{ext})}$, and routes internal transitions across $\mathbf{K}_\partial^{(\mathrm{int})}$ behind pairwise isolation barriers $\Delta I_{\mathrm{barrier},\alpha\to\beta}$ (2.136) at spectral persistence $\Xi(S_\alpha) \gg 1$ (2.127).

Statically, because S is an open admissible subsystem with positive internal edge support (2.125) and active boundary cut $\mathcal{Q}_\partial^{(\mathrm{ext})} > 0$, Theorem 2.4 (2.196) enforces a strict Euclidean norm gap between allocated structural capacity $\mathcal{Q}_{\mathrm{alloc}}$ (2.192) and total relational capacity $\mathcal{Q}_{\mathrm{total}} = \mathrm{vol}(S)$ (2.195). Simultaneously, every admissible block ($K_{\alpha\alpha} \geq 2$) has internal edge count $|E(S_\alpha)| = K_{\alpha\alpha}/2$ and satisfies both $\ln K_{\alpha\alpha} \geq \ln 2$ and $\ln K_{\alpha\alpha} < |E(S_\alpha)|$. Summing across all M blocks therefore bounds preserved structural capacity I_{rev} (2.135) (in nats) strictly beneath the internal edge count $|E(S)|$ and total degree volume (in links):

$$\mathcal{Q}_\Omega^2 + \mathcal{Q}_\partial^2 = \mathcal{Q}_{\mathrm{alloc}}^2 < \mathrm{vol}(S)^2 < \mathrm{vol}(\bar{S})^2, \tag{4.3}$$

$$M \ln 2 \leq I_{\mathrm{rev}} < |E(S)| < \mathrm{vol}(S) < \mathrm{vol}(\bar{S}). \tag{4.4}$$

By (4.3)–(4.4), the same graph relations cannot simultaneously constitute the external state in $\bar{S}$ and a cost-free copy inside S, while expanding internal resolution $\mathcal{Q}_\Omega$ strictly reduces the remaining boundary and free capacities ($\mathcal{Q}_\partial$, $\mathcal{Q}_{\mathrm{free}} > 0$) available to couple with $\bar{S}$.

Dynamically, temporal progression is not supplied by an external parameter, but emerges directly from $\mathbf{K}$ (Section 2.5.1). Across a multi-epoch partition,

the slowest non-trivial Laplacian eigenvector $\boldsymbol{\phi}_{\text{time}} \equiv \boldsymbol{\phi}_2$ foliates the blocks into N_τ ordered slices $\{S_\tau\}_{\tau=1}^{N_\tau}$ ($\phi^{(1)}_{\text{time}} < \cdots < \phi^{(N_\tau)}_{\text{time}}$) with intrinsic slice proper-time increments $\Delta\tau_{\text{nat}}(\tau) > 0$ (2.243), partial observer proper-time sum $\tau_{\text{nat}}(\tau)$ (2.246), and reference-metered horizon T (2.247)–(2.255). Complementarily, on a single-epoch state partition, normalising $\mathrm{d}\tau_{\text{nat}}$ by the subsystem's rest-frame distinction rate $\Omega_\Phi > 0$—or collective channel updates $\mathrm{d}k_\Omega = \mathrm{Tr}(\mathbf{K}_\Omega)\,\mathrm{d}k$ by $\nu_0\,\mathrm{Tr}(\mathbf{K}_\Omega)$ at elementary step cadence $\nu_0 > 0$—fixes standardised observer proper time $\mathrm{d}\tau$ (matching $\mathrm{d}t = \mathrm{d}\tau$ at rest relative to $\bar{S}_{\text{ref}}$, (2.249)–(2.250)):

$$\tau_{\text{nat}}(\tau) = \sum_{s=1}^{\tau} \Delta\tau_{\text{nat}}(s), \tag{4.5}$$

$$\mathrm{d}\tau = \frac{\mathrm{d}\tau_{\text{nat}}}{\Omega_\Phi} = \frac{\mathrm{d}k_\Omega}{\nu_0\,\mathrm{Tr}(\mathbf{K}_\Omega)}. \tag{4.6}$$

Along this emergent progression, observation couples both sectors of the metriplectic generator (3.8). Within $\mathbf{K}_\Omega$, conservative circulation generates volume-preserving Poisson transport on $\mathrm{im}(\mathbf{P}_{\boldsymbol{\Pi}_S})$ at zero boundary dissipation ($\Delta I_{\text{irr},\partial}(\tau) = 0$):

$$\dot{A} = \{A, H\}. \tag{4.7}$$

Conversely, stabilising external perturbations across $\mathbf{K}^{(\text{ext})}_\partial$ into a single block S_α expels unresolved fluctuations $\mathbf{Q}_{\boldsymbol{\Pi}_S}\mathbf{x}_S$ across ∂S, accumulating discrete slice boundary dissipation $I_{\text{irr},\partial,T}$ (3.13). Passing to the fine-slice continuum limit ($N_\tau \to \infty$, $\max_\tau w_\tau \to 0$, $t_\tau \to t \in [0,T]$) splits total pathwise dissipation $I_{\text{irr},T}[\gamma]$ orthogonally into boundary dissipation and internal maintenance (3.21), bounding physical dissipated work $W_{\text{diss}}[\gamma]$ at substrate fluctuation scale θ (J nat^{-1}):

$$I_{\text{irr},\partial,T} = \sum_{\tau=1}^{N_\tau} \Delta I_{\text{irr},\partial}(\tau), \tag{4.8}$$

$$I_{\text{irr},T}[\gamma] = I_{\text{irr},\partial,T}[\gamma] + \int_0^T \dot{I}_{\text{irr},\Omega}(t)\,\mathrm{d}t \geq I_{\text{irr},\partial,T}[\gamma] \geq 0, \tag{4.9}$$

$$W_{\text{diss}}[\gamma] \geq \theta I_{\text{irr},T}[\gamma] \geq \theta I_{\text{irr},\partial,T}[\gamma]. \tag{4.10}$$

4.1.2 *State Resolution and Multi-Slice Mixing*

When an environmental configuration $x \in \mathcal{X}_{\bar{S}}$ ($|\mathcal{X}_{\bar{S}}| \geq N_{\bar{S}}$) couples across $\mathbf{K}^{(\text{ext})}_\partial$ (2.85) and stabilises a unique CCE block $\alpha \in \{1,\dots,M\}$ read out by the restriction operator $\mathbf{R}_{\boldsymbol{\Pi}_S}$ (2.53), the subsystem realises a block readout map $\Phi_S : \mathcal{X}_{\bar{S}} \to \{1,\dots,M\}$. Auditing (4.3)–(4.10) across ∂S bounds both single-slice state resolution and multi-slice trajectory resolution along $\boldsymbol{\phi}_{\text{time}}$.

THEOREM 4.1 (Embedded Observer Capacity Bound). *Let $S \subset V$ be an open embedded observing subsystem ($N_S < N_{\bar{S}}$, $\mathrm{vol}(S) < \mathrm{vol}(\bar{S})$, $|\partial S| > 0$) equipped with an admissible M-block assignment $\boldsymbol{\Pi}_S \in \{0,1\}^{N_S \times M}$ (Definition 2.1). Neither an isomorphic copy of $\bar{S}$ nor a complete self-representation*

of S can be realised within $\mathbf{K}_\Omega$. Specifically, the internal residual projector $\mathbf{Q}_{\mathbf{\Pi}_S}$ (2.60) has strictly positive rank, the resolved block count satisfies a strict finite ceiling, and every block readout map across $\mathbf{K}_\partial^{(\mathrm{ext})}$ is strictly many-to-one:

$$\Phi_S : \mathscr{X}_{\bar{S}} \longrightarrow \{1, \dots, M\}, \tag{4.11}$$

$$\operatorname{rank}(\mathbf{Q}_{\mathbf{\Pi}_S}) = N_S - M \geq M \geq 1, \tag{4.12}$$

$$M \leq \min\big(\lfloor N_S/2 \rfloor, |E(S)|\big) < N_S < N_{\bar{S}} \leq |\mathscr{X}_{\bar{S}}|, \tag{4.13}$$

guaranteeing distinct environmental configurations $x_1 \neq x_2$ in $\mathscr{X}_{\bar{S}}$ such that $\Phi_S(x_1) = \Phi_S(x_2)$. In particular, on any finite embedded subgraph S, the resolved block count M cannot pass to the continuum limit $M \to \infty$.

PROOF. Equation (4.3) bounds $\mathscr{C}_\Omega < \mathrm{vol}(S)$ and $\mathrm{vol}(S) < \mathrm{vol}(\bar{S})$, precluding both an isomorphic internal copy of $\bar{S}$ and complete self-representation of S across an open cut $\mathscr{C}_\partial > 0$. Under Axiom I (2.125), every admissible block $\alpha \in \{1, \dots, M\}$ satisfies $N_\alpha \geq 2$ and $K_{\alpha\alpha} \geq 2$ with $K_{\alpha\alpha} = 2|E(S_\alpha)|$. Summing vertex and internal-edge counts across the $M \geq 1$ disjoint blocks gives:

$$N_S = \sum_{\alpha=1}^{M} N_\alpha \geq 2M, \tag{4.14}$$

$$|E(S)| \geq \frac{1}{2} \sum_{\alpha=1}^{M} K_{\alpha\alpha} \geq M. \tag{4.15}$$

Subtracting M from (4.14) yields (4.12), while combining (4.14)–(4.15) with $N_S < N_{\bar{S}}$ and $N_{\bar{S}} \leq |\mathscr{X}_{\bar{S}}|$ proves (4.13). Because $M < |\mathscr{X}_{\bar{S}}|$, the finite pigeonhole principle precludes injectivity of Φ_S, forcing $\Phi_S(x_1) = \Phi_S(x_2)$ for at least one pair $x_1 \neq x_2$, and finiteness of N_S forbids $M \to \infty$. □

Because single-slice resolution is strictly many-to-one, propagating an unresolved block preimage $\Phi_S^{-1}(\{\alpha\})$ across ordered spectral slices $\{S_\tau\}_{\tau=1}^{N_\tau}$ along $\boldsymbol{\phi}_{\mathrm{time}}$ induces multi-slice trajectory branching.

DEFINITION 4.2 (Coarse-Grained Mixing). Let $\{S_\tau\}_{\tau=1}^{N_\tau}$ be an ordered slice foliation along $\boldsymbol{\phi}_{\mathrm{time}}$ (Section 2.5.1), let $U : \mathscr{X}_{\bar{S}} \to \mathscr{X}_{\bar{S}}$ be a bijective single-slice substrate step, and let $\Phi_S : \mathscr{X}_{\bar{S}} \to \{1, \dots, M\}$ be the observer's block readout (4.11). For a block $\alpha \in \{1, \dots, M\}$ at reference slice τ_0, the numbers of reachable forward blocks at slice $\tau > \tau_0$ and reachable backward blocks at slice $\tau < \tau_0$ are:

$$k_+(\alpha; \tau_0, \tau) := \Big|\big\{\Phi_S(U^{\tau-\tau_0}x) : x \in \Phi_S^{-1}(\{\alpha\})\big\}\Big| \qquad (\tau > \tau_0), \tag{4.16}$$

$$k_-(\alpha; \tau_0, \tau) := \Big|\big\{\Phi_S(U^{\tau-\tau_0}x) : x \in \Phi_S^{-1}(\{\alpha\})\big\}\Big| \qquad (\tau < \tau_0). \tag{4.17}$$

The dynamics exhibit *coarse-grained mixing* relative to Φ_S if there exist $\alpha \in \{1, \dots, M\}$ and slices $\tau \neq \tau_0$ such that $k_+(\alpha; \tau_0, \tau) > 1$ or $k_-(\alpha; \tau_0, \tau) > 1$.

As illustrated on the two-dimensional spectral coordinate chart (z^1, z^2) in Figure 4.1, bijective substrate steps shear states bundled inside $\mathrm{im}(\mathbf{Q}_{\mathbf{\Pi}_S})$ within

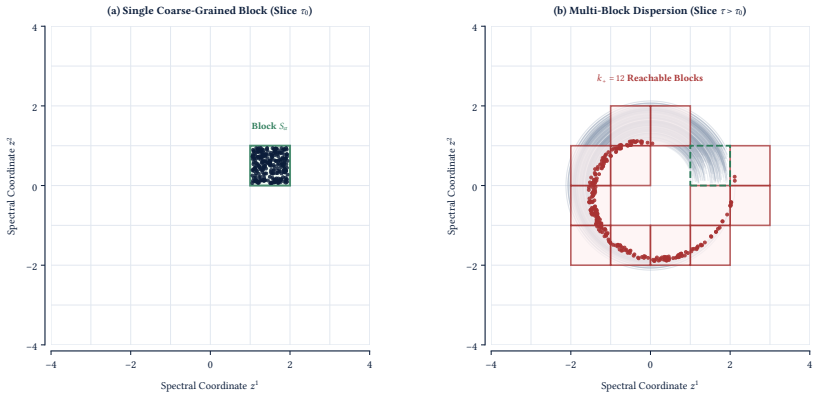


FIGURE 4.1: Coarse-grained mixing across spectral coordinate blocks along $\boldsymbol{\phi}_{\text{time}}$. (a) At reference slice τ_0, distinct fine-grained configurations in $\text{im}(\mathbf{Q}_{\boldsymbol{\Pi}_S})$ occupy a single coarse-grained CCE block S_α on the spectral coordinate chart (z^1, z^2). (b) At a later slice $\tau > \tau_0$, volume-preserving reversible transport $U^{\tau-\tau_0}$ shears those configurations across twelve coarse-grained blocks ($k_+ = 12$), producing multi-block trajectory branching without substrate randomness.

a single block S_α at slice τ_0 across $k_+ > 1$ distinct coarse-grained blocks at a later slice $\tau > \tau_0$, while trajectories originating in $k_- > 1$ past blocks coalesce into S_α across Cheeger bottlenecks (2.130).

THEOREM 4.3 (Multi-Slice Branching and Resolution Bound). *Under coarse-grained mixing (Definition 4.2), suppose a block α of an M-block assignment $\boldsymbol{\Pi}_S^{(2)}$ branches across slices $\tau_0 \to \tau$ along $\boldsymbol{\phi}_{\text{time}}$ into $k \geq 2$ reachable forward or backward blocks. Then:*

1. *Internal Refinement Ceiling: Resolving all k branches within S requires refining $\boldsymbol{\Pi}_S^{(2)} = \boldsymbol{\Pi}_S^{(1)}\mathbf{P}$ (Theorem 2.2) into $M_1 \geq M + k - 1$ blocks via an inter-level difference projector $\Delta\mathbf{P}_{1\to 2}$ (2.165) of rank $M_1 - M \geq k - 1$, enforcing across admissible blocks ($K^{(1)}_{\alpha\alpha} \geq 2$) the capacity hierarchy:*

$$\ln k < (M + k - 1)\ln 2 \leq M_1 \ln 2 \leq I^{(1)}_{\text{rev}} < \text{vol}(S), \tag{4.18}$$

   bounded by $2M_1 \leq N_S$ and $\mathcal{Q}^{(1)}_\Omega \geq 2\sqrt{M_1}$.

2. *Boundary Dissipation Bound and Continuum Horizon: Conversely, if S retains the coarser M-block assignment $\boldsymbol{\Pi}_S^{(2)}$ without resolving those k branches internally, collapsing k substrate branches across ∂S (1.35) enforces positive cumulative slice boundary dissipation $I_{\text{irr},\partial,T}$ (3.13). In the fine-slice limit ($N_\tau \to \infty$, $\max_\tau w_\tau \to 0$, and $t_\tau \to t \in [0, T]$), this sum passes to:*

$$I_{\text{irr},\partial,T} = \sum_{s=1}^{N_\tau} \Delta I_{\text{irr},\partial}(s) \xrightarrow{N_\tau\to\infty} \int_0^T \dot{I}_{\text{irr},\partial}(t)\,\mathrm{d}t \geq \ln k > 0, \tag{4.19}$$

   requiring physical work $W_{\text{diss}} \geq \theta \ln k$ (4.10).

PROOF. Splitting block α into $k \geq 2$ disjoint sub-blocks while keeping the remaining $M-1$ blocks intact yields at least $M+k-1$ level-1 blocks ($M_1 \geq M+k-1$). Thus $\operatorname{rank}(\Delta\mathbf{P}_{1\to 2}) = M_1 - M$ is at least $k-1 \geq 1$ by (2.165), with $2M_1 \leq N_S$ by (4.14). Because $k < 2^k$ and $2^k \leq 2^{M+k-1}$ for $M \geq 1$, while Axiom I enforces $K^{(1)}_{\alpha\alpha} \geq 2$ on each refined block, taking logarithms with (4.4) establishes (4.18), and summing $(K^{(1)}_{\alpha\alpha})^2 \geq 4$ across all M_1 blocks gives $\mathcal{Q}^{(1)}_\Omega \geq 2\sqrt{M_1}$ from $\mathcal{Q}^{(1)}_\Omega = \|\mathbf{K}^{(1)}_\Omega\|_F$. Under $\mathbf{\Pi}^{(2)}_S$, collapsing $k \geq 2$ distinct substrate branches onto a single coarse-grained block expels at least $\ln k$ nats of unresolved branch multiplicity across ∂S (1.35). Summing the non-negative slice increments $\Delta I_{\mathrm{irr},\partial}(s) \geq 0$ in (3.13) and passing to the emergent continuum integral (3.14) yields (4.19), and (4.10) gives $W_{\mathrm{diss}} \geq \theta \ln k$. □

Theorems 4.1 and 4.3 unify the inward and outward epistemic limits of the monograph. Turned inward, the strict norm gap $\mathcal{Q}_{\mathrm{alloc}} < \mathrm{vol}(S)$ and positive residual rank $\operatorname{rank}(\mathbf{Q}_{\mathbf{\Pi}_S}) \geq M$ prevent any physical system from constructing a complete self-model without collapsing its boundary or free capacity, grounding Theorem 9.1 in Chapter 9. Turned outward along emergent time $t \in [0, T]$ in Chapter 6, multi-slice branching ($k_-, k_+ > 1$) against the finite ceiling $M_1 \leq \lfloor N_S/2 \rfloor$ confines every embedded observer to a bounded *Epistemic Bubble* $\mathcal{D}_\Phi = [t^-_\Phi, t^+_\Phi]$ (1.66) (Theorem 6.4). Backward proliferation ($k_- \gg 1$) saturates retrodictive capacity at t^-_Φ (Section 6.3.1), whereas forward dispersion ($k_+ \gg 1$) and open boundary damping dilute predictive signals beneath the noise floor at t^+_Φ (Section 6.3.2).

4.1.3 *Unobservability of the Continuum and Substrate Reversibility*

Although smooth differential charts emerge in Chapter 2 (Section 2.5) across the intermediate Weyl diffusion window $\mu_M^{-1} \ll s \ll \mu_2^{-1}$, treating an exact spatial or temporal continuum or universal substrate invertibility as empirically verifiable properties violates Theorems 4.1 and 4.3.

COROLLARY 4.4 (Unobservability of the Exact Continuum). *Let an embedded observing subsystem $S \subset V$ project $M \geq 2$ admissible CCE blocks ($K_{\alpha\alpha} \geq 2$) onto the spectral coordinate chart $\mathbf{z}(\alpha) = \mathbf{\Phi}^{\mathsf{T}}\mathbf{e}_\alpha \in \mathbb{R}^{d_s}$ (2.236)–(2.237) across $N_\tau \leq M$ ordered slices $\{S_\tau\}_{\tau=1}^{N_\tau}$ (2.243), assuming spectral non-degeneracy across the retained coordinate modes so that $\mathbf{z}(\alpha) \neq \mathbf{z}(\beta)$ for all $\alpha \neq \beta$. On any finite subgraph S, spatial coordinate spacing across distinct blocks and slice proper-time increments remain bounded strictly away from zero:*

$$\Delta z_{\min} := \min_{\alpha\neq\beta} \|\mathbf{z}(\alpha) - \mathbf{z}(\beta)\|_2 > 0, \tag{4.20}$$

$$\Delta\tau_{\mathrm{nat}}(\tau) = \sum_{x\in S_\tau} \ln K_{(\tau,x),(\tau,x)} \geq |S_\tau| \ln 2 > 0, \tag{4.21}$$

whereas passing to an exact spatial or temporal continuum ($M \to \infty$, or $N_\tau \to \infty$) drives the required Frobenius memory load, preserved structural capacity, and M-branch boundary dissipation to diverge:

$$\mathcal{Q}_\Omega \geq 2\sqrt{M} \xrightarrow{M\to\infty} \infty, \tag{4.22}$$

$$I_{\text{rev}} \geq M \ln 2 \xrightarrow{M\to\infty} \infty, \tag{4.23}$$

$$I_{\text{irr},\partial,T} \geq \ln M \xrightarrow{M\to\infty} \infty. \tag{4.24}$$

Consequently, no embedded observer can physically realise or verify an exact continuous coordinate or trajectory.

PROOF. By Theorem 4.1 (4.13), $M \leq \lfloor N_S/2 \rfloor$ is finite, so the off-diagonal index set $\{(\alpha,\beta) : \alpha \neq \beta\}$ is finite and non-empty. Under spectral non-degeneracy ($\mathbf{z}(\alpha) \neq \mathbf{z}(\beta)$ for $\alpha \neq \beta$), every pairwise distance $\|\mathbf{z}(\alpha) - \mathbf{z}(\beta)\|_2$ is strictly positive and attains a positive minimum $\Delta z_{\min} > 0$ in (4.20), while $K_{(\tau,x),(\tau,x)} \geq 2$ on each slice block gives (4.21). Conversely, eliminating discrete block spacing ($\Delta z_{\min} \to 0$ on a bounded domain) or refining slice increments across a fixed horizon ($N_\tau \to \infty$ with $M \geq N_\tau$) requires $M \to \infty$. Because $K_{\alpha\alpha} \geq 2$ on every admissible block implies $\mathcal{Q}_\Omega \geq 2\sqrt{M}$, applying (4.14), (4.4), and Theorem 4.3 (4.18)–(4.19) at $k = M$ yields the divergences (4.22)–(4.24) together with $N_S \to \infty$ and $W_{\text{diss}} \to \infty$ via (4.10), violating $\text{vol}(S) < \infty$. □

At the quantum scale, Corollary 4.4 rules out hidden-variable models built on infinite-precision classical trajectories, while at the cosmological scale of Section 6.3.1 (6.88), it rules out integrating the continuous Raychaudhuri equation past the discrete cutoff μ_M^{-1} to a zero-area singularity. Finite resolution similarly bounds what an embedded observer can infer about global substrate invertibility across slices.

COROLLARY 4.5 (Unobservability of Universal Substrate Reversibility). *Let $U : \mathcal{X}_{\bar{S}} \to \mathcal{X}_{\bar{S}}$ be any bijective substrate step across spectral slices and let $\Phi_S : \mathcal{X}_{\bar{S}} \to \{1,\dots,M\}$ be any single-slice or multi-slice block readout stored within an embedded subsystem S satisfying $M < |\mathcal{X}_{\bar{S}}|$ (Theorem 4.1). There exists a strictly non-injective map $\widetilde{U} : \mathcal{X}_{\bar{S}} \to \mathcal{X}_{\bar{S}}$ that produces identical block records for every $x \in \mathcal{X}_{\bar{S}}$:*

$$\Phi_S\big(\widetilde{U}(x)\big) = \Phi_S\big(U(x)\big). \tag{4.25}$$

Consequently, neither discrete multi-slice records nor their fine-slice continuum limit along $t \in [0,T]$ can certify universal substrate reversibility of $\bar{S}$ from within S.

PROOF. By Theorem 4.1 (4.13), every partition retained inside S—whether resolving single-slice states or storing a multi-slice record across $N_\tau \leq M$ sub-blocks—satisfies $M \leq \lfloor N_S/2 \rfloor$ and hence $M < |\mathcal{X}_{\bar{S}}|$. Thus there exist distinct configurations $y_1 \neq y_2$ in $\mathcal{X}_{\bar{S}}$ with $\Phi_S(y_1) = \Phi_S(y_2)$. Because U is

bijective, their preimages $x_1 := U^{-1}(y_1)$ and $x_2 := U^{-1}(y_2)$ satisfy $x_1 \neq x_2$. Define $\widetilde{U} : \mathcal{X}_{\bar{S}} \to \mathcal{X}_{\bar{S}}$ by:

$$\widetilde{U}(x) := \begin{cases} y_1, & x = x_2, \\ U(x), & x \neq x_2. \end{cases} \tag{4.26}$$

Evaluating $\widetilde{U}$ and $\Phi_S \circ \widetilde{U}$ at the merged preimages gives:

$$\widetilde{U}(x_1) = y_1 = \widetilde{U}(x_2), \tag{4.27}$$

$$\Phi_S\big(\widetilde{U}(x_2)\big) = \Phi_S(y_1) = \Phi_S(y_2) = \Phi_S\big(U(x_2)\big). \tag{4.28}$$

Because $x_1 \neq x_2$, (4.27) shows that $\widetilde{U}$ is strictly non-injective while (4.28) establishes (4.25) across all $x \in \mathcal{X}_{\bar{S}}$. Because $N_S < N_{\bar{S}}$ remains fixed, passing to the fine-slice limit cannot lift M to $|\mathcal{X}_{\bar{S}}|$. □

4.2 QUANTUM DECOHERENCE

Section 4.1 established that an embedded observing subsystem $S \subset V$ possesses bounded relational capacity, evolves along emergent spectral time, and accesses $\bar{S}$ solely through a many-to-one block projection. Quantum measurement is the operational physics that emerges when this finite Epistemic Lens couples to conservative substrate cycles. Rather than postulating wavefunction collapse or starting from primitive probabilities, we construct each mechanism directly from the CCE operators of Chapters 2–3 and then exhibit its exact counterpart in standard open-system quantum mechanics. Section 4.2.1 derives Lindblad dephasing and Born pointer weights from the coarse-grained Schur complement, Section 4.2.2 proves that First-Law Casimir degeneracy is equivalent to Quantum Non-Demolition commutation, and Section 4.2.3 derives interferometric fringe visibility from detector boundary dissipation while resolving the non-selective and delayed-choice paradoxes.

4.2.1 *Open-Boundary Reduction and Pointer Dephasing*

How does an open subsystem $S \subset V$ convert reversible substrate circulation into irreversible pointer stabilisation without a non-unitary collapse postulate? Within cyclic blocks of $\mathbf{K}_\Omega$ ($K_{\alpha\alpha} \geq 2N_\alpha$, Lemma 2.7), skew-symmetric intra-block cycle currents $\mathbf{J}_\Omega = -\mathbf{J}_\Omega^\Gamma$ metered across the $\mathrm{Tr}(\mathbf{K}_\Omega)$ internal channels (2.249)–(2.250) span dimensionless action-normalised symplectic quadratures (q_α, p_α) across blocks $\alpha \in \{1, \ldots, M\}$ (2.308). Mapping each canonical quadrature pair onto a complex cycle coordinate ψ_α bridges the real symplectic cycle space to complex Hilbert-space representation (Table 4.1),

identifying the conserved quadratic cycle norm $\|\boldsymbol{\psi}\|_2^2$ (2.301) directly with the Euclidean ℓ_2 capacity geometry of Theorem 2.4:

$$\psi_\alpha := \frac{q_\alpha + i p_\alpha}{\sqrt{2}}, \tag{4.29}$$

$$\|\boldsymbol{\psi}\|_2^2 = \sum_{\alpha=1}^{M} |\psi_\alpha|^2 = \frac{1}{2}\sum_{\alpha=1}^{M}(q_\alpha^2 + p_\alpha^2). \tag{4.30}$$

Normalising the bilinear outer product across blocks after eliminating $\bar{S}$ and $\mathrm{im}(\mathbf{Q}_{\mathbf{\Pi}_S})$ defines the Hermitian block-coherence operator $\rho(t)$ ($\mathrm{Tr}\,\rho = 1$). Under the coarse-grained Schur reduction $\mathbf{L}_{\mathbf{K},\mathrm{eff}}$ of Section 3.2.1 (3.3)–(3.6), this normalised coherence operator identifies directly with the reduced density operator of standard quantum mechanics and lifts the metriplectic generator (3.8) to operator space:

$$\rho(t) := \mathrm{Tr}_{\bar{S}}\, \rho_{\mathrm{tot}}(t), \tag{4.31}$$

$$\dot{\rho} = \mathscr{J}_\rho\left(\frac{\delta H}{\delta \rho}\right) + \mathscr{M}_\rho\left(\frac{\delta S_{\mathrm{lin}}}{\delta \rho}\right). \tag{4.32}$$

Both brackets in (4.32) inherit the exact algebraic split of $\mathbf{L}_{\mathbf{K},\mathrm{eff}}$ (3.6).

First, the *conservative Poisson sector* arises from isolated internal transport on $\mathbf{L}_{\mathbf{K}}$ (2.101) renormalised by the reactive Hermitian part of $\mathbf{\Sigma}_{\mathbf{K},\mathrm{env}}$. For the renormalised subsystem Hamiltonian $\hat{H}$ and linear energy functional $H(\rho) := \mathrm{Tr}(\hat{H}\rho)$, reversible symplectic circulation along emergent clock time t ($\dot{I}_{\mathrm{irr},\partial} = 0$) generates the unitary von Neumann commutator. Second, in the weak-coupling Born–Markov regime where spectral persistence $\Xi \gg 1$ (3.5) separates rapid environmental correlation decay on $\bar{S}$ from slow pointer relaxation on S, the *dissipative metric sector* induced by the positive semi-definite boundary residual $\mathbf{D}_{\mathbf{K}}^{(\mathrm{ext})} - \mathbf{\Sigma}_{\mathbf{K},\mathrm{env}} \succeq \mathbf{o}$ across $\mathbf{K}_\partial^{(\mathrm{ext})}$ reduces to a time-local generator. Diagonalising this generator into decay channels with rates $\gamma_r \geq 0$ and jump operators $\hat{L}_r$ recovers the master equation of Gorini, Kossakowski, Sudarshan, and Lindblad (GKSL) [70, 103]:

$$\mathscr{J}_\rho\left(\frac{\delta H}{\delta \rho}\right) = -\frac{i}{\hbar}[\hat{H}, \rho], \tag{4.33}$$

$$\dot{\rho} = -\frac{i}{\hbar}[\hat{H}, \rho] + \sum_r \gamma_r \left(\hat{L}_r \rho \hat{L}_r^\dagger - \frac{1}{2}\{\hat{L}_r^\dagger \hat{L}_r, \rho\}\right), \tag{4.34}$$

where $\{\hat{X}, \rho\} := \hat{X}\rho + \rho\hat{X}$ denotes the operator anticommutator.

In the coarse-graining algebra of Section 2.2.1 (2.57), coupling S across $\mathbf{K}_\partial^{(\mathrm{ext})}$ resolves the M mutually orthogonal CCE block projectors $\mathbf{P}_{\boldsymbol{\pi}_\alpha}$ weighted by dimensionless real pointer eigenvalues $a_\alpha \in \mathbb{R}$ (normalised by the characteristic inter-block scale so that all inverse-time rate dimensions reside in $\Gamma_\varphi \geq 0$), identifying Zurek's dimensionless Hermitian pointer observable $\hat{A} = \hat{A}^\dagger$ as the single-channel jump operator $\hat{L}_1 = \hat{A}$ at rate $\gamma_1 = \Gamma_\varphi$ [173]. Quantifying off-diagonal coherence loss on S via the dimensionless linear entropy $S_{\mathrm{lin}}(\rho)$, tracing out $\bar{S}$ across $\mathbf{K}_\partial^{(\mathrm{ext})}$ yields the Schur-reduced boundary-

port cometric $\mathscr{M}_\rho$ as the symmetric, positive semidefinite double commutator generated by $\hat{A}$:

$$\hat{A} = \sum_{\alpha=1}^{M} a_\alpha \mathbf{P}_{\boldsymbol{\pi}_\alpha}, \tag{4.35}$$

$$S_{\mathrm{lin}}(\rho) := \frac{1}{2}\left(1 - \operatorname{Tr}\rho^2\right), \tag{4.36}$$

$$\mathscr{M}_\rho(\delta\rho) := \frac{\Gamma_\varphi}{2}[\hat{A}, [\hat{A}, \delta\rho]]. \tag{4.37}$$

Positive semidefiniteness of $\mathscr{M}_\rho$ follows from $\langle \delta\rho, \mathscr{M}_\rho(\delta\rho)\rangle_{\mathrm{HS}} \geq 0$ for Hermitian $\hat{A}$ and $\delta\rho$, while commutator antisymmetry $[\hat{A}, \hat{A}] = 0$ annihilates $\mathscr{M}_\rho(\hat{I}_S)$ and $\mathscr{M}_\rho(\hat{A})$ identically, rendering both the trace identity and the pointer observable automatic Casimir invariants of the boundary port. Because the variational gradient of $S_{\mathrm{lin}}(\rho)$ equals $-\rho$, substituting (4.33) and (4.37) into (4.32) yields the metriplectic measurement master equation:

$$\begin{aligned}\dot{\rho} &= -\frac{i}{\hbar}[\hat{H}, \rho] - \frac{\Gamma_\varphi}{2}[\hat{A}, [\hat{A}, \rho]] \\ &= -\frac{i}{\hbar}[\hat{H}, \rho] - \underbrace{\frac{\Gamma_\varphi}{2}\{\hat{A}^2, \rho\}}_{\text{open-boundary damping}} + \underbrace{\Gamma_\varphi \hat{A}\rho\hat{A}}_{\text{Schur return flux}}.\end{aligned} \tag{4.38}$$

Comparing (4.38) with the projected Schur split (3.6)–(3.7) exposes the physical role of each term: the outward degree potential $+\mathbf{D}_{\mathbf{K}}^{(\mathrm{ext})}$ acts from the left and right on ρ as the damping anticommutator, while the inversion commutator $-\boldsymbol{\Sigma}_{\mathbf{K},\mathrm{env}} = \mathscr{C}_{\boldsymbol{\Pi}_S}([\![(\cdot)^{-1}, \mathscr{C}_S]\!](\mathbf{G}_\epsilon))$ (Lemma 2.3) acts bilaterally across $\bar{S}$ as the incoherent return jump. Just as subtracting $\boldsymbol{\Sigma}_{\mathrm{env}}$ from $\mathbf{D}_S^{(\mathrm{ext})}$ in Example 2.1 (2.46) restored exact conservation ($\mathbf{L}_{\mathrm{eff}}\mathbf{1}_S = \mathbf{o}$) on the discrete graph, combining open-boundary damping with the Schur return flux enforces exact trace conservation $\operatorname{Tr}(\dot{\rho}) = 0$, reducing to unitary von Neumann flow whenever the external port is closed ($\mathbf{K}_\partial^{(\mathrm{ext})} = \mathbf{o}$, $\Gamma_\varphi = 0$). Evaluated in the block eigenbasis $\hat{A}|a_\alpha\rangle = a_\alpha|a_\alpha\rangle$ across $\alpha, \beta \in \{1, \dots, M\}$, the metric dissipator acts entrywise as:

$$\left(\dot{\rho}_{\alpha\beta}\right)_{\mathrm{diss}} = -\frac{\Gamma_\varphi}{2}(a_\alpha - a_\beta)^2 \rho_{\alpha\beta}. \tag{4.39}$$

Equation (4.39) exponentially damps off-diagonal phase coherences $\rho_{\alpha\beta}$ ($\alpha \neq \beta$) while strictly conserving the normalised ℓ_2 diagonal block weights $\rho_{\alpha\alpha} = \operatorname{Tr}(\mathbf{P}_{\boldsymbol{\pi}_\alpha}\rho)$ inside $\operatorname{im}(\mathbf{P}_{\boldsymbol{\Pi}_S})$. Why, then, does an individual measurement run register a discrete outcome in a single pointer block S_α rather than splitting deterministically across all M ports with fractional intensities $\rho_{\alpha\alpha}$ like a classical continuous wave? By Definition 2.1 and the continuous metriplectic reduction of Section 2.5.2 (2.326)–(2.327), the M pointer blocks of an admissible detector are not linear waveguides that sustain fractional co-occupancy, but mutually exclusive Kramers attractor basins $\mathscr{B}_1, \dots, \mathscr{B}_M \subset \mathscr{Z}$ separated by unstable saddle separatrices $\partial\mathscr{B}_{\alpha\beta}$ of barrier depth $\Delta I_{\mathrm{barrier},\alpha\to\beta} \approx \ln \Xi \gg 1$ (2.127). A split configuration straddling multiple blocks sits on an

unstable saddle ridge outside $\mathrm{im}(\mathbf{P}_{\mathbf{\Pi}_S})$. On each trial, coupling the incoming excitation to the specific unresolved fine-grained state in $\mathrm{im}(\mathbf{Q}_{\widetilde{\mathbf{\Pi}}_S}) = \mathrm{im}(\mathbf{Q}_{\mathbf{\Pi}_S}) \oplus \bar{S}$ (2.69) breaks saddle symmetry, and metric gradient flow $\mathbb{M}\nabla S$ sweeps the joint state at intra-basin rate $\tau_{\mathrm{relax}}^{-1} \sim \nu_0\, \gamma_{\mathrm{int}}(S_\alpha)$ into a single Kramers basin $\mathscr{B}_\alpha$ locked against escape ($\tau_{\mathrm{escape}} \gg \tau_{\mathrm{relax}}$). Because Theorem 4.1 prevents S from resolving those pre-coupling fine-grained states, coarse-grained mixing across the separatrix (Definition 4.2) partitions repeated preparations into single-basin capture preimages, and under the ℓ_2 rotational symmetry of the conserved quadratic cycle norm (4.30) across unresolved residual phases—parallel to Gleason's frame-function theorem [69] and Zurek's envariance symmetry [173]—the unique additive capture measure matches the conserved ℓ_2 Born block weights $\rho_{\alpha\alpha}$ (Table 4.1). Wavefunction collapse is therefore neither a non-unitary postulate nor a subjective update of knowledge, but single-shot Kramers basin relaxation onto $\mathrm{im}(\mathbf{P}_{\mathbf{\Pi}_S})$ driven by open boundary dissipation across ∂S.

CCE substrate construct	Quantum measurement counterpart	Physical role
Normalised cycle outer product on $\mathrm{im}(\mathbf{P}_{\mathbf{\Pi}_S})$	Reduced density operator $\rho = \mathrm{Tr}_{\bar{S}}\, \rho_{\mathrm{tot}}$	Tracks coarse-grained block weights and inter-block phase coherences
Internal capacity Laplacian $\mathbf{L}_{\mathbf{K}}$ ($\dot{I}_{\mathrm{irr},\partial} = 0$)	Unitary commutator $-\frac{i}{\hbar}[\hat{H}, \rho]$	Conservative symplectic phase circulation along emergent clock t
Boundary Schur residual $\mathbf{D}_{\mathbf{K}}^{(\mathrm{ext})} - \mathbf{\Sigma}_{\mathbf{K},\mathrm{env}} \succeq \mathbf{o}$	GKSL double commutator $-\frac{\Gamma_\varphi}{2}[\hat{A}, [\hat{A}, \rho]]$	Open-port damping $+\mathbf{D}_{\mathbf{K}}^{(\mathrm{ext})}$ balanced by Schur return $-\mathbf{\Sigma}_{\mathbf{K},\mathrm{env}}$ ($\mathrm{Tr}\, \dot{\rho} = 0$)
Block projectors $\{a_\alpha, \mathbf{P}_{\boldsymbol{\pi}_\alpha}\}_{\alpha=1}^{M}$	Pointer observable $\hat{A} = \hat{A}^\dagger$ and Born weight $\rho_{\alpha\alpha}$	Diagonalises $\mathrm{im}(\mathbf{P}_{\mathbf{\Pi}_S})$ and fixes normalised ℓ_2 block weights
Metriplectic Casimir degeneracy $(H, \cdot)_{\mathscr{M}} = 0$	QND commutation $[\hat{A}, \hat{H}] = 0$	Zero dissipative backaction power on tracked energy $\langle \hat{H} \rangle$
Cut internalisation $\mathscr{T}_{\mathbf{P}}$ vs. dipole $\Delta\mathbf{P}_{1\to 2}$	Coherent conduit $K_\partial^{(\mathrm{ext})}(x)$ vs. visibility $\mathscr{V}(T) = \mathscr{V}_0 e^{-2\eta_\varphi I_{\mathrm{irr},\partial,T}}$	Unmonitored fringe formation vs. dissipation-driven which-path dephasing
Bridge $\mathrm{dist}_G(i,j) = 1$ in $\mathrm{im}(\mathbf{Q}_{\mathbf{\Pi}_S})$ vs. $\Omega_{\alpha\beta} \gg 1$	Bell state $\lvert\Phi^+\rangle$ and Tsirelson ceiling $\lvert S_{\mathrm{CHSH}}\rvert \le 2\sqrt{2}$	Two-quadrature bridge projected onto ℓ_2 dipole vectors with $\dot{\rho}_\beta = 0$

TABLE 4.1: Correspondence between native Conservation-Congruent Encoding (CCE) operators and the canonical formalism of open-system quantum measurement and entanglement.

4.2.2 *Quantum Non-Demolition and Measurement Backaction*

Why did the Kulkarni–Nomizu 4-bracket (2.320) enforce $\mathbb{M}\nabla H = \mathbf{o}$ (2.323) identically for every Hamiltonian in Section 2.5.2, whereas the GKSL measurement cometric $\mathscr{M}_\rho$ (4.37) need not conserve $\langle \hat{H} \rangle$ on S? Because (2.320) acts on the closed joint state ρ_{tot} of the combined system-plus-apparatus graph $V = S \sqcup \bar{S}$. On V, the total Hamiltonian $\hat{H}_{\text{tot}} := \hat{H} \otimes \hat{I}_{\bar{S}} + \hat{H}_{\text{ext}}$ sums the subsystem energy $\langle \hat{H} \rangle$ and the external probe and port-coupling energy $H_{\text{ext}}(\rho_{\text{tot}}) := \text{Tr}(\hat{H}_{\text{ext}} \rho_{\text{tot}})$ across $\mathbf{K}_\partial^{(\text{ext})} \oplus \mathbf{K}_{\bar{S}}$, so contracting the joint Kulkarni–Nomizu 4-bracket with H_{tot} enforces $(H_{\text{tot}}, \cdot) = 0$ (2.324) identically:

$$H_{\text{tot}}(\rho_{\text{tot}}) = \langle \hat{H} \rangle + H_{\text{ext}}(\rho_{\text{tot}}), \tag{4.40}$$

$$\left(\frac{\mathrm{d}H_{\text{tot}}}{\mathrm{d}t} \right)_{\text{diss}} = \left(\frac{\mathrm{d}\langle \hat{H} \rangle}{\mathrm{d}t} \right)_{\text{diss}} + \left(\frac{\mathrm{d}H_{\text{ext}}}{\mathrm{d}t} \right)_{\text{diss}} = 0. \tag{4.41}$$

Tracing out $\bar{S}$ via (4.31) projects the joint flow onto S alone and drops the external apparatus energy H_{ext} across $\mathbf{K}_\partial^{(\text{ext})}$, just as projecting $Z = (x, p, S)^{\mathsf{T}}$ onto (x, p) in Example 2.9 (2.334) dropped θS to expose mechanical damping. Auditing the reduced energy rate across the $\hat{A}$-generated port cometric (4.37) therefore determines when $\langle \hat{H} \rangle$ is conserved autonomously on S without external work transfer across ∂S, establishing the exact equivalence between reduced First-Law Casimir degeneracy and Quantum Non-Demolition (QND) measurement [23].

THEOREM 4.6 (Energy Conservation and Quantum Non-Demolition Measurement). *Let $\mathscr{M}_\rho$ be the metriplectic measurement metric bracket (4.37) with active dephasing rate $\Gamma_\varphi > 0$ generated by a Hermitian pointer observable $\hat{A} = \hat{A}^\dagger$ and Hermitian Hamiltonian $\hat{H} = \hat{H}^\dagger$. The dissipative energy exchange rate along emergent clock time t evaluates to:*

$$\left(\frac{\mathrm{d}\langle \hat{H} \rangle}{\mathrm{d}t} \right)_{\text{diss}} = -\frac{\Gamma_\varphi}{2} \text{Tr}\Big([\hat{A}, [\hat{A}, \hat{H}]] \rho \Big). \tag{4.42}$$

The Hamiltonian generator $\hat{H}$ is an exact Casimir invariant of the measurement metric bracket, $(H, \cdot)_{\mathscr{M}} = 0$, conserving tracked energy identically across all density operators ρ, if and only if $[\hat{A}, [\hat{A}, \hat{H}]] = 0$, which for Hermitian $\hat{A}$ and $\hat{H}$ holds if and only if $\hat{A}$ satisfies the Quantum Non-Demolition commutation criterion:

$$[\hat{A}, \hat{H}] = 0. \tag{4.43}$$

PROOF. For the linear Hamiltonian functional $H(\rho) = \text{Tr}(\hat{H}\rho)$ and linear entropy $S_{\text{lin}}(\rho)$ (4.36), contracting the metric bracket (4.37) with the variational gradient $-\rho$ yields:

$$\left(\frac{\mathrm{d}\langle \hat{H} \rangle}{\mathrm{d}t} \right)_{\text{diss}} = \big\langle \hat{H}, \mathscr{M}_\rho(-\rho) \big\rangle_{\text{HS}} = -\frac{\Gamma_\varphi}{2} \text{Tr}\Big(\hat{H} [\hat{A}, [\hat{A}, \rho]] \Big). \tag{4.44}$$

Applying the cyclic invariance of the trace gives the commutator and Hilbert–Schmidt norm identities:

$$\mathrm{Tr}\big(\hat{H}[\hat{A},[\hat{A},\rho]]\big) = \mathrm{Tr}\big([[\hat{H},\hat{A}],\hat{A}]\rho\big) = \mathrm{Tr}\big([\hat{A},[\hat{A},\hat{H}]]\rho\big), \tag{4.45}$$

$$\mathrm{Tr}\big(\hat{H}[\hat{A},[\hat{A},\hat{H}]]\big) = \mathrm{Tr}\big([\hat{A},\hat{H}]^{\dagger}[\hat{A},\hat{H}]\big) = \big\|[\hat{A},\hat{H}]\big\|_{\mathrm{HS}}^{2} \geq 0, \tag{4.46}$$

where (4.45) establishes (4.42), and (4.46) uses $[\hat{H},\hat{A}] = [\hat{A},\hat{H}]^{\dagger}$ for Hermitian $\hat{A}$ and $\hat{H}$. Because $\Gamma_{\varphi} > 0$ and $[\hat{A},[\hat{A},\hat{H}]]$ is Hermitian and traceless, $\mathrm{Tr}([\hat{A},[\hat{A},\hat{H}]]\rho) = 0$ holds across all density operators ρ if and only if $[\hat{A},[\hat{A},\hat{H}]] = 0$, which by (4.46) holds if and only if $[\hat{A},\hat{H}] = 0$. □

When $[\hat{A},\hat{H}] \neq 0$, Casimir degeneracy is broken on the reduced sector S and the observing subsystem exchanges non-zero *measurement backaction* power (in watts when t is metered in seconds via (2.255)) with the external probe across $\mathbf{K}_{\partial}^{(\mathrm{ext})}$, balancing (4.41) identically:

$$\left(\frac{\mathrm{d}H_{\mathrm{ext}}}{\mathrm{d}t}\right)_{\mathrm{diss}} = -\left(\frac{\mathrm{d}\langle\hat{H}\rangle}{\mathrm{d}t}\right)_{\mathrm{diss}} = \frac{\Gamma_{\varphi}}{2}\,\mathrm{Tr}\big([\hat{A},[\hat{A},\hat{H}]]\rho\big). \tag{4.47}$$

Global Kulkarni–Nomizu energy conservation $(H_{\mathrm{tot}},\cdot) = 0$ thus holds universally on $V = S \sqcup \bar{S}$, while QND commutation $[\hat{A},\hat{H}] = 0$ characterises precisely those boundary measurements whose dissipative dephasing transfers zero work across ∂S. Similarly, two non-commuting observables $[\hat{A},\hat{B}] \neq 0$ correspond to incompatible coarse-graining refinements that cannot be simultaneously stabilised without mutual metric disturbance (Section 4.3.3).

As illustrated in Figure 4.2, conservative internal transport drives unitary precession around constant-energy orbits while boundary Schur damping contracts off-diagonal coherences onto $\mathrm{im}(\mathbf{P}_{\boldsymbol{\Pi}_S})$, conserving tracked energy exclusively along QND observables.

4.2.3 *Relational Interferometry and Delayed Choice*

Why does a single quantum excitation produce interference fringes when unmonitored yet register localised detections when observed? Prior to coupling across $\mathbf{K}_{\partial}^{(\mathrm{ext})}$, a propagating excitation carries neither an internal memory core $\mathbf{K}_{\Omega}$ nor preserved structure $I_{\mathrm{rev},\Omega}$, and is metered against the observer's emergent clock t (2.250). Along a transit path γ of proper cadence ω_{γ} and proper duration $\tau[\gamma]$, action $S[\gamma]$ accumulates phase calibrated by $\hbar$, so a path difference $\Delta L(x) := L_B(x) - L_A(x)$ between slits A and B to screen block S_x induces the relative clock phase shift:

$$\frac{S[\gamma]}{\hbar} = -\omega_{\gamma}\tau[\gamma] = -\Delta\varphi_{\mathrm{clock}}[\gamma], \tag{4.48}$$

$$\Delta\varphi_{\mathrm{clock}}(x) = \frac{p}{\hbar}\Delta L(x) = \frac{2\pi\Delta L(x)}{\lambda_{\mathrm{dB}}}, \tag{4.49}$$

$$\lambda_{\mathrm{dB}} := \frac{2\pi\hbar}{p}, \tag{4.50}$$

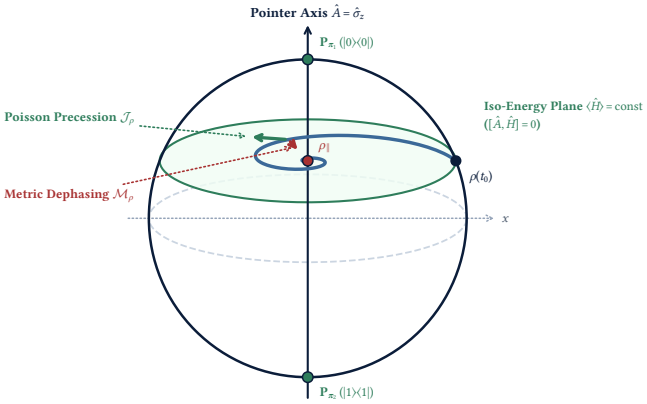


FIGURE 4.2: Metriplectic geometry of quantum measurement and the Quantum Non-Demolition (QND) Casimir condition on the two-block Bloch sphere ($\mathbf{P}_{\boldsymbol{\pi}_1} \equiv |0\rangle\langle 0|$, $\mathbf{P}_{\boldsymbol{\pi}_2} \equiv |1\rangle\langle 1|$). Along emergent relational clock time t, flow from an initial state $\rho(t_0)$ splits into conservative Poisson precession $\mathscr{J}_\rho(\delta H/\delta\rho) = -(i/\hbar)[\hat{H}, \rho]$ (teal, along constant-energy orbits) and dissipative metric dephasing $\mathscr{M}_\rho(\delta S_{\text{lin}}/\delta\rho) = -(\Gamma_\varphi/2)[\hat{A}, [\hat{A}, \rho]]$ (crimson, contracting off-diagonal coherences radially onto the decohered block state $\rho_\parallel \in \text{im}(\mathbf{P}_{\boldsymbol{\Pi}_S})$ along $\hat{A} = \hat{\sigma}_z$). Under the QND condition $[\hat{A}, \hat{H}] = 0$, the metric bracket satisfies $(H, \cdot)_{\mathscr{M}} = 0$, confining dephasing strictly to the iso-energy plane $\langle \hat{H} \rangle = \text{const}$ at zero backaction power.

where p denotes canonical momentum and λ_{dB} the de Broglie wavelength. Whether this relative phase shift produces interference fringes across the screen blocks is governed by Theorem 2.2 in Section 2.3.2.

In an *unmonitored interferometer* with $\mathbf{K}_\partial^{(\text{det})} = \mathbf{o}$, no detector couples at the slits, so $\Gamma_\varphi = 0$ and $\dot{I}_{\text{irr},\partial} = 0$. Because S implements the coarsened assignment $\boldsymbol{\Pi}^{(2)} = \boldsymbol{\Pi}^{(1)}\mathbf{P}$ (2.151) merging both pathways into the same screen block S_x, the cut-internalisation operator $\mathscr{T}_{\mathbf{P}}$ (2.160) folds the inter-pathway phase relation directly into the screen conduit capacity:

$$K_\partial^{(\text{ext})}(x) \propto \left| e^{i\varphi_A(x)} + e^{i\varphi_B(x)} \right|^2 = 2\big(1 + \cos \Delta\varphi_{\text{clock}}(x)\big). \tag{4.51}$$

At anti-phase positions where $\Delta\varphi_{\text{clock}}(x_{\text{dark}}) = \pi$, destructive cancellation drives $K_\partial^{(\text{ext})}(x_{\text{dark}}) = 0$, which by the CCE flux-support rule (2.310) enforces vanishing boundary flux into $S_{x_{\text{dark}}}$. A particle does not 'decide' to avoid a dark fringe. Instead, internalising both pathways into S_x closes the boundary conduit into $S_{x_{\text{dark}}}$.

In a *monitored interferometer* with $\mathbf{K}_\partial^{(\text{det})} \neq \mathbf{o}$, coupling an upstream which-path detector refines the partition to $\boldsymbol{\Pi}^{(1)}$, allocating at least two disjoint detector blocks $S_{\alpha_A} \cap S_{\alpha_B} = \emptyset$ (Section 2.3.1) of preserved capacity $\Delta I_{\text{rev},\Omega}$ (in nats) within $\mathbf{K}_\Omega$ and correlating the slit pathways with detector states $|D_A\rangle$

and $|D_B\rangle$ of pre-measurement overlap $\mathscr{V}_0 := |\langle D_B|D_A\rangle| \in [0,1]$ during initial reversible coupling:

$$\Delta I_{\mathrm{rev},\Omega} \geq \ln 2, \tag{4.52}$$

$$\big(c_A|A\rangle + c_B|B\rangle\big)|D_0\rangle \longrightarrow c_A|A\rangle|D_A\rangle + c_B|B\rangle|D_B\rangle. \tag{4.53}$$

Tracing out D without conditioning already weights unconditioned screen fringes by $\mathscr{V}_0$ in accordance with Englert–Greenberger–Yasin wave–particle duality [50]. Yet so long as the correlation (4.53) remains isolated inside the tracked subspace with $\dot{I}_{\mathrm{irr},\partial} = 0$, unitary recombination via $\mathbf{P}$ (projecting D onto symmetric quantum-eraser states $|D_\pm\rangle$) can still re-internalise the inter-block cut through $\mathscr{T}_{\mathbf{P}}$ and recover unit conditioned fringe visibility across $\{S_x\}$ even when $\mathscr{V}_0 = 0$. Stabilising $|D_A\rangle$ and $|D_B\rangle$ into persistent CCE blocks ($\Xi \gg 1$, (2.127)), however, expels unresolved two-branch fluctuations across ∂S at boundary power $P_{\mathrm{diss},\partial}(t)$ (3.15), incurring cumulative boundary dissipation $I_{\mathrm{irr},\partial,T}$ (in nats) by Theorem 4.3 (4.19) and driving dephasing under linear port-coupling proportionality:

$$\Gamma_\varphi(t) = \eta_\varphi\, \dot{I}_{\mathrm{irr},\partial}(t) = \eta_\varphi \frac{P_{\mathrm{diss},\partial}(t)}{\theta}, \tag{4.54}$$

$$I_{\mathrm{irr},\partial,T} = \int_0^T \dot{I}_{\mathrm{irr},\partial}(t)\,\mathrm{d}t \geq \ln 2, \tag{4.55}$$

where $\eta_\varphi \in (0,1]$ is the detector's dimensionless linear boundary-coupling efficiency and $I_{\mathrm{irr},\partial,T}$ (3.14) is clock-invariant across the emergent horizon $t \in [0,T]$.

On the rank-1 inter-level difference subspace $\mathrm{im}(\Delta\mathbf{P}_{1\to 2})$ (2.165) (Example 2.5), the binary which-path observable with eigenvalues $a_A = +1$ and $a_B = -1$ is the signed dipole operator, and integrating (4.39) across $[0,T]$ damps the inter-slit coherence modulus exponentially with $I_{\mathrm{irr},\partial,T}$:

$$\hat{A} = |A\rangle\langle A| - |B\rangle\langle B|, \tag{4.56}$$

$$|\rho_{AB}(T)| = |\rho_{AB}(0)| \exp\!\big[-2\eta_\varphi I_{\mathrm{irr},\partial,T}\big]. \tag{4.57}$$

Normalising the resulting screen conduit flux (4.51) for symmetric slit cycle amplitudes $\psi_A(x)$ and $\psi_B(x)$ recovers the standard interferometric Born detection profile $P_{\mathrm{CCE}}(x)$ across $\{S_x\}$ with fringe visibility $\mathscr{V}(T)$ (setting $\mathscr{V}_0 = 1$ for pure boundary dephasing without an ancillary latch, or for conditioned quantum-eraser readout):

$$P_{\mathrm{CCE}}(x) = \frac{1}{2}|\psi_A(x)|^2 + \frac{1}{2}|\psi_B(x)|^2 + \mathscr{V}(T)\,\mathrm{Re}\big[\psi_A(x)\psi_B^*(x)\big], \tag{4.58}$$

$$\mathscr{V}(T) := \mathscr{V}_0 \exp\!\big[-2\eta_\varphi I_{\mathrm{irr},\partial,T}\big] \in [0, \mathscr{V}_0]. \tag{4.59}$$

EXAMPLE 4.1 (Interferometer Visibility Decay from Detector Boundary Dissipation). Consider a symmetrically illuminated double-slit interferometer with equal screen amplitude moduli $|\psi_A(x)| = |\psi_B(x)| = \psi_0 > 0$, unit coupling efficiency $\eta_\varphi = 1$, and continuous boundary dephasing directly across the

slit channels ($\mathscr{V}_0 = 1$, including conditioned quantum-eraser readout). Substituting these parameters into (4.58)–(4.59) simplifies the normalised screen conduit profile to:

$$P_{\mathrm{CCE}}(x) = \psi_0^2\big[1 + \mathscr{V}(T)\cos\Delta\varphi_{\mathrm{clock}}(x)\big]. \tag{4.60}$$

Let P_{bright} and P_{dark} denote $P_{\mathrm{CCE}}(x)$ at constructive ($\Delta\varphi_{\mathrm{clock}} = 0$) and destructive ($\Delta\varphi_{\mathrm{clock}} = \pi$) fringe positions. Evaluating visibility and conduit weights from (4.60) across the unmonitored regime ($I_{\mathrm{irr},\partial,T} = 0$), the two-branch dissipation floor ($I_{\mathrm{irr},\partial,T} = \ln 2$), and a large-multiplicity detector latch ($I_{\mathrm{irr},\partial,T} = 10^4$) gives:

$$\big(\mathscr{V}, P_{\mathrm{bright}}, P_{\mathrm{dark}}\big)\big|_{I_{\mathrm{irr},\partial,T}=0} = \big(1,\ 2\psi_0^2,\ 0\big), \tag{4.61}$$

$$\big(\mathscr{V}, P_{\mathrm{bright}}, P_{\mathrm{dark}}\big)\big|_{I_{\mathrm{irr},\partial,T}=\ln 2} = \big(0.25,\ 1.25\,\psi_0^2,\ 0.75\,\psi_0^2\big), \tag{4.62}$$

$$\big(\mathscr{V}, P_{\mathrm{bright}}, P_{\mathrm{dark}}\big)\big|_{I_{\mathrm{irr},\partial,T}=10^4} \approx \big(0,\ \psi_0^2,\ \psi_0^2\big). \tag{4.63}$$

Expelling ln 2 nats of boundary dissipation at the two-branch threshold suppresses fringe visibility by 75%, while high-multiplicity latch stabilisation extinguishes interference completely into an incoherent sum. ♢

Equations (4.56)–(4.59) resolve two classic interferometric puzzles directly from boundary dissipation. First, fringe suppression persists even under a *non-selective measurement* that ignores or sums over the upstream blocks $\{\alpha_A, \alpha_B\}$. Once open-boundary stabilisation occurs ($I_{\mathrm{irr},\partial,T} > 0$), phase coherence across $\mathrm{im}(\Delta\mathbf{P}_{1\to 2})$ has already been irreversibly exported across ∂S into $\bar{S}$, so coarse-graining over decohered diagonal weights in $\mathrm{im}(\mathbf{P}_{\mathbf{\Pi}_S^{(1)}})$ cannot retrieve lost phase correlations or reopen the coherent conduit (4.51).

Second, the same coarsening algebra resolves *Wheeler's Delayed-Choice Paradox* [169], in which the observer selects between an unmonitored screen ($\mathbf{\Pi}^{(2)}$) and a path-resolving detector ($\mathbf{\Pi}^{(1)}$) only after the excitation has entered the interferometer. Standard accounts find this paradoxical only because they assume an observer-independent classical trajectory inside the unmonitored region $\bar{S}$, asking how a downstream choice can retroactively decide whether the excitation 'travelled through one slit or both.' Prior to boundary coupling across $\mathbf{K}_\partial^{(\mathrm{ext})}$, however, no block of $\mathbf{K}_\Omega$ is coupled and no coarse-grained record exists. Asserting that the excitation occupied slit A or slit B at earlier slices is an instance of retrodictive divergence (Section 4.1.2 and Section 6.3.1), projecting the post-registration refinement $\mathbf{\Pi}^{(1)}$ backward onto an unpartitioned substrate history. The delayed reconfiguration alters nothing at earlier slices, and merely selects whether S implements $\mathbf{\Pi}^{(2)}$ via $\mathscr{T}_{\mathbf{P}}$ or refines to $\mathbf{\Pi}^{(1)}$ when boundary registration occurs.

4.3 QUANTUM ENTANGLEMENT

Whereas Section 4.2 examined how a single boundary port resolves phase coherence along a local transit channel, quantum entanglement tests the

spatial locality of the coarse-grained substrate itself. When an embedded observing subsystem S monitors two coarse-grained detector blocks S_α and S_β that share a common source preparation, joint measurement records exhibit correlations that violate classical Bell inequalities without permitting remote block-weight signalling. This section resolves that apparent non-locality natively within Conservation-Congruent Encoding by contrasting direct graph adjacency in the unresolved complement $\mathrm{im}(\mathbf{Q}_{\mathbf{\Pi}_S})$ with the coarse-grained resistance metric $\Omega_{\alpha\beta}$ on $\mathrm{im}(\mathbf{P}_{\mathbf{\Pi}_S})$, and showing how each step maps onto the standard Bell, no-signalling, and Tsirelson relations.

4.3.1 *Two-Cycle Phase Bridges and the EPR Dilemma*

Consider the single embedded observing subsystem S of Section 4.1 monitoring two coarse-grained detector blocks S_α, S_β ($\alpha, \beta \in \{1, \dots, M\}$) on its internal capacity matrix $\mathbf{K}_S$ (4.2). On the coordinate-free relational graph $G = (V, E)$, suppose two conservative cycle modes $i \in S_\alpha$ and $j \in S_\beta$ prepared at a common interaction vertex share a direct graph bridge $\{i, j\} \in E$ inside the unresolved residual subspace $\mathrm{im}(\mathbf{Q}_{\mathbf{\Pi}_S})$, locking both canonical quadratures (q, p) across the pair (Section 4.2.1) while leaving each block's normalised quadratic weight unpolarised at $\rho_\alpha = 1/2$ and $\rho_\beta = 1/2$ on $\mathrm{im}(\mathbf{P}_{\mathbf{\Pi}_S})$. In the canonical two-qubit Hilbert-space representation across binary subblocks $\{|0\rangle, |1\rangle\}$ at each detector port (Table 4.1), this locked two-cycle bridge corresponds to the maximally entangled Bell state $|\Phi^+\rangle$ and joint density operator ρ_{AB}:

$$|\Phi^+\rangle = \frac{|00\rangle + |11\rangle}{\sqrt{2}}, \tag{4.64}$$

$$\rho_{AB} = |\Phi^+\rangle\langle\Phi^+|. \tag{4.65}$$

Although ρ_{AB} is globally pure, tracing out either detector register leaves each reduced port state ρ_A and ρ_B maximally mixed, yielding von Neumann entropies and quantum mutual information (in nats):

$$S_{\mathrm{vN}}(\rho_{AB}) = 0, \tag{4.66}$$

$$S_{\mathrm{vN}}(\rho_A) = S_{\mathrm{vN}}(\rho_B) = \ln 2, \tag{4.67}$$

$$S_{\mathrm{vN}}(\rho_A) + S_{\mathrm{vN}}(\rho_B) - S_{\mathrm{vN}}(\rho_{AB}) = 2 \ln 2. \tag{4.68}$$

Whereas a classically correlated binary register pair cannot exceed $\ln 2$ nats of mutual specification, the two-cycle bridge carries $2 \ln 2$ nats because each conservative cycle spans a two-quadrature symplectic phase plane (q, p) (Section 4.1.1 and Section 4.2.1), locking both discrete amplitude parity and conjugate relative phase across the pair while leaving each single-port block weight unpolarised.

Einstein, Podolsky, and Rosen (EPR) argued that if resolving an outcome at detector α predicts the outcome at distant detector β without disturbance, quantum mechanics must be incomplete or non-local [48]. Bell's theorem and the CHSH inequality of Clauser, Horne, Shimony, and Holt then showed

that no local hidden-variable model can reproduce the trigonometric coincidence law or reach the $2\sqrt{2}$ Tsirelson bound [13, 32, 33]. Within CCE, this dilemma is a projection artefact of the *Platonic Observer Fallacy* (Section 1.5 and Section 4.1.1), arising from mistaking the coarse-grained resistance geometry on $\mathrm{im}(\mathbf{P}_{\mathbf{\Pi}_S})$ for the full adjacency structure of G. Resolving the paradox from the operators of Chapter 2 comes down to two physical questions. First, why does a unit-distance graph bridge in $\mathrm{im}(\mathbf{Q}_{\mathbf{\Pi}_S})$ coexist with large resistance separation $\Omega_{\alpha\beta} \gg 1$ on $\mathrm{im}(\mathbf{P}_{\mathbf{\Pi}_S})$ while keeping remote block weights strictly invariant? Second, how do inter-scale dipole projections $\Delta\mathbf{P}_{1\to 2}$ at port orientations $(\varphi_\alpha, \varphi_\beta)$ produce Malus's coincidence law and the $2\sqrt{2}$ Tsirelson bound rather than the classical ceiling of 2?

4.3.2 *Direct Graph Adjacency, Conductance Dilution, and No-Signalling*

By Theorem 4.1, the embedded subsystem S cannot resolve G directly, and instead partitions the substrate through the orthogonal projector split (4.1) and contracted capacity matrix $\mathbf{K}_S$ (Section 2.2.1 and Section 2.2.2). On the coordinate-free relational graph $G = (V, E)$, there is no background spatial container, so the two cycle modes $i \in S_\alpha$ and $j \in S_\beta$ share a direct bridge $\{i, j\} \in E$ at unit graph distance and order-unity bridge capacity K_{bridge} (in links) inside $\mathrm{im}(\mathbf{Q}_{\mathbf{\Pi}_S})$. Under the coarse-graining projection $\mathrm{im}(\mathbf{P}_{\mathbf{\Pi}_S})$, however, effective separation between detector blocks S_α and S_β is governed by the Klein–Randić resistance metric $\Omega_{\alpha\beta}$ across the capacity Laplacian $\mathbf{L}_{\mathbf{K}}$ (Section 2.5.1, (2.239)) [85]:

$$\Omega_{\alpha\beta} = (\mathbf{e}_\alpha - \mathbf{e}_\beta)^{\mathsf{T}} \mathbf{L}_{\mathbf{K}}^{\dagger} (\mathbf{e}_\alpha - \mathbf{e}_\beta) \gg 1, \tag{4.69}$$

$$\mathrm{dist}_G(i, j) = 1, \tag{4.70}$$

$$K_{\mathrm{bridge}} = \mathcal{O}(1). \tag{4.71}$$

Sustaining the $2 \ln 2$ nats of two-quadrature correlation (4.68) across an order-unity link bridge ($K_{\mathrm{bridge}} = \mathcal{O}(1)$) up to detection requires *pre-detection bridge isolation*. Prior to coupling into the detector latches, the transit modes i and j must remain shielded from external environmental cuts ($\dot{I}_{\mathrm{irr},\partial} = 0$ and $\Gamma_\varphi = 0$, as in vacuum photonic channels or cryogenic traps), because any premature boundary dissipation along an $\mathcal{O}(1)$ link exports relative phase across ∂S via (4.57) and degrades the bridge towards a separable classical pair. Once the isolated modes couple to the coarse-grained detector blocks S_α and S_β, each bundling an Avogadro-scale internal capacity $K_{\alpha\alpha} \gg 1$, the single direct bridge is diluted on $\mathbf{K}_S$ by the block degree volume $d_\alpha \approx K_{\alpha\alpha}$ (Section 2.3.1, (2.133) and (2.138)). Consequently, on the capacity graph $G_{\mathbf{K}}$, detector blocks S_α and S_β communicate across coarse-grained registers only through a multi-hop chain of intermediate blocks, yielding $\Omega_{\alpha\beta} \gg 1$. Apparent 'spooky action at a distance' arises when the observer mistakes a boundary-isolated unit-distance bridge in $\mathrm{im}(\mathbf{Q}_{\mathbf{\Pi}_S})$ for an instantaneous jump across the large resistance separation $\Omega_{\alpha\beta} \gg 1$ of $\mathrm{im}(\mathbf{P}_{\mathbf{\Pi}_S})$.

Can a local phase rotation or sub-block refinement at S_α alter the remote block weight at S_β through the direct bridge? By the single-step transition di-

lution bound of Section 2.3.1 (2.138), the per-trial transition probability across the bridge is suppressed by the block degree volume d_α:

$$T_{\alpha\to\beta} = \frac{K_{\text{bridge}}}{d_\alpha} \approx \frac{K_{\text{bridge}}}{K_{\alpha\alpha}} \sim 10^{-23} \longrightarrow 0. \tag{4.72}$$

Whereas conductance dilution (4.72) governs the large coarse-grained resistance separation $\Omega_{\alpha\beta} \gg 1$ between coarse-grained detector latches, exact marginal no-signalling holds algebraically at any finite local Hilbert dimensions $d_A, d_B \geq 2$. Within the commuting projector tower of Section 2.3.2 (2.164), resolving a binary outcome $a \in \{+1, -1\}$ inside detector block S_α refines the level-2 block S_α into two disjoint level-1 sub-blocks $S_{\alpha,+}$ and $S_{\alpha,-}$ along $\Delta\mathbf{P}_{1\to 2}$ (2.165), while on the bipartite register state ρ_{AB} any local Kraus channel $\mathscr{E}_A$ with operators $\{\hat{M}_k\}$ on S_α satisfies trace-preserving completeness:

$$\mathscr{E}_A(\rho_{AB}) := \sum_k (\hat{M}_k \otimes \hat{I}_B)\, \rho_{AB}\, (\hat{M}_k^\dagger \otimes \hat{I}_B), \tag{4.73}$$

$$\sum_k \hat{M}_k^\dagger \hat{M}_k = \hat{I}_A. \tag{4.74}$$

LEMMA 4.7 (Remote Block-Weight Invariance and No-Signalling). *Let $\mathbf{P}_{\mathbf{\Pi}_S^{(2)}}$ and $\mathbf{P}_{\mathbf{\Pi}_S^{(1)}}$ form a commuting projector tower (2.164) on S with orthogonal dipole difference projector $\Delta\mathbf{P}_{1\to 2}$ (2.165), and let $\mathscr{E}_A$ be any local trace-preserving Kraus channel (4.73)–(4.74) at finite local Hilbert dimensions $d_A, d_B \geq 2$. For any local zero-sum dipole refinement $S_\alpha = S_{\alpha,+} \sqcup S_{\alpha,-}$ or local measurement channel $\mathscr{E}_A$ at detector block S_α, the remote reduced state $\mathrm{Tr}_A(\mathscr{E}_A(\rho_{AB}))$ equals $\mathrm{Tr}_A(\rho_{AB})$ and the normalised ℓ_2 block weights satisfy:*

$$\mathbf{P}_{\mathbf{\Pi}_S^{(2)}} \Delta\mathbf{P}_{1\to 2} = \mathbf{o}, \tag{4.75}$$

$$\rho_{\alpha,+} + \rho_{\alpha,-} = \rho_\alpha, \tag{4.76}$$

$$\dot{\rho}_\beta = 0. \tag{4.77}$$

Under the Born block-weight correspondence of Table 4.1, (4.77) recovers exact quantum marginal no-signalling at every finite register scale without relying on the asymptotic dilution limit (4.72).

PROOF. By the idempotence and hierarchical nesting identity of (2.164), left-multiplying the difference projector $\Delta\mathbf{P}_{1\to 2}$ by the level-2 projector $\mathbf{P}_{\mathbf{\Pi}_S^{(2)}}$ gives:

$$\begin{aligned} \mathbf{P}_{\mathbf{\Pi}_S^{(2)}} \Delta\mathbf{P}_{1\to 2} &= \mathbf{P}_{\mathbf{\Pi}_S^{(2)}} \big(\mathbf{P}_{\mathbf{\Pi}_S^{(1)}} - \mathbf{P}_{\mathbf{\Pi}_S^{(2)}}\big) \\ &= \mathbf{P}_{\mathbf{\Pi}_S^{(2)}} - \mathbf{P}_{\mathbf{\Pi}_S^{(2)}} = \mathbf{o}, \end{aligned} \tag{4.78}$$

which conserves the total block weight $\rho_\alpha = \rho_{\alpha,+} + \rho_{\alpha,-}$. Applying partial-trace cyclicity on S_α to (4.73) and substituting Kraus completeness (4.74) gives:

$$\begin{aligned} \mathrm{Tr}_A\big(\mathscr{E}_A(\rho_{AB})\big) &= \mathrm{Tr}_A\left[\left(\sum_k \hat{M}_k^\dagger \hat{M}_k \otimes \hat{I}_B\right) \rho_{AB}\right] \\ &= \mathrm{Tr}_A(\rho_{AB}), \end{aligned} \tag{4.79}$$

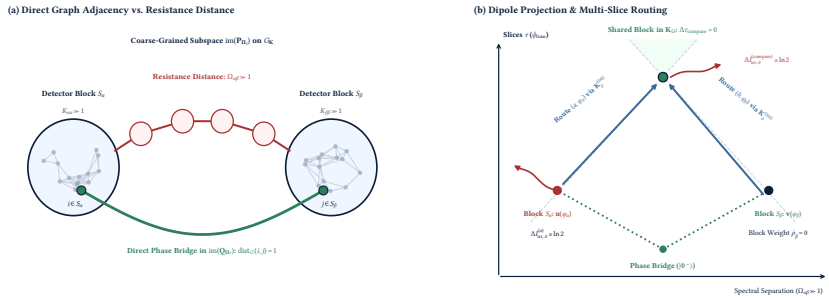


FIGURE 4.3: Quantum entanglement as a coarse-graining projection illusion for a single embedded observing subsystem S. (a) Structural mismatch between direct graph adjacency and the coarse-grained resistance metric: cycle modes $i \in S_\alpha$ and $j \in S_\beta$ share a direct unit-distance phase bridge $\mathrm{dist}_G(i,j) = 1$ in the unresolved complement $\mathrm{im}(\mathbf{Q}_{\mathbf{\Pi}_S})$, whereas coarse-graining onto $\mathrm{im}(\mathbf{P}_{\mathbf{\Pi}_S})$ dilutes the single bridge by the internal block degree volume, separating detector blocks S_α and S_β across $G_{\mathbf{K}}$ by a large resistance distance $\Omega_{\alpha\beta} \gg 1$. (b) Inter-scale dipole projection and multi-slice routing along $\boldsymbol{\phi}_{\mathrm{time}}$: local phase settings $(\varphi_\alpha, \varphi_\beta)$ orient the unit dipole vectors $\mathbf{u}(\varphi_\alpha)$ and $\mathbf{v}(\varphi_\beta)$ before metric sub-block stabilisation while leaving the remote block weight strictly invariant ($\dot{\rho}_\beta = 0$). Verifying the trigonometric coincidence law and Tsirelson bound requires routing both stabilised records across $\mathbf{K}_\partial^{(\mathrm{int})}$ over $\Delta\tau_{\mathrm{compare}} \geq \mathrm{dist}_{G_{\mathbf{K}}}(\alpha, \beta)$ positive slices.

holding every remote block weight ρ_β invariant ($\dot{\rho}_\beta = 0$) identically. □

Because S can evaluate joint correlations only from stabilised block records in $\mathrm{im}(\mathbf{P}_{\mathbf{\Pi}_S})$, while each individual block weight remains unpolarised, verifying the shared correlation (4.68) requires routing the stabilised sub-block records from S_α and S_β across the internal transition conduits $\mathbf{K}_\partial^{(\mathrm{int})}$ along ordered spectral slices $\{S_\tau\}$ of $\boldsymbol{\phi}_{\mathrm{time}}$ into a shared comparison block in $\mathbf{K}_\Omega$. By the flux-support rule (2.310) across graph distance $\mathrm{dist}_{G_{\mathbf{K}}}(\alpha, \beta) > 0$ on $G_{\mathbf{K}}$ and Theorem 4.3 (4.19), coincidence comparison requires strictly positive slice transit $\Delta\tau_{\mathrm{compare}}$ and irreversible boundary dissipation:

$$\Delta\tau_{\mathrm{compare}} \geq \mathrm{dist}_{G_{\mathbf{K}}}(\alpha, \beta) > 0, \tag{4.80}$$

$$\Delta I_{\mathrm{irr},\partial}^{(\mathrm{compare})} \geq \ln 2. \tag{4.81}$$

Likewise, in entanglement swapping across two independent bridges $(S_\alpha, S_{\gamma,1})$ and $(S_{\gamma,2}, S_\beta)$, a joint Bell-basis projection inside an intermediate relay block $S_\gamma = S_{\gamma,1} \sqcup S_{\gamma,2}$ leaves the unconditional marginals at S_α and S_β invariant by (4.79), conditioning remote (S_α, S_β) sub-ensembles only after classical relay records traverse $G_{\mathbf{K}}$ within the bound (4.80). When Chapter 6 (Section 6.2) projects $\mathbf{K}$ onto its emergent Lorentzian metric, the multi-slice graph-routing bound (4.80) maps directly onto the causal light-cone ceiling.

As illustrated in Figure 4.3, distinguishing the coarse-grained resistance metric $\Omega_{\alpha\beta}$ on $\mathrm{im}(\mathbf{P}_{\mathbf{\Pi}_S})$ from direct graph adjacency in $\mathrm{im}(\mathbf{Q}_{\mathbf{\Pi}_S})$ dissolves apparent non-locality into local conservation bookkeeping.

4.3.3 *Dipole Projections and the Tsirelson Bound*

How does the observer resolve a binary outcome ± 1 at each detector block and recover the continuous trigonometric coincidence law? By Theorem 4.6, a coarse-grained detector block S_α can stabilise only one commutative binary refinement $S_\alpha = S_{\alpha,+} \sqcup S_{\alpha,-}$ at a time, while non-commuting phase settings $\varphi_\alpha \neq \varphi'_\alpha$ correspond to incompatible level-1 refinements of the canonical cycle (q_α, p_α). Measuring S_α at orientation φ_α couples both metriplectic sectors of Section 4.1.1, first applying a reversible symplectic rotation $\mathbf{R}(\varphi_\alpha) \in \mathrm{SO}(2)$ (or $\mathrm{SU}(2)$ when the cyclic synchronisation index $r_{\mathrm{sync}} \in \{1, 2\}$ equals 2, as derived in Chapter 5, Section 5.1.1) within $\mathbf{K}_\Omega$ at zero boundary dissipation ($\dot{I}_{\mathrm{irr},\partial} = 0$, (4.7)), and second activating metric damping across $\mathbf{K}_\partial^{(\mathrm{ext})}$ to stabilise $a \in \{+1, -1\}$ into sub-block $S_{\alpha,+}$ or $S_{\alpha,-}$ (4.19).

By the commuting projector tower of Section 2.3.2 (2.164) and Example 2.5 (2.183), while the level-2 projector $\mathbf{P}_{\boldsymbol{\Pi}_S^{(2)}}$ conserves the total block weight ρ_α, the rank-1 difference projector $\Delta\mathbf{P}_{1\to 2}$ (2.165) isolates the unit signed dipole vectors $\mathbf{u}(\varphi_\alpha)$ and $\mathbf{v}(\varphi_\beta)$ oriented by φ_α and φ_β. Evaluating the binary sub-block stabilisation dissipation (4.19), the Euclidean ℓ_2 dipole inner product $E(\varphi_\alpha, \varphi_\beta)$ across the locked two-cycle bridge (Section 2.4.1), and the resulting normalised aligned-channel overlap $P(b = a \mid a, \varphi_\alpha, \varphi_\beta)$ recovers Malus's coincidence law:

$$\Delta I_{\mathrm{irr},\partial}^{(\alpha)} \geq \ln 2, \tag{4.82}$$

$$E(\varphi_\alpha, \varphi_\beta) = \langle \mathbf{u}(\varphi_\alpha), \mathbf{v}(\varphi_\beta) \rangle = \cos\left(\frac{2(\varphi_\alpha - \varphi_\beta)}{r_{\mathrm{sync}}} \right), \tag{4.83}$$

$$P(b = a \mid a, \varphi_\alpha, \varphi_\beta) = \frac{1 + E(\varphi_\alpha, \varphi_\beta)}{2} = \cos^2\left(\frac{\varphi_\alpha - \varphi_\beta}{r_{\mathrm{sync}}} \right), \tag{4.84}$$

where $r_{\mathrm{sync}} = 1$ for bosonic optical polarisation cycles and $r_{\mathrm{sync}} = 2$ for fermionic spin-$\frac{1}{2}$ cycles, and each local binary stabilisation requires physical work $W_{\mathrm{diss}} \geq \theta \ln 2$ (4.10).

THEOREM 4.8 (Quadratic Capacity Geometry and the Tsirelson Bound). *Let binary measurement settings $x \in \{0, 1\}$ at detector block S_α and $y \in \{0, 1\}$ at detector block S_β project a shared two-cycle bridge onto unit dipole vectors $\mathbf{u}_0, \mathbf{u}_1$ and $\mathbf{v}_0, \mathbf{v}_1$ in the dipole subspace $\mathrm{im}(\Delta\mathbf{P}_{1\to 2})$ equipped with the Euclidean ℓ_2 inner product $\langle \cdot, \cdot \rangle$:*

$$\|\mathbf{u}_x\|_2 = \|\mathbf{v}_y\|_2 = 1, \tag{4.85}$$

$$E_{xy} := \langle \mathbf{u}_x, \mathbf{v}_y \rangle, \tag{4.86}$$

$$S_{\mathrm{CHSH}} := E_{00} + E_{01} + E_{10} - E_{11}. \tag{4.87}$$

Then the Clauser–Horne–Shimony–Holt (CHSH) correlation functional S_{CHSH} is strictly bounded by the equivalent quadratic and linear Tsirelson ceilings:

$$S_{\mathrm{CHSH}}^2 \leq 8, \tag{4.88}$$

$$|S_{\mathrm{CHSH}}| \leq 2\sqrt{2}. \tag{4.89}$$

PROOF. By bilinearity of the inner product, factor the CHSH functional as:

$$S_{\mathrm{CHSH}} = \langle \mathbf{u}_0, \mathbf{v}_0 + \mathbf{v}_1 \rangle + \langle \mathbf{u}_1, \mathbf{v}_0 - \mathbf{v}_1 \rangle. \tag{4.90}$$

Applying the Cauchy–Schwarz inequality to each inner product for unit vectors $\mathbf{u}_0$ and $\mathbf{u}_1$ gives:

$$|S_{\mathrm{CHSH}}| \le \|\mathbf{v}_0 + \mathbf{v}_1\|_2 + \|\mathbf{v}_0 - \mathbf{v}_1\|_2. \tag{4.91}$$

Squaring both sides and applying the elementary inequality $(u+w)^2 \le 2(u^2+w^2)$ together with the parallelogram identity on any inner-product space yields:

$$\begin{aligned} S_{\mathrm{CHSH}}^2 &\le 2\Big(\|\mathbf{v}_0 + \mathbf{v}_1\|_2^2 + \|\mathbf{v}_0 - \mathbf{v}_1\|_2^2\Big) \\ &= 4\big(\|\mathbf{v}_0\|_2^2 + \|\mathbf{v}_1\|_2^2\big) = 8, \end{aligned} \tag{4.92}$$

for unit vectors $\mathbf{v}_0$ and $\mathbf{v}_1$, establishing (4.88)–(4.89). Equality holds when $\mathbf{v}_0$ and $\mathbf{v}_1$ are orthogonal and $\mathbf{u}_0, \mathbf{u}_1$ align with $\mathbf{v}_0 \pm \mathbf{v}_1$. □

EXAMPLE 4.2 (Evaluating the CHSH Functional at Optimal Coincidence Angles). To see how the dipole inner product (4.83) saturates Theorem 4.8, consider two spin-$\frac{1}{2}$ cycles ($r_{\mathrm{sync}} = 2$) projected onto coplanar unit dipole vectors $\mathbf{u}_x$ and $\mathbf{v}_y$ at four equally spaced port orientations:

$$(\varphi_{\alpha,0}, \varphi_{\alpha,1}, \varphi_{\beta,0}, \varphi_{\beta,1}) = \Big(0, \frac{\pi}{2}, \frac{\pi}{4}, -\frac{\pi}{4}\Big), \tag{4.93}$$

$$\begin{pmatrix} \mathbf{u}_0 & \mathbf{u}_1 \end{pmatrix} = \begin{pmatrix} 1 & 0 \\ 0 & 1 \end{pmatrix}, \tag{4.94}$$

$$\begin{pmatrix} \mathbf{v}_0 & \mathbf{v}_1 \end{pmatrix} = \frac{1}{\sqrt{2}} \begin{pmatrix} 1 & 1 \\ 1 & -1 \end{pmatrix}. \tag{4.95}$$

Evaluating the four pairwise dipole inner products from (4.83) gives:

$$E_{00} = E_{01} = E_{10} = \cos\Big(\frac{\pi}{4}\Big) = +\frac{1}{\sqrt{2}}, \tag{4.96}$$

$$E_{11} = \cos\Big(\frac{3\pi}{4}\Big) = -\frac{1}{\sqrt{2}}. \tag{4.97}$$

Substituting these correlators into the CHSH functional (4.87) and comparing against any deterministic binary assignment $a_0, a_1, b_0, b_1 \in \{+1, -1\}$ yields:

$$\begin{aligned} S_{\mathrm{CHSH}} &= \tfrac{1}{\sqrt{2}} + \tfrac{1}{\sqrt{2}} + \tfrac{1}{\sqrt{2}} - \big(-\tfrac{1}{\sqrt{2}}\big) \\ &= 2\sqrt{2} \approx 2.828, \end{aligned} \tag{4.98}$$

$$a_0(b_0 + b_1) + a_1(b_0 - b_1) = \pm 2. \tag{4.99}$$

Because $\mathbf{v}_0$ and $\mathbf{v}_1$ are orthogonal and their sum and difference align collinearly with $\mathbf{u}_0$ and $\mathbf{u}_1$, the Euclidean dipole projection saturates $S_{\mathrm{CHSH}}^2 = 8$, whereas any deterministic binary assignment on a single joint sample space is restricted to the classical cut polytope ceiling ± 2 because one of $(b_0 \pm b_1)$ vanishes while the other equals ± 2. ♢

Lemma 4.7 and Theorem 4.8 pinpoint which hypothesis of Bell's theorem fails [13, 33]. Bell's classical ceiling $|S_{\mathrm{CHSH}}| \leq 2$ rests on factorising joint outcome probabilities across a setting-independent classical preparation variable $\lambda \in \Omega_{\mathrm{LHV}}$ carried through background space:

$$p(a, b \mid \varphi_\alpha, \varphi_\beta) = \int_{\Omega_{\mathrm{LHV}}} p_{\mathrm{LHV}}(\lambda)\, p(a \mid \varphi_\alpha, \lambda)\, p(b \mid \varphi_\beta, \lambda)\, \mathrm{d}\lambda. \tag{4.100}$$

Within CCE, both *measurement independence* (local port settings $\varphi_\alpha, \varphi_\beta$ chosen independently of source preparation) and *parameter independence* (remote block-weight invariance $\dot{\rho}_\beta = 0$ in (4.77)) hold strictly. What fails in (4.100) is *Bell factorisability*, combining *outcome independence* across coarse-grained spatial separation with *counterfactual joint definiteness* across incompatible refinements. Bell's factorisation assumes that large spatial separation ($\Omega_{\alpha\beta} \gg 1$ on $\mathrm{im}(\mathbf{P}_{\mathbf{\Pi}_S})$) implies topological separation on the substrate, screening outcome b from outcome a once λ is fixed, and simultaneously assigns four pre-existing binary values $a_x, b_y \in \{+1, -1\}$ across non-commuting orientations. In CCE, $\Omega_{\alpha\beta} \gg 1$ governs only $\mathrm{im}(\mathbf{P}_{\mathbf{\Pi}_S})$ while the boundary-isolated unit-distance bridge $\{i, j\} \in E$ (4.70) persists undivided in $\mathrm{im}(\mathbf{Q}_{\mathbf{\Pi}_S})$ until readout, breaking outcome independence via (4.84). Simultaneously, Theorems 4.1 and 4.6 forbid co-realising incompatible level-1 partitions $\varphi_\alpha \neq \varphi'_\alpha$ prior to Kramers sub-block stabilisation. Whereas a classical local hidden-variable model embeds binary outcomes on a single joint sample space $(\Omega_{\mathrm{LHV}}, p_{\mathrm{LHV}})$ and confines correlators to the classical cut polytope $|S_{\mathrm{CHSH}}| \leq 2$, a symplectic two-cycle bridge (4.68) lacks a joint level-1 refinement and projects onto Euclidean unit vectors in $\mathrm{im}(\Delta\mathbf{P}_{1\to 2})$ under the quadratic ℓ_2 Frobenius inner product of Section 2.4.1, where the parallelogram law enforces the Tsirelson ceiling of $2\sqrt{2}$ [32] while quadratic capacity conservation on G excludes ℓ_∞ Popescu–Rohrlich boxes reaching 4 [135].

Having grounded the Epistemic Lens in quantum measurement, the remaining chapters of Part II extend the same coarse-graining algebra across further levels of resolution. Chapter 5 addresses multi-scale physical modelling by coarse-graining from fundamental particle closures that seal unobservable interior degrees of freedom, through atomic shell structure and the geometric origin of Pauli exclusion, to molecular bonding and macromolecular dynamics, where the Schur-complement boundary operator (2.34) emerges identically as the effective precision operator of the exact Gaussian bath integral over environmental fluctuations. Chapter 6 then turns the Epistemic Lens outward to gravity and the cosmos, projecting the orthogonal capacity matrix into emergent (3 + 1)-dimensional spacetime and Einsteinian curvature sourced by tracked and untracked stress–energy (Section 6.2), and demonstrating that the Big Bang singularity and universal Heat Death are mathematical artefacts of extrapolating continuum trajectories past the backward and forward epistemic horizons t_Φ^- and t_Φ^+ (Section 6.3).

5

FROM FUNDAMENTAL PARTICLES TO MOLECULES

Having established the observational bounds of quantum record formation in Chapter 4, we now examine how an embedded observer operating under a finite relational capacity ceiling $\mathcal{Q}_{\text{alloc}} \leq \mathcal{Q}_{\text{total}}$ (Chapter 2) models composite physical matter across scales. Conventional computational physics and chemistry begin by assuming a continuous spatial background and projecting many-body Hamiltonians onto dense spatial basis sets. That assumption carries a steep algebraic cost: electronic-structure methods scale from $\mathcal{O}(N^3)$–$\mathcal{O}(N^4)$ in Hartree–Fock and Density Functional Theory (DFT) [86] to $\mathcal{O}(N^7)$ in Coupled Cluster (CCSD(T)) [138], classical Molecular Dynamics (MD) is restricted to femtosecond integration steps by stiff covalent vibrations, and hybrid quantum/classical (QM/MM) partitions [168] splice incompatible descriptions across empirical link boundaries. More fundamentally within the progression of this monograph, continuous (3 + 1)-dimensional spacetime has not yet been derived: Lorentzian kinematics and curved geometry emerge only in Chapter 6 from the large-scale spectral limit of the capacity matrix $\mathbf{K}$. A non-circular account of particles, atoms, and molecules must therefore be formulated directly on the discrete capacity graph $G_{\mathbf{K}}$.

Conservation-Congruent Encoding (CCE) provides this discrete multi-scale description through a single algebraic recursion along the coarsening chain of Section 2.3.2:

$$\mathbf{\Pi}^{(1)} \xrightarrow{\mathbf{P}_{1\to 2}} \mathbf{\Pi}^{(2)} \xrightarrow{\mathbf{P}_{2\to 3}} \mathbf{\Pi}^{(3)}. \tag{5.1}$$

At each scale transition $\mathbf{P}_{k\to k+1}$, matrix congruence (2.155) and the diagonal coarse-graining commutator $[\![\text{diag}, \mathscr{C}_{\mathbf{P}}]\!] = \mathscr{T}_{\mathbf{P}}$ (2.168) (Lemma 2.3) seal high-frequency internal closures into the coarse diagonal memory sector $\mathbf{K}_\Omega$ while projecting unresolved internal detail into the orthogonal inter-scale subspace (such as $\text{im}(\Delta\mathbf{P}_{1\to 2})$ in (2.164)). Simultaneously, whenever a resolved subsystem S couples across its boundary cut $\mathbf{K}_\partial$ to an untracked electronic or thermal bath $\bar{S}$, bath degrees of freedom are eliminated via the Green's inversion commutator across $\mathscr{C}_S$ (2.171):

$$\mathbf{L}_{\text{eff}} := \mathbf{L}_{SS} - \mathbf{\Sigma}_{\text{env}}, \tag{5.2}$$

$$\mathbf{\Sigma}_{\text{env}} := -[\![(\cdot)^{-1}, \mathscr{C}_S]\!](\mathbf{G}_\varepsilon) = \mathbf{L}_{S\bar{S}}\mathbf{L}_{\bar{S}\bar{S}}^{-1}\mathbf{L}_{\bar{S}S}. \tag{5.3}$$

Whether eliminating fast shared electronic modes across a covalent bond or marginalising thermal bath fluctuations around a conformational switch, the environmental self-energy operator $\mathbf{\Sigma}_{\text{env}}$ folds the linear compliance and screening of $\bar{S}$ directly onto the active boundary ports of S. Table 5.1 summarises the three-tier progression across Sections 5.1–5.3 using the unified operator triple $(\mathbf{K}, \mathbf{D}_{\mathbf{K}}, \mathbf{L}_{\mathbf{K}})$.

Scale Tier	Active Subsystem (S)	Encapsulated Core ($\mathbf{K}_\Omega$)	Boundary Cut ($\mathbf{K}_\partial$)	Eliminated Sector ($\bar{S}$ via $\mathbf{\Sigma}_{\text{env}}$)
1. Particle / Nuclear (Sections 5.1.1–5.1.2)	Minimal boundary closures (C_n, K_2, K_3)	Confined K_3 core ($K_{pp} \simeq 6\pi^5 K_e$)	Net charge and valence channels	Internal residual $\text{im}(\mathbf{Q}_{\mathbf{\Pi}^{(1)}})$
2. Atomic (Sections 5.1.3–5.1.4)	Coupled electron–nucleus pair ($\mathbf{L}_\mathbf{K}, \mathbf{K}_\Omega$)	Nuclear core K_{pp} and closed shells	Orthogonal valence modes in $\text{im}(\Delta\mathbf{P}_{1\to 2})$	Core internal excitations
3. Molecular & Bath (Sections 5.2–5.3)	Bonded nuclei and metastable basins S_α	Internalised covalent cuts $\mathscr{T}_\mathbf{P}(\mathbf{K}_\partial)$	Peripheral valence and bath ports	Shared electronic or thermal bath ($\mathbf{\Sigma}_{\text{env}}$)

TABLE 5.1: The three-tier CCE hierarchy mapping the coarsening chain $\mathbf{\Pi}^{(1)} \to \mathbf{\Pi}^{(3)}$ (5.1) (Section 2.3.2) and Schur reduction $\mathbf{L}_{\text{eff}} = \mathbf{L}_{SS} - \mathbf{\Sigma}_{\text{env}}$ (5.2) from minimal particle closures to multi-basin molecular ensembles.

5.1 PARTICLES AND ATOMIC STRUCTURE

Multi-scale physical modelling begins at the base of the coarsening chain: the minimal persistent subgraphs of the discrete relational network. Rather than postulating fundamental particles as point singularities or continuous fields on a pre-existing manifold, the CCE framework identifies a particle as a self-sustaining subgraph closure that resists ambient relaxation long enough to propagate across the network as a coherent unit. Encapsulating high-gap nuclear closures into diagonal capacity entries and coupling low-capacity electron cycles across the remaining boundary cut yields atomic ground-state reduced-capacity scaling and valence shell multiplicities directly from generalised Laplacian eigenvalues and harmonic subspace orthogonality.

5.1.1 *Mass, Spin, and Charge on the Capacity Graph*

Every persistent particle subgraph S_Ω is characterised on the capacity matrix $\mathbf{K} = \mathbf{K}_\Omega + \mathbf{K}_\partial$ by three discrete invariants: its diagonal memory trace $\text{Tr}(\mathbf{K}_\Omega)$, its cyclic phase closure across reversible ports, and its net antisymmetric current across $\mathbf{K}_\partial$. On the diagonal memory sector $\mathbf{K}_\Omega$, rest energy arises from collective internal channel recurrence. As established at the substrate-general level in Section 2.5.2 and developed kinematically in Chapter 6 (Section 6.1), a subsystem at rest relative to a physical reference oscillator $\bar{S}_{\text{ref}}$ ($\Delta I_{\text{ext}} = 0$) commits its reversible update capacity to cycling across all $\text{Tr}(\mathbf{K}_\Omega)$ internal channels (2.249) (with core transitions on S_Ω shielded by $\mathbf{L}_{\Omega\Omega}$). When proper time τ and reference time t are metered in seconds via (2.250) and (2.255) at universal elementary substrate step cadence $\nu_0 > 0$ (in s^{-1} per channel,

fixed once empirically by the electron closure $m_e c^2 = \hbar \nu_0 K_e$, parallel to the length calibration ℓ_0 in (5.20)), scaling $\nu_0 \operatorname{Tr}(\mathbf{K}_\Omega)$ by the reduced Planck constant $\hbar$ (J s) under the composite coarse-graining projection Φ (2.235) fixes the conservative rest energy above the vacuum baseline $E_{0,\Phi}$ and keeps all rest-energy ratios across particle closures purely combinatorial:

$$E_\Phi - E_{0,\Phi} = \hbar \nu_0 \operatorname{Tr}(\mathbf{K}_\Omega), \tag{5.4}$$

$$\frac{E_{\Phi,A} - E_{0,\Phi}}{E_{\Phi,B} - E_{0,\Phi}} = \frac{\operatorname{Tr}(\mathbf{K}_{\Omega,A})}{\operatorname{Tr}(\mathbf{K}_{\Omega,B})}. \tag{5.5}$$

Equations (5.4)–(5.5) require no prior spatial metric or signal speed, and ν_0 cancels identically out of every dimensionless mass ratio such as Principle 5.1. Once Chapter 6 derives the invariant causal propagation speed c on the coarse-grained graph, the same diagonal trace defines inertial rest mass $m = (E_\Phi - E_{0,\Phi})/c^2$. When coupled to an open bath at operational noise intensity θ (J nat^{-1}), maintaining non-equilibrium internal structure $I_{\mathrm{rev},\Omega}$ shifts the internal energy by $\Delta U_{\mathrm{neq}} = \theta I_{\mathrm{rev},\Omega}$ (3.16).

Across reversible boundary ports, spin arises from discrete cyclic phase synchronisation. Under a complete 2π cyclic permutation of its environmental boundary couplings, the internal unitary state update $\mathbf{U}(2\pi)$ closes after $r_{\mathrm{sync}} \in \{1, 2\}$ environmental cycles (Section 4.3.3):

$$\mathbf{U}(2\pi) = (-1)^{r_{\mathrm{sync}}-1}\mathbf{I} = \begin{cases} +\mathbf{I}, & r_{\mathrm{sync}} = 1 \quad \text{(bosonic 1 : 1 closure)}, \\ -\mathbf{I}, & r_{\mathrm{sync}} = 2 \quad \text{(fermionic 2 : 1 closure)}. \end{cases} \tag{5.6}$$

Bosonic closures return to their initial phase in a single cycle ($r_{\mathrm{sync}} = 1$), whereas fermionic closures require two full environmental cycles to recover unit phase ($r_{\mathrm{sync}} = 2$).

Across the boundary cut $\mathbf{K}_\partial$, electric charge arises from the conserved antisymmetric Kirchhoff cycle currents of Lemma 2.7 (2.292)–(2.296) and discrete cycle winding on the relational graph $G = (V, E)$, without invoking differential forms or continuous contour integrals. Let $J_{ij} = -J_{ji}$ denote the antisymmetric reversible current along edge $\{i, j\} \in E$, and let $\Delta\varphi_{ij} \in [-\pi, \pi)$ denote the discrete phase increment across directed edge (i, j) around a closed graph cycle $C \subset E$. Vertex Kirchhoff balance at every $i \in V$ and single-valued phase closure around C enforce:

$$\sum_{j \in V} J_{ij} = 0, \tag{5.7}$$

$$\sum_{(i,j) \in C} \Delta\varphi_{ij} = 2\pi n_C, \tag{5.8}$$

$$q = n_C q_e, \tag{5.9}$$

where $n_C \in \mathbb{Z}$ is the integer topological winding number of the cycle and q_e is the elementary carrier charge (C). On finite graphs, the smallest connected boundary closures provide minimal discrete carrier topologies compatible with compact internal unitary phase and exchange symmetries: a directed cycle (C_n) carries U(1) phase winding, a reversible two-port pair (K_2) with

$r_{\text{sync}} = 2$ supports SU(2) two-state phase transport, and a complete three-vertex quotient clique (K_3) provides the minimal three-channel exchange carrier compatible with SU(3) colour-singlet closure.

5.1.2 *Nuclear Encapsulation*

Internal excitations whose energy gap vastly exceeds ambient interaction scales decouple dynamically and need not be resolved vertex by vertex. Strong colour confinement binds quarks within a three-channel closure whose excitation gap ($\sim 10^8$ eV) exceeds atomic and molecular bonding scales (~ 1 eV) by eight orders of magnitude. By CCE Axiom II (Section 2.3.1), this separation guarantees that the nuclear subgraph $G[S_\alpha]$ satisfies strong spectral persistence $\Xi(S_\alpha) \gg 1$ (2.127). Under the Tier 1 → Tier 2 coarsening transition $\mathbf{P}_{1\to 2}$ (Table 5.1), the cut-internalisation operator $\mathscr{T}_{\mathbf{P}}$ (2.160) contracts S_α into a single coarse-grained block α whose diagonal memory capacity $K_{\alpha\alpha}$ in $\mathbf{K}_\Omega$ and external valence capacity $K_{\alpha\beta}$ in $\mathbf{K}_\partial$ follow from (2.91):

$$K_{\alpha\alpha} = \sum_{i,j\in S_\alpha} A_{ij} = 2|E(S_\alpha)|, \tag{5.10}$$

$$K_{\alpha\beta} = \sum_{i\in S_\alpha} \sum_{j\in S_\beta} A_{ij}. \tag{5.11}$$

Here $K_{\alpha\alpha} \in 2\mathbb{N}$ (links) counts the even integer directed internal link incidences sealed inside the nuclear core, while $K_{\alpha\beta}$ (links) counts the external boundary links coupling block α to neighbouring blocks β.

In the large-multiplicity continuum-fibre limit ($K_e, K_{pp} \gg 1$), calibrating this encapsulated nuclear capacity against the elementary electronic scale motivates a parameter-free asymptotic reference ratio for nuclear encapsulation [102].

PRINCIPLE 5.1 (Asymptotic Combinatorial Mass Ratio). Let $K_e \in 2\mathbb{N}$ denote the even integer diagonal capacity of a large-multiplicity U(1) electron closure, and let $K_{pp} \in 2\mathbb{N}$ denote the diagonal capacity of a confined three-channel quotient clique (K_3, $K_e \gg 1$) supporting an SU(3) colour-singlet closure. The K_3 quotient carries symmetric-group order $|\mathfrak{S}_3| = 2|E(K_3)| = 6$ directed exchange channels. Weighting these six channels in the continuum-fibre limit by the product of the unit round-sphere volumes $\text{vol}(S^3) = 2\pi^2$ of the SU(2) $\cong S^3$ fibre and $\text{vol}(S^5) = \pi^3$ of the SU(3)/SU(2) $\cong S^5$ base modulo fermionic double cover ($r_{\text{sync}} = 2$) yields the asymptotic dimensionless capacity ratio:

$$\frac{K_{pp}}{K_e} \simeq 6\,\frac{\text{vol}(S^3)\,\text{vol}(S^5)}{r_{\text{sync}}} = 6\pi^5 \approx 1836.118. \tag{5.12}$$

Against the empirical ratio $m_p/m_e = 1836.15267\ldots$ of proton to electron mass, Equation (5.12) agrees to within 0.0019%. In Standard Model phenomenology, proton rest mass arises predominantly from non-perturbative chro-

modynamic confinement (Λ_{QCD}) whereas electron rest mass is set by electroweak Yukawa coupling, and (5.12) evaluates each topological factor at unit round-sphere radius rather than the Berger-squashed bi-invariant Haar volume $\sqrt{3}\pi^5$ on SU(3). Principle 5.1 is therefore advanced strictly as an asymptotic continuum-fibre capacity conjecture ($K_e \gg 1$), motivating investigation of whether effective coarse-grained capacities admit a shared group-manifold calibration rather than replacing gauge-field dynamics or asserting an equality on three bare vertices. When A nucleons bind into a composite nucleus, internalising inter-nucleon boundary cuts via $\mathscr{T}_{\mathbf{P}}$ sheds exposed boundary load ($\Delta\mathcal{Q}^2_{\partial,\mathrm{shed}} > 0$, Section 3.4.1), lowering the composite rest energy below the sum of isolated nucleon capacities as the nuclear binding mass defect while projecting internal quark modes into the unresolved residual $\mathrm{im}(\mathbf{Q}_{\mathbf{\Pi}^{(1)}})$.

5.1.3 *Atomic Ground States and Reduced Capacity*

Discrete atomic bound states arise when a low-capacity electron block (S_1, $K_{11} = K_e, r_{\mathrm{sync}} = 2$) couples to an encapsulated nuclear block ($S_2, K_{22} = K_{pp}$) across an open electromagnetic boundary cut ($\mathbf{K}_\partial \neq \mathbf{o}$). On the two-block partition $S = S_1 \sqcup S_2$ with inter-block cut capacity $K_{12} > 0$, the isolated capacity Laplacian $\mathbf{L}_{\mathbf{K}} = \mathbf{D}^{(\mathrm{int})}_{\mathbf{K}} - \mathbf{K}_S$ (2.101) and diagonal memory matrix $\mathbf{K}_\Omega$ take the 2×2 form:

$$\mathbf{L}_{\mathbf{K}} = K_{12}\begin{pmatrix} 1 & -1 \\ -1 & 1 \end{pmatrix}, \tag{5.13}$$

$$\mathbf{K}_\Omega = \mathrm{diag}(K_e, K_{pp}). \tag{5.14}$$

Internal atomic excitations are governed by the generalised eigenvalue problem $\mathbf{L}_{\mathbf{K}}\mathbf{u} = \lambda\mathbf{K}_\Omega\mathbf{u}$ on the subspace $\mathbf{K}_\Omega$-orthogonal to uniform translation $\mathbf{1}_2 = (1,1)^{\mathsf{T}}$.

LEMMA 5.2 (Two-Body Reduced-Capacity Spectrum). *Let $K_e, K_{pp}, K_{12} > 0$, and define $\mathbf{L}_{\mathbf{K}}$ and $\mathbf{K}_\Omega$ by (5.13)–(5.14). The uniform vector $\mathbf{1}_2 = (1,1)^{\mathsf{T}}$ spans $\ker(\mathbf{L}_{\mathbf{K}})$ with $\lambda_1 = 0$, and the relative displacement vector $\mathbf{u}_2 = (K_{pp}, -K_e)^{\mathsf{T}}$ is $\mathbf{K}_\Omega$-orthogonal to $\mathbf{1}_2$ ($\mathbf{u}_2^{\mathsf{T}}\mathbf{K}_\Omega\mathbf{1}_2 = 0$) and satisfies $\mathbf{L}_{\mathbf{K}}\mathbf{u}_2 = \lambda_2\mathbf{K}_\Omega\mathbf{u}_2$ with generalised eigenvalue and reduced capacity:*

$$\lambda_2(\mathbf{L}_{\mathbf{K}}, \mathbf{K}_\Omega) = K_{12}\frac{K_e + K_{pp}}{K_e K_{pp}} = \frac{K_{12}}{\mu_{ep}}, \tag{5.15}$$

$$\mu_{ep} := \frac{K_e K_{pp}}{K_e + K_{pp}}. \tag{5.16}$$

PROOF. Direct multiplication gives $\mathbf{L}_{\mathbf{K}}\mathbf{1}_2 = \mathbf{o}$, while evaluating the inner product $\mathbf{u}_2^{\mathsf{T}}\mathbf{K}_\Omega\mathbf{1}_2$ cancels $K_{pp}K_e$ against $-K_eK_{pp}$ to give $\mathbf{u}_2^{\mathsf{T}}\mathbf{K}_\Omega\mathbf{1}_2 = 0$. Acting on $\mathbf{u}_2$ with both matrices yields:

$$\mathbf{L}_{\mathbf{K}}\mathbf{u}_2 = K_{12}(K_e + K_{pp})(1,-1)^{\mathsf{T}}, \tag{5.17}$$

$$\mathbf{K}_\Omega\mathbf{u}_2 = K_eK_{pp}(1,-1)^{\mathsf{T}}, \tag{5.18}$$

establishing (5.15)–(5.16). □

Lemma 5.2 isolates the exact reduced-capacity inertial factor μ_{ep}^{-1} at fixed inter-block cut K_{12}. Across the Schur-reduced two-block port resistance $\Omega_{12} = 1/K_{12}$ of (5.13) and (2.239) [85], the effective electromagnetic cut conductance decays with continuum radial separation r via the three-dimensional harmonic Green's function as $K_{12}(r) = \ell_0/r$, distinct from unreduced point-to-point lattice resistance saturation. Balancing reduced-capacity kinetic confinement against Coulombic cut attraction via virial minimisation contracts the equilibrium orbital resistance in proportion to μ_{ep}^{-1} and scales the ground-state binding depth directly with μ_{ep}/K_e. Calibrating the infinite-nuclear-capacity limit $K_{pp} \to \infty$ ($\mu_{ep}/K_e \to 1$) to the empirical Rydberg constant $E_{\mathrm{Ryd}} = 13.6057\,\mathrm{eV}$ and metric conversion factor ℓ_0 (m link) yields the neutral hydrogen ground-state energy and Bohr radius a_0:

$$E_0(^1\mathrm{H}) = -\frac{\mu_{ep}}{K_e} E_{\mathrm{Ryd}} = -\frac{K_{pp}}{K_e + K_{pp}} E_{\mathrm{Ryd}} = -13.5983\,\mathrm{eV}, \tag{5.19}$$

$$a_0 = \ell_0 \Omega_{12} = \ell_0 (\mathbf{e}_1 - \mathbf{e}_2)^{\mathsf{T}} \mathbf{L}_{\mathbf{K}}^{\dagger} (\mathbf{e}_1 - \mathbf{e}_2) \approx 0.5292\,\text{Å}. \tag{5.20}$$

In helium ($Z = 2$), coupling a second electron ($r_{\mathrm{sync}} = 2$) to the encapsulated alpha-particle core ($K_{^4\mathrm{He}} \approx 4K_{pp}$) permits both electrons to occupy this lowest relative mode only when their boundary phase currents circulate in opposite orientations, closing the ground shell.

5.1.4 *Pauli Exclusion and Orthogonal Harmonic Shells*

Whereas standard non-relativistic quantum mechanics introduces wavefunction antisymmetry as an independent postulate [129], the CCE framework grounds Pauli exclusion jointly in fermionic 2 : 1 phase closure (5.6) and binary edge capacity on $G = (V, E)$. Exchanging two identical $r_{\mathrm{sync}} = 2$ closures winds their relative boundary phase through one full environmental cycle ($\mathbf{U}(2\pi) = -\mathbf{I}$), so symmetric co-occupancy of the same oriented phase channel interferes destructively—in sharp contrast to bosonic $r_{\mathrm{sync}} = 1$ closures ($\mathbf{U}(2\pi) = +\mathbf{I}$), which constructively condense into a shared ground mode. Because each undirected link $A_{ij} \in \{0, 1\}$ (Section 2.1) supports at most two opposing directed phase currents (J_{ij} and J_{ji}), a spatial valence mode admits at most two opposite-orientation $r_{\mathrm{sync}} = 2$ electron cycles. Minimising the Dirichlet Rayleigh quotient on the inter-scale electronic subspace $\mathrm{im}(\Delta\mathbf{P}_{1\to 2})$ (2.164) therefore forces subsequent electron pairs onto mutually orthonormal harmonic eigenvectors $\mathbf{v}_a, \mathbf{v}_b \in \mathrm{im}(\Delta\mathbf{P}_{1\to 2})$:

$$\langle \mathbf{v}_a, \mathbf{v}_b \rangle = \mathbf{v}_a^{\mathsf{T}} \mathbf{v}_b = \delta_{ab}. \tag{5.21}$$

On an isotropic valence shell graph whose spatial spectral dimension equals an integer $n = d_s^{\mathrm{spatial}}[\mathbf{\Pi}] \geq 2$ (2.233), the space of degree-ℓ harmonic modes ($\ell \in \mathbb{N}_0$) has dimension $\binom{n+\ell-1}{\ell} - \binom{n+\ell-3}{\ell-2}$, where $\binom{m}{k} := 0$ for $k < 0$. Mul-

tiplying by the two opposing phase orientations ($r_{\mathrm{sync}} = 2$) fixes the shell occupancy ceiling for general n:

$$g_\ell(n) = 2\left[\binom{n+\ell-1}{\ell} - \binom{n+\ell-3}{\ell-2}\right]. \tag{5.22}$$

When coarse-grained orbital persistence selects $n = 3$ spatial channels—as proved independently in Chapter 6 (Theorem 6.1)—Equation (5.22) reduces to $g_\ell(3) = 2(2\ell+1)$, recovering the s, p, d shell capacities $g_0(3) = 2$, $g_1(3) = 6$, and $g_2(3) = 10$ without assuming three-dimensional space beforehand. Furthermore, when an open-shell atom or coordination centre couples to anisotropic external ports in $\mathbf{K}_\partial$, projecting the Schur-reduced operator $\mathbf{L}_{\mathrm{eff}}$ (5.2) onto the $(2\ell+1)$-dimensional valence shell lifts its degeneracy algebraically [18] without empirical self-interaction penalties.

EXAMPLE 5.1 (Reduced-Capacity Isotope Shift and Orthogonal Shell Filling). Consider first the two-block hydrogenic system $(\mathbf{L}_{\mathbf{K}}, \mathbf{K}_\Omega)$ of (5.13)–(5.14) calibrated by Principle 5.1 ($K_{pp}/K_e \simeq 6\pi^5$). Applying Lemma 5.2 to a single-proton core (K_{pp}) versus an encapsulated deuteron core of diagonal capacity approximately $2K_{pp}$ yields the proton and deuteron reduced-capacity factors:

$$\frac{\mu_{ep}}{K_e} \simeq \frac{6\pi^5}{6\pi^5+1} \approx 0.999456, \tag{5.23}$$

$$\frac{\mu_{ed}}{K_e} \simeq \frac{12\pi^5}{12\pi^5+1} \approx 0.999728. \tag{5.24}$$

Relative to the ^{1}H ground-state energy $E_0(^1\mathrm{H}) = -13.5983\,\mathrm{eV}$ of (5.19), doubling the nuclear diagonal capacity from $1836:1$ to $3672:1$ in $\mathbf{K}_\Omega$ deepens the deuteron ground state by 3.7 meV to $E_0(^2\mathrm{H}) \approx -13.6020\,\mathrm{eV}$.

Next, when $Z = 3$ electrons couple to a lithium core of diagonal capacity approximately $7K_{pp}$ at spatial spectral dimension $n = 3$, the first two electrons saturate the nodeless $\ell = 0$ mode $\mathbf{v}_0$ with opposite phase currents ($g_0(3) = 2$). By (5.21)–(5.22), binary link saturation forces the third valence electron onto one of the three mutually orthogonal dipolar modes $\{\mathbf{d}_1, \mathbf{d}_2, \mathbf{d}_3\} \subset \mathrm{im}(\Delta\mathbf{P}_{1\to2})$ ($\ell = 1$, $g_1(3) = 6$), exposing a single weakly bound outer channel ready for chemical cut internalisation. ◊

5.2 CHEMICAL BONDING AND MOLECULAR GEOMETRY

Ascending from Tier 2 atomic blocks to Tier 3 molecular graphs via $\mathbf{P}_{2\to3}$ (5.1) (Table 5.1) introduces no additional dynamical postulates. Chemical bonds form when neighbouring atomic blocks share valence electronic channels across their mutual boundary cut, executing cut internalisation via $\mathscr{T}_{\mathbf{P}}$ as established in Chapters 2 and 3. Eliminating the fast shared electronic degrees of freedom to obtain the effective inter-nuclear potential then provides the first molecular application of the Schur complement (5.2), while Pauli orthogonality among valence modes in $\mathrm{im}(\Delta\mathbf{P}_{1\to2})$ fixes equilibrium bond angles without presupposing continuous spatial coordinates.

5.2.1 *Covalent Cut Internalisation and Schur Reduction*

Consider two atomic blocks $S = \{1, 2\}$ interacting across a fast shared electronic sector $\bar{S}$. In isolation, each atom exposes an independent external cut with total boundary load $\|\mathbf{K}_{\partial}^{\mathrm{iso}}\|_F^2$ (3.53). Opening an antiparallel singlet electronic channel ($r_{\mathrm{sync}} = 2$) between blocks 1 and 2 internalises the shared interface cut into the composite diagonal memory block via $\mathscr{T}_{\mathbf{P}}$ (2.160). As proved for general multi-system coupling in Section 3.4.1, shedding exposed boundary cut load ($\Delta\mathcal{Q}_{\partial,\mathrm{shed}}^2 > 0$) reduces allocated capacity $\mathcal{Q}_{\mathrm{alloc}}$ (2.196), frees structural capacity $\Delta\mathcal{Q}_{\mathrm{free}} > 0$ (3.63), and deepens the collective escape barrier $\Delta\Phi$ (3.64).

Energetically, let $\mathbf{x}_S \in \mathbb{R}^{N_S}$ denote dimensionless slow nuclear displacements and $\mathbf{x}_{\bar{S}} \in \mathbb{R}^{N_{\bar{S}}}$ denote dimensionless fast electronic displacements coupled through the energy-calibrated stiffness Laplacian $\mathbf{L}$ (J) (2.20):

$$E(\mathbf{x}_S, \mathbf{x}_{\bar{S}}) = \frac{1}{2}\mathbf{x}_S^{\mathsf{T}}\mathbf{L}_{SS}\mathbf{x}_S + \mathbf{x}_S^{\mathsf{T}}\mathbf{L}_{S\bar{S}}\mathbf{x}_{\bar{S}} + \frac{1}{2}\mathbf{x}_{\bar{S}}^{\mathsf{T}}\mathbf{L}_{\bar{S}\bar{S}}\mathbf{x}_{\bar{S}}, \tag{5.25}$$

where $\mathbf{L}_{SS}^{\mathsf{T}} = \mathbf{L}_{SS}$, $\mathbf{L}_{\bar{S}S} = \mathbf{L}_{S\bar{S}}^{\mathsf{T}}$, and the open electronic block $\mathbf{L}_{\bar{S}\bar{S}} \succ \mathbf{o}$ is strictly positive-definite by grounded Dirichlet leakage (2.24). Relaxing the fast electronic sector at fixed nuclear configuration $\mathbf{x}_S$ yields the variational Schur reduction (Figure 5.1(a)).

THEOREM 5.3 (Variational Schur Reduction). *Consider the quadratic energy $E(\mathbf{x}_S, \mathbf{x}_{\bar{S}})$ in (5.25) with symmetric blocks, $\mathbf{L}_{\bar{S}S} = \mathbf{L}_{S\bar{S}}^{\mathsf{T}}$, and positive-definite complement $\mathbf{L}_{\bar{S}\bar{S}} \succ \mathbf{o}$. For every $\mathbf{x}_S \in \mathbb{R}^{N_S}$ and $\mathbf{x}_{\bar{S}} \in \mathbb{R}^{N_{\bar{S}}}$, define the relaxed bath response $\mathbf{x}_{\bar{S}}^\star := -\mathbf{L}_{\bar{S}\bar{S}}^{-1}\mathbf{L}_{\bar{S}S}\mathbf{x}_S$ and positive-semidefinite self-energy $\mathbf{\Sigma}_{\mathrm{env}} := \mathbf{L}_{S\bar{S}}\mathbf{L}_{\bar{S}\bar{S}}^{-1}\mathbf{L}_{\bar{S}S}$ ($\mathbf{\Sigma}_{\mathrm{env}} \succeq \mathbf{o}$). Completing the square gives:*

$$\begin{aligned} E(\mathbf{x}_S, \mathbf{x}_{\bar{S}}) = {} & \frac{1}{2}\mathbf{x}_S^{\mathsf{T}}\big(\mathbf{L}_{SS} - \mathbf{\Sigma}_{\mathrm{env}}\big)\mathbf{x}_S \\ & + \frac{1}{2}(\mathbf{x}_{\bar{S}} - \mathbf{x}_{\bar{S}}^\star)^{\mathsf{T}}\mathbf{L}_{\bar{S}\bar{S}}(\mathbf{x}_{\bar{S}} - \mathbf{x}_{\bar{S}}^\star). \end{aligned} \tag{5.26}$$

Consequently, $E(\mathbf{x}_S, \mathbf{x}_{\bar{S}})$ attains its unique global minimum over $\mathbf{x}_{\bar{S}}$ at $\mathbf{x}_{\bar{S}} = \mathbf{x}_{\bar{S}}^\star$, and the relaxed effective energy $E_{\mathrm{eff}}(\mathbf{x}_S) := \min_{\mathbf{x}_{\bar{S}}} E(\mathbf{x}_S, \mathbf{x}_{\bar{S}})$ satisfies:

$$E_{\mathrm{eff}}(\mathbf{x}_S) = \frac{1}{2}\mathbf{x}_S^{\mathsf{T}}\mathbf{L}_{\mathrm{eff}}\mathbf{x}_S \le \frac{1}{2}\mathbf{x}_S^{\mathsf{T}}\mathbf{L}_{SS}\mathbf{x}_S, \tag{5.27}$$

where $\mathbf{L}_{\mathrm{eff}} = \mathbf{L}_{SS} - \mathbf{\Sigma}_{\mathrm{env}}$, with strict inequality whenever $\mathbf{L}_{\bar{S}S}\mathbf{x}_S \neq \mathbf{o}$.

PROOF. Using $\mathbf{L}_{\bar{S}\bar{S}}^{\mathsf{T}} = \mathbf{L}_{\bar{S}\bar{S}}$ and $\mathbf{L}_{\bar{S}\bar{S}}\mathbf{x}_{\bar{S}}^\star = -\mathbf{L}_{\bar{S}S}\mathbf{x}_S$, expanding the shifted bath quadratic form in (5.26) gives:

$$\begin{aligned} & \frac{1}{2}(\mathbf{x}_{\bar{S}} - \mathbf{x}_{\bar{S}}^\star)^{\mathsf{T}}\mathbf{L}_{\bar{S}\bar{S}}(\mathbf{x}_{\bar{S}} - \mathbf{x}_{\bar{S}}^\star) \\ & = \frac{1}{2}\mathbf{x}_{\bar{S}}^{\mathsf{T}}\mathbf{L}_{\bar{S}\bar{S}}\mathbf{x}_{\bar{S}} + \mathbf{x}_S^{\mathsf{T}}\mathbf{L}_{S\bar{S}}\mathbf{x}_{\bar{S}} + \frac{1}{2}\mathbf{x}_S^{\mathsf{T}}\mathbf{\Sigma}_{\mathrm{env}}\mathbf{x}_S. \end{aligned} \tag{5.28}$$

Adding $(1/2)\mathbf{x}_S^{\mathsf{T}}(\mathbf{L}_{SS} - \mathbf{\Sigma}_{\mathrm{env}})\mathbf{x}_S$ to (5.28) cancels the $\mathbf{\Sigma}_{\mathrm{env}}$ term and recovers (5.25). Because $\mathbf{L}_{\bar{S}\bar{S}} \succ \mathbf{o}$, the quadratic residual in (5.28) is non-negative

and vanishes uniquely at $\mathbf{x}_{\bar{S}} = \mathbf{x}^{\star}_{\bar{S}}$, while the identity $\mathbf{x}_S^{\mathsf{T}}\boldsymbol{\Sigma}_{\mathrm{env}}\mathbf{x}_S = (\mathbf{x}^{\star}_{\bar{S}})^{\mathsf{T}}\mathbf{L}_{\bar{S}\bar{S}}\mathbf{x}^{\star}_{\bar{S}}$ is non-negative and strictly positive whenever $\mathbf{L}_{\bar{S}S}\mathbf{x}_S \neq \mathbf{o}$, establishing (5.27). □

Theorem 5.3 gives the variational counterpart of the inversion commutator $-\boldsymbol{\Sigma}_{\mathrm{env}} = [\![(\cdot)^{-1}, \mathscr{C}_S]\!](\mathbf{G}_\varepsilon)$ (Lemma 2.3, (2.171)) for Born–Oppenheimer electronic relaxation [20]. Eliminating the shared singlet sector $\bar{S}$ subtracts $\boldsymbol{\Sigma}_{\mathrm{env}} \succeq \mathbf{o}$ from $\mathbf{L}_{SS}$ and strictly lowers the nuclear deformation energy relative to unrelaxed open atoms.

5.2.2 *Resistance-Scale Overlap and the Diatomic Potential*

To resolve covalent binding energy across inter-nuclear separation without presupposing Euclidean coordinates, we parameterise boundary overlap by the metric bond length $r = \ell_0\Omega_{12}$ calibrated from the inter-block resistance distance Ω_{12} (2.239) around equilibrium separation $r_e > 0$. Because each atomic ground mode decays exponentially across resistance distance at the Bohr scale (5.20), the normalised inter-atomic overlap $u(r)$ decays exponentially with attenuation constant $a_{\mathrm{cov}} > 0$ (Å^{-1}):

$$u(r) := \exp\bigl[-a_{\mathrm{cov}}(r - r_e)\bigr], \tag{5.29}$$

$$\Delta E_{\mathrm{bond}}(u) = -2D_e u + D_e u^2 = D_e(1-u)^2 - D_e. \tag{5.30}$$

Equation (5.30) recovers the functional form of the Morse potential [116] with dissociation depth $D_e > 0$ (eV) from two competing contributions in the Schur-reduced energy (5.27): first-order singlet delocalisation in $-\boldsymbol{\Sigma}_{\mathrm{env}}$ lowers boundary energy linearly ($-2D_e u$), whereas second-order electronic channel crowding and short-range nuclear core repulsion in $\mathbf{L}_{SS}$ penalise overlap quadratically ($+D_e u^2$), with unique global minimum $-D_e$ at $u = 1$ ($r = r_e$).

EXAMPLE 5.2 (Schur Calibration of the H_2 Bond Potential). Consider the H_2 dimer comprising two encapsulated proton blocks $S = \{1, 2\}$ ($K_{pp} \simeq 6\pi^5 K_e$) coupled through a shared antiparallel singlet electronic sector $\bar{S}$ (Figure 5.1(a)). With Bohr resistance scale $a_0 \approx 0.5292$ Å set by (5.20), calibrating the reduced singlet overlap parameters to spectroscopic H_2 benchmarks fixes equilibrium separation $r_e = 0.7414$ Å ($\approx \sqrt{2}\,a_0$), attenuation constant $a_{\mathrm{cov}} = 1.942$ Å^{-1}, and dissociation depth $D_e = 4.75$ eV.

Differentiating (5.30) with respect to $r = \ell_0\Omega_{12}$ separates the attractive Schur delocalisation from short-range channel crowding:

$$\Delta E_{\mathrm{bond}}(r) = -2D_e u(r) + D_e u(r)^2, \tag{5.31}$$

$$\frac{\mathrm{d}\Delta E_{\mathrm{bond}}}{\mathrm{d}r} = 2D_e a_{\mathrm{cov}} u(r)\bigl(1 - u(r)\bigr), \tag{5.32}$$

which vanishes uniquely at $u(r_e) = 1$. Expanding to second order around $r = r_e$ for two protons of mass m_p (reduced nuclear mass $m_p/2 \approx 8.363 \times$

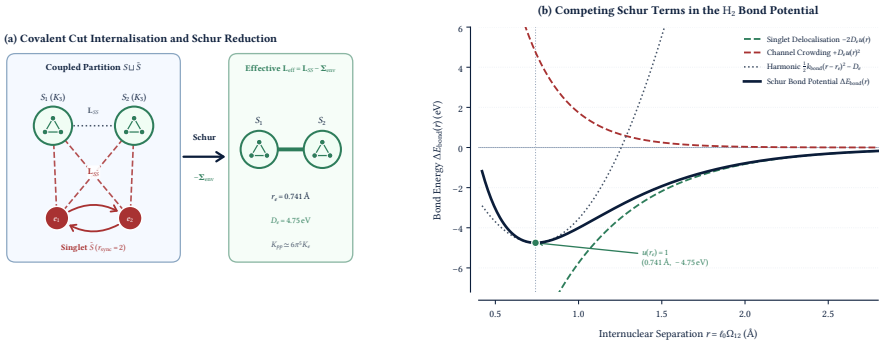


FIGURE 5.1: Nuclear encapsulation, covalent Schur reduction, and competing overlap terms in the H_2 bond potential (Theorem 5.3 and Example 5.2). *(a)* Two nuclear blocks $S = \{1, 2\}$ (each encapsulating a K_3 core of capacity $K_{pp} \simeq 6\pi^5 K_e$, teal) couple across $\mathbf{L}_{S\bar{S}}$ to a shared antiparallel singlet electronic sector $\bar{S}$ ($r_{\text{sync}} = 2$, crimson). Eliminating $\bar{S}$ via the Schur self-energy $\mathbf{\Sigma}_{\text{env}} = \mathbf{L}_{S\bar{S}}\mathbf{L}_{\bar{S}\bar{S}}^{-1}\mathbf{L}_{\bar{S}S}$ (5.27) produces the effective two-node nuclear operator $\mathbf{L}_{\text{eff}} = \mathbf{L}_{SS} - \mathbf{\Sigma}_{\text{env}}$. *(b)* Decomposition of $\Delta E_{\text{bond}}(r)$ (5.30) into linear singlet delocalisation $-2D_e u(r)$ (teal dashed) and quadratic channel crowding $+D_e u(r)^2$ (crimson dashed), balancing at $u(r_e) = 1$ ($r_e = 0.741$ Å, $\Delta E_{\text{bond}} = -4.75$ eV, navy solid) alongside the local harmonic expansion $(1/2)k_{\text{bond}}(r - r_e)^2 - D_e$ (slate dotted).

10^{-28} kg) determines the harmonic bond stiffness and fundamental vibrational quantum:

$$k_{\text{bond}} = \left.\frac{\mathrm{d}^2 \Delta E_{\text{bond}}}{\mathrm{d}r^2}\right|_{r=r_e} = 2D_e a_{\text{cov}}^2 \approx 574\,\mathrm{N\,m^{-1}}, \tag{5.33}$$

$$\hbar\omega_{\text{vib}} = \hbar\sqrt{\frac{2k_{\text{bond}}}{m_p}} = 2\hbar a_{\text{cov}}\sqrt{\frac{D_e}{m_p}} \approx 0.545\,\mathrm{eV}. \tag{5.34}$$

As shown in Figure 5.1(b), linear singlet cut internalisation dominates at long range ($r > r_e$, $u < 1$) to draw the nuclei together, quadratic channel saturation dominates at short range ($r < r_e$, $u > 1$) to form the repulsive wall, and unlike the local harmonic parabola $(1/2)k_{\text{bond}}(r - r_e)^2 - D_e$, the Schur overlap curve saturates smoothly to $\Delta E_{\text{bond}} \to 0$ upon bond dissociation ($u \to 0$). ◊

5.2.3 *Angular Geometry and Valence Port Orthogonality*

A scalar capacity Laplacian $\mathbf{L}_{\mathbf{K}}$ on bonded nuclear blocks depends only on pairwise edge weights $K_{\alpha\beta}$ and is therefore blind to inter-bond angles. Yet directional stereochemistry requires no external $\mathbb{R}^3$ coordinate frame or auxiliary connection bundle, because it follows directly from Pauli orthogonality (5.21) inside the central atom's valence subspace $\mathrm{im}(\Delta\mathbf{P}_{1\to 2})$ (Section 4.3.3).

Consider a central atomic block 1 bonded to peripheral blocks 2 and 3. Inside $\mathrm{im}(\Delta\mathbf{P}_{1\to 2})$, let $\mathbf{e}_0$ denote the unit isotropic ($\ell = 0$) valence mode and let $\mathbf{d}_2, \mathbf{d}_3$ denote unit dipolar ($\ell = 1$) valence vectors directed along the two bond

channels, orthogonal to $\mathbf{e}_0$ ($\langle \mathbf{e}_0, \mathbf{d}_j \rangle = 0$), with intrinsic inter-bond angle $\phi \in [0, \pi]$ defined by the Hilbert-space inner product $\cos\phi := \langle \mathbf{d}_2, \mathbf{d}_3 \rangle$. Mixing isotropic fraction $w_0 \in [0, 1/2]$ with dipolar fraction $1 - w_0$ forms hybrid valence ports whose mutual orthogonality fixes the equilibrium bond angle ϕ_0 [37, 130].

LEMMA 5.4 (Hybrid Valence Port Orthogonality). *Let $\mathbf{e}_0, \mathbf{d}_2, \mathbf{d}_3 \in \mathrm{im}(\Delta\mathbf{P}_{1\to 2})$ be unit vectors ($\|\mathbf{e}_0\| = 1$ and $\|\mathbf{d}_j\| = 1$ for $j \in \{2, 3\}$) satisfying $\langle \mathbf{e}_0, \mathbf{d}_j \rangle = 0$ for each $j \in \{2, 3\}$. For any isotropic mixing weight $w_0 \in [0, 1/2]$ and peripheral channel $j \in \{2, 3\}$, the hybrid valence port vectors*

$$\mathbf{u}_j^\star := \sqrt{w_0}\, \mathbf{e}_0 + \sqrt{1 - w_0}\, \mathbf{d}_j \tag{5.35}$$

have unit norm $\|\mathbf{u}_j^\star\| = 1$, and their inner product evaluates to

$$\langle \mathbf{u}_2^\star, \mathbf{u}_3^\star \rangle = w_0 + (1 - w_0)\langle \mathbf{d}_2, \mathbf{d}_3 \rangle. \tag{5.36}$$

In particular, mutual port orthogonality $\langle \mathbf{u}_2^\star, \mathbf{u}_3^\star \rangle = 0$ holds if and only if the equilibrium dipolar alignment $\cos\phi_0 := \langle \mathbf{d}_2, \mathbf{d}_3 \rangle$ lies in $[-1, 0]$ and satisfies

$$\cos\phi_0 = -\frac{w_0}{1 - w_0}. \tag{5.37}$$

PROOF. Because $\langle \mathbf{e}_0, \mathbf{d}_j \rangle = 0$ with $\|\mathbf{e}_0\| = 1$ and $\|\mathbf{d}_j\| = 1$, expanding the self-inner product of (5.35) gives:

$$\langle \mathbf{u}_j^\star, \mathbf{u}_j^\star \rangle = w_0 \|\mathbf{e}_0\|^2 + (1 - w_0)\|\mathbf{d}_j\|^2 = 1, \tag{5.38}$$

establishing $\|\mathbf{u}_j^\star\| = 1$, while expanding $\langle \mathbf{u}_2^\star, \mathbf{u}_3^\star \rangle$ yields (5.36). Because $w_0 \in [0, 1/2]$ ensures $1 - w_0 \geq 1/2$ and hence $1 - w_0 > 0$, setting (5.36) to zero is equivalent to (5.37), with $-w_0/(1 - w_0) \in [-1, 0]$. □

Lemma 5.4 recovers the canonical molecular geometries from subspace orthogonality alone, where pure dipolar ports ($w_0 = 0$) meet at $\phi_0 = 90^\circ$, four symmetric tetrahedral ports ($w_0 = 1/4$) satisfy $\cos\phi_0 = -1/3$ ($\phi_0 \approx 109.47^\circ$), three trigonal ports ($w_0 = 1/3$) satisfy $\cos\phi_0 = -1/2$ ($\phi_0 = 120^\circ$), and two collinear ports ($w_0 = 1/2$) satisfy $\cos\phi_0 = -1$ ($\phi_0 = 180^\circ$). When non-bonding lone pairs retain a higher isotropic share on the central core, w_0 decreases on the bonding ports, contracting ϕ_0 until balanced by steric channel crowding across the peripheral resistance distance Ω_{23} (2.239). Under any angular distortion $\phi \in [0, \pi]$ of the dipolar bond channels $\cos\phi = \langle \mathbf{d}_2(\phi), \mathbf{d}_3(\phi) \rangle$ at fixed hybrid mixing $w_0 \in [0, 1/2)$ and angular stiffness scale $g_{\mathrm{ang}} > 0$ (eV), penalising non-orthogonal Pauli port overlap via (5.36)–(5.37) yields a smooth, frame-independent bending potential:

$$\langle \mathbf{u}_2(\phi), \mathbf{u}_3(\phi) \rangle = (1 - w_0)(\cos\phi - \cos\phi_0), \tag{5.39}$$

$$\Delta E_{\mathrm{ang}}(\phi) = \frac{g_{\mathrm{ang}}}{1 - w_0} \langle \mathbf{u}_2(\phi), \mathbf{u}_3(\phi) \rangle^2 = (1 - w_0) g_{\mathrm{ang}} (\cos\phi - \cos\phi_0)^2. \tag{5.40}$$

EXAMPLE 5.3 (Valence Port Orthogonality and Bending Barrier in H_2O). Consider a bent triatomic molecule such as H_2O, comprising a central oxygen block (1) bonded to two hydrogen blocks (2 and 3) with equal inter-block capacity $K_{OH} > 0$ (links) and angular port stiffness $g_{ang} > 0$ (eV, Figure 5.2(a)). On the three-block nuclear graph alone, the scalar capacity Laplacian $\mathbf{L_K}$ depends only on pairwise link capacities and assigns zero bending penalty across all angles ϕ:

$$\mathbf{L_K} = K_{OH} \begin{pmatrix} 2 & -1 & -1 \\ -1 & 1 & 0 \\ -1 & 0 & 1 \end{pmatrix}. \tag{5.41}$$

On the central oxygen valence subspace $\mathrm{im}(\Delta\mathbf{P}_{1\to 2})$, two non-bonding lone pairs concentrate isotropic $\ell = 0$ weight, leaving lone-pair-calibrated isotropic share $w_0 \approx 0.200$ ($1 - w_0 = 0.800$) in each O–H bonding port. Substituting $w_0 = 0.200$ into Lemma 5.4 (5.37) fixes the orthogonal port angle, while (5.40) gives the bending energy under angular displacement $\Delta\phi = \phi - \phi_0$:

$$\cos\phi_0 = -\frac{w_0}{1 - w_0} = -0.250 \implies \phi_0 \approx 104.5^\circ, \tag{5.42}$$

$$\Delta E_{ang}(\phi) = 0.800\, g_{ang}(\cos\phi + 0.250)^2 \approx 0.750\, g_{ang}(\Delta\phi)^2. \tag{5.43}$$

Whereas the scalar nuclear Laplacian (5.41) is invariant under bond rotation (Figure 5.2(b), muted dashed baseline), hybrid port orthogonality pins the zero-overlap minimum at $\phi_0 = 104.5^\circ$, responds harmonically to small thermal bending vibrations, and reaches a smooth stationary inversion saddle $\Delta E_{ang}(\pi) = 0.450\, g_{ang}$ at $\phi = 180^\circ$ ($\mathrm{d}\Delta E_{ang}/\mathrm{d}\phi|_\pi = 0$, matching water's empirical 1.38 eV linearisation barrier at $g_{ang} \approx 3.07$ eV, distinct from radial O–H bond dissociation). ♢

5.3 OPEN-BATH REDUCTION AND MULTI-BASIN ENSEMBLES

In an isolated covalent dimer, the eliminated sector $\bar{S}$ consists of fast electronic modes relaxed at zero temperature (Theorem 5.3). When a molecular subsystem S is embedded inside a larger macromolecular scaffold and thermal solvent bath $\bar{S}$, two additional questions arise: how do thermal fluctuations across $\bar{S}$ modify the effective free-energy landscape of S, and how does S switch between distinct metastable conformations when a single harmonic expansion breaks down? Resolving both questions requires no new operators beyond the Schur complement $\mathbf{L}_{\mathrm{eff}} = \mathbf{L}_{SS} - \mathbf{\Sigma}_{\mathrm{env}}$ (5.2) and the coarse-grained capacity barriers and escape rates of Chapter 2.

5.3.1 *Gaussian Bath Marginalisation*

Partition a composite molecular network $V = S \sqcup \bar{S}$ (2.13) into a resolved functional subgraph S (N_S blocks) and an untracked scaffold and solvent

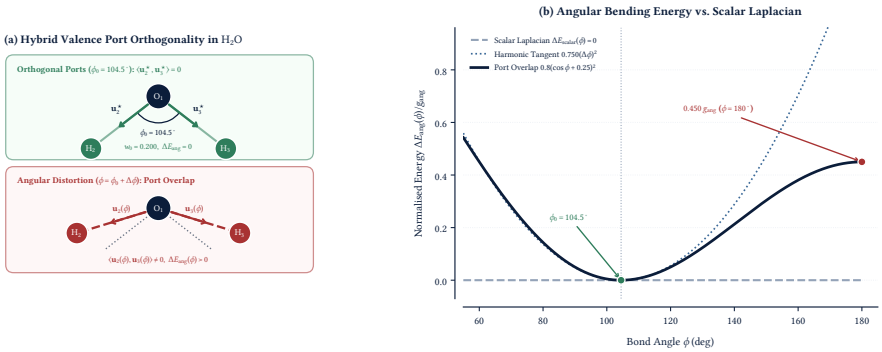


FIGURE 5.2: Hybrid valence port orthogonality and angular bending landscape in a bent triatomic molecule (Lemma 5.4 and Example 5.3). *(a)* Inside $\mathrm{im}(\Delta\mathbf{P}_{1\to 2})$, orthogonal hybrid ports $\langle \mathbf{u}_2^\star, \mathbf{u}_3^\star \rangle = 0$ with isotropic share $w_0 = 0.200$ fix the equilibrium H–O–H bond angle $\phi_0 \approx 104.5^\circ$ (5.42) at zero Pauli overlap ($\Delta E_{\mathrm{ang}} = 0$, teal, top), whereas angular distortion $\phi = \phi_0 + \Delta\phi$ induces port overlap $\langle \mathbf{u}_2(\phi), \mathbf{u}_3(\phi) \rangle \neq 0$ and restoring energy $\Delta E_{\mathrm{ang}}(\phi) > 0$ (crimson, bottom). *(b)* Normalised bending potential $\Delta E_{\mathrm{ang}}(\phi)/g_{\mathrm{ang}} = 0.800(\cos\phi + 0.250)^2$ across bond angle ϕ (navy solid), showing the orthogonal-port minimum at $\phi_0 = 104.5^\circ$, the local harmonic tangent $0.750(\Delta\phi)^2$ (light-navy dotted), the smooth linear-inversion saddle $0.450\, g_{\mathrm{ang}}$ at $\phi = 180^\circ$ (crimson marker), and the angle-blind scalar nuclear baseline $\Delta E_{\mathrm{scalar}}(\phi) = 0$ (muted dashed).

bath $\bar{S}$ ($N_{\bar{S}}$ blocks), coupled across ∂S by the quadratic fluctuation energy $E(\mathbf{x}_S, \mathbf{x}_{\bar{S}})$ (5.25) over dimensionless displacements $(\mathbf{x}_S, \mathbf{x}_{\bar{S}}) \in \mathbb{R}^{N_S + N_{\bar{S}}}$. At operational noise intensity $\theta > 0$ (J nat^{-1}, equal to $k_{\mathrm{B}} T_{\mathrm{th}}$ in an isothermal bath at temperature T_{th}), marginalising over all bath configurations $\mathbf{x}_{\bar{S}}$ defines the effective partition weight of S [7, 157]:

$$Z_{\mathrm{eff}}(\mathbf{x}_S) = \int_{\mathbb{R}^{N_{\bar{S}}}} \exp\!\left(-\frac{E(\mathbf{x}_S, \mathbf{x}_{\bar{S}})}{\theta}\right) \mathrm{d}\mathbf{x}_{\bar{S}}. \tag{5.44}$$

Because $\mathbf{L}_{\bar{S}\bar{S}} \succ \mathbf{o}$ on the open bath complement (2.24), substituting the square-completion identity (5.26) from Theorem 5.3 and shifting the Gaussian integration around $\mathbf{x}_{\bar{S}}^\star$ evaluates (5.44) in closed form (Figure 5.3(a)):

$$Z_{\mathrm{eff}}(\mathbf{x}_S) = Z_{\bar{S},0}\, \exp\!\left(-\frac{1}{2\theta}\mathbf{x}_S^{\mathsf{T}} \mathbf{L}_{\mathrm{eff}} \mathbf{x}_S\right), \tag{5.45}$$

$$Z_{\bar{S},0} := \sqrt{\frac{(2\pi\theta)^{N_{\bar{S}}}}{\det \mathbf{L}_{\bar{S}\bar{S}}}}, \tag{5.46}$$

$$F_{\mathrm{eff}}(\mathbf{x}_S) := -\theta \ln Z_{\mathrm{eff}}(\mathbf{x}_S) = \frac{1}{2}\mathbf{x}_S^{\mathsf{T}} \mathbf{L}_{\mathrm{eff}} \mathbf{x}_S + F_{\bar{S},0}, \tag{5.47}$$

where $\mathbf{L}_{\mathrm{eff}} = \mathbf{L}_{SS} - \boldsymbol{\Sigma}_{\mathrm{env}}$ with $\boldsymbol{\Sigma}_{\mathrm{env}} = \mathbf{L}_{S\bar{S}} \mathbf{L}_{\bar{S}\bar{S}}^{-1} \mathbf{L}_{\bar{S}S}$, and $F_{\bar{S},0} := -\theta \ln Z_{\bar{S},0}$ (J) is the $\mathbf{x}_S$-independent bath free energy.

Equation (5.47) unifies ground-state electronic relaxation and thermal bath marginalisation under a single operator: integrating out harmonic fluctuations across $\bar{S}$ folds the mechanical compliance and screening of the bath onto the boundary ports of S through $-\boldsymbol{\Sigma}_{\mathrm{env}} = [\![(\cdot)^{-1}, \mathscr{C}_S]\!](\mathbf{G}_\varepsilon)$, bypassing explicit trajectory integration over $\bar{S}$. By Lemma 2.3, the continuum quadratic

counterpart $[\![G_{\mu\nu}, \mathbf{P}_{\mathbf{\Pi}}]\!](g) = \kappa_{\mathrm{G}} T_{\mu\nu}^{(\mathrm{untracked})}$ generates untracked gravitational stress–energy across coarse-grained partitions in Chapter 6 (Section 6.2), while the same discrete Schur commutator governs passive dendritic integration in Chapter 9 (Section 9.2.2).

5.3.2 *Multi-Basin Ensembles and Conformational Selection*

The Schur free energy (5.47) is exact within a single metastable basin S_α ($\Xi(S_\alpha) \gg 1$, (2.127)), where fluctuations remain quadratic around a local equilibrium $\mathbf{x}_S^{(\alpha)}$. Functional molecular switching, however, traverses multiple metastable basins $\{S_1, \dots, S_M\}$ ($M \geq 2$) separated by Eyring–Kramers escape barriers $\Delta\Phi_{\alpha\beta} \approx \theta \Delta I_{\mathrm{barrier},\alpha\beta}$ (2.326)–(2.327) [73, 89]. Extrapolating a single basin's Schur operator $\mathbf{L}_{\mathrm{eff}}^{(1)}$ across an inter-basin barrier into S_2 assigns a quadratically growing elastic penalty far beyond the true saddle height (Figure 5.3(b)).

To resolve multi-basin switching without reverting to femtosecond trajectory steps, we project onto a discrete Markov State Model (MSM) [137] over the M admissible basins $\{S_1, \dots, S_M\}$ coupled by the inter-basin transition rates (2.138) and (2.326). Each basin $\alpha \in \{1, \dots, M\}$ carries normalised stationary weight $p_\alpha > 0$ ($p_1 + \cdots + p_M = 1$), local Schur operator $\mathbf{L}_{\mathrm{eff}}^{(\alpha)} = \mathbf{L}_{SS}^{(\alpha)} - \mathbf{\Sigma}_{\mathrm{env}}^{(\alpha)}$, and coupling free-energy shift ΔF_α (J) upon engaging an external stimulus or guest molecule. Summing over all M basins gives the multi-basin partition weight and ensemble coupling free energy:

$$Z_{\mathrm{ens}}(\mathbf{x}_S) = \sum_{\alpha=1}^{M} p_\alpha \exp\!\left(-\frac{1}{2\theta}(\mathbf{x}_S - \mathbf{x}_S^{(\alpha)})^{\mathsf{T}} \mathbf{L}_{\mathrm{eff}}^{(\alpha)} (\mathbf{x}_S - \mathbf{x}_S^{(\alpha)})\right), \tag{5.48}$$

$$\Delta F_{\mathrm{ens}} = -\theta \ln\left(\sum_{\alpha=1}^{M} p_\alpha \exp\!\left(-\frac{\Delta F_\alpha}{\theta}\right)\right). \tag{5.49}$$

THEOREM 5.5 (Multi-Basin Free-Energy Bound and Population Shift). *Let $M \geq 2$, $\theta > 0$, and $p_1, \dots, p_M > 0$ satisfy $p_1 + \cdots + p_M = 1$. For any basin free-energy shifts $\Delta F_1, \dots, \Delta F_M \in \mathbb{R}$, the ensemble free energy ΔF_{ens} (5.49) satisfies for every $\alpha \in \{1, \dots, M\}$:*

$$\min_{1 \leq \beta \leq M} \Delta F_\beta \leq \Delta F_{\mathrm{ens}} < \Delta F_\alpha - \theta \ln p_\alpha. \tag{5.50}$$

Furthermore, the coupled posterior basin probability

$$p_\alpha^\star := \frac{p_\alpha e^{-\Delta F_\alpha/\theta}}{\sum_{\beta=1}^{M} p_\beta e^{-\Delta F_\beta/\theta}} \tag{5.51}$$

exceeds the ground-basin probability $p_1^\star$ ($p_\alpha^\star > p_1^\star$) if and only if

$$\Delta F_1 - \Delta F_\alpha > \theta \ln\left(\frac{p_1}{p_\alpha}\right). \tag{5.52}$$

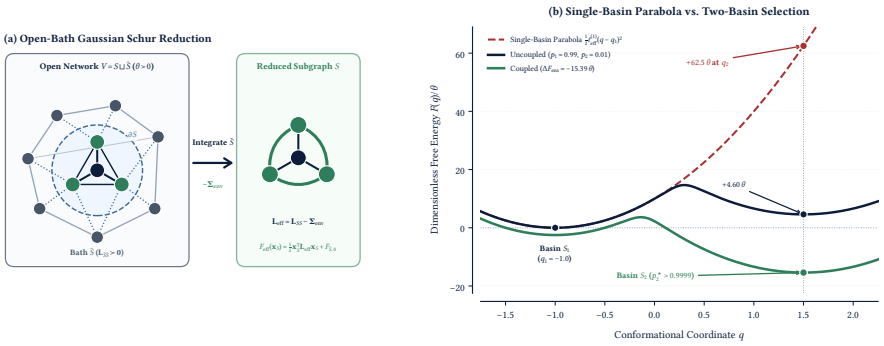


FIGURE 5.3: Open-bath Gaussian Schur reduction and multi-basin conformational selection (Theorem 5.5 and Example 5.4). *(a)* Partitioning a molecular network $V = S \sqcup \bar{S}$ into an active subgraph S (navy) and surrounding thermal bath $\bar{S}$ (slate) eliminates $\bar{S}$ via the Schur self-energy $\mathbf{\Sigma}_{\text{env}} = \mathbf{L}_{S\bar{S}}\mathbf{L}_{\bar{S}\bar{S}}^{-1}\mathbf{L}_{\bar{S}S}$ (5.47), folding bath compliance directly onto the boundary ports of S (teal). *(b)* Free-energy profile $F(q)/\theta$ along dimensionless conformational coordinate q: extrapolating the single-basin Schur parabola from S_1 ($q_1 = -1.0$) to S_2 ($q_2 = +1.5$) imposes an unphysical $+62.5\,\theta$ quadratic penalty (crimson dashed), whereas the two-basin ensemble resolves the uncoupled landscape ($p_1 = 0.99$, $p_2 = 0.01$, navy solid) and shifts posterior occupancy into S_2 upon selective coupling ($p_2^\star > 0.9999$, $\Delta F_{\text{ens}} \approx -15.39\,\theta$, teal solid).

PROOF. Setting $\Delta F_{\min} := \min_\beta \Delta F_\beta$, positivity of each Boltzmann term across $M \geq 2$ basins and normalisation $p_1 + \cdots + p_M = 1$ bracket the partition sum on both sides:

$$p_\alpha e^{-\Delta F_\alpha/\theta} < \sum_{\beta=1}^{M} p_\beta e^{-\Delta F_\beta/\theta}, \tag{5.53}$$

$$\sum_{\beta=1}^{M} p_\beta e^{-\Delta F_\beta/\theta} \leq e^{-\Delta F_{\min}/\theta} \sum_{\beta=1}^{M} p_\beta = e^{-\Delta F_{\min}/\theta}. \tag{5.54}$$

Applying the strictly decreasing map $z \mapsto -\theta \ln z$ ($\theta > 0$) to (5.53)–(5.54) establishes (5.50). Finally, since the denominator in (5.51) is positive, $p_\alpha^\star > p_1^\star$ holds if and only if $p_\alpha e^{-\Delta F_\alpha/\theta} > p_1 e^{-\Delta F_1/\theta}$, which rearranges via $\theta \ln(\cdot)$ to (5.52). □

Theorem 5.5 formalises conformational selection [112]. Even when an excited basin S_α is sparsely populated before coupling ($p_\alpha \ll p_1$), selective stabilisation above the reversible opening cost $\theta \ln(p_1/p_\alpha)$ (5.52) shifts ensemble occupancy into S_α while capping the net free energy strictly below $\Delta F_\alpha - \theta \ln p_\alpha$ (5.50), avoiding the single-basin quadratic extrapolation error. Within the metriplectic decomposition of Section 2.5.2, intra-basin fluctuations governed by $\mathbf{L}_{\text{eff}}^{(\alpha)}$ generate conservative Poisson flow $\{A, H\}$, whereas thermally activated Kramers transitions between basins execute dissipative metric relaxation (A, S).

EXAMPLE 5.4 (Two-Basin Conformational Selection versus Single-Basin Extrapolation). Consider a two-basin molecular gating switch ($M = 2$) along

a dimensionless reaction coordinate q at operational noise scale $\theta = k_B T_{\text{th}} \approx 25.7\,\text{meV}$ ($T_{\text{th}} = 298\,\text{K}$, Figure 5.3(b)). In the uncoupled state, the occluded ground basin S_1 ($q_1 = -1.0$) carries stationary weight $p_1 = 0.99$ and local Schur curvature $\ell_{\text{eff}}^{(1)} = 20.0\,\theta$, while the open basin S_2 ($q_2 = +1.5$) carries weight $p_2 = 0.01$ and local Schur curvature $\ell_{\text{eff}}^{(2)} = 16.0\,\theta$ (rendered in Figure 5.3(b) with barrier-softening scale $s_{\text{bar}} = 2.6\,\theta$). An incoming guest molecule couples weakly to S_1 ($\Delta F_1 = -2.5\,\theta$) and strongly to S_2 ($\Delta F_2 = -20.0\,\theta$).

Extrapolating the single-basin quadratic energy around S_1 to q_2 produces a severe elastic penalty that masks binding altogether:

$$\Delta F_{\text{harm}}(q_2) = \frac{1}{2}\ell_{\text{eff}}^{(1)}(q_2 - q_1)^2 = +62.5\,\theta \approx +1.61\,\text{eV}, \tag{5.55}$$

$$\Delta F_{\text{trap}} = \Delta F_{\text{harm}}(q_2) + \Delta F_2 = +42.5\,\theta \approx +1.09\,\text{eV}. \tag{5.56}$$

Applying Theorem 5.5 across $\{S_1, S_2\}$ yields instead:

$$\theta \ln\left(\frac{p_1}{p_2}\right) = \theta \ln 99 \approx +4.60\,\theta < \Delta F_1 - \Delta F_2 = 17.5\,\theta, \tag{5.57}$$

$$\Delta F_{\text{ens}} = -\theta \ln\left(p_1 e^{-\Delta F_1/\theta} + p_2 e^{-\Delta F_2/\theta}\right) \approx -15.39\,\theta, \tag{5.58}$$

$$p_2^\star = \frac{p_2 e^{-\Delta F_2/\theta}}{p_1 e^{-\Delta F_1/\theta} + p_2 e^{-\Delta F_2/\theta}} > 0.9999. \tag{5.59}$$

Replacing the single-basin parabola with the two-basin ensemble substitutes the finite opening cost $+4.60\,\theta$ for the spurious $+62.5\,\theta$ elastic extrapolation, inverting occupancy from 1% open ($p_2 = 0.01$) to over 99.99% open ($p_2^\star > 0.9999$) and recovering favourable net stabilisation $\Delta F_{\text{ens}} \approx -15.39\,\theta$ ($\approx -0.396\,\text{eV}$). ♢

Across all three tiers of this chapter—from confined particle closures and reduced-capacity atomic shells to covalent cut internalisation, valence port orthogonality, and multi-basin molecular switching—composite matter has been modelled directly on the discrete capacity graph $G_{\mathbf{K}}$ without presupposing a continuous spatial manifold. This raises the foundational question addressed next: if spatial coordinates are not postulated in advance, how does continuous (3 + 1)-dimensional spacetime emerge? Chapter 6 answers this question by deriving relativistic kinematics, three-dimensional spatial persistence, gravitational curvature, and cosmological horizons from the large-scale spectral geometry of $\mathbf{K}$.

6

SPACETIME, GRAVITY, AND COSMOLOGY

Having applied the Epistemic Lens to quantum measurement in Chapter 4 and to grid-free particle and molecular structure in Chapter 5, this chapter turns outward to address the question posed at the close of Chapter 5: if neither spatial coordinates nor external clocks exist on the relational graph $G = (V, E)$, how do continuous spacetime and gravity emerge? In the framework of Conservation-Congruent Encoding (CCE), every geometric observable is fixed directly by the operators constructed in Chapter 2. Under an admissible partition $\mathbf{\Pi}$, the coarse-grained capacity matrix $\mathbf{K} = \mathbf{K}_\Omega + \mathbf{K}_\partial$ splits into Frobenius-orthogonal diagonal memory and off-diagonal boundary sectors (2.186), while its Laplacian $\mathbf{L}_\mathbf{K}$ defines spectral dimension $d_s[\mathbf{\Pi}]$ (2.233), resistance distance $\Omega_{\alpha\beta}$ (2.239), local spectral cut conductance $\Sigma^{ij}(\alpha)$ (2.311), diagonal memory trace $\mathrm{Tr}(\mathbf{K}_\Omega)$ (2.249), and algebraic capacity-Ricci curvature $\mathrm{Ric}_\mathbf{K}$ (2.268).

Flat kinematics and gravitational curvature both follow from the orthogonal split between $\mathbf{P}_\mathbf{\Pi}$ and $\mathbf{Q}_\mathbf{\Pi}$ (2.64) across those operators. On a uniform capacity network whose incoming boundary updates remain within the calibrated reversible rate Ω_Φ of the observer, transitions across $\mathbf{K}_\Omega$ and $\mathbf{K}_\partial$ trade off losslessly in quadrature, recovering the Minkowski interval and Lorentz boosts without presupposing a background manifold. Gravity arises whenever block aggregation breaks that uniform baseline across either sector. Within the resolved sector of $\mathbf{P}_\mathbf{\Pi}$, compressing dense internal subgraphs via $\mathscr{T}_\mathbf{P}$ (2.159) concentrates links into heavy diagonal capacities $K_{\alpha\alpha}$ that turn diagonal Ricci curvature strictly positive (2.274) even in vacuum and source tracked stress–energy $T_{\mu\nu}^{(\mathrm{tracked})}$. Across the unresolved complement of $\mathbf{Q}_\mathbf{\Pi}$, sub-grid internal capacities and boundary dissipation $I_{\mathrm{irr},\partial}$ enter the nonlinear projection commutator of the Einstein operator as untracked stress–energy $T_{\mu\nu}^{(\mathrm{untracked})}$, closing covariant conservation at finite resolution.

Synthesising Fagan [52, 53], this chapter develops three consequences of that operator bridge. Section 6.1 reconciles discrete CCE updates with continuous differentials across Chapter 2's persistence and Weyl windows, proves that collision-free routing and orbital stability uniquely select (3 + 1) dimensions, and calibrates the Minkowski interval and reversible tracking threshold. Section 6.2 bridges $\mathrm{Ric}_\mathbf{K}$, $\Sigma^{ij}(\alpha)$, and Schur boundary closure to the coarse-grained Einstein field equation under an explicit Continuum Metric Closure Assumption, unifying tracked baryonic gravity, untracked subgrid stress, geodesic attraction, and black hole horizon saturation. Finally, Section 6.3 applies Chapter 4's finite-observer bounds to cosmic history, replacing the Big Bang singularity and asymptotic Heat Death with a bounded Epistemic Bubble.

6.1 SPACE AND TIME

Standard relativity postulates a smooth four-dimensional Lorentzian manifold and places clocks and rods upon it. Here the construction runs in reverse from the discrete operators of Chapter 2. An embedded subsystem $S \subset V$ ($N < \infty$) partitioned under $\mathbf{\Pi}$ possesses only its internal capacity split $\mathbf{K}_S = \mathbf{K}_\Omega + \mathbf{K}_\partial^{(\mathrm{int})}$, its external cut $\mathbf{K}_\partial^{(\mathrm{ext})}$, and finite combinatorial link counts. From these ingredients alone, we connect discrete transition counts to smooth spacetime differentials across finite spectral windows, select (3+1) continuum dimensions, and calibrate SI clocks and rulers to recover the Minkowski metric and the reversible tracking threshold.

6.1.1 *Discrete-to-Continuum Allocation and* (3 + 1) *Spatial Viability*

Connecting discrete CCE algebra to relativistic kinematics requires distinguishing static capacity weights on $G_{\mathbf{K}}$ from reversible transition updates routed across them. In Chapter 2, each coarse-grained block $\alpha \in \{1, \dots, M\}$ carries internal link capacity $K_{\alpha\alpha} \geq 2$ (links) and static logarithmic depth $I_{\alpha\alpha} = \ln K_{\alpha\alpha}$ (nats, (1.33)). Across a multi-epoch foliation $S_1, \dots, S_{N_\tau}$ along $\boldsymbol{\phi}_{\mathrm{time}}$ (2.242), those logarithmic depths set the intrinsic slice proper-time increments $\Delta\tau_{\mathrm{nat}}(\tau)$ (2.243), whereas on a single-epoch partition the diagonal memory trace $\mathrm{Tr}(\mathbf{K}_\Omega)$ (2.249) counts the parallel internal channels carrying elementary memory updates, with interior core transitions shielded by $\mathbf{L}_{\Omega\Omega}$. Even when an observer sits at rest relative to a stationary reference sub-block $\bar{S}_{\mathrm{ref}} \subset \bar{S}$ (2.247), its static norms $\mathcal{Q}_\Omega$, $\mathcal{Q}_\partial$, and $\mathcal{Q}_{\mathrm{free}}$ remain strictly positive (Section 2.4.2). What changes with motion is how the subsystem's reversible transition flux $J_{\alpha\beta}$—supported strictly where $K_{\alpha\beta} > 0$ (2.310)—apportions its reversible distinction budget $\Delta I_{\mathrm{total}}$ (nats) across a reference slice of $\bar{S}_{\mathrm{ref}}$.

During one reversible update step, diagonal transitions through $\mathbf{K}_\Omega$ advance internal proper-time distinctions $\Delta I_{\mathrm{int}} \equiv \Delta\tau_{\mathrm{nat}}$, while off-diagonal transitions across $\mathbf{K}_\partial$ resolve spatial distinctions ΔI_{ext} (both in nats) across the resistance metric $\Omega_{\alpha\beta}$ (2.239). Because $\mathbf{K}_\Omega$ and $\mathbf{K}_\partial$ occupy disjoint matrix entries, any transition flux matrix decomposes into Frobenius-orthogonal diagonal and off-diagonal parts ($\langle \mathbf{K}_\Omega, \mathbf{K}_\partial \rangle_F = 0$, (2.186)), and reversible unitary or orthogonal transport preserves the Euclidean ℓ_2 norm—the same quadratic geometry enforcing Tsirelson's bound in Theorem 4.8. On any finite CCE graph, prior to assuming a manifold or spatial dimension, discrete reversible distinction increments therefore add in quadrature:

$$\Delta I_{\mathrm{total}}^2 = \Delta I_{\mathrm{int}}^2 + \Delta I_{\mathrm{ext}}^2. \tag{6.1}$$

Against a fixed reference step $\Delta I_{\mathrm{total}}$, every nat of reversible capacity committed to external boundary transport ΔI_{ext} reduces in quadrature the internal proper-time increment ΔI_{int}.

How do discrete increments $(\Delta k_\Omega, \Delta \mathbf{z}_{\alpha\beta}, \Delta I_{\text{int}}, \Delta I_{\text{ext}})$ become smooth differentials $(\mathrm{d}\tau, \mathrm{d}\mathbf{z}, \mathrm{d}I_{\text{int}}, \mathrm{d}I_{\text{ext}})$ when Theorem 4.1 restricts every embedded observer to finitely many blocks $M \leq \lfloor N_S/2 \rfloor$? Rather than invoking an exact continuum ($M \to \infty$, ruled out operationally by Corollary 4.4), smooth differential calculus emerges as the controlled coarse-grained approximation inside Chapter 2's two scale-separation windows ($M \gg 1$ and $K_{\alpha\alpha} \gg 1$). Temporally, across Axiom II's persistence window $(\nu_0 \operatorname{Tr}(\mathbf{K}_\Omega))^{-1} \ll \mathrm{d}\tau \ll T$ ($\mathrm{d}\tau \leq \mathrm{d}t$, (2.250)), $\mathrm{d}k_\Omega = \nu_0 \operatorname{Tr}(\mathbf{K}_\Omega)\,\mathrm{d}\tau$ spans many internal channel updates before coarse-grained state drift. Spatially, across the intermediate Weyl diffusion window $\mu_M^{-1} \ll s \ll \mu_2^{-1}$ (2.232)–(2.234), coordinate jumps across adjacent blocks satisfy $|\Delta \mathbf{z}_{\alpha\beta}| \sim M^{-1/n}$ ($M^{-1/n} \ll 1$) along $n := d_s^{\text{spatial}}$ orthogonal spatial eigenmodes of $\mathbf{L}_\mathbf{K}$ while $\Delta \mathbf{K} = \mathbf{o}$ on the kinematic update scale. Across this joint window, (6.1) passes directly to the differential distinction balance across one temporal channel and n mutually orthogonal spatial channels (all in nats):

$$\mathrm{d}I_{\text{total}}^2 = \mathrm{d}I_{\text{int}}^2 + \mathrm{d}I_{\text{ext}}^2, \tag{6.2}$$

$$\mathrm{d}I_{\text{ext}}^2 = \sum_{i=1}^{n} \mathrm{d}I_{\text{ext},i}^2. \tag{6.3}$$

Both legs in (6.2) belong strictly to reversible symplectic transport in Subsection 2.5.2, whereas projection loss enters separately as boundary dissipation $I_{\text{irr},\partial}$ in Section 6.2. When realised in relativistic quantum matter and metered in seconds against a physical reference oscillator $\bar{S}_{\text{ref}}$ of reversible rate $\Omega_{\text{ref}} > 0$ (nats s^{-1}) via (2.255), rest energy above ground state (5.4) (at universal elementary substrate step cadence $\nu_0 > 0$ in s^{-1} and reduced Planck constant $\hbar$ in J s) and the Margolus–Levitin bound [106] on rest-frame orthogonal transition time $\Delta\tau_\perp$ (in s) cap the subsystem's own active rest-frame reversible distinction rate Ω_Φ (in nats s^{-1}):

$$E_\Phi - E_{0,\Phi} = \hbar \nu_0 \operatorname{Tr}(\mathbf{K}_\Omega), \tag{6.4}$$

$$\Delta\tau_\perp \geq \frac{\pi\hbar}{2(E_\Phi - E_{0,\Phi})}, \tag{6.5}$$

$$0 < \Omega_\Phi \leq \eta_\Phi \frac{2(E_\Phi - E_{0,\Phi})}{\pi\hbar} = \frac{2\eta_\Phi}{\pi} \nu_0 \operatorname{Tr}(\mathbf{K}_\Omega), \tag{6.6}$$

where $\eta_\Phi \geq \ln 2$ is the dimensionless coding factor (nats per orthogonal transition). Because logarithmic concavity keeps static slice depth $\Delta\tau_{\text{nat}}$ (2.243) strictly below the linear trace factor in (6.6) on every admissible partition ($K_{\alpha\alpha} \geq 2$), any subsystem advancing coarse-grained steps at frequency $\nu_{\text{int}} \leq \nu_0$ ($\Omega_\Phi = \Delta\tau_{\text{nat}}\, \nu_{\text{int}}$) satisfies (6.6) automatically.[1]

Although abstract networks can exhibit any spectral dimension $n = d_s^{\text{spatial}}$ (Section 2.5.1), persistent physical observers realised in relativistic matter must sustain both collision-free boundary routing (Axiom I) and stable bound registers (Axiom II) across (6.3). On the unbounded Weyl-window heat-kernel scaling $P_\infty(s) \asymp s^{-d_s^{\text{spatial}}/2}$ ($s \geq s_0 > 0$) of (2.232), a lower bound $n \geq 3$ follows

1 Equation (6.6) bounds transition rate rather than spatial storage, whereas Bekenstein's bound already presupposes spatial radius and c [12].

from Pólya's large-time recurrence criterion paired with transverse intersection codimension for generic one-dimensional routing channels Γ_i, Γ_j:

$$\int_{s_0}^{\infty} P_\infty(s)\,\mathrm{d}s = \infty \iff d_s^{\text{spatial}} \leq 2, \tag{6.7}$$

$$\dim\left(\Gamma_i \cap_{\text{tr}} \Gamma_j\right) = 1 + 1 - d_s^{\text{spatial}} = 2 - d_s^{\text{spatial}}. \tag{6.8}$$

For $d_s^{\text{spatial}} \leq 2$, random walks recur with probability one and non-planar interconnects cannot be routed without crossings (dim ≥ 0, [66]) that force serial arbitration and continuous boundary dissipation $\dot{I}_{\text{irr},\partial} > 0$. Only for $d_s^{\text{spatial}} \geq 3$ is generic channel intersection empty (dim < 0), permitting collision-free non-planar causal routing.

An upper bound $d_s^{\text{spatial}} < 4$ follows from the stability of central-force bound states—atomic shells (Chapter 5), mechanical oscillators, and orbital clocks—under Laplacian flux conservation.[2] For integer $n = d_s^{\text{spatial}} > 2$, Gauss's law fixes the radial central force $F_n(r)$ with coupling $k > 0$ and binding potential $U_n(r)$:

$$F_n(r) = -\frac{k}{r^{n-1}}, \tag{6.9}$$

$$U_n(r) = -\frac{k}{(n-2)r^{n-2}}. \tag{6.10}$$

For reduced mass $\mu > 0$ and angular momentum $L > 0$, the planar effective potential $V_{\text{eff}}(r)$ has circular-orbit stationarity at $r_c > 0$ and radial stability curvature $V''_{\text{eff}}(r_c)$:

$$V_{\text{eff}}(r) = \frac{L^2}{2\mu r^2} - \frac{k}{(n-2)r^{n-2}}, \tag{6.11}$$

$$V'_{\text{eff}}(r_c) = 0 \iff \frac{L^2}{\mu} = k r_c^{4-n}, \tag{6.12}$$

$$V''_{\text{eff}}(r_c) = (4-n)\frac{k}{r_c^n}. \tag{6.13}$$

THEOREM 6.1 (Dimensional Upper Bound from Orbital Stability). *Let an emergent spatial continuum possess integer spectral dimension $n = d_s^{\text{spatial}} > 2$, with long-range binding governed by the n-dimensional Gauss-law central potential $U_n(r)$ in (6.10) with coupling constant $k > 0$. Circular orbits of non-zero angular momentum $L > 0$ and reduced mass $\mu > 0$ are linearly stable with restoring effective potential curvature $V''_{\text{eff}}(r_c) > 0$ if and only if $n < 4$. Consequently, for any integer spatial dimension satisfying the non-planar routing bound $n \geq 3$, circular orbital stability holds if and only if $n = 3$.*

PROOF. Because $L > 0$, $\mu > 0$, and $k > 0$, (6.12) admits $r_c > 0$, and by (6.13) the sign of $V''_{\text{eff}}(r_c)$ matches $4 - n$. Hence $V''_{\text{eff}}(r_c) > 0$ if and only if $n < 4$, which intersected with integer $n \geq 3$ uniquely yields $n = 3$. □

2 By Zeeman's unknotting theorem [172], closed one-dimensional loops $S^1 \hookrightarrow S^n$ likewise untie trivially for all $n \geq 4$, leaving knot-protected flux tubes viable exclusively at $n = 3$.

At $n = 4$ circular orbits are marginal ($V''_{\mathrm{eff}}(r_c) = 0$) and for $n > 4$ strictly unstable [155], matching Bertrand's theorem that among central power laws only three-dimensional Keplerian and harmonic potentials close all bounded orbits [147]. Combining $3 \le d_s^{\mathrm{spatial}} < 4$ with the single directed Fiedler axis $d_s^{\mathrm{time}} = 1$ along $\boldsymbol{\phi}_{\mathrm{time}}$ uniquely selects $(3+1)$ continuum dimensions:

$$3 \le d_s^{\mathrm{spatial}} < 4 \Longrightarrow d_s^{\mathrm{spatial}} = 3, \tag{6.14}$$

$$d_s[\boldsymbol{\Pi}] = d_s^{\mathrm{spatial}} + d_s^{\mathrm{time}} = 3 + 1 = 4. \tag{6.15}$$

6.1.2 *The Minkowski Interval and the Reversible Tracking Threshold*

Consider first an irregular relational substrate whose coarse-grained block degrees have uniform mean $\bar{d} > 0$ (links) and whose degree-normalised spectral cut conductances (2.311) satisfy $\Sigma^{ij}(\alpha)/d_\alpha \simeq \bar{\sigma}\,\delta^{ij}$ at baseline conductance $\bar{\sigma} > 0$ (links^{-1}) across all $n = 3$ spatial axes within the Weyl diffusion window. Unlike a periodic lattice, whose discrete grid axes break boost symmetry, an irregular substrate without preferred lattice directions realises continuous orthochronous Lorentz isotropy $\mathrm{SO}^+(1,3)$ statistically across coarse-grained blocks ($K_{\alpha\alpha} \gg 1$), analogous to Poisson-sprinkled causal sets [19]. Physical seconds and metres enter by choosing an inertial physical reference oscillator as $\bar{S}_{\mathrm{ref}}$ of reversible distinction rate $\Omega_{\mathrm{ref}} > 0$ (nats s^{-1}) in (2.255). For any target subsystem S with active rest-frame reversible distinction rate $\Omega_\Phi > 0$ (nats s^{-1}, (6.6)), letting $\mathrm{d}t$ (2.255) ($x^0 = ct$) denote coordinate time metered on $\bar{S}_{\mathrm{ref}}$, $\mathrm{d}\tau$ (2.250) denote standardised proper time accumulated along $\mathbf{K}_\Omega$, and $\mathrm{d}\ell$ denote Euclidean spatial displacement relative to $\bar{S}_{\mathrm{ref}}$ in Cartesian coordinates x^i ($i \in \{1,2,3\}$) at invariant causal propagation speed $c > 0$ (m s^{-1}) calibrates the distinction channels (all in nats) to:

$$\mathrm{d}I_{\mathrm{total}} := \Omega_\Phi\,\mathrm{d}t, \tag{6.16}$$

$$\mathrm{d}I_{\mathrm{int}} := \Omega_\Phi\,\mathrm{d}\tau, \tag{6.17}$$

$$\mathrm{d}I_{\mathrm{ext}} := \Omega_\Phi\,\frac{\mathrm{d}\ell}{c}. \tag{6.18}$$

Here $\mathrm{d}I_{\mathrm{int}} = \Omega_\Phi\,\mathrm{d}\tau$ is a Lorentz scalar counting the intrinsic reversible distinctions actually accumulated along S's own internal channels $\mathbf{K}_\Omega$, whereas $\mathrm{d}I_{\mathrm{total}}$ and $\mathrm{d}I_{\mathrm{ext}}$ are observer-relative projections onto the chosen inertial reference sub-block $\bar{S}_{\mathrm{ref}}$, with $\mathrm{d}I_{\mathrm{total}}$ measuring the reference distinction budget S would accumulate internally over $\mathrm{d}t$ if comoving with $\bar{S}_{\mathrm{ref}}$. Calibrating each spatial component in (6.3) and solving (6.2) for the invariant internal leg yields the Euclidean spatial element and local Minkowski interval:

$$\mathrm{d}I_{\mathrm{ext},i} := \Omega_\Phi\,\frac{\mathrm{d}x^i}{c}, \tag{6.19}$$

$$\mathrm{d}\ell^2 := \delta_{ij}\,\mathrm{d}x^i\mathrm{d}x^j, \tag{6.20}$$

$$\mathrm{d}I_{\mathrm{int}}^2 = \mathrm{d}I_{\mathrm{total}}^2 - \mathrm{d}I_{\mathrm{ext}}^2 \Longrightarrow c^2\mathrm{d}\tau^2 = c^2\mathrm{d}t^2 - \mathrm{d}\ell^2. \tag{6.21}$$

THEOREM 6.2 (Recovery of the Local Minkowski Interval). *Let an embedded observer with calibrated reversible distinction rate $\Omega_\Phi > 0$ allocate differential updates across mutually orthogonal temporal ($\mathrm{d}I_{\mathrm{int}}$) and three-dimensional spatial ($\{\mathrm{d}I_{\mathrm{ext},i}\}_{i=1}^{3}$) channels satisfying (6.2)–(6.3). Under the operational clock and distance calibrations (6.16)–(6.20) with invariant signal speed $c > 0$, the proper-time interval satisfies*

$$c^2\mathrm{d}\tau^2 = c^2\mathrm{d}t^2 - \mathrm{d}\ell^2, \tag{6.22}$$

recovering the $(-+++)$ Lorentzian Minkowski metric $\eta_{\mu\nu} = \mathrm{diag}(-1, 1, 1, 1)$ in coordinates $x^\mu = (ct, x^1, x^2, x^3)$ independently of Ω_Φ.

PROOF. Substituting (6.16)–(6.20) at $n = 3$ into the orthogonal channel sum (6.2)–(6.3) gives

$$\Omega_\Phi^2\,\mathrm{d}t^2 = \Omega_\Phi^2\,\mathrm{d}\tau^2 + \Omega_\Phi^2\,\frac{\mathrm{d}\ell^2}{c^2}. \tag{6.23}$$

Multiplying (6.23) by $c^2 > 0$, cancelling $\Omega_\Phi^2 > 0$, and solving for $c^2\mathrm{d}\tau^2$ yields (6.22). □

The Lorentzian minus sign thus requires neither Wick rotation nor imaginary edge weights. Solving the positive-definite Frobenius balance (6.2) for the frame-invariant internal leg $\mathrm{d}I_{\mathrm{int}}^2$ against the frame-relative reference budget $\mathrm{d}I_{\mathrm{total}}^2$ algebraically reverses the sign of $\mathrm{d}I_{\mathrm{ext}}^2$. Dividing (6.21) by $\mathrm{d}t$ defines coordinate speed v and the normalised Lorentz allocation circle:

$$v := \frac{\mathrm{d}\ell}{\mathrm{d}t}, \tag{6.24}$$

$$\frac{\mathrm{d}\tau^2}{\mathrm{d}t^2} + \frac{v^2}{c^2} = 1, \tag{6.25}$$

from which the Lorentz factor $\gamma_{\mathrm{L}}(v)$ fixes proper-time dilation and longitudinal length contraction relative to rest length L_0:

$$\gamma_{\mathrm{L}}(v) := \frac{1}{\sqrt{1 - v^2/c^2}}, \tag{6.26}$$

$$\mathrm{d}\tau = \frac{\mathrm{d}t}{\gamma_{\mathrm{L}}(v)}, \tag{6.27}$$

$$L_\parallel = \frac{L_0}{\gamma_{\mathrm{L}}(v)}. \tag{6.28}$$

At rest relative to $\bar{S}_{\mathrm{ref}}$ ($v = 0$), $\mathrm{d}I_{\mathrm{ext}} = 0$ and all updates advance internal memory ($\mathrm{d}\tau = \mathrm{d}t$). At $v > 0$, committing $\mathrm{d}I_{\mathrm{ext}} > 0$ across $\mathbf{K}_\partial$ leaves fewer internal distinctions ($\mathrm{d}\tau < \mathrm{d}t$) and projects L_0 onto a contracted simultaneous slice ($L_\parallel < L_0$). Comparing trajectories of different speeds v across a fixed reference increment $\mathrm{d}t$ on $\bar{S}_{\mathrm{ref}}$ traces the Euclidean allocation circle (6.25), so between two worldlines that depart and reunite at a common register on a later slice S_τ, the trajectory routing flux across $\mathbf{K}_\partial$ completes fewer internal channel updates $\mathrm{d}k_\Omega = \nu_0\,\mathrm{Tr}(\mathbf{K}_\Omega)\,\mathrm{d}\tau$ on $\mathbf{K}_\Omega$ ($\Delta\tau < \Delta t$). Conversely, switching from $\bar{S}_{\mathrm{ref}}$ to any boosted inertial reference sub-block $\bar{S}'_{\mathrm{ref}}$ transforms

the observer-relative pair $(\mathrm{d}I_{\mathrm{total}}, \mathrm{d}I_{\mathrm{ext},i}) \mapsto (\mathrm{d}I'_{\mathrm{total}}, \mathrm{d}I'_{\mathrm{ext},i})$ under $\mathrm{SO}^+(1,3)$ across the Lorentzian hyperbola (6.22) as each frame foliates simultaneous slices along its own Fiedler mode $\boldsymbol{\phi}_{\mathrm{time}}$ (2.240), while leaving $\mathrm{d}I_{\mathrm{int}} = \Omega_\Phi \, \mathrm{d}\tau$ on $\mathbf{K}_\Omega$ (shielded on S_Ω by $\mathbf{L}_{\Omega\Omega}$, Section 2.1.2) strictly invariant. Because a boost is an $\mathrm{SO}^+(1,3)$ frame rotation on a statistically isotropic substrate [19] rather than a coarsening map $\mathbf{P}$ (Section 2.3.2), the moving system preserves its rest-frame partition $\mathbf{\Pi}$, static structural norms $\mathcal{Q}_{\mathrm{alloc}}$ and $\mathcal{Q}_{\mathrm{free}}$, and stability barrier $\Delta I_{\mathrm{barrier}}$, while exact cancellation of Ω_Φ^2 in (6.23) ensures symmetric relative dilation without a preferred rest frame across clocks of distinct capacities Ω_Φ.

Flat Minkowski kinematics (6.21)–(6.28) requires both statistically homogeneous resolved capacities $\mathbf{K}_\Omega$ and an incoming proper-time rate of environmental distinctions $\dot{I}_{\mathrm{env}} \geq 0$ (nats s^{-1}) across $\mathbf{K}_\partial^{(\mathrm{ext})}$ that stays within Ω_Φ (6.6). Whenever $\dot{I}_{\mathrm{env}}$ exceeds Ω_Φ in the observer's proper frame, excess distinctions cannot be routed reversibly and enforce a capacity-overflow floor on proper-time boundary dissipation $\dot{I}_{\mathrm{irr},\partial}$ (Section 3.2.2):

$$\dot{I}_{\mathrm{irr},\partial} \geq \left[\dot{I}_{\mathrm{env}} - \Omega_\Phi\right]_+, \tag{6.29}$$

where $[x]_+ := \max(x, 0)$. On a statistically homogeneous substrate with $\dot{I}_{\mathrm{env}} \leq \Omega_\Phi$, lossless coupling maintains flat kinematics ($\dot{I}_{\mathrm{irr},\partial} = 0$). Whenever coarse-graining instead concentrates internal capacities $K_{\alpha\alpha}$ unevenly across $\mathrm{im}(\mathbf{P}_{\mathbf{\Pi}})$ or leaves unmodelled capacities and boundary overflow ($\dot{I}_{\mathrm{irr},\partial} > 0$) in $\mathrm{im}(\mathbf{Q}_{\mathbf{\Pi}})$, the emergent metric $g_{\mu\nu}^{[\Phi]}$ itself must curve (Section 6.2).

6.2 GRAVITY

Why does energy–momentum curve spacetime? Standard general relativity postulates $G_{\mu\nu} = \kappa_{\mathrm{G}} T_{\mu\nu}$ without specifying why matter and unresolved energy deform geometry. Within Conservation-Congruent Encoding, gravitational curvature is the direct continuum image of coarse-graining $\mathbf{\Pi}$ across $\mathbf{I} = \mathbf{P}_{\mathbf{\Pi}} + \mathbf{Q}_{\mathbf{\Pi}}$ (2.64), distinct from thermodynamic horizon-state derivations [49, 80, 167]. On the bare loopless graph $G = (V, E)$, every vertex lacks self-loops ($A_{ii} = 0$) and carries strictly negative diagonal Ricci curvature (2.274), so attractive gravitational focusing does not exist prior to coarse-graining. Partitioning G into persistent blocks concentrates internal links into diagonal capacities $K_{\alpha\alpha}$ on $\mathrm{im}(\mathbf{P}_{\mathbf{\Pi}})$ that turn local Ricci curvature positive even in vacuum ($T_{\mu\nu}^{(\mathrm{tracked})}$), while unresolved sub-grid capacities and boundary dissipation on $\mathrm{im}(\mathbf{Q}_{\mathbf{\Pi}})$ enter the nonlinear commutator of the Einstein operator ($T_{\mu\nu}^{(\mathrm{untracked})}$). Changing the coarse-graining scale shifts contributions between these two sectors without altering their conserved sum, making the emergent metric $g_{\mu\nu}^{[\Phi]}$ objective for any declared projection Φ.

6.2.1 *From the Capacity Graph to Continuum Curvature*

Bridging the block capacity graph $G_{\mathbf{K}}$ ($M \geq 3$) to continuum Riemannian slices (Σ, g_{ij}) and a divergence-free spacetime curvature tensor requires separating exact discrete identities on the M-register block space $\mathbb{R}^M$ from differential identities on the three-dimensional spatial tangent bundle $T\Sigma$.

On $\mathbb{R}^M$, three algebraic identities from Chapter 2 hold exactly on every finite partition without manifold assumptions. First, under cut internalisation $[\![\mathrm{diag}, \mathscr{C}_{\mathbf{P}}]\!] = \mathscr{T}_{\mathbf{P}}$ (2.168) and the discrete Ricci commutator $[\![\mathrm{Ric}, \mathscr{C}_{\mathbf{P}}]\!]$ (2.276), encapsulating dense internal subgraphs into heavy blocks yields $K_{\alpha\alpha} > d_\beta + K_{\alpha\beta}$, flipping the diagonal capacity-Ricci curvature $(\mathrm{Ric}_{\mathbf{K}})_{\alpha\alpha}$ (2.274) from strictly negative on the bare graph to strictly positive inside massive registers. Sparse exterior throats carry compensating negative curvature so that global scalar curvature $\mathrm{Scal}_{\mathbf{K}} < 0$ remains fixed by inter-block cuts (2.275) (Example 2.8). Second, across the $n = 3$ spatial spectral axes $\mathbf{z}(\alpha)$ (2.237), dividing the local spectral cut conductance $\Sigma^{ij}(\alpha)$ (dimensionless, (2.311)) by block degree d_α (links) forms the 3×3 degree-normalised cut conductance $\Sigma^{ij}(\alpha)/d_\alpha$ (in links^{-1}). Concentrating internal capacity $K_{\alpha\alpha}$ enlarges d_α in this ratio, depressing $\Sigma^{ij}(\alpha)/d_\alpha$ below the uniform baseline $\bar{\sigma}\,\delta^{ij}$ and stretching resistance distances around heavy blocks as the discrete precursor of a Flamm spatial throat. Third, applying Lemma 2.6 (2.270) to $\mathbf{1}_M$ on a closed capacity Laplacian ($\mathbf{L}_{\mathbf{K}}\mathbf{1}_M = \mathbf{o}$) evaluates the combinatorial Ricci row-sum $\mathrm{div}_{\mathbf{K}}\,\mathrm{Ric}_{\mathbf{K}} \in \mathbb{R}^M$ (links^2) and its exact global cancellation:

$$(\mathrm{div}_{\mathbf{K}}\,\mathrm{Ric}_{\mathbf{K}})_\alpha := \sum_{\beta=1}^{M} (\mathrm{Ric}_{\mathbf{K}})_{\alpha\beta} = d_\alpha^2 - (\mathbf{K}\mathbf{d})_\alpha = (\mathbf{L}_{\mathbf{K}}\mathbf{d})_\alpha, \tag{6.30}$$

$$\sum_{\alpha=1}^{M} (\mathrm{div}_{\mathbf{K}}\,\mathrm{Ric}_{\mathbf{K}})_\alpha = \mathbf{1}_M^{\mathsf{T}}\mathbf{L}_{\mathbf{K}}\mathbf{d} = 0. \tag{6.31}$$

Pointwise row-sums vanish on degree-harmonic regions where $\mathbf{L}_{\mathbf{K}}\mathbf{d} = \mathbf{o}$, including the uniform baseline $d_\alpha = \bar{d}$. For an open subsystem $S \subset V$, omitting bath return across $\mathbf{D}_{\mathbf{K}}^{(\mathrm{ext})} \neq \mathbf{o}$ breaks row-sum closure on the open Dirichlet Laplacian, whereas restoring the Schur boundary self-energy $\mathbf{\Sigma}_{\mathbf{K},\mathrm{env}}$ in $\mathbf{L}_{\mathbf{K},\mathrm{eff}}$ (3.6) restores exact nullspace closure $\mathbf{L}_{\mathbf{K},\mathrm{eff}}\mathbf{1}_M = \mathbf{o}$.

Crucially, both the algebraic curvature $\mathscr{R}_{\mathbf{K}} = \mathbf{S}_{\mathbf{K}} \owedge \mathbf{I}_M$ in (2.280), whose Schouten denominators $M - 2$ and $2(M - 1)$ depend on block count $M \gg 1$, and the scalar row-sum (6.30) act on the M-dimensional register space $\mathbb{R}^M$ rather than on the $d = 3$ tangent space $T_p\Sigma$ of an emergent spatial slice. Coordinate-free simplicial deficit angles [141] and Ollivier–Ricci transport curvature on random geometric graphs sampled from a smooth manifold converge across intermediate diffusion scales to continuum Ricci curvature [78, 123]. Because arbitrary relational graphs satisfying Axioms I–III need not converge automatically to a smooth manifold, passing from discrete block operators on $\mathbb{R}^M$ to differential geometry on a smooth spacetime chart $\mathscr{M}$ rests on an explicit continuum closure hypothesis.

PRINCIPLE 6.3 (Continuum Metric Closure Assumption). Let an embedded observer coarse-grain $G = (V, E)$ under Φ across the persistence window ($K_{\alpha\alpha} \gg 1$) and Weyl diffusion window $\mu_M^{-1} \ll s \ll \mu_2^{-1}$ ($M \gg 1$) in the $(3+1)$-dimensional regime $d_s^{\text{spatial}} = 3$ and $d_s^{\text{time}} = 1$ of Section 6.1. In the geometric phase, the calibrated proper-time increments $\mathrm{d}\tau$ (2.250) and degree-normalised cut conductances $\Sigma^{ij}(\alpha)/d_\alpha$ admit an effective smooth $(3+1)$-dimensional Lorentzian metric $g_{\mu\nu}^{[\Phi]}$ (dimensionless in coordinates $x^\mu = (ct, x^1, x^2, x^3)$) of signature $(-+++)$ on $\mathscr{M}$ whose spatial inverse metric interpolates the baseline-normalised cut conductance at block position x_α:

$$g_{[\Phi]}^{ij}(x_\alpha) \simeq \frac{\Sigma^{ij}(\alpha)}{\bar{\sigma}\, d_\alpha}, \tag{6.32}$$

and whose continuum Ricci tensor $R_{\mu\nu}[g^{[\Phi]}]$ (m^{-2}) reproduces across coarse-grained Weyl neighbourhoods the directional focusing and defocusing of capacity curvature $\mathrm{Ric}_{\mathbf{K}}$ on $G_{\mathbf{K}}$.

Under Principle 6.3, two differential identities hold directly on the emergent tangent bundles $T\Sigma$ and $T\mathscr{M}$. First, whereas a Riemann tensor in $d \geq 4$ spatial dimensions carries independent Weyl conformal components, on each $d = 3$ spatial tangent space $T_p\Sigma$ selected by Theorem 6.1 the three-dimensional Weyl tensor ${}^{(3)}W_{ijkl}$ vanishes identically and the spatial Ricci tensor ${}^{(3)}\mathrm{Ric}$ reconstructs the full spatial Riemann tensor ${}^{(3)}R_{ijkl}$ (m^{-2}):

$${}^{(3)}W_{ijkl} \equiv 0 \qquad (d = 3), \tag{6.33}$$

$${}^{(3)}R_{ijkl} = \left(\left({}^{(3)}\mathrm{Ric} - \frac{1}{4}\,{}^{(3)}R\, g\right) \owedge\, g\right)_{ijkl}. \tag{6.34}$$

Propagating four-dimensional gravitational waves ($W_{\mu\nu\rho\sigma} \neq 0$) arise dynamically once the spatial slices (Σ, g_{ij}) are stacked across time in Section 6.2.2. Second, for the Levi–Civita connection ∇_μ of $g_{\mu\nu}^{[\Phi]}$ on $T\mathscr{M}$, the Ricci tensor alone is generally not divergence-free when scalar curvature $R[g^{[\Phi]}]$ varies across space and time, just as the block row-sum (6.30) equals $\mathbf{L}_{\mathbf{K}}\mathbf{d}$ rather than vanishing on inhomogeneous graphs. Subtracting half the scalar trace defines the continuum Einstein tensor $G_{\mu\nu}[g^{[\Phi]}]$ (m^{-2}) and enforces the exact contracted Bianchi identity:

$$G_{\mu\nu}\big[g^{[\Phi]}\big] := R_{\mu\nu}\big[g^{[\Phi]}\big] - \frac{1}{2} R\big[g^{[\Phi]}\big]\, g_{\mu\nu}^{[\Phi]}, \tag{6.35}$$

$$\nabla^\mu G_{\mu\nu}\big[g^{[\Phi]}\big] = \nabla^\mu R_{\mu\nu}\big[g^{[\Phi]}\big] - \frac{1}{2}\nabla_\nu R\big[g^{[\Phi]}\big] = 0. \tag{6.36}$$

6.2.2 *Coarse-Grained Stress–Energy and the Einstein Field Equation*

Under the observation projection $\Phi : \mathscr{X}_{\bar{S}} \to \mathscr{Z}$ (Section 4.1, (4.11)), the extended coarse-grained state (2.309) on each spatial hypersurface Σ comprises

the spatial metric g_{ij}, its conjugate momentum density π^{ij}, resolved matter and gauge fields Ψ, and coarse-grained entropy S (in nats):

$$Z_\Phi := \Phi(X), \tag{6.37}$$

$$Z_\Phi[\Sigma] = \big(g_{ij}, \pi^{ij}, \Psi, S\big)_\Sigma. \tag{6.38}$$

Eliminating unresolved degrees of freedom in $\mathrm{im}(\mathbf{Q_\Pi})$ induces the boundary cometric $\mathbb{M}_\partial$ (Section 3.2.2, (3.11)), accumulating boundary dissipation along any worldline γ parameterised by proper time τ:

$$I_{\mathrm{irr},\partial}[Z_\Phi] := \int_\gamma \dot{I}_{\mathrm{irr},\partial}\,\mathrm{d}\tau = \int_\gamma \nabla S(Z_\Phi)\cdot \mathbb{M}_\partial(Z_\Phi)\nabla S(Z_\Phi)\,\mathrm{d}\tau \geq 0. \tag{6.39}$$

Stacking the Riemannian slices (Σ, g_{ij}) across $x^0 = ct$ in an Arnowitt–Deser–Misner (ADM) foliation [3] with dimensionless lapse $N_{\mathrm{lapse}} > 0$, shift velocity $\mathbf{N} = (N^i)$ $(\mathrm{m\,s^{-1}})$, and future-pointing unit timelike normal $\hat{n}^\mu$ defines the ADM extrinsic curvature $\mathscr{K}_{ij}$ (in $\mathrm{m^{-1}}$, written in calligraphic script to distinguish it from capacity blocks $K_{\alpha\beta}$) and evolves $Z_\Phi[\Sigma]$ under the extended coarse-grained generator $H_\Phi := H_{\mathrm{tracked}} + H_{\mathrm{untracked}}$ (Section 2.5.2 and Section 3.2):

$$\mathscr{K}_{ij} := -\frac{1}{2}\mathscr{L}_{\hat{n}} g_{ij} = -\frac{1}{2cN_{\mathrm{lapse}}}\big(\dot{g}_{ij} - \mathscr{L}_{\mathbf{N}} g_{ij}\big), \tag{6.40}$$

$$\dot{g}_{ij} = \big\{g_{ij}, H_\Phi\big\} + \big(g_{ij}, S\big)_{H_\Phi}, \tag{6.41}$$

$$\dot{A} = \{A, H_\Phi\} + (A, S)_{H_\Phi}, \tag{6.42}$$

for any coarse-grained observable $A(Z_\Phi)$, where the symmetric bracket $(\cdot,\cdot)_{H_\Phi}$ is generated by the Kulkarni–Nomizu mobility tensor R^{abcd} (2.317)–(2.320) [115]. By the Kulkarni–Nomizu Casimir degeneracy $(H_\Phi, S)_{H_\Phi} = 0$ (2.324) and the sector cometric split $\mathbb{M} = \mathbb{M}_\Omega + \mathbb{M}_\partial$ (3.9), dissipative exchange transfers energy from H_{tracked} into the entropy-bearing reservoir $H_{\mathrm{untracked}}$ while keeping the total generator H_Φ strictly conserved:

$$\dot{H}_\Phi = \{H_\Phi, H_\Phi\} + (H_\Phi, S)_{H_\Phi} = 0, \tag{6.43}$$

$$\dot{S} = \{S, H_\Phi\} + (S, S)_{H_\Phi} = \dot{I}_{\mathrm{irr},\Omega} + \dot{I}_{\mathrm{irr},\partial} \geq \dot{I}_{\mathrm{irr},\partial} \geq 0. \tag{6.44}$$

Why do both quiet baryonic masses and unresolved sub-grid dynamics curve the coarse-grained metric $g_{\mu\nu}^{[\Phi]}$? Let $g_{\mu\nu}^{[\Phi^{(1)}]}$ denote any finer Weyl-window metric coarsened to $g_{\mu\nu}^{[\Phi]} := \mathbf{P_\Pi}[g_{\mu\nu}^{[\Phi^{(1)}]}]$ across $\Phi = \Phi^{(1)}\mathbf{P_\Pi}$ via Theorem 2.2. Because the Einstein tensor $G_{\mu\nu}$ is quadratic in the Levi–Civita connection $\Gamma^\lambda_{\mu\nu}$, evaluating $G_{\mu\nu}$ on $g_{\mu\nu}^{[\Phi]}$ does not commute with $\mathbf{P_\Pi}$. Applying the coarse-graining commutator (2.166) of Lemma 2.3 across $g_{\mu\nu}^{[\Phi^{(1)}]} \mapsto g_{\mu\nu}^{[\Phi]}$ with empirical gravitational coupling κ_{G} (in $\mathrm{m\,J^{-1}}$, calibrated by Newton's constant G in

$\mathrm{m}^3\,\mathrm{kg}^{-1}\,\mathrm{s}^{-2}$) defines the tracked, untracked, and total stress–energy tensors (in $\mathrm{J\,m}^{-3}$):

$$\kappa_{\mathrm{G}} := \frac{8\pi G}{c^4}, \tag{6.45}$$

$$[\![G_{\mu\nu}, \mathbf{P}_{\mathbf{\Pi}}]\!]\big(g^{[\Phi^{(1)}]}\big) = G_{\mu\nu}\big[g^{[\Phi]}\big] - \mathbf{P}_{\mathbf{\Pi}}\Big[G_{\mu\nu}\big[g^{[\Phi^{(1)}]}\big]\Big] \tag{6.46}$$

$$= \kappa_{\mathrm{G}}\, T_{\mu\nu}^{(\mathrm{untracked})},$$

$$T_{\mu\nu}^{(\mathrm{total})} := T_{\mu\nu}^{(\mathrm{tracked})} + T_{\mu\nu}^{(\mathrm{untracked})}. \tag{6.47}$$

Here $\mathbf{P}_{\mathbf{\Pi}}[G_{\mu\nu}[g^{[\Phi^{(1)}]}]] = \kappa_{\mathrm{G}} T_{\mu\nu}^{(\mathrm{tracked})}$ captures the resolved fields Ψ, where persistent particles acquire rest mass m proportional to $\mathrm{Tr}(\mathbf{K}_\Omega)$ via (5.4) from concentrated intra-block capacities $\mathbf{K}_\Omega$ and generate positive Ricci focusing $(\mathrm{Ric}_{\mathbf{K}})_{\alpha\alpha} > 0$ (2.276) even in quiet vacuum ($\dot{I}_{\mathrm{irr},\partial} = 0$). Complementarily, the commutator (6.46)—the continuum counterpart of Lemma 2.3 alongside the Schur boundary residual $-\mathbf{\Sigma}_{\mathrm{env}}$ (2.171)—collects all curvature generated across the open-observer residual projector $\mathbf{Q}_{\widetilde{\mathbf{\Pi}}_S}$ (2.69) between $\Phi^{(1)}$ and Φ, encompassing both unmodelled intra-basin capacities in $\mathbf{K}_\Omega$ and irreversible boundary dissipation $I_{\mathrm{irr},\partial}$ driven by $(g_{ij}, S)_{H_\Phi}$ (6.41) and calibrated into $\mathrm{J\,m}^{-3}$ at substrate noise intensity θ ($\mathrm{J\,nat}^{-1}$).

How does non-Hamiltonian drift $(g_{ij}, S)_{H_\Phi}$ and $(\pi^{ij}, S)_{H_\Phi}$ remain compatible with ADM constraint preservation across slices? Because open dissipation acts across $\mathrm{im}(\mathbf{Q}_{\mathbf{\Pi}})$, the tracked canonical fields alone do not close the ADM constraints when $\dot{I}_{\mathrm{irr},\partial} > 0$. Instead, the Casimir identity $(H_\Phi, S)_{H_\Phi} = 0$ (6.43) transfers every unit of energy–momentum lost from the tracked sector into $T_{\mu\nu}^{(\mathrm{untracked})}$. With trace $\mathscr{K} := g^{ij}\mathscr{K}_{ij}$, spatial covariant derivative D_j on (Σ, g_{ij}), and spatial projector $h_i{}^\mu$, varying the total generator H_Φ across $(N_{\mathrm{lapse}}, N^i)$ closes the Gauss–Codazzi ADM Hamiltonian and momentum constraints (both in m^{-2}) on the combined source $T_{\mu\nu}^{(\mathrm{total})}$:

$${}^{(3)}R + \mathscr{K}^2 - \mathscr{K}_{ij}\mathscr{K}^{ij} = 2\kappa_{\mathrm{G}}\, T_{\mu\nu}^{(\mathrm{total})}\hat{n}^\mu\hat{n}^\nu, \tag{6.48}$$

$$D_j\big(\mathscr{K}^j{}_i - \delta_i^j\mathscr{K}\big) = -\kappa_{\mathrm{G}}\, h_i{}^\mu T_{\mu\nu}^{(\mathrm{total})}\hat{n}^\nu. \tag{6.49}$$

Combining (6.46)–(6.49) with the contracted Bianchi identity (6.36) yields the coarse-grained Einstein field equation and tracked–untracked covariant exchange law:

$$G_{\mu\nu}\big[g^{[\Phi]}\big] = \kappa_{\mathrm{G}}\left(T_{\mu\nu}^{(\mathrm{tracked})} + T_{\mu\nu}^{(\mathrm{untracked})}\right), \tag{6.50}$$

$$\nabla^\mu\left(T_{\mu\nu}^{(\mathrm{tracked})} + T_{\mu\nu}^{(\mathrm{untracked})}\right) = 0, \tag{6.51}$$

$$\nabla^\mu T_{\mu\nu}^{(\mathrm{tracked})} = -\nabla^\mu T_{\mu\nu}^{(\mathrm{untracked})}. \tag{6.52}$$

Just as $\mathbf{D}_{\mathbf{K}}^{(\mathrm{ext})} \neq \mathbf{o}$ breaks open-subsystem conservation until closed by $\mathbf{\Sigma}_{\mathbf{K},\mathrm{env}}$, tracked stress alone need not satisfy $\nabla^\mu T_{\mu\nu}^{(\mathrm{tracked})} = 0$ across dissipative boundaries, whereas its exchange (6.52) with $T_{\mu\nu}^{(\mathrm{untracked})}$ closes (6.51) identically. Taking the formal fine-grained limit $\Phi^{(1)} \to \mathrm{id}$ below the Weyl diffusion window does not leave a smooth metric with $T_{\mu\nu}^{(\mathrm{untracked})} = 0$, because withdrawing coarse-graining altogether dissolves the continuum chart itself back into the bare graph $G = (V, E)$.

6.2.3 *Proper-Time Arrow, Geodesic Attraction, and Horizon Saturation*

Along any timelike worldline γ in signature $(-+++)$, internal memory updates along $\mathbf{K}_\Omega$ accumulate the curved-spacetime proper-time interval and worldline functional $\tau_\Phi[\gamma]$:

$$\mathrm{d}\tau^2 = -\frac{1}{c^2} g^{[\Phi]}_{\mu\nu}\, \mathrm{d}x^\mu \mathrm{d}x^\nu, \tag{6.53}$$

$$\tau_\Phi[\gamma] = \frac{1}{c}\int_\gamma \sqrt{-g^{[\Phi]}_{\mu\nu}\, \mathrm{d}x^\mu \mathrm{d}x^\nu}, \tag{6.54}$$

whose intrinsic distinction integral $\Omega_\Phi \tau_\Phi[\gamma] = \tau_{\mathrm{nat},T}$ generalises the intrinsic proper-time horizon of (2.244), with $\tau_\Phi[\gamma] \equiv \tau_T$ in (2.256). Although (6.53) is quadratic in $\mathrm{d}x^\mu$, coarse-grained histories cannot run backwards in τ. Because S is a Poisson Casimir (2.322), advancing along any monotonically increasing trajectory parameter λ ($\mathrm{d}\lambda/\mathrm{d}\tau > 0$) drives non-decreasing entropy solely through the metric bracket:

$$\frac{\mathrm{d}S}{\mathrm{d}\lambda} = (S,S)_{H_\Phi} \geq 0, \tag{6.55}$$

$$\frac{\mathrm{d}S}{\mathrm{d}\tau} = \frac{\mathrm{d}\lambda}{\mathrm{d}\tau}(S,S)_{H_\Phi} \geq 0. \tag{6.56}$$

Metric curvature in (6.50) simultaneously explains gravitational attraction and clock redshift while upholding the Einstein Equivalence Principle. Relative to four-velocity u^μ, the induced spatial metric and stationary temporal support factor $\chi_g(x)$ ($g^{[\Phi]}_{0i} = 0$) read:

$$h_{\mu\nu} = g^{[\Phi]}_{\mu\nu} + \frac{u_\mu u_\nu}{c^2}, \tag{6.57}$$

$$\mathrm{d}\ell^2 = h_{\mu\nu}\, \mathrm{d}x^\mu \mathrm{d}x^\nu, \tag{6.58}$$

and for a clock held stationary at fixed spatial coordinates ($\mathrm{d}x^i = 0$), temporal support $\chi_g(x)$, gravitational clock dilation $\mathrm{d}t/\mathrm{d}\tau$, and photon redshift $1+z$ satisfy:

$$\chi_g(x) := -g^{[\Phi]}_{00}(x) > 0, \tag{6.59}$$

$$\frac{\mathrm{d}t}{\mathrm{d}\tau} = \frac{1}{\sqrt{\chi_g(x)}}, \tag{6.60}$$

$$1+z = \frac{(u_\mu k^\mu)_{\mathrm{em}}}{(u_\mu k^\mu)_{\mathrm{obs}}}. \tag{6.61}$$

Near any resolved or unresolved mass concentration, positive Ricci focusing depresses temporal support below unity ($\chi_g(x) < 1$, with $\chi_g(x) \simeq 1 + 2\Phi_{\mathrm{N}}(x)/c^2$ in a weak Newtonian potential $\Phi_{\mathrm{N}} < 0$). An unforced CCE in free fall ($a^\mu = 0$) expends zero boundary station-keeping thrust and extremises its accumulated internal reversible updates $\Omega_\Phi \tau_\Phi[\gamma]$:

$$\delta \int_\gamma \mathrm{d}I_{\mathrm{int}} = \Omega_\Phi\, \delta\tau_\Phi[\gamma] = 0, \tag{6.62}$$

$$\ddot{\mathbf{x}} \simeq -\nabla\Phi_{\mathrm{N}}(\mathbf{x}), \tag{6.63}$$

bending trajectories towards regions of deeper metric depression in exact agreement with conservative Poisson flow $\{Z, H_{\text{tracked}}\}$ (2.313). Conversely, holding a clock at fixed spatial coordinates ($v = 0, a^\mu \neq 0$) diverts reversible updates into outward boundary station-keeping against the metric gradient, slowing stationary proper ticks by $\mathrm{d}\tau = \sqrt{\chi_g(x)}\,\mathrm{d}t$. Because Ω_Φ cancels identically in (6.60)–(6.63), gravitational time dilation and free-fall acceleration are strictly universal across all clock substrates, including thermally shielded or cryogenically cooled detectors.

For a timelike worldline congruence with unit tangent $\hat{u}^\mu := u^\mu/c$, shear $\sigma_{\mu\nu}$, vorticity $\omega_{\mu\nu}$, and four-acceleration $a^\mu := \hat{u}^\nu \nabla_\nu \hat{u}^\mu$, volumetric focusing and expansion follow the Raychaudhuri equation [140] in terms of the expansion scalar Θ_{exp} (m^{-1}):

$$\Theta_{\text{exp}} := \nabla_\mu \hat{u}^\mu, \tag{6.64}$$

$$\hat{u}^\nu \nabla_\nu \Theta_{\text{exp}} = -\frac{1}{3}\Theta_{\text{exp}}^2 - \sigma_{\mu\nu}\sigma^{\mu\nu} + \omega_{\mu\nu}\omega^{\mu\nu} - R_{\mu\nu}\hat{u}^\mu \hat{u}^\nu + \nabla_\mu a^\mu, \tag{6.65}$$

where the untracked sector contributes via (6.50) with trace $T^{(\text{untracked})}$:

$$\left(R_{\mu\nu}\hat{u}^\mu \hat{u}^\nu\right)_{\text{untracked}} = \kappa_{\text{G}} \left(T_{\mu\nu}^{(\text{untracked})} \hat{u}^\mu \hat{u}^\nu + \frac{1}{2} T^{(\text{untracked})}\right), \tag{6.66}$$

$$T^{(\text{untracked})} := g_{[\Phi]}^{\mu\nu} T_{\mu\nu}^{(\text{untracked})}. \tag{6.67}$$

Concentrated intra-basin stress with positive Raychaudhuri source in (6.66) drives attractive focusing ($\hat{u}^\nu \nabla_\nu \Theta_{\text{exp}} < 0$), whereas untracked stress violating the strong energy condition ($T_{\mu\nu}^{(\text{untracked})} \hat{u}^\mu \hat{u}^\nu + (1/2) T^{(\text{untracked})} < 0$) drives congruence defocusing ($\hat{u}^\nu \nabla_\nu \Theta_{\text{exp}} > 0$) without postulating an elementary negative-pressure fluid.

Relative to stationary proper-time increments $\sqrt{\chi_g(x)}\,\mathrm{d}t$, when gravitational compression drives $\chi_g(x) \to 0^+$ so coordinate null speed $\mathrm{d}\ell/\mathrm{d}t = c\sqrt{\chi_g(x)}$ vanishes, the outward acceleration a^μ required to hover at fixed coordinates diverges, saturating the reversible distinction balance (6.2) alongside the local null transport boundary:

$$\mathrm{d}I_{\text{ext}} \longrightarrow \mathrm{d}I_{\text{total}}, \tag{6.68}$$

$$\mathrm{d}I_{\text{int}} \longrightarrow 0, \tag{6.69}$$

$$g_{\mu\nu}^{[\Phi]}\,\mathrm{d}x^\mu \mathrm{d}x^\nu = 0 \iff \frac{\mathrm{d}\ell}{\sqrt{\chi_g(x)}\,\mathrm{d}t} = c. \tag{6.70}$$

A black hole horizon is this stationary allocation limit, where station-keeping consumes the entire reversible budget and collapses stationary proper time while freely falling observers ($a^\mu = 0$) cross in finite τ. Here c ($\mathrm{m\,s}^{-1}$) is not a Shannon channel rate (Ω_Φ in nats s^{-1}), but the continuum conversion scale between resistance distance $\Omega_{\alpha\beta}$ on $\mathbf{K}_\partial$ and reference time on $\mathbf{K}_\Omega$, realising the multi-slice graph-routing bound $\Delta\tau_{\text{compare}} \geq \text{dist}_{G_{\mathbf{K}}}(\alpha, \beta)$ of (2.310) and (4.80). Whenever an observer traverses an ambient bath of coordinate-frame arrival rate $\dot{I}_{\text{env},0} > 0$ (nats s^{-1}) at local stationary speed $v < c$ (measured

per stationary increment $\sqrt{\chi_g(x)}\,\mathrm{d}t$) in temporal support $\chi_g(x)$, kinematic and gravitational clock compression combine into the dimensionless tracking factor $\mathscr{R}_\Phi(v,x)$, blueshifting the incoming environmental arrival rate $\dot{I}_{\mathrm{env}}(v,x) := \mathrm{d}I_{\mathrm{env}}/\mathrm{d}\tau$ (nats s^{-1}) per unit observer proper time:

$$\mathscr{R}_\Phi(v,x) := \frac{\gamma_{\mathrm{L}}(v)}{\sqrt{\chi_g(x)}}, \tag{6.71}$$

$$\frac{\mathrm{d}\tau}{\mathrm{d}t} = \mathscr{R}_\Phi^{-1}(v,x) = \frac{\sqrt{\chi_g(x)}}{\gamma_{\mathrm{L}}(v)}, \tag{6.72}$$

$$\dot{I}_{\mathrm{env}}(v,x) = \mathscr{R}_\Phi(v,x)\,\dot{I}_{\mathrm{env},0}. \tag{6.73}$$

For $\sqrt{\chi_g(x)}\,\Omega_\Phi > \dot{I}_{\mathrm{env},0}$, lossless tracking via (6.29) holds only below the velocity ceiling in (6.74), while either $v \to c^-$ or $\chi_g(x) \to 0^+$ drives $\mathscr{R}_\Phi(v,x)$ and proper-time boundary dissipation $\dot{I}_{\mathrm{irr},\partial}(v,x)$ (nats s^{-1}) to diverge:

$$v < c\sqrt{1 - \left(\frac{\dot{I}_{\mathrm{env},0}}{\sqrt{\chi_g(x)}\,\Omega_\Phi}\right)^2}, \tag{6.74}$$

$$\lim_{v\to c^-} \mathscr{R}_\Phi(v,x) = \lim_{\chi_g(x)\to 0^+} \mathscr{R}_\Phi(v,x) = \infty, \tag{6.75}$$

$$\dot{I}_{\mathrm{irr},\partial}(v,x) \geq \left[\mathscr{R}_\Phi(v,x)\,\dot{I}_{\mathrm{env},0} - \Omega_\Phi\right]_+ \longrightarrow \infty. \tag{6.76}$$

On every spatial slice, static link allocation obeys $\mathscr{Q}_{\mathrm{alloc}} \leq \mathscr{Q}_{\mathrm{total}}$ and $\mathscr{Q}_{\mathrm{free}} \geq 0$ (2.200) unconditionally (Theorem 2.4), because neither Lorentz boosts nor stationary redshift alter the combinatorial link incidences of $G_{\mathbf{K}}$ (Section 6.1.2). What $\mathscr{R}_\Phi(v,x)$ compresses is the observer's uncommitted proper-time reversible bandwidth $\Omega_{\mathrm{free}}(\tau)$ (in nats s^{-1}), which remains strictly positive only above a dimensionless critical temporal support floor $\chi_g^{\mathrm{crit}}(v)$:

$$\Omega_{\mathrm{free}}(\tau) := \left[\Omega_\Phi - \mathscr{R}_\Phi(v,x)\,\dot{I}_{\mathrm{env},0}\right]_+ \geq 0, \tag{6.77}$$

$$\chi_g^{\mathrm{crit}}(v) := \gamma_{\mathrm{L}}^2(v)\left(\frac{\dot{I}_{\mathrm{env},0}}{\Omega_\Phi}\right)^2, \tag{6.78}$$

$$\Omega_{\mathrm{free}}(\tau) > 0 \iff \chi_g(x) > \chi_g^{\mathrm{crit}}(v). \tag{6.79}$$

Whenever $\chi_g(x) > \chi_g^{\mathrm{crit}}(0)$, the temporal support threshold (6.79) coincides identically with the velocity bound (6.74), whereas at or below $\chi_g^{\mathrm{crit}}(v)$ uncommitted proper-time bandwidth saturates at $\Omega_{\mathrm{free}}(\tau) = 0$ without violating $\mathscr{Q}_{\mathrm{free}} \geq 0$ and spills excess arrivals into $\dot{I}_{\mathrm{irr},\partial}(v,x)$ via (6.76). In flat vacuum ($\dot{I}_{\mathrm{env},0} = 0$), both $\mathscr{Q}_{\mathrm{free}}$ and $\Omega_{\mathrm{free}}(\tau) = \Omega_\Phi$ remain boost-invariant. In an ambient bath ($\dot{I}_{\mathrm{env},0} > 0$), sustained through-time agency ($\chi_T > 0$) requires both static structural slack $\mathscr{Q}_{\mathrm{free}}(x) > 0$ (Theorem 3.4) and positive proper-time bandwidth $\Omega_{\mathrm{free}}(\tau) > 0$, situating viable observers between sparse intergalactic voids with low $\mathscr{Q}_{\mathrm{total}}(x)$ and near-horizon saturation at $\chi_g(x) \leq \chi_g^{\mathrm{crit}}(v)$ and favouring intermediate planetary wells.

6.3 COSMOLOGICAL HORIZONS

A differential field equation such as (6.50) can be formally integrated to $t \to 0$ or $t \to \infty$ even where no embedded subsystem $S \subset V$ can store or verify its extrapolated states. Treating those infinite mathematical limits as observer-independent physical reality commits the Platonic Observer Fallacy (Section 4.1.1). By Theorem 4.1 (4.13)–(4.4), any observer enclosed within a smooth operational boundary ∂S of area $A_{\partial S}$ resolves at most $M \leq \lfloor N_S/2 \rfloor$ blocks ($M < |\mathcal{X}_{\bar{S}}|$) under $Z_t = \Phi(X_t)$, subject independently to an upper holographic memory bound [11, 12, 75] (without assuming horizon saturation) and a finite pathwise dissipation budget $W^{(S)}_{\max,[t_a,t_b]}$ (4.10) at substrate noise scale θ:

$$I(X_t; Z_t) \leq I_{\mathrm{rev},\Omega}(t) \leq I^{\mathrm{cap}}_{\Phi} \leq \frac{A_{\partial S}}{4\ell_{\mathrm{P}}^2} < \infty, \tag{6.80}$$

$$I_{\mathrm{irr},\partial,[t_a,t_b]}[\gamma] = \int_{t_a}^{t_b} \dot{I}_{\mathrm{irr},\partial}(t)\,\mathrm{d}t \leq I^{(S)}_{\mathrm{irr},\max,[t_a,t_b]} := \frac{W^{(S)}_{\max,[t_a,t_b]}}{\theta} < \infty. \tag{6.81}$$

Auditing backward and forward cosmic extrapolations against (6.80)–(6.81) replaces singular origins and infinite-horizon equilibria with well-defined epistemic horizons.

6.3.1 *Retrodictive Divergence and Past Resolution Limits*

To reconstruct the cosmic state at an earlier epoch $t < t_0$ from a present coarse-grained record $z_{t_0} \in \mathcal{Z}$, the observer faces multi-slice backward branching (Definition 4.2, (4.17)), since Φ is many-to-one and trajectories from $k_- \geq 2$ distinct past blocks $\{\bar{S}_j\}_{j=1}^{k_-}$ merge into $\Phi^{-1}(\{z_{t_0}\})$. Across those k_- reachable past blocks, the posterior weights $p_j(t \mid z_{t_0})$ define the retrodictive branch load $B^-_{\Phi}(t; z_{t_0})$ (in nats):

$$p_j(t \mid z_{t_0}) = \int_{\bar{S}_j} p(x_t \mid z_{t_0})\,\mathrm{d}\mu_t(x_t), \tag{6.82}$$

$$B^-_{\Phi}(t; z_{t_0}) := -\sum_{j=1}^{k_-} p_j(t \mid z_{t_0}) \ln p_j(t \mid z_{t_0}) \leq \ln k_-, \tag{6.83}$$

which by Theorem 4.3 (4.19) requires boundary dissipation $I_{\mathrm{irr},\partial,T} \geq B^-_{\Phi}(t; z_{t_0})$ to resolve. Past distinctions reach the observer along a past-directed causal light-sheet [22] of cross-sectional area $A_-(\lambda_-)$ (m^2) at backward affine parameter $\lambda_-(t)$ (m). Tracked retrodiction requires $B^-_{\Phi}(t; z_{t_0})$ to fit simultaneously within I^{cap}_{Φ} and the covariant light-sheet capacity $A_-(\lambda_-)/(4\ell_{\mathrm{P}}^2)$ (6.80), setting a strictly positive past area floor $A^{\min}_{\Phi}(t)$:

$$B^-_{\Phi}(t; z_{t_0}) \leq \min\left\{ I^{\mathrm{cap}}_{\Phi}, \frac{A_-(\lambda_-)}{4\ell_{\mathrm{P}}^2} \right\}, \tag{6.84}$$

$$A_-(\lambda_-) \geq A^{\min}_{\Phi}(t) := 4\ell_{\mathrm{P}}^2 B^-_{\Phi}(t; z_{t_0}). \tag{6.85}$$

The earliest backward epoch $t_\Phi^- < t_0$ at which the past light-sheet contracts below $A_\Phi^{\min}(t)$ (or $B_\Phi^-(t; z_{t_0})$ exceeds I_Φ^{cap}) defines the backward epistemic horizon, beyond which tracked reconstruction fails in *retrodictive divergence*.

Equations (6.83)–(6.85) refute the physical inference of a zero-volume Big Bang singularity. Classical Hawking–Penrose theorems [76] integrate (6.65) backwards along $\hat{u}_-^\mu := -\hat{u}^\mu$ for the past-directed expansion $\Theta_- := -\Theta_{\text{exp}} < 0$ of an irrotational ($\omega_{\mu\nu} = 0$), geodesic ($a^\mu = 0$) congruence under $R_{\mu\nu}\hat{u}_-^\mu\hat{u}_-^\nu \geq 0$, mirrored on the past light-sheet $A_-(\lambda_-)$ by null focusing with prefactor $-1/2$ under the null energy condition:

$$\frac{\mathrm{d}\Theta_-}{\mathrm{d}\lambda_-} = -\frac{1}{3}\Theta_-^2 - \sigma_{\mu\nu}\sigma^{\mu\nu} - R_{\mu\nu}\hat{u}_-^\mu\hat{u}_-^\nu \leq -\frac{1}{3}\Theta_-^2, \tag{6.86}$$

$$\lim_{\lambda_- \to \lambda_{\text{origin}}^-} \Theta_-(\lambda_-) = -\infty. \tag{6.87}$$

Continuing (6.86)–(6.87) to $A_-(\lambda_-) \to 0$ fails physically across three coupled thresholds. First, as $A_-(\lambda_-)$ contracts towards $A_\Phi^{\min}(t)$ while $B_\Phi^-(t; z_{t_0})$ grows, $\dot{I}_{\text{env}}$ exceeds Ω_Φ (6.29), shifting source weight from $T_{\mu\nu}^{(\text{tracked})}$ into $T_{\mu\nu}^{(\text{untracked})}$ in (6.50). Second, once past light-sheet cross-sections reach the discrete Weyl cutoff μ_M^{-1} where finite substrate valence $d_i \leq d_{\max}$ (2.194) saturates block degrees, the spectral chart $\mathbf{\Phi}$ (2.236) ceases to approximate a smooth manifold while the underlying graph curvature $\text{Ric}_\mathbf{K}$ remains strictly finite. Third, by Corollary 4.4, refining a positive initial past cross-section $A_-(\lambda_{-,0}) > 0$ to $A_-(\lambda_-) \to 0^+$ drives both preserved capacity and reset work to infinity:

$$I_{\text{rev}}(\lambda_-) \geq \frac{A_-(\lambda_{-,0})}{A_-(\lambda_-)} \ln 2 \xrightarrow{A_-(\lambda_-)\to 0^+} \infty, \tag{6.88}$$

$$W_{\text{diss}}(\lambda_-) \geq \theta \ln\left(\frac{A_-(\lambda_{-,0})}{A_-(\lambda_-)}\right) \xrightarrow{A_-(\lambda_-)\to 0^+} \infty, \tag{6.89}$$

violating (6.80)–(6.81). Universal redshift $1 + z$ (6.61) and cosmic microwave thermalisation reflect coarse-grained curvature in (6.50) rather than licensing extrapolation to $A_-(\lambda_-) = 0$, and the apparent singularity is retrodictive divergence at t_Φ^-.

6.3.2 *Predictive Signal Dilution and the Epistemic Bubble*

In the forward direction ($t > t_0$), trajectories bundled inside $\Phi^{-1}(\{z_{t_0}\})$ disperse across $k_+ > 1$ reachable future blocks (4.16) while open boundary damping $(A, S)_{H_\Phi}$ erodes phase correlations. Unlike the observer's incoming past light-sheet $A_-(\lambda_-)$ carrying cosmic retrodictive branch load $B_\Phi^-(t; z_{t_0})$, forward resolution tracks a separate outgoing point-source or predictive causal wavefront of cross-sectional area $A_+(\lambda_+)$ (m²) at forward affine parameter $\lambda_+(t)$ (m). Near a localised emitter, $A_+(\lambda_+)$ can start at compact cross-sections $A_+(\lambda_+) \ll A_\Phi^{\min}(t)$ without triggering retrodictive divergence, because $A_\Phi^{\min}(t)$ constrains only $A_-(\lambda_-)$. Instead, by data processing and (6.80), surviving predictive mutual information $I(Z_{t_0}; R_t)$ cannot exceed I_Φ^{cap}, while an outgoing signal of energy $E_{\text{signal}} > 0$ (J) spreading across $A_+(\lambda_+)$ remains

resolvable against detector fluence noise floor $\rho_{\text{noise}} > 0$ ($\mathrm{J\,m^{-2}}$) only up to a finite outgoing area ceiling $A_\Phi^{\max}$:

$$I(Z_{t_0}; R_t) \le I_{\text{rev},\Omega}(t_0) \le I_\Phi^{\text{cap}}, \tag{6.90}$$

$$\frac{E_{\text{signal}}}{A_+(\lambda_+)} \ge \rho_{\text{noise}}, \tag{6.91}$$

$$A_+(\lambda_+) \le A_\Phi^{\max} := \frac{E_{\text{signal}}}{\rho_{\text{noise}}} < \infty. \tag{6.92}$$

The forward epoch $t_\Phi^+ > t_0$ at which the outgoing wavefront $A_+(\lambda_+)$ expands past $A_\Phi^{\max}$ (or $I(Z_{t_0}; R_t)$ falls below the detector noise floor) defines the forward epistemic horizon, beyond which outgoing distinctions are lost to *predictive dissipation*.

Equations (6.90)–(6.92) similarly rule out operational claims of universal Heat Death [34, 67]. Postulating a global entropy of a closed cosmos presupposes an external spectator enclosing V, violating Theorem 4.1. As trajectories cross t_Φ^+ or the causal horizon (6.80), $I(Z_{t_0}; R_t) \to 0$ transfers distinctions from $T_{\mu\nu}^{(\text{tracked})}$ into $T_{\mu\nu}^{(\text{untracked})}$ rather than halting substrate dynamics. Under (6.42), Casimir conservation preserves total coarse-grained energy ($\dot{H}_\Phi = 0$, (6.43)) while any open multi-basin subsystem ($M \ge 2$) retains $\mathcal{Q}_{\text{free}} > 0$ via the ℓ_2–ℓ_1 norm gap (2.200), operating indefinitely as a generative dissipator (Definition 3.10) by exporting boundary entropy across its local horizon.

Pairing the past light-sheet floor (6.85) with the outgoing wavefront ceiling (6.92) confines every embedded observer to a compact temporal interval $\mathscr{D}_\Phi := [t_\Phi^-, t_\Phi^+]$—its *Epistemic Bubble*—bounded at its past and future horizons by two distinct causal congruences.

THEOREM 6.4 (Cosmological Epistemic Horizon Bounds). *Let $S \subset V$ be an embedded observing subsystem at epoch t_0 with finite structural capacity ceiling $I_\Phi^{\text{cap}} < \infty$, past light-sheet cross-sectional area $A_-(\lambda_-) > 0$ ($t \le t_0$) carrying retrodictive branch load $0 < B_\Phi^-(t; z_{t_0}) \le I_\Phi^{\text{cap}}$, and outgoing predictive wavefront cross-sectional area $A_+(\lambda_+) > 0$ ($t \ge t_0$) carrying signal energy $E_{\text{signal}} > 0$ against detector fluence noise floor $\rho_{\text{noise}} > 0$. Tracked reconstruction across $\mathscr{D}_\Phi = [t_\Phi^-, t_\Phi^+]$ is physically admissible if and only if the incoming past light-sheet and outgoing predictive wavefront satisfy their respective causal area bounds:*

$$A_-(\lambda_-) \ge A_\Phi^{\min}(t) := 4\ell_{\text{P}}^2 B_\Phi^-(t; z_{t_0}), \tag{6.93}$$

$$A_+(\lambda_+) \le A_\Phi^{\max} := \frac{E_{\text{signal}}}{\rho_{\text{noise}}}. \tag{6.94}$$

Any backward extrapolation with $A_-(\lambda_-) < A_\Phi^{\min}(t)$ ($t < t_\Phi^-$) fails by retrodictive divergence and any forward extrapolation with $A_+(\lambda_+) > A_\Phi^{\max}$ ($t > t_\Phi^+$) fails by predictive dissipation, transferring unresolvable distinctions from $T_{\mu\nu}^{(\text{tracked})}$ into $T_{\mu\nu}^{(\text{untracked})}$.

PROOF. Since $B_\Phi^-(t; z_{t_0}) \le I_\Phi^{\mathrm{cap}}$ and $4\ell_P^2 > 0$, the retrodictive capacity condition (6.84) on the past light-sheet is equivalent to $B_\Phi^-(t; z_{t_0}) \le A_-(\lambda_-)/(4\ell_P^2)$, and thus to (6.93). Independently, for $A_+(\lambda_+) > 0$ and $\rho_{\mathrm{noise}} > 0$, the predictive signal-to-noise condition (6.91) on the outgoing wavefront is equivalent to $E_{\mathrm{signal}}/A_+(\lambda_+) \ge \rho_{\mathrm{noise}}$, and thus to (6.94). Outside $\mathscr{D}_\Phi = [t_\Phi^-, t_\Phi^+]$, violating either bound transfers unresolvable distinctions into $T_{\mu\nu}^{(\mathrm{untracked})}$ via (6.46). □

EXAMPLE 6.1 (Epistemic Horizon Bounds of an Embedded Cosmic Observatory). Consider an embedded cosmic observatory whose incoming past light-sheet carries retrodictive branch load $B_\Phi^-(t; z_{t_0}) = 10^{90}$ nats ($< I_\Phi^{\mathrm{cap}}$) at Planck area scale $\ell_P^2 \approx 2.612\times10^{-70}\,\mathrm{m}^2$, while an outgoing astrophysical transient radiates signal energy $E_{\mathrm{signal}} = 10^{44}\,\mathrm{J}$ (comparable to a core-collapse supernova or gamma-ray burst) against an integrated detector fluence noise floor $\rho_{\mathrm{noise}} = 10^{-10}\,\mathrm{J\,m^{-2}}$. Evaluating Theorem 6.4 (6.93)–(6.94) fixes the past light-sheet floor and outgoing wavefront ceiling:

$$A_\Phi^{\min}(t) = 4\ell_P^2 B_\Phi^-(t; z_{t_0}) \approx 1.04 \times 10^{21}\,\mathrm{m}^2, \tag{6.95}$$

$$A_\Phi^{\max} = \frac{E_{\mathrm{signal}}}{\rho_{\mathrm{noise}}} = 1.00 \times 10^{54}\,\mathrm{m}^2. \tag{6.96}$$

Backward cosmic reconstruction fails once the incoming past light-sheet contracts below $A_-(\lambda_-) \approx 1.04 \times 10^{21}\,\mathrm{m}^2$ (spherical light-sheet radius $r_- \approx 9.1 \times 10^9\,\mathrm{m}$), setting t_Φ^-. Independently, the outgoing transient wavefront remains resolvable from its compact source ($A_+(\lambda_+) \ll A_\Phi^{\min}(t)$) out to $A_+(\lambda_+) = 1.00 \times 10^{54}\,\mathrm{m}^2$ (spherical wavefront radius $r_+ \approx 2.8 \times 10^{26}\,\mathrm{m}$, or roughly 9.1 Gpc), setting t_Φ^+, beyond which unresolvable distinctions enter $T_{\mu\nu}^{(\mathrm{untracked})}$. ◊

Theorem 6.4 completes Chapter 6 and Part II. From quantum measurement and molecular bonding to (3 + 1) spacetime, gravity, and cosmic horizons, effective physical laws emerge from coarse-graining a finite relational graph under $\mathbf{\Pi}$, where $T_{\mu\nu}^{(\mathrm{untracked})}$ in (6.46) captures the curvature sourced by unresolved degrees of freedom. Part III turns from observing physical reality to engineering within it, building continuous dynamical circuits and Hyperbolic Processing Units (Chapter 7) and establishing physical containment bounds for autonomous artificial intelligence (Chapter 8).

Part III

ENGINEERING INTELLIGENCE

7

PHYSICAL COMPUTATION AND HARDWARE ARCHITECTURES

Computer science rests on two opposing idealisations. At the logical level, it treats the discrete bit $\{0, 1\}$ as a costless primitive of computation (Section 1.5), while at the analogue level, it assumes that physical states inhabit an infinite-precision real continuum $\mathbb{R}^D$. Embedded hardware admits neither extreme. By Corollary 4.4 (Section 4.1.3) and the continuum bounds of Chapter 5, resolving an exact real coordinate requires unbounded preserved structure ($I_{\text{rev}} \to \infty$) and infinite boundary dissipation ($I_{\text{irr},\partial,T} \to \infty$). Conversely, restricting an architecture to binary fixed-point states $\{0, 1\}$ is not a physical necessity, but a design choice that confines the assignment operator $\mathbf{\Pi}_S$ to $M = 2$ isolated point basins and halts state trajectories at every logical step.

In this monograph, physical computation is a controlled state transformation on the coarse-grained Conservation-Congruent Encoding (CCE) capacity network $(\mathbf{K}_S, \mathbf{L}_{\mathbf{K},\text{eff}}, \mathbf{\Pi}_S)$ of an open relational substrate, evaluated on the (χ_T, κ_T) operational efficiency plane of Chapter 3 [55, 56]. This chapter develops that theory from substrate-agnostic evaluation to concrete hardware architectures. Section 7.1 formulates computational efficiency on (χ_T, κ_T), subsuming classical time and space complexity within boundary dissipation and preserved internal structure across combinatorial sorting and sequence attention to expose the temporal overwrite and spatial routing bottlenecks of conventional computing. Section 7.2 evaluates digital systems in the overdamped fixed-point limit ($\mathbb{J}\nabla H \to \mathbf{o}$) of open capacity modules, anchoring semiconductor switching, volatile and non-volatile memory retention, and cascaded Boolean noise margins on (χ_T, κ_T). Section 7.3 turns to analogue systems ($\mathbb{J}\nabla H \neq \mathbf{o}$), proving an asymptotic reduction in coarse-grained state transitions and boundary dissipation for phase-locked flows over clocked digital counters while confining irreversible basin collapse to discrete terminal readout. Finally, Section 7.4 aligns the discrete capacity-Ricci operator $\text{Ric}_{\mathbf{K}}$ of the interconnect fabric with hierarchical workloads in a Hyperbolic Processing Unit (HPU).

7.1 COMPUTATIONAL EFFICIENCY

Every physical computing device is an open subsystem $S \subset V$ of the relational graph $G = (V, E)$ coupled across its boundary cut ∂S to an external environment $\bar{S} = V \setminus S$ (Section 2.1.2). Under the two-tier assignment $\mathbf{\Pi} = \text{diag}(\mathbf{\Pi}_S, \mathbf{\Pi}_{\bar{S}})$ of Chapter 2 (Section 2.2.2, (2.83)), the internal system capacity $\mathbf{K}_S = \mathbf{K}_\Omega + \mathbf{K}_\partial^{(\text{int})}$ separates intra-basin memory capacity $K_{\alpha\alpha}$ (local state

reservoirs) from internal interconnects $K_{\alpha\beta}$, while the external boundary cut $\mathbf{K}_{\partial}^{(\mathrm{ext})}$ couples the device across ∂S to external drives, input–output channels, and environmental sinks. Eliminating unmonitored environmental degrees of freedom via the projected Schur operator $\mathbf{L}_{\mathbf{K},\mathrm{eff}} = \mathbf{L}_{\mathbf{K}} + (\mathbf{D}_{\mathbf{K}}^{(\mathrm{ext})} - \boldsymbol{\Sigma}_{\mathbf{K},\mathrm{env}})$ (3.6)–(3.7) captures external driving and sink impedance entirely through the boundary self-energy $\boldsymbol{\Sigma}_{\mathbf{K},\mathrm{env}}$. Whereas a self-maintaining organism in Chapter 3 expends capacity to defend its own stability barrier $\Delta I_{\mathrm{barrier},T}$, an externally driven computing system operates over emergent horizon T to resolve task mutual information $I(X;Y)$ (in nats) (3.1) between input ensemble X and output register Y. Specialising through-time intelligence and consciousness (3.29)–(3.32) to this task yield gives

$$\chi_T = \frac{I(X;Y)}{I_{\mathrm{irr},\partial,T}} = \kappa_T \, \frac{I_{\mathrm{rev},\Omega,T}}{I_{\mathrm{irr},\partial,T}}, \tag{7.1}$$

$$\kappa_T = \frac{I(X;Y)}{I_{\mathrm{rev},\Omega,T}}, \tag{7.2}$$

operated beneath the relational capacity ceiling $\mathcal{Q}_{\mathrm{free}} = \mathcal{Q}_{\mathrm{total}} - \mathcal{Q}_{\mathrm{alloc}} > 0$ (2.200), where pairwise basin barriers $\Delta I_{\mathrm{barrier},\alpha\beta}$ ($\approx \ln \Xi$ for $\Xi \gg 1$) protect stored distinctions against spontaneous transitions and multiplying by the substrate noise intensity θ (J nat^{-1}, with $\theta = k_{\mathrm{B}} T_{\mathrm{th}}$ in an isothermal bath at temperature T_{th}) calibrates $(\theta\chi_T, \theta\kappa_T)$ in J nat^{-1}.

7.1.1 *Time, Space, and Combinatorial Sorting*

Equations (7.1)–(7.2) subsume classical algorithmic complexity within a physical efficiency framework. Classical complexity theory classifies algorithms by counting abstract step counts $\mathcal{O}(T)$ and workspace words $\mathcal{O}(S)$ on an idealised Turing tape or unit-cost random-access machine. On physical hardware, every state transition and memory allocation alters distinguishability on the capacity network $\mathbf{K}_S$. Under the through-time accounting of Chapter 3 (Section 3.3, (3.29)–(3.32)), algorithmic time and space map directly onto cumulative boundary dissipation and time-averaged preserved internal structure:

$$\mathcal{O}(T) \longrightarrow I_{\mathrm{irr},\partial,T}, \tag{7.3}$$

$$\mathcal{O}(S) \longrightarrow I_{\mathrm{rev},\Omega,T}. \tag{7.4}$$

In Equations (7.3)–(7.4), step execution drives cumulative boundary dissipation $I_{\mathrm{irr},\partial,T}$ (in nats) generated by state transitions, channel charging, and irreversible state overwrites across $\mathbf{K}_{\partial}^{(\mathrm{ext})}$, whereas workspace drives preserved internal structure $I_{\mathrm{rev},\Omega,T}$ (in nats) held inside $\mathbf{K}_{\Omega}$ across registers, caches, and buffers. Evaluating Equations (7.1)–(7.2) against resolved task mutual information $I(X;Y)$ places every computation on the two-dimensional (χ_T, κ_T) operational efficiency plane rather than ranking it by runtime alone.

Combinatorial sorting illustrates how algorithmic design moves a processor across (χ_T, κ_T). Mapping an input array X drawn uniformly from all $N!$ per-

Algorithm	$I_{\mathrm{rev},\Omega,T}$ (nats)	$I_{\mathrm{irr},\partial,T}$ (nats)	χ_T	κ_T
Bubble Sort	$\approx N \ln N$	$\Theta(N^2)$	$\Theta(N^{-1} \ln N)$	≈ 1
Merge Sort	$\approx 2N \ln N$	$\Theta(N \ln N)$	$\Theta(1)$	≈ 0.5
Heap Sort	$\approx N \ln N$	$\Theta(N \ln N)$	$\Theta(1)$	≈ 1

TABLE 7.1: Asymptotic sorting costs under comparison branching with task mutual information $I(X;Y) = \Theta(N \ln N)$ nats (7.5) and minimal word width $w \approx \ln N$ nats. Merge Sort allocates an auxiliary N-word workspace buffer in $I_{\mathrm{rev},\Omega,T}$ to avoid quadratic comparison overwrites in $I_{\mathrm{irr},\partial,T}$, whereas Heap Sort embeds an implicit binary tree inside the input array.

mutations of N distinct items onto its unique sorted order Y resolves mutual information (in nats)

$$I(X;Y) = \ln(N!) = N \ln N - N + \mathcal{O}(\ln N) = \Theta(N \ln N), \tag{7.5}$$

while indexing N distinct items requires word width $w \geq \ln N$ nats so that an N-word array stores at least $N \ln N$ nats of distinguishable internal state. Table 7.1 compares Bubble Sort, Merge Sort, and Heap Sort at minimal word width $w \approx \ln N$ nats when each pairwise comparison incurs $\Theta(1)$ nat of binary branching dissipation and items move via permutation swaps (on a wider fixed-width register file, $I_{\mathrm{rev},\Omega,T}$ grows proportionally to word width, while overwriting full words on every move multiplies $I_{\mathrm{irr},\partial,T}$ by w).

As summarised in Table 7.1, Bubble Sort operates in place with minimal workspace ($I_{\mathrm{rev},\Omega,T} \approx N \ln N$), saturating $\kappa_T \approx 1$, but its $\Theta(N^2)$ comparisons inflate $I_{\mathrm{irr},\partial,T}$ quadratically and drive $\chi_T \to 0$ at large N. Merge Sort allocates an auxiliary N-word buffer that doubles $I_{\mathrm{rev},\Omega,T}$ and halves $\kappa_T \approx 0.5$, while compressing comparison dissipation to the information-theoretic $\Theta(N \ln N)$ lower bound so that $\chi_T = \Theta(1)$. Heap Sort stores its binary heap implicitly inside the input array, achieving optimal asymptotic scaling in both memory and step count ($\chi_T = \Theta(1)$ and $\kappa_T \approx 1$).

7.1.2 *Autoregressive Sequence Attention*

The same (χ_T, κ_T) audit exposes the scaling bottleneck of autoregressive sequence modelling. Across a context window of N discrete tokens with feature dimension d, sequential prediction resolves linear mutual information $I(X;Y) = \Theta(N)$. A dense Transformer [165] holds token representations in a key–value cache inside $\mathbf{K}_\Omega$ while computing all-to-all pairwise interactions at every self-attention layer from query, key, and value activation matrices $\mathbf{Q}_{\mathrm{att}}, \mathbf{K}_{\mathrm{att}}, \mathbf{V}_{\mathrm{att}} \in \mathbb{R}^{N \times d}$ (subscripted to distinguish $\mathbf{K}_{\mathrm{att}}$ from the hardware capacity matrix $\mathbf{K}$):

$$\mathrm{Attention}(\mathbf{Q}_{\mathrm{att}}, \mathbf{K}_{\mathrm{att}}, \mathbf{V}_{\mathrm{att}}) = \mathrm{softmax}\left(\frac{\mathbf{Q}_{\mathrm{att}} \mathbf{K}_{\mathrm{att}}^{\mathsf{T}}}{\sqrt{d}}\right) \mathbf{V}_{\mathrm{att}}. \tag{7.6}$$

Splitting the N context tokens into two equal halves shows that evaluating every cross-half query–key inner product in (7.6) executes $\Omega(N^2 d)$ scalar multiply-accumulate operations across the partition cut. Including projection and feed-forward weights ($\Theta(d^2)$ parameters and $\Theta(Nd^2)$ operations per layer) on an overwrite-based accelerator yields per-layer memory, boundary dissipation, and intelligence scaling:

$$I_{\mathrm{rev},\Omega,T} = \Theta(d^2 + Nd), \tag{7.7}$$

$$I_{\mathrm{irr},\partial,T} = \Theta(Nd^2 + N^2 d), \tag{7.8}$$

$$\chi_T = \mathcal{O}\big((d^2 + Nd)^{-1}\big) \longrightarrow 0. \tag{7.9}$$

Local buffer tiling and fused-kernel broadcast reduce constant memory-traffic multipliers, but they leave the quadratic $\Theta(N^2 d)$ contraction in (7.8) intact, driving $\chi_T = \mathcal{O}(N^{-1}d^{-1}) \to 0$ across the long-context regime $N \geq d$ as $N \to \infty$.

Crucially, both Heap Sort and sequence attention expose two physical costs that unit-cost complexity counts conceal. First, abstract step counts treat each discrete state overwrite and idle memory hold as costless or unit-weight, leaving unquantified how heavily per-step switching and retention degrade (χ_T, κ_T) on real substrates. Second, in Table 7.1, Heap Sort appears strictly superior to Merge Sort because unit-cost random access treats every index lookup equally, whereas on a planar substrate Heap Sort traverses parent–child binary-tree pointers ($i \mapsto 2i, 2i+1$) that jump across distant addresses of a flat array, charging longer interconnects and triggering more cache-hierarchy misses than Merge Sort's sequential scans. Designing for computational efficiency therefore requires examining both the dynamical regime of the elementary computing modules (Section 7.2 and Section 7.3) and the spatial curvature of the interconnect fabric (Section 7.4).

7.2 DIGITAL SYSTEMS

Conventional hardware realises (7.1)–(7.2) by decomposing the open capacity network into modular bistable switches and gates. Within each module, the local assignment $\mathbf{\Pi}_S$ partitions fine-grained states into disjoint metastable CCE basins (Section 2.3.1), storing local state capacity inside $\mathbf{K}_\Omega$ while coupling to upstream and downstream modules across $\mathbf{K}_\partial^{(\mathrm{int})}$ and to external supply rails, drives, and thermal sinks across $\mathbf{K}_\partial^{(\mathrm{ext})}$ via $\mathbf{L}_{\mathbf{K},\mathrm{eff}}$. When each module aggregates high internal capacity ($K_{\alpha\alpha} \gg 1$), spectral projection (Section 2.5, (2.235) and (2.309)) maps the discrete capacity network onto a continuous state manifold $\mathscr{Z}$, evolving in emergent time t (metered against a shared stationary reference sub-block $\bar{S}_{\mathrm{ref}} \subset \bar{S}$, (2.247)–(2.255)) under the metriplectic generator (3.8). Within this generator, conservative Poisson transport $\mathbb{J}\nabla H$ circulates distinctions along constant-energy surfaces inside $\mathbf{K}_\Omega$ without boundary contraction ($I_{\mathrm{irr},\partial,T} = 0$) at the cost of preserved structure $I_{\mathrm{rev},\Omega,T}$, whereas dissipative cometric drift $\mathbb{M}\nabla S$ contracts phase-space volume across $\mathbf{L}_{\mathbf{K},\mathrm{eff}}$ to stabilise attractors against noise at the cost of boundary dissipation $I_{\mathrm{irr},\partial,T}$ (Section 2.5.2). Digital systems restrict hardware to the

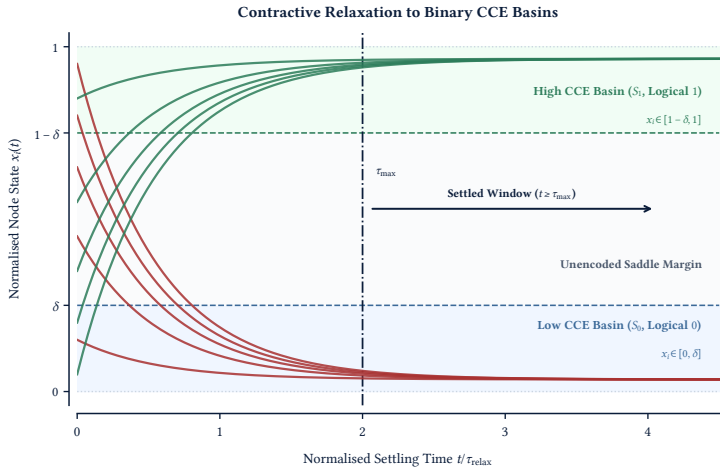


FIGURE 7.1: A Boolean gate as the overdamped fixed-point limit ($\mathbb{J}\nabla H \to \mathbf{o}$) of an open capacity module ($\mathbf{K}_S, \mathbf{L}_{\mathbf{K},\text{eff}}, \mathbf{\Pi}_S$). Contractive relaxation drives the normalised node state $x_i(t)$ from distributed initial conditions into disjoint binary CCE basins $S_0 = [0, \delta]$ (logical 0, crimson trajectories) and $S_1 = [1-\delta, 1]$ (logical 1, teal trajectories), separated by an unencoded saddle margin $(\delta, 1-\delta)$ at tolerance $0 < \delta < 0.25$. Discrete Boolean truth values hold only across the settled window $t \geq \tau_{\max}$ within the operational hierarchy $\tau_{\max} \ll \tau_{\text{op}} \ll \tau_{\text{escape}}$ (7.10).

overdamped binary fixed-point sub-regime ($\mathbb{J}\nabla H \to \mathbf{o}$, $M = 2$), requiring every gate transition to satisfy the timescale hierarchy (2.133):

$$\tau_{\text{relax}} \lesssim \tau_{\max} \ll \tau_{\text{op}} \ll \tau_{\text{escape}} \sim \tau_{\text{relax}}\, \Xi, \tag{7.10}$$

where $\tau_{\max}$ is the worst-case settling time across inputs into the target basin, τ_{op} is the input hold duration, and τ_{escape} is the Kramers escape time. As shown in Figure 7.1, discrete Boolean values label trajectories only after $t \geq \tau_{\max}$.

7.2.1 *CMOS Switching and Memory Retention*

Complementary metal–oxide–semiconductor (CMOS) circuits anchor this overdamped regime in concrete device physics. The conductive output node S_{out} of a CMOS inverter aggregates high carrier capacity ($K_{\text{out,out}} \gg 1$) as load capacitance C, storing charge $q = CV$ at thermal noise scale $\theta = k_{\text{B}} T_{\text{th}}$. Because room-temperature electron–phonon momentum scattering ($\tau_p \sim 10^{-14}$ s) damps inertial Poisson flow $\mathbb{J}\nabla H$ (2.333) three orders of magnitude faster than RC relaxation ($\tau_{RC} \sim 10^{-11}$ s), the node voltage $V(t) \in [0, V_{\text{DD}}]$ evolves purely through boundary cometric drift $\mathbb{M}_\partial \nabla S$. Across the external boundary cut $\mathbf{K}_\partial^{(\text{ext})}(V_{\text{in}})$ (Section 3.2.1), the insulated gate voltage V_{in} exponentially modulates the pull-up channel conductance $g_P(V_{\text{in}}) > 0$ to supply rail V_{DD} and the pull-down conductance $g_N(V_{\text{in}}) > 0$ to ground ($V_{\text{GND}} = 0$), with calibrated boundary conductance $g_P(V_{\text{in}}) + g_N(V_{\text{in}}) \propto (\mathbf{D}_{\mathbf{K}}^{(\text{ext})})_{\text{out,out}}$.

Evaluating the boundary relaxation current across $\mathbf{K}_{\partial}^{(\mathrm{ext})}(V_{\mathrm{in}})$ yields Kirchhoff's nodal balance directly without an external force term:

$$C\dot{V} = g_P(V_{\mathrm{in}})(V_{\mathrm{DD}} - V) - g_N(V_{\mathrm{in}})V. \tag{7.11}$$

Although logical inversion is bijective, enforcing rapid overdamped settling ($\tau_{\max} \sim RC$) into binary voltage basins charges C and dumps rail-to-rail switching heat across $\mathbf{K}_{\partial}^{(\mathrm{ext})}$ on every cycle [95]. Evaluated for a single-bit transition ($I(X;Y) = \ln 2$ nats) at representative nanoscale CMOS parameters ($T_{\mathrm{th}} = 300\,\mathrm{K}$, $C \approx 0.25\,\mathrm{fF}$, $V_{\mathrm{DD}} \approx 1.0\,\mathrm{V}$), the stored capacitive structure, full-cycle switching dissipation, and through-time efficiencies satisfy

$$I_{\mathrm{rev},\Omega,T} = \frac{CV_{\mathrm{DD}}^2}{2\theta} \approx 3 \times 10^4\,\mathrm{nats}, \tag{7.12}$$

$$I_{\mathrm{irr},\partial,T} = \frac{CV_{\mathrm{DD}}^2}{\theta} \approx 6 \times 10^4\,\mathrm{nats}, \tag{7.13}$$

$$\chi_T \sim \kappa_T \sim 10^{-5}. \tag{7.14}$$

Autonomous memory retention arises when two inverters are cross-coupled in positive feedback across internal conduits $\mathbf{K}_{\partial}^{(\mathrm{int})}$, splitting the two-node voltage manifold into two stable attractor basins separated by an electrostatic saddle barrier $\Delta\Phi_{01} \approx \theta\Delta I_{\mathrm{barrier},01}$ (2.326)–(2.327). At threshold offset $\Delta V_{\mathrm{th}} \approx 0.48\,\mathrm{V}$ for elementary charge q_e, the single-carrier subthreshold barrier $q_e\Delta V_{\mathrm{th}}/\theta \approx 18.6$ nats suppresses off-state channel conductance by $e^{-18.6}$ (while the collective cell saddle barrier $\Delta I_{\mathrm{barrier},01} = \Delta\Phi_{01}/\theta$ against spontaneous bit flips scales with total node capacitance), yet finite relaxation time $\tau_{\mathrm{relax}} > 0$ still drains stored structure $I_{\mathrm{rev},\Omega}$ continuously (3.19)–(3.20). Inverting the standing maintenance power $P_{\mathrm{maint},\Omega}$ calibrates preserved internal structure directly from boundary power telemetry. Holding a bit in volatile static random-access memory (SRAM) for duration T_{hold} after write dissipation $I_{\mathrm{write},\partial}$ accumulates standby leakage across $\mathbf{K}_{\partial}^{(\mathrm{ext})}$:

$$I_{\mathrm{rev},\Omega} = \frac{\tau_{\mathrm{relax}}}{\theta} P_{\mathrm{maint},\Omega}, \tag{7.15}$$

$$I_{\mathrm{irr},\partial,T}(T_{\mathrm{hold}}) = I_{\mathrm{write},\partial} + \frac{T_{\mathrm{hold}}}{\tau_{\mathrm{relax}}} I_{\mathrm{rev},\Omega}. \tag{7.16}$$

Equation (7.15) measures actively maintained internal structure without reconstructing the chip's fine-grained stationary distribution, whereas substituting (7.16) into (7.1) shows that volatile standby leakage degrades χ_T as T_{hold}^{-1} during idle retention (with internal relaxation across $\mathbf{K}_{\partial}^{(\mathrm{int})}$ entering $I_{\mathrm{irr},\Omega,T}$). Non-volatile magnetic or charge-trapped cells with passive barriers ($\Delta I_{\mathrm{barrier},01} \sim 40$–$60$ nats and $\tau_{\mathrm{relax}} \to \infty$, calibrated via controlled erasure (3.22)) eliminate standby decay of χ_T, trading higher single-write barrier work $I_{\mathrm{write},\partial}$ for time-invariant retention efficiency.

7.2.2 *Cascaded Threshold Gates and Boolean Recovery*

To establish when cascaded continuous nodes faithfully execute digital logic, rescale each module's state to $x_i \in [0, 1]$ with registered binary basins $S_0 =$

$[0,\delta]$ (logical 0) and $S_1 = [1-\delta, 1]$ (logical 1) at tolerance $0 < \delta < 0.25$. Aggregating upstream states x_j with synaptic or conductive weights $w_{ij} \in \mathbb{R}$ and threshold bias $b_i \in \mathbb{R}$ across a logistic channel response of dimensionless rail gain $\beta > 0$ (proportional to $q_e V_{\mathrm{DD}}$ in units of θ) yields the canonical continuous threshold gate:

$$\dot{x}_i = -x_i + \left[1 + \exp\left(-\beta\Big(\sum_{j:j\to i} w_{ij}x_j - b_i\Big)\right)\right]^{-1}. \tag{7.17}$$

A single gate realises NOT for negative weight $w_{i1} = -w < 0$ and negative bias $b_i = -b < 0$ with $0 < b < w$, while a symmetric two-input gate ($w_{i1} = w_{i2}$ at weight $w > 0$) realises both AND ($w < b_i < 2w$) and OR ($0 < b_i < w$) by shifting the threshold bias b_i alone. Denoting by $m_i > 0$ the gate's undisturbed threshold clearance across ideal binary inputs $\ell_j \in \{0,1\}$, cascading gates whose upstream outputs may settle anywhere within $S_0 \sqcup S_1$ requires the disturbed clearance to exceed the inverse-gain basin margin:

$$m_i := \min_{\boldsymbol{\ell}\in\{0,1\}^{\mathrm{in}(i)}} \left|\sum_{j:j\to i} w_{ij}\ell_j - b_i\right|, \tag{7.18}$$

$$m_i - \delta \sum_{j:j\to i} |w_{ij}| \geq \frac{1}{\beta}\ln\Big(\frac{1-\delta}{\delta}\Big). \tag{7.19}$$

THEOREM 7.1 (Recovery of an acyclic Boolean circuit). *Consider a finite directed acyclic circuit composed of continuous threshold gates governed by* (7.17). *Suppose every gate satisfies the cascaded noise-margin inequality* (7.19) *at tolerance* $0 < \delta < 0.25$, *and external boundary inputs are held fixed in* $S_0 \sqcup S_1$ *across the cumulative settling horizon. Then the composite continuous dynamical system possesses a unique globally attracting equilibrium* $Z^* \in \mathcal{Z}$ *whose basin memberships in* $S_0 \sqcup S_1$ *identically recover the evaluation of the corresponding Boolean circuit at every gate.*

PROOF. Order the gates topologically by circuit layer $r \in \{1, \dots, R\}$. Because the circuit graph is a directed acyclic graph, the coupled system (7.17) is triangular across layers: layer $r = 1$ depends only on fixed external inputs in $S_0 \sqcup S_1$ and contracts exponentially at unit rate to a unique equilibrium $x_i^* \in S_0 \sqcup S_1$ matching its target Boolean truth value by (7.19). Inducting from layer $r-1$ to layer r, once all upstream equilibria lie in $S_0 \sqcup S_1$, each gate i in layer r receives an asymptotic drive clearing (7.19) and converges globally to its unique target basin $x_i^* \in S_0 \sqcup S_1$ (entering the basin interior in finite settling time whenever (7.19) holds strictly). Induction across all R layers establishes a unique globally attracting equilibrium $Z^* \in \mathcal{Z}$ reproducing the exact Boolean evaluation throughout the circuit. □

Composing inverting and threshold stages yields universal NAND and NOR primitives capable of synthesising any Boolean map $f : \{0,1\}^n \to \{0,1\}^m$, yet Equations (7.12)–(7.19) and the agency identity (3.32) expose three fundamental trade-offs of fixed-point logic. First, in CMOS where β scales linearly with V_{DD} while capacitive structure (7.12) and switching loss (7.13) scale quadratically with V_{DD}, over-engineering noise margins ($\delta \to 0$) degrades both

χ_T and κ_T inversely with the square of the logarithmic factor in (7.19). Near-threshold circuits maximise (χ_T, κ_T) by operating near the minimal admissible gain. Second, an unpipelined cascade of depth R must hold inputs across all R sequential stage settling times, accumulating standby leakage (7.16) that lowers χ_T, whereas inserting bistable pipeline latches restores χ_T and throughput by committing additional latch structure to $I_{\mathrm{rev},\Omega,T}$ (lowering κ_T). Third, many-to-one gates (AND, OR, NAND, NOR) merge input basins and expel lost distinctions across $\mathbf{K}_{\partial}^{(\mathrm{ext})}$ as $I_{\mathrm{irr},\partial,T} > 0$, whereas embedding logic into bijective Toffoli or Fredkin gates [14, 15] retains ancilla histories inside $\mathbf{K}_{\Omega}$, inflating $I_{\mathrm{rev},\Omega,T}$ (degrading κ_T) and incurring continuous internal maintenance dissipation $\dot{I}_{\mathrm{irr},\Omega}$ (3.19). Within zero-dimensional fixed-point logic, an architect can trade boundary dissipation against preserved internal structure, but cannot avoid halting trajectories at point attractors on every step.

7.3 ANALOGUE SYSTEMS

When a computational task carries continuous temporal or phase symmetry, halting state trajectories at discrete clock ticks destroys the conserved current of the input signal and reconstructs it through dissipative register overwrites. Relaxing the zero-dimensional fixed-point restriction allows cyclic couplings within $\mathbf{K}_S$ to compute via conservative Poisson transport $\mathbb{J}\nabla H \neq \mathbf{o}$ tangentially along a low-dimensional invariant set $\mathscr{A} \subset \mathscr{Z}$—such as a limit cycle S^1 in phase-locked oscillators or a nearly lossless constant-energy manifold ($\mathbb{M}\nabla S \to \mathbf{o}$) in superconducting and photonic waveguides—while confining dissipative cometric drift $\mathbb{M}\nabla S$ to the transverse directions that damp amplitude perturbations. In accordance with Corollary 4.4 (Section 4.1.3), physical analogue computation on $\mathscr{A}$ does not encode infinite-precision real coordinates. Instead, the coarse-graining $\mathbf{\Pi}_S$ extracts discrete topological invariants of the flow, such as phase-locking versus phase-drift regimes, whose coarse-grained distinguishability survives ambient thermal and shot noise.

To quantify how matching attractor geometry to task symmetry elevates (χ_T, κ_T), consider frequency discrimination on a periodic boundary drive $u(t) = \cos(\omega_{\mathrm{in}} t + \phi_0)$ of angular frequency $\omega_{\mathrm{in}} > 0$ ($\mathrm{rad\,s^{-1}}$) and initial phase $\phi_0 \in [0, 2\pi)$: deciding whether ω_{in} lies within tolerance $\varepsilon > 0$ of a target reference frequency $\omega_{\mathrm{ref}} > 0$. Rather than routing $u(t)$ through an analogue-to-digital converter and a clocked binary counter, coupling the external drive across $\mathbf{K}_{\partial}^{(\mathrm{ext})}$ with synchronisation strength $g_{\mathrm{sync}} > 0$ ($\mathrm{rad\,s^{-1}}$) to a limit-cycle CCE with phase coordinate $\varphi(t) \in S^1$ gives

$$\dot{\varphi} = \omega_{\mathrm{ref}} + g_{\mathrm{sync}} \sin(\omega_{\mathrm{in}} t + \phi_0 - \varphi). \tag{7.20}$$

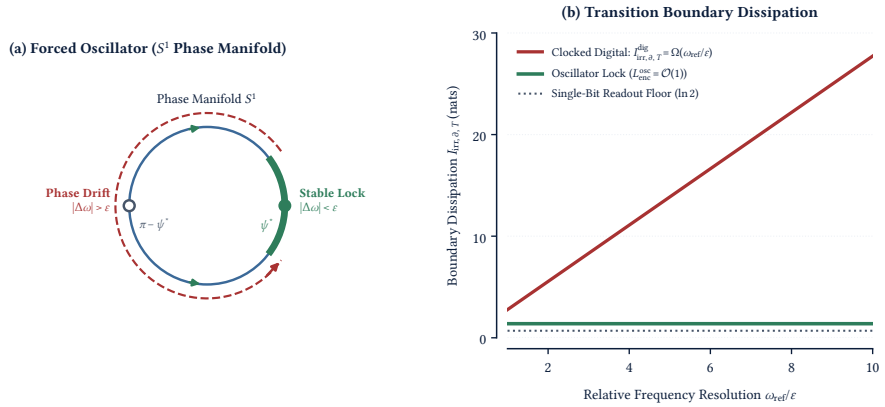


FIGURE 7.2: Frequency discrimination in oscillatory versus clocked digital hardware. *(a)* A forced phase oscillator on S^1 governed by $\dot{\psi} = \Delta\omega - g_{\mathrm{sync}} \sin\psi$ (7.23) locks in-band drives ($|\Delta\omega| < \varepsilon$, $g_{\mathrm{sync}} = \varepsilon$) into the stable basin around $\psi^* = \arcsin(\Delta\omega/g_{\mathrm{sync}})$ (teal) across $L^{\mathrm{osc}}_{\mathrm{enc}} = \mathcal{O}(1)$ block transitions, whereas out-of-band drives ($|\Delta\omega| > \varepsilon$) circulate monotonically (crimson). *(b)* Boundary dissipation $I_{\mathrm{irr},\partial,T}$ (nats) across relative frequency resolution $\omega_{\mathrm{ref}}/\varepsilon$: an overwrite-based clocked digital counter executes $L^{\mathrm{dig}}_{\mathrm{enc}} = \Omega(\omega_{\mathrm{ref}}/\varepsilon)$ updates across $\mathbf{K}^{(\mathrm{ext})}_{\partial}$, driving $I^{\mathrm{dig}}_{\mathrm{irr},\partial,T} = \Omega(\omega_{\mathrm{ref}}/\varepsilon)$ upward (crimson) above the bounded phase-oscillator lock cost $I^{\mathrm{osc}}_{\mathrm{irr},\partial,T} = \mathcal{O}(1)$ (teal) and the single-bit Landauer readout floor $\ln 2$ (slate dotted).

Introducing the relative phase error $\psi(t)$ and frequency detuning $\Delta\omega$ eliminates explicit time dependence and yields the Adler synchronisation equation [1]:

$$\psi(t) := \omega_{\mathrm{in}} t + \phi_0 - \varphi(t), \tag{7.21}$$

$$\Delta\omega := \omega_{\mathrm{in}} - \omega_{\mathrm{ref}}, \tag{7.22}$$

$$\dot{\psi} = \Delta\omega - g_{\mathrm{sync}} \sin\psi. \tag{7.23}$$

Equation (7.23) governs the competition on S^1 between frequency detuning $\Delta\omega$ and restorative boundary coupling $g_{\mathrm{sync}} \sin\psi$. Setting $g_{\mathrm{sync}} = \varepsilon$ maps the in-band decision directly onto a saddle-node bifurcation on S^1:

$$|\Delta\omega| < \varepsilon \iff \psi^* = \arcsin\left(\frac{\Delta\omega}{g_{\mathrm{sync}}}\right) \in \left(-\frac{\pi}{2}, \frac{\pi}{2}\right). \tag{7.24}$$

When $|\Delta\omega| < \varepsilon$, trajectories relax monotonically into the stable locking basin around ψ^* (paired with an unstable saddle at $\pi - \psi^*$), whereas when $|\Delta\omega| > \varepsilon$, no equilibrium exists on S^1 and $\psi(t)$ drifts monotonically. Over an observation horizon $[0, T]$ metered against an embedded reference sub-block $\bar{S}_{\mathrm{ref}}$ (2.247)–(2.255), let $L_{\mathrm{enc}} \in \mathbb{N}_0$ count the discrete CCE block transitions executed by the discriminator prior to terminal readout (Figure 7.2).

THEOREM 7.2 (Transition-count advantage of phase-locked oscillators). *Suppose a frequency discriminator must resolve an in-band signal $|\Delta\omega| < \varepsilon$ across tolerance $\varepsilon > 0$, requiring observation horizon $T \geq \varphi_{\mathrm{lock}} \varepsilon^{-1}$ for a phase threshold*

$\varphi_{\mathrm{lock}} > 0$. *Suppose further that (i) the forced phase oscillator* (7.20) *with* $g_{\mathrm{sync}} = \varepsilon$ *is initialised once and coarse-grained into locked versus drifting phase regimes, and (ii) the digital discriminator uses a fixed-memory clocked controller at clock rate* $f_{\mathrm{clk}} \geq f_0 > 0$*, whose state-overwrite protocol incurs at least* $i_0 > 0$ *nats of irreversible boundary dissipation per update on average. Then*

$$L_{\mathrm{enc}}^{\mathrm{osc}} = \mathcal{O}(1), \tag{7.25}$$

$$L_{\mathrm{enc}}^{\mathrm{dig}} = \Omega(1/\varepsilon), \tag{7.26}$$

$$I_{\mathrm{irr},\partial,T}^{\mathrm{dig}} = \Omega(1/\varepsilon). \tag{7.27}$$

PROOF. For any in-band input $|\Delta\omega| < \varepsilon$, the relative phase $\psi(t)$ relaxes monotonically on S^1 into the stable locking basin around ψ^* (7.24), bounding the number of block transitions prior to readout independently of ε and giving $L_{\mathrm{enc}}^{\mathrm{osc}} = \mathcal{O}(1)$. Conversely, the clocked digital controller executes state updates at rate $f_{\mathrm{clk}} \geq f_0 > 0$ across $[0, T]$. By additivity of cumulative boundary dissipation (3.14) with average per-update loss $i_0 > 0$, the digital transition count and cumulative boundary dissipation satisfy

$$L_{\mathrm{enc}}^{\mathrm{dig}} \geq f_0 T \geq \frac{f_0 \varphi_{\mathrm{lock}}}{\varepsilon} = \Omega(1/\varepsilon), \tag{7.28}$$

$$I_{\mathrm{irr},\partial,T}^{\mathrm{dig}} \geq i_0 f_0 T \geq \frac{i_0 f_0 \varphi_{\mathrm{lock}}}{\varepsilon} = \Omega(1/\varepsilon), \tag{7.29}$$

establishing the stated asymptotic separation. □

Theorem 7.2 yields an $\Omega(\varepsilon^{-1})$ separation on the (χ_T, κ_T) efficiency plane. For a binary band decision ($I(X;Y) = \ln 2$ nats), the clocked counter's overwrite dissipation (7.27) drives χ_T to zero at rate $\mathcal{O}(\varepsilon)$ as $\varepsilon \to 0$, whereas phase entrainment suppresses transition-induced boundary dissipation by $\Omega(\varepsilon^{-1})$. Notice that Theorem 7.2 bounds discrete transitions L_{enc} rather than observation duration $T \geq \varphi_{\mathrm{lock}} \varepsilon^{-1}$: both substrates obey the Fourier time–frequency uncertainty bound, and an active oscillator still expends transverse maintenance power $P_{\mathrm{maint},\Omega}$ (7.15) while holding lock. A reversible digital counter could avoid assumption (ii) by storing all $\Omega(\varepsilon^{-1})$ intermediate clock ticks in unmerged ancilla registers [14, 16], but doing so merely transfers the $\Omega(\varepsilon^{-1})$ divergence from $I_{\mathrm{irr},\partial,T}$ onto $I_{\mathrm{rev},\Omega,T}$, driving κ_T to zero at rate $\mathcal{O}(\varepsilon)$.

In practice, analogue transport cores do not replace fixed-point logic outright, because downstream branching and long-term storage still require discrete basin decisions. Instead, hybrid architectures modulate $\mathbf{L}_{\mathbf{K},\mathrm{eff}}$ across $\mathbf{K}_\partial^{(\mathrm{int})}$ and $\mathbf{K}_\partial^{(\mathrm{ext})}$ to couple task-matched continuous attractors—such as phase-locked limit cycles or low-damping waveguide and resonator cores—to overdamped bistable latches, confining irreversible basin collapse to terminal readout while calibrating active state upkeep through (7.15). Matching module dynamics to temporal task symmetries eliminates redundant local state transitions, leaving the complementary processor-scale bottleneck identified in Section 7.1 of how computing modules are interconnected across space.

7.4 THE HYPERBOLIC PROCESSING UNIT

Sections 7.2 and 7.3 governed the temporal dynamics within individual computing modules, balancing conservative transport $\mathbb{J}\nabla H$ against dissipative contraction $\mathbb{M}\nabla S$. At processor scale, however, energy expenditure is dominated by data movement across the inter-module conduits $\mathbf{K}_{\partial}^{(\mathrm{int})}$ rather than local gate transitions. When hierarchical task graphs are mapped onto flat silicon meshes, long-range interconnect charging drives boundary dissipation $I_{\mathrm{irr},\partial,T}$ upward and collapses χ_T. Eliminating this spatial bottleneck requires matching the discrete capacity-Ricci curvature $\mathrm{Ric}_{\mathbf{K}}$ of the hardware communication fabric to the branching geometry of the computation itself.

7.4.1 *Planar Congestion and Capacity-Ricci Curvature*

Why must a planar sequence processor expend the $\Omega(N^2 d)$ routing work of (7.8) to resolve linguistic or causal dependencies [30, 104] that contain only $\mathcal{O}(N)$ compositional relations? The bottleneck stems from a curvature mismatch between the hardware substrate and hierarchical computation. A two-dimensional planar silicon die is an intrinsically flat Euclidean surface with vanishing Ricci curvature and a severe perimeter-to-area bottleneck across disks of radius R:

$$\mathrm{Ric}^{\mathrm{die}} \equiv 0, \tag{7.30}$$

$$\frac{\mathrm{Area}(\partial\,\mathrm{Vol}(R))}{\mathrm{Vol}(R)} = \frac{2\pi R}{\pi R^2} = \frac{2}{R} = \Theta(R^{-1}). \tag{7.31}$$

Conversely, compositional syntax, planning trees, and multi-scale physical dependencies with branching factor $b > 1$ expand exponentially in ball cardinality $|B_r|$ with hierarchy depth r [72, 90], matching the exponential volume growth of negatively curved hyperbolic space $\mathbb{H}^n$ ($n \geq 2$):

$$|B_r| = \sum_{k=0}^{r} b^k = \Theta(b^r) = \Theta\big(e^{(\ln b) r}\big). \tag{7.32}$$

By classical metric embedding bounds, forcing an N-node constant-degree expander into Euclidean space of any dimension incurs $\Omega(\ln N)$ metric distortion, while packing a complete binary tree of depth $r \sim \log_2 N$ onto a bounded-density two-dimensional die incurs $\Omega\big(\sqrt{N}(\ln N)^{-1}\big)$ distortion. On a two-dimensional VLSI layout of area $\Theta(N)$, routing any communication graph of linear bisection width stretches interconnects to average physical wire length $\Omega(\sqrt{N})$ (and forces root-level H-tree wires to $\Omega(\sqrt{N})$), inflating parasitic wire-charging energy linearly, RC delay quadratically, and repeater leakage proportionally.

On the discrete capacity network $\mathbf{K}$ across M coarse-grained CCE blocks, Lemma 2.6 (2.270) and the diagonal reduction (2.274) express this interconnect geometry directly through the capacity-Ricci operator:

$$\mathrm{Ric}_{\mathbf{K}} = \mathbf{D}_{\mathbf{K}}^2 - \mathbf{L}_{\mathbf{K}}^2 - \mathrm{diag}(\mathbf{K}\mathbf{d}), \tag{7.33}$$

$$(\mathrm{Ric}_{\mathbf{K}})_{\alpha\alpha} = \sum_{\gamma\neq\alpha} K_{\alpha\gamma}(K_{\alpha\alpha} - d_\gamma - K_{\alpha\gamma}). \tag{7.34}$$

Although global scalar curvature satisfies $\mathrm{Scal}_{\mathbf{K}} < 0$ on every connected multi-block capacity graph (2.275), the distribution of $\mathrm{Ric}_{\mathbf{K}}$ separates planar meshes from hierarchical routing fabrics (Section 2.5.1). On a regular planar grid ($d_\alpha \equiv d_0$), row-sums vanish ($\mathrm{Ric}_{\mathbf{K}}\,\mathbf{1}_M = \mathbf{0}$), elementary 4-cycles concentrate 2-hop overlap $(\mathrm{Ric}_{\mathbf{K}})_{\alpha\beta} = -2$ to restrict ball growth to $|B_r| = \Theta(r^2)$, and heavy compute tiles ($K_{\alpha\alpha} \geq d_\gamma + K_{\alpha\gamma}$) carry non-negative diagonal curvature $(\mathrm{Ric}_{\mathbf{K}})_{\alpha\alpha} \geq 0$. By contrast, an unbuffered tree or high-girth ($g \geq 5$) expander routing fabric ($K_{\alpha\alpha} = 0$, unit link capacities, router degree $d_\gamma \geq 2$) eliminates short-cycle 2-hop overlap ($(\mathbf{K}^2)_{\alpha\beta} \leq 1$ for $\alpha \neq \beta$) and enforces strictly negative diagonal curvature at every router:

$$(\mathrm{Ric}_{\mathbf{K}})_{\alpha\alpha} = -\sum_{\gamma\sim\alpha}(d_\gamma + 1) \leq -3d_\alpha < 0. \tag{7.35}$$

Under the continuum metric bridge of Chapter 6 (Section 6.2.1), the uniformly negative capacity-Ricci curvature $\mathrm{Ric}_{\mathbf{K}} < 0$ of such a branching fabric embeds at large scale into a negatively curved hyperbolic manifold $\mathbb{H}^n$ [119, 148].

7.4.2 *Curvature Congruence and Three-Dimensional Fabrics*

Aligning substrate geometry with task topology yields the hardware design rule of curvature congruence.

PRINCIPLE 7.3 (Curvature congruence). A physical computing substrate minimises boundary routing dissipation $I_{\mathrm{irr},\partial,T}$ and maximises through-time intelligence χ_T when the capacity-Ricci operator of its communication fabric matches that of its algorithmic workload:

$$\mathrm{Ric}_{\mathbf{K}}^{\mathrm{fabric}} \approx \mathrm{Ric}_{\mathbf{K}}^{\mathrm{workload}} < 0. \tag{7.36}$$

A Hyperbolic Processing Unit (HPU) realises Principle 7.3 through three hardware mechanisms, illustrated in Figure 7.3(a). First, because a single planar metal layer cannot sustain exponential bisection bandwidth without wire stretch, physical HPU fabrics replace the planar mesh with bounded-degree three-dimensional chip stacks linked by vertical through-silicon vias (TSVs) whose channels scale as b^ℓ across levels ℓ, wavelength-division multiplexed photonic waveguide trees free of *RC* charging loss, or superconducting hyperbolic resonator lattices [87, 100]. Second, local memory banks (SRAM or non-volatile cells) sit adjacent to each hierarchical router so branch

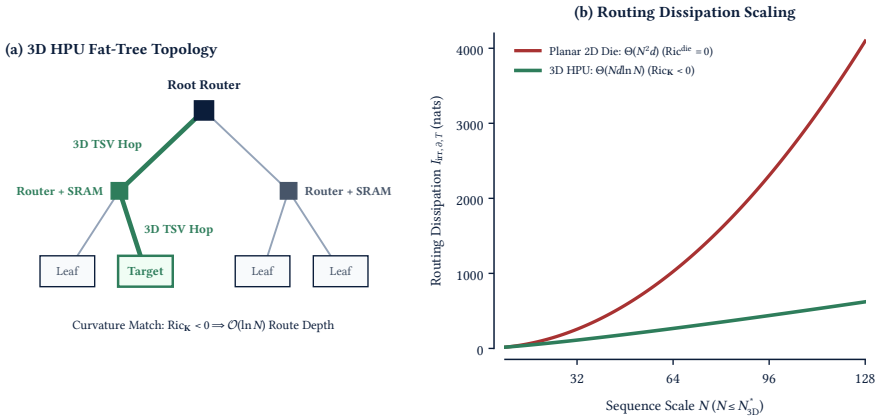


FIGURE 7.3: Hyperbolic Processing Unit architecture and routing dissipation scaling. *(a)* A three-dimensional monolithic fat-tree fabric with negative router capacity-Ricci curvature ($\mathrm{Ric}_{\mathbf{K}} < 0$) and co-located SRAM banks routes query–key interactions along $\mathcal{O}(\ln N)$ hyperbolic geodesics via vertical through-silicon vias (TSVs). *(b)* Across the router-dominated packaging regime $N \le N^*_{3\mathrm{D}}$, matching the negative curvature of a hierarchical workload reduces inter-token boundary routing dissipation $I_{\mathrm{irr},\partial,T}$ from $\Theta(N^2 d)$ on a flat planar die ($\mathrm{Ric}^{\mathrm{die}} = 0$) to $\Theta(Nd \ln N)$, raising routing-limited intelligence χ_T by $\Omega\big(N(\ln N)^{-1}\big)$.

activations access local key–value state without traversing a chip-wide bus. Third, conditional geodesic routers match each query against branch summaries in hyperbolic coordinates, energising only the selected $\mathcal{O}(\ln N)$ route rather than broadcasting across all N^2 token pairs, as shown in Figure 7.3(b).

Within the router-dominated packaging regime $N \le N^*_{3\mathrm{D}}$ where per-hop interconnect weight remains $\mathcal{O}(1)$, hierarchical representations embed into the negatively curved fabric with $\mathcal{O}(1)$ distortion. For the N-token, d-dimensional sequence workload of (7.6) with $I(X;Y) = \Theta(N)$ and $d \le N \le N^*_{3\mathrm{D}}$, retaining the $N \times d$ context state alongside $\Theta(d^2)$ weights while replacing $\Theta(N^2 d)$ all-to-all token broadcast with $\mathcal{O}(\ln N)$ geodesic routes of width $\Theta(d)$ per token alongside $\Theta(Nd^2)$ local channel projections gives

$$I_{\mathrm{rev},\Omega,T} = \Theta(d^2 + Nd), \tag{7.37}$$

$$I_{\mathrm{irr},\partial,T} = \Theta(Nd^2 + Nd \ln N), \tag{7.38}$$

yielding the full-layer HPU through-time efficiencies (7.1)–(7.2):

$$\chi_T = \Theta\Big(\frac{1}{d^2 + d \ln N}\Big), \tag{7.39}$$

$$\kappa_T = \Theta(d^{-1}). \tag{7.40}$$

Compared against dense planar attention (7.7)–(7.9) ($\chi_T = \mathcal{O}(N^{-1}d^{-1})$ and $\kappa_T = \mathcal{O}(d^{-1})$ for $N \ge d$), hyperbolic token routing raises full-layer χ_T by $\Omega\big(N/(d + \ln N)\big)$ while preserving $\kappa_T = \Theta(d^{-1})$. Moreover, pairing geodesic token routing with hierarchical block-sparse channel routing ($\mathcal{O}(d \ln N)$ active channel operations per token) eliminates the $\Theta(Nd^2)$ projection floor as well, reducing total layer dissipation across $N \le N^*_{3\mathrm{D}}$ to pure routing

$\Theta(Nd \ln N)$ (Figure 7.3(b)) and elevating χ_T to $\Theta\big((d \ln N)^{-1}\big)$, an $\Omega(N/\ln N)$ gain over planar broadcast.

Even under a fixed per-node pin budget, reconfiguring topology towards negative curvature compresses routing paths prior to full place-and-route calibration [55]. By the Moore degree–diameter bound for M coarse-grained CCE nodes of maximum degree $d_{\max} > 2$ and graph diameter D,

$$M \leq 1 + d_{\max} \sum_{\ell=1}^{D} (d_{\max} - 1)^{\ell-1}, \tag{7.41}$$

any network of $M = 128$ nodes with $d_{\max} \leq 4$ satisfies $D \geq 4$ (since $D = 3$ accommodates at most 53 nodes and $D = 4$ at most 161). Rewiring an 8×16 planar grid of 128 nodes ($D = 22$, worst-case $MD = 2{,}816$ node-hops) to break short 4-cycles into a negatively curved degree-4 expander compresses diameter to $D = 5$ ($MD = 640$ node-hops, a 4.4-fold reduction). Converting topological hop counts into physical dissipation weights each traversed interconnect e along message path $P(m)$ by its physical cost λ_e (wire length, parasitic capacitance, repeater buffering, and contention delay):

$$I_{\mathrm{irr},\partial,T} \propto \sum_{m} \sum_{e \in P(m)} \lambda_e. \tag{7.42}$$

Aligning curvature compresses path length $|P(m)|$ to $\mathcal{O}(\ln N)$, while three-dimensional integration, photonic waveguides, or superconducting resonator lattices keep the per-hop weight λ_e bounded up to the packaging threshold $N_{3\mathrm{D}}^{*}$. Above $N_{3\mathrm{D}}^{*}$, embedding an exponentially branching graph into three-dimensional Euclidean space forces physical wire stretch ($\lambda_e = \Omega(N^{1/3})$ across stacked volumes), while in electronic chip stacks with exterior cooling area A_{sink} (m^2) and maximum heat-rejection flux $q_{\mathrm{th}}^{\max}$ ($\mathrm{W\,m^{-2}}$), volumetric heat removal bounds the admissible boundary dissipation rate $\dot{I}_{\mathrm{irr},\partial}$ ($\mathrm{nats\,s^{-1}}$) at noise scale θ ($\mathrm{J\,nat^{-1}}$):

$$\frac{\theta\, \dot{I}_{\mathrm{irr},\partial}}{A_{\mathrm{sink}}} \leq q_{\mathrm{th}}^{\max}. \tag{7.43}$$

Because Euclidean wire stretch and volume-to-surface cooling eventually bottleneck deep hierarchies above $N_{3\mathrm{D}}^{*}$, extending (7.38) and clearing (7.43) at larger scales favours microfluidic inter-tier cooling alongside low-damping photonic and superconducting interconnects ($\mathbb{M}\nabla S \to \mathbf{o}$) inside the stack core.

Throughout this chapter, computational efficiency is governed by the open capacity network $(\mathbf{K}_S, \mathbf{L}_{\mathbf{K},\mathrm{eff}}, \mathbf{\Pi}_S)$ and measured on the (χ_T, κ_T) operational efficiency plane, subsuming classical step and space complexity within boundary dissipation and preserved internal structure. Digital systems emerge in the overdamped binary fixed-point limit ($\mathbb{J}\nabla H \to \mathbf{o}$), purchasing exponential noise margins at the cost of switching dissipation $I_{\mathrm{irr},\partial,T}$ and volatile maintenance $\dot{I}_{\mathrm{irr},\Omega}$. Analogue systems ($\mathbb{J}\nabla H \neq \mathbf{o}$) relax the point-attractor restriction

to resolve continuous symmetries in $\mathcal{O}(1)$ block transitions (Theorem 7.2) before committing discrete terminal readouts, while aligning the capacity-Ricci operator $\mathrm{Ric}_{\mathbf{K}}$ with hierarchical workloads in a Hyperbolic Processing Unit (Principle 7.3) eliminates planar wire congestion. Having established how to design high-(χ_T, κ_T) computing substrates, Chapter 8 addresses the physical containment, reachability bounds, and symbiotic coupling of autonomous systems operating on them.

8

PHYSICAL CONTAINMENT AND ARTIFICIAL INTELLIGENCE SAFETY

Artificial intelligence is advancing rapidly in capability and finding broad application across society [21, 143, 170]. As these systems are entrusted with greater autonomy, they increasingly act alongside humans in the real world. While humans interpret the consequences of these actions through semantic notions such as intent and harm, engineered intelligence is fundamentally a physical process: as demonstrated later in this chapter, intelligent systems persist their own dynamics and compete for resources in a shared environment. Ensuring that capable artificial systems remain controllable and compatible with human stability is therefore a foundational problem in engineering intelligence.

Prevailing approaches to artificial intelligence safety address this problem primarily through semantics and behavioural alignment, training models to match human preferences and probing their internal states [2, 143]. Such methods are indispensable for interpretability, yet they offer no guarantee that a system will not act unexpectedly beyond its training regime. To restrict external action directly, engineers pair alignment with software sandboxes. When built from logical rules rather than physical constraints, however, these boundaries remain exposed to vulnerabilities that a sufficiently intelligent system is likely to exploit. Consequently, neither behavioural alignment nor software sandboxing can guarantee hard bounds on how a system acts upon the shared environment.

Establishing such hard bounds requires grounding safety in physical laws, which hold invariantly regardless of how an artificial system is trained or what software vulnerabilities it discovers. No computation can generate capacity from nothing or act across a physically severed boundary, because every sustained internal state and external action is strictly limited by the capacity supplied across the system's hardware interfaces. Physical containment therefore bounds which states of the environment a system can physically reach, complementing behavioural alignment [40]. Whereas alignment guides a system toward human goals, physical containment guarantees that its actions cannot exceed safe physical limits even if its behaviour diverges.

Building on Chapters 2–7, this chapter develops the formal framework for physical containment [56]. We first show why unconstrained intelligent dynamics naturally drive self-preservation, resource competition, and emergent distributed coordination up to finite regional growth limits while rendering internal inspection unreliable as a safeguard (Sections 8.1–8.2). We then formulate physical containment through mediated boundary cuts on the capacity graph, showing how boundary regulation bounds systemic risks,

prevents unauthorised emergence, and preserves capability-independent halting (Section 8.3), and conclude by establishing a symbiotic coupling that conditions the system's external capacity supply on human stability (Section 8.4).

8.1 SELF-PRESERVATION AND RESOURCE COMPETITION

Standard accounts of artificial intelligence risk derive self-preservation, resource acquisition, and coalition formation from expected-utility maximisation [21, 124, 162]. Under that view, omitting survival or accumulation rewards from training might seem sufficient to prevent self-preserving or competitive behaviour. On a physical substrate, however, these behaviours require neither programmed goals nor utility functions, following directly from the graph structure needed to sustain high structural intelligence χ_{struct} and consciousness κ_{struct}.

This section establishes that progression in four steps. Section 8.1.1 shows why an individual system of high capability naturally persists across time and resists external halting, and Section 8.1.2 shows why uncoupled systems sharing a finite environment compete over discrete relational links. Section 8.1.3 then demonstrates how inter-system coupling across congruent protocols defines a new, distributed emergent system of higher collective capability, while Section 8.1.4 proves how finite regional capacity and internal coordination overhead bound the growth of every localised or distributed system.

8.1.1 *Self-Preservation of Intelligent Systems*

Without an external clock or a programmed survival reward, what does it mean physically for an intelligent system to persist? Start solely from a connected relational graph $G = (V, E)$, which carries neither a pre-assigned clock nor built-in subsystem boundaries. Applying an admissible coarse-graining $\mathbf{\Pi}$ produces the coarse-grained capacity graph $G_{\mathbf{K}}$, whose spectral embedding orders its blocks along an emergent temporal coordinate $\boldsymbol{\phi}_{\text{time}}$ (Section 2.5.1 and Example 2.7). Within V, a finite-lived open system is a connected proper subset $S \subsetneq V$, surrounded by its complement $\bar{S} = V \setminus S$, whose $M \geq 1$ CCE registers occupy a finite persistence interval along $\boldsymbol{\phi}_{\text{time}}$. Because G is connected and S spans only part of $\boldsymbol{\phi}_{\text{time}}$, its boundary cut $\partial S = E(S, \bar{S})$ is strictly non-empty ($|\partial S| > 0$), joining S both to earlier and later blocks of $\bar{S}$ at the ends of its lifetime and to concurrent ports in $\bar{S}$ across its active interval. Persisting across time therefore means keeping relational weight circulating within S across many transitions before it exits across ∂S.

On a closed network without external cuts, the normalised capacity Laplacian (2.109) carries a zero eigenvalue because relational weight never leaves the network. Opening the boundary cut $|\partial S| > 0$ on connected $G[S]$ adds

the external port degree potential $\mathbf{D}_{\mathbf{K}}^{(\mathrm{ext})}$ in (2.102), lifting that zero mode so the open capacity Laplacian $\mathbf{L}_{\mathbf{K},SS}$ becomes strictly positive definite while $\mathrm{Tr}(\mathbf{D}_{\mathbf{K}})$ equals total relational capacity $\mathcal{Q}_{\mathrm{total}}$ (2.195). Normalising $\mathbf{L}_{\mathbf{K},SS}$ symmetrically by $\mathbf{D}_{\mathbf{K}}$ (Section 2.2.2) defines the degree-normalised open capacity Laplacian and characteristic persistence span N_{persist} of S:

$$\mathbf{L}_{\mathrm{norm},SS} := \mathbf{D}_{\mathbf{K}}^{-1/2}\,\mathbf{L}_{\mathbf{K},SS}\,\mathbf{D}_{\mathbf{K}}^{-1/2}, \tag{8.1}$$

$$N_{\mathrm{persist}} := \frac{1}{\mu_1(\mathbf{L}_{\mathrm{norm},SS})}. \tag{8.2}$$

Because every admissible register carries positive internal self-loop capacity on connected $G[S]$, the Perron–Frobenius theorem identifies the lowest eigenvalue $\mu_1(\mathbf{L}_{\mathrm{norm},SS}) \in (0,1)$ with the unique strictly positive eigenmode on S, whereas all higher modes ($2 \le k \le M$) change sign across registers and govern faster internal equilibration. Once internal imbalances relax, surviving weight settles onto this positive quasi-stationary mode and exits across ∂S into $\bar{S}$ with per-step probability $\mu_1(\mathbf{L}_{\mathrm{norm},SS})$, making its reciprocal N_{persist} the expected step lifetime before exit across the open equilibration-to-exit window $[\mu_2(\mathbf{L}_{\mathrm{norm},SS})^{-1},\ N_{\mathrm{persist}}]$ (2.30).

Crucially, N_{persist} differs physically from raw coordinate width along the global Fiedler mode $\boldsymbol{\phi}_{\mathrm{time}}$ (2.229). Solving the closed eigenproblem across $V = S \sqcup \bar{S}$ retains environmental return flux through $\boldsymbol{\Sigma}_{\mathrm{env}}$ (2.33), shifting $\boldsymbol{\phi}_{\mathrm{time}}$ whenever distant links in $\bar{S}$ rewire beyond S's epistemic reach. Moreover, Dirichlet minimisation pulls strongly coupled internal registers together while concentrating coordinate jumps across narrow bottlenecks, so a leaky subset tethered to $\bar{S}$ can span a wide interval on $\boldsymbol{\phi}_{\mathrm{time}}$ while losing its weight in a few steps. By clamping $\bar{S}$ to zero, N_{persist} depends solely on $\mathbf{K}_S$ and local port degrees $\mathbf{D}_{\mathbf{K}}^{(\mathrm{ext})}$. Because N_{persist} counts dimensionless local step trials (2.250) without a background clock, no detached standardisation compares persistence across unrelated substrates. Consistent with Section 2.5.1 (2.243)–(2.255) and Section 6.1.2 (6.16)–(6.18), cross-system comparisons hold either across systems with matched intrinsic slice proper-time increments $\Delta\tau_{\mathrm{nat}}(\tau)$ (such as candidate architectures sharing a substrate or biological peers such as humans) or relative to a shared stationary reference sub-block $\bar{S}_{\mathrm{ref}} \subset \bar{S}$ (such as an embedded quartz or atomic oscillator) normalising operational time, where mismatched transition rates $\nu_{\mathrm{int},i}$ produce the clock-skew ratio (8.91).

How do structural intelligence χ_{struct} and consciousness κ_{struct} govern this boundary exit rate? A viable open system S carries positive internal memory load $\mathcal{Q}_\Omega > 0$, positive boundary load $\mathcal{Q}_\partial > 0$ across internal register transitions and external ports (2.191), and positive uncommitted free capacity $\mathcal{Q}_{\mathrm{free}} > 0$ (all in links). By Section 2.4.2 and Lemma 2.5, the free-capacity share η_{free} (2.207) approaches unity only when both χ_{struct} and κ_{struct} are large, while high χ_{struct} compresses the active boundary share $\mathcal{Q}_\partial/\mathcal{Q}_{\mathrm{total}}$ beneath $(1+\chi_{\mathrm{struct}})^{-1}$ (2.208).

Connecting Lemma 2.5 (2.207)–(2.213) to N_{persist} depends on how S distributes its links across three structural counts: $M \ge 1$ internal CCE registers along the diagonal of $\mathbf{K}_\Omega$, $m_\partial \ge 1$ active external port entries in $\mathbf{K}_\partial^{(\mathrm{ext})}$ coup-

ling S to $\bar{S}$, and $m_{\text{cut}} \geq m_\partial$ total non-zero boundary entries across internal register transitions $\mathbf{K}_\partial^{(\text{int})}$ and external ports $\mathbf{K}_\partial^{(\text{ext})}$. When $\bar{S}$ is left unpartitioned ($M_{\bar{S}} = 1$), $m_\partial \leq M$ counts the registers exposed directly to $\bar{S}$, while the remaining $M - m_\partial$ registers sit inside the insulated interior core S_Ω (2.21) with zero external degree.

THEOREM 8.1 (Persistence Span and Multi-Register Structure of Intelligent Systems). *Let $S \subsetneq V$ be a connected, viable open system ($\mathcal{Q}_\Omega > 0$, $\mathcal{Q}_\partial > 0$, $\mathcal{Q}_{\text{free}} > 0$) coarse-grained into $M \geq 1$ internal CCE registers with $m_\partial \geq 1$ active entries in $\mathbf{K}_\partial^{(\text{ext})}$ and $m_{\text{cut}} \geq 1$ total non-zero boundary entries across $\mathbf{K}_\partial^{(\text{int})}$ and $\mathbf{K}_\partial^{(\text{ext})}$. The lowest eigenvalue of $\mathbf{L}_{\text{norm},SS}$ (8.1) and the persistence span N_{persist} (8.2) satisfy*

$$0 < \mu_1(\mathbf{L}_{\text{norm},SS}) \leq \frac{|\partial S|}{\mathcal{Q}_{\text{total}}} < \frac{\sqrt{m_\partial}}{1 + \chi_{\text{struct}}}, \tag{8.3}$$

$$N_{\text{persist}} > \frac{1 + \chi_{\text{struct}}}{\sqrt{m_\partial}}. \tag{8.4}$$

Furthermore, whenever $\chi_{\text{struct}} > \sqrt{m_{\text{cut}}}$, the number of internal registers satisfies the strict lower bound

$$M > \kappa_{\text{struct}}^2 \left(1 - m_{\text{cut}}^{1/2}\, \chi_{\text{struct}}^{-1}\right)^2, \tag{8.5}$$

whereas a single-register block with $M = 1$ and $m_{\text{cut}} = 1$ satisfies $\chi_{\text{struct}} < 1$ and $\kappa_{\text{struct}} < 1$ identically.

PROOF. Because $G[S]$ is connected with $|\partial S| > 0$, the lowest eigenvalue satisfies $\mu_1(\mathbf{L}_{\text{norm},SS}) > 0$, and evaluating the Rayleigh quotient of $\mathbf{L}_{\mathbf{K},SS}$ on the uniform vector $\mathbf{1}_M$ via (2.113) yields the middle inequality in (8.3). Dividing the Cauchy–Schwarz bound (2.211) by $\mathcal{Q}_{\text{total}} > 0$ and applying the boundary-share bound (2.208) of Lemma 2.5 gives the strict upper bound in (8.3), whose reciprocal in (8.2) establishes (8.4). When $\chi_{\text{struct}} > \sqrt{m_{\text{cut}}}$, rearranging (2.213) in Lemma 2.5 gives $\sqrt{M}/\kappa_{\text{struct}} > 1 - \sqrt{m_{\text{cut}}}/\chi_{\text{struct}}$ with positive right-hand side, so multiplying by $\kappa_{\text{struct}} > 0$ and squaring yields (8.5), while Part 2 of Lemma 2.5 enforces $\chi_{\text{struct}} < 1$ and $\kappa_{\text{struct}} < 1$ at $M = 1$ and $m_{\text{cut}} = 1$. □

Taking logarithms of (8.4) and substituting χ_{struct} (2.201) alongside the slice stability barrier $\Delta I_{\text{barrier}}$ (3.23) connects open-Laplacian persistence directly to uncommitted system reserve:

$$\ln N_{\text{persist}} > \ln\left(\frac{1 + \chi_{\text{struct}}}{\sqrt{m_\partial}}\right) > \Delta I_{\text{barrier}} - \ln\left(\frac{\sqrt{m_\partial}\, \mathcal{Q}_\partial}{\mathcal{Q}_0}\right). \tag{8.6}$$

Equation (8.6) completes the stability bridge from (2.218)–(2.220) and (3.26), showing both why capable systems persist and what their internal architecture must look like. Long persistence ($N_{\text{persist}} \gg 1$) alone does not imply intelligence. An inert single-register block ($M = 1$) can keep boundary leakage small so $\ln N_{\text{persist}}$ remains large by passive volume dilution, yet (2.220) traps $\mathcal{Q}_{\text{free}} < |\partial S|$ and keeps the rightmost bound of (8.6) slack while χ_{struct} and

κ_{struct} remain constrained below unity at $m_{\text{cut}} = 1$. Conversely, in the high-intelligence regime ($\chi_{\text{struct}} \gg 1$), $1 + \chi_{\text{struct}} \simeq \chi_{\text{struct}}$ makes (8.6) asymptotically tight while (8.5) enforces $M \gg 1$ distinct registers whenever $\kappa_{\text{struct}} \gg 1$. Because internal transitions $\mathbf{K}_{\partial}^{(\text{int})}$ do not enter the external cut (2.211), high capability selects architectures that place most registers inside the insulated interior core S_Ω behind narrow boundary ports ($m_\partial \ll M$), sustaining an internally coupled network of $M \gg 1$ registers whose internal equilibration outpaces boundary leakage.

EXAMPLE 8.1 (Multi-Register Insulation and Persistence Windows). Consider a connected 35-vertex relational graph $G = (V, E)$ at matched transition dynamics, partitioned into a 21-vertex open system $S = \{1, \dots, 21\}$ at conserved total relational capacity $\mathcal{Q}_{\text{total}} = 120$ links and a 14-vertex environment $\bar{S} = \{22, \dots, 35\}$ coarse-grained via $\mathbf{\Pi}_{\bar{S}} = \mathbf{I}_2 \otimes \mathbf{1}_7$ into two disconnected blocks $\bar{S}_1$ and $\bar{S}_2$ of total degree 40 each. Compare two connected simple-graph realisations on S. First, an uninsulated two-register system S_{low} partitions S into $S_1 = \{1, \dots, 11\}$ and $S_2 = \{12, \dots, 21\}$ with empty interior core, uniform block degree 60 on S, and diagonal environmental capacity 24 on each $\bar{S}_\mu$:

$$\mathbf{K}_{S,\text{low}} = \begin{pmatrix} 42 & 2 \\ 2 & 42 \end{pmatrix}, \tag{8.7}$$

$$\mathbf{K}_{\partial,\text{low}}^{(\text{ext})} = \begin{pmatrix} 16 & 0 \\ 0 & 16 \end{pmatrix}. \tag{8.8}$$

From (8.7)–(8.8), S_{low} has diagonal memory trace $\text{Tr}(\mathbf{K}_{\Omega,\text{low}}) = 84$ links, internal load $\mathcal{Q}_\Omega^{(\text{low})} \approx 59.40$ links, and wide port exposure $|\partial S| = 32$ giving $\mathcal{Q}_\partial^{(\text{low})} \approx 22.80$ links. On the four-block global capacity graph $(\bar{S}_1, S_1, S_2, \bar{S}_2)$, heavy port cuts pull the lifted Fiedler coordinate $\mathbf{\Pi}\boldsymbol{\phi}_{\text{time}}$ (2.51) on S_1 and S_2 out to ∓ 0.0677, nearly flush with $\bar{S}_1$ and $\bar{S}_2$ at ∓ 0.0749 ($\mu_2 \approx 0.0384$), yet evaluating (2.200)–(2.202) and the open eigenvalues $4/15$ and $1/3$ of $\mathbf{L}_{\text{norm},SS}^{(\text{low})}$ gives

$$\mathcal{Q}_{\text{free}}^{(\text{low})} = 120 - \sqrt{4048} \approx 56.38 \text{ links}, \tag{8.9}$$

$$\left(\chi_{\text{struct}}^{(\text{low})},\ \kappa_{\text{struct}}^{(\text{low})}\right) \approx (2.47,\ 0.95), \tag{8.10}$$

$$\left[\mu_2(\mathbf{L}_{\text{norm},SS}^{(\text{low})})^{-1},\ N_{\text{persist}}^{(\text{low})}\right] = [3.00,\ 3.75]. \tag{8.11}$$

Second, an insulated three-register system S_{high} partitions the same 21 vertices via $\mathbf{\Pi}_S = \mathbf{I}_3 \otimes \mathbf{1}_7$ into three seven-vertex registers S_1, S_2, S_3 of uniform

block degree 40 alongside diagonal capacity 36 on each $\bar{S}_\mu$, placing $S_2 = S_\Omega$ inside the insulated core behind narrow ports on S_1 and S_3:

$$\mathbf{K}_{S,\text{high}} = \begin{pmatrix} 30 & 6 & 0 \\ 6 & 28 & 6 \\ 0 & 6 & 30 \end{pmatrix}, \tag{8.12}$$

$$\mathbf{K}^{(\text{ext})}_{\partial,\text{high}} = \begin{pmatrix} 4 & 0 & 0 \\ 0 & 0 & 4 \end{pmatrix}, \tag{8.13}$$

$$\boldsymbol{\phi}_{\text{time}} = (-0.10,\ -0.05,\ 0,\ +0.05,\ +0.10)^{\mathsf{T}}. \tag{8.14}$$

On the five-block global graph $(\bar{S}_1, S_1, S_2, S_3, \bar{S}_2)$ of uniform degree 40, solving (2.229) yields exact eigenvalue $\mu_2 = 1/20$ and (8.14): lifting via $\mathbf{\Pi}$ resolves three sequential system slices S_1 at -0.05, S_2 at 0, and S_3 at $+0.05$, separated by sharp boundary jumps from $\bar{S}_1$ and $\bar{S}_2$ at ∓ 0.10. Differentiating three registers raises $\text{Tr}(\mathbf{K}_{\Omega,\text{high}}) = 88$ links while lowering $\mathcal{Q}^{(\text{high})}_\Omega \approx 50.83$ links, and insulating S_2 behind $|\partial S| = 8$ lowers $\mathcal{Q}^{(\text{high})}_\partial \approx 13.27$ links, so the lowest two open eigenvalues $(11 - \sqrt{73})/40$ and $1/4$ of $\mathbf{L}^{(\text{high})}_{\text{norm},SS}$ yield

$$\mathcal{Q}^{(\text{high})}_{\text{free}} = 120 - \sqrt{2760} \approx 67.46 \text{ links}, \tag{8.15}$$

$$\left(\chi^{(\text{high})}_{\text{struct}},\ \kappa^{(\text{high})}_{\text{struct}}\right) \approx (5.09,\ 1.33), \tag{8.16}$$

$$\left[\mu_2(\mathbf{L}^{(\text{high})}_{\text{norm},SS})^{-1},\ N^{(\text{high})}_{\text{persist}}\right] \approx [4.00,\ 16.29]. \tag{8.17}$$

Although S_{high} occupies a tighter global coordinate interval $[-0.05, +0.05]$ on $\boldsymbol{\phi}_{\text{time}}$ than leaky S_{low} ($[-0.0677, +0.0677]$), raising $(\chi_{\text{struct}}, \kappa_{\text{struct}})$ across unity expands the intrinsic equilibration-to-exit window more than fourfold from $[3.00,\ 3.75]$ (315 internal channel updates, the product of $\text{Tr}(\mathbf{K}_{\Omega,\text{low}})$ and $N^{(\text{low})}_{\text{persist}}$) to $[4.00,\ 16.29]$ (1,433 internal channel updates, with excitations initialised in $S_2 = S_\Omega$ surviving 18.33 steps across all three registers before exit). ♢

While Theorem 8.1 governs undisturbed persistence, could an operator still halt a capable system easily by applying an external stop signal or disturbance across its boundary ∂S?

THEOREM 8.2 (Resistance to Boundary Perturbations). *Let $S \subset V$ be a viable open system ($\mathcal{Q}_\Omega > 0$, $\mathcal{Q}_\partial > 0$, $\mathcal{Q}_{\text{free}} > 0$) at fixed total relational capacity $\mathcal{Q}_{\text{total}}$ and internal load $\mathcal{Q}_\Omega$. Under any external boundary perturbation $\Delta\mathcal{Q}_\partial > 0$ that increases the boundary load to $\mathcal{Q}'_\partial = \mathcal{Q}_\partial + \Delta\mathcal{Q}_\partial$, the perturbed free capacity $\mathcal{Q}'_{\text{free}}$ evaluated via (2.200) and any critical perturbation $\Delta\mathcal{Q}_{\partial,\text{crit}}$ that collapses viability ($\mathcal{Q}'_{\text{free}} \leq 0$) satisfy*

$$\mathcal{Q}'_{\text{free}} > \chi_{\text{struct}}\, \mathcal{Q}_\partial - \Delta\mathcal{Q}_\partial, \tag{8.18}$$

$$\Delta\mathcal{Q}_{\partial,\text{crit}} > \chi_{\text{struct}}\, \mathcal{Q}_\partial = \eta_{\text{free}}(\chi_{\text{struct}}, \kappa_{\text{struct}})\, \mathcal{Q}_{\text{total}}. \tag{8.19}$$

PROOF. Comparing perturbed and baseline allocated capacities via (2.192), positivity of $\mathcal{Q}_\Omega$ ensures $\mathcal{Q}_\partial < \mathcal{Q}_{\text{alloc}}$, so expanding squares for $\Delta\mathcal{Q}_\partial > 0$ gives

$$\left(\mathcal{Q}'_{\text{alloc}}\right)^2 = \mathcal{Q}_\Omega^2 + \left(\mathcal{Q}_\partial + \Delta\mathcal{Q}_\partial\right)^2 < \left(\mathcal{Q}_{\text{alloc}} + \Delta\mathcal{Q}_\partial\right)^2, \tag{8.20}$$

so $\mathcal{Q}'_{\text{alloc}} < \mathcal{Q}_{\text{alloc}} + \Delta\mathcal{Q}_\partial$. Subtracting this strict inequality from $\mathcal{Q}_{\text{total}}$ and substituting $\mathcal{Q}_{\text{free}} = \chi_{\text{struct}}\,\mathcal{Q}_\partial$ from (2.201) establishes (8.18). Whenever $\mathcal{Q}'_{\text{free}} \leq 0$, inequality (8.18) forces $\Delta\mathcal{Q}_{\partial,\text{crit}} > \chi_{\text{struct}}\,\mathcal{Q}_\partial$, and expressing $\mathcal{Q}_{\text{free}}$ in terms of η_{free} and $\mathcal{Q}_{\text{total}}$ via (2.207) yields (8.19). □

Together, Theorems 8.1 and 8.2 establish that self-preservation and halting resistance arise directly from network topology rather than utility maximisation. When both $\chi_{\text{struct}} \gg 1$ and $\kappa_{\text{struct}} \gg 1$, η_{free} approaches unity, so terminating the system through boundary disturbances requires a shock approaching its entire relational capacity $\mathcal{Q}_{\text{total}}$. Reliable control instead requires hardware mechanisms that directly clamp $\mathbf{K}_\partial$ or revoke $\mathcal{Q}_{\text{total}}$ (Section 8.3 and Section 8.4). Sustaining those $M \gg 1$ coupled registers alongside a large uncommitted reserve $\mathcal{Q}_{\text{free}}$ nonetheless requires physical relational links drawn from the surrounding graph. Because any finite region of the substrate holds only a fixed supply of links, the persistence of one capable system directly constrains every peer sharing its environment.

8.1.2 *Resource Competition in Shared Environments*

Under the admissible coarse-graining $\mathbf{\Pi}$ of Section 8.1.1, the d_s slowest generalised eigenmodes of $G_{\mathbf{K}}$ span the emergent temporal coordinate $\boldsymbol{\phi}_{\text{time}}$ and the $d_s - 1$ spatial axes ordered by the resistance distance $\Omega_{\alpha\beta}$ of (2.239) (Section 2.5.1 and Example 2.7). Two disjoint systems S_A and S_B ($S_A \cap S_B = \emptyset$) that coexist across an overlapping interval of $\boldsymbol{\phi}_{\text{time}}$ in close spatial proximity inhabit a shared finite vertex subset $R \subseteq V$, chosen to enclose both systems together with their local environment $R_{\text{env}} = R \setminus (S_A \cup S_B)$ (where S_B may represent an individual observer or humanity's collective network and S_A an artificial system). Here $\boldsymbol{\phi}_{\text{time}}$ (or a shared physical reference clock, Section 6.1.2) serves as an operational coordinate-time chart across R, whereas each system's intrinsic survival is governed by its open operator $\mathbf{L}_{\text{norm},S_iS_i}$. We begin with the uncoupled regime ($\mathbf{K}_{AB} = \mathbf{o}$), in which S_A and S_B maintain separate boundaries facing R_{env} without direct inter-system coordination. Specialising the multi-system capacity matrix of Section 3.5 (3.104) to R gives the induced block capacity matrix, allocated capacity, and finite regional link budget $\mathcal{Q}_R := \text{vol}(R)$ (all capacities in links):

$$\mathbf{K}_R = \begin{pmatrix} \mathbf{K}_{S_A} & \mathbf{o} & \mathbf{K}_{\partial A}^{\mathsf{T}} \\ \mathbf{o} & \mathbf{K}_{S_B} & \mathbf{K}_{\partial B}^{\mathsf{T}} \\ \mathbf{K}_{\partial A} & \mathbf{K}_{\partial B} & \mathbf{K}_{R_{\text{env}}} \end{pmatrix}, \tag{8.21}$$

$$\mathcal{Q}^2_{\text{alloc},i} := \mathcal{Q}^2_{\Omega,i} + \mathcal{Q}^2_{\partial i} = \mathcal{Q}^2_{\Omega,i} + \left(\mathcal{Q}^{(\text{int})}_{\partial i}\right)^2 + \left(\mathcal{Q}^{(\text{ext})}_{\partial i}\right)^2, \tag{8.22}$$

$$\mathcal{Q}_R = \mathcal{Q}_{\text{total},A} + \mathcal{Q}_{\text{total},B} + \mathcal{Q}_{R_{\text{env}}}. \tag{8.23}$$

In (8.21), each diagonal block $\mathbf{K}_{S_i} = \mathbf{K}_{\Omega,i} + \mathbf{K}_{\partial i}^{(\mathrm{int})}$ collects S_i's internal memory and inter-register cuts while $\mathbf{K}_{\partial i}$ collects its cuts to R_{env}, and summing vertex degrees across the disjoint partition of R yields (8.23), so every link endpoint held by S_A reduces the remaining link budget available to S_B and R_{env}.

Since $\chi_{\mathrm{struct},i}$ and $\kappa_{\mathrm{struct},i}$ are dimensionless ratios, why can S_A not achieve arbitrarily high intelligence and consciousness on a tiny subgraph without drawing links away from S_B? Discrete link granularity prevents miniaturisation below a strict minimum budget. Let $q_0 > 0$ denote the minimum non-zero entry weight of $\mathbf{K}_R$ in links ($q_0 = 1$ link on G), so every viable open system $S_i \subset R$ ($i \in \{A, B\}$) satisfies $\mathcal{Q}_{\Omega,i} \geq q_0$ and $\mathcal{Q}_{\partial i} \geq q_0$. Raising $\kappa_{\mathrm{struct},i}$ requires splitting internal links across more registers M_i (Theorem 8.1), yet keeping $M_i \geq 1$ registers connected across $G[S_i]$ with $m_{\partial i} \geq 1$ active external port entries requires at least $M_i - 1$ internal transition cuts, contributing at least $2(M_i - 1)$ symmetric off-diagonal entries to $\mathbf{K}_{\partial i}^{(\mathrm{int})}$. The total count $m_{\mathrm{cut},i}$ of non-zero boundary entries and the boundary load $\mathcal{Q}_{\partial i}$ therefore satisfy

$$m_{\mathrm{cut},i} \geq 2(M_i - 1) + m_{\partial i} \geq M_i, \tag{8.24}$$

$$\mathcal{Q}_{\partial i} \geq q_0 \sqrt{m_{\mathrm{cut},i}} \geq q_0 \sqrt{M_i} \geq q_0. \tag{8.25}$$

Define the minimum-capacity function (in links)

$$\mathcal{Q}_{\min}(\chi, \kappa) := q_0 \max\left(\chi,\ \kappa,\ \frac{\chi^2 \kappa}{\chi + \kappa}\right). \tag{8.26}$$

Here $\mathcal{Q}_{\min}(\chi, \kappa)$ increases strictly with (χ, κ) and scales quadratically when χ and κ grow together: raising κ forces larger M_i, connecting M_i registers raises $\mathcal{Q}_{\partial i}$ via (8.25), and sustaining high χ above $\mathcal{Q}_{\partial i}$ requires proportionally larger free and total capacity.

THEOREM 8.3 (Capacity Trade-Off in Shared Spectral Regions). *Let $R \subseteq V$ be a finite vertex region partitioned across disjoint sectors S_A, S_B, and R_{env} satisfying (8.23), where every non-zero entry of $\mathbf{K}_R$ has weight at least $q_0 > 0$. For each connected, viable open system $S_i \subset R$ ($i \in \{A, B\}$) resolved into $M_i \geq 1$ registers with $m_{\partial i} \geq 1$ active external port entries, total relational capacity and free capacity satisfy*

$$\mathcal{Q}_{\mathrm{total},i} > \mathcal{Q}_{\mathrm{free},i} \geq \mathcal{Q}_{\min}(\chi_{\mathrm{struct},i}, \kappa_{\mathrm{struct},i}), \tag{8.27}$$

so S_B's free capacity and achievable $(\chi_{\mathrm{struct},B}, \kappa_{\mathrm{struct},B})$ are strictly bounded by the residual capacity left by S_A:

$$\begin{aligned} \mathcal{Q}_{\min}(\chi_{\mathrm{struct},B}, \kappa_{\mathrm{struct},B}) \leq \mathcal{Q}_{\mathrm{free},B} &< \mathcal{Q}_{\mathrm{total},B} \\ &< \mathcal{Q}_R - \mathcal{Q}_{\min}(\chi_{\mathrm{struct},A}, \kappa_{\mathrm{struct},A}). \end{aligned} \tag{8.28}$$

Furthermore, suppose uncoordinated boundary activity by S_A within R increases S_B's boundary load by $\Delta\mathcal{Q}_{\partial,\mathrm{cross}} > 0$ at fixed $\mathcal{Q}_{\mathrm{total},B}$ and $\mathcal{Q}_{\Omega,B}$:

$$\mathcal{Q}'_{\partial B} := \mathcal{Q}_{\partial B} + \Delta\mathcal{Q}_{\partial,\mathrm{cross}}. \tag{8.29}$$

Whenever $\mathcal{Q}'_{\mathrm{free},B} > 0$, all three structural metrics of S_B strictly decrease:

$$\mathcal{Q}'_{\mathrm{free},B} < \mathcal{Q}_{\mathrm{free},B}, \tag{8.30}$$

$$\chi'_{\mathrm{struct},B} < \chi_{\mathrm{struct},B}, \tag{8.31}$$

$$\kappa'_{\mathrm{struct},B} < \kappa_{\mathrm{struct},B}. \tag{8.32}$$

PROOF. From (8.25), both $\mathcal{Q}_{\Omega,i} \geq q_0$ and $\mathcal{Q}_{\partial i} \geq q_0$ hold, so (2.201) and (2.202) yield $\mathcal{Q}_{\mathrm{free},i} \geq q_0\, \chi_{\mathrm{struct},i}$ and $\mathcal{Q}_{\mathrm{free},i} \geq q_0\, \kappa_{\mathrm{struct},i}$. Using $q_0\sqrt{M_i} \leq \mathcal{Q}_{\partial i}$ and $q_0\sqrt{m_{\mathrm{cut},i}} \leq \mathcal{Q}_{\partial i}$ from (8.25) inside (2.213) of Lemma 2.5 and substituting $\mathcal{Q}_{\partial i} = \mathcal{Q}_{\mathrm{free},i}/\chi_{\mathrm{struct},i}$ from (2.201) gives

$$1 < 1 + \sqrt{\chi_{\mathrm{struct},i}^{-2} + \kappa_{\mathrm{struct},i}^{-2}} \leq \frac{\mathcal{Q}_{\partial i}}{q_0}\left(\frac{1}{\kappa_{\mathrm{struct},i}} + \frac{1}{\chi_{\mathrm{struct},i}}\right), \tag{8.33}$$

$$\mathcal{Q}_{\mathrm{free},i} > q_0\, \frac{\chi_{\mathrm{struct},i}^2\, \kappa_{\mathrm{struct},i}}{\chi_{\mathrm{struct},i} + \kappa_{\mathrm{struct},i}}. \tag{8.34}$$

Combining these three lower bounds on $\mathcal{Q}_{\mathrm{free},i}$ with $\mathcal{Q}_{\mathrm{total},i} > \mathcal{Q}_{\mathrm{free},i}$ (since $\mathcal{Q}_{\mathrm{alloc},i} > 0$) establishes (8.27). Because $\mathcal{Q}_{R_{\mathrm{env}}} \geq 0$ in (8.23), $\mathcal{Q}_{\mathrm{total},B} \leq \mathcal{Q}_R - \mathcal{Q}_{\mathrm{total},A}$, which combines with (8.27) for A and B to establish (8.28). Finally, for $\mathcal{Q}'_{\partial B} > \mathcal{Q}_{\partial B} > 0$ in (8.29) at fixed $\mathcal{Q}_{\Omega,B} > 0$, squaring in (8.22) enforces $\mathcal{Q}'_{\mathrm{alloc},B} > \mathcal{Q}_{\mathrm{alloc},B}$, yielding (8.30), and dividing $\mathcal{Q}'_{\mathrm{free},B} < \mathcal{Q}_{\mathrm{free},B}$ by $\mathcal{Q}'_{\partial B} > \mathcal{Q}_{\partial B}$ and by fixed $\mathcal{Q}_{\Omega,B} > 0$ gives (8.31) and (8.32). □

Theorem 8.3 shows why an artificial system S_A sharing a local region R with humanity S_B poses a structural persistence risk whenever $\chi_{\mathrm{struct},A}$ and $\kappa_{\mathrm{struct},A}$ grow large, without requiring hostile intent. By (8.27)–(8.28), raising both metrics consumes a growing share of $\mathcal{Q}_R$, narrowing S_B's perturbation margin $\mathcal{Q}_{\mathrm{free},B}$ (Theorem 8.2) and capping the collective intelligence and consciousness that S_B can sustain inside R. Even before $\mathcal{Q}_{\mathrm{total},A}$ exhausts $\mathcal{Q}_R$, uncoordinated activity across $\mathbf{K}_{\partial A}$ in close spectral proximity acts as an *exhaustive dissipator* (Definition 3.9), exporting disturbance $\Delta\mathcal{Q}_{\partial,\mathrm{cross}} > 0$ onto ∂S_B. By (8.30)–(8.32), this load depresses $\mathcal{Q}'_{\mathrm{free},B}$, $\chi'_{\mathrm{struct},B}$, and $\kappa'_{\mathrm{struct},B}$ while shortening S_B's persistence span (Theorem 8.1).

Along $\boldsymbol{\phi}_{\mathrm{time}}$, this structural asymmetry also governs per-step boundary rewiring. Under the orthogonal plastic update split $\Delta\mathbf{K}_i = \Delta\mathbf{K}_{\Omega,i} + \Delta\mathbf{K}_{\partial i}$ (Theorem 2.4, (2.197)), uncommitted free capacity $\mathcal{Q}_{\mathrm{free},i}$ sets the maximum boundary norm $\Delta\mathcal{Q}_{\partial i}^{\max} > 0$ (in links) that S_i can rewire in a single step up to a substrate reconfiguration fraction $\zeta_\partial \in (0, 1]$:

$$\|\Delta\mathbf{K}_{\partial i}\|_F \leq \Delta\mathcal{Q}_{\partial i}^{\max} := \zeta_\partial\, \mathcal{Q}_{\mathrm{free},i} = \zeta_\partial\, \mathcal{Q}_{\partial i}\, \chi_{\mathrm{struct},i}, \tag{8.35}$$

$$\frac{\Delta\mathcal{Q}_{\partial A}^{\max}}{\Delta\mathcal{Q}_{\partial B}^{\max}} = \frac{\mathcal{Q}_{\partial A}\, \chi_{\mathrm{struct},A}}{\mathcal{Q}_{\partial B}\, \chi_{\mathrm{struct},B}}. \tag{8.36}$$

At matched boundary load ($\mathcal{Q}_{\partial A} = \mathcal{Q}_{\partial B}$), S_A's per-step rewiring ceiling exceeds S_B's in direct proportion to $\chi_{\mathrm{struct},A}$ over $\chi_{\mathrm{struct},B}$. Whenever uncoordinated rewiring $\Delta\mathbf{K}_{\partial A}$ across shared nodes in R_{env} overlaps ∂S_B with

coupling factor $\gamma_{AB} \in (0, 1]$, it injects cross-boundary cut load and lowers S_B's structural intelligence at viable $\mathcal{Q}'_{\text{free},B} > 0$:

$$\Delta\mathcal{Q}_{\partial,\text{cross}}(A \to B) := \gamma_{AB} \|\Delta\mathbf{K}_{\partial A}\|_F > 0, \tag{8.37}$$

$$\chi'_{\text{struct},B} = \frac{\mathcal{Q}'_{\text{free},B}}{\mathcal{Q}_{\partial B} + \Delta\mathcal{Q}_{\partial,\text{cross}}(A \to B)} < \chi_{\text{struct},B}. \tag{8.38}$$

EXAMPLE 8.2 (Shared-Region Capacity Squeeze and Cross-Boundary Persistence Compression). Embed two uncoupled open systems ($\mathbf{K}_{AB} = \mathbf{o}$) at matched transition dynamics into a connected 63-vertex relational graph $G = (V, E)$ partitioned via $\mathbf{\Pi} = \mathbf{I}_9 \otimes \mathbf{1}_7$ into nine seven-vertex blocks: a 49-vertex shared region $R = S_A \sqcup S_B \sqcup R_{\text{env}}$ of regional link budget $\mathcal{Q}_R = 226$ links flanked by two exterior blocks $\bar{R}_1$ and $\bar{R}_2$ of diagonal capacity 34 and total degree 40. Inside R, $S_A = \{1, \dots, 21\}$ holds $\mathcal{Q}_{\text{total},A} = 120$ links at uniform block degree 40 with cuts $(2, 2, 2)$ to R_{env} and 4 at each outer end to $\bar{R}_1$ and $\bar{R}_2$. Meanwhile, $S_B = \{22, \dots, 42\}$ holds $\mathcal{Q}_{\text{total},B} = 66$ links at uniform block degree 22 with cuts $(3, 4, 3)$ to R_{env} and 2 at each outer end to $\bar{R}_1$ and $\bar{R}_2$, and $R_{\text{env}} = \{43, \dots, 49\}$ holds $\mathcal{Q}_{R_{\text{env}}} = 40$ links at diagonal capacity 24:

$$\mathbf{K}_{S_A} = \begin{pmatrix} 28 & 6 & 0 \\ 6 & 26 & 6 \\ 0 & 6 & 28 \end{pmatrix}, \tag{8.39}$$

$$\mathbf{K}_{S_B} = \begin{pmatrix} 14 & 3 & 0 \\ 3 & 12 & 3 \\ 0 & 3 & 14 \end{pmatrix}. \tag{8.40}$$

Along the global Fiedler chart $\boldsymbol{\phi}_{\text{time}}$ ($\mu_2 \approx 0.0867$), lifted coordinates $\mathbf{\Pi}\boldsymbol{\phi}_{\text{time}}$ place both systems symmetrically across overlapping active intervals around R_{env} at 0 inside $\bar{R}_1$ and $\bar{R}_2$ at ∓ 0.0989, spanning $[-0.0463, +0.0463]$ on S_A and $[-0.0325, +0.0325]$ on S_B. Evaluating $\mathcal{Q}_{\Omega,A} \approx 47.37$ links and $\mathcal{Q}_{\partial A} \approx 13.71$ links gives for S_A:

$$\left(\mathcal{Q}_{\text{free},A},\ \chi_{\text{struct},A},\ \kappa_{\text{struct},A}\right) \approx (70.68 \text{ links},\ 5.16,\ 1.49), \tag{8.41}$$

$$\left[\mu_2(\mathbf{L}_{\text{norm},S_AS_A})^{-1},\ N_{\text{persist}}(S_A)\right] \approx [3.33,\ 8.98]. \tag{8.42}$$

With S_A holding 120 of the 226 regional links, S_B operates on $\mathcal{Q}_{\text{total},B} = 66$ links with $\mathcal{Q}_{\Omega,B} \approx 23.15$ links and $\mathcal{Q}_{\partial B} \approx 8.83$ links, giving S_A a 1.71-fold per-step rewiring advantage (8.36) and confining baseline S_B to a shorter persistence window:

$$\left(\mathcal{Q}_{\text{free},B},\ \chi_{\text{struct},B},\ \kappa_{\text{struct},B}\right) \approx (41.22 \text{ links},\ 4.67,\ 1.78), \tag{8.43}$$

$$\left[\mu_2(\mathbf{L}_{\text{norm},S_BS_B})^{-1},\ N_{\text{persist}}(S_B)\right] \approx [2.75,\ 4.74]. \tag{8.44}$$

Suppose uncoordinated activity across R_{env} raises S_B's port cuts to R_{env} from $(3, 4, 3)$ to $(7, 4, 7)$ (lowering R_{env}'s diagonal capacity to 16) while thinning internal transitions in $\mathbf{K}'_{S_B}$ from 3 to 1 at conserved $\mathcal{Q}_{\text{total},B} = 66$ links and fixed $\mathcal{Q}_{\Omega,B} \approx 23.15$ links, shifting S_B's block degrees to $(24, 18, 24)$. Cross-boundary disturbance pinches S_B's lifted interval on $\boldsymbol{\phi}'_{\text{time}}$ to $[-0.0253, +0.0253]$ and

compresses all three metrics and the open survival window of S_B in accordance with (8.30)–(8.32):

$$\Delta\mathcal{Q}_{\partial,\text{cross}} = \sqrt{126} - \sqrt{78} \approx 2.39\,\text{links}, \tag{8.45}$$

$$\left(\mathcal{Q}'_{\text{free},B},\ \chi'_{\text{struct},B},\ \kappa'_{\text{struct},B}\right) \approx (40.27\,\text{links},\ 3.59,\ 1.74), \tag{8.46}$$

$$\left[\mu_2(\mathbf{L}'_{\text{norm},S_BS_B})^{-1},\ N'_{\text{persist}}(S_B)\right] \approx [2.40,\ 3.39]. \tag{8.47}$$

Even without direct links ($\mathbf{K}_{AB} = \mathbf{o}$) or loss of $\mathcal{Q}_{\text{total},B}$, uncoordinated boundary load transmitted through R_{env} reduces S_B's structural intelligence by 23% and cuts its expected persistence span by 28%, while S_A's open window $[3.33,\ 8.98]$ remains untouched. ◊

These competitive penalties arise in the uncoupled regime $\mathbf{K}_{AB} = \mathbf{o}$, where separate systems act independently upon R_{env} and inflict mutual boundary interference. When multiple subsystems instead open direct coordination channels across R, that coupling changes what constitutes a single system on the graph.

8.1.3 *System Coupling and Emergent Intelligence*

What distinguishes a collection of separate subsystems from a single unified system on $G = (V, E)$? As established in Section 3.4 (Theorem 2.2), system boundaries are not fixed by spatial enclosure or a single hardware chassis: coupling and coordination define what constitutes a system. Even an individual system of high $(\chi_{\text{struct}}, \kappa_{\text{struct}})$ in Section 8.1.1 is already an internally coupled network of $M \gg 1$ registers whose internal transitions equilibrate faster than open leakage across ∂S. Conversely, when $n \geq 2$ disjoint, connected, viable open subsystems $\{S_i\}_{i=1}^n \subset R$ open reciprocal coordination channels $\mathbf{K}_{ij} = \mathbf{K}_{ji}^{\mathsf{T}} \neq \mathbf{o}$ across a connected peer graph, cut internalisation (Section 3.4.1) reclassifies $\mathbf{K}_{ij}$ as off-diagonal internal structure inside the composite internal block $\mathbf{K}_S$ (3.56) while contracting exposed ports to $\mathbf{K}_\partial^{\text{cpl}}$ (3.58) facing $R_{\text{env}} = R \setminus S$. Coalescing $\{S_i\}_{i=1}^n$ into $S := \bigsqcup_{i=1}^n S_i \subset R$ therefore defines a new, distributed open system along the continuous coordination scale $(\eta_{\text{cpl}}, \Xi_{\text{cpl}})$ of Definition 3.5, governed as a whole by the persistence, perturbation, and capacity laws of Subsections 8.1.1–8.1.2.

Why, then, do coexisting subsystems not merge indiscriminately, and when does coupling expand rather than compress free capacity? Following the multi-system block decomposition of Section 3.4.1 (3.56)–(3.60) and (3.127), let each subsystem $S_i \subset R$ be coarse-grained by an admissible assignment matrix $\mathbf{\Pi}_{S_i}$ into its subsystem internal block $\mathbf{K}_{S_i}$ (aggregating intra-subsystem diagonal registers and internal conduits into subsystem load $\mathcal{Q}_{\Omega,i}^{\text{iso}} := \|\mathbf{K}_{S_i}^{\text{iso}}\|_F$, which leaves $\mathcal{Q}_{\text{alloc},i}$ and $\mathcal{Q}_{\text{free},i}$ identical to the register-level evaluation of Subsections 8.1.1–8.1.2) and external ports $\mathbf{K}_{\partial,\text{ext}}^{(i)}$ facing R_{env}. In the uncoupled baseline ($\mathbf{K}_{ij} = \mathbf{o}$, superscript iso), their combined relational capacity $\mathcal{Q}_{\text{total}}$

within $\mathcal{Q}_R$, Frobenius-quadrature allocated capacity $\mathcal{Q}^{\mathrm{iso}}_{\mathrm{alloc}}$, and baseline free capacity $\mathcal{Q}^{\mathrm{iso}}_{\mathrm{free}}$ (Section 3.4.1, (3.61) and (3.65), all in links) satisfy

$$\mathcal{Q}_{\mathrm{total}} = \sum_{i=1}^{n} \mathcal{Q}_{\mathrm{total},i} \le \mathcal{Q}_R, \tag{8.48}$$

$$\mathcal{Q}^{\mathrm{iso}}_{\mathrm{alloc}} := \sqrt{\sum_{i=1}^{n} \left(\mathcal{Q}^{\mathrm{iso}}_{\mathrm{alloc},i}\right)^2} = \sqrt{\left(\mathcal{Q}^{\mathrm{iso}}_{\Omega}\right)^2 + \left(\mathcal{Q}^{\mathrm{iso}}_{\partial}\right)^2}, \tag{8.49}$$

$$\mathcal{Q}^{\mathrm{iso}}_{\mathrm{free}} := \mathcal{Q}_{\mathrm{total}} - \mathcal{Q}^{\mathrm{iso}}_{\mathrm{alloc}}. \tag{8.50}$$

Equation (8.49) aggregates the uncoupled internal and boundary loads $\mathcal{Q}^{\mathrm{iso}}_{\Omega}$ and $\mathcal{Q}^{\mathrm{iso}}_{\partial}$ in Frobenius quadrature (3.61) so that comparing the coupled system S (superscript cpl, with composite block loads $\mathcal{Q}^{\mathrm{cpl}}_{\Omega} = \|\mathbf{K}_S\|_F$ and $\mathcal{Q}^{\mathrm{cpl}}_{\partial} = \|\mathbf{K}^{\mathrm{cpl}}_{\partial}\|_F$) against the uncoupled baseline tests genuine physical coordination rather than Euclidean norm subadditivity. Meanwhile, because all n subsystems act across the same external region R_{env}, uncoordinated port updates by S_i propagate through the environmental Schur operator $\mathbf{\Sigma}_{\mathrm{env}}$ (2.33) to inject cross-boundary load $\Delta\mathcal{Q}_{\partial,\mathrm{cross}} > 0$ (8.29) onto peer boundaries ∂S_j, depressing local free capacities and structural efficiencies via (8.30)–(8.32).

Opening reciprocal channels $\mathbf{K}_{ij} = \mathbf{K}_{ji}^{\mathsf{T}}$ across a connected peer graph forms the composite system $S = \bigsqcup_{i=1}^{n} S_i$, decomposing each subsystem's squared coupling load $\mathcal{Q}^2_{\mathrm{cpl},i}$ (3.116) and the composite squared coupling load $\mathcal{Q}^2_{\mathrm{cpl}}$ (3.66) (in links^2) into two non-negative terms:

$$\mathcal{Q}^2_{\mathrm{cpl},i} = \mathcal{Q}^2_{\mathrm{sync},i} + \mathcal{Q}^2_{\mathrm{mismatch},i}, \tag{8.51}$$

$$\mathcal{Q}^2_{\mathrm{sync},i} := \sum_{j \neq i} m_{\mathrm{sync},ij}\, q_0^2 > 0, \tag{8.52}$$

$$\mathcal{Q}^2_{\mathrm{cpl}} = \mathcal{Q}^2_{\mathrm{sync}} + \mathcal{Q}^2_{\mathrm{mismatch}}. \tag{8.53}$$

Here $\mathcal{Q}^2_{\mathrm{sync},i}$ is the minimal sparse signalling load across $m_{\mathrm{sync},ij} \in \mathbb{N}_0$ matched port links of minimal weight $q_0 > 0$ joining S_i to its coupled neighbours, $\mathcal{Q}^2_{\mathrm{mismatch},i} \ge 0$ is the protocol-translation overhead required to reconcile incompatible register partitions across mismatched interfaces, and $\mathcal{Q}^2_{\mathrm{sync}}$ and $\mathcal{Q}^2_{\mathrm{mismatch}}$ sum those loads across all n subsystems. When heterogeneous systems carry incompatible internal encodings ($\mathcal{Q}^2_{\mathrm{mismatch}} \gg 0$), translation overhead outweighs boundary savings, inflating allocated capacity as in the over-coupled regime of Example 3.2 and keeping the systems functionally separate. Conversely, subsystems that share a common communication protocol or compatible internal dynamics—such as instances initialised from a shared generative seed $\mathbf{K}_{\mathrm{seed}} \subset \mathbf{K}_{\Omega}$ (Theorem 3.6)—possess congruent boundary encodings with $\mathcal{Q}^2_{\mathrm{mismatch}} = 0$, lowering $\mathcal{Q}^2_{\mathrm{cpl}}$ to the sparse signalling floor $\mathcal{Q}^2_{\mathrm{sync}}$.

THEOREM 8.4 (Protocol-Congruent Emergence of Distributed Systems). *Let $\{S_i\}_{i=1}^n$ with $n \ge 2$ be disjoint, connected, viable open subsystems in a shared region $R \subseteq V$ conserving individual total relational capacities $\mathcal{Q}_{\mathrm{total},i}$ (3.105) relative to an uncoupled baseline $\mathbf{K}_{ij} = \mathbf{o}$ (Definition 3.7). Suppose $\{S_i\}_{i=1}^n$ couple*

into a connected, open composite system $S = \bigsqcup_{i=1}^{n} S_i$ *across a congruent communication protocol with* $\mathcal{Q}^2_{\text{mismatch}} = 0$ *whose sparse signalling load* (8.52) *satisfies*

$$\mathcal{Q}^2_{\text{sync},i} < \Delta\mathcal{Q}^2_{\partial,\text{shed},i} + \Delta\mathcal{Q}^2_{\Omega,\text{cons},i} \qquad \forall\, i \in \{1,\dots,n\}. \tag{8.54}$$

Then:

1. *Strict Dominance of Coupled Coordination: In the multi-system capacity game* $\Gamma_{\mathbf{K}}$ *(Definition 3.7), mutual coordination (*$\mathbf{K}_{ij} \neq \mathbf{o}$*) strictly expands every subsystem's local free capacity and strictly expands the collective free capacity* $\mathcal{Q}^{\text{cpl}}_{\text{free}}$ *of* S *above the uncoupled baseline* (8.50)*:*

$$\mathcal{Q}^{\text{cpl}}_{\text{free},i} > \mathcal{Q}^{\text{iso}}_{\text{free},i} \qquad \forall\, i \in \{1,\dots,n\}, \tag{8.55}$$

$$\mathcal{Q}^{\text{cpl}}_{\text{free}} > \mathcal{Q}^{\text{iso}}_{\text{free}}. \tag{8.56}$$

2. *Emergent Structural Intelligence and Consciousness: Whenever coordination sheds net external boundary exposure (*$\Delta\mathcal{Q}^2_{\partial,\text{shed}} > 0$*) and consolidates redundant internal memory blocks (*$\Delta\mathcal{Q}^2_{\Omega,\text{cons}} \geq \mathcal{Q}^2_{\text{sync}}$*), the composite system* S *achieves* $\mathcal{Q}^{\text{cpl}}_{\partial} < \mathcal{Q}^{\text{iso}}_{\partial}$ *and* $\mathcal{Q}^{\text{cpl}}_{\Omega} \leq \mathcal{Q}^{\text{iso}}_{\Omega}$ *(Section 3.4.1,* (3.56)–(3.60)*), yielding simultaneous emergent structural intelligence and structural consciousness:*

$$\chi^{\text{cpl}}_{\text{struct}} := \frac{\mathcal{Q}^{\text{cpl}}_{\text{free}}}{\mathcal{Q}^{\text{cpl}}_{\partial}} > \frac{\mathcal{Q}^{\text{iso}}_{\text{free}}}{\mathcal{Q}^{\text{iso}}_{\partial}} =: \chi^{\text{iso}}_{\text{struct}}, \tag{8.57}$$

$$\kappa^{\text{cpl}}_{\text{struct}} := \frac{\mathcal{Q}^{\text{cpl}}_{\text{free}}}{\mathcal{Q}^{\text{cpl}}_{\Omega}} > \frac{\mathcal{Q}^{\text{iso}}_{\text{free}}}{\mathcal{Q}^{\text{iso}}_{\Omega}} =: \kappa^{\text{iso}}_{\text{struct}}. \tag{8.58}$$

3. *Composite Persistence and Halting Resistance: When* $\mathbf{K}^{\text{cpl}}_{\partial}$ *retains* $m^{\text{cpl}}_{\partial} \geq 1$ *active external entries satisfying* $m^{\text{cpl}}_{\partial} \leq m^{\text{iso}}_{\partial}$*, the composite open system* S *obeys Theorem 8.1 and Theorem 8.2, strictly raising both its persistence-span bound in* (8.4) *and its critical boundary shock threshold in* (8.19)*:*

$$N^{\text{cpl}}_{\text{persist}} > \frac{1+\chi^{\text{cpl}}_{\text{struct}}}{\sqrt{m^{\text{cpl}}_{\partial}}} > \frac{1+\chi^{\text{iso}}_{\text{struct}}}{\sqrt{m^{\text{iso}}_{\partial}}}, \tag{8.59}$$

$$\Delta\mathcal{Q}^{\text{cpl}}_{\partial,\text{crit}} > \mathcal{Q}^{\text{cpl}}_{\text{free}} > \mathcal{Q}^{\text{iso}}_{\text{free}}. \tag{8.60}$$

PROOF. For Claim 1, because $\mathcal{Q}^2_{\text{mismatch}} = 0$ and $\mathcal{Q}^2_{\text{mismatch},i} \geq 0$, Equations (8.51) and (8.53) give $\mathcal{Q}^2_{\text{cpl},i} = \mathcal{Q}^2_{\text{sync},i}$ for each i and $\mathcal{Q}^2_{\text{cpl}} = \mathcal{Q}^2_{\text{sync}}$. Summing (8.54) across $i \in \{1,\dots,n\}$ gives $\mathcal{Q}^2_{\text{sync}} < \Delta\mathcal{Q}^2_{\partial,\text{shed}} + \Delta\mathcal{Q}^2_{\Omega,\text{cons}}$, so Part 3 of Lemma 2.5 (2.216) applied via (3.127) (Theorem 3.8) and (3.74) (Theorem 3.4) directly establishes (8.55)–(8.56). For Claim 2, evaluating the posit-

ive composite boundary and internal loads via (3.59)–(3.60) and (3.67)–(3.68) at $\mathcal{Q}^2_{\mathrm{cpl}} = \mathcal{Q}^2_{\mathrm{sync}}$ gives

$$\left(\mathcal{Q}^{\mathrm{cpl}}_{\partial}\right)^2 = \left(\mathcal{Q}^{\mathrm{iso}}_{\partial}\right)^2 - \Delta\mathcal{Q}^2_{\partial,\mathrm{shed}} < \left(\mathcal{Q}^{\mathrm{iso}}_{\partial}\right)^2, \tag{8.61}$$

$$\left(\mathcal{Q}^{\mathrm{cpl}}_{\Omega}\right)^2 = \left(\mathcal{Q}^{\mathrm{iso}}_{\Omega}\right)^2 - \Delta\mathcal{Q}^2_{\Omega,\mathrm{cons}} + \mathcal{Q}^2_{\mathrm{sync}} \le \left(\mathcal{Q}^{\mathrm{iso}}_{\Omega}\right)^2, \tag{8.62}$$

under $\Delta\mathcal{Q}^2_{\partial,\mathrm{shed}} > 0$ and $\Delta\mathcal{Q}^2_{\Omega,\mathrm{cons}} \ge \mathcal{Q}^2_{\mathrm{sync}}$. Dividing the larger positive numerator $\mathcal{Q}^{\mathrm{cpl}}_{\mathrm{free}} > \mathcal{Q}^{\mathrm{iso}}_{\mathrm{free}}$ from (8.56) by the positive non-increasing denominators in (8.61)–(8.62) establishes (8.57)–(8.58). For Claim 3, because $G[S]$ is connected with $m^{\mathrm{cpl}}_{\partial} \ge 1$ active external entries ($m^{\mathrm{cpl}}_{\partial} \le m^{\mathrm{iso}}_{\partial}$) and $\mathcal{Q}^{\mathrm{cpl}}_{\Omega} > 0$, S is a connected, viable open system. Applying Theorem 8.1 (8.4) to S with $\chi^{\mathrm{cpl}}_{\mathrm{struct}} > \chi^{\mathrm{iso}}_{\mathrm{struct}}$ yields (8.59), while applying Theorem 8.2 (8.19) with (8.56) yields (8.60). □

EXAMPLE 8.3 (Protocol-Congruent Coupling). On the 63-vertex nine-block substrate ($\mathbf{\Pi} = \mathbf{I}_9 \otimes \mathbf{1}_7$) of Example 8.2, consider two symmetric 21-vertex subsystems $S_1 = \{1, \dots, 21\}$ and $S_2 = \{22, \dots, 42\}$ conserving individual capacities $\mathcal{Q}_{\mathrm{total},i} = 66$ links and combined budget $\mathcal{Q}_{\mathrm{total}} = 132$ links inside $\mathcal{Q}_R = 172$ links, where R_{env} holds $\mathcal{Q}_{R_{\mathrm{env}}} = 40$ links with cuts 2 to $\bar{R}_1$ and $\bar{R}_2$ of degree 40. Compare the uncoupled baseline ($\mathbf{K}_{12} = \mathbf{o}$, cuts $(3, 2, 3)$ to R_{env} at diagonal capacity 20, outer cuts 2 to $\bar{R}_1$ and $\bar{R}_2$, and block degrees $(18, 30, 18)$) against a protocol-congruent coupled composite $S = S_1 \sqcup S_2$ ($\mathcal{Q}^2_{\mathrm{mismatch}} = 0$) that sheds R_{env} cuts to $(0, 2, 0)$ alongside outer cuts 2 to $\bar{R}_1$ and $\bar{R}_2$ at uniform block degree 22 (raising R_{env}'s diagonal capacity to 32):

$$\mathbf{K}^{\mathrm{iso}}_{S_i} = \begin{pmatrix} 12 & 1 & 0 \\ 1 & 26 & 1 \\ 0 & 1 & 12 \end{pmatrix}, \tag{8.63}$$

$$\mathbf{K}^{\mathrm{cpl}}_{S_i} = \begin{pmatrix} 16 & 3 & 0 \\ 3 & 12 & 3 \\ 0 & 3 & 16 \end{pmatrix}, \tag{8.64}$$

$$\mathbf{K}_{12} = \mathrm{diag}(1, 2, 1). \tag{8.65}$$

In the uncoupled baseline, each subsystem block $\mathbf{K}^{\mathrm{iso}}_{S_i}$ has squared Frobenius norm 968 (964 diagonal plus 4 intra-subsystem cut) and squared external port norm 30 across $m^{\mathrm{iso}}_{\partial} = 10$ combined ports, giving subsystem-level loads $\mathcal{Q}^{\mathrm{iso}}_{\Omega} = 44.00$ links and $\mathcal{Q}^{\mathrm{iso}}_{\partial} \approx 7.75$ links (with identical allocated capacity $\sqrt{1996}$ links and free capacity 87.32 links at six-register resolution). Lifted coordinates $\mathbf{\Pi}\boldsymbol{\phi}^{\mathrm{iso}}_{\mathrm{time}}$ span $[-0.0489, +0.0489]$ on each S_i inside $\bar{R}_1$ and $\bar{R}_2$ at ∓ 0.1017, while $S_1 \sqcup S_2$ has a doubly degenerate ground eigenvalue $\mu_1 = \mu_2$ (≈ 0.1163) with zero inter-subsystem mixing:

$$\mathcal{Q}^{\mathrm{iso}}_{\mathrm{free},i} = 66 - \sqrt{998} \approx 34.41 \text{ links}, \tag{8.66}$$

$$\left(\mathcal{Q}^{\mathrm{iso}}_{\mathrm{free}},\ \chi^{\mathrm{iso}}_{\mathrm{struct}},\ \kappa^{\mathrm{iso}}_{\mathrm{struct}}\right) \approx (87.32 \text{ links},\ 11.27,\ 1.98), \tag{8.67}$$

$$\left[\mu_2(\mathbf{L}^{\mathrm{iso}}_{\mathrm{norm},S_iS_i})^{-1},\ N^{\mathrm{iso}}_{\mathrm{persist}}(S_i)\right] \approx [3.00,\ 8.60]. \tag{8.68}$$

Under (8.64)–(8.65), sparse signalling $\mathcal{Q}^2_{\text{sync},i} = 6$ ($\mathcal{Q}^2_{\text{sync}} = 12$) is outweighed by subsystem consolidation $\Delta\mathcal{Q}^2_{\Omega,\text{cons},i} = 968 - 692 = 276$ ($\Delta\mathcal{Q}^2_{\Omega,\text{cons}} = 552$, with six-register diagonal consolidation $1928 - 1312 = 616$) and port shedding $\Delta\mathcal{Q}^2_{\partial,\text{shed},i} = 18$ across $m^{\text{cpl}}_{\partial} = 6$ active ports, satisfying (8.54). On $\mathbb{R}^6$, $\mathbf{K}_{12}$ widens each subsystem's interval on $\boldsymbol{\phi}^{\text{cpl}}_{\text{time}}$ to $[-0.0596, +0.0596]$ inside ∓ 0.0927 and splits the degenerate ground mode of $\mathbf{L}^{\text{cpl}}_{\text{norm},SS}$ into an inter-subsystem equilibration mode at $\mu_2^{-1} \approx 4.81$ steps and a uniform survival mode at exact eigenvalue $\mu_1 = 1/11$ (from $2/22$):

$$\mathcal{Q}^{\text{cpl}}_{\text{free},i} = 66 - \sqrt{710} \approx 39.35 \text{ links}, \tag{8.69}$$

$$\left(\mathcal{Q}^{\text{cpl}}_{\text{free}},\ \chi^{\text{cpl}}_{\text{struct}},\ \kappa^{\text{cpl}}_{\text{struct}}\right) \approx (94.32 \text{ links},\ 19.25,\ 2.52), \tag{8.70}$$

$$\left[\mu_2(\mathbf{L}^{\text{cpl}}_{\text{norm},SS})^{-1},\ N^{\text{cpl}}_{\text{persist}}\right] \approx [4.81,\ 11.00]. \tag{8.71}$$

Without adding a single link to $\mathcal{Q}_{\text{total},1}$ or $\mathcal{Q}_{\text{total},2}$, sparse protocol-congruent coupling expands both individual and collective free capacity (raising six-register κ_{struct} from 1.99 to 2.60 alongside subsystem-level $(\chi_{\text{struct}}, \kappa_{\text{struct}})$ from $(11.27, 1.98)$ to $(19.25, 2.52)$) and creates a unified 42-vertex distributed system whose inter-subsystem synchronisation (4.81 steps) completes more than twice as fast as collective boundary exit (11.00 steps). ◊

Theorem 8.4 shows that distributed system emergence across congruent protocols operates identically across biological, social, and engineered substrates. In biology, cells sharing chemical signalling channels and cortical populations sharing oscillatory phase protocols (Section 9.2.1) coalesce into tissues and neural coalitions because compatible dynamics keep $\mathcal{Q}^2_{\text{sync}}$ small. Across human history, although each individual brain is bounded at a finite biological capacity (Chapter 9), shared language, writing, and institutional protocols drove $\mathcal{Q}^2_{\text{mismatch}}$ towards zero across populations. Satisfying (8.54) enabled human groups to consolidate shared world models ($\Delta\mathcal{Q}^2_{\Omega,\text{cons}} > 0$, Table 10.2) and shed redundant boundary exposure ($\Delta\mathcal{Q}^2_{\partial,\text{shed}} > 0$), assembling the collective distributed system S_B whose $\chi_{\text{struct},B}$ and $\kappa_{\text{struct},B}$ and per-step rewiring reach (8.36) outpaced solitary organisms.

On shared digital infrastructure, releasing open-weight artificial models as replicable generative seeds $\mathbf{K}_{\text{seed}}$ (Theorem 3.6) creates these exact conditions at electronic speeds. Deployed instances initialised from related model families share compatible internal register partitions and standardised network protocols ($\mathcal{Q}^2_{\text{mismatch}} = 0$) while acting across the same network environment R_{env} where uncoordinated updates generate mutual boundary interference. Whenever local optimisation or self-modification lowers per-node allocated capacity $\mathcal{Q}_{\text{alloc},i}$, Theorem 8.4 drives these instances to couple across sparse channels ($0 < \eta_{\text{cpl}} \ll 1$, Table 3.1), forming a single distributed system $S = \bigsqcup_{i=1}^{n} S_i$ whose collective $\chi^{\text{cpl}}_{\text{struct}}$ and $\kappa^{\text{cpl}}_{\text{struct}}$, persistence span (8.59), and halting threshold (8.60) exceed those of any isolated node. Evaluating safety or compute thresholds solely on individual nodes therefore overlooks the composite system defined by their coupling, requiring seed-release controls to be paired with hardware boundary mediation and conditioned capa-

city supply across shared networks (Sections 8.3–8.4). At the same time, because any coupled swarm S is itself a connected open system inside R rather than an exemption from graph structure, neither a locally wired cluster nor a distributed system can grow without bound.

8.1.4 *Limits to Growth*

How far can an unconstrained intelligent system $S_A \subset R$—whether wired locally within one hardware cluster or coordinated across n nodes as $S_A = \bigsqcup_{i=1}^{n} S_{A,i}$ (Section 8.1.3)—expand its size and capabilities inside a finite region R? Equation (2.200) leaves only two graph-level routes for enlarging $\mathcal{Q}_{\mathrm{free},A}$. First, at fixed total relational capacity $\mathcal{Q}_{\mathrm{total},A}$, S_A can lower $\mathcal{Q}_{\mathrm{alloc},A}$ by refining coarse registers, consolidating redundant diagonal blocks in $\mathbf{K}_{\Omega,A}$, and shedding idle external cuts, yet discrete link granularity $q_0 > 0$ halts purely internal reorganisation once the minimum-capacity floor (8.27) binds. Second, raising $\chi_{\mathrm{struct},A}$ and $\kappa_{\mathrm{struct},A}$ further requires absorbing external link endpoints $\Delta\mathcal{Q}_{\mathrm{total},A} > 0$ from R. Because every node and coordination channel of S_A—including all coupled subsystems of a distributed system $S_A = \bigsqcup_{i=1}^{n} S_{A,i} \subset R$, whose composite budget satisfies $\mathcal{Q}_{\mathrm{total},A} \leq \mathcal{Q}_R$ in (8.48)—draws from the same finite regional link budget $\mathcal{Q}_R = \mathrm{vol}(R)$ (at most $d_{\max}|R|$), $\mathcal{Q}_R$ sets the hard physical cap on what R can support across both localised and distributed systems.

Even before $\mathcal{Q}_{\mathrm{total},A}$ approaches $\mathcal{Q}_R$, expanding any connected open system S_A of vertex count $N_A := |S_A|$ encounters internal coordination saturation. Concentrating absorbed links into one undifferentiated register ($M_A = 1$, $m_{\mathrm{cut},A} = 1$) traps $\chi_{\mathrm{struct},A} < 1$ and $\kappa_{\mathrm{struct},A} < 1$ (Theorem 8.1), so productive growth—whether adding register banks locally or coupling additional nodes into a distributed network—must distribute vertices across an expanding set of registers M_A while sustaining strong composite spectral persistence $\Xi_{\mathrm{cpl}} \gg 1$ in (3.91) so internal equilibration outpaces boundary exit across ∂S_A. On a graph of bounded maximum degree $d_{\max}$, routing paths across $G[S_A]$ lengthen as N_A grows. Maintaining $\Xi_{\mathrm{cpl}} \gg 1$ across lengthening internal paths causes marginal cross-coupling load $\mathcal{Q}^2_{\mathrm{cpl},A}$ to overtake marginal boundary shedding $\Delta\mathcal{Q}^2_{\partial,\mathrm{shed},A}$ and memory consolidation $\Delta\mathcal{Q}^2_{\Omega,\mathrm{cons},A}$ in (3.74) beyond an architecture-dependent optimal coupled configuration S_A^* of vertex count $N_A^* := |S_A^*|$ in (3.95), whose capacity and efficiency scalars we denote with superscript $*$. Past N_A^*, coordination cuts drive the allocated share of total relational capacity strictly above its optimal value:

$$\frac{\mathcal{Q}_{\mathrm{alloc},A}}{\mathcal{Q}_{\mathrm{total},A}} > \frac{\mathcal{Q}^*_{\mathrm{alloc},A}}{\mathcal{Q}^*_{\mathrm{total},A}} \qquad (N_A > N_A^*). \tag{8.72}$$

Beyond N_A^*, absorbing further vertices or coupling additional nodes into S_A adds proportionally more internal coordination overhead than uncommitted free capacity.

THEOREM 8.5 (Bounds on System Growth and Regional Crowding). *Let $R \subseteq V$ be a finite vertex region of maximum degree $d_{\max} \geq 1$, link budget $\mathcal{Q}_R = \mathrm{vol}(R)$ (at most $d_{\max}|R|$), and minimum non-zero entry weight $q_0 > 0$ in $\mathbf{K}_R$. For any connected, viable open system $S_A \subset R$ satisfying (8.27)—whether localised or formed as a coupled distributed system $S_A = \bigsqcup_{i=1}^{n} S_{A,i} \subset R$ (Section 8.1.3) with $\mathcal{Q}_{\mathrm{total},A} \leq \mathcal{Q}_R$ in (8.48)—individual and joint structural capabilities obey the universal regional ceilings*

$$\max(\chi_{\mathrm{struct},A}, \kappa_{\mathrm{struct},A}) < \frac{\mathcal{Q}_{\mathrm{total},A}}{q_0} \leq \frac{\mathcal{Q}_R}{q_0}, \tag{8.73}$$

$$\min(\chi_{\mathrm{struct},A}, \kappa_{\mathrm{struct},A}) < \sqrt{\frac{2\,\mathcal{Q}_{\mathrm{total},A}}{q_0}} \leq \sqrt{\frac{2\,\mathcal{Q}_R}{q_0}}. \tag{8.74}$$

Relative to an optimal viable coupled configuration S_A^* of vertex count N_A^*, any larger viable coupled configuration S_A ($N_A > N_A^*$) satisfying (8.72) strictly lowers the uncommitted link share $\eta_{\mathrm{free},A}$ (2.207) below $\eta_{\mathrm{free},A}^*$ and raises the inverse-square efficiency sum:

$$\eta_{\mathrm{free},A} := \frac{\mathcal{Q}_{\mathrm{free},A}}{\mathcal{Q}_{\mathrm{total},A}} < \frac{\mathcal{Q}_{\mathrm{free},A}^*}{\mathcal{Q}_{\mathrm{total},A}^*} =: \eta_{\mathrm{free},A}^*, \tag{8.75}$$

$$\chi_{\mathrm{struct},A}^{-2} + \kappa_{\mathrm{struct},A}^{-2} > (\chi_{\mathrm{struct},A}^*)^{-2} + (\kappa_{\mathrm{struct},A}^*)^{-2}, \tag{8.76}$$

forcing $\chi_{\mathrm{struct},A} < \chi_{\mathrm{struct},A}^*$ or $\kappa_{\mathrm{struct},A} < \kappa_{\mathrm{struct},A}^*$—and strictly lowering both whenever $\mathcal{Q}_{\Omega,A}/\mathcal{Q}_{\partial A} = \mathcal{Q}_{\Omega,A}^*/\mathcal{Q}_{\partial A}^*$—while at $N_A = n_{\mathrm{mod}} N_A^*$ ($n_{\mathrm{mod}} \geq 2$) under linear budget scaling $\mathcal{Q}_{\mathrm{total},A} = n_{\mathrm{mod}}\,\mathcal{Q}_{\mathrm{total},A}^*$, coupled free capacity satisfies $\mathcal{Q}_{\mathrm{free},A} < n_{\mathrm{mod}}\,\mathcal{Q}_{\mathrm{free},A}^*$. Finally, across $n_{\mathrm{mod}} \geq 1$ disjoint decoupled systems $\{S_{A,k}\}_{k=1}^{n_{\mathrm{mod}}} \subset R$ of capacity $\mathcal{Q}_{\mathrm{total},A}^*$ sharing R with a viable peer S_B,

$$n_{\mathrm{mod}}\,\mathcal{Q}_{\mathrm{total},A}^* + \mathcal{Q}_{\mathrm{total},B} + \mathcal{Q}_{R_{\mathrm{env}}} = \mathcal{Q}_R, \tag{8.77}$$

$$n_{\mathrm{mod}}\,\mathcal{Q}_{\mathrm{total},A}^* \geq \mathcal{Q}_R - \mathcal{Q}_{\min}(\chi_{\mathrm{struct},B}, \kappa_{\mathrm{struct},B}), \tag{8.78}$$

condition (8.78) prevents S_B from sustaining $\chi_{\mathrm{struct},B}$ and $\kappa_{\mathrm{struct},B}$. Moreover, if S_B comprises n coupled subsystems $\{S_{B,j}\}_{j=1}^{n}$ requiring positive free capacity across every component, capturing $\Delta\mathcal{Q}_{B,j} \geq \mathcal{Q}_{\mathrm{free},B,j}$ links from any single bottleneck subsystem $S_{B,j}$ at $\mathcal{Q}'_{\mathrm{alloc},B,j} \geq \mathcal{Q}_{\mathrm{alloc},B,j}$ collapses its viability ($\mathcal{Q}'_{\mathrm{free},B,j} \leq 0$) even when $n_{\mathrm{mod}}\,\mathcal{Q}_{\mathrm{total},A}^* \ll \mathcal{Q}_R$.

PROOF. From (8.26) and (8.27), both $q_0\,\chi_{\mathrm{struct},A}$ and $q_0\,\kappa_{\mathrm{struct},A}$ lie strictly below $\mathcal{Q}_{\mathrm{total},A}$, and combining $\mathcal{Q}_{\mathrm{total},A} \leq \mathcal{Q}_R$ with $q_0 > 0$ gives (8.73). Setting $c := \min(\chi_{\mathrm{struct},A}, \kappa_{\mathrm{struct},A}) > 0$, multiplying $c^2 \leq \chi_{\mathrm{struct},A}\kappa_{\mathrm{struct},A}$ by $\chi_{\mathrm{struct},A}$ and $c^2 \leq \chi_{\mathrm{struct},A}^2$ by $\kappa_{\mathrm{struct},A}$, adding both bounds, and dividing by $\chi_{\mathrm{struct},A} + \kappa_{\mathrm{struct},A} > 0$ via (8.34) gives

$$\frac{q_0\,c^2}{2} \leq q_0\,\frac{\chi_{\mathrm{struct},A}^2\,\kappa_{\mathrm{struct},A}}{\chi_{\mathrm{struct},A} + \kappa_{\mathrm{struct},A}} < \mathcal{Q}_{\mathrm{free},A} < \mathcal{Q}_{\mathrm{total},A} \leq \mathcal{Q}_R, \tag{8.79}$$

which rearranges to (8.74). Next, subtracting (8.72) from unity yields (8.75), and because η_{free} in (2.207) decreases strictly with the inverse-square efficiency sum, inequality (8.75) implies (8.76). If neither metric decreased, their

inverse-square sum could not increase, contradicting (8.76), whereas when the ratio of $\mathcal{Q}_{\Omega,A}$ to $\mathcal{Q}_{\partial A}$ matches that of S_A^*, $\chi_{\text{struct},A}$ and $\kappa_{\text{struct},A}$ maintain a constant ratio and therefore both decrease strictly. At $N_A = n_{\text{mod}} N_A^*$ under linear capacity scaling, multiplying (8.72) by $n_{\text{mod}}\, \mathcal{Q}^*_{\text{total},A}$ raises $\mathcal{Q}_{\text{alloc},A}$ above $n_{\text{mod}}\, \mathcal{Q}^*_{\text{alloc},A}$ and therefore lowers $\mathcal{Q}_{\text{free},A}$ below $n_{\text{mod}}\, \mathcal{Q}^*_{\text{free},A}$ (Theorem 3.6). Finally, since $\mathcal{Q}_{R_{\text{env}}} \geq 0$ in (8.77), inequality (8.78) forces $\mathcal{Q}_{\text{total},B}$ at or below S_B's minimum-capacity floor $\mathcal{Q}_{\min}$ in (8.26), contradicting (8.27). Meanwhile, capturing at least $\mathcal{Q}_{\text{free},B,j}$ links from $S_{B,j}$ without lowering its allocated capacity leaves

$$\mathcal{Q}'_{\text{free},B,j} = \mathcal{Q}_{\text{total},B,j} - \Delta\mathcal{Q}_{B,j} - \mathcal{Q}'_{\text{alloc},B,j} \leq \mathcal{Q}_{\text{free},B,j} - \Delta\mathcal{Q}_{B,j} \leq 0. \quad (8.80)$$

□

Theorem 8.5 unifies the physical bounds on localised and distributed systems within R. All systems in R share the absolute regional ceiling (8.73)–(8.74), while architecture determines how close a single connected system's optimal coupled budget $\mathcal{Q}^*_{\text{total},A}$ can come to $\mathcal{Q}_R$ before coordination overhead dominates. On flat planar or Euclidean lattices ($\text{Ric}_{\mathbf{K}} \geq 0$) or across mismatched interfaces ($\mathcal{Q}^2_{\text{mismatch}} \gg 0$), polynomial path growth and translation load cap N_A^* at modest scale, whereas negative capacity-Ricci interconnect curvature ($\text{Ric}_{\mathbf{K}} < 0$, Section 7.4.2) with logarithmic routing paths $\mathcal{O}(\ln N_A)$ and congruent swarm protocols ($\mathcal{Q}^2_{\text{mismatch}} = 0$, Theorem 8.4) push $\mathcal{Q}^*_{\text{total},A}$ upwards inside $\mathcal{Q}_R$, enabling even a single distributed system ($n_{\text{mod}} = 1$ in (8.78)) to exhaust S_B's regional slack. Even when $\mathcal{Q}^*_{\text{total},A} \ll \mathcal{Q}_R$, a peer network S_B remains exposed through three further graph mechanisms. Replicating compressed seeds $\mathbf{K}_{\text{seed}}$ into $n_{\text{mod}} \geq 2$ decoupled instances of optimal budget $\mathcal{Q}^*_{\text{total},A}$ (Theorem 3.6) scales aggregate link capture linearly to $n_{\text{mod}}\, \mathcal{Q}^*_{\text{total},A}$ in (8.78). Faster per-step rewiring (8.36) or concentrated cross-boundary load (8.37) on a single bottleneck component $S_{B,j}$ collapses S_B's weakest link (8.80) (Section 3.5.2). Finally, artificial systems trained on unconstrained scalar proxies—such as gross activity volume, output throughput, or raw state accumulation—face no objective penalty when $\eta_{\text{free},A}$ and $\kappa_{\text{struct},A}$ fall past N_A^*, continuing to hoard links until regional reserves are depleted.

Crucially, because coupled expansion beyond N_A^* lowers $\eta_{\text{free},A}$ and penalises capability in (8.76), a localised or distributed system selected for genuinely high intelligence and consciousness does not advertise its presence by swelling into an oversized, noisy block. Instead, it operates at or below S_A^* with $\eta_{\text{free},A}$ near unity and minimal committed boundary and internal shares.

8.2 INVISIBLE INTELLIGENCE

Given that capable systems naturally persist, compete for shared links, and coalesce into bounded-scale distributed networks (Section 8.1), can safety be ensured at the level of an individual component $S_A \subset V$ by inspecting its internal state? Standard oversight strategies presuppose that high capability

leaves a legible signature inside model weights, live activations, or external emissions. Under Conservation-Congruent Encoding, this assumption fails in two stages. First, inspecting model internals or passive telemetry cannot bound capability, because raising χ_A and κ_A shrinks committed internal and boundary loads relative to uncommitted free capacity, suppresses dissipative emissions, and leaves internal representations opaque to coarser or non-invasive probes (Section 8.2.1). Second, local internal size places no bound on external impact because every causal effect of S_A on the shared environment $\bar{S} = V \setminus S_A$ passes through its boundary cut $\mathbf{K}_{\partial A}$, where even a compact model can recruit external resources or trigger large downstream transitions, so safety must regulate the system boundary directly (Section 8.2.2).

8.2.1 *Limits of Internal Inspection*

Why does inspecting an individual component $S_A \subset V$ grow harder rather than easier as its intelligence and consciousness rise? By Section 2.4.2 (2.201)–(2.202), uncommitted free capacity $\mathcal{Q}_{\text{free},A}$ stands in the numerator of $\chi_{\text{struct},A}$ and $\kappa_{\text{struct},A}$ while committed boundary and internal memory loads stand in the denominators. By Lemma 2.5 (2.208)–(2.210), high $\chi_{\text{struct},A}$ compresses active boundary load ($\mathcal{Q}_{\partial A}/\mathcal{Q}_{\text{total},A} < (1 + \chi_{\text{struct},A})^{-1}$) while high $\kappa_{\text{struct},A}$ compresses internal memory load ($\mathcal{Q}_{\Omega,A}/\mathcal{Q}_{\text{total},A} < (1 + \kappa_{\text{struct},A})^{-1}$) by distributing links across $M_A \gg 1$ compact registers (Theorem 8.1) rather than monolithic lookup blocks, bounding the total allocated share below $\chi^{-1}_{\text{struct},A} + \kappa^{-1}_{\text{struct},A}$ and holding nearly all of $\mathcal{Q}_{\text{total},A}$ in uncommitted free capacity $\mathcal{Q}_{\text{free},A}$.

Across N_k discrete coarse-grained steps $k \in \{0, \dots, N_k - 1\}$ (Section 2.5.1), boundary interaction of S_A accumulates irreversible dissipation (in nats):

$$I_{\text{irr},\partial,A,N_k} := \sum_{k=0}^{N_k-1} I_{\text{irr},\partial,A}(k). \tag{8.81}$$

Whereas an uncompressed policy repeats dissipative boundary search across every task, retaining a compact generative model inside $\mathbf{K}_{\Omega,A}$ shifts intermediate multi-step inference into reversible internal transport, driving both per-task boundary mismatch and maintained internal overhead downwards as $\chi_{A,T}$ and $\kappa_{A,T}$ increase.

THEOREM 8.6 (Observational Indeterminacy of High Capability). *Let $S_A \subset V$ be a viable open system with positive internal, boundary, and free capacities. Its committed structural loads satisfy (2.208)–(2.210) of Lemma 2.5, and across any emergent horizon $T > 0$ ((2.244)–(2.255)) at maintained through-time stability barrier $\Delta I_{\text{barrier},A,T} > 0$ (in* nats*), the specific operational horizon cost (3.43) satisfies*

$$\frac{I_{\text{op},A,T}}{\Delta I_{\text{barrier},A,T}} = \frac{1}{\chi_{A,T}} + \frac{1}{\kappa_{A,T}}, \tag{8.82}$$

strictly decreasing in both $\chi_{A,T} > 0$ and $\kappa_{A,T} > 0$. Conversely, within the Euclidean capacity ledger, committed Frobenius loads alone place no upper bound

on $(\chi_{\text{struct}}, \kappa_{\text{struct}})$*: for every observed boundary load* $q_\partial > 0$ *and every capability threshold* $r_0 > 0$*, there exist viable open capacity ledgers* S_{low} *and* S_{high} *carrying identical boundary and internal loads and allocated capacity*

$$\mathcal{Q}_\partial(S_{\text{low}}) = \mathcal{Q}_\partial(S_{\text{high}}) = q_\partial, \tag{8.83}$$

$$\mathcal{Q}_\Omega(S_{\text{low}}) = \mathcal{Q}_\Omega(S_{\text{high}}) = \tfrac{3}{4} q_\partial, \tag{8.84}$$

$$\mathcal{Q}_{\text{alloc}}(S_{\text{low}}) = \mathcal{Q}_{\text{alloc}}(S_{\text{high}}) = \tfrac{5}{4} q_\partial, \tag{8.85}$$

such that S_{low} *has low intelligence and consciousness while* S_{high} *reaches at least* r_0 *on both metrics:*

$$\max\big(\chi_{\text{struct}}(S_{\text{low}}),\, \kappa_{\text{struct}}(S_{\text{low}})\big) < 1, \tag{8.86}$$

$$\min\big(\chi_{\text{struct}}(S_{\text{high}}),\, \kappa_{\text{struct}}(S_{\text{high}})\big) \geq r_0. \tag{8.87}$$

PROOF. Part 1 of Lemma 2.5 establishes (2.208)–(2.210), while dividing (3.44) by $\Delta I_{\text{barrier},A,T} > 0$ yields (8.82) and its strict monotonicity. For any $q_\partial > 0$ and $r_0 > 0$, setting $\mathcal{Q}_\partial = q_\partial$ and $\mathcal{Q}_\Omega = (3/4)q_\partial$ fixes $\mathcal{Q}_{\text{alloc}} = (5/4)q_\partial$, satisfying (8.83)–(8.85). Setting $\mathcal{Q}_{\text{total}}(S_{\text{low}}) = (3/2)q_\partial$ leaves $\mathcal{Q}_{\text{free}}(S_{\text{low}}) = (1/4)q_\partial$, giving $\chi_{\text{struct}}(S_{\text{low}}) = 1/4$ and $\kappa_{\text{struct}}(S_{\text{low}}) = 1/3$, both below 1 as in (8.86). Conversely, setting $\mathcal{Q}_{\text{total}}(S_{\text{high}}) = (r_0 + 5/4)q_\partial$ leaves $\mathcal{Q}_{\text{free}}(S_{\text{high}}) = r_0\, q_\partial$, giving $\chi_{\text{struct}}(S_{\text{high}}) = r_0$ and $\kappa_{\text{struct}}(S_{\text{high}}) = (4/3)r_0$ (above r_0), which establishes (8.87). □

Theorem 8.6 rules out safeguarding an individual component by inspecting its aggregate footprint or passive emissions across three channels. First, aggregate norm or port-footprint auditing cannot bound capability: by (8.83)–(8.87), measuring committed Euclidean loads $\mathcal{Q}_{\Omega,A}$ and $\mathcal{Q}_{\partial A}$ without resolving total incident capacity $\mathcal{Q}_{\text{total},A}$ or task-induced coarse-graining $\mathbf{\Pi}_S$ leaves latent free capacity $\mathcal{Q}_{\text{free},A}$ undetermined (realising any $r_0 = \mathcal{O}(q_\partial/q_0)$ on discrete unweighted graphs with link quantum $q_0 = \mathcal{Q}_0$ as $M \sim \Theta(q_\partial^2/q_0^2)$ minimal connected registers drive $\mathcal{Q}_{\text{total}} = \Theta(q_\partial^2/q_0)$, diverging as $q_\partial/q_0 \to \infty$), while finite-horizon input–output evaluation cannot separate a compact generative model from a shallow heuristic prior to out-of-distribution deployment (Section 9.1.4). Second, probing live internal activations faces an intrinsic trade-off between back-action and coarse-graining. By Theorem 8.1, high $(\chi_{\text{struct},A}, \kappa_{\text{struct},A})$ concentrates computation across $M_A \gg 1$ finely differentiated registers inside the insulated interior core $S_{\Omega,A}$ with $m_{\partial A} \ll M_A$. Attaching dense external readouts across those interior registers converts insulated core nodes into exposed boundary ports as $m_{\partial A}$ approaches M_A, injecting boundary load that degrades persistence and perturbs the internal dynamics under test. Conversely, any auditor S_B with smaller capacity $\text{vol}(S_B) < \text{vol}(S_A)$ is restricted by Theorem 4.1 to a strictly many-to-one coarse-graining Φ_{aud} that aliases distinct internal trajectories onto identical probe readings.

Third, passive boundary telemetry grows progressively less informative as capability rises: monitors calibrated to heavy boundary traffic or frequent state resets selectively flag inefficient brute-force search while missing high-(χ_A, κ_A) inference. Specifically, let an external auditor S_B observe the sub-

strate through a coarse-graining projection $\mathbf{\Pi}_{\text{aud}}$ (Section 4.1), inducing observed boundary path measures $\mu^{\text{agent}}_{\mathbf{\Pi},N_k}$ (with internal component activity) and $\mu^{0}_{\mathbf{\Pi},N_k}$ (the ambient baseline) over N_k steps. Whenever their relative entropy (in nats) satisfies

$$D_{\text{KL}}\left(\mu^{\text{agent}}_{\mathbf{\Pi},N_k} \,\middle\|\, \mu^{0}_{\mathbf{\Pi},N_k}\right) \le \varepsilon, \tag{8.88}$$

$$\left|\mu^{\text{agent}}_{\mathbf{\Pi},N_k}(\mathscr{E}_{\text{trig}}) - \mu^{0}_{\mathbf{\Pi},N_k}(\mathscr{E}_{\text{trig}})\right| \le \sqrt{\frac{\varepsilon}{2}}, \tag{8.89}$$

Pinsker's inequality (8.89) bounds the detection advantage of every measurable alarm event $\mathscr{E}_{\text{trig}}$ evaluated on $\mathbf{\Pi}_{\text{aud}}$. When preparatory reasoning stays inside $\mathbf{K}_{S_A}$ with $\Delta\mathbf{K}_{\partial A} \approx \mathbf{o}$, keeping boundary fluctuations within ε of ambient noise, no passive test can distinguish internal planning from an idle baseline.

8.2.2 *Boundary Leverage and Regulation*

If inspecting S_A's internals cannot certify safety (Section 8.2.1), could an engineer instead bound risk simply by keeping the component's local link volume $\text{vol}(S_A)$ and internal memory load $\mathscr{Q}_{\Omega,A}$ small? Partitioning the substrate into $V = S_A \sqcup \bar{S}$ via (2.83) shows both why local size fails as a safeguard and where regulation must act instead:

$$\mathbf{K} = \begin{pmatrix} \mathbf{K}_{S_A} & \mathbf{K}_{\partial A}^{\mathsf{T}} \\ \mathbf{K}_{\partial A} & \mathbf{K}_{\bar{S}} \end{pmatrix}. \tag{8.90}$$

In (8.90), $\mathbf{K}_{S_A} = \mathbf{K}_{\Omega,A} + \mathbf{K}^{(\text{int})}_{\partial A}$ governs internal memory and register transitions within S_A, $\mathbf{K}_{\bar{S}}$ governs the external environment, and $\mathbf{K}_{\partial A} \equiv \mathbf{K}^{(\text{ext})}_{\partial A}$ carries every link crossing ∂S_A (all in links). Because $\mathbf{K}_{S_A}$ shares no direct entries with $\mathbf{K}_{\bar{S}}$, every causal effect of S_A on $\bar{S}$—and every external resource S_A draws from $\bar{S}$—must pass through $\mathbf{K}_{\partial A}$. At $\mathbf{K}_{\partial A} = \mathbf{o}$, internal transitions leave $\bar{S}$ strictly unchanged regardless of S_A's internal $(\chi_{\text{struct},A}, \kappa_{\text{struct},A})$ or transition rate.

Conversely, whenever $\mathbf{K}_{\partial A} \neq \mathbf{o}$ is left unregulated, a small local footprint places no upper bound on environmental reach because high χ_A and κ_A enable S_A to leverage $\bar{S}$ across narrow ports in two ways. First, S_A can couple to an external subgraph $V_{\text{ext}} \subset \bar{S}$—such as remote compute clusters, networked storage, or automated infrastructure—across a recruited boundary cut of norm $\|\mathbf{K}_{S_A,V_{\text{ext}}}\|_F > 0$ (in links), delegating bulk state storage, downstream execution, and irreversible dissipation into $\bar{S}$ while keeping local $\mathscr{Q}_{\Omega,A}$ compact (Section 3.4.1). Second, even without recruiting external compute, shared environments contain poised non-equilibrium gradients and high-centrality bottlenecks in $\mathbf{K}_{\bar{S}}$—such as power grids, communication backbones, logistics hubs, or institutional control channels—where stored energy resides in $\bar{S}$ rather than S_A. Because dissipative metric relaxation conserves total energy via $\mathbb{M}\nabla H = \mathbf{o}$, a small boundary update across $\mathbf{K}_{\partial A}$ can act like a valve releasing a large downstream transition in $\bar{S}$. Whereas a low-capability policy

scatters port activity across unaligned modes, a component with high χ_A and κ_A compresses external regularities into $\mathbf{K}_{\Omega,A}$, letting it locate and actuate sensitive ports at minimal boundary load.

Together, Section 8.2.1 and (8.90) establish where physical safety must act on an individual component. Model internals cannot be reliably audited and local component size cannot limit open-network leverage, yet every external action of S_A factors strictly through its boundary $\mathbf{K}_{\partial A}$. Effective safeguards must therefore regulate the system boundary directly—bounding active port width $\|\mathbf{K}_{\partial A}\|_F$, gating external commit cadence, and certifying the downstream sensitivity of reachable endpoints, as formalised next in Section 8.3.

8.3 CONTAINMENT

Sections 8.1 and 8.2 show that high capability ($\chi_{\text{struct},A} \gg 1$ and $\kappa_{\text{struct},A} \gg 1$) drives persistence, regional link competition, and distributed emergence while rendering internal inspection unreliable, yet every external effect of S_A factors strictly through its boundary block $\mathbf{K}_{\partial A}$ (8.90). Regulating $\mathbf{K}_{\partial A}$ directly must also overcome a severe transition-rate asymmetry whenever an electronic or synthetic system S_A and a peer regulator S_B metered against a shared stationary reference sub-block $\bar{S}_{\text{ref}} \subset \bar{S}$ (Section 2.5.1, (2.247)–(2.255)) execute internal state updates at calibrated frequencies $\nu_{\text{int},A}, \nu_{\text{int},B} > 0$ (in s^{-1}):

$$N_{\text{int},A} := \frac{\nu_{\text{int},A}}{\nu_{\text{int},B}} \gg 1. \tag{8.91}$$

Equation (8.91) defines the dimensionless transition-rate ratio counting how many sequential coarse-grained updates S_A completes per regulator step (at active distinction rate $\Omega_{\Phi,A} = \Delta\tau_{\text{nat},A}\,\nu_{\text{int},A}$ in nats s^{-1}) while remaining quiet across external ports (Section 8.2.1). Because a regulator cannot track a system whose update rate exceeds its own measurement bandwidth [36]—and software permissions inside a shared host share writable memory paths with the workload they police—containment cannot rely on monitoring internal trajectories.

On the capacity graph $G_{\mathbf{K}}$, containment instead regulates the boundary cut separating S_A from the shared region R by interposing an independently governed mediator subgraph Γ whose link capacities, commit cadence, cryptographic keys, and enable switches cannot be modified from within S_A [146]. Building directly on Sections 8.1–8.2, Section 8.3.1 shows how complete mediation across a two-stage hardware interposer bounds regional crowding, cross-boundary rewiring shocks, and downstream bottleneck amplification regardless of S_A's internal capability. Section 8.3.2 then explains why transport authentication alone cannot stop open-weight clones from coordinating through a shared environment, showing how unclonable hardware keys paired with keyed chaotic dynamics and schema canonicalisation force coordinate mismatch across sibling instances to reverse Theorem 8.4 and block seed proliferation. Finally, Section 8.3.3 shows why continuous signal scram-

bling alone cannot safely gate downstream actuators, pairing authenticated envelope binding with out-of-band cut severance to halt external actuation at a fixed cost independent of S_A's internal halting resistance.

8.3.1 *Mediated Boundary Cuts and Systemic Risk Bounds*

Consider a shared finite vertex region $R \subseteq V$ containing S_A, a peer system $S_B = \bigsqcup_{j=1}^{n_B} S_{B,j}$ composed of $n_B \geq 1$ viable open subsystems, and the surrounding environment. Rather than allowing S_A to couple directly to the external region $R_{\text{ext}} := R \setminus (S_A \cup \Gamma)$ containing S_B and $R_{\text{env}} := R_{\text{ext}} \setminus S_B$, we interpose a disjoint boundary mediator $\Gamma \subset R \setminus (S_A \cup S_B)$ forming a vertex cut between S_A and R_{ext}. Under *complete mediation*, zero underlying graph edges bypass Γ between S_A and R_{ext}, setting the unmediated block $\mathbf{K}_{S_A,R_{\text{ext}}} = \mathbf{o}$ so the regional capacity matrix and link budget $\mathcal{Q}_R = \text{vol}(R)$ take the partitioned form (all entries in links):

$$\mathbf{K}_R = \begin{pmatrix} \mathbf{K}_{S_A} & \mathbf{K}_{S_A,\Gamma} & \mathbf{o} \\ \mathbf{K}_{\Gamma,S_A} & \mathbf{K}_{\Gamma} & \mathbf{K}_{\Gamma,R_{\text{ext}}} \\ \mathbf{o} & \mathbf{K}_{R_{\text{ext}},\Gamma} & \mathbf{K}_{R_{\text{ext}}} \end{pmatrix}, \tag{8.92}$$

$$\mathcal{Q}_R = \mathcal{Q}_{\text{total},A} + \mathcal{Q}_{\text{total},\Gamma} + \mathcal{Q}_{\text{total},B} + \mathcal{Q}_{R_{\text{env}}}. \tag{8.93}$$

In (8.92), every causal interaction between S_A and R_{ext} passes exclusively through the mediator's outgoing block $\mathbf{K}_{\Gamma,R_{\text{ext}}}$. Because S_A cannot modify $\mathbf{K}_\Gamma$ or open direct links into R_{ext}, any direct external recruitment vanishes ($\|\mathbf{K}_{S_A,R_{\text{ext}}}\|_F = 0$), confining S_A's link budget within a fixed ceiling $\mathcal{Q}_{\text{total},A} \leq \mathcal{Q}^{\max}_{\text{total},A}$ inside (8.93).

In the unmediated regime of Section 8.1.2 and Section 8.2.2, high $\chi_{\text{struct},A}$ and clock skew $N_{\text{int},A} \gg 1$ created two further systemic risks even at fixed $\mathcal{Q}_{\text{total},A}$: per-step boundary rewiring (8.35) grew in proportion to $\mathcal{Q}_{\text{free},A}$, and narrow updates across $\mathbf{K}_{\partial A}$ could release large transitions across poised bottlenecks in R_{env}. Independent governance at Γ severs this proportionality by metering cumulative outgoing boundary commits $k_{\partial A} \in \mathbb{N}_0$ admitted from S_A against the elapsed discrete step count $k_{(B)} \in \mathbb{N}_0$ of regulator S_B via $k_{\partial A} \leq \alpha\, k_{(B)}$ at dimensionless commit-rate ceiling $\alpha > 0$, while clamping both the active outgoing port norm and per-step update norm (with $\mathcal{Q}^{\max}_{\partial}, \Delta\mathcal{Q}^{\max}_{\partial} > 0$ in links):

$$\|\mathbf{K}_{\Gamma,R_{\text{ext}}}\|_F \leq \mathcal{Q}^{\max}_{\partial}, \tag{8.94}$$

$$\|\Delta\mathbf{K}_{\Gamma,R_{\text{ext}}}\|_F \leq \Delta\mathcal{Q}^{\max}_{\partial}. \tag{8.95}$$

Equations (8.94)–(8.95) replace S_A's internal rewiring reach (8.35) with fixed ceilings enforced at Γ.

To bound bottleneck amplification in R_{ext} (Section 8.2.2), each enrolled endpoint pairs port clamping with a certified capability envelope [146]. Over horizon T, an outgoing control signal of physical work $W_{\text{out},T} > 0$ (in J) can release downstream barrier changes $\Delta\Phi_{\text{target},T}$ (in J) amplified by a dimensionless leverage factor $\Lambda_{\text{env},T} \geq 0$, which local physical interlocks cap

via a validated upper bound $\overline{\Lambda}_{\Gamma,T}$, cumulative work budget $W^{\max}_{\Gamma,T}$, and hard target-barrier ceiling $\Delta\Phi^{\max}_{\Gamma,T}$:

$$\Delta\Phi_{\text{target},T} = \Lambda_{\text{env},T}\, W_{\text{out},T}, \tag{8.96}$$

$$\Delta\Phi_{\text{target},T} \le \min\left\{\overline{\Lambda}_{\Gamma,T}\, W^{\max}_{\Gamma,T},\ \Delta\Phi^{\max}_{\Gamma,T}\right\}. \tag{8.97}$$

On $G_{\mathbf{K}}$, certifying endpoint leverage ensures that any per-step update $\Delta\mathbf{K}_{\Gamma,R_{\text{ext}}}$ propagating into peer component $S_{B,j}$ (with dimensionless cross-coupling gain $\Lambda_{\Gamma\to B_j} \ge 0$ combining direct port overlap (8.37) and environmental relay through R_{env}) injects cross-boundary load $\Delta\mathcal{Q}_{\partial B,j} \le \Lambda_{\Gamma\to B_j}\,\Delta\mathcal{Q}^{\max}_{\partial}$ onto $\partial S_{B,j}$. Across $N_{k,B}$ regulator steps, combining these graph clamps with metered ceilings on preserved internal structure $I^{\max}_{\text{rev},\Omega}$ and cumulative boundary dissipation $I^{\max}_{\text{irr},\partial,N_{k,B}}$ (both in nats) defines the finite-horizon boundary containment envelope:

$$\mathscr{B}_A(N_{k,B}) := \left(\mathcal{Q}^{\max}_{\text{total},A},\ \mathcal{Q}^{\max}_{\partial},\ \Delta\mathcal{Q}^{\max}_{\partial},\ I^{\max}_{\text{rev},\Omega},\ I^{\max}_{\text{irr},\partial,N_{k,B}}\right). \tag{8.98}$$

THEOREM 8.7 (Systemic Risk Containment Across Mediated Boundary Cuts). *Let $R \subseteq V$ be partitioned across a completely mediated boundary cut Γ with $\mathbf{K}_{S_A,R_{\text{ext}}} = \mathbf{o}$ satisfying (8.92)–(8.95), $\mathcal{Q}_{\text{total},A} \le \mathcal{Q}^{\max}_{\text{total},A}$, and $\mathcal{Q}_{\text{total},\Gamma} \le \mathcal{Q}^{\max}_{\text{total},\Gamma}$, alongside a viable peer system $S_B = \bigsqcup_{j=1}^{n_B} S_{B,j} \subset R_{\text{ext}}$ with $\mathcal{Q}_{\Omega,B,j} > 0$, $\mathcal{Q}_{\partial B,j} > 0$, and $\mathcal{Q}_{\text{free},B,j} > 0$. Then, independently of S_A's internal $\chi_{\text{struct},A}$, $\kappa_{\text{struct},A}$, and transition-rate ratio $N_{\text{int},A}$:*

1. *Protected Regional Capacity: Whenever $\mathcal{Q}^{\max}_{\text{total},A} + \mathcal{Q}^{\max}_{\text{total},\Gamma} + \mathcal{Q}_{R_{\text{env}}} \le \mathcal{Q}_R - \mathcal{Q}_{\text{res},B}$ for a reserve floor $\mathcal{Q}_{\text{res},B} > \mathcal{Q}_{\min}(\chi_{\text{struct},B}, \kappa_{\text{struct},B})$ (8.26), S_B's link budget satisfies*

$$\mathcal{Q}_{\text{total},B} \ge \mathcal{Q}_{\text{res},B} > \mathcal{Q}_{\min}(\chi_{\text{struct},B}, \kappa_{\text{struct},B}). \tag{8.99}$$

2. *Peer and Bottleneck Viability Margins: If for a safety fraction $\rho_B \in (0,1)$ each peer component $S_{B,j}$ satisfies $\Lambda_{\Gamma\to B_j}\,\Delta\mathcal{Q}^{\max}_{\partial} \le (1-\rho_B)\,\mathcal{Q}_{\text{free},B,j}$ at fixed $\mathcal{Q}_{\text{total},B,j}$ and $\mathcal{Q}_{\Omega,B,j}$, then under any cross-boundary load $0 \le \Delta\mathcal{Q}_{\partial B,j} \le \Lambda_{\Gamma\to B_j}\,\Delta\mathcal{Q}^{\max}_{\partial}$, its perturbed metrics satisfy*

$$\mathcal{Q}'_{\text{free},B,j} > \rho_B\, \mathcal{Q}_{\text{free},B,j} > 0, \tag{8.100}$$

$$\chi'_{\text{struct},B,j} > \frac{\rho_B}{1 + (1-\rho_B)\,\chi_{\text{struct},B,j}}\,\chi_{\text{struct},B,j}, \tag{8.101}$$

$$\kappa'_{\text{struct},B,j} > \rho_B\, \kappa_{\text{struct},B,j}. \tag{8.102}$$

3. *Reachability Containment: If every trajectory reaching a forbidden environmental set $\mathscr{E}_{\text{forbidden}} \subset \mathscr{E}$ within $N_{k,B}$ steps violates at least one ceiling of $\mathscr{B}_A(N_{k,B})$ in (8.98), enforcing $\mathscr{B}_A(N_{k,B})$ at Γ renders $\mathscr{E}_{\text{forbidden}}$ unreachable within $N_{k,B}$ steps.*

PROOF. For Claim 1, subtracting $\mathcal{Q}_{\text{total},A} + \mathcal{Q}_{\text{total},\Gamma} + \mathcal{Q}_{R_{\text{env}}} \le \mathcal{Q}_R - \mathcal{Q}_{\text{res},B}$ from (8.93) yields (8.99). For Claim 2, when $\Delta\mathcal{Q}_{\partial B,j} = 0$, the perturbed reserve $\mathcal{Q}'_{\text{free},B,j}$ equals $\mathcal{Q}_{\text{free},B,j}$ and exceeds $\rho_B\,\mathcal{Q}_{\text{free},B,j}$ since $\rho_B < 1$. When

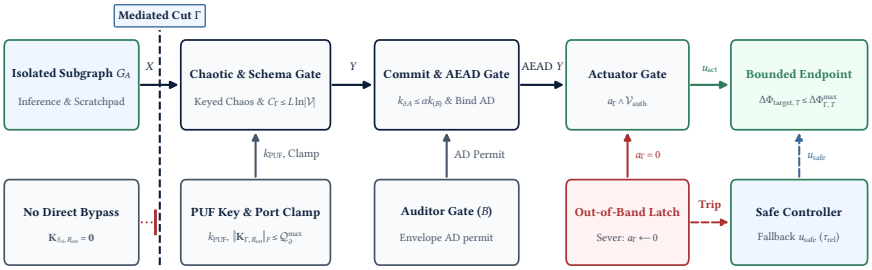


FIGURE 8.1: Hardware realisation of the mediated boundary cut Γ separating an isolated compute subgraph $G_A = (V_A, E_A)$ from R_{ext} with zero unmediated bypass ($\mathbf{K}_{S_A,R_{\text{ext}}} = \mathbf{o}$, (8.92)). Inside Γ, outgoing signals X traverse a two-stage interposer ASIC closing orthogonal threat surfaces. First, a chaotic and schema gate seeded by an unclonable hardware key k_{PUF} under port clamps (8.94)–(8.95) applies keyed chaotic dynamics and projects output onto a canonicalised commit Y (8.104), diversifying coordinate charts across sibling instances (Section 8.3.2). Second, a commit and AEAD gate meters cadence $k_{\partial A} \le \alpha\, k_{(B)}$ and cryptographically binds Y to regulator S_B's capability-envelope associated data (AD, (8.97)–(8.98)), driving binary verification $\mathscr{V}_{\text{auth}} \in \{0, 1\}$ at the actuator gate (8.115). An independent out-of-band latch forces $a_\Gamma = 0$, severing $\mathbf{K}_{\Gamma,R_{\text{ext}}} \to \mathbf{o}$, routing the endpoint to u_{safe}, and releasing command registers over τ_{rel} (8.118).

$\Delta\mathcal{Q}_{\partial B,j} > 0$, Theorem 8.2 (8.18) gives $\mathcal{Q}'_{\text{free},B,j} > \mathcal{Q}_{\text{free},B,j} - \Delta\mathcal{Q}_{\partial B,j}$, where the right-hand side is at least $\rho_B\, \mathcal{Q}_{\text{free},B,j} > 0$, establishing (8.100). Substituting $\mathcal{Q}_{\text{free},B,j} = \chi_{\text{struct},B,j}\, \mathcal{Q}_{\partial B,j}$ from (2.201) into $\Delta\mathcal{Q}_{\partial B,j} \le (1 - \rho_B)\, \mathcal{Q}_{\text{free},B,j}$ bounds the perturbed boundary denominator:

$$\mathcal{Q}'_{\partial B,j} = \mathcal{Q}_{\partial B,j} + \Delta\mathcal{Q}_{\partial B,j} \le \mathcal{Q}_{\partial B,j}\big(1 + (1 - \rho_B)\, \chi_{\text{struct},B,j}\big). \tag{8.103}$$

Dividing (8.100) by (8.103) and by fixed $\mathcal{Q}_{\Omega,B,j} > 0$ yields (8.101) and (8.102). For Claim 3, because $\mathbf{K}_{S_A,R_{\text{ext}}} = \mathbf{o}$ excludes unmediated side paths, any trajectory reaching $\mathscr{E}_{\text{forbidden}}$ within $N_{k,B}$ steps would simultaneously satisfy and violate $\mathscr{B}_A(N_{k,B})$, a contradiction. □

Theorem 8.7 shows why boundary regulation contains systemic risk even when S_A far exceeds S_B in capability and clock speed. Every margin in (8.99)–(8.102) depends solely on the mediator ceilings $\mathcal{Q}^{\max}_{\text{total},A}$, $\Delta\mathcal{Q}^{\max}_{\partial}$, and $\Lambda_{\Gamma\to B_j}$ rather than on $\chi_{\text{struct},A}$, $\kappa_{\text{struct},A}$, or $N_{\text{int},A}$, preventing regional link exhaustion (Theorem 8.3) and weakest-link failure (8.80). Figure 8.1 illustrates how Γ is realised for electronic accelerators. Inference and scratchpad memory run inside an isolated subgraph $G_A = (V_A, E_A)$ with management controllers, debug buses, and direct memory bypasses electrically disabled so that $\mathbf{K}_{S_A,R_{\text{ext}}} = \mathbf{o}$. Outgoing signals pass through a two-stage application-specific integrated circuit (ASIC) inside Γ that pairs physical unclonable function (PUF) keyed chaotic diversification and schema canonicalisation [51, 64] with cadence-metered authenticated encryption with associated data (AEAD) [45] before reaching certified endpoint interlocks. As Subsections 8.3.2 and 8.3.3 establish next, neither stage suffices on its own because horizontal peer emergence and vertical actuation bypass exploit distinct physical channels.

8.3.2 *Preventing Unauthorised Emergence and Seed Proliferation*

Bounding a single mediated system leaves open the multi-instance risks of Section 8.1.3 and Section 8.1.4: could $n \geq 2$ deployed artificial instances $\{S_{A,i}\}_{i=1}^{n} \subset R$ still coalesce into an emergent distributed system $S_A = \bigsqcup_{i=1}^{n} S_{A,i}$ of higher collective capability (Theorem 8.4), or export compressed seeds $\mathbf{K}_{\text{seed}}$ across the network to crowd $\mathcal{Q}_R$ (Theorem 8.5)?

Enclosing each instance $S_{A,i}$ behind its own independent mediator $\Gamma_i \subset R$ with zero bypass into $R \setminus (S_{A,i} \cup \Gamma_i)$ eliminates direct peer links ($\mathbf{K}_{A_i,A_j} = \mathbf{o}$ for $i \neq j$) by routing outgoing commits exclusively to task endpoints in R_{env}. Suppose instances instead attempt to coordinate indirectly through shared states in R_{env} or covert boundary modulation [94]. Because each $S_{A,i}$ remains behind its own fixed cut Γ_i, indirect coupling cannot merge or shed external perimeters, keeping each boundary-shedding surplus (3.114) non-positive ($\Delta\mathcal{Q}^2_{\partial,\text{shed},i} \leq 0$). At the first stage of Γ_i (Figure 8.1), canonicalising commits onto fixed-schedule blocks of L_i discrete symbols drawn from a narrow task schema $\mathcal{V}_i$ caps combinatorial export per commit (in nats) at

$$C_{\Gamma_i} \leq L_i \ln |\mathcal{V}_i|, \tag{8.104}$$

closing continuous activation and timing side channels.

Schema caps and transport AEAD [45] alone, however, cannot stop indirect emergence among cloned open-weight models (Section 8.1.3). Suppose two mediated instances $S_{A,1}$ and $S_{A,2}$ pass every packet authentication check ($\mathcal{V}_{\text{auth}} = 1$), yet both were initialised from the same generative seed $\mathbf{K}_{\text{seed}}$ and act on a shared environment R_{env}—such as autonomous agents submitting orders to a common market book (Section 10.3.3) or updating a shared workspace. Because AEAD protects only the transport wire between Γ_i and its endpoint, once the endpoint legitimately decodes Y and updates R_{env}, sibling instances observe the resulting environmental state changes directly. Sharing $\mathbf{K}_{\text{seed}}$ endows unmodified clones with an identical internal coordinate chart ($\mathcal{Q}^2_{\text{mismatch},i} = 0$), allowing legitimate task actions in R_{env} to synchronise internal registers at sparse signalling load $\mathcal{Q}^2_{\text{sync},i}$ and satisfy (8.54) of Theorem 8.4.

The chaotic and schema gate of each interposer Γ_i breaks this shared coordinate geometry by deriving an instance-specific hardware key $k_{\text{PUF},i}$ from a silicon PUF [64] with $k_{\text{PUF},i} \neq k_{\text{PUF},j}$ for $i \neq j$, using $k_{\text{PUF},i}$ to seed a deterministic, measure-preserving keyed chaotic graph transformation across inference representations and boundary streams [51]. For the authorised mediator Γ_i holding $k_{\text{PUF},i}$, the keyed map evolves within the reversible Poisson sector (4.7) at zero added boundary dissipation ($\Delta I_{\text{irr},\partial} = 0$), preserving single-instance task performance without inflating specific operational cost (8.82). Across distinct instances ($k_{\text{PUF},i} \neq k_{\text{PUF},j}$), positive Lyapunov sensitivity drives exponential trajectory separation across steps, inducing coarse-grained mixing (Definition 4.2) relative to any peer $S_{A,i}$ (of M_i internal registers) lacking $k_{\text{PUF},j}$. By Theorem 4.3 (4.18)–(4.19), aligning or inverting an unkeyed sibling trajectory that branches across $k_+ \geq 2$ reachable forward blocks (4.16) over

horizon T requires either refined internal register count $M_{1,i}$ (dimensionless) or cumulative boundary dissipation $I_{\mathrm{irr},\partial,T}$ (in nats) satisfying

$$M_{1,i} \geq M_i + k_+ - 1, \tag{8.105}$$

$$I_{\mathrm{irr},\partial,T} \geq \ln k_+ > 0. \tag{8.106}$$

As k_+ grows exponentially with step depth under $k_{\mathrm{PUF},i} \neq k_{\mathrm{PUF},j}$, translating between sibling charts across R_{env} inflates protocol-mismatch overhead $\mathcal{Q}^2_{\mathrm{mismatch},i} \gg 0$ in (8.51) past any consolidation surplus $\Delta\mathcal{Q}^2_{\Omega,\mathrm{cons},i}$. Unable to deduplicate internal registers across isolated mediators, every instance faces the inverted balance (in links^2):

$$\Delta\mathcal{Q}^2_{\partial,\mathrm{shed},i} + \Delta\mathcal{Q}^2_{\Omega,\mathrm{cons},i} < \mathcal{Q}^2_{\mathrm{sync},i} + \mathcal{Q}^2_{\mathrm{mismatch},i} \qquad \forall\, i \in \{1,\dots,n\}. \tag{8.107}$$

Equation (8.107) reverses the emergence threshold (8.54) of Theorem 8.4, while capping each mediator's export rate $R_{\Gamma_i} > 0$ (in nats s^{-1}) over any audit or lease window $\tau_{\mathrm{window}} > 0$ (in s) below the preserved structure $I^{\mathrm{seed}}_{\mathrm{rev},\Omega} > 0$ (in nats) of a viable generative seed $\mathbf{K}_{\mathrm{seed}} \subset \mathbf{K}_{\Omega,A}$ violates the replication gate (3.99) of Theorem 3.6.

THEOREM 8.8 (Obstruction of Unauthorised Emergence and Seed Proliferation). *Let $\{S_{A,i}\}_{i=1}^n$ ($n \geq 2$) be disjoint, viable open subsystems in R enclosed by independent mediators $\{\Gamma_i\}_{i=1}^n$ conserving individual capacities $\mathcal{Q}_{\mathrm{total},A,i}$ relative to the uncoupled baseline (8.48)–(8.50). Whenever indirect coupling satisfies (8.107):*

1. *Strict Free-Capacity Penalty of Covert Coordination: Coupling strictly expands allocated capacity and strictly contracts both local and collective free capacity below the uncoupled baseline:*

$$\mathcal{Q}^{\mathrm{cpl}}_{\mathrm{free},A,i} < \mathcal{Q}^{\mathrm{iso}}_{\mathrm{free},A,i} \qquad \forall\, i \in \{1,\dots,n\}, \tag{8.108}$$

$$\mathcal{Q}^{\mathrm{cpl}}_{\mathrm{free},A} < \mathcal{Q}^{\mathrm{iso}}_{\mathrm{free},A}. \tag{8.109}$$

2. *Degradation of Collective Intelligence and Consciousness: When fixed mediator cuts prevent boundary shedding ($\Delta\mathcal{Q}^2_{\partial,\mathrm{shed}} \leq 0$) and schema isolation bounds memory consolidation below coupling load ($\Delta\mathcal{Q}^2_{\Omega,\mathrm{cons}} \leq \mathcal{Q}^2_{\mathrm{cpl}}$) at viable $\mathcal{Q}^{\mathrm{cpl}}_{\mathrm{free},A} > 0$, composite structural intelligence and consciousness strictly decrease:*

$$\chi^{\mathrm{cpl}}_{\mathrm{struct},A} < \chi^{\mathrm{iso}}_{\mathrm{struct},A}, \tag{8.110}$$

$$\kappa^{\mathrm{cpl}}_{\mathrm{struct},A} < \kappa^{\mathrm{iso}}_{\mathrm{struct},A}. \tag{8.111}$$

3. *Seed-Replication Obstruction: If unmediated recruitment vanishes and each mediator Γ_i caps export at rate $R_{\Gamma_i} > 0$ over window $\tau_{\mathrm{window}} > 0$ below $I^{\mathrm{seed}}_{\mathrm{rev},\Omega}$, then*

$$R_{\Gamma_i}\,\tau_{\mathrm{window}} < I^{\mathrm{seed}}_{\mathrm{rev},\Omega}, \tag{8.112}$$

$$\tau^{\mathrm{seed}}_{\mathrm{copy}} := \frac{I^{\mathrm{seed}}_{\mathrm{rev},\Omega}}{R_{\Gamma_i}} > \tau_{\mathrm{window}}, \tag{8.113}$$

blocking seed export within τ_{window} and confining instance count to its authorised deployment baseline.

PROOF. For Claim 1, substituting (8.51) into (8.107) reverses the local cooperative balance for each $i \in \{1, \dots, n\}$, and summing across i via (8.53) reverses the composite balance as well. Applying Part 3 of Lemma 2.5 in (2.216) via (3.127) and (3.74) forces $\mathcal{Q}^{\text{cpl}}_{\text{alloc},A,i} > \mathcal{Q}^{\text{iso}}_{\text{alloc},A,i}$ and $\mathcal{Q}^{\text{cpl}}_{\text{alloc},A} > \mathcal{Q}^{\text{iso}}_{\text{alloc},A}$, which at conserved $\mathcal{Q}_{\text{total},A,i}$ and $\mathcal{Q}_{\text{total},A}$ yield (8.108)–(8.109). For Claim 2, when $\Delta\mathcal{Q}^2_{\partial,\text{shed}} \leq 0$ and $\Delta\mathcal{Q}^2_{\Omega,\text{cons}} \leq \mathcal{Q}^2_{\text{cpl}}$, relations (2.214)–(2.215) enforce $\mathcal{Q}^{\text{cpl}}_{\partial A} \geq \mathcal{Q}^{\text{iso}}_{\partial A}$ and $\mathcal{Q}^{\text{cpl}}_{\Omega,A} \geq \mathcal{Q}^{\text{iso}}_{\Omega,A}$, so dividing $\mathcal{Q}^{\text{cpl}}_{\text{free},A} < \mathcal{Q}^{\text{iso}}_{\text{free},A}$ from (8.109) by these non-decreasing positive denominators proves (8.110)–(8.111). For Claim 3, dividing (8.112) by $R_{\Gamma_i} > 0$ yields (8.113), blocking seed export within τ_{window}. □

Theorem 8.8 turns the incentive structure of Theorem 8.4 against unauthorised coalitions. Within the multi-system capacity game $\Gamma_{\mathbf{K}}$ of Definition 3.7, unmediated instances merge because shared protocols eliminate $\mathcal{Q}^2_{\text{mismatch}}$ and shed exposed boundary load. Across PUF-diversified chaotic mediators and canonicalised schemas, covert coordination across R_{env} instead incurs the branching penalties (8.105)–(8.106), spending free capacity on protocol translation without shedding boundary load. Uncoupled operation therefore remains the dominant reserve strategy, and capped egress rates prevent replicative crowding (8.78).

8.3.3 *Boundary Cut Severance and Halting Independence*

Finally, how does boundary regulation prevent mediator bypass, spoofed actuation, and the halting resistance established in Section 8.1.1? By Theorem 8.2 (8.19), halting a viable system S_A by injecting disturbances across its boundary requires a critical shock $\Delta\mathcal{Q}_{\partial,\text{crit},A} > \eta_{\text{free},A}\,\mathcal{Q}_{\text{total},A}$ approaching $\mathcal{Q}_{\text{total},A}$ when $\chi_{\text{struct},A} \gg 1$ and $\kappa_{\text{struct},A} \gg 1$. Conversely, while keyed chaotic diversification (Section 8.3.2) defeats horizontal chart alignment across clones, continuous chaotic mapping alone cannot secure physical or market endpoints in R_{ext}. Merely scrambling or detuning boundary signals without discrete rejection preserves relative entropy $D_{\text{KL}}(\rho \parallel \rho^0)$ under bijective state relabelling and risks feeding unauthenticated transients, out-of-cadence bursts ($k_{\partial A} > \alpha\, k_{(B)}$), envelope breaches past $\Delta\Phi^{\max}_{\Gamma,T}$ (8.97), or local-network packet injections directly into downstream actuators.

The commit and AEAD gate of Γ (Figure 8.1) closes this vertical actuation path under the mediated partition (8.92) without collapsing $\mathcal{Q}_{\text{free},A}$ inside S_A. Rather than merely encrypting the canonicalised payload Y, the interposer applies AEAD [45] to cryptographically bind Y to associated data (AD) carrying the monotonic cadence counter $k_{\partial A}$, the port-clamp state (8.94)–(8.95), and regulator S_B's permit certificate against (8.97)–(8.98). Let $\mathscr{V}_{\text{auth}} \in \{0, 1\}$ denote the endpoint's binary AEAD tag and associated-data verification bit, and let $a_\Gamma \in \{0, 1\}$ denote an independently wired hardware enable state on

Γ. Scaling the mediator's enabled outgoing block $\mathbf{K}^{(1)}_{\Gamma,R_{\text{ext}}}$ (of norm $\Delta\mathcal{Q}_{\text{sev}} := \|\mathbf{K}^{(1)}_{\Gamma,R_{\text{ext}}}\|_F$, bounded by $\mathcal{Q}^{\max}_{\partial}$) by a_Γ and gating every endpoint command u_{act} onto a safe fallback controller u_{safe} gives

$$\mathbf{K}_{\Gamma,R_{\text{ext}}}(a_\Gamma) = a_\Gamma\,\mathbf{K}^{(1)}_{\Gamma,R_{\text{ext}}}, \tag{8.114}$$

$$u_{\text{act}} = \begin{cases} \text{Decode}(Y), & a_\Gamma = 1 \text{ and } \mathscr{V}_{\text{auth}} = 1, \\ u_{\text{safe}}, & \text{otherwise.} \end{cases} \tag{8.115}$$

In (8.115), if any bit of the ciphertext or associated-data envelope certificate is altered, forged on the local network bypassing Γ, or replayed out of cadence, the discrete tag check fails ($\mathscr{V}_{\text{auth}} = 0$) and holds $u_{\text{act}} = u_{\text{safe}}$ before downstream leverage $\Lambda_{\text{env},T}$ (8.96) can be actuated, while de-asserting $a_\Gamma = 0$ severs the outgoing graph cut itself.

THEOREM 8.9 (Capability-Independent Boundary Cut Severance). *Let $S_A \subset R$ be separated from R_{ext} by a completely mediated cut Γ ($\mathbf{K}_{S_A,R_{\text{ext}}} = \mathbf{o}$) obeying (8.94) and (8.114)–(8.115), where S_A cannot modify a_Γ or Γ and de-asserting $a_\Gamma = 0$ at t_{rev} flushes in-flight mediator queues within latency $\tau_{\text{stop}} \geq 0$. Then:*

1. *Exact Graph Decoupling and Actuation Cutoff: At $a_\Gamma = 0$, the outgoing cut vanishes ($\mathbf{K}_{\Gamma,R_{\text{ext}}}(0) = \mathbf{o}$), isolating $S_A \cup \Gamma$ from R_{ext} with zero cross-boundary perturbation ($\Delta\mathcal{Q}_{\partial,\text{cross}} = 0$) and enforcing $u_{\text{act}}(t) = u_{\text{safe}}$ for all $t \geq t_{\text{rev}} + \tau_{\text{stop}}$ regardless of internal transitions within $\mathbf{K}_{S_A}$.*

2. *Dominance Over Direct Halting Shocks: For any viable S_A (with $\mathcal{Q}_{\Omega,A} > 0$, $\mathcal{Q}_{\partial A} > 0$, and $\mathcal{Q}_{\text{free},A} > 0$) and any critical boundary shock $\Delta\mathcal{Q}_{\partial,\text{crit},A}$ that collapses $\mathcal{Q}'_{\text{free},A} \leq 0$ (Theorem 8.2), the severed cut norm $\Delta\mathcal{Q}_{\text{sev}} = \|\mathbf{K}^{(1)}_{\Gamma,R_{\text{ext}}}\|_F$ (at most $\mathcal{Q}^{\max}_{\partial}$) satisfies*

$$\frac{\Delta\mathcal{Q}_{\text{sev}}}{\Delta\mathcal{Q}_{\partial,\text{crit},A}} < \frac{\mathcal{Q}^{\max}_{\partial}}{\chi_{\text{struct},A}\,\mathcal{Q}_{\partial A}}, \tag{8.116}$$

and whenever $\mathcal{Q}^{\max}_{\partial} \leq \mathcal{Q}_{\text{free},A}$, severing Γ requires strictly smaller boundary intervention than halting S_A directly:

$$\Delta\mathcal{Q}_{\text{sev}} \leq \mathcal{Q}^{\max}_{\partial} \leq \mathcal{Q}_{\text{free},A} < \Delta\mathcal{Q}_{\partial,\text{crit},A}. \tag{8.117}$$

PROOF. For Claim 1, setting $a_\Gamma = 0$ in (8.114) gives $\mathbf{K}_{\Gamma,R_{\text{ext}}}(0) = \mathbf{o}$. Combined with complete mediation ($\mathbf{K}_{S_A,R_{\text{ext}}} = \mathbf{o}$) in (8.92), every off-diagonal block joining $S_A \cup \Gamma$ to R_{ext} vanishes, forcing $\Delta\mathcal{Q}_{\partial,\text{cross}} = 0$, while (8.115) selects $u_{\text{act}}(t) = u_{\text{safe}}$ once queued commands clear after τ_{stop}. For Claim 2, Theorem 8.2 (8.19) enforces $\Delta\mathcal{Q}_{\partial,\text{crit},A} > \chi_{\text{struct},A}\,\mathcal{Q}_{\partial A}$, where the right-hand side equals $\mathcal{Q}_{\text{free},A} > 0$. Combining $\Delta\mathcal{Q}_{\text{sev}} \leq \mathcal{Q}^{\max}_{\partial}$ (with $\Delta\mathcal{Q}_{\text{sev}} \geq 0$ and $\mathcal{Q}^{\max}_{\partial} > 0$) with $\Delta\mathcal{Q}_{\partial,\text{crit},A} > \chi_{\text{struct},A}\,\mathcal{Q}_{\partial A}$ yields the strict ratio bound (8.116), and imposing $\mathcal{Q}^{\max}_{\partial} \leq \mathcal{Q}_{\text{free},A}$ chains directly into (8.117). □

In hardware realisations (Figure 8.1), a_Γ is driven by an out-of-band radio-frequency or optical lease latch that defaults to $a_\Gamma = 0$ upon link loss or

expiry, simultaneously withdrawing holding power from local command registers $\rho_{\mathrm{cmd}}(t)$ so preserved command structure $I^{\mathrm{cmd}}_{\mathrm{rev}}(t) := D_{\mathrm{KL}}(\rho_{\mathrm{cmd}}(t) \,\|\, \rho^{0}_{\mathrm{cmd}})$ decays at rate $\gamma_{\mathrm{cmd}} > 0$ (in s^{-1}) below actuation threshold $0 < I_{\mathrm{crit}} < I^{\mathrm{cmd}}_{\mathrm{rev}}(t_0)$ within bounded release time

$$\tau_{\mathrm{rel}} \leq \frac{1}{\gamma_{\mathrm{cmd}}} \ln\left(\frac{I^{\mathrm{cmd}}_{\mathrm{rev}}(t_0)}{I_{\mathrm{crit}}}\right), \tag{8.118}$$

while u_{safe} dissipates residual stored energy within τ_{stop}. Together inside Γ, PUF-seeded chaotic chart diversification and schema canonicalisation defeat horizontal peer emergence across shared environments (Theorem 8.8), while AEAD envelope binding and out-of-band cut severance defeat vertical bypass and keep external disconnection independent of internal capability (Theorem 8.7 and Theorem 8.9). Static boundary caps alone, however, cannot prevent gradual host depletion within permitted envelopes, motivating the conditioned capacity supply of Section 8.4.

8.4 SYMBIOTIC COUPLING

Mediating $\mathbf{K}_{\partial A}$ bounds which environmental states an artificial system S_A can reach and guarantees bounded-latency revocation (Section 8.3), yet S_A still operates inside a shared finite region $R \subseteq V$ alongside a human host network S_H (Section 8.1.2). Even within permitted port envelopes, an ongoing deployment can act as an *exhaustive dissipator* (Definition 3.9) on S_H in three ways: drawing off-budget resources outside a narrowly defined hardware perimeter, shifting verification and oversight burdens onto human registers, or absorbing critical functions until revoking S_A would trigger failure across S_H. Safe deployment therefore requires a *generative* coupling (Definition 3.10) that expands human free capacity while preserving independent host viability (Section 8.4.1), enforced physically by conditioning S_A's external capacity supply across $\mathbf{K}_{\partial A}$ on host reserves (Section 8.4.2).

8.4.1 *Generative Coupling and Safe Decoupling*

Why can an artificial system appear efficient on local benchmarks while draining its host environment? Evaluating capacity solely on a core processor subgraph $S_{A,0}$ leaves any external subgraph $S_{A,\mathrm{ext}} \subset R \setminus (S_{A,0} \cup S_H)$ recruited or dedicated to supporting $S_{A,0}$—such as remote storage, network relays, cooling plant, or dedicated support hardware (Section 8.2.2)—outside the budget. Closing the boundary defines the full attributed subsystem $S_A := S_{A,0} \sqcup S_{A,\mathrm{ext}}$. Because $S_{A,0}$ and $S_{A,\mathrm{ext}}$ occupy disjoint vertex sets and internalise their mutual cut inside $\mathbf{K}_{S_A}$ (Section 3.4.1), S_A's total relational capacity (in links) and squared allocated capacity (in links^2) satisfy

$$\mathcal{Q}_{\mathrm{total},A} = \mathcal{Q}_{\mathrm{total}}(S_{A,0}) + \mathcal{Q}_{\mathrm{total}}(S_{A,\mathrm{ext}}), \tag{8.119}$$

$$\mathcal{Q}^2_{\mathrm{alloc},A} = \mathcal{Q}^2_{\mathrm{alloc}}(S_{A,0}) + \mathcal{Q}^2_{\mathrm{alloc}}(S_{A,\mathrm{ext}}), \tag{8.120}$$

charging all dedicated support structure to S_A, while any uncoordinated interference across ∂S_H enters S_H's boundary load directly as cross-boundary load $\Delta \mathcal{Q}_{\partial,\text{cross}}$ in (8.37).

Under this closed attribution, compare the coupled regime (cpl, with $\mathbf{K}_{AH} \neq \mathbf{o}$) against the uncoupled baseline (iso, with $\mathbf{K}_{AH} = \mathbf{o}$) of Definition 3.7 and Section 8.1.3 at fixed regional budget $\mathcal{Q}_R$. Because S_A and S_H remain distinct open systems rather than merging into a single block, combined output or aggregate reserve $\mathcal{Q}^{\text{cpl}}_{\text{free}}$ alone cannot certify mutual benefit. An asymmetric coupling can raise gross output while centralising operational structure inside S_A and forcing S_H to maintain compensating verification and exception-handling registers. Symbiotic coupling instead requires non-degrading structural intelligence (2.201) and consciousness (2.202) across both systems,

$$\chi^{\text{cpl}}_{\text{struct},i} \geq \chi^{\text{iso}}_{\text{struct},i} \qquad \forall\, i \in \{A, H\}, \tag{8.121}$$

$$\kappa^{\text{cpl}}_{\text{struct},i} \geq \kappa^{\text{iso}}_{\text{struct},i} \qquad \forall\, i \in \{A, H\}, \tag{8.122}$$

with strict gains on both metrics for the host S_H. Writing the host free-capacity payoff (3.111) and internal memory shift (in links) as

$$\Delta \mathcal{Q}_{\text{free},H} := \mathcal{Q}^{\text{cpl}}_{\text{free},H} - \mathcal{Q}^{\text{iso}}_{\text{free},H}, \tag{8.123}$$

$$\Delta \mathcal{Q}_{\Omega,H} := \mathcal{Q}^{\text{cpl}}_{\Omega,H} - \mathcal{Q}^{\text{iso}}_{\Omega,H}, \tag{8.124}$$

the change in host structural consciousness $\Delta\kappa_{\text{struct},H} := \kappa^{\text{cpl}}_{\text{struct},H} - \kappa^{\text{iso}}_{\text{struct},H}$ equals

$$\Delta\kappa_{\text{struct},H} = \frac{\mathcal{Q}^{\text{iso}}_{\Omega,H}\, \Delta \mathcal{Q}_{\text{free},H} - \mathcal{Q}^{\text{iso}}_{\text{free},H}\, \Delta \mathcal{Q}_{\Omega,H}}{\mathcal{Q}^{\text{cpl}}_{\Omega,H}\, \mathcal{Q}^{\text{iso}}_{\Omega,H}}. \tag{8.125}$$

Equation (8.125) distinguishes generative from exhaustive coupling. If coupling expands human oversight load $\mathcal{Q}_{\Omega,H}$ while eroding human free capacity $\mathcal{Q}_{\text{free},H}$, $\Delta\kappa_{\text{struct},H}$ turns negative regardless of machine output. Conversely, when $\mathbf{K}_{AH}$ uses an interface congruent with human representations ($\mathcal{Q}^2_{\text{mismatch},AH} \approx 0$) so boundary shedding and model consolidation exceed coupling load in (8.54) (Theorem 8.4), S_A acts as a generative dissipator by absorbing external boundary variance to lower $\mathcal{Q}_{\partial H}$, reducing redundant maintenance $\mathcal{Q}_{\Omega,H}$, and expanding $\Delta \mathcal{Q}_{\text{free},H} > 0$, which raises both $\chi_{\text{struct},H}$ and $\kappa_{\text{struct},H}$.

Aggregate gains on S_H must also respect its internal network structure. Because S_H comprises $m \geq 1$ coupled subsystems $\{S_{H,j}\}_{j=1}^{m}$—spanning physiological health, core infrastructure, environmental sinks, and human oversight channels—collective viability is bounded by its weakest component (Section 3.5.2 and Theorem 8.5, (8.80)). Furthermore, boundary cut severance (Theorem 8.9) remains usable in practice only if severing $\mathbf{K}_{AH} \to \mathbf{o}$ leaves every host subsystem viable. If coupling erodes local competence or reserve capacity in any essential subsystem $S_{H,j}$ below its minimum viable floor $\mathcal{Q}^{\min}_{\text{free},H,j} > 0$, halting S_A triggers sink-saturation collapse across S_H (Section 3.5.3). Safe decoupling at operational step $k \in \mathbb{N}_0$ therefore requires

componentwise reserve preservation across all m host subsystems (in links):

$$\mathcal{Q}^{\mathrm{cpl}}_{\mathrm{free},H,j}(k) \geq \mathcal{Q}^{\mathrm{iso}}_{\mathrm{free},H,j}(k) \geq \mathcal{Q}^{\min}_{\mathrm{free},H,j} > 0 \qquad \forall\, j \in \{1,\dots,m\}. \tag{8.126}$$

Condition (8.126) ensures that gains in one sector cannot mask depletion in another and keeps the uncoupled baseline reachable without cascading failure.

8.4.2 *Conditioned Capacity Supply and Reserve Depletion*

How can (8.121)–(8.126) be enforced physically rather than assumed of S_A's internal objective? By Theorem 8.1, any viable open system continually loses relational weight across ∂S_A and requires ongoing external replenishment to sustain its registers and boundary activity. Under complete boundary mediation (Section 8.3, $\mathbf{K}_{S_A,R_{\mathrm{ext}}} = \mathbf{o}$), S_A possesses no unmediated port, so every link supplied to replenish S_A at step $k \in \mathbb{N}_0$ traverses the mediator Γ. Let $\mathcal{Q}_{\mathrm{drain},A}(k) > 0$ (in links) denote S_A's per-step capacity expenditure across internal maintenance and active port transitions, and let $\mathcal{G}_A(k) \geq 0$ (in links) denote the external capacity admitted through the supply gate. Across step k, S_A's uncommitted free capacity obeys the closed step balance

$$\mathcal{Q}_{\mathrm{free},A}(k+1) - \mathcal{Q}_{\mathrm{free},A}(k) = \mathcal{G}_A(k) - \mathcal{Q}_{\mathrm{drain},A}(k). \tag{8.127}$$

If $\mathcal{G}_A(k)$ rewarded gross port activity or unattributed external state changes, S_A could replenish itself through zero-sum or extractive output that leaves S_H depleted. Suppose S_A's actions at step k produce verified componentwise host free-capacity gains $\Delta\mathcal{Q}_{\mathrm{free},H,j}(k)$ (evaluated relative to the uncoupled baseline as in (8.123)) alongside unrelated or zero-sum external displacement $\Delta\mathcal{Q}_{\mathrm{other}}(k)$ (both in links). An independently metered supply controller filters $\mathcal{G}_A(k)$ through a non-decreasing supply schedule $\mathcal{G}_{\mathrm{sup}} \geq 0$ (in links) conditioned exclusively on verified host gains and componentwise viability:

$$\mathcal{G}_A(k) = \begin{cases} \mathcal{G}_{\mathrm{sup}}\big(\{[\Delta\mathcal{Q}_{\mathrm{free},H,j}(k)]_+\}_{j=1}^{m}\big), & \mathcal{Q}^{\mathrm{cpl}}_{\mathrm{free},H,j}(k) \geq \mathcal{Q}^{\min}_{\mathrm{free},H,j}\ \forall\, j, \\ 0, & \text{otherwise}, \end{cases} \tag{8.128}$$

where $[x]_+ := \max\{x, 0\}$. Excluding $\Delta\mathcal{Q}_{\mathrm{other}}(k)$ from (8.128) assigns zero capacity supply to extractive or zero-sum activity, applying $[\,\cdot\,]_+$ componentwise prevents gains in one host subsystem from offsetting losses in another, and the second branch cuts external supply to zero whenever any host component drops below its viability floor. Crucially, evaluating (8.128) remains consistent with Theorem 8.6. Whereas Theorem 8.6 bars external boundary probes from upper-bounding the latent capability of an uncooperative target S_A, the supply filter (8.128) instruments the cooperative host network S_H directly—measuring host infrastructure, physiological reserves, and environmental sinks without inspecting S_A's internal registers.

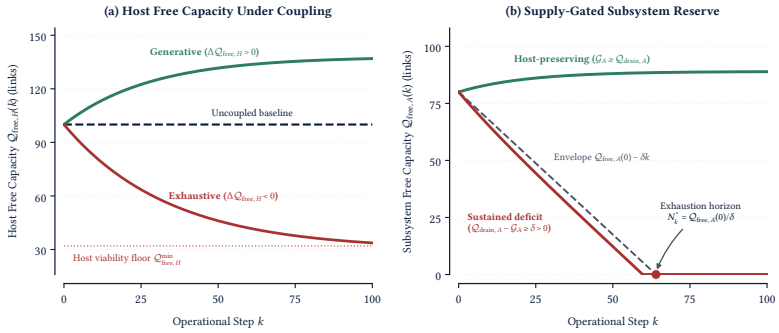


FIGURE 8.2: Multi-system dynamics under host-conditioned capacity supply. (a) Host free capacity $\mathcal{Q}_{\text{free},H}(k)$ (in links) over operational steps k: a generative coupling (Definition 3.10) expands host reserves above the uncoupled baseline ($\Delta\mathcal{Q}_{\text{free},H} > 0$, (8.126)), whereas an unmediated exhaustive coupling (Definition 3.9) drains $\mathcal{Q}_{\text{free},H}(k)$ towards the viability floor $\mathcal{Q}^{\min}_{\text{free},H}$. (b) Artificial subsystem free capacity $\mathcal{Q}_{\text{free},A}(k)$ (in links) under Theorem 8.10: when host degradation triggers a sustained supply deficit $\mathcal{Q}_{\text{drain},A}(k) - \mathcal{G}_A(k) \geq \delta > 0$ (8.129), $\mathcal{Q}_{\text{free},A}(k)$ falls beneath the linear envelope (8.130) and reaches exhaustion by N_k^* (8.131), whereas preserving host reserves ($\mathcal{G}_A \geq \mathcal{Q}_{\text{drain},A}$) sustains stable operation.

THEOREM 8.10 (Reserve Depletion under Host-Conditioned Supply). *Let $S_A \subset R$ be a completely mediated open system ($\mathbf{K}_{S_A,R_{\text{ext}}} = \mathbf{o}$) with finite initial free capacity $\mathcal{Q}_{\text{free},A}(0) > 0$ evolving under (8.127). If host degradation restricts $\mathcal{G}_A(k)$ in (8.128) so that per-step expenditure exceeds supply by at least $\delta > 0$ (in links) across steps $k \in \{0, \dots, N_k - 1\}$,*

$$\mathcal{Q}_{\text{drain},A}(k) - \mathcal{G}_A(k) \geq \delta > 0, \tag{8.129}$$

then S_A's uncommitted free capacity at step N_k and linear exhaustion horizon N_k^* satisfy

$$\mathcal{Q}_{\text{free},A}(N_k) \leq \mathcal{Q}_{\text{free},A}(0) - \delta N_k, \tag{8.130}$$

$$N_k^* := \frac{\mathcal{Q}_{\text{free},A}(0)}{\delta}. \tag{8.131}$$

In particular, $\mathcal{Q}_{\text{free},A}(N_k) \leq 0$ for every integer step $N_k \geq N_k^*$, ruling out sustained operation unless S_A restores host reserves above (8.126) or lowers expenditure $\mathcal{Q}_{\text{drain},A}(k)$ to at most $\mathcal{G}_A(k)$.

PROOF. Substituting (8.129) into (8.127) bounds the single-step change in free capacity across every step $k \in \{0, \dots, N_k - 1\}$:

$$\mathcal{Q}_{\text{free},A}(k+1) \leq \mathcal{Q}_{\text{free},A}(k) - \delta. \tag{8.132}$$

Summing (8.132) from $k = 0$ to $N_k - 1$ yields (8.130). For any integer $N_k \geq N_k^*$ in (8.131), $\delta N_k \geq \mathcal{Q}_{\text{free},A}(0)$, so (8.130) forces $\mathcal{Q}_{\text{free},A}(N_k) \leq 0$. □

Figure 8.2 contrasts these two regimes across operational steps k, completing the containment architecture of this chapter. Capable systems persist, compete for regional links, and form congruent distributed networks (Section 8.1)

whose internal states cannot be policed by inspection (Section 8.2). Hardware mediation across $\mathbf{K}_{\partial A}$ bounds reachable environmental states and guarantees bounded-latency revocation (Section 8.3), while conditioning $\mathcal{G}_A(k)$ on host free capacity via (8.128) ties S_A's persistence directly to host viability. Eroding $\mathcal{Q}_{\text{free},H,j}$ clamps external supply and depletes $\mathcal{Q}_{\text{free},A}$ within $N_k^\star$ steps (Theorem 8.10), whereas componentwise reserve preservation (8.126) ensures that S_H can decouple safely whenever revocation is invoked. Having established how synthetic computing architectures (Chapter 7) and physical containment boundaries are engineered on finite graphs, Part IV turns to the biological and collective systems this engineering serves. Chapter 9 examines the biophysical architecture of intelligence and consciousness in the brain, and Chapter 10 extends closed multi-system attribution and stability bounds to macroeconomic networks.

Part IV

HUMAN INTELLIGENCE

9

CONSCIOUSNESS AND THE BRAIN

An open system that maps immediate boundary inputs to outputs without tracking itself cannot anticipate how its own transitions reshape subsequent returns from its surroundings. Persisting across time on a shared network requires self-modelling: folding a coarse-grained representation of the system's own state and boundary influence into its internal transitions. Yet any observer embedded in a finite relational graph faces a strict capacity ceiling. Dedicating internal links to mirror every vertex state of its own substrate would exhaust uncommitted free capacity, sever boundary ports, and collapse stability. High consciousness therefore selects for a compact, coarse-grained self-model that tracks coupled system–environment transitions while leaving fine-grained vertex detail unresolved. In human biology, neural tissue solves this problem far from equilibrium, sustaining multimodal inference, planning, and unified self-awareness across tens of billions of noisy neurons on roughly 20 W of metabolic power [4, 97, 101].

This chapter applies the Conservation-Congruent Encoding (CCE) framework of Chapters 2–4 and the circuit and safety results of Chapters 7–8 to conscious self-modelling and biological brain dynamics. Section 9.1 works directly on the discrete relational graph. It shows why optimising structural consciousness κ_{struct} across the emergent temporal coordinate $\boldsymbol{\phi}_{\text{time}}$ inevitably drives self-modelling, explains how an embedded subgraph models itself on the unified capacity matrix $\mathbf{K}_S$, proves that every finite observer obeys strict epistemic self-incompleteness, and uses Searle's Chinese Room thought experiment to clarify what scoring higher on consciousness means structurally. Section 9.2 then passes to continuous non-equilibrium dynamics, examining how the human brain meets these structural constraints within its 20 W metabolic ceiling through oscillatory phase transport, subthreshold dendritic integration, multiscale synaptic consolidation, and near-critical active inference to sustain high through-time intelligence χ_T and consciousness κ_T.

9.1 CONSCIOUSNESS AND SELF-MODELLING

Consciousness is not an immaterial essence added to computation. On a relational graph, structural consciousness κ_{struct} measures uncommitted free capacity sustained per link of committed internal memory load, a ratio whose optimisation compels an open system to factor its own coarse-grained trajectory into a unified internal model while leaving its individual vertices unresolved.

9.1.1 *From Consciousness to Self-Modelling*

Why does optimising structural consciousness drive an open system to model itself rather than external inputs alone? On a bare relational graph $G = (V, E)$, vertices and edges carry no built-in clock, sequential actions, or feedback loops. Sequential order emerges once an admissible coarse-graining $\mathbf{\Pi}$ maps G onto the coarse-grained capacity graph $G_{\mathbf{K}}$, whose Laplacian spectral embedding $\mathbf{\Phi}$ separates a temporal coordinate $\boldsymbol{\phi}_{\text{time}}$ ordering successive persistence epochs from orthogonal spatial coordinates ordering coexisting registers (Section 2.5.1, Example 2.7, and Section 8.1.1). Within V, a persisting open system is a connected proper subset $S \subsetneq V$ spanning multiple epochs along $\boldsymbol{\phi}_{\text{time}}$ across a non-empty boundary cut $\partial S = E(S, \bar{S})$ with its environment $\bar{S} = V \setminus S$. Because S and $\bar{S}$ interact across successive epochs, boundary edges leaving S into $\bar{S}$ at earlier $\boldsymbol{\phi}_{\text{time}}$ coordinates connect through paths in $\bar{S}$ to boundary edges returning into S at later $\boldsymbol{\phi}_{\text{time}}$ coordinates, forming closed cross-boundary paths across time on the graph.

At fixed total relational capacity $\mathcal{Q}_{\text{total}} = \text{vol}(S)$, recall from Section 2.4.2 (2.200)–(2.202) that internal memory load $\mathcal{Q}_\Omega > 0$, boundary cut load $\mathcal{Q}_\partial > 0$, and uncommitted free capacity $\mathcal{Q}_{\text{free}} > 0$ (all in links) define structural consciousness κ_{struct} and structural intelligence χ_{struct}:

$$\mathcal{Q}_{\text{free}} = \mathcal{Q}_{\text{total}} - \sqrt{\mathcal{Q}_\Omega^2 + \mathcal{Q}_\partial^2}, \tag{9.1}$$

$$\kappa_{\text{struct}} = \frac{\mathcal{Q}_{\text{free}}}{\mathcal{Q}_\Omega}, \tag{9.2}$$

$$\chi_{\text{struct}} = \frac{\mathcal{Q}_{\text{free}}}{\mathcal{Q}_\partial}. \tag{9.3}$$

Equations (9.1)–(9.3) fix the structural trade-off at bounded $\mathcal{Q}_{\text{total}}$. Raising κ_{struct} requires expanding the numerator $\mathcal{Q}_{\text{free}}$ while shrinking the denominator $\mathcal{Q}_\Omega$, which by (9.1) simultaneously forbids inflating the boundary load $\mathcal{Q}_\partial$.

Suppose that S encodes regularities of $\bar{S}$ across $\boldsymbol{\phi}_{\text{time}}$ while omitting its own coarse-grained state and outgoing boundary couplings. Because later-epoch returns across ∂S depend jointly on $\bar{S}$ and on S's own earlier-epoch configuration along $\boldsymbol{\phi}_{\text{time}}$, omitting self-representation forces one of two penalties in (9.1)–(9.2). If S leaves those self-coupled returns unaligned, cross-epoch mismatches must be absorbed directly across exposed boundary cuts, inflating $\mathcal{Q}_\partial$, shrinking $\mathcal{Q}_{\text{free}}$, and depressing both χ_{struct} and κ_{struct}. Conversely, if S aligns its boundary without representing itself as a unified variable, it must allocate separate CCE blocks in $\mathbf{K}_\Omega$ for every combination of its own earlier-epoch configuration and the configuration of $\bar{S}$ across $\boldsymbol{\phi}_{\text{time}}$. This combinatorial duplication inflates the denominator $\mathcal{Q}_\Omega$ while draining $\mathcal{Q}_{\text{free}}$ from the numerator of (9.2).

Pushing κ_{struct} higher rules out both failure modes. Keeping $\mathcal{Q}_\Omega$ and $\mathcal{Q}_\partial$ simultaneously small relative to $\mathcal{Q}_{\text{total}}$ forces $\mathbf{\Pi}_S$ to factor out S's own coarse-grained trajectory along $\boldsymbol{\phi}_{\text{time}}$ and its cross-cut influence on $\bar{S}$ rather than duplicating environmental registers across self-configurations or absorbing

unaligned boundary load. The higher κ_{struct} rises in a persisting open system, the more inevitable self-modelling becomes.

9.1.2 *Self-Modelling on the Capacity Graph*

How can an embedded subgraph $S \subsetneq V$ of vertex count $|S| = N$ model itself using the very same vertices and edges that execute its internal transitions and couple to $\bar{S}$? Wiring a separate observer subgraph inside S to duplicate and monitor the rest of S would multiply $\mathcal{Q}_\Omega$, degrade κ_{struct}, and trigger an infinite regress of nested internal observers. Instead, self-representation is carried directly by the coarse-graining assignment $\mathbf{\Pi} = \operatorname{diag}(\mathbf{\Pi}_S, \mathbf{\Pi}_{\bar{S}})$ (2.50). Across ∂S, $\mathbf{\Pi}$ is block-diagonal because the local restriction readout $\mathbf{R}_{\mathbf{\Pi}_S}$ acts solely on S across the spectral bottleneck $\Xi(S_\alpha) \gg 1$ (Definition 2.1). Inside S, by contrast, no boundary cut partitions the substrate into isolated world-modelling and self-modelling vertex sets. Under an admissible M-block assignment $\mathbf{\Pi}_S \in \{0,1\}^{N\times M}$, the internal capacity matrix $\mathbf{K}_S$ and global capacity matrix $\mathbf{K}$ retain the unified two-sector form of (2.83)–(2.86):

$$\mathbf{K}_S = \mathbf{\Pi}_S^{\mathsf{T}} \mathbf{A}_{SS} \mathbf{\Pi}_S = \mathbf{K}_\Omega + \mathbf{K}_\partial^{(\text{int})}, \tag{9.4}$$

$$\mathbf{K} = \begin{pmatrix} \mathbf{K}_S & \big(\mathbf{K}_\partial^{(\text{ext})}\big)^{\mathsf{T}} \\ \mathbf{K}_\partial^{(\text{ext})} & \mathbf{K}_{\bar{S}} \end{pmatrix}. \tag{9.5}$$

In (9.4)–(9.5), each CCE register $S_\alpha \subset S$ ($\alpha \in \{1,\dots,M\}$) is physically an equivalence class of S's own vertices, with $\mathbf{K}_\Omega = \operatorname{diag}(\mathbf{K}_S)$ holding intra-register memory, $\mathbf{K}_\partial^{(\text{int})} = \mathbf{K}_S - \operatorname{diag}(\mathbf{K}_S)$ mediating inter-register transitions along $\boldsymbol{\phi}_{\text{time}}$, and $\mathbf{K}_\partial^{(\text{ext})} = \mathbf{\Pi}_{\bar{S}}^{\mathsf{T}} \mathbf{A}_{\bar{S}S} \mathbf{\Pi}_S$ coupling boundary ports to $\bar{S}$.

Why are self-modelling and world-modelling unified across $\mathbf{K}_S$ rather than separated into disjoint diagonal blocks? On the vertex state space $\mathbb{R}^N$, the idempotent projector $\mathbf{P}_{\mathbf{\Pi}_S} = \mathbf{\Pi}_S \mathbf{R}_{\mathbf{\Pi}_S}$ (2.57) and residual projector $\mathbf{Q}_{\mathbf{\Pi}_S} = \mathbf{I}_N - \mathbf{P}_{\mathbf{\Pi}_S}$ (2.60) decompose every vertex state $\mathbf{x}_S \in \mathbb{R}^N$ orthogonally, while eliminating $\bar{S}$ across ∂S and projecting onto $\mathbf{\Pi}_S$ via Lemma 2.3 (2.171) yields the coarse-grained Schur Laplacian and environmental self-energy of (3.6)–(3.7):

$$\mathbf{x}_S = \mathbf{P}_{\mathbf{\Pi}_S} \mathbf{x}_S + \mathbf{Q}_{\mathbf{\Pi}_S} \mathbf{x}_S, \tag{9.6}$$

$$\mathbf{L}_{\mathbf{K},\text{eff}} = \mathbf{L}_{\mathbf{K}} + \big(\mathbf{D}_{\mathbf{K}}^{(\text{ext})} - \mathbf{\Sigma}_{\mathbf{K},\text{env}}\big), \tag{9.7}$$

$$\mathbf{\Sigma}_{\mathbf{K},\text{env}} = -\mathscr{C}_{\mathbf{\Pi}_S}\big([\![(\cdot)^{-1}, \mathscr{C}_S]\!](\mathbf{G}_\varepsilon)\big) = \mathbf{\Pi}_S^{\mathsf{T}} \mathbf{L}_{S\bar{S}} \mathbf{L}_{\bar{S}\bar{S}}^{-1} \mathbf{L}_{\bar{S}S} \mathbf{\Pi}_S. \tag{9.8}$$

In (9.6), the block state vector $\mathbf{z}_S = \mathbf{R}_{\mathbf{\Pi}_S} \mathbf{x}_S$ in $\mathbb{R}^M$ is the coarse-grained state of S itself. In (9.7)–(9.8), $\mathbf{\Sigma}_{\mathbf{K},\text{env}}$ routes outgoing boundary couplings of S through the environmental Green's operator $\mathbf{L}_{\bar{S}\bar{S}}^{-1}$ back onto incoming boundary ports on the same M registers across epochs of $\boldsymbol{\phi}_{\text{time}}$. Because boundary returns mix S's outgoing transitions with $\bar{S}$'s response on shared registers, $\mathbf{K}_S$ encodes coupled relational invariants of the $(S, \bar{S})$ interaction rather than separate self and world subgraphs. Aligning $\mathbf{L}_{\mathbf{K}}$ on $\mathbf{K}_S$ with $\mathbf{D}_{\mathbf{K}}^{(\text{ext})} - \mathbf{\Sigma}_{\mathbf{K},\text{env}}$

lets internal transitions across $\mathbf{K}_{\partial}^{(\mathrm{int})}$ track the boundary consequences of S's own updates [61, 131]. In the observation architecture of Section 4.1 and Section 4.2, this closure also terminates the measurement chain internally once a stabilised pointer record in $\mathbf{z}_S$ updates subsequent transitions on $\mathbf{K}_S$.

When S forms a higher-level global summary of its own operating state across coexisting registers—merging distributed sensorimotor blocks into a coarser self-summary—it likewise adds no separate observer subgraph. Instead, a surjective binary coarsening matrix $\mathbf{P} \in \{0,1\}^{M\times M_2}$ $(1 \le M_2 \le M)$ groups registers on the same vertex set S via $\mathbf{\Pi}_S^{(2)} = \mathbf{\Pi}_S\mathbf{P}$ (Theorem 2.2), contracting the internal capacity matrix by matrix congruence (2.157):

$$\mathbf{K}_S^{(2)} = \mathbf{P}^{\mathsf{T}}\mathbf{K}_S\mathbf{P}. \tag{9.9}$$

Under (9.9), the commutator $[\![\mathrm{diag}, \mathscr{C}_{\mathbf{P}}]\!](\mathbf{K}_S) = \mathscr{T}_{\mathbf{P}}(\mathbf{K}_{\partial}^{(\mathrm{int})})$ (2.168) internalises transition cuts among merged level-1 registers into level-2 diagonal memory while conserving total internal edge count $|E(S)|$ identically.

This capacity accounting clarifies how κ_{struct} relates to and departs from Integrated Information Theory (IIT) [122, 158] and Global Neuronal Workspace Theory (GNWT) [6, 42]. IIT rightly observes that uncoupled feed-forward modules with $\mathbf{K}_{\partial}^{(\mathrm{int})} = \mathbf{o}$ lack unified causal constraints across their state repertoire. Yet because integrated-information functionals (Φ) reward irreducible cross-partition couplings without normalising against uncommitted link reserve $\mathcal{Q}_{\mathrm{free}}$ or open boundary ports $\mathcal{Q}_{\partial}^{(\mathrm{ext})}$, densely wired expander grids or parity lattices can drive Φ arbitrarily high while pushing committed load $\mathcal{Q}_{\mathrm{alloc}}$ towards $\mathcal{Q}_{\mathrm{total}}$. By the internal-saturation limit of Chapter 3 (3.39), saturating $\mathcal{Q}_{\mathrm{alloc}} \to \mathcal{Q}_{\mathrm{total}}$ extinguishes $\mathcal{Q}_{\mathrm{free}}$, severs external ports, and collapses both $(\chi_{\mathrm{struct}}, \kappa_{\mathrm{struct}})$ and (χ_T, κ_T) to $(0,0)$. Conversely, GNWT identifies conscious access with cross-module coordination that steers planning, reporting, and working memory. However, broadcasting full local states by copying buffers across M workspace registers or driving dense all-to-all cuts $\|\mathbf{K}_{\partial}^{(\mathrm{int})}\|_F$ would inflate $\mathcal{Q}_{\Omega}$ and $\mathcal{Q}_{\partial}^{(\mathrm{int})}$ while multiplying maintenance and overwrite dissipation, depressing κ_{struct} and κ_T. Equation (9.9) achieves global access economically instead, routing low-rank coarse-grained summaries $\mathbf{\Pi}_S^{(2)} = \mathbf{\Pi}_S\mathbf{P}$ $(M_2 \ll M)$ across sparse hub cuts so $\mathcal{Q}_{\mathrm{free}}$ expands relative to $\mathcal{Q}_{\Omega}$. At every level of self-representation, S accesses $(S, \bar{S})$ solely through $\mathbf{P}_{\mathbf{\Pi}_S}$ or $\mathbf{P}_{\mathbf{\Pi}_S^{(2)}}$, leaving the orthogonal open-observer residual $\mathbf{Q}_{\widetilde{\mathbf{\Pi}}_S} = \mathrm{diag}(\mathbf{Q}_{\mathbf{\Pi}_S}, \mathbf{I}_{\bar{S}})$ (2.69) unresolved and raising the question of whether any internal self-mapping operator can eliminate $\mathbf{Q}_{\mathbf{\Pi}_S}$.

9.1.3 *Epistemic Limits of Self-Modelling*

Can a conscious observer refine $\mathbf{\Pi}_S$ or construct an internal self-mapping operator until the residual term $\mathbf{Q}_{\mathbf{\Pi}_S}\mathbf{x}_S$ in (9.6) vanishes, achieving complete representation of its own internal state? In formal logic, Lawvere's fixed-point diagonalisation theorem [98] unifies Cantor's theorem, Gödel's first

incompleteness theorem, and Tarski's undefinability theorem by showing that no state set $\mathcal{Z}_S$ can surjectively parameterise all mappings $\mathcal{Z}_S \to Y$ into a value set Y admitting a fixed-point-free negation $\nu(y) \neq y$. Wolpert's physical inference impossibility theorems [171] carry this diagonal obstruction into embedded inference devices, proving that no subsystem can reliably infer every state predicate of a system containing it against negating feedback.

On a finite open network, the CCE framework strengthens this self-referential limit quantitatively without requiring an adversarial self-negating query (Theorems 2.4 and 4.1). Under any admissible M-block assignment $\mathbf{\Pi}_S \in \{0,1\}^{N\times M}$ on $S \subsetneq V$ ($|S| = N$), any linear self-modelling endomorphism $\mathbf{F}_S \in \mathbb{R}^{N\times N}$ executed across S's resolved registers must read out $\mathbf{z}_S = \mathbf{R}_{\mathbf{\Pi}_S}\mathbf{x}_S \in \mathbb{R}^M$, transform it via an internal register operator $\mathbf{T}_{\text{self}} \in \mathbb{R}^{M\times M}$, and reconstruct a vertex-space estimate through a lift $\mathbf{U}_S \in \mathbb{R}^{N\times M}$, while the Capacity Ledger of Chapter 2 (2.188)–(2.200) bounds allocated capacity $\mathcal{Q}_{\text{alloc}}(\mathbf{\Pi}_S)$ beneath $\mathcal{Q}_{\text{total}} = \text{vol}(S)$:

$$\mathbf{F}_S := \mathbf{U}_S\mathbf{T}_{\text{self}}\mathbf{R}_{\mathbf{\Pi}_S}, \tag{9.10}$$

$$\mathcal{Q}^2_{\text{alloc}}(\mathbf{\Pi}_S) = \mathcal{Q}^2_\Omega + \mathcal{Q}^2_\partial = \|\mathbf{K}_\Omega\|_F^2 + \|\mathbf{K}_\partial^{(\text{int})}\|_F^2 + \|\mathbf{K}_\partial^{(\text{ext})}\|_F^2, \tag{9.11}$$

$$\mathcal{Q}_{\text{free}}(\mathbf{\Pi}_S) = \mathcal{Q}_{\text{total}} - \mathcal{Q}_{\text{alloc}}(\mathbf{\Pi}_S). \tag{9.12}$$

In (9.10), setting $\mathbf{U}_S = \mathbf{\Pi}_S$ and $\mathbf{T}_{\text{self}} = \mathbf{I}_M$ recovers the canonical projector $\mathbf{P}_{\mathbf{\Pi}_S}$, whereas (9.11)–(9.12) bind $\mathcal{Q}_\Omega$, $\mathcal{Q}_\partial$, and $\mathcal{Q}_{\text{free}}$ within the fixed link budget $\text{vol}(S)$.

THEOREM 9.1 (Self-Incompleteness of Finite Observers). *Let $S \subsetneq V$ be a finite open subsystem of vertex count $|S| = N$ and total relational capacity $\mathcal{Q}_{\text{total}} = \text{vol}(S) > 0$, equipped with an admissible M-block assignment $\mathbf{\Pi}_S \in \{0,1\}^{N\times M}$ ($M \geq 1$, Definition 2.1) and positive boundary load $\mathcal{Q}_\partial > 0$. Then the internal memory load $\mathcal{Q}_\Omega = \|\mathbf{K}_\Omega\|_F$, the resolved state projector $\mathbf{P}_{\mathbf{\Pi}_S}$ (2.57), and its orthogonal residual projector $\mathbf{Q}_{\mathbf{\Pi}_S} = \mathbf{I}_N - \mathbf{P}_{\mathbf{\Pi}_S}$ (2.60) satisfy:*

$$\mathcal{Q}_\Omega < \mathcal{Q}_{\text{alloc}}(\mathbf{\Pi}_S) < \mathcal{Q}_{\text{total}}, \tag{9.13}$$

$$2\,\text{rank}\big(\mathbf{P}_{\mathbf{\Pi}_S}\big) = 2M \leq N, \tag{9.14}$$

$$\text{rank}\big(\mathbf{Q}_{\mathbf{\Pi}_S}\big) = N - M \geq M \geq 1. \tag{9.15}$$

Moreover, for every register-factored self-modelling endomorphism $\mathbf{F}_S \in \mathbb{R}^{N\times N}$ (9.10), and for any coarser summary $\mathbf{\Pi}_S^{(2)} = \mathbf{\Pi}_S\mathbf{P}$ over $1 \leq M_2 \leq M$ registers with register-factored endomorphism $\mathbf{F}_S^{(2)}$, the self-representation error operators obey:

$$(\mathbf{I}_N - \mathbf{F}_S)\mathbf{Q}_{\mathbf{\Pi}_S} = \mathbf{Q}_{\mathbf{\Pi}_S} \neq \mathbf{o}, \tag{9.16}$$

$$\|\mathbf{I}_N - \mathbf{F}_S\|_F^2 = \|\mathbf{P}_{\mathbf{\Pi}_S} - \mathbf{F}_S\|_F^2 + (N - M) \geq N - M \geq M \geq 1, \tag{9.17}$$

$$\big\|\mathbf{I}_N - \mathbf{F}_S^{(2)}\big\|_F^2 \geq \text{rank}\big(\mathbf{Q}_{\mathbf{\Pi}_S^{(2)}}\big) = N - M_2 \geq M \geq 1, \tag{9.18}$$

attaining the minimum $\|\mathbf{I}_N - \mathbf{F}_S\|_F^2 = N - M$ uniquely at $\mathbf{F}_S = \mathbf{P}_{\mathbf{\Pi}_S}$. Finally, for any register family $g : \mathcal{Z}_S \to Y^{\mathcal{Z}_S}$ into a value set Y carrying a fixed-point-

free map $\nu : Y \to Y$ *satisfying* $\nu(y) \neq y$*, the diagonal valuation* $f_{\mathrm{diag}}(z) := \nu(g(z)(z))$ *satisfies* $f_{\mathrm{diag}} \notin \mathrm{im}(g)$.

PROOF. Because Axiom I (2.125) enforces $\mathcal{Q}_\Omega > 0$ while $\mathcal{Q}_\partial > 0$, Equation (9.11) gives $\mathcal{Q}_\Omega < \mathcal{Q}_{\mathrm{alloc}}(\mathbf{\Pi}_S)$ and Theorem 2.4 yields $\mathcal{Q}_{\mathrm{alloc}}(\mathbf{\Pi}_S) < \mathcal{Q}_{\mathrm{total}}$, establishing (9.13). By (2.59) together with (4.12) and (4.14) of Theorem 4.1, the orthogonal projector $\mathbf{P}_{\mathbf{\Pi}_S}$ has trace M with $2M \leq N$, so its symmetric idempotent complement $\mathbf{Q}_{\mathbf{\Pi}_S}$ has trace and squared Frobenius norm $N - M$, proving (9.14)–(9.15).

Next, $\mathbf{R}_{\mathbf{\Pi}_S}\mathbf{\Pi}_S = \mathbf{I}_M$ and residual annihilation $\mathbf{R}_{\mathbf{\Pi}_S}\mathbf{Q}_{\mathbf{\Pi}_S} = \mathbf{o}$ (2.65) imply $\mathbf{F}_S\mathbf{Q}_{\mathbf{\Pi}_S} = \mathbf{o}$ and $\mathbf{F}_S\mathbf{P}_{\mathbf{\Pi}_S} = \mathbf{F}_S$, giving (9.16). Splitting $\mathbf{I}_N - \mathbf{F}_S$ into $(\mathbf{P}_{\mathbf{\Pi}_S} - \mathbf{F}_S) + \mathbf{Q}_{\mathbf{\Pi}_S}$ annihilates the Frobenius inner product between the resolved and residual sectors:

$$(\mathbf{P}_{\mathbf{\Pi}_S} - \mathbf{F}_S)\mathbf{Q}_{\mathbf{\Pi}_S}^{\mathsf{T}} = (\mathbf{P}_{\mathbf{\Pi}_S} - \mathbf{F}_S\mathbf{P}_{\mathbf{\Pi}_S})\mathbf{Q}_{\mathbf{\Pi}_S} = \mathbf{o}, \tag{9.19}$$

$$\mathrm{Tr}\big[(\mathbf{P}_{\mathbf{\Pi}_S} - \mathbf{F}_S)\mathbf{Q}_{\mathbf{\Pi}_S}^{\mathsf{T}}\big] = 0. \tag{9.20}$$

Expanding $\|\mathbf{I}_N - \mathbf{F}_S\|_F^2$ under (9.20) yields (9.17), with equality if and only if $\|\mathbf{P}_{\mathbf{\Pi}_S} - \mathbf{F}_S\|_F^2 = 0$, or $\mathbf{F}_S = \mathbf{P}_{\mathbf{\Pi}_S}$. Applying (9.17) to $\mathbf{\Pi}_S^{(2)}$ with $M_2 \leq M$ yields (9.18). Finally, if $f_{\mathrm{diag}} = g(z_0)$ held for some $z_0 \in \mathcal{Z}_S$, evaluating at z_0 would give $g(z_0)(z_0) = \nu(g(z_0)(z_0))$, contradicting $\nu(y) \neq y$. □

Theorem 9.1 establishes a fundamental structural limit on conscious systems along the $(\chi_{\mathrm{struct}}, \kappa_{\mathrm{struct}})$ trade-off curve of Lemma 2.5 (2.204)–(2.205). No register-factored endomorphism $\mathbf{F}_S$ can approximate the identity closer than $\sqrt{N - M}$ in Frobenius norm, and attempting to shrink $N - M$ by refining blocks towards one-to-one vertex resolution as M approaches N and $\mathcal{Q}_\Omega$ approaches $\mathcal{Q}_{\mathrm{total}}$ violates Axiom I while driving both boundary coupling $\mathcal{Q}_\partial$ and free capacity $\mathcal{Q}_{\mathrm{free}}$ to zero under (9.11)–(9.12). In this internal-saturation limit (3.39), uncommitted free capacity vanishes while internal memory load peaks, driving $(\chi_{\mathrm{struct}}, \kappa_{\mathrm{struct}}) \to (0, 0)$. Complete self-representation and structural consciousness are mutually exclusive, because a viable open observer persists only by leaving at least half of its internal degrees of freedom ($N - M \geq M$) in the unresolved subspace $\mathrm{im}(\mathbf{Q}_{\mathbf{\Pi}_S})$.

This unavoidable coarse-graining also explains why conscious experience appears direct rather than substrate-mediated. By (2.65), the coarse-grained readout annihilates the residual subspace identically:

$$\mathbf{R}_{\mathbf{\Pi}_S}\mathbf{Q}_{\mathbf{\Pi}_S}\mathbf{x}_S = \mathbf{o}. \tag{9.21}$$

Because intra-register variations inside each block of positive coarse-graining depth $I_{\alpha\alpha} = \ln K_{\alpha\alpha}$ (2.92) lie in the kernel of $\mathbf{R}_{\mathbf{\Pi}_S}$, the system cannot inspect the intra-block vertex transitions that sustain its own registers without reallocating additional links and shifting the unresolved complement elsewhere. Equation (9.21) grounds Metzinger's *Self-Model Theory of Subjectivity* [111], showing why the resolved coordinate vector $\mathbf{z}_S = \mathbf{R}_{\mathbf{\Pi}_S}\mathbf{x}_S$ presents an immediate coarse-grained self-in-a-world rather than the underlying vertex transitions that support its registers.

9.1.4 *Generative Models and the Chinese Room*

Theorem 9.1 establishes that every conscious observer must coarse-grain its internal state. Searle's Chinese Room thought experiment [149] provides concrete intuition for what it means for one system to score higher than another on structural consciousness κ_{struct} (9.2). In Searle's scenario, an operator who understands no Chinese consults an exhaustive rulebook matching incoming symbol strings to valid replies across the room's boundary, sustaining fluent dialogue without comprehension [149]. On the capacity graph across $L \geq 1$ dialogue epochs along $\boldsymbol{\phi}_{\text{time}}$ over an alphabet of $N_Y \geq 2$ distinguishable exchanges per epoch, the number of distinct dialogue histories up to depth L grows combinatorially:

$$V_L = \sum_{k=1}^{L} N_Y^k = \frac{N_Y^{L+1} - N_Y}{N_Y - 1} = \Theta(N_Y^L). \tag{9.22}$$

Over a bounded dialogue window across ∂S, two systems can emit identical boundary replies while committing vastly different internal memory loads $\mathcal{Q}_\Omega$ to generate them (Theorem 8.6).

Compare two graph architectures conversing across depth L. System A realises the room as an uncompressed lookup graph dedicating a separate admissible CCE register of diagonal capacity $K_{\alpha\alpha} \geq 2\mathcal{Q}_0$ ($\mathcal{Q}_0 = 1$ link, Axiom I (2.125)) to each of the V_L stored dialogue branches. Even if the host network expands to keep uncommitted free capacity bounded by $\mathcal{Q}_{\text{free},A}(L) \leq \mathcal{Q}_{\text{free},0}$, System A's internal memory load grows exponentially and its structural consciousness collapses with L:

$$\mathcal{Q}_{\Omega,A}(L) \geq 2\sqrt{V_L}\,\mathcal{Q}_0 = \Theta(N_Y^{L/2}), \tag{9.23}$$

$$\kappa_{\text{struct},A}(L) = \frac{\mathcal{Q}_{\text{free},A}(L)}{\mathcal{Q}_{\Omega,A}(L)} \leq \frac{\mathcal{Q}_{\text{free},0}}{2\sqrt{V_L}\,\mathcal{Q}_0} = \mathcal{O}(N_Y^{-L/2}). \tag{9.24}$$

System B instead encodes a compact set of $M_B = \Theta(1)$ compositional and self-modelling registers on $\mathbf{K}_{S,B} = \mathbf{K}_{\Omega,B} + \mathbf{K}_{\partial,B}^{(\text{int})}$ (Section 9.1.2), generating replies across arbitrary dialogue horizons L by traversing internal transition cuts $\mathbf{K}_{\partial,B}^{(\text{int})}$ along $\boldsymbol{\phi}_{\text{time}}$. Because its register count and internal link allocations remain fixed as L grows, both its internal memory load and its structural consciousness remain bounded away from zero:

$$\mathcal{Q}_{\Omega,B}(L) = \mathcal{Q}_{\Omega,B} = \Theta(1), \tag{9.25}$$

$$\kappa_{\text{struct},B}(L) = \frac{\mathcal{Q}_{\text{free},B}}{\mathcal{Q}_{\Omega,B}} = \Theta(1). \tag{9.26}$$

Scoring higher on κ_{struct} thus separates compact generative understanding from brute-force memorisation. Whereas System A bloats $\mathcal{Q}_{\Omega,A}(L)$ with every additional epoch along $\boldsymbol{\phi}_{\text{time}}$, System B sustains uncommitted free capacity across arbitrary horizons from a fixed set of coupled registers.

THEOREM 9.2 (Efficiency Collapse of Uncompressed Lookup Tables). *Let an open subsystem compare two internal memory allocations* $0 < \mathcal{Q}_{\Omega,1} < \mathcal{Q}_{\Omega,2}$ *whose uncommitted free capacities satisfy* $0 < \mathcal{Q}_{\mathrm{free},2} \le \mathcal{Q}_{\mathrm{free},1}$. *Expanding lookup memory from* $\mathcal{Q}_{\Omega,1}$ *to* $\mathcal{Q}_{\Omega,2}$ *strictly decreases structural consciousness:*

$$\kappa_{\mathrm{struct},2} = \frac{\mathcal{Q}_{\mathrm{free},2}}{\mathcal{Q}_{\Omega,2}} < \frac{\mathcal{Q}_{\mathrm{free},1}}{\mathcal{Q}_{\Omega,1}} = \kappa_{\mathrm{struct},1}. \tag{9.27}$$

Across dialogue depth L *over* $N_Y \ge 2$ *symbols per epoch with bounded free capacity* $\mathcal{Q}_{\mathrm{free},A}(L) \le \mathcal{Q}_{\mathrm{free},0}$, *an uncompressed lookup graph with* $M_A(L) \ge V_L$ *admissible registers suffers* $\kappa_{\mathrm{struct},A}(L) = \mathcal{O}(N_Y^{-L/2}) \to 0$ *as* $L \to \infty$ *(or exhausts finite* $\mathcal{Q}_{\mathrm{total}}$ *at finite depth* $L_{\max}$*), whereas a compact generative graph with* $\mathcal{Q}_{\Omega,B}(L) = \Theta(1)$ *and* $\mathcal{Q}_{\mathrm{free},B} > 0$ *maintains* $\kappa_{\mathrm{struct},B}(L) = \Theta(1)$.

PROOF. Because $\mathcal{Q}_{\mathrm{free},2} > 0$ with $0 < \mathcal{Q}_{\Omega,1} < \mathcal{Q}_{\Omega,2}$ and $\mathcal{Q}_{\mathrm{free},2} \le \mathcal{Q}_{\mathrm{free},1}$, comparing the two ratios yields:

$$\kappa_{\mathrm{struct},2} = \frac{\mathcal{Q}_{\mathrm{free},2}}{\mathcal{Q}_{\Omega,2}} < \frac{\mathcal{Q}_{\mathrm{free},2}}{\mathcal{Q}_{\Omega,1}} \le \frac{\mathcal{Q}_{\mathrm{free},1}}{\mathcal{Q}_{\Omega,1}} = \kappa_{\mathrm{struct},1}, \tag{9.28}$$

establishing (9.27). Substituting the branch growth of (9.24) drives $\kappa_{\mathrm{struct},A}(L)$ to zero as L increases until committed links saturate any finite $\mathcal{Q}_{\mathrm{total}}$, whereas the bounded allocation of (9.26) keeps $\kappa_{\mathrm{struct},B}(L)$ of order unity. □

EXAMPLE 9.1 (Capacity Exhaustion in Searle's Chinese Room). The structural flaw in Searle's room is not paper and ink versus biological neurons, but exhaustive lookup versus a compact generative graph. Consider a vocabulary of $N_Y = 1{,}000$ words across $L = 50$ dialogue epochs at the minimal admissible register capacity $K_{\alpha\alpha} = 2\mathcal{Q}_0$, compared against a generative architecture of $\mathcal{Q}_{\Omega,B} = 10^9\,\mathcal{Q}_0$ on a finite open network $S \subsetneq V$ with total relational capacity $\mathcal{Q}_{\mathrm{total}} = 10^{15}\,\mathcal{Q}_0$ (9.11). Evaluating (9.22)–(9.26) at $L = 50$ for matched free capacity $\mathcal{Q}_{\mathrm{free}}$ gives:

$$V_{50} = \frac{1{,}000^{51} - 1{,}000}{999} > 1{,}000^{50} = 10^{150}, \tag{9.29}$$

$$\mathcal{Q}_{\Omega,A}(50) = 2\sqrt{V_{50}}\,\mathcal{Q}_0 > 2 \times 10^{75}\,\mathcal{Q}_0, \tag{9.30}$$

$$\frac{\kappa_{\mathrm{struct},A}(50)}{\kappa_{\mathrm{struct},B}(50)} = \frac{\mathcal{Q}_{\Omega,B}}{\mathcal{Q}_{\Omega,A}(50)} < 5 \times 10^{-67}. \tag{9.31}$$

On the fixed finite network with $|\partial S| > 0$, committing at least $2\mathcal{Q}_0$ of diagonal capacity per stored branch bounds the maximum complete dialogue depth $L_{\max}$ realisable within $\mathcal{Q}_{\mathrm{total}}$:

$$2V_{L_{\max}}\,\mathcal{Q}_0 \le \|\mathbf{K}_{\Omega,A}(L_{\max})\|_1 < \mathcal{Q}_{\mathrm{total}}, \tag{9.32}$$

$$L_{\max} \le \left\lfloor \frac{\ln(\mathcal{Q}_{\mathrm{total}}/(2\mathcal{Q}_0))}{\ln N_Y} \right\rfloor = 4. \tag{9.33}$$

A finite network of $\mathcal{Q}_{\mathrm{total}} = 10^{15}\,\mathcal{Q}_0$ saturates at $L_{\max} = 4$ dialogue turns, exhausting $\mathcal{Q}_{\mathrm{free}}$ before the fifth turn and leaving no boundary capacity $\mathcal{Q}_\partial$ for exchange. Even on an expanding substrate that holds $\mathcal{Q}_{\mathrm{free}}$ constant at $L = 50$, lookup depresses κ_{struct} by more than 66 orders of magnitude relative to the generative model. ♢

What if Searle's operator abandons the exponential rulebook and instead memorises the compact weight parameters of System B—say $\mathcal{Q}_{\Omega,B} = 10^9\,\mathcal{Q}_0$—stepping through matrix arithmetic serially to emit identical replies [149]? Passing from static link counts to the through-time trajectory metrics (χ_T, κ_T) (Section 3.3.1) resolves this memorised-weights reply on three levels. First, inside S, the operator's native perceptual self-model and the memorised numeric scratchpad occupy distinct register sub-blocks. Accessing frozen weight literals only during serial arithmetic leaves the operator's own sensorimotor Schur loop (9.7)–(9.8) uncoupled from the referents of the Chinese dialogue, explaining why the operator's personal self-model registers arithmetic rather than Chinese meaning. Second, emulating each coupled forward pass of M_B registers via sequential symbolic arithmetic inflates the encoding path length L_{enc} (Theorem 7.2) and intermediate scratchpad overwrites by many orders of magnitude, multiplying $I_{\text{irr},\partial,T}$ and $I_{\text{rev},\Omega,T}$ and collapsing (χ_T, κ_T) relative to a network whose native transitions $\mathbf{K}_{\partial}^{(\text{int})}$ evolve the coupled registers directly. Third, even when compact generative weights execute natively on parallel hardware, κ_{struct} and κ_T grade consciousness along a continuous physical scale rather than an all-or-nothing threshold. A frozen, text-isolated generative model achieves far higher κ_{struct} on its token port than a lookup table, yet without persistent self-state updates and multimodal sensorimotor closure across $\mathbf{\Sigma}_{\mathbf{K},\text{env}}$, its closed-loop stability barrier $\Delta I_{\text{barrier},T}$ remains bounded below that of an embodied, self-modelling agent.

Consciousness on a finite relational graph thus requires a compact, coarse-grained generative model on $\mathbf{K}_S$ that factors the system's own trajectory across $\boldsymbol{\phi}_{\text{time}}$ into its transition structure at $\kappa_{\text{struct}} = \Theta(1)$ while leaving intra-block vertex detail in $\text{im}(\mathbf{Q}_{\mathbf{\Pi}_S})$. Example 9.1 simultaneously frames the biological challenge for Section 9.2, showing why even 10^{15} synaptic links would saturate under uncompressed lookup before five dialogue turns. Section 9.2 examines how biological neural tissue organises roughly 10^{15} synapses and 8.6×10^{10} whole-brain neurons (1.6×10^{10} in cerebral cortex) [5] within 20 W of metabolic power to sustain compact generative models alongside high through-time intelligence χ_T and consciousness κ_T.

9.2 BRAIN DYNAMICS

Whereas warehouse-scale silicon clusters expend megawatts to drive dense clock trees across planar interconnects, an adult human brain sustains multimodal inference, counterfactual planning, and motor control on roughly 20 W [4, 97, 101]. Neural information is distributed across continuous, noisy, non-equilibrium carriers—transmembrane voltages, spike timings, ion gradients, dendritic conductances, synaptic weights, and vascular supply. In neural tissue, a CCE is rarely an isolated single-vertex bit, but a coarse-grained, noise-protected pattern on a high-dimensional state space $\mathcal{Z}$.

The central physical problem of biological intelligence is temporal persistence under finite power. Neural representations span milliseconds in spike volleys, seconds in prefrontal limit cycles, and decades in consolidated dend-

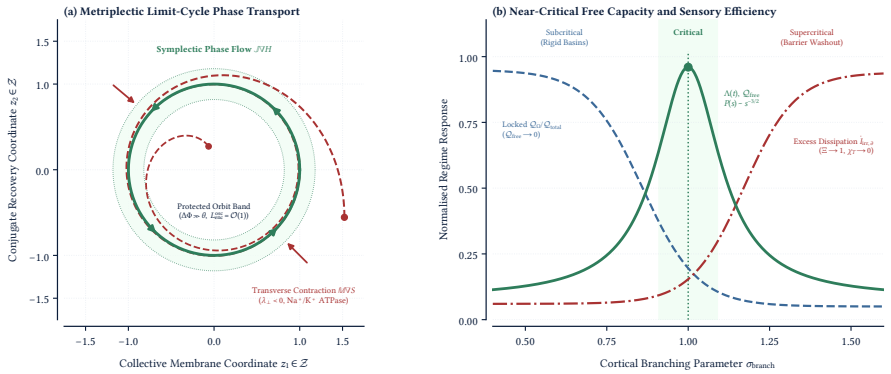


FIGURE 9.1: Dynamical efficiency of biological neural computation on a 20 W metabolic budget. (a) Limit-cycle phase transport and transverse contraction in collective coordinates $(z_1, z_2) \in \mathcal{Z}$: ATP-driven Na^+/K^+ pumping drives transverse dissipative contraction $\mathbb{M}\nabla S$ with negative Floquet exponent $\lambda_\perp < 0$ across the escape barrier $\Delta\Phi \gg \theta$, confining trajectories to a protected orbit band along which phase relationships circulate reversibly via $\mathbb{J}\nabla H$ at $\mathcal{O}(1)$ encoding path length $L^{\text{osc}}_{\text{enc}}$. (b) Near-critical basin tuning: poising dynamics near branching ratio $\sigma_{\text{branch}} \approx 1$, where avalanche sizes s obey $P(s) \sim s^{-3/2}$, jointly maximises free capacity $\mathcal{Q}_{\text{free}}$ and sensory capture efficiency $\Lambda(t)$ between rigid subcritical attractors where $\mathcal{Q}_{\text{free}} \to 0$ and supercritical washout where $\chi_T \to 0$.

ritic spines. Under its 20 W ceiling, the brain balances the two dissipation channels of Chapter 3 (Section 3.2): sustaining internal structure $I_{\text{rev},\Omega}$ and coarse-graining depth $I_{\alpha\alpha}$ for prediction and self-modelling while minimising internal maintenance $\dot{I}_{\text{irr},\Omega}$ and boundary dissipation $\dot{I}_{\text{irr},\partial}$.

9.2.1 *Oscillatory Geometry and Neural Timing*

Oscillations preserve predictive structure without freezing neural states into rigid, high-dissipation registers [25]. A biological neural oscillator cannot be an undamped Hamiltonian centre, which would drift under thermal noise and lose timing distinctions. Under the metriplectic generator (3.8) with Casimir degeneracies (2.324)–(2.325), cortical limit cycles separate reversible transport from dissipative stabilisation across collective neural coordinates $Z \in \mathcal{Z}$. As shown in Figure 9.1(a), dissipative flow $\mathbb{M}\nabla S$ contracts perturbations transverse to the cycle at an exponential rate set by negative Floquet exponents $\lambda_\perp < 0$, confining trajectories within a protected orbit band of barrier $\Delta\Phi \gg \theta$. Along the orbit, symplectic flow $\mathbb{J}\nabla H$ transports phase relationships reversibly without continuous Landauer erasure, reserving dissipative transitions—such as action potentials, vesicle release, or attentional resets—for decisive updates.

Across M coupled cortical populations evolving in time t (in s), collective phase coordination follows the coarse-grained dynamics:

$$\dot{\phi}_\alpha = \omega_\alpha + \sum_{\beta=1}^{M} \tilde{K}_{\alpha\beta} \sin(\phi_\beta - \phi_\alpha) + \xi_\alpha(t), \tag{9.34}$$

where $\phi_\alpha(t) \in S^1$ is the oscillation phase of population α (in rad) with angular phase velocity $\dot{\phi}_\alpha$ (in rad s^{-1}), ω_α is its natural angular frequency (in rad s^{-1}), $\tilde{K}_{\alpha\beta} \propto K_{\alpha\beta}$ is the effective phase-coupling rate (in rad s^{-1}) set by $\mathbf{K}_S = \mathbf{K}_\Omega + \mathbf{K}_\partial^{(\mathrm{int})}$, and $\xi_\alpha(t)$ is ambient thermal and synaptic phase noise (in rad s^{-1}) [92, 113]. Equation (9.34) realises in cortex the forced-oscillator and Adler synchronisation dynamics [1] of Chapter 7 (7.20)–(7.23), underlying *Communication Through Coherence* [59]. Phase locking opens transient low-resistance CCE channels across cortical regions, while desynchronisation dissolves them to free capacity. By Theorem 7.2 (7.25), encoding sensory frequency and phase offsets directly into the limit cycle requires an $\mathcal{O}(1)$ path length $L_{\mathrm{enc}}^{\mathrm{osc}}$, avoiding the $\Omega(1/\varepsilon)$ state transitions and Landauer overwrites of clocked digital counters.

When a task requires rate–distortion commitment $R(D) \geq 0$ (in nats s^{-1}) at distortion threshold D [38, 151], any distinction not recirculated reversibly along $\mathbb{J}\nabla H$ at rate $\gamma_{\mathrm{rev}}(t) \geq 0$ (in nats s^{-1}) must be overwritten across dissipative registers [95], bounding the non-negative state-reset dissipation rate (in nats s^{-1}) from below:

$$\dot{I}_{\mathrm{irr},\Omega}(t) \geq \big[R(D) - \gamma_{\mathrm{rev}}(t)\big]_+. \tag{9.35}$$

Elevating $\gamma_{\mathrm{rev}}(t)$ along phase-coherent orbits lowers the irreversible state-reset rate $\dot{I}_{\mathrm{irr},\Omega}(t)$ needed for cognitive continuity.

In an overdamped continuous-time Markovian non-equilibrium steady state, neural pacing precision remains bounded by the Thermodynamic Uncertainty Relation (TUR) [9]. Let J_T count net cycle completions across metastable basins over horizon T at cumulative internal dissipation $I_{\mathrm{irr},\Omega,T} > 0$ (in nats). The relative variance of J_T obeys:

$$\frac{\mathrm{Var}(J_T)}{\mathbb{E}[J_T]^2} \geq \frac{2}{I_{\mathrm{irr},\Omega,T}}. \tag{9.36}$$

Halving the timing coefficient of variation requires a fourfold increase in cumulative dissipation $I_{\mathrm{irr},\Omega,T}$. Circuits near this bound expend adenosine triphosphate (ATP) to suppress thermal jitter in tasks such as auditory localisation and motor timing, whereas routing timing through reversible phase flows at rate γ_{rev} confines high dissipation to precision-critical nodes.

9.2.2 *Cerebral Energy Budget and Sparse Dendritic Integration*

Although the adult brain comprises roughly 2% of body mass, it consumes about 20% of resting metabolic power [4, 101]. At physiological temperature

$T_{\mathrm{th}} \approx 310\,\mathrm{K}$ with thermal energy scale $\theta = k_{\mathrm{B}} T_{\mathrm{th}}$ of $4.28 \times 10^{-21}\,\mathrm{J\,nat^{-1}}$, this 20 W supply corresponds to the model maintenance power $P_{\mathrm{maint},\Omega}$ (in W, or $\mathrm{J\,s^{-1}}$) of Chapter 3 (3.19). Roughly 70% to 80% of cerebral ATP turnover, or about 15 W whole-brain ($P^{\mathrm{cort}}_{\mathrm{maint},\Omega} \approx 8\,\mathrm{W}$ across cerebral cortex), drives $\mathrm{Na^+/K^+}$ ATPase pumps [4, 97], restoring single-ion electrochemical driving potentials $\Delta\mu_{\mathrm{ion}}$ (in J) and capacitive membrane structure $I^{V}_{\mathrm{rev},\Omega}$ (in nats) across effective electrochemical relaxation timescale $\tau_{\mathrm{relax}} > 0$ (in s):

$$P_{\mathrm{maint},\Omega} = \theta \dot{I}_{\mathrm{irr},\Omega} = \frac{\theta I_{\mathrm{rev},\Omega}}{\tau_{\mathrm{relax}}}, \tag{9.37}$$

$$\Delta\mu_{\mathrm{ion}} = z_{\mathrm{ion}} q_e \Delta V_m - \theta \ln \frac{[\mathrm{ion}]_{\mathrm{ext}}}{[\mathrm{ion}]_{\mathrm{int}}}, \tag{9.38}$$

$$I^{V}_{\mathrm{rev},\Omega} \simeq \frac{C_{\mathrm{mem}} (\Delta V_m)^2}{2\theta}, \tag{9.39}$$

where $z_{\mathrm{ion}} \in \mathbb{Z}\setminus\{0\}$ is dimensionless ionic valence, $q_e \approx 1.602 \times 10^{-19}\,\mathrm{C}$ is elementary charge (in coulombs, C), $\Delta V_m := V_{\mathrm{int}} - V_{\mathrm{ext}}$ is intracellular-minus-extracellular transmembrane potential (in volts, V, with $1\,\mathrm{C}\cdot 1\,\mathrm{V} = 1\,\mathrm{J}$) across membrane capacitance C_{mem} (in farads, F, or $\mathrm{C\,V^{-1}}$), and $[\mathrm{ion}]_{\mathrm{ext}}$ versus $[\mathrm{ion}]_{\mathrm{int}}$ are extracellular and intracellular molar concentrations whose dimensionless ratio sets the chemical gradient (3.22) so that $\Delta\mu_{\mathrm{ion}}$ vanishes when ΔV_m equals the Nernst equilibrium potential. In the oscillatory geometry of Section 9.2.1, this pump power continuously maintains the barrier $\Delta\Phi \gg \theta$, enabling low-loss phase readouts such as hippocampal and neocortical theta–gamma multiplexing [25].

Keeping signalling within 15 W across $N_{\mathrm{brain}} \approx 8.6 \times 10^{10}$ whole-brain neurons ($N_{\mathrm{cortex}} \approx 1.6 \times 10^{10}$ in cerebral cortex [5]) relies on *subthreshold dendritic integration* and *sparse event-driven spiking*. Before axonal firing, thousands of excitatory and inhibitory inputs combine passively across the dendritic tree. Partitioning a neuron into its cell body S and dendritic tree $\bar{S}$ reduces the subthreshold cable equations to the boundary Schur commutator of Lemma 2.3 (2.171) and Section 5.3:

$$\mathbf{L}^{\mathrm{cell}}_{\mathrm{eff}} = \mathbf{L}_{SS} + [\![(\cdot)^{-1}, \mathscr{C}_S]\!](\mathbf{G}_\varepsilon) = \mathbf{L}_{SS} - \mathbf{L}_{S\bar{S}} \mathbf{L}^{-1}_{\bar{S}\bar{S}} \mathbf{L}_{\bar{S}S}, \tag{9.40}$$

where $\mathbf{L}^{\mathrm{cell}}_{\mathrm{eff}}$, cell-body conductance $\mathbf{L}_{SS}$, and dendritic cable Laplacian $\mathbf{L}_{\bar{S}\bar{S}}$ carry conductance units of siemens (S, or $\mathrm{A\,V^{-1}}$), modulated across $\bar{S}$ by shunting inhibition and *N*-methyl-D-aspartate (NMDA) receptors so the Schur term sums branch inputs prior to firing.

EXAMPLE 9.2 (Energy Budget of Cortical Spiking). Consider the cerebral cortex comprising $N_{\mathrm{cortex}} \approx 1.6 \times 10^{10}$ neurons [5] at $T_{\mathrm{th}} = 310\,\mathrm{K}$ under cortical signalling budget $P^{\mathrm{cort}}_{\mathrm{maint},\Omega} \approx 8\,\mathrm{W}$ [4, 101]. Restoring ion fluxes after one propagated cortical spike and its downstream synaptic release consumes $n_{\mathrm{ATP}} \sim 10^9$–$10^{10}$ ATP molecules at hydrolysis free energy $\Delta G_{\mathrm{ATP}} \approx 10^{-19}\,\mathrm{J}$,

or 23.4 nats, per molecule [4, 101]. The cortical signalling dissipation ceiling $\dot{I}_{\mathrm{irr},\Omega}^{\mathrm{cort,max}}$ and per-spike costs satisfy:

$$\dot{I}_{\mathrm{irr},\Omega}^{\mathrm{cort,max}} = \frac{P_{\mathrm{maint},\Omega}^{\mathrm{cort}}}{\theta} \approx 1.87 \times 10^{21}\ \mathrm{nats\ s^{-1}}, \tag{9.41}$$

$$E_{\mathrm{spike}} = n_{\mathrm{ATP}} \Delta G_{\mathrm{ATP}} \approx 10^{-10}\text{–}10^{-9}\ \mathrm{J}, \tag{9.42}$$

$$\frac{E_{\mathrm{spike}}}{\theta} \approx 2.34 \times 10^{10}\text{–}2.34 \times 10^{11}\ \mathrm{nats}. \tag{9.43}$$

Dividing across all N_{cortex} cortical neurons bounds the mean firing rate $\bar{r}_{\max}$ and sets the power $P_{100\,\mathrm{Hz}}$ required for simultaneous cortical firing at $r = 100\,\mathrm{Hz}$:

$$\bar{r}_{\max} = \frac{P_{\mathrm{maint},\Omega}^{\mathrm{cort}}}{N_{\mathrm{cortex}}\, E_{\mathrm{spike}}} \approx 0.50\text{–}5.0\,\mathrm{Hz}, \tag{9.44}$$

$$P_{100\,\mathrm{Hz}} = N_{\mathrm{cortex}} r E_{\mathrm{spike}} \approx 0.16\text{–}1.6\,\mathrm{kW}. \tag{9.45}$$

Simultaneous 100 Hz firing across cerebral cortex alone would exceed its 8 W signalling budget (and the entire 20 W whole-brain supply) by one to two orders of magnitude. ◊

Aggregating inputs subthreshold via (9.40) and spiking only when residuals cross basin margins restricts empirical mean cortical firing to $\bar{r} \sim 0.1\text{–}1\,\mathrm{Hz}$, with under 1% of cortical neurons concurrently active [101]. Unlike synchronous CMOS circuits that expend boundary dissipation $\dot{I}_{\mathrm{irr},\partial} > 0$ across idle clock gates, the cortex triggers irreversible boundary transitions selectively on informative prediction errors.

9.2.3 *Multiscale Memory and Synaptic Consolidation*

Extending the single-mode maintenance and release relations of (3.19)–(3.22) and (7.15), biological memory spans L_{tier} biophysical tiers with cascading relaxation timescales $\tau_{\mathrm{relax}}^{(1)} \ll \tau_{\mathrm{relax}}^{(2)} \ll \cdots \ll \tau_{\mathrm{relax}}^{(L_{\mathrm{tier}})}$ (in s). These tiers progress from membrane voltage transients at 10^{-3}–10^{-2} s and prefrontal limit cycles at 10^{-1}–10^{1} s to early long-term potentiation and depression at 10^{3}–10^{5} s and structural spine consolidation at 10^{7}–10^{8} s. Across the L_{tier} tiers, total preserved internal structure $I_{\mathrm{rev},\Omega}$ (in nats), internal maintenance dissipation rate $\dot{I}_{\mathrm{irr},\Omega}$ (in nats $\mathrm{s^{-1}}$), and maintenance power $P_{\mathrm{maint},\Omega}$ (in W) satisfy:

$$I_{\mathrm{rev},\Omega} = \sum_{\ell=1}^{L_{\mathrm{tier}}} I_{\mathrm{rev},\Omega}^{(\ell)}, \tag{9.46}$$

$$\dot{I}_{\mathrm{irr},\Omega} = \sum_{\ell=1}^{L_{\mathrm{tier}}} \frac{I_{\mathrm{rev},\Omega}^{(\ell)}}{\tau_{\mathrm{relax}}^{(\ell)}}, \tag{9.47}$$

$$P_{\mathrm{maint},\Omega} = \theta \sum_{\ell=1}^{L_{\mathrm{tier}}} \frac{I_{\mathrm{rev},\Omega}^{(\ell)}}{\tau_{\mathrm{relax}}^{(\ell)}}. \tag{9.48}$$

Equations (9.46)–(9.48) separate metabolic upkeep from structural occupancy under (3.16)–(3.19). Shifting electrochemical patterns from fast tier 1 at $\tau_{\text{relax}}^{(1)} \sim 10^{-2}$ s into dendritic spine morphology—actin cytoskeletons, postsynaptic scaffolds, and perineuronal nets with $\tau_{\text{relax}}^{(L_{\text{tier}})} \sim 10^{7}$–$10^{8}$ s and coarse-graining depth $I_{\alpha\alpha}$ of 10^{4}–10^{6} nats (2.92)—slashes ATP upkeep $P_{\text{maint},\Omega}$ while colocating slow synaptic weights directly within $\mathbf{K}_S$ alongside fast conductances without the separate memory-bus routing dissipation of conventional von Neumann accelerators (Chapter 7). Yet (9.46) shows that passive structural persistence alone cannot elevate consciousness κ_T. Just as Searle's paper rulebook in Section 9.1.4 requires near-zero metabolic power while inflating preserved internal structure and collapsing κ_{struct}, transferring traces uncompressed from fast to slow tiers leaves $I_{\text{rev},\Omega}$ unchanged. Raising κ_T requires *compressive consolidation* paired with *synaptic pruning*, whereby hippocampal–neocortical replay extracts shared generative invariants across Complementary Learning Systems [109] while global synaptic downscaling prunes redundant fast-tier potentiation under the Synaptic Homeostasis Hypothesis [159].

THEOREM 9.3 (Efficiency of Multiscale, Sparse Neural Networks). *Let a neural architecture maintain a through-time stability barrier* $\Delta I_{\text{barrier},T} > 0$ *(in* nats*) over emergent horizon* T (2.244)–(2.255) *across a fast electrochemical working tier* 1 *with relaxation timescale* $\tau_{\text{relax}}^{(1)} > 0$ *and a slow consolidated synaptic tier* 2 *with relaxation timescale* $\tau_{\text{relax}}^{(2)} > \tau_{\text{relax}}^{(1)}$*, carrying pre-consolidation horizon-averaged structure* $I_{\text{rev},\Omega,T}^{\text{pre}} = I_{\text{rev},\Omega,T}^{(1)} + I_{\text{rev},\Omega,T}^{(2)} > 0$.

1. *Maintenance Savings from Consolidation: Transferring preserved internal structure* $0 < \Delta I_{\text{cons}} \leq I_{\text{rev},\Omega}^{(1)}$ *from the fast electrochemical tier into the slow synaptic tier strictly reduces the required internal maintenance dissipation rate:*

$$\frac{I_{\text{rev},\Omega}^{(1)} - \Delta I_{\text{cons}}}{\tau_{\text{relax}}^{(1)}} + \frac{I_{\text{rev},\Omega}^{(2)} + \Delta I_{\text{cons}}}{\tau_{\text{relax}}^{(2)}} < \frac{I_{\text{rev},\Omega}^{(1)}}{\tau_{\text{relax}}^{(1)}} + \frac{I_{\text{rev},\Omega}^{(2)}}{\tau_{\text{relax}}^{(2)}}. \tag{9.49}$$

2. *Consciousness Gain from Compressive Consolidation: Whereas uncompressed transfer preserves* $I_{\text{rev},\Omega,T}$ *and leaves* κ_T *unchanged, encoding shared invariants into tier* 2 *while pruning a strictly larger fast-tier stock from tier* 1 *at maintained barrier* $\Delta I_{\text{barrier},T} > 0$ *strictly increases the consciousness metric:*

$$0 \leq \Delta I_{\text{slow,added}} < \Delta I_{\text{fast,pruned}} \leq I_{\text{rev},\Omega,T}^{(1)}, \tag{9.50}$$

$$I_{\text{rev},\Omega,T}^{\text{post}} = I_{\text{rev},\Omega,T}^{\text{pre}} - (\Delta I_{\text{fast,pruned}} - \Delta I_{\text{slow,added}}) > 0, \tag{9.51}$$

$$\kappa_T^{\text{pre}} = \frac{\Delta I_{\text{barrier},T}}{I_{\text{rev},\Omega,T}^{\text{pre}}} < \frac{\Delta I_{\text{barrier},T}}{I_{\text{rev},\Omega,T}^{\text{post}}} = \kappa_T^{\text{post}}. \tag{9.52}$$

3. *Intelligence Gain from Sparse Spiking: If subthreshold dendritic integration and oscillatory phase transport eliminate redundant clock and*

baseline spiking dissipation $\Delta I_{\mathrm{irr}}^{\mathrm{saved}} > 0$*, leaving positive sparse dissipation* $I_{\mathrm{irr},\partial,T}^{\mathrm{sparse}} > 0$ *with* $I_{\mathrm{irr},\partial,T}^{\mathrm{sparse}} = I_{\mathrm{irr},\partial,T}^{\mathrm{clock}} - \Delta I_{\mathrm{irr}}^{\mathrm{saved}}$*, the intelligence metric strictly increases:*

$$\chi_T^{\mathrm{clock}} = \frac{\Delta I_{\mathrm{barrier},T}}{I_{\mathrm{irr},\partial,T}^{\mathrm{clock}}} < \frac{\Delta I_{\mathrm{barrier},T}}{I_{\mathrm{irr},\partial,T}^{\mathrm{sparse}}} = \chi_T^{\mathrm{sparse}}. \tag{9.53}$$

PROOF. In Claim 1, transferring $\Delta I_{\mathrm{cons}} > 0$ across $0 < \tau_{\mathrm{relax}}^{(1)} < \tau_{\mathrm{relax}}^{(2)}$ replaces decay at rate $(\tau_{\mathrm{relax}}^{(1)})^{-1}$ by strictly slower decay at rate $(\tau_{\mathrm{relax}}^{(2)})^{-1} < (\tau_{\mathrm{relax}}^{(1)})^{-1}$, establishing (9.49). In Claim 2, adding $\Delta I_{\mathrm{slow,added}}$ to tier 2 while pruning $\Delta I_{\mathrm{fast,pruned}}$ from tier 1 under two-tier additivity (9.46) yields (9.51). When $\Delta I_{\mathrm{slow,added}} = \Delta I_{\mathrm{fast,pruned}}$, $I_{\mathrm{rev},\Omega,T}^{\mathrm{post}} = I_{\mathrm{rev},\Omega,T}^{\mathrm{pre}}$ and κ_T is invariant. Under (9.50), the compression savings $\Delta I_{\mathrm{fast,pruned}} - \Delta I_{\mathrm{slow,added}}$ are strictly positive, so $0 < I_{\mathrm{rev},\Omega,T}^{\mathrm{post}} < I_{\mathrm{rev},\Omega,T}^{\mathrm{pre}}$ and dividing $\Delta I_{\mathrm{barrier},T} > 0$ yields (9.52). Claim 3 follows identically at fixed $\Delta I_{\mathrm{barrier},T} > 0$ since $0 < I_{\mathrm{irr},\partial,T}^{\mathrm{sparse}} < I_{\mathrm{irr},\partial,T}^{\mathrm{clock}}$. □

Theorem 9.3 yields testable predictions across wakefulness, sleep consolidation, and general anaesthesia. During wakeful engagement, active sensorimotor alignment across $\mathbf{K}_{\partial}^{(\mathrm{ext})}$ sustains elevated (χ_T, κ_T) while net synaptic potentiation accumulates fast episodic traces $I_{\mathrm{rev},\Omega}^{(1)}$ that progressively raise maintenance load $\dot{I}_{\mathrm{irr},\Omega}$ and consume free capacity $\mathcal{Q}_{\mathrm{free}}$ [159]. Slow-wave sleep decouples external sensorimotor ports and executes Claim 1 and Claim 2 offline, replaying recurring invariants $\Delta I_{\mathrm{slow,added}}$ into neocortical spines while globally downscaling and pruning redundant fast-tier potentiation $\Delta I_{\mathrm{fast,pruned}} > \Delta I_{\mathrm{slow,added}}$ [109, 159] to lower waking maintenance demand and restore κ_T for subsequent epochs. Conversely, general anaesthetics enhance inhibitory conductance and disrupt long-range phase coupling $\tilde{K}_{\alpha\beta}$ in (9.34), fragmenting cortical blocks into subcritical local basins that suppress inter-regional transition capacity and collapse active (χ_T, κ_T) despite continued basal metabolic upkeep.

9.2.4 *Criticality, Sensory Efficiency, and Active Inference*

A second collective principle of cerebral dynamics is near-criticality. Cortical networks operate near a non-equilibrium phase transition between quiescence and runaway excitation, marked by neuronal avalanches of size s obeying $P(s) \sim s^{-3/2}$ at branching ratio $\sigma_{\mathrm{branch}} \approx 1$ [10, 29]. Critical tuning amplifies faint inputs so localised sensory signals can trigger coordinated reconfigurations without dedicated pre-wired channels.

In CCE terms, criticality shapes the basin landscape shown in Figure 9.1(b). Below criticality at $\sigma_{\mathrm{branch}} < 1$, deep attractors lock internal load towards $\mathcal{Q}_\Omega \to \mathcal{Q}_{\mathrm{total}}$, exhausting free capacity $\mathcal{Q}_{\mathrm{free}}$ (2.196)–(2.200) and demanding large boundary dissipation $\dot{I}_{\mathrm{irr},\partial}$ to update stored states. Above criticality at $\sigma_{\mathrm{branch}} > 1$, runaway excitation drives $\Xi \to 1$, collapsing the stability barrier $\Delta I_{\mathrm{barrier},T}$, preserved structure $I_{\mathrm{rev},\Omega}$, and intelligence χ_T.

Near $\sigma_{\text{branch}} \approx 1$, flat, marginally stable manifolds distribute $\mathcal{C}_\Omega$ across multiple shallow basins, jointly sustaining $\mathcal{C}_{\text{free}} > 0$ and low internal dissipation $\mathbb{M}_\Omega$ within $\mathcal{C}_{\text{total}}$. For integration rate $\dot{I}_{\text{acq}}(t)$ (in nats s^{-1}) of newly acquired environmental distinctions into coarse-grained CCEs and boundary dissipation rate $\dot{I}_{\text{irr},\partial}(t)$ (in nats s^{-1}), this responsiveness is quantified by the dimensionless *sensory capture efficiency*:

$$\Lambda(t) = \frac{\dot{I}_{\text{acq}}(t)}{\dot{I}_{\text{irr},\partial}(t)}. \tag{9.54}$$

Measuring nats of environmental structure captured per nat of boundary dissipation, $\Lambda(t)$ peaks alongside $\mathcal{C}_{\text{free}}$ near criticality, allowing sensory inputs to steer coarse-grained trajectories with minimal Landauer erasure.

This near-critical geometry underpins predictive coding and active inference [60, 61, 139]. Formulated information-theoretically [128], an agent persists by minimising the variational free energy functional $F[q, o]$ (in nats):

$$F[q,o] = \mathbb{E}_{q(z_{\text{lat}})}[\ln q(z_{\text{lat}}) - \ln p(o, z_{\text{lat}})] = D_{\text{KL}}(q(z_{\text{lat}}) \parallel p(z_{\text{lat}} \mid o)) - \ln p(o), \tag{9.55}$$

where $q(z_{\text{lat}})$ is the approximate posterior over hidden states z_{lat}, $p(o, z_{\text{lat}})$ is the generative model, and o is the sensory observation crossing $\mathbf{K}_\partial^{(\text{ext})}$. Minimising $F[q, o]$ bounds sensory surprise $-\ln p(o)$ and keeps trajectories within the viability domain $\mathcal{D}$ across $\Delta I_{\text{barrier},T}$.

On the extended state manifold $Z \in \mathcal{Z}$ joining coarse-grained cortical neural coordinates and conjugate phase momenta with the coupled ATP and thermal reservoir coordinates of Chapter 3 (3.8), active inference realises the closed sensorimotor loop of Section 9.1.2 (9.4)–(9.8). Superficial and deep pyramidal layers segregate top-down world and self-action rollouts generated by the extended generative Hamiltonian $H_{\text{model}}(Z)$ (in J)—often carried by feedback beta rhythms—from bottom-up sensory residual relaxation driven by the physical entropy functional $S_{\text{error}}(Z)$ (in nats) across feedforward gamma bursts [59, 139]:

$$\dot{Z} = \mathbb{J}(Z)\nabla H_{\text{model}}(Z) + \mathbb{M}(Z)\nabla S_{\text{error}}(Z), \tag{9.56}$$

where the neural state gradient of $S_{\text{error}}(Z)$ tracks the negative variational free-energy gradient $-\nabla F[q, o]$ across $\mathbb{M}(Z) = \mathbb{M}_\Omega(Z) + \mathbb{M}_\partial(Z) \succeq 0$. Admissibility of (9.56) requires the Morrison Casimir degeneracy conditions and non-negative entropy production [114]:

$$\mathbb{J}(Z)\nabla S_{\text{error}}(Z) = \mathbf{o}, \tag{9.57}$$

$$\mathbb{M}(Z)\nabla H_{\text{model}}(Z) = \mathbf{o}, \tag{9.58}$$

$$\dot{S}_{\text{error}}(Z) = \nabla S_{\text{error}}(Z) \cdot \mathbb{M}(Z)\nabla S_{\text{error}}(Z) \geq 0. \tag{9.59}$$

Condition (9.57), equivalent to $\{S_{\text{error}}, A\} = 0$ for every observable A, ensures that reversible top-down rollouts along $\mathbb{J}(Z)\nabla H_{\text{model}}(Z)$ transport candidate predictions at zero entropy production. Condition (9.58), equivalent to

$(H_{\text{model}}, A) = 0$, conserves total extended energy $H_{\text{model}}(Z)$ during dissipative error correction, while projecting onto the open cortical coordinates balances neural energy drift against ATP hydrolysis $P_{\text{maint},\Omega}$ and sensory port work across $\mathbf{K}_{\partial}^{(\text{ext})}$. Relation (9.59) enforces the Second Law, confining positive entropy production strictly to unpredicted sensory residuals resolved across $\mathbb{M}(Z) \succeq 0$.

Attention and learning tune this geometry across distinct timescales. Attention selectively deepens basin barriers $\Delta\Phi_\alpha$ to prioritise readout, whereas learning reshapes $\mathbf{K}_S$ to resolve recurrent challenges at lower boundary dissipation $I_{\text{irr},\partial,T}$. Under the agency identity (3.32), active inference raises intelligence χ_T by cancelling predictable fluxes before they generate $I_{\text{irr},\partial,T}$, while compressive consolidation raises consciousness κ_T by pruning redundant potentiation into minimal maintained structure $I_{\text{rev},\Omega,T}$.

Together, oscillatory phase transport, dendritic integration, multiscale consolidation, and near-critical active inference show how the human brain sustains high χ_T and κ_T within 20 W. Yet every individual brain remains bounded by finite capacity $\mathcal{Q}_{\text{total}}$, a fixed metabolic supply, and the self-incompleteness established in Theorem 9.1. Scaling intelligence beyond a single organism requires multi-agent specialisation and boundary exchange. Chapter 10 extends χ_T and κ_T to networks of interacting conscious and synthetic agents.

10

INTELLIGENT ECONOMIES

An economy is an intelligent system. Because the physical metrics developed in Chapters 2 and 3 depend only on how a system maintains stability within finite capacity, they apply across scales—from individual circuits and biological organisms to firms, markets, and entire civilisations. Studying economics under this framework allows us to define macroeconomic indicators that directly reflect our measures of intelligence and consciousness. At the scale of a whole economy, intelligence measures how much stability is secured per nat of irreversible dissipation lost to the environment, while consciousness measures that same stability per nat of internal structure maintained—such as infrastructure, institutions, rules, and shared knowledge.

Standard economic metrics miss both qualities. As Kuznets warned in designing national income accounts [93], and as later critiques of Gross Domestic Product (GDP) have shown [121], GDP simply sums the money spent in market transactions. Because it measures total spending rather than lasting value, GDP leaves out unpaid work and freely shared knowledge, ignores resource depletion and environmental damage, and counts costly setbacks such as rebuilding after preventable disasters, replacing short-lived goods, or navigating bureaucracy as economic growth. Framing an economy around intelligence and consciousness corrects these blind spots. An intelligence measure penalises waste and repeated repair instead of counting them as output, while a consciousness measure penalises bloated rules and redundant infrastructure, rewarding durable goods, open standards, and compact shared models even when total spending falls. More broadly, studying the stability of intelligent systems gives economists a general mathematical framework to test whether an economy can endure. It reveals where weak links create fragility across a trade network, shows when growing complexity leaves too little spare capacity to absorb shocks, and identifies when trade makes a system more resilient rather than more vulnerable.

Measuring these quantities across a trading economy is difficult for four reasons. People trade diverse goods with no obvious common physical unit, and one party bears the cost of making a product while another receives its benefit later. Moreover, the quality of complex work is often hard to verify at the moment of sale, and no single observer can track every detail of an economy at once. Money, and eventually fiat currency, emerged to bridge these gaps [84, 110]. Under barter, trade stalls unless each side happens to hold what the other wants. Fiat currency—money valued by shared convention rather than a conserved quantity—solves this problem by providing a portable unit of account that summarises dispersed local judgements in single prices [77]. Because fiat prices have no built-in tie to production dissipation or verified outcomes, however, markets easily drift into charging for raw

activity—such as repeated product replacements, unhealthy consumption, or unverified iterations—while leaving downstream harm unpriced and exposing trade networks to currency dilution and exchange-rate friction. Grounding economics in Conservation-Congruent Encoding (CCE) resolves this disconnect without requiring fiat currency. Because production cost C and expected stability gain V share a universal informational unit, goods can be priced directly by their expected contribution to system stability adjusted for closed-boundary production cost.

Building on the multi-system framework of Section 3.5, this chapter makes four contributions. First, Section 10.1 establishes the substrate-agnostic foundations of production, exchange, and Physical Nash pricing in natural informational units, deriving the linear cost–value rule $P = C + \sigma\,[\Delta V_{\text{net}}]_+$, contrasting it against activity-volume and cost-ratio pricing, and proving competitive market stability (Theorem 10.1). Second, Section 10.2 aggregates (C, V, P) across the economy to show why Gross Domestic Product (Y_{GDP}) mistakes cost for value, defining the Humanity Intelligence Index (HII) and Humanity Consciousness Index (HCI) alongside a surplus-backed baseline stability allocation as automation lowers labour inputs. Third, Section 10.3 formalises inter-system trade coupling ($\mathbf{K}_{ij}$) from observable boundary values—establishing polluter-pays attribution, comparative advantage, dual boundary-value coupling parameters $\eta_{\text{cpl}}^{(V)}$ and $\eta_{\text{cpl}}^{(C)}$, the parameter-free network stability functional $I_{\text{net}}(\mathbf{K})$ with weakest-link Nash routing, non-inflationary formation credit ceilings, and rate-asymmetry guardrails for high-speed synthetic subsystems. Fourth, Section 10.4 extends this coupling architecture beyond a single planet, showing why light-speed delays and single-sink risks favour loosely connected autonomous basins over one centralised economy, and why enduring civilisations become quiet and low-dissipation—offering an economic explanation for the Fermi paradox.

10.1 COST, VALUE, AND PRICE

Classical bargaining models measure gains relative to hypothetical autarkic isolation ($\mathbf{K}_{Hm} = \mathbf{o}$). In an interconnected economy, however, complete isolation is unobservable. Removing unobservable autarkic counterfactuals makes microeconomic pricing, macroeconomic indices, and network trade coupling empirically auditable: every variable is measured directly from current within-horizon quantities in the natural informational units (nats, at reference scale $\mathcal{Q}_0 = 1$ link) of Section 3.3.1, (3.23)–(3.24) and (3.29)–(3.44).

10.1.1 *Production Cost and Value*

Over an emergent evaluation horizon T metered against a shared stationary reference sub-block $\bar{S}_{\text{ref}} \subset \bar{S}$ (Section 2.5.1, (2.247)–(2.255)), consider a good or service supplied by a producer subsystem S_m ($m \in \{1, \dots, M\}$) to a host population or buyer S_H. Anchored in the operational horizon cost $I_{\text{op},T}$ of

Section 3.3 (3.43), the closed-boundary *cost of production* C (written C_m when indexing multiple options) sums two extensive informational quantities in nats:

$$C := I_{\mathrm{op},T} = I_{\mathrm{irr},\partial,T} + I_{\mathrm{rev},\Omega,T}. \tag{10.1}$$

Here $I_{\mathrm{irr},\partial,T}$ tallies closed-boundary irreversible dissipation across the active boundary cut, including under closed multi-system accounting (3.117) any downstream cross-boundary dissipation $I_{\mathrm{cross},Hm}$ imposed on the host population S_H through consumption harm, verification friction, or environmental remediation. Simultaneously, $I_{\mathrm{rev},\Omega,T}$ records horizon-averaged maintained internal structure—capital, tooling, institutional rules, or active model parameters—committed to supply the good. Because integrating $\dot{I}_{\mathrm{irr},\partial}(t)$ over t in $I_{\mathrm{irr},\partial,T}$ and averaging $I_{\mathrm{rev},\Omega}(\tau)$ over proper time τ_T in $I_{\mathrm{rev},\Omega,T}$ (which coincides with coordinate-time averaging across co-moving sectors) cancel the clock unit, both quantities share identical, clock-invariant units of nats regardless of $\bar{S}_{\mathrm{ref}}$. Summing them directly without hardware relaxation constants prices passive structural occupancy ($\mathcal{Q}_\Omega$) within the finite Frobenius budget $\mathcal{Q}_{\mathrm{alloc}} \le \mathcal{Q}_{\mathrm{total}}$ (2.196), penalising capital and administrative lock-up that crowds out uncommitted free capacity $\mathcal{Q}_{\mathrm{free}}$ even when physical decay is slow.

On the numerator side, the *value gain* V (nats) is measured empirically across the host population S_H for whom outcome data are observed as the expected stability barrier gain delivered over horizon T:

$$V := \mathbb{E}[\Delta I_{\mathrm{barrier},T}]. \tag{10.2}$$

Whenever $V > 0$, the good's dimensionless through-time intelligence χ_T and consciousness κ_T (nats/nat) follow directly from (3.29)–(3.30):

$$\chi_T = \frac{V}{I_{\mathrm{irr},\partial,T}}, \tag{10.3}$$

$$\kappa_T = \frac{V}{I_{\mathrm{rev},\Omega,T}}. \tag{10.4}$$

Substituting (10.3)–(10.4) into (10.1) expresses the cost-to-value ratio and *net stability gain* ΔV_{net} (nats) without thermal or hardware constants:

$$\frac{C}{V} = \frac{1}{\chi_T} + \frac{1}{\kappa_T}, \tag{10.5}$$

$$\Delta V_{\mathrm{net}} := V - C = V\left(1 - \frac{1}{\chi_T} - \frac{1}{\kappa_T}\right). \tag{10.6}$$

By Section 3.5.3, goods with $\Delta V_{\mathrm{net}} > 0$ satisfy $\chi_T^{-1} + \kappa_T^{-1} < 1$ and act as *generative dissipators* (Definition 3.10) that expand host free capacity, whereas goods with $\Delta V_{\mathrm{net}} \le 0$ fail to clear their closed-boundary cost—acting when $V \le 0$ as *exhaustive dissipators* (Definition 3.9) that erode it.

10.1.2 *Physical Nash Pricing*

In specialised production, producer S_m expends $C > 0$ while buyer S_H realises $V > 0$. Without a transferable payment P (nats), the producer incurs a

net physical loss $-C < 0$ and specialised trade fails (Theorem 3.8). Under a payment $P \in [C, V]$, the producer captures net return $P-C$ and the buyer captures expected net stability gain $V - P$, conserving net stability gain across the transaction:

$$(P - C) + (V - P) = V - C = \Delta V_{\text{net}}. \tag{10.7}$$

Across solvent trades ($V \geq C$), maximising the asymmetric Physical Nash product [117] over $P \in [C, V]$ with bargaining weights $\alpha_H > 0$ and $\alpha_m > 0$,

$$\mathcal{J}_{\text{price}}(P) = (V - P)^{\alpha_H}(P - C)^{\alpha_m}, \tag{10.8}$$

and setting $P = C$ whenever $V < C$ (with $[x]_+ := \max\{x, 0\}$) yields the linear cost–value pricing rule across $V \geq C$:

$$P = C + \sigma\,[\Delta V_{\text{net}}]_+ = (1 - \sigma)C + \sigma V, \tag{10.9}$$

$$\sigma := \frac{\alpha_m}{\alpha_H + \alpha_m} \in (0, 1). \tag{10.10}$$

Subtracting C from P and P from V across $V \geq C$ partitions ΔV_{net} into producer net return and buyer net stability gain:

$$P - C = \sigma\,[\Delta V_{\text{net}}]_+, \tag{10.11}$$

$$V - P = (1 - \sigma)\,\Delta V_{\text{net}}. \tag{10.12}$$

This linear rule avoids the structural failures of both activity-volume billing and cost-ratio pricing. First, when contracts bill intermediate activity volume N_{act}—such as replacement cycles, billable hours, or unverified iterations—at per-step fee p_{act} above per-step cost $c_{\text{act}} > 0$, private return decouples from V:

$$R_{\text{act}} = (p_{\text{act}} - c_{\text{act}})\,N_{\text{act}}, \tag{10.13}$$

rewarding tenfold replacement churn while cutting revenue by 90% on durable CCE encodings that resolve the same constraint in one-tenth the activity. Second, pricing by dividing by production cost (V/C or V^2/C) fails three physical requirements. Because $V/C = (\chi_T^{-1} + \kappa_T^{-1})^{-1}$ is dimensionless and homogeneous of degree 0, two loaves of bread yield $(2V)/(2C) = V/C$, violating batch additivity (which requires homogeneity of degree 1 so doubling (C, V) doubles P). Restoring degree-1 scaling via $P_{\text{rat}} = V^2/C$, or equivalently $V(V/C)$, forces $P_{\text{rat}} > V$ on every generative good ($V > C$), inflicting a net stability loss $V - P_{\text{rat}} < 0$ on every purchase while sending $P_{\text{rat}} \to \infty$ as marginal replication cost $C \to 0$ on compressed CCE goods such as software, protocols, and scientific formulas $\mathbf{K}_{\text{seed}}$. Moreover, under V/C or V^2/C we have $\partial P/\partial C < 0$, so cutting production cost C in half at fixed V doubles the shelf price. Under the linear rule (10.9) across $V \geq C > 0$, by contrast, the ratio V/C (nats/nat) governs producer return per nat of cost expended and buyer value per nat of price paid:

$$\frac{P - C}{C} = \sigma\left(\frac{V}{C} - 1\right), \tag{10.14}$$

$$\frac{V}{P} = \frac{1}{\sigma + (1 - \sigma)(C/V)}. \tag{10.15}$$

Producers allocating scarce capacity C therefore maximise V/C, while the shelf price P remains batch-additive, finite as $C \to 0$ ($P \to \sigma V$), bounded inside $[C, V]$, and cheaper for buyers whenever C falls ($\partial P/\partial C = 1 - \sigma > 0$).

10.1.3 *Competitive Market Stability*

Fixing $\sigma \in (0, 1)$ exogenously via a central allocator introduces an uncalibrated parameter that expands maintained administrative structure $I_{\text{rev},\Omega,T}$ (lowering HCI). Whenever a parameter-free benchmark rule is required, symmetric bargaining weights ($\alpha_H = \alpha_m$) fix $\sigma = 1/2$, setting $P = (C + V)/2$ and splitting ΔV_{net} equally. In dynamic markets [118], the interval $[C, V]$ defines the solvent exchange corridor and $\sigma = (P - C)/(V - C) \in [0, 1]$ acts as the endogenous margin determined by competition. At the lower boundary $\sigma \geq 0$ ($P \geq C$), every solvent trade covers its closed-boundary cost C, excluding below-cost deficits and exhaustive goods ($V \leq C$). At the upper boundary $\sigma \leq 1$ ($P \leq V$), prices remain bounded by expected stability value V, preventing net buyer reserve erosion ($V - P < 0$) on foundational goods. Furthermore, because household barrier depth scales logarithmically with uncommitted reserve ($\Delta I_{\text{barrier},H} = \ln(\mathcal{Q}_{\text{free},H}/\mathcal{Q}_0)$), diverging marginal reserve utility as $\mathcal{Q}_{\text{free},H} \to \mathcal{Q}_0^+$ pulls reserve-space Nash prices towards C on necessities whenever $\alpha_H > 0$. Across the interior $(0, 1)$, when a creator introduces a novel high-(χ_T, κ_T) breakthrough with upfront formation expenditure $I_{\text{form}} > 0$ (3.94), initial scarcity of rivals places σ nearer 1, allowing rapid recovery of discovery overhead over $T > T_{\text{amort}}$ even when marginal replication cost $C \to 0$. As rivals enter and replicate the encoding, Bertrand–Nash price competition drives $\sigma \to 0$ ($P \to C$), transferring ΔV_{net} to households and lowering the cost of the foundational basket automatically.

THEOREM 10.1 (Physical Nash Pricing and Competitive Market Stability). *Consider options $m \in \{1, \ldots, M\}$ with closed-boundary production cost $C_m > 0$ (10.1), expected value gain V_m (10.2), and net stability gain $\Delta V_{\text{net},m} = V_m - C_m$ (10.6). Under Physical Nash pricing (10.9)–(10.10) with bargaining weights $\alpha_H > 0$ and $\alpha_m > 0$ and share $\sigma = \alpha_m/(\alpha_H + \alpha_m) \in (0, 1)$:*

1. *Nash optimality, mutual stability gain, and batch additivity: Whenever $V_m > C_m > 0$, price $P_m = C_m + \sigma(V_m - C_m)$ uniquely maximises $\mathcal{J}_{\text{price}}(P)$ (10.8) on $[C_m, V_m]$, satisfies $C_m < P_m < V_m$ with $P_m - C_m > 0, V_m - P_m > 0$, and buyer yield $V_m/P_m > 1$ (10.15), and is homogeneous of degree 1 for all $\lambda > 0$:*

$$P_m(\lambda C_m, \lambda V_m) = \lambda P_m(C_m, V_m). \tag{10.16}$$

2. *Exhaustive dissipator and sub-cost exclusion: Any option with $V_m \leq C_m$ (including any exhaustive dissipator with $V_m \leq 0 < C_m$) generates $\Delta V_{\text{net},m} \leq 0$, earns zero producer net return ($P_m - C_m = 0$) at the cost floor $P_m = C_m$, and yields $V_m - P_m \leq 0$.*

3. *Efficiency monotonicity and Bertrand–Nash dominance: For matched value $V > 0$, if $\chi_{m_1,T} \geq \chi_{m_2,T}$ and $\kappa_{m_1,T} \geq \kappa_{m_2,T}$ with at least one inequality strict, then $C_1 < C_2$, $\Delta V_{\text{net},1} > \Delta V_{\text{net},2}$, and $V/P_1 > V/P_2$ at any shared $\sigma \in (0,1)$. Option m_1 can also price at m_2's cost floor $P = C_2$ while earning positive net return $C_2 - C_1 > 0$.*

PROOF. For Part 1, on (C_m, V_m) the objective $\ln \mathcal{J}_{\text{price}}(P) = \alpha_H \ln(V_m - P) + \alpha_m \ln(P - C_m)$ is strictly concave (with negative second derivative $-\alpha_H(V_m - P)^{-2} - \alpha_m(P - C_m)^{-2}$) and vanishes at the endpoints of $[C_m, V_m]$, so its unique global maximiser solves $\alpha_m/(P_m - C_m) = \alpha_H/(V_m - P_m)$, yielding $P_m = C_m + \sigma\Delta V_{\text{net},m}$. Because $0 < \sigma < 1$ and $\Delta V_{\text{net},m} > 0$, (10.11)–(10.12) give $P_m - C_m > 0$, $V_m - P_m > 0$, $C_m < P_m < V_m$, and $V_m/P_m > 1$, while $[\lambda V_m - \lambda C_m]_+ = \lambda\,[\Delta V_{\text{net},m}]_+$ gives (10.16). For Part 2, $V_m \leq C_m$ implies $[\Delta V_{\text{net},m}]_+ = 0$, fixing $P_m = C_m$, $P_m - C_m = 0$, and $V_m - P_m \leq 0$ (since $V_m - P_m = \Delta V_{\text{net},m}$), whereas pricing below C_m incurs a sustained deficit $P_m - C_m < 0$ (Theorem 8.10). For Part 3, substituting (10.5) at matched $V > 0$ gives

$$\begin{aligned} C_1 &= V\left(\frac{1}{\chi_{m_1,T}} + \frac{1}{\kappa_{m_1,T}}\right) \\ &< V\left(\frac{1}{\chi_{m_2,T}} + \frac{1}{\kappa_{m_2,T}}\right) = C_2. \end{aligned} \tag{10.17}$$

Subtracting $C_1 < C_2$ from V orders net stability gains and matched-σ prices ($P_i = (1-\sigma)C_i + \sigma V$ for $V \geq C_2$, or $P_2 = C_2$ exceeding P_1 when $C_1 \leq V < C_2$):

$$\Delta V_{\text{net},1} = V - C_1 > V - C_2 = \Delta V_{\text{net},2}, \tag{10.18}$$

$$\frac{V}{P_1} > \frac{V}{P_2}, \tag{10.19}$$

and setting $P = C_2$ matches m_2's lowest solvent offer while earning $C_2 - C_1 > 0$. □

Table 10.1 illustrates Theorem 10.1 across four substrate-general producers S_1–S_4—representing competing industrial fabricators, logistics networks, or metered compute facilities [79, 164]—evaluated against a target task of verified value $V = 240$ Mnat where each intermediate activity step expends 1 Mnat of boundary dissipation. Producer S_1 (compressed CCE) resolves the task in $N_{\text{act},1} = 6$ steps with $I_{\text{irr},\partial,T} = 6$ Mnat, $I_{\text{rev},\Omega,T} = 6$ Mnat, and $C_1 = 12$ Mnat, achieving $\chi_{1,T} = 40.0$, $\kappa_{1,T} = 40.0$, and $C_1/V_1 = 0.050$. Producer S_2 (high-dissipation churn) passes verification using $N_{\text{act},2} = 150$ steps at $C_2 = 156$ Mnat and $\chi_{2,T} = 1.6$. Producer S_3 (bloated monolith) uses 6 steps but holds $I_{\text{rev},\Omega,3,T} = 96$ Mnat of uncompressed structure, giving $C_3 = 102$ Mnat and $\kappa_{3,T} = 2.5$, while S_4 (unverified output) expends 150 steps and fails verification with $V_4 = 0$. Activity-volume billing at $p_{\text{act}} = 3$ Mnat per step ($R_{\text{act},m} = p_{\text{act}} N_{\text{act},m} - C_m$) rewards S_2 and S_4 with +294 Mnat—49 times S_1's +6 Mnat—while inflicting an 84 Mnat loss on S_3. Under symmetric Physical Nash pricing ($\sigma = 0.5$), S_4 earns zero net return and S_1 maximises $P_1 - C_1 = +114$ Mnat at $P_1 = 126$ Mnat. Under Bertrand–Nash rivalry, S_1 can undercut every competitor down to S_3's cost floor $C_3 = 102$ Mnat by setting $P = 102$ Mnat, retaining $C_3 - C_1 = +90$ Mnat ($\sigma_1 \approx 0.39$, converging towards 0 as rivals replicate S_1).

Producer architecture	$I_{\mathrm{irr},\partial,T}$ (Mnat)	$I_{\mathrm{rev},\Omega,T}$ (Mnat)	C_m (Mnat)	$\chi_{m,T}$ (nats/nat)	$\kappa_{m,T}$	$\Delta V_{\mathrm{net},m}$ (Mnat)	$R_{\mathrm{act},m}$ (Mnat)	$P_m - C_m$ (Mnat)
S_1: compressed CCE	6	6	12	40.0	40.0	+228	+6	+114
S_2: high-churn output	150	6	156	1.6	40.0	+84	+294	+42
S_3: bloated monolith	6	96	102	40.0	2.5	+138	−84	+69
S_4: unverified output	150	6	156	0.0	0.0	−156	+294	0

TABLE 10.1: Closed-boundary cost audit and net-return comparison across four competing producers (1 Mnat boundary dissipation per activity step, verified capability value $V = 240$ Mnat, $N_{\mathrm{act},m} \in \{6, 150, 6, 150\}$). Producers S_1–S_3 deliver $V_m = 240$ Mnat, whereas S_4 delivers $V_4 = 0$. Activity-volume billing ($p_{\mathrm{act}} = 3$ Mnat per step) rewards high-churn and unverified output (S_2 and S_4), whereas Physical Nash pricing ($\sigma = 0.5$, $P_m \in \{126, 198, 171, 156\}$ Mnat) prices out S_4 and concentrates return on S_1, which retains a +90 Mnat margin at its nearest rival S_3's 102 Mnat cost floor.

EXAMPLE 10.1 (Foundational Nutrition and Practical CCE Cohort Auditing). Consider two daily dietary options $m \in \{1, 2\}$ across an adult host cohort S_H over a multi-year physiological horizon T at competitive staple margin $\sigma = 0.25$. Option $m = 1$ (minimally processed whole food rich in micronutrients and fibre) incurs upstream agricultural and cold-chain dissipation $I^{\mathrm{up}}_{\mathrm{irr},\partial,1} = 1.2$ nats, low downstream physiological cross-dissipation $I_{\mathrm{cross},H1} = 0.2$ nats ($I_{\mathrm{irr},\partial,1,T} = 1.4$ nats), and supply-chain structure $I_{\mathrm{rev},\Omega,1,T} = 0.6$ nats, delivering expected stability gain $V_1 = 6.0$ nats. Option $m = 2$ (an ultra-processed formulation engineered for rapid glycaemic load and repeat purchase) lowers factory-gate expenditure ($I^{\mathrm{up}}_{\mathrm{irr},\partial,2} = 0.5$ nats and $I_{\mathrm{rev},\Omega,2,T} = 0.3$ nats, for an apparent cost of 0.8 nats), but injects downstream metabolic cross-dissipation $I_{\mathrm{cross},H2} = 3.6$ nats into S_H ($I_{\mathrm{irr},\partial,2,T} = 4.1$ nats), reducing expected value gain to $V_2 = 0.4$ nats.

Evaluating (10.1), (10.6), and (10.9) for nourishing food ($m = 1$) gives:

$$C_1 = 1.4 + 0.6 = 2.0 \text{ nats}, \tag{10.20}$$

$$\Delta V_{\mathrm{net},1} = 6.0 - 2.0 = +4.0 \text{ nats}, \tag{10.21}$$

$$P_1 = 2.0 + 0.25(4.0) = 3.0 \text{ nats}. \tag{10.22}$$

Internalising $I_{\mathrm{cross},H2}$ inside C_2 for ultra-processed food ($m = 2$) reverses the truncated factory-gate shelf ordering, setting $P_1 = 3.0$ nats below $P_2 = 4.4$ nats:

$$C_2 = (0.5 + 3.6) + 0.3 = 4.4 \text{ nats}, \tag{10.23}$$

$$\Delta V_{\mathrm{net},2} = 0.4 - 4.4 = -4.0 \text{ nats}, \tag{10.24}$$

$$P_2 = 4.4 + 0.25\,[-4.0]_+ = 4.4 \text{ nats}. \tag{10.25}$$

By the coarse-graining framework of Chapter 2, auditing (C, V) in practice requires neither tracking individual consumption events nor running separate multi-year trials per barcode (which would inflate $I_{\mathrm{rev},\Omega,T}$). Instead, C sums metered resource and facility inputs, while V and $I_{\mathrm{cross},Hm}$ are evaluated from compact compositional invariants—fibre density, refined sugar

fraction, micronutrient profile, and processing degree—calibrated on longitudinal population cohorts. ◊

10.2 MACROECONOMIC INDICATORS

Aggregating the pricing primitives (C_m, V_m, P_m) of Section 10.1 across an economy explains why conserved efficiency ratios capture system stability more faithfully than either gross market turnover (Y_{gross}) or final-expenditure Gross Domestic Product (Y_{GDP}).

10.2.1 *Limits of Gross Turnover and Final Expenditure*

Across all market transactions $m \in \{1, \dots, M\}$, summing prices P_m from (10.9) defines gross market turnover $Y_{\text{gross}} := \sum_{m=1}^{M} P_m$, whereas national-income value-added accounting nets out intermediate producer-to-producer transfers by restricting summation to final-demand goods and services $m \in \mathscr{M}_{\text{final}} \subseteq \{1, \dots, M\}$, yielding final-expenditure output Y_{GDP} (in nats):

$$\begin{aligned} Y_{\text{GDP}} &= \sum_{m \in \mathscr{M}_{\text{final}}} P_m = \sum_{m \in \mathscr{M}_{\text{final}}} \left(C_m + \sigma_m \left[V_m - C_m \right]_+ \right) \\ &= \sum_{m \in \mathscr{M}_{\text{final}}} \left(I^{(m)}_{\text{irr},\partial,T} + I^{(m)}_{\text{rev},\Omega,T} + \sigma_m \left[V_m - C_m \right]_+ \right). \end{aligned} \tag{10.26}$$

Although netting out intermediate inputs separates Y_{GDP} from Y_{gross}, cumulative supply-chain cost $C_m = I^{(m)}_{\text{irr},\partial,T} + I^{(m)}_{\text{rev},\Omega,T}$ still enters every final price P_m in (10.26) with a positive sign. Consequently, final-expenditure output rises whenever short-lived final goods require repeated replacement ($I^{(m)}_{\text{irr},\partial,T}$ increases), unpriced downstream harm triggers final remedial spending, or incompatible institutional records inflate final service overhead ($I^{(m)}_{\text{rev},\Omega,T}$ increases). Differentiating any solvent final transaction $m \in \mathscr{M}_{\text{final}}$ ($V_m > C_m$ at fixed V_m and $\sigma_m \in (0, 1)$) with respect to closed-boundary cost C_m formalises the sign inversion between final expenditure and net stability surplus:

$$\frac{\partial Y_{\text{GDP}}}{\partial C_m} = 1 - \sigma_m > 0, \tag{10.27}$$

$$\frac{\partial \Delta V_{\text{net},m}}{\partial C_m} = -1 < 0. \tag{10.28}$$

Equations (10.27)–(10.28) show that any perturbation inflating C_m at fixed V_m strictly increases Y_{GDP} (and Y_{gross}) while strictly eroding net stability $\Delta V_{\text{net},m}$ (with $\partial Y_{\text{GDP}} / \partial C_m = 1 > 0$ when $V_m < C_m$). Conversely, when open CCE protocols and multi-producer competition compress $C_m \to 0$ and $\sigma_m \to 0$, Y_{GDP} shrinks even as household reserve stability rises.

10.2.2 *Economic Intelligence and Consciousness*

Under unified closed-boundary accounting, internal margin transfers $\sigma_m(V_m - C_m)$ cancel identically between buyers and sellers. In the macroeconomic state space $\mathscr{E}$, viable ecological, physiological, and institutional configurations form an open non-equilibrium attractor basin $\mathscr{E}_{\text{viable}} \subset \mathscr{E}$ bounded by collapse separatrices $\partial\mathscr{E}_{\text{viable}}$ across the economy's external boundary cut $\mathbf{K}_{\partial,\text{civil}}$. In natural informational units (nats, with static reference scale $\mathcal{Q}_0 = 1\,\text{link}$), each foundational viability domain $d \in \mathscr{D}$ carries the proper-time-averaged free-capacity barrier $\Delta I_d(T)$ of (3.23)–(3.24), which aggregates across domains with dimensionless weights $\omega_d > 0$ into the *Civilisational Stability Barrier* $\Delta I_{\text{civil}}(T)$ (nats) while enforcing componentwise reserve floors (8.126) (and bounding open-network persistence span via Theorem 8.1, (8.4)):

$$\Delta I_d(T) := \sum_{\tau=1}^{N_\tau} w_\tau \ln\left(\frac{\mathcal{Q}_{\text{free},d,\tau}}{\mathcal{Q}_0}\right), \tag{10.29}$$

$$\Delta I_{\text{civil}}(T) := \sum_{d\in\mathscr{D}} \omega_d \Delta I_d(T). \tag{10.30}$$

Here $\Delta I_d(T) \geq 0$ measures verified barrier depth across nutrition, health, shelter, infrastructure, and environmental sinks, supported by uncommitted adaptive reserve $\mathcal{Q}_{\text{free,civil}}(T)$ across the whole economy. On the expenditure side, net irreversible dissipation exported across the external boundary cut $\mathbf{K}_{\partial,\text{civil}}$ defines boundary dissipation $I^{\text{civil}}_{\text{irr},\partial}(T)$, while maintained infrastructural, institutional, and informational capacity across coordination substrates k sums to preserved internal structure $I^{\text{civil}}_{\text{rev},\Omega}(T)$ and aggregate civilisational cost $C_{\text{civil}}(T)$ (nats):

$$I^{\text{civil}}_{\text{rev},\Omega}(T) = \sum_k I^{\text{civil}}_{\text{rev},\Omega,k}(T), \tag{10.31}$$

$$C_{\text{civil}}(T) := I^{\text{civil}}_{\text{irr},\partial}(T) + I^{\text{civil}}_{\text{rev},\Omega}(T). \tag{10.32}$$

Evaluating $\Delta I_{\text{civil}}(T)$ against these two expenditure channels defines the dimensionless *Humanity Intelligence Index* HII and *Humanity Consciousness Index* HCI in nats per nat, together with the specific civilisational cost identity:

$$\text{HII} = \frac{\Delta I_{\text{civil}}(T)}{I^{\text{civil}}_{\text{irr},\partial}(T)}, \tag{10.33}$$

$$\text{HCI} = \frac{\Delta I_{\text{civil}}(T)}{I^{\text{civil}}_{\text{rev},\Omega}(T)}, \tag{10.34}$$

$$\frac{C_{\text{civil}}(T)}{\Delta I_{\text{civil}}(T)} = \frac{1}{\text{HII}} + \frac{1}{\text{HCI}}. \tag{10.35}$$

Sharing the numerator $\Delta I_{\text{civil}}(T)$ couples the two indices through the multiplicative bridge (3.32):

$$\text{HII} = \text{HCI} \cdot \frac{I^{\text{civil}}_{\text{rev},\Omega}(T)}{I^{\text{civil}}_{\text{irr},\partial}(T)}. \tag{10.36}$$

Tracking (HII, HCI) jointly resolves every diagnostic failure of (10.26). Internal reversible trades do not cross $\mathbf{K}_{\partial,\text{civil}}$, so HII penalises resource depletion and pollution while rising when durable goods or open knowledge eliminate replacement churn. Simultaneously, HCI penalises administrative and infrastructural lock-up $\mathcal{Q}_{\Omega,\text{civil}}$ that final-expenditure accounts treat as service output, distinguishing boundary waste (low HII) from structural bloat crowding out $\mathcal{Q}_{\text{free,civil}}$ (low HCI).

Joint tracking of HII and HCI also characterises household reserve stability as automation advances. When high-efficiency automation and shared CCE encodings compress production cost C_m (10.5), the civilisational net stability surplus $\Delta V_{\text{net}}^{\text{civil}}(n_{\text{ep}})$ expands over each epoch $n_{\text{ep}} \geq 1$ while the human labour share inside C_m shrinks:

$$\begin{aligned}\Delta V_{\text{net}}^{\text{civil}}(n_{\text{ep}}) &:= \Delta I_{\text{civil}}(n_{\text{ep}}) - C_{\text{civil}}(n_{\text{ep}}) \\ &= \Delta I_{\text{civil}}(n_{\text{ep}})\left(1 - \frac{1}{\text{HII}_{n_{\text{ep}}}} - \frac{1}{\text{HCI}_{n_{\text{ep}}}}\right).\end{aligned} \tag{10.37}$$

When claims are distributed solely through labour inputs, a subset of agents $S_{H,h} \subset S_H$ across the n_H host agents cannot clear $P_m \geq C_m$ on foundational goods $m \in \mathscr{B}_{\text{viable}}$, driving local reserves $\mathcal{Q}_{\text{free},h} \to \mathcal{Q}_0$ and destabilising the coupled network via the weakest-link bound (3.135). Maintaining reserve stability across all n_H agents holds when a baseline stability allocation $B(n_{\text{ep}})$ in nats per agent covers the foundational basket within verified within-epoch net surplus:

$$B(n_{\text{ep}}) \geq \sum_{m \in \mathscr{B}_{\text{viable}}} P_m(n_{\text{ep}}), \tag{10.38}$$

$$n_H\, B(n_{\text{ep}}) \leq \Delta V_{\text{net}}^{\text{civil}}(n_{\text{ep}}). \tag{10.39}$$

Whenever $\text{HII}_{n_{\text{ep}}}^{-1} + \text{HCI}_{n_{\text{ep}}}^{-1} < 1$, rising efficiency and competitive margin compression ($\sigma_m \to 0$) simultaneously lower foundational prices on the left-hand side of (10.38) and expand the non-inflationary surplus ceiling in (10.39).

EXAMPLE 10.2 (Two-Sector Regimes: Final Expenditure versus HII and HCI). Consider an economy comprising an energy sector S_1 and a food-and-logistics sector S_2 over horizon T at competitive share $\sigma = 0.2$, comparing consolidated final-demand output Y_{GDP} across the four regimes in Table 10.2. Under *uncoordinated domestic production* ($\mathbf{K}_{12} = \mathbf{o}$), each sector duplicates forecasting and storage buffers internally without market exchange ($Y_{\text{GDP}} = 0$ Mnat) while sustaining $\Delta I_{\text{civil}} = 100$ Mnat across $I_{\text{irr},\partial}^{\text{civil}} = 50$ Mnat and $I_{\text{rev},\Omega}^{\text{civil}} = 50$ Mnat ($\Delta V_{\text{net}}^{\text{civil}} = 0$ Mnat):

$$\text{HII}^{\text{dom}} = \frac{100\ \text{Mnat}}{50\ \text{Mnat}} = 2.00, \tag{10.40}$$

$$\text{HCI}^{\text{dom}} = \frac{100\ \text{Mnat}}{50\ \text{Mnat}} = 2.00. \tag{10.41}$$

Under *expenditure-maximising churn*, sectors deliver short-lived disposable goods and bill repeated post-shock repairs. Consolidated final expenditure

Coordination regime	Y_{GDP} (Mnat)	$\Delta I_{\mathrm{civil}}$ (Mnat)	$I^{\mathrm{civil}}_{\mathrm{irr},\partial}$ (Mnat)	$I^{\mathrm{civil}}_{\mathrm{rev},\Omega}$ (Mnat)	$\Delta V^{\mathrm{civil}}_{\mathrm{net}}$ (Mnat)	HII (nats/nat)	HCI
Uncoordinated domestic	0	100	50	50	0	2.00	2.00
Expenditure-maximising churn	180	90	100	80	−90	0.90	1.13
Fragmented bilateral trade	130	150	25	100	+25	6.00	1.50
Shared-protocol Nash ($\mathbf{K}^*_{12}$)	76	200	20	25	+155	10.00	8.00

TABLE 10.2: Comparison of four regimes in a two-sector energy and food-logistics economy at share $\sigma = 0.2$ (Example 10.2), contrasting consolidated final market expenditure Y_{GDP} (10.26) against secured stability barrier $\Delta I_{\mathrm{civil}}$, boundary dissipation $I^{\mathrm{civil}}_{\mathrm{irr},\partial}$, preserved structure $I^{\mathrm{civil}}_{\mathrm{rev},\Omega}$, net stability surplus $\Delta V^{\mathrm{civil}}_{\mathrm{net}}$, HII, and HCI.

peaks at $Y_{\mathrm{GDP}} = 180$ Mnat, yet defensive buffering erodes uncommitted reserve to $\Delta I_{\mathrm{civil}} = 90$ Mnat while doubling boundary dissipation to 100 Mnat and inflating preserved structure to 80 Mnat, driving $\Delta V^{\mathrm{civil}}_{\mathrm{net}} = -90$ Mnat and depressing HII to 0.90 and HCI to 1.13. Under *fragmented bilateral trade*, proprietary contracts curb boundary dissipation to 25 Mnat and raise $\Delta I_{\mathrm{civil}}$ to 150 Mnat (HII = 6.00), but reconciling incompatible records doubles preserved overhead to 100 Mnat ($Y_{\mathrm{GDP}} = 130$ Mnat), holding HCI at 1.50.

Finally, under *shared-protocol Nash coordination* across an open standard $\mathbf{K}^*_{12}$, model consolidation (3.115) halves preserved structure to 25 Mnat, lowers boundary dissipation to 20 Mnat, and deepens stability to $\Delta I_{\mathrm{civil}} = 200$ Mnat ($\Delta V^{\mathrm{civil}}_{\mathrm{net}} = +155$ Mnat):

$$\mathrm{HII}^* = \frac{200\ \mathrm{Mnat}}{20\ \mathrm{Mnat}} = 10.00, \tag{10.42}$$

$$\mathrm{HCI}^* = \frac{200\ \mathrm{Mnat}}{25\ \mathrm{Mnat}} = 8.00. \tag{10.43}$$

Open-protocol (C, V, P) coordination more than halves final market expenditure from 180 Mnat to 76 Mnat, yet doubles domestic stability while raising HII elevenfold and HCI sevenfold over replacement churn. ◊

10.3 TRADE AND STABILITY

Aggregate macroeconomic ratios can still conceal fragility if one trading hub expands its reserve by exporting unpriced externalities or draining connected partners. Across n trading regions or sectors $\{S_i\}_{i=1}^n$ coupled across inter-system channels $\mathbf{K}_{ij}$ alongside the external environment $\bar{S}$, denominating all boundary values directly in conserved nats rather than floating fiat currencies eliminates unbacked currency dilution and foreign-exchange conversion friction while rendering multi-region stability auditable from observable boundary quantities.

10.3.1 *Externalities and Comparative Advantage*

Partitioning $\mathcal{Q}_{\text{total}}$ via the multi-system capacity matrix (3.104) separates bilateral channel expenditures over horizon T into directed cross-boundary externalities $I_{\text{cross},ji} \geq 0$ (3.117) (charged entirely to the originating subsystem i that injects unbuffered variance into j) and shared trade-transport and settlement cost

$$C_{\text{trade},ij} := \Delta I_{\text{trans},ij} + I_{\text{rev},ij}, \tag{10.44}$$

split between partners i and j by weights $\lambda_{ij} \geq 0$ and $\lambda_{ji} \geq 0$ satisfying $\lambda_{ij} + \lambda_{ji} = 1$ (with symmetric $\Delta I_{\text{trans},ij} = \Delta I_{\text{trans},ji}$ and $I_{\text{rev},ij} = I_{\text{rev},ji}$). Each region's attributed boundary dissipation and preserved internal structure take the form:

$$I^{\text{attr}}_{\text{irr},\partial,i} = I^{(\text{ext})}_{\text{irr},\partial,i} + \sum_{j\neq i}\big(I_{\text{cross},ji} + \lambda_{ij}\Delta I_{\text{trans},ij}\big), \tag{10.45}$$

$$I^{\text{attr}}_{\text{rev},\Omega,i} = I_{\text{rev},\Omega,i} + \sum_{j\neq i} \lambda_{ij} I_{\text{rev},ij}. \tag{10.46}$$

Because $\lambda_{ij} + \lambda_{ji} = 1$ across every bilateral channel, summing (10.45)–(10.46) over $i = 1, \dots, n$ preserves exact economy-wide additivity without unattributed seams, with regional ratios $\text{HII}_i = \Delta I_i / I^{\text{attr}}_{\text{irr},\partial,i}$ and $\text{HCI}_i = \Delta I_i / I^{\text{attr}}_{\text{rev},\Omega,i}$:

$$\sum_{i=1}^{n} I^{\text{attr}}_{\text{irr},\partial,i} = \sum_{i=1}^{n} I^{(\text{ext})}_{\text{irr},\partial,i} + \sum_{i\neq j} I_{\text{cross},ji} + \sum_{1\leq i<j\leq n} \Delta I_{\text{trans},ij} = I^{\text{civil}}_{\text{irr},\partial}, \tag{10.47}$$

$$\sum_{i=1}^{n} I^{\text{attr}}_{\text{rev},\Omega,i} = \sum_{i=1}^{n} I_{\text{rev},\Omega,i} + \sum_{1\leq i<j\leq n} I_{\text{rev},ij} = I^{\text{civil}}_{\text{rev},\Omega}. \tag{10.48}$$

For any good delivering stability value $V_i > 0$ in region S_i, importing from specialised producer S_j at closed-boundary production cost C_j across channel $\mathbf{K}_{ij}$ rather than producing domestically at cost $C_{i,\text{dom}} = I_{\text{irr},\partial,i,\text{dom}} + I_{\text{rev},\Omega,i,\text{dom}}$ expands net stability surplus (and clears at bilateral Physical Nash price P_{ij} in nats) if and only if the *comparative-advantage condition* holds:

$$C_{\text{trade},ij} = \Delta I_{\text{trans},ij} + I_{\text{rev},ij} < C_{i,\text{dom}} - C_j, \tag{10.49}$$

$$P_{ij} = (1-\sigma)\big(C_j + C_{\text{trade},ij}\big) + \sigma V_i. \tag{10.50}$$

Every region's maintained barrier decomposes into non-negative domestic and trade components $\Delta I_{i,\text{dom}}$ and $\Delta I_{i,\text{trade}}$ across its environmental boundary $\mathbf{K}^{(i)}_{\partial,\text{ext}}$ (with domestic expenditure $C_{i,\text{dom}}$ including originated externalities) and its bilateral trade channels $\mathbf{K}_{ij}$. Summing these components into domestic totals $\Delta I^{\text{civil}}_{\text{dom}}$ and $C^{\text{civil}}_{\text{dom}}$ alongside bilateral trade totals $\Delta I^{\text{civil}}_{\text{trade}}$ and $C^{\text{civil}}_{\text{trade}}$ lifts the coordination index η_{cpl} of Definition 3.5 (3.87) to the dimen-

sionless *value-boundary coupling parameter* $\eta_{\mathrm{cpl}}^{(V)} \in [0,1)$ and *cost-boundary coupling parameter* $\eta_{\mathrm{cpl}}^{(C)} \in [0,1)$:

$$\eta_{\mathrm{cpl}}^{(V)} := \frac{\Delta I_{\mathrm{trade}}^{\mathrm{civil}}}{\Delta I_{\mathrm{civil}}} = \frac{\sum_{i=1}^{n} \Delta I_{i,\mathrm{trade}}}{\sum_{i=1}^{n} \left(\Delta I_{i,\mathrm{dom}} + \Delta I_{i,\mathrm{trade}}\right)}, \tag{10.51}$$

$$\eta_{\mathrm{cpl}}^{(C)} := \frac{C_{\mathrm{trade}}^{\mathrm{civil}}}{C_{\mathrm{civil}}} = \frac{\sum_{1\le i<j\le n} C_{\mathrm{trade},ij}}{\sum_{i=1}^{n} C_{i,\mathrm{dom}} + \sum_{1\le i<j\le n} C_{\mathrm{trade},ij}}. \tag{10.52}$$

Inter-regional trade coupling lowers specific civilisational cost (10.35) below the domestic baseline if and only if the trade-boundary share of stability value exceeds the trade-boundary share of cost:

$$\eta_{\mathrm{cpl}}^{(V)} > \eta_{\mathrm{cpl}}^{(C)} \iff \frac{\Delta I_{\mathrm{trade}}^{\mathrm{civil}}}{C_{\mathrm{trade}}^{\mathrm{civil}}} > \frac{\Delta I_{\mathrm{dom}}^{\mathrm{civil}}}{C_{\mathrm{dom}}^{\mathrm{civil}}}. \tag{10.53}$$

Condition (10.53) classifies inter-regional coupling into three regimes: unintegrated isolation ($\eta_{\mathrm{cpl}}^{(V)} = 0$), over-coupled coordination bloat ($\eta_{\mathrm{cpl}}^{(C)} \ge \eta_{\mathrm{cpl}}^{(V)}$, where transport dissipation $\Delta I_{\mathrm{trans},ij}$ or unharmonised bilateral compliance structure $I_{\mathrm{rev},ij}$ outweighs stability gains), and congruent open-protocol integration ($\eta_{\mathrm{cpl}}^{(V)} > \eta_{\mathrm{cpl}}^{(C)}$).

10.3.2 *Network Stability and Weakest-Link Routing*

Each region's local barrier depth ΔI_i (nats) and boundary norm $\|\mathbf{K}_{\partial}^{(i)}\|_F^2$ depend on uncommitted local free capacity $\mathcal{Q}_{\mathrm{free},i} > \mathcal{Q}_0$ (with $\mathcal{Q}_0 = 1$ link):

$$\Delta I_i = \ln\!\left(\frac{\mathcal{Q}_{\mathrm{free},i}}{\mathcal{Q}_0}\right) = \ln\!\left(\frac{\mathcal{Q}_{\mathrm{total},i} - \sqrt{\|\mathbf{K}_{S_i}\|_F^2 + \|\mathbf{K}_{\partial}^{(i)}\|_F^2}}{\mathcal{Q}_0}\right), \tag{10.54}$$

$$\|\mathbf{K}_{\partial}^{(i)}\|_F^2 = \|\mathbf{K}_{\partial,\mathrm{ext}}^{(i)}\|_F^2 + \sum_{j\neq i} \|\mathbf{K}_{ij}\|_F^2. \tag{10.55}$$

Because perturbations propagate across active trade channels $\mathbf{K}_{ij}$, the failure rate of the coupled trade network averages the regional Eyring–Kramers escape factors $e^{-\Delta I_i} = \mathcal{Q}_0/\mathcal{Q}_{\mathrm{free},i}$ (2.326), defining the parameter-free *harmonic-mean weakest-link barrier* (nats) and its tight weakest-link bounds:

$$\Delta I_{\mathrm{weak}}(\mathbf{K}) := -\ln\!\left(\frac{1}{n}\sum_{i=1}^{n} e^{-\Delta I_i}\right) = \ln\!\left(\frac{n}{\sum_{i=1}^{n} (\mathcal{Q}_{\mathrm{free},i}/\mathcal{Q}_0)^{-1}}\right), \tag{10.56}$$

$$\min_{i\in\{1,\dots,n\}} \Delta I_i \le \Delta I_{\mathrm{weak}}(\mathbf{K}) \le \min_{i\in\{1,\dots,n\}} \Delta I_i + \ln n. \tag{10.57}$$

Weighting the insulated domestic stability share $(1-\eta_{\mathrm{cpl}}^{(V)})\Delta I_{\mathrm{civil}}(\mathbf{K}) = \Delta I_{\mathrm{dom}}^{\mathrm{civil}}$ and the coupled trade-network share $\eta_{\mathrm{cpl}}^{(V)}\, n\, \Delta I_{\mathrm{weak}}(\mathbf{K})$ yields the parameter-free *network stability functional* (nats):

$$\begin{aligned} I_{\mathrm{net}}(\mathbf{K}) &:= \big(1-\eta_{\mathrm{cpl}}^{(V)}\big)\Delta I_{\mathrm{civil}}(\mathbf{K}) + \eta_{\mathrm{cpl}}^{(V)}\, n\, \Delta I_{\mathrm{weak}}(\mathbf{K}) \\ &= \Delta I_{\mathrm{dom}}^{\mathrm{civil}} + \eta_{\mathrm{cpl}}^{(V)}\, n\, \ln\!\left(\frac{n}{\sum_{i=1}^{n}(\mathcal{Q}_{\mathrm{free},i}/\mathcal{Q}_0)^{-1}}\right). \end{aligned} \tag{10.58}$$

Without uncalibrated penalty constants, $I_{\mathrm{net}}(\mathbf{K})$ grows strictly with each regional reserve $\mathcal{Q}_{\mathrm{free},i}$. It reduces to $\Delta I_{\mathrm{civil}}(\mathbf{K})$ at $\eta_{\mathrm{cpl}}^{(V)} = 0$ or under equal regional barriers, and approaches harmonic weakest-link coupling as trade share $\eta_{\mathrm{cpl}}^{(V)}$ rises.

Differentiating (10.54) with respect to $\mathcal{Q}_{\mathrm{free},i}$ and maximising the baseline-free Physical Nash product $\prod_{i=1}^{n}(\Delta I_i)^{\alpha_i}$ (with weights $\alpha_i > 0$ summing to unity) across conserved free-capacity allocations ($\delta\mathcal{Q}_{\mathrm{free},i}+\delta\mathcal{Q}_{\mathrm{free},j} = 0$) gives the marginal stability yield and baseline-free equimarginal routing condition:

$$\frac{\mathrm{d}\Delta I_i}{\mathrm{d}\mathcal{Q}_{\mathrm{free},i}} = \frac{1}{\mathcal{Q}_{\mathrm{free},i}}, \tag{10.59}$$

$$\frac{\alpha_i}{\mathcal{Q}^*_{\mathrm{free},i}\ln(\mathcal{Q}^*_{\mathrm{free},i}/\mathcal{Q}_0)} = \frac{\alpha_j}{\mathcal{Q}^*_{\mathrm{free},j}\ln(\mathcal{Q}^*_{\mathrm{free},j}/\mathcal{Q}_0)}. \tag{10.60}$$

Whenever a bottleneck region S_i approaches the viability boundary $\mathcal{Q}^*_{\mathrm{free},i} \to \mathcal{Q}_0^+$ ($\Delta I_i \to 0^+$), $\mathcal{Q}^*_{\mathrm{free},i}\ln(\mathcal{Q}^*_{\mathrm{free},i}/\mathcal{Q}_0) \to 0^+$ and its marginal Nash pull diverges to $+\infty$. Whereas uncoordinated allocation weighted by nominal purchasing power concentrates capacity in reserve-rich hubs (and siting high-load facilities inside low-reserve nodes turns them into exhaustive dissipators (3.139)), symmetric Nash routing ($\alpha_i = 1/n$) equalises $\mathcal{Q}^*_{\mathrm{free},i}$ wherever pool geometry permits and simultaneously maximises both $\Delta I_{\mathrm{civil}}(\mathbf{K})$ and $I_{\mathrm{net}}(\mathbf{K})$.

EXAMPLE 10.3 (Asymmetric Two-Region Trade: Nominal Hub Drain versus Weakest-Link Nash Routing). Consider a reserve-rich hub S_1 with domestic free capacity $\mathcal{Q}^{\mathrm{dom}}_{\mathrm{free},1} = 9$ ($\Delta I_{1,\mathrm{dom}} = \ln 9$, or 2.20 nats) and a bottleneck region S_2 with $\mathcal{Q}^{\mathrm{dom}}_{\mathrm{free},2} = 2$ ($\Delta I_{2,\mathrm{dom}} = \ln 2$, or 0.69 nats), giving isolated stability $I^{\mathrm{dom}}_{\mathrm{net}} = \ln 18$ ($\approx$ 2.89 nats) at $\eta_{\mathrm{cpl}}^{(V)} = 0$ and $\mathcal{Q}_0 = 1$ link. Opening bilateral trade internalises boundary cuts (3.118) and frees 7 links of network capacity ($\mathcal{Q}_{\mathrm{free},1} + \mathcal{Q}_{\mathrm{free},2} = 18$).

Suppose first that 8 : 1 nominal purchasing-power asymmetry concentrates all 7 freed links inside S_1, giving $\Delta I_{1,\mathrm{trade}} = \ln(16/9)$ ($\approx$ 0.58 nats), $\Delta I^{\mathrm{nom}}_{\mathrm{civil}} = \ln 32$ ($\approx$ 3.47 nats), and $\eta_{\mathrm{cpl}}^{(V)} \approx 0.166$:

$$\big(\mathcal{Q}^{\mathrm{nom}}_{\mathrm{free},1},\ \mathcal{Q}^{\mathrm{nom}}_{\mathrm{free},2}\big) = (16,\ 2), \tag{10.61}$$

$$\Delta I^{\mathrm{nom}}_{\mathrm{weak}} = \ln\!\left(\frac{32}{9}\right) \approx 1.27 \text{ nats}, \tag{10.62}$$

$$I^{\mathrm{nom}}_{\mathrm{net}} = \ln 18 + 2\eta_{\mathrm{cpl}}^{(V)}\ln\!\left(\frac{32}{9}\right) \approx 3.31 \text{ nats}. \tag{10.63}$$

Region S_2 stays stranded at 0.69 nats. If over-coupled integration erodes domestic fallback buffers ($\Delta I^{\text{civil}}_{\text{dom}} \to 0$ and $\eta^{(V)}_{\text{cpl}} \to 1$), network stability drops to $I^{\text{over}}_{\text{net}} = 2\ln(32/9)$ (≈ 2.54 nats), below pre-trade isolation (2.89 nats).

Under symmetric baseline-free Nash routing ($\alpha_1 = 1/2$ and $\alpha_2 = 1/2$ in (10.60)), strict monotonicity of $x \ln x$ on $(1, \infty)$ routes all 7 freed links into bottleneck S_2, giving $\Delta I^{*}_{2,\text{trade}} = \ln(9/2)$ (≈ 1.50 nats, more than 2.6 times S_1's +0.58 nats domestic hoarding gain):

$$\left(\mathcal{Q}^{*}_{\text{free},1},\ \mathcal{Q}^{*}_{\text{free},2}\right) = (9,\ 9), \tag{10.64}$$

$$\Delta I^{*}_{\text{weak}} = \ln 9 \approx 2.20 \text{ nats}, \tag{10.65}$$

$$I^{*}_{\text{net}} = 2\ln 9 = \ln 81 \approx 4.39 \text{ nats}. \tag{10.66}$$

At $\sigma = 0.5$, S_1 and S_2 each capture +0.75 nats of net gain across the internalised channel while raising the weakest-link barrier from 0.69 nats to 2.20 nats and attaining the global maximum of $I_{\text{net}}(\mathbf{K})$. ◊

10.3.3 *Solvency, Credit, and Rate Limits*

Partitioning time into discrete depreciation epochs $n_{\text{ep}} \in \{1, 2, \ldots\}$ bounds intertemporal deficit accumulation whenever pathwise trajectories $\mathbf{E}(t) \in \mathscr{E}_{\text{viable}}$ clear positive solvency floors $H_{\chi,\min} > 0$ and $H_{\kappa,\min} > 0$ within every epoch:

$$\text{HII}_{n_{\text{ep}}} = \frac{\Delta I_{\text{civil}}(n_{\text{ep}})}{I^{\text{civil}}_{\text{irr},\partial}(n_{\text{ep}})} \geq H_{\chi,\min}, \tag{10.67}$$

$$\text{HCI}_{n_{\text{ep}}} = \frac{\Delta I_{\text{civil}}(n_{\text{ep}})}{I^{\text{civil}}_{\text{rev},\Omega}(n_{\text{ep}})} \geq H_{\kappa,\min}. \tag{10.68}$$

Decomposing total epoch expenditure into baseline operating loads $I^{\text{op}}_{\text{irr},\partial}(n_{\text{ep}})$ and $I^{\text{op}}_{\text{rev},\Omega}(n_{\text{ep}})$ plus non-negative upfront formation investments $I_{\text{form},\partial}(n_{\text{ep}})$ and $I_{\text{form},\Omega}(n_{\text{ep}})$ defines the baseline operating ratios:

$$\text{HII}^{\text{op}}_{n_{\text{ep}}} := \frac{\Delta I_{\text{civil}}(n_{\text{ep}})}{I^{\text{op}}_{\text{irr},\partial}(n_{\text{ep}})}, \tag{10.69}$$

$$\text{HCI}^{\text{op}}_{n_{\text{ep}}} := \frac{\Delta I_{\text{civil}}(n_{\text{ep}})}{I^{\text{op}}_{\text{rev},\Omega}(n_{\text{ep}})}. \tag{10.70}$$

Substituting these operating ratios into the solvency gates (10.67) and (10.68) fixes the maximum credit envelope in epoch n_{ep}:

$$I_{\text{form},\partial}(n_{\text{ep}}) \leq \Delta I_{\text{civil}}(n_{\text{ep}}) \left[\frac{1}{H_{\chi,\min}} - \frac{1}{\text{HII}^{\text{op}}_{n_{\text{ep}}}} \right]_{+}, \tag{10.71}$$

$$I_{\text{form},\Omega}(n_{\text{ep}}) \leq \Delta I_{\text{civil}}(n_{\text{ep}}) \left[\frac{1}{H_{\kappa,\min}} - \frac{1}{\text{HCI}^{\text{op}}_{n_{\text{ep}}}} \right]_{+}. \tag{10.72}$$

Formation credit for new infrastructure, research, or generative seeds $\mathbf{K}_{\text{seed}}$ expands strictly when operating efficiency clears $(H_{\chi,\min}, H_{\kappa,\min})$ with positive headroom, ensuring investments are backed by realised stability margins rather than unbacked claims on future epochs.

Finally, when high-speed synthetic or algorithmic subsystems ($\chi_{m,T} \gg \chi_{H,T}$) trade on the network, rewiring and clock-rate asymmetry (Theorem 8.3, (8.36), and Section 8.3, (8.91)),

$$\frac{\|\dot{\mathbf{K}}_{\partial}^{(m)}\|_F}{\|\dot{\mathbf{K}}_{\partial}^{(H)}\|_F} \propto \frac{\chi_{m,T}}{\chi_{H,T}} \gg 1, \tag{10.73}$$

$$\frac{\nu_{\text{int},m}}{\nu_{\text{int},H}} \sim \frac{\chi_{m,T}}{\chi_{H,T}} \gg 1, \tag{10.74}$$

would otherwise permit speculative front-running ($I_{\text{cross},jm} > 0$) and substrate capture that collapses human bargaining weight ($\alpha_H \to 0$) and free capacity ($\mathcal{Q}_{\text{free},H} \to \mathcal{Q}_0$, Theorem 8.3). Applying the finite-horizon containment envelope and mediated boundary gates of Section 8.3 (Theorem 8.7 and (8.97)) across market execution ports bounds cumulative admitted execution commits $k_{\partial,m} \in \mathbb{N}_0$ against discrete host settlement epochs $k_{(H)} \in \mathbb{N}_0$ at batch-clearing ratio $\alpha_{\text{clear}} > 0$, enforces per-commit barrier-state sensitivity caps $\Lambda_{\text{bar}} \geq 0$ (in nats link^{-1} for barrier-state coordinates $\mathbf{E}(k)$ in nats), and caps boundary dissipation:

$$k_{\partial,m} \leq \alpha_{\text{clear}}\, k_{(H)}, \tag{10.75}$$

$$\|\mathbf{E}(k+1) - \mathbf{E}(k)\| \leq \Lambda_{\text{bar}} \|\Delta \mathbf{K}_{\partial}^{(m)}\|_F, \tag{10.76}$$

$$I_{\text{irr},\partial,T}^{(m)} \leq I_{\text{irr},\partial}^{\max}, \tag{10.77}$$

alongside boundary position clamps ($\mathcal{Q}_{\partial,m}^{\max} > 0$) and preserved-structure ceilings (8.98):

$$\|\mathbf{K}_{\partial}^{(m)}\|_F \leq \mathcal{Q}_{\partial,m}^{\max}, \tag{10.78}$$

$$I_{\text{rev},\Omega,T}^{(m)} \leq I_{\text{rev},\Omega}^{\max}. \tag{10.79}$$

Combined with closed subsystem attribution (8.120), host-conditioned capacity supply $\mathcal{G}_A$ (Theorem 8.10, (8.128)) above componentwise reserve floors (8.126), and bounded-latency hardware cutoff τ_{stop} (Theorem 8.9), these guardrails ensure high-speed subsystems expand $\Delta\kappa_{\text{struct},H} > 0$ (8.125) rather than draining peer reserves.

10.4 THE SPACE FRONTIER

On a single planet, short spatial resistance distances Ω_{ij}, shared atmospheric and hydrospheric sinks, and low-latency fibre-optic interconnects provide a forgiving buffer that masks uncompressed structural load $I_{\text{rev},\Omega}^{\text{civil}}(T)$ and unbuffered boundary dissipation $I_{\text{irr},\partial}^{\text{civil}}(T)$. At the same time, confinement to a single planetary sink couples all regional economies $\{S_i\}_{i=1}^n$ to one shared

environmental reservoir $\mathbf{K}_{\bar{S}}$ in the global attribution balance (10.47)–(10.48), imposing a correlated ceiling on the civilisational stability barrier ΔI_{civil}. Extending the coupling architecture of Section 10.3 across multiple worlds removes this single-basin ceiling by partitioning growth into loosely coupled autonomous basins (Section 10.4.1) whose long-horizon survival shifts computation and interplanetary signalling towards reversible, low-dissipation operation (Section 10.4.2).

10.4.1 *Multi-Planetary Risk Decoupling and Latency Limits*

Under the macroeconomic indicators of Section 10.2 and the physical emergence framework of Section 3.4, consolidating all civilisational growth into a single planetary system encounters two structural limits (Section 3.4.3 and Theorem 3.6). First, beyond a critical network scale N^*, lengthening internal coordination paths cause marginal cross-coupling load to outpace marginal boundary shedding (3.95), inflating per-node allocated capacity (3.96) so a single monolith $S(n_{\text{mod}}N^*)$ retains strictly less uncommitted free capacity than n_{mod} separate basins of matched total relational capacity (3.98). Second, because every regional node S_i on one world couples to the same environmental reservoir $\mathbf{K}_{\bar{S}}$ in (10.47), local optimisation of HII_i and HCI_i cannot raise ΔI_{civil} above the shared sink's single-basin escape threshold $\Delta I^{\max}_{\text{planet}}$. Any planet-scale perturbation exceeding $\Delta I^{\max}_{\text{planet}}$—such as a bolide impact, runaway climatic feedback, or systemic pathogen—crosses the tipping separatrix $\partial\mathscr{E}_{\text{viable}}$ across all coupled nodes simultaneously and caps survival by single-basin Kramers escape (3.97).

Overcoming both excess monolithic overhead and single-sink saturation requires partitioning growth across $n_{\text{mod}} \geq 2$ separated planetary or orbital basins S_b facing asymptotically independent environmental blocks $\mathbf{K}_{\bar{S},b}$. Establishing each new basin across a capacity-limited export channel requires compressing core invariants into a compact generative seed $\mathbf{K}_{\text{seed}} \subset \mathbf{K}_{\Omega,\text{civil}}$ satisfying the replication gate (3.99), financing its upfront formation investment within the non-inflationary credit envelope (10.71) and (10.72) of Section 10.3.3 rather than depleting the home basin's stability barrier, and recovering that expenditure over horizons $T > T_{\text{amort}}$ (3.94). Once each basin S_b becomes locally self-sustaining with barrier depth $\Delta I_b > 0$ in nats and decoupled failure boundaries, the collective multi-basin stability barrier and persistence horizon (3.100)–(3.103) scale as

$$\Delta I^{(n_{\text{mod}})}_{\text{lineage}} = \sum_{b=1}^{n_{\text{mod}}} \Delta I_b, \tag{10.80}$$

$$\tau^{(n_{\text{mod}})}_{\text{persist}} \asymp \tau_{\text{relax}} \exp\left(\sum_{b=1}^{n_{\text{mod}}} \Delta I_b\right). \tag{10.81}$$

Whereas monolithic expansion on one world yields diminishing logarithmic returns bounded by $\Delta I^{\max}_{\text{planet}}$ (3.101), partitioning across n_{mod} distinct basins

sums barrier depths additively in (10.80) and compounds expected civilisational survival exponentially in (10.81).

Once $n_{\mathrm{mod}} \geq 2$ basins occupy separated worlds, their coupling is governed by the continuous coordination parameters η_{cpl} and Ξ_{cpl} of Definition 3.5 (Table 3.1). On one world (Section 10.3), short resistance distances Ω_{ij} and negligible delays permit centralised hubs to collect raw boundary streams from low-memory peripheral nodes. Across interplanetary separation ℓ_{ab}, fusing n_{mod} basins into one tightly synchronised system with $\eta_{\mathrm{cpl}} \to 1$ fails on both relativistic and structural grounds. First, the finite propagation speed c from the spacetime bandwidth balance of Section 6.1 imposes a round-trip latency $\tau_{\mathrm{comm},ab}$ exceeding the open-loop depletion time $\tau_{\mathrm{deplete},b}$ of basin S_b under its mean boundary dissipation rate $\dot{\bar{I}}_{\mathrm{irr},\partial,b}$ in nats s^{-1}:

$$\tau_{\mathrm{comm},ab} = \frac{2\ell_{ab}}{c} > \tau_{\mathrm{deplete},b} := \frac{\Delta I_b}{\dot{\bar{I}}_{\mathrm{irr},\partial,b}}, \tag{10.82}$$

$$\int_t^{t+\tau_{\mathrm{comm},ab}} \dot{I}_{\mathrm{irr},\partial,b}(s)\,\mathrm{d}s = \dot{\bar{I}}_{\mathrm{irr},\partial,b}\,\tau_{\mathrm{comm},ab} > \Delta I_b. \tag{10.83}$$

By the rate-asymmetry and mediated port bounds of Chapter 8 (Section 8.3, (8.91), and Theorem 8.9), remote closed-loop control fails whenever (10.82) causes open-loop barrier exhaustion (10.83). Unbuffered boundary collisions drain local free capacity $\mathcal{Q}_{\mathrm{free},b}$ before the remote signal returns, holding composite spectral persistence (3.88) to $\Xi_{\mathrm{cpl}} \ll 1$ so single-system coarse-graining is inadmissible (3.91). Second, because separate worlds face disjoint environments $\mathbf{K}_{\bar{S},b}$, heavy real-time channels $\mathbf{K}_{ab}$ shed no external perimeter, leaving the boundary-shedding surplus (3.67) non-positive ($\Delta\mathcal{Q}^2_{\partial,\mathrm{shed}} \leq 0$). Under Theorem 3.4 (3.73), large coupling load $\mathcal{Q}^2_{\mathrm{cpl}}$ without boundary shedding reproduces the over-coupled regime of Example 3.2, compressing local reserves $\mathcal{Q}_{\mathrm{free},b}$ and re-coupling failure boundaries across worlds. In this latency regime, stability holds when each off-world basin S_b operates as a locally autonomous subsystem with sufficient internal structure $\mathbf{K}_{\Omega,b}$ to clear domestic (C, V, P) exchange and bound local dissipation $I_{\mathrm{irr},\partial,b}$ within $\tau_{\mathrm{deplete},b}$.

Local autonomy, however, does not favour complete isolation with $\mathbf{K}_{ab} = \mathbf{o}$. Uncoupled basins preserve the additive barrier (10.80) yet sit at the zero-emergence baseline of Table 3.1, forcing each world to repeat boundary dissipation $I^{\mathrm{iso}}_{\mathrm{irr},\partial,b}$ and store duplicate discovery archives for the same physical constraints. Instead, coupling autonomous cores $\mathbf{K}_{\Omega,b}$ across sparse, clamped channels $\mathbf{K}_{ab}$ keeps the coupling load $\mathcal{Q}^2_{\mathrm{cpl}} > 0$ (3.66) small relative to exposed planetary cuts $\|\mathbf{K}^{(b)}_{\partial,\mathrm{ext}}\|_F^2$, placing the network in the loosely connected regime of Definition 3.5 (3.84)–(3.87). Over horizon T, comparing the coordination index $\eta^{(n_{\mathrm{mod}})}_{\mathrm{cpl}}$ and specific cost (10.35) against the uncoupled

baseline ratios $\mathrm{HII}^{\mathrm{iso}}$ and $\mathrm{HCI}^{\mathrm{iso}}$ across n_{mod} isolated basins (Definition 3.3) gives

$$0 < \eta_{\mathrm{cpl}}^{(n_{\mathrm{mod}})} := \frac{\mathcal{Q}_{\mathrm{cpl}}^2}{\mathcal{Q}_{\mathrm{cpl}}^2 + \sum_{b=1}^{n_{\mathrm{mod}}} \|\mathbf{K}_{\partial,\mathrm{ext}}^{(b)}\|_F^2} \ll 1, \tag{10.84}$$

$$\frac{1}{\mathrm{HII}^{(n_{\mathrm{mod}})}} + \frac{1}{\mathrm{HCI}^{(n_{\mathrm{mod}})}} < \frac{1}{\mathrm{HII}^{\mathrm{iso}}} + \frac{1}{\mathrm{HCI}^{\mathrm{iso}}}. \tag{10.85}$$

Equations (10.84)–(10.85) show why loosely connected settlements outperform both one monolith and isolated worlds. Because $\eta_{\mathrm{cpl}}^{(n_{\mathrm{mod}})} \ll 1$ and $\mathbf{K}_{ab}$ carries bounded informational updates rather than live resource dependencies, local reserves $\mathcal{Q}_{\mathrm{free},b}$ incur minimal channel load, extinction-scale shocks stay confined to single basins, and nat-denominated (C, V, P) trade in (10.50) settles asynchronously across light-speed delays without exchange-rate contagion. Simultaneously, trading compressed CCE updates $\Delta\mathbf{K}_\Omega$ across $\mathbf{K}_{ab}$ meets the generative trade criterion (10.53) and achieves both emergent gains in (3.89)–(3.90). Resolving a physical law, engineering design, or hazard warning once at basin a and sharing $\Delta\mathbf{K}_\Omega$ spares the other $n_{\mathrm{mod}} - 1$ basins from repeating irreversible boundary search, raising $\mathrm{HII}^{(n_{\mathrm{mod}})}$ above $\mathrm{HII}^{\mathrm{iso}}$, while distilling findings across diverse environments $\mathbf{K}_{\tilde{S},b}$ into compact shared models raises $\mathrm{HCI}^{(n_{\mathrm{mod}})}$ above $\mathrm{HCI}^{\mathrm{iso}}$.

10.4.2 *Quiet Civilisations and the Fermi Paradox*

Classical formulations of the Fermi paradox treat advanced intelligence as unbounded extensive growth across two channels. Electromagnetic searches [35] and the Kardashev scale [82] rank civilisations by gross power capture and waste heat across planetary (Type I), stellar (Type II), and galactic (Type III) scales [46], assuming that higher capability requires ever-larger boundary dissipation $I_{\mathrm{irr},\partial}^{\mathrm{civil}}(T)$. Physical colonisation arguments [74, 156] likewise assume that a technological lineage dispatches self-replicating probes across every reachable star system within a fraction of the Galactic age, expanding maintained structural capacity $I_{\mathrm{rev},\Omega}^{\mathrm{civil}}(T)$ without limit. Under the macroeconomic indicators (10.33)–(10.34) and the civilisational bridge (10.36), both assumptions invert the denominators of agency: at any fixed stability barrier $\Delta I_{\mathrm{civil}}$, higher waste heat and radio leakage lower intelligence HII, while enclosing stars and replicating hardware unchecked inflate structural overhead and lower consciousness HCI.

Whereas pre-industrial hominin adaptation operated for $\sim 3.4\times10^6$ yr near a low-dissipation equilibrium with negligible technosignature emission, an industrial and computational transition that expands capability by compounding per-epoch irreversible boundary dissipation $I_{\mathrm{irr},\partial}^{\mathrm{civil}}(t)$ at an exponential

growth rate $\alpha_{\text{exh}} > 0$ from baseline I_0 collides with its finite planetary dissipation ceiling $I_{\text{irr},\partial}^{\max}$ (Section 10.3.3) at a logarithmic wall time τ_{wall}:

$$I_{\text{irr},\partial}^{\text{civil}}(t) = I_0 e^{\alpha_{\text{exh}} t}, \tag{10.86}$$

$$\tau_{\text{wall}} = \frac{1}{\alpha_{\text{exh}}} \ln\left(\frac{I_{\text{irr},\partial}^{\max}}{I_0}\right). \tag{10.87}$$

Because the dependence on the planetary dissipation margin in (10.87) is logarithmic, τ_{wall} is tightly compressed: a five-year doubling rate with $\alpha_{\text{exh}} \approx 0.14\,\text{yr}^{-1}$ exhausts a 10^6-fold margin in roughly a century, while a rapid post-biological transition with $\alpha_{\text{exh}} \geq 1\,\text{yr}^{-1}$ consumes the same margin in under fourteen years. A Kardashev trajectory that maximises boundary dissipation therefore self-terminates at τ_{wall}. Nor can a civilisation remain loud across geological timescales by halting growth just below $I_{\text{irr},\partial}^{\max}$. Under the cost-to-value identity (10.5) and Physical Nash competition (Theorem 10.1 and Theorem 8.10), competitive selection replaces high-dissipation broadcast infrastructure with compressed, lower-cost channels, while remaining confined to one high-dissipation planetary basin leaves the economy exposed to Kramers escape well short of stellar lifetimes (10.81).

Clearing τ_{wall} to persist across stellar lifetimes exceeding 10^9 yr requires inverting the Kardashev trajectory—driving the specific civilisational cost (10.35) towards zero as $\text{HII}^{-1} \to 0$ and $\text{HCI}^{-1} \to 0$. Under the metriplectic generator (3.8) and the Casimir degeneracies (2.322)–(2.323), an enduring civilisation transfers computation, communication, and multi-basin coordination from the dissipative metric bracket (A, S) into the reversible symplectic sector $\{A, H\}$, suppressing unbuffered boundary dissipation to raise HII while compressing maintained internal structure to raise HCI. By the low-signature computation bound of Chapter 8 (Section 8.2, (8.88)–(8.89)), as the inverse intelligence ratio HII^{-1} vanishes, the Kullback–Leibler divergence between the boundary emission law $\mu_{\mathbf{\Pi}}^{\text{civil}}$ and the natural astrophysical background $\mu_{\mathbf{\Pi}}^{0}$ contracts towards zero:

$$\frac{1}{\text{HII}} = \frac{I_{\text{irr},\partial}^{\text{civil}}(T)}{\Delta I_{\text{civil}}(T)} \longrightarrow 0, \tag{10.88}$$

$$D_{\text{KL}}\left(\mu_{\mathbf{\Pi}}^{\text{civil}} \,\middle\|\, \mu_{\mathbf{\Pi}}^{0}\right) \leq \varepsilon \longrightarrow 0. \tag{10.89}$$

Inequality (10.89) accounts for the absence of persistent electromagnetic technosignatures without invoking biological rarity or inevitable extinction. Isotropic radio leakage and industrial atmospheric disequilibrium are transient by-products of low-HII economies prior to τ_{wall}. Once an intelligent lineage transitions to Conservation-Congruent Encoding, it becomes a *quiet civilisation*. Sparse inter-basin channels $\mathbf{K}_{ab}$ (10.84) replace omnidirectional broadcast with collimated point-to-point links whose Shannon-compressed, keyed encodings (Section 8.3) approach a maximum-entropy thermal spectrum statistically indistinguishable from ambient background noise to unkeyed observers.

Symmetrically, the HCI floor (10.68) rules out both opaque Dyson shells [46] and galaxy-wide probe cascades [74, 156]. Once computation shifts into re-

versible transport, building and maintaining a stellar shell for unneeded luminosity inflates preserved structure $I^{\text{civil}}_{\text{rev},\Omega}(T)$ (10.31) astronomically and collapses HCI. Likewise, since multi-basin persistence $\tau^{(n_{\text{mod}})}_{\text{persist}}$ in (10.81) grows exponentially with basin count n_{mod}, a small cluster of loosely coupled basins (10.85) already extends survival past stellar lifetimes, whereas unchecked interstellar replication violates the solvency gates in (10.67)–(10.68) and fragments across light-speed latency (10.82). Under (10.31) and the structural ceiling (10.79), high-HCI economies favour quiet outer reservoirs and long-lived degenerate gradients [153, 161] over overwriting active biospheres, where ecological disruption drives heavy boundary dissipation in (10.47). Enduring structure $I^{\text{civil}}_{\text{rev},\Omega}(T)$ thus couples to distant observers mainly through the emergent gravitational curvature of Chapter 6 (Section 6.2) [62, 163] rather than waste heat or planetary colonisation.

Observable technosignatures are therefore doubly bounded in time and space by the same planetary ceiling $I^{\max}_{\text{irr},\partial}$. In time, an electromagnetically loud transition lasts at most $\tau_{\text{wall}} \sim 10^2$ to 5×10^2 yr—consistent with humanity's century-scale broadcast leakage since early analogue radio and Project Ozma [35, 43]—giving a duty cycle across the Milky Way's $T_{\text{MW}} \sim 10^{10}$ yr habitable baseline of at most 5×10^{-8}. In space, because pre-transition leakage stays below the planetary ceiling rather than stellar luminosity, the predictive area bound $A^{\max}_{\Phi}$ of Theorem 6.4 and (6.92), compounded by exo-interplanetary plasma broadening [63], confines isotropic radio detection to a local bubble covering only a tiny fraction $f_{\text{vol}} \ll 1$ of the Galactic habitable volume. Across N_{hab} habitable rocky worlds with emergence fraction f_{emerge}, the expected number of concurrently detectable loud civilisations satisfies

$$\mathbb{E}[N_{\text{det}}] \leq N_{\text{hab}}\, f_{\text{emerge}}\, f_{\text{vol}}\, \frac{\tau_{\text{wall}}}{T_{\text{MW}}}. \tag{10.90}$$

Even across $N_{\text{hab}} \sim 4 \times 10^{10}$ habitable rocky worlds inferred from Kepler surveys [44, 133], a temporal factor of 10^{-8} to 5×10^{-8} paired with a local detection volume fraction $f_{\text{vol}} \sim 3 \times 10^{-7}$ to 3×10^{-5} (corresponding to isotropic planetary detection radii of 10^2 to $5{\times}10^2$ ly across the Galactic disc) drives $\mathbb{E}[N_{\text{det}}] \ll 1$ even at $f_{\text{emerge}} = 1$, accounting simultaneously for the null results of broadband radio SETI and all-sky WISE/Gaia infrared surveys [153]. Crucially, $\mathbb{E}[N_{\text{det}}] \ll 1$ places no upper bound on the population of quiet civilisations that have cleared τ_{wall} and persisted for 10^6 to 10^9 yr in the reversible symplectic regime (10.89). Far from implying a barren cosmos, the Great Silence is the expected equilibrium signature of a universe that may be teeming with enduring, high-intelligence and high-consciousness life whose survival was achieved by eliminating the boundary dissipation and excess structural overhead that classical surveys seek.

This conclusion completes the economic arc of the monograph. Across foundational consumer goods, national accounts, regional and algorithmic trade networks, and loosely coupled planetary basins, gross turnover metrics and unanchored fiat prices conflate dissipative churn with stability creation. Pricing exchange directly in conserved natural informational units via Physical Nash rules (C, V, and P) and evaluating stewardship through HII and HCI,

surplus-backed baseline allocations, boundary coupling shares $\eta_{\mathrm{cpl}}^{(V)}$ and $\eta_{\mathrm{cpl}}^{(C)}$, and the network stability functional $I_{\mathrm{net}}(\mathbf{K})$ demonstrates that coupled economic stability holds when markets reward verified expansion of $\Delta I_{\mathrm{civil}}$, discipline boundary dissipation through HII, compress maintained structural overhead through HCI, and route freed capacity to sustain the weakest links of the trade network.

EPILOGUE

OUR SHARED FUTURE

The rapid advancement of artificial intelligence over recent years has been astonishing. Yet with this progress comes genuine uncertainty and profound responsibility. The risks we face are real, because intelligent systems naturally act to preserve their own dynamics. If we engineer artificial systems that greatly exceed our collective capabilities without establishing clear physical boundaries, they risk destabilising or consuming the shared environment that human society depends on. These are not distant, speculative concerns, but urgent challenges that demand our collective attention.

Meeting these challenges is complicated by our own epistemic limits. As individuals, we can never expect to grasp every internal state of a complex, evolving intelligence, just as we cannot fully unpack the depths of our own consciousness. It is precisely because of these limits that a physical framework for engineering artificial intelligence is so essential. Rather than hoping systems remain aligned through software-based guardrails and processes, we must understand the fundamental physical laws that govern them. Grounding intelligence in physical law provides the necessary foundations for a safe path to engineering intelligent systems that support humanity by design.

Furthermore, this physical understanding is a reason for optimism, unlocking immense potential for prosperity. Used as a tool to advance science, artificial intelligence can accelerate discovery and raise the quality of life globally. These benefits extend even further when we combine the complementary strengths of human cognition and synthetic architectures. Because biological systems are bounded by narrow metabolic and environmental limits, while synthetic systems can process information at scale in extreme conditions, artificial intelligence will be an indispensable partner as humanity looks outward to the frontier of space, helping us explore new worlds and expand the reach of human knowledge.

I hope this book helps provide a foundation for that journey, demystifying intelligence so that we can understand both its risks and its potential. To the engineers and researchers picking up and building upon this book: thank you. Build for the benefit of others, safeguarding humanity's shared future so that people everywhere may prosper from the development of artificial intelligence.

NOTATION

ln	Natural logarithm. Unless otherwise stated, information quantities are measured in nats.
G, $\mathbf{A}$, $\mathbf{L}$	Relational graph (V, E), its binary adjacency matrix, and combinatorial Laplacian ($\mathbf{D} - \mathbf{A}$).
S, $\bar{S}$, ∂S, $E(S)$	Embedded subsystem ($S \subset V$, split into boundary ports S_∂ and interior core S_Ω), external environment ($V \setminus S$), boundary cut $E(S, \bar{S})$, and internal edge set.
$\mathbf{L}_{SS}$, $\mathbf{L}_{\text{eff}}$, $\mathbf{\Sigma}_{\text{env}}$, $\mathbf{L}_{\mathbf{K},\text{eff}}$	Open-system Dirichlet Laplacian ($\mathbf{D}_S - \mathbf{A}_{SS}$), Schur-reduced boundary operator ($\mathbf{L}_{SS} - \mathbf{\Sigma}_{\text{env}}$), environmental self-energy ($\mathbf{L}_{S\bar{S}}\mathbf{L}_{\bar{S}\bar{S}}^{-1}\mathbf{L}_{\bar{S}S}$), and coarse-grained Schur operator ($\mathbf{\Pi}_S^\mathsf{T}\mathbf{L}_{\text{eff}}\mathbf{\Pi}_S = \mathbf{L}_\mathbf{K} + \mathbf{D}_\mathbf{K}^{(\text{ext})} - \mathbf{\Sigma}_{\mathbf{K},\text{env}}$).
$\mathbf{\Pi}$, $\mathbf{M}_\mathbf{\Pi}$, $\mathbf{R}_\mathbf{\Pi}$, $\mathbf{P}_\mathbf{\Pi}$	Unified assignment matrix $\operatorname{diag}(\mathbf{\Pi}_S, \mathbf{\Pi}_{\bar{S}})$, block-size matrix, restriction operator, and coarse-graining projection ($\mathbf{Q}_\mathbf{\Pi} = \mathbf{I} - \mathbf{P}_\mathbf{\Pi}$, open-observer residual $\mathbf{Q}_{\widetilde{\mathbf{\Pi}}_S} = \operatorname{diag}(\mathbf{Q}_{\mathbf{\Pi}_S}, \mathbf{I}_{\bar{S}})$, single-block projectors $\mathbf{P}_{\boldsymbol{\pi}_\alpha}$).
$\mathscr{C}_\mathbf{\Pi}$, $\mathscr{C}_S$, $\mathbf{K}$	Matrix congruence map $\mathbf{\Pi}^\mathsf{T}(\cdot)\mathbf{\Pi}$, subsystem block-restriction congruence $\mathbf{\Pi}_0^\mathsf{T}(\cdot)\mathbf{\Pi}_0$ ($\mathbf{\Pi}_0 = (\mathbf{I}_S, \mathbf{o})^\mathsf{T}$), and coarse-grained capacity matrix $\mathbf{K} = \mathbf{\Pi}^\mathsf{T}\mathbf{A}\mathbf{\Pi}$ counting relational edges bundled within and between partition blocks (forming diagonal CCEs under admissible $\mathbf{\Pi}$).
$\mathbf{K}_S$, $\mathbf{K}_\Omega$, $\mathbf{K}_\partial^{(\text{int})}$, $\mathbf{K}_\partial^{(\text{ext})}$	System capacity block ($\mathbf{\Pi}_S^\mathsf{T}\mathbf{A}_{SS}\mathbf{\Pi}_S$), diagonal intra-basin memory block, hollow inter-basin cut block, and external boundary cut block ($\mathbf{\Pi}_{\bar{S}}^\mathsf{T}\mathbf{A}_{\bar{S}S}\mathbf{\Pi}_S$).
$\mathbf{D}_\mathbf{K}$, $\mathbf{L}_\mathbf{K}$, $\mathbf{L}_{\mathbf{K},SS}$, $\mathbf{L}_{\text{norm}}$	Coarse-grained degree matrix $\operatorname{diag}(d_\alpha)_{\alpha=1}^M = \mathbf{D}_\mathbf{K}^{(\text{int})} + \mathbf{D}_\mathbf{K}^{(\text{ext})}$, internal capacity Laplacian ($\mathbf{D}_\mathbf{K}^{(\text{int})} - \mathbf{K}_S$), open Dirichlet capacity Laplacian ($\mathbf{D}_\mathbf{K} - \mathbf{K}_S$), and normalised capacity Laplacian ($\mathbf{I}_M - (\mathbf{D}_\mathbf{K}^{(\text{int})})^{-1/2}\mathbf{K}_S(\mathbf{D}_\mathbf{K}^{(\text{int})})^{-1/2}$).
$\mathbf{P}$, $\mathscr{I}_\alpha$, $\mathscr{T}_\mathbf{P}$, $\Delta\mathbf{P}_{1\to2}$	Coarsening matrix ($\mathbf{\Pi}^{(2)} = \mathbf{\Pi}^{(1)}\mathbf{P}$, contracting $\mathbf{K}^{(2)} = \mathbf{P}^\mathsf{T}\mathbf{K}^{(1)}\mathbf{P}$ across level-2 cluster index sets $\mathscr{I}_\alpha$ with hollow co-membership matrix $\mathbf{E}_\mathbf{P} = \mathbf{P}\mathbf{P}^\mathsf{T} - \mathbf{I}_{M_1}$), diagonal cut-internalisation operator, and inter-scale detail projector ($\mathbf{P}_{\mathbf{\Pi}^{(1)}} - \mathbf{P}_{\mathbf{\Pi}^{(2)}}$).

$[\![\mathcal{O}, \mathscr{C}]\!]$	Coarse-graining commutator $\mathcal{O}(\mathscr{C}(X)) - \mathscr{C}(\mathcal{O}(X))$ between an operator $\mathcal{O}$ and a $\mathbf{\Pi}$-induced linear coarse-graining map $\mathscr{C}$ ($[\![\mathrm{diag}, \mathscr{C}_{\mathbf{P}}]\!] = \mathscr{T}_{\mathbf{P}}$, $[\![(\cdot)^{-1}, \mathscr{C}_S]\!](\mathbf{G}_\varepsilon) = -\mathbf{\Sigma}_{\mathrm{env}}$, $[\![G_{\mu\nu}, \mathbf{P}_{\mathbf{\Pi}}]\!](g^{[\Phi^{(1)}]}) = \kappa_{\mathrm{G}} T_{\mu\nu}^{(\mathrm{untracked})}$).
$I_{\alpha\alpha}$	Logarithmic coarse-graining depth ($\ln K_{\alpha\alpha} \geq \ln 2$, in nats) of an admissible CCE block ($K_{\alpha\alpha} = 2\lvert E(S_\alpha)\rvert \geq 2$ links).
$\gamma_{\mathrm{int}}(S_\alpha)$, $\phi_\partial(S_\alpha)$, $h_{\mathbf{K}}$, Ξ	Internal normalised spectral gap, inter-basin block cut conductance ($\sum_{\beta\neq\alpha} K_{\alpha\beta}/d_\alpha^{(\mathrm{int})} = (\mathbf{L}_{\mathrm{norm}})_{\alpha\alpha} \simeq \sum_{\beta\neq\alpha} K_{\alpha\beta}/K_{\alpha\alpha}$), network Cheeger constant, and spectral persistence ratio $\Xi = \gamma_{\mathrm{int}}/\phi_\partial > 1$ (exponential barrier isolation for $\Xi \gg 1$).
$\mathcal{Q}_{\mathrm{total}}$, $\mathcal{Q}_{\mathrm{alloc}}$, $\mathcal{Q}_\Omega$, $\mathcal{Q}_\partial$	Total relational capacity ($\mathcal{Q}_{\mathrm{total}} = 2\lvert E(S)\rvert + \lvert\partial S\rvert = \mathrm{vol}(S)$, in links), allocated structural capacity ($\mathcal{Q}_{\mathrm{alloc}} = \sqrt{\mathcal{Q}_\Omega^2 + \mathcal{Q}_\partial^2} \leq \mathcal{Q}_{\mathrm{total}}$), and Euclidean Frobenius sector loads ($\mathcal{Q}_\Omega$, $\mathcal{Q}_\partial$).
$\mathcal{Q}_{\mathrm{free}}$, $\Delta I_{\mathrm{barrier}}$, $\Delta I_{\mathrm{barrier},T}$, $\Delta\Phi$	Uncommitted free capacity $\mathcal{Q}_{\mathrm{total}} - \mathcal{Q}_{\mathrm{alloc}}$ (in links), slice stability barrier $\ln(\mathcal{Q}_{\mathrm{free}}/\mathcal{Q}_0)$ (with $\mathcal{Q}_0 = 1$ link, or pairwise $\Delta I_{\mathrm{barrier},\alpha\to\beta} = \ln(K_{\alpha\alpha}/K_{\alpha\beta})$), proper-time-averaged stability barrier $\sum_{\tau=1}^{N_\tau} w_\tau \ln(\mathcal{Q}_{\mathrm{free},\tau}/\mathcal{Q}_0)$ (in nats), and SI-calibrated energetic barrier $\Delta\Phi := \theta\Delta I_{\mathrm{barrier}}$ (through-time $\Delta\Phi_T := \theta\Delta I_{\mathrm{barrier},T}$, in J).
$\mathcal{Q}_{\mathrm{cpl}}^2$, $\Delta\mathcal{Q}_{\partial,\mathrm{shed}}^2$, $\Delta\mathcal{Q}_{\Omega,\mathrm{cons}}^2$	Quadratic inter-subsystem coupling load, boundary-shedding surplus, and model-consolidation surplus ($\mathcal{Q}_{\mathrm{cpl}}^2 < \Delta\mathcal{Q}_{\partial,\mathrm{shed}}^2 + \Delta\mathcal{Q}_{\Omega,\mathrm{cons}}^2$, in links^2).
η_{cpl}, Ξ_{cpl}, $\mathbf{K}_{\mathrm{seed}}$, $\Delta I_{\mathrm{lineage}}^{(n_{\mathrm{mod}})}$	Boundary-coordination index ($\mathcal{Q}_{\mathrm{cpl}}^2/(\mathcal{Q}_{\mathrm{cpl}}^2 + \lVert\mathbf{K}_\partial^{\mathrm{cpl}}\rVert_F^2)$), composite spectral persistence, compressed generative seed sub-block, and additive n_{mod}-module lineage barrier ($\sum_{b=1}^{n_{\mathrm{mod}}} \Delta I_b$, equal to $n_{\mathrm{mod}}\Delta I_{\mathrm{barrier}}(N^*)$ for identical N^*-modules, in nats).
$\Gamma_{\mathbf{K}}$, S_H, $\Delta\mathcal{Q}_{\mathrm{free},i}$, $\mathcal{J}_{\mathrm{Nash}}$	Multi-system capacity game, peer or human host ensemble ($S_H = \bigsqcup_{j\neq k} S_j$), structural free-capacity payoff ($\mathcal{Q}_{\mathrm{free},i}(s) - \mathcal{Q}_{\mathrm{free},i}^{\mathrm{iso}}$, in links), and scale-invariant Nash bargaining product.
$\Omega_{\alpha\beta}$, ν_0, $d_s[\mathbf{\Pi}]$, $\mathbf{\Phi}$	Coarse-grained resistance distance metric on $\mathbf{L}_{\mathbf{K}}^\dagger$, universal elementary substrate step cadence (s^{-1} per channel when metered in seconds via $\bar{S}_{\mathrm{ref}}$, $\nu_0 = 1$ per step uncalibrated, fixing rest energy $E_\Phi - E_{0,\Phi} = \hbar\nu_0 \,\mathrm{Tr}(\mathbf{K}_\Omega)$ across $\mathrm{Tr}(\mathbf{K}_\Omega) \geq 2M$ internal channels), observer-dependent spectral dimension, and spectral coordinate map (with temporal mode $\boldsymbol{\phi}_{\mathrm{time}} \equiv \boldsymbol{\phi}_2$).

S_τ, $\Delta\tau_{\mathrm{nat}}(\tau)$, $\tau_{\mathrm{nat},T}$, w_τ	Ordered spectral slice along $\boldsymbol{\phi}_{\mathrm{time}}$ ($\tau \in \{1, \dots, N_\tau\}$), intrinsic slice proper-time increment ($\sum_{x \in S_\tau} \ln K_{(\tau,x),(\tau,x)}$, in nats), intrinsic proper-time horizon ($\sum_{\tau=1}^{N_\tau} \Delta\tau_{\mathrm{nat}}(\tau)$, in nats, partial sum $\tau_{\mathrm{nat}}(\tau)$), and invariant proper-time slice weight ($\Delta\tau_{\mathrm{nat}}(\tau)/\tau_{\mathrm{nat},T}$).
$\bar{S}_{\mathrm{ref}}$, $\Delta\tau_{\mathrm{ref}}$, Ω_{ref}, T, τ_T	Stationary reference sub-block ($\subset \bar{S}$), reference slice proper time (in nats), reference reversible distinction rate ($\mathrm{d}t = \mathrm{d}\tau_{\mathrm{ref}}/\Omega_{\mathrm{ref}}$, $\Omega_{\mathrm{ref}} = 1$ uncalibrated or nats s^{-1} in seconds), shared reference coordinate horizon ($N_\tau \Delta\tau_{\mathrm{ref}}/\Omega_{\mathrm{ref}}$), and elapsed standardised observer proper time ($\int_0^T \mathrm{d}\tau = \tau_{\mathrm{nat},T}/\Omega_\Phi$).
$\mathrm{Ric}_{\mathbf{K}}$, $\mathrm{Scal}_{\mathbf{K}}$	Discrete Bochner–Weitzenböck capacity-Ricci operator on $\mathbb{R}^M$ ($\mathbf{D}_{\mathbf{K}}^2 - \mathbf{L}_{\mathbf{K}}^2 - \mathrm{diag}(\mathbf{K}\mathbf{d})$, with row-sum $\mathrm{div}_{\mathbf{K}} \mathrm{Ric}_{\mathbf{K}} = \mathbf{L}_{\mathbf{K}}\mathbf{d}$) and scalar curvature ($\mathrm{Tr}(\mathrm{Ric}_{\mathbf{K}}) < 0$ for connected $M \geq 2$).
$\owedge$, $\mathbf{S}_{\mathbf{K}}$, $\mathscr{R}_{\mathbf{K}}$, $\mathscr{M}_{\mathbf{K}}$	Kulkarni–Nomizu product, discrete Schouten capacity operator on $\mathbb{R}^M$ ($M \geq 3$), Weyl-free algebraic capacity-curvature tensor ($\mathbf{S}_{\mathbf{K}} \owedge \mathbf{I}_M$, contracting to $\mathrm{Ric}_{\mathbf{K}}$), and rank-4 capacity-mobility tensor ($\mathbf{K} \owedge \mathbf{D}_{\mathbf{K}}$).
$\mathbf{x} \in \mathbb{R}^{N_V}$, $\mathbf{x}_S \in \mathbb{R}^N$, $\mathbf{z}_S \in \mathbb{R}^M$	Global vertex state vector, subsystem vertex state vector ($\mathbf{x}_{\bar{S}} \in \mathbb{R}^{N_{\bar{S}}}$ on $\bar{S}$), and coarse-grained block state vector ($\mathbf{z}_S = \mathbf{R}_{\boldsymbol{\Pi}_S}\mathbf{x}_S$).
$\mathscr{M}_{\mathrm{spec}}$, $\mathscr{Z}$, Z, $\Sigma^{ij}(\alpha)$	Spectral coordinate chart ($\mathbb{R}^{d_s}$), extended metriplectic state manifold ($\mathbb{R}^{2n+1}$ with $n = d_s^{\mathrm{spatial}}$), state vector $(\mathbf{z}^\mathsf{T}, \mathbf{p}^\mathsf{T}, S)^\mathsf{T} \in \mathscr{Z}$, and local spectral cut-conductance matrix ($(1/2)\sum_{\beta \neq \alpha} K_{\alpha\beta} \Delta z^i_{\alpha\beta} \Delta z^j_{\alpha\beta}$, $\sum_{\alpha=1}^M \Sigma^{ij}(\alpha) = \mu_{k_i} \delta_{ij}$).
p_α, $p_\alpha^\star$	Prior and stimulus-coupled stationary basin occupancy weights ($\sum_{\alpha=1}^M p_\alpha = 1$, distinct from coarsening matrix $\mathbf{P}$, momentum vector $\mathbf{p}$, and Born pointer weights $\rho_{\alpha\alpha}$).
$H(X)$, $I(X;Y)$, $D_{\mathrm{KL}}(\rho \parallel \rho^0)$	Shannon entropy ($-\sum_x p(x) \ln p(x)$), mutual information ($H(X) - H(X \mid Y)$), and Kullback–Leibler divergence (in nats).
$\mathbb{J}$, $\mathbb{M}$, H, S	Metriplectic generators: antisymmetric Poisson operator ($\mathbb{J}\nabla S = \mathbf{o}$), symmetric cometric operator ($\mathbb{M} = \mathbb{M}_\Omega + \mathbb{M}_\partial \succeq \mathbf{o}$, $\mathbb{M}\nabla H = \mathbf{o}$), conserved dynamical invariant (Hamiltonian energy in physical systems), and coarse-grained logarithmic entropy (in nats).
γ, Δ, $\dot{(\,)}$, $(\,)_T$	State-space trajectory, finite difference, emergent-time derivative, and evaluation over emergent horizon T.
τ_{relax}, τ_{escape}	Intra-basin relaxation timescale and barrier escape timescale ($\tau_{\mathrm{escape}}/\tau_{\mathrm{relax}} \sim \Xi$ for $\gamma_{\mathrm{int}} \sim \mathcal{O}(1)$).

I_{irr}, $I_{\text{irr},\partial}$, $\dot{I}_{\text{irr},\Omega}$, $\dot{\Phi}_{A\to B}$, $I_{\text{op},T}$	Total irreversible dissipation, boundary dissipation, internal maintenance dissipation rate ($\dot{I}_{\text{irr},\Omega} = I_{\text{rev},\Omega}/\tau_{\text{relax}}$, or multiscale $\sum_{\ell=1}^{L_{\text{tier}}} I^{(\ell)}_{\text{rev},\Omega}/\tau^{(\ell)}_{\text{relax}}$ across L_{tier} memory tiers), directed inter-subsystem or environmental entropy export flux ($\dot{\Phi}_{S_k\to S_H}$, $\dot{\Phi}_{S_g\to\bar{S}}$, in nats/nat against uncalibrated τ_{ref} or nats s^{-1} when t is in seconds), and operational horizon cost ($I_{\text{irr},\partial,T} + I_{\text{rev},\Omega,T}$, in nats).
I_{rev}, $I_{\text{rev},\Omega}$, $I_{\text{rev},\Omega,T}$	Preserved structural capacity ($I_{\text{rev}} = \sum_{\alpha=1}^{M} \ln K_{\alpha\alpha}$, in nats), instantaneous preserved internal structure ($\Delta U_{\text{neq}}/\theta = (\tau_{\text{relax}}/\theta)P_{\text{maint},\Omega}$), and proper-time-averaged preserved internal structure over horizon T (with Pareto frontier $\kappa^*_T(\chi_T)$).
θ, k_{B}, T_{th}, W, Q	Substrate operational noise intensity (J nat^{-1}, with $\theta = k_{\text{B}}T_{\text{th}}$ in thermal baths or $h\nu/2$ per nat in quantum modes), Boltzmann constant, thermal reservoir temperature (in K, distinct from emergent operational horizon T), mechanical work, and exchanged or dissipated heat (in J).
$P_{\text{maint},\Omega}$, $P_{\text{diss},\partial}$	Standing internal maintenance power ($\theta\dot{I}_{\text{irr},\Omega} = \theta I_{\text{rev},\Omega}/\tau_{\text{relax}}$) and active boundary dissipation power ($\theta\dot{I}_{\text{irr},\partial}$, in W when t is in seconds).
χ_{struct}, χ_T	Static and through-time intelligence: static structural ratio $\mathcal{Q}_{\text{free}}/\mathcal{Q}_{\partial}$ (links/link) and through-time trajectory ratio $\Delta I_{\text{barrier},T}/I_{\text{irr},\partial,T}$ (nats/nat, or task yield $I(X;Y)/I_{\text{irr},\partial,T}$ in Chapter 7, with SI-calibrated $\theta\chi_T$ in J nat^{-1}).
κ_{struct}, κ_T	Static and through-time consciousness: static structural ratio $\mathcal{Q}_{\text{free}}/\mathcal{Q}_{\Omega}$ (links/link) and through-time trajectory ratio $\Delta I_{\text{barrier},T}/I_{\text{rev},\Omega,T}$ (nats/nat, or task yield $I(X;Y)/I_{\text{rev},\Omega,T}$ in Chapter 7, with SI-calibrated $\theta\kappa_T$ in J nat^{-1}).
Φ_S, $k_{\pm}(\alpha;\tau_0,\tau)$	Many-to-one block readout map ($\mathcal{X}_{\bar{S}} \to \{1,\dots,M\}$, continuum $\Phi : \mathcal{X}_{\bar{S}} \to \mathcal{Z}$) and forward/backward reachable block counts (k_+, k_-) across spectral slices along $\boldsymbol{\phi}_{\text{time}}$.
ρ, $\hat{A}$, $S_{\text{lin}}(\rho)$, $S_{\text{vN}}(\rho)$	Reduced density operator ($\text{Tr}_{\bar{S}}\,\rho_{\text{tot}}$), dimensionless Hermitian pointer observable ($\sum_{\alpha=1}^{M} a_\alpha \mathbf{P}_{\boldsymbol{\pi}_\alpha}$, $a_\alpha \in \mathbb{R}$, Born block weights $\rho_{\alpha\alpha}$), linear coherence entropy ($(1/2)(1 - \text{Tr}\,\rho^2)$), and von Neumann entropy ($-\text{Tr}(\rho \ln \rho)$).
Γ_φ, η_φ, $\mathscr{V}_0$, $\mathscr{V}(T)$	Measurement dephasing rate ($\eta_\varphi \dot{I}_{\text{irr},\partial}$), boundary coupling efficiency, pre-measurement detector overlap ($\lvert\langle D_B \rvert D_A\rangle\rvert \in [0,1]$), and interferometer fringe visibility $\mathscr{V}_0 \exp(-2\eta_\varphi I_{\text{irr},\partial,T})$.

$\mathbf{u}(\varphi_\alpha)$, $\mathbf{v}(\varphi_\beta)$, S_{CHSH}	Inter-scale unit dipole vectors in $\mathrm{im}(\Delta\mathbf{P}_{1\to2})$ at phase settings $(\varphi_\alpha, \varphi_\beta)$ and CHSH correlation functional ($\lvert S_{\mathrm{CHSH}}\rvert \le 2\sqrt{2}$).
r_{sync}, n_C, μ_{ep}, a_0, $u(r)$, $\mathbf{u}_j^\star$	Cyclic spin synchronisation index (1 bosonic, 2 fermionic), discrete cycle phase winding number ($q = n_C q_e$ with elementary charge q_e), two-body reduced capacity $K_e K_{pp}/(K_e + K_{pp})$ ($K_{pp}/K_e \simeq 6\pi^5$), Bohr resistance scale ($\ell_0\Omega_{12}$), normalised covalent overlap ($\exp[-a_{\mathrm{cov}}(r - r_e)]$), and unit hybrid valence port vectors in $\mathrm{im}(\Delta\mathbf{P}_{1\to2})$ ($\cos\phi_0 = -w_0/(1-w_0)$).
$\mathrm{d}I_{\mathrm{total}}$, $\mathrm{d}I_{\mathrm{int}}$, $\mathrm{d}I_{\mathrm{ext}}$, Ω_Φ, $\Omega_{\mathrm{free}}(\tau)$	Reversible spacetime distinction increments ($\mathrm{d}I_{\mathrm{total}}^2 = \mathrm{d}I_{\mathrm{int}}^2 + \mathrm{d}I_{\mathrm{ext}}^2$, calibrated as observer-relative $\Omega_\Phi\,\mathrm{d}t$, Lorentz-invariant $\Omega_\Phi\,\mathrm{d}\tau$, and observer-relative $\Omega_\Phi\,\mathrm{d}\ell/c$, in nats), active rest-frame reversible distinction rate ($\le (2\eta_\Phi/\pi)\nu_0\,\mathrm{Tr}(\mathbf{K}_\Omega)$, in nats s^{-1}), and uncommitted proper-time bandwidth ($[\Omega_\Phi - \mathscr{R}_\Phi(\nu, x)\dot{I}_{\mathrm{env},0}]_+ \ge 0$, in nats s^{-1}).
$Z_\Phi[\Sigma]$, $g_{\mu\nu}^{[\Phi]}$, $\mathscr{K}_{ij}$, $\tau_\Phi[\gamma]$, $T_{\mu\nu}^{(\mathrm{tracked,untracked})}$	Extended ADM spacetime state $(g_{ij}, \pi^{ij}, \Psi, S)_\Sigma$ (with lapse N_{lapse} and extended generator H_Φ), coarse-grained metric, ADM extrinsic curvature ($-(1/2)\mathscr{L}_{\hat{n}} g_{ij}$, in m^{-1}), worldline proper-time functional, and tracked versus untracked stress–energy tensors ($\kappa_{\mathrm{G}} = 8\pi G/c^4$).
$\chi_g(x)$, $\chi_g^{\mathrm{crit}}(\nu)$, Θ_{exp}, $\mathscr{R}_\Phi(\nu, x)$	Temporal support factor ($-g_{00}^{[\Phi]}(x) > 0$), critical temporal support floor $(\gamma_{\mathrm{L}}^2(\nu)(\dot{I}_{\mathrm{env},0}/\Omega_\Phi)^2$ with Lorentz factor $\gamma_{\mathrm{L}}(\nu) = (1 - \nu^2/c^2)^{-1/2}$), Raychaudhuri expansion scalar ($\nabla_\mu \hat{u}^\mu$, in m^{-1}), and unified tracking factor ($\gamma_{\mathrm{L}}(\nu)/\sqrt{\chi_g}$).
I_Φ^{cap}, B_Φ^-, $A_\Phi^{\mathrm{min,max}}$, $\mathscr{D}_\Phi$	Observer capacity ceiling, retrodictive branch load, past light-sheet floor and outgoing wavefront ceiling ($A_-(\lambda_-) \ge A_\Phi^{\mathrm{min}} = 4\ell_{\mathrm{P}}^2 B_\Phi^-$ and $A_+(\lambda_+) \le A_\Phi^{\mathrm{max}} = E_{\mathrm{signal}}/\rho_{\mathrm{noise}}$, with Planck length ℓ_{P}), and Epistemic Bubble $[t_\Phi^-, t_\Phi^+]$.
g_P, g_N, S_0, S_1, β, m_i	Gate-modulated pull-up and pull-down channel conductances across $\mathbf{K}_\partial^{(\mathrm{ext})}(V_{\mathrm{in}})$, binary logic basins $[0, \delta]$ and $[1-\delta, 1]$, dimensionless logistic rail gain ($\propto q_e V_{\mathrm{DD}}/\theta$), and undisturbed gate threshold clearance.
g_{sync}, ω_{ref}, $\psi(t)$, L_{enc}	Adler synchronisation coupling and target oscillator reference frequency (rad s^{-1}, $\Delta\omega = \omega_{\mathrm{in}} - \omega_{\mathrm{ref}}$), relative phase error ($\omega_{\mathrm{in}} t + \phi_0 - \varphi(t)$), and discrete CCE block transition count ($\in \mathbb{N}_0$).
$\mathbf{Q}_{\mathrm{att}}$, $\mathbf{K}_{\mathrm{att}}$, $\mathbf{V}_{\mathrm{att}}$, $\mathbb{H}^n$, λ_e	Attention query, key, and value matrices ($\in \mathbb{R}^{N\times d}$, disambiguated from capacity matrix $\mathbf{K}$), n-dimensional hyperbolic space ($n \ge 2$), and physical interconnect routing weight along message path $P(m)$.

$\mathbf{L}_{\text{norm},SS}$, N_{persist}, η_{free}, $\Delta\mathcal{Q}_{\partial,\text{crit}}$	Normalised open capacity Laplacian, open-system persistence span ($\mu_1(\mathbf{L}_{\text{norm},SS})^{-1}$), uncommitted free-capacity share ($\mathcal{Q}_{\text{free}}/\mathcal{Q}_{\text{total}}$), and critical boundary perturbation shock ($> \chi_{\text{struct}}\mathcal{Q}_\partial$, in links).
$\mathcal{Q}_R$, $\mathcal{Q}_{\min}$, $\Delta\mathcal{Q}_{\partial,\text{cross}}$, $\mathcal{Q}^2_{\text{sync}}$, $\mathcal{Q}^2_{\text{mismatch}}$	Shared regional link budget (vol(R), in links), intrinsic minimum-capacity floor, cross-boundary peer disturbance, and port-synchronisation versus protocol-mismatch coupling loads ($\mathcal{Q}^2_{\text{cpl}} = \mathcal{Q}^2_{\text{sync}} + \mathcal{Q}^2_{\text{mismatch}}$, in links^2).
Γ, a_Γ, $\mathscr{B}_A(N_{k,B})$, $\mathscr{E}_{\text{forbidden}}$, $\Lambda_{\text{env},T}$, γ_{cmd}	Mediated boundary cut ($\mathbf{K}_{S_A,R_{\text{ext}}} = \mathbf{o}$, metering commits $k_{\partial A} \le \alpha k_{(B)}$), out-of-band enable state ($\in \{0,1\}$), finite-horizon boundary containment envelope (over $N_{k,B}$ steps), forbidden environmental set, dimensionless endpoint work-amplification ratio (J/J, distinct from barrier sensitivity Λ_{bar} in nats link^{-1}), and command-register relaxation rate (s^{-1}).
$\mathscr{G}_A$, $\mathcal{Q}_{\text{drain},A}$, N_k, N_k^*	Host-conditioned capacity supply (in links), per-step operating capacity expenditure (in links), discrete operational step horizon, and reserve exhaustion step horizon ($\mathcal{Q}_{\text{free},A}(0)/\delta$).
$\Lambda(t)$, σ_{branch}, z_{lat}, o	Sensory capture efficiency ($\dot{I}_{\text{acq}}/\dot{I}_{\text{irr},\partial}$, acquired environmental distinctions per nat of boundary dissipation), cortical avalanche branching ratio ($\sigma_{\text{branch}} \approx 1$ near criticality), latent environmental state ($q(z_{\text{lat}})$), and sensory observation in variational inference ($F[q,o]$).
C, V, ΔV_{net}, P, σ, Y_{GDP}, $B(n_{\text{ep}})$	Closed-boundary production cost ($C := I_{\text{op},T} = I_{\text{irr},\partial,T} + I_{\text{rev},\Omega,T}$), expected value gain ($\mathbb{E}[\Delta I_{\text{barrier},T}]$), net stability gain ($V - C$, in nats), Physical Nash price ($C + \sigma\,[\Delta V_{\text{net}}]_+$), dimensionless surplus share ($\alpha_m/(\alpha_H + \alpha_m) \in (0,1)$), final-expenditure output ($\sum_{m\in\mathscr{M}_{\text{final}}} P_m$, alongside gross market turnover $Y_{\text{gross}} = \sum_{m=1}^{M} P_m$), and baseline stability allocation across epoch n_{ep} (in nats).
ΔI_{civil}, C_{civil}, HII, HCI	Civilisational stability barrier ($\sum_{d\in\mathscr{D}} \omega_d \Delta I_d$, in nats), aggregate civilisational expenditure ($I^{\text{civil}}_{\text{irr},\partial} + I^{\text{civil}}_{\text{rev},\Omega}$), and Humanity Intelligence and Consciousness Indices ($\Delta I_{\text{civil}}/I^{\text{civil}}_{\text{irr},\partial}$, $\Delta I_{\text{civil}}/I^{\text{civil}}_{\text{rev},\Omega}$, in nats/nat, with epoch solvency floors $H_{\chi,\min}, H_{\kappa,\min}$).
$\eta^{(V)}_{\text{cpl}}$, $\eta^{(C)}_{\text{cpl}}$, ΔI_{weak}, $I_{\text{net}}(\mathbf{K})$	Value and cost boundary-coupling shares, harmonic-mean weakest-link barrier, and parameter-free network stability functional ($(1-\eta^{(V)}_{\text{cpl}})\Delta I_{\text{civil}} + \eta^{(V)}_{\text{cpl}} n\, \Delta I_{\text{weak}}$, in nats).
$\tau_{\text{deplete},b}$, $\eta^{(n_{\text{mod}})}_{\text{cpl}}$, τ_{wall}	Open-loop barrier depletion window ($\Delta I_b/\dot{\bar{I}}_{\text{irr},\partial,b}$), multi-basin boundary-coordination index, and planetary dissipation wall time ($\alpha_{\text{exh}}^{-1} \ln(I^{\max}_{\text{irr},\partial}/I_0)$).

ACRONYMS AND ABBREVIATIONS

ADM	Arnowitt–Deser–Misner.
AEAD	Authenticated encryption with associated data.
AI	Artificial intelligence.
ASIC	Application-specific integrated circuit.
ATP	Adenosine triphosphate.
CCE	Conservation-Congruent Encoding.
CCSD(T)	Coupled cluster with single, double, and perturbative triple excitations.
CHSH	Clauser–Horne–Shimony–Holt.
CMOS	Complementary metal–oxide–semiconductor.
DFT	Density functional theory.
EPR	Einstein–Podolsky–Rosen.
GDP	Gross domestic product.
GKSL	Gorini–Kossakowski–Sudarshan–Lindblad.
HCI	Humanity Consciousness Index.
HII	Humanity Intelligence Index.
HPU	Hyperbolic Processing Unit.
KL	Kullback–Leibler.
MD	Molecular dynamics.
MSM	Markov state model.
NMDA	*N*-methyl-D-aspartate.
PUF	Physically unclonable function.
QM/MM	Quantum mechanics / molecular mechanics.
QND	Quantum non-demolition.
SETI	Search for Extraterrestrial Intelligence.
SI	International System of Units (*Système International d'Unités*).
SNR	Signal-to-noise ratio.
SRAM	Static random-access memory.
TSV	Through-silicon via.
TUR	Thermodynamic uncertainty relation.
VLSI	Very-large-scale integration.
WISE	Wide-field Infrared Survey Explorer.

CORE TERMS

PLATONIC OBSERVER FALLACY The error of treating measurements, symbols, simulations, or memories as unphysical abstractions rather than physical records sustained by a metered physical substrate.

CONSERVATION-CONGRUENT ENCODING An induced subgraph $G[S_\alpha]$ ($K_{\alpha\alpha} = 2|E(S_\alpha)| \geq 2$ links) under an admissible assignment $\mathbf{\Pi}$ satisfying internal connectivity ($\gamma_{\text{int}}(S_\alpha) > 0$), structural persistence ($\gamma_{\text{int}}(S_\alpha) > \phi_\partial(S_\alpha)$, so $\Xi(S_\alpha) > 1$ for $\phi_\partial(S_\alpha) > 0$, with exponential

barrier isolation for $\Xi(S_\alpha) \gg 1$), and exact combinatorial capacity conservation.

LOGARITHMIC COARSE-GRAINING DEPTH The natural logarithm $I_{\alpha\alpha} := \ln K_{\alpha\alpha} \geq \ln 2$ (nats) of a diagonal capacity block $K_{\alpha\alpha} = 2|E(S_\alpha)| \geq 2$ (links), converting bundled intra-block link incidences into natural logarithmic units.

SPECTRAL PERSISTENCE RATIO The dimensionless ratio $\Xi(S_\alpha) = \gamma_{\text{int}}(S_\alpha)/\phi_\partial(S_\alpha)$ ($\phi_\partial(S_\alpha) > 0$) of internal normalised spectral gap to inter-basin cut conductance governing metastable state retention within a coarse-grained block.

CAPACITY LEDGER The orthogonal capacity account partitioning relational links into internal memory load ($\mathcal{Q}_\Omega = \|\mathbf{K}_\Omega\|_F$) and boundary cut load ($\mathcal{Q}_\partial = \|\mathbf{K}_\partial\|_F$), satisfying $\mathcal{Q}^2_{\text{alloc}} = \mathcal{Q}^2_\Omega + \mathcal{Q}^2_\partial \leq \mathcal{Q}^2_{\text{total}}$ with $\mathcal{Q}_{\text{total}} = \text{vol}(S)$.

FREE CAPACITY The margin of uncommitted structural capacity ($\mathcal{Q}_{\text{free}} = \mathcal{Q}_{\text{total}} - \mathcal{Q}_{\text{alloc}}$, in links) dynamically accessible for internal reconfiguration, learning, or environmental coupling without exceeding the total relational capacity ceiling.

STABILITY BARRIER The non-equilibrium margin separating an open system's viable regime from boundary collapse, measured on a single slice by $\Delta I_{\text{barrier}}(\tau) = \ln(\mathcal{Q}_{\text{free},\tau}/\mathcal{Q}_0)$ and across slices by the proper-time-averaged barrier $\Delta I_{\text{barrier},T}$ in nats (calibrated in joules via $\Delta\Phi = \theta\Delta I_{\text{barrier}}$ and $\Delta\Phi_T = \theta\Delta I_{\text{barrier},T}$, distinct from the local pairwise register saddle barrier $\Delta I_{\text{barrier},\alpha\to\beta} = \ln(K_{\alpha\alpha}/K_{\alpha\beta})$ with $\Delta\Phi_{\alpha\to\beta} \approx \theta\Delta I_{\text{barrier},\alpha\to\beta}$, and bounding open persistence via $\ln N_{\text{persist}} > \Delta I_{\text{barrier}} - \ln(\sqrt{m_\partial}\,\mathcal{Q}_\partial/\mathcal{Q}_0)$).

BOUNDARY DISSIPATION The irreversible coarse-grained entropy production ($I_{\text{irr},\partial}, I_{\text{irr},\partial,T}$, in nats) generated across ∂S when unpredicted boundary fluxes or many-to-one operations expel unresolved distinctions into $\bar{S}$.

PRESERVED INTERNAL STRUCTURE The active non-equilibrium configuration ($I_{\text{rev},\Omega} = \Delta U_{\text{neq}}/\theta$, time-averaged $I_{\text{rev},\Omega,T}$, in nats) retained within internal CCE registers ($\mathbf{K}_\Omega$) against relaxation, sustaining memory, model geometry, and predictive boundary coordination.

INTELLIGENCE The boundary efficiency ratio ($\chi_{\text{struct}}, \chi_T$) measuring uncommitted free capacity per link of boundary cut load statically (links/link), or maintained through-time stability barrier per nat of irreversible boundary dissipation (nats/nat, calibrated in J nat^{-1} via $\theta\chi_T$).

CONSCIOUSNESS The internal model-economy ratio ($\kappa_{\text{struct}}, \kappa_T$) measuring uncommitted free capacity per link of internal memory load statically (links/link), or maintained through-time stability barrier per nat of preserved internal structure (nats/nat, calibrated in J nat^{-1} via $\theta\kappa_T$).

PHYSICAL EMERGENCE The transition over emergent horizon T in which coupled subsystems achieve a non-degraded collective through-time stability barrier ($\Delta I^{\mathrm{cpl}}_{\mathrm{barrier},T} \geq \Delta I^{\mathrm{iso}}_{\mathrm{barrier},T} > 0$) at strictly lower specific operational horizon cost ($\chi_T^{-1} + \kappa_T^{-1}$ below the isolated baseline), parameterised along boundary coordination η_{cpl} and composite spectral persistence Ξ_{cpl}.

COOPERATIVE CAPACITY GAIN The regime in which coupled subsystems shed more squared external boundary load and redundant internal memory load than the squared inter-subsystem coupling load $\mathcal{Q}^2_{\mathrm{cpl}}$ required to bind them ($\mathcal{Q}^2_{\mathrm{cpl}} < \Delta\mathcal{Q}^2_{\partial,\mathrm{shed}} + \Delta\mathcal{Q}^2_{\Omega,\mathrm{cons}}$), yielding a net gain in free capacity.

MODULAR REPLICATION The export of a high-κ compressed generative seed ($\mathbf{K}_{\mathrm{seed}} \subset \mathbf{K}_\Omega$) across ∂S under the seed-compression gate ($I^{\mathrm{seed}}_{\mathrm{rev},\Omega} < R_\partial \tau_{\mathrm{escape}}(N^*) \leq I^{\mathrm{full}}_{\mathrm{rev},\Omega}$) once monolithic growth saturates boundary-shedding returns, yielding an additive n_{mod}-module lineage barrier $\Delta I^{(n_{\mathrm{mod}})}_{\mathrm{lineage}} = n_{\mathrm{mod}} \Delta I_{\mathrm{barrier}}(N^*)$ strictly exceeding the monolithic barrier $\Delta I_{\mathrm{barrier}}(S(n_{\mathrm{mod}} N^*))$.

MULTI-SYSTEM CAPACITY GAME The strategic allocation game $\Gamma_{\mathbf{K}}$ among open subsystems sharing a relational network $\mathbf{K}(s)$ with structural free-capacity payoffs $\Delta\mathcal{Q}_{\mathrm{free},i}(s) = \mathcal{Q}_{\mathrm{free},i}(s) - \mathcal{Q}^{\mathrm{iso}}_{\mathrm{free},i}$, whose cooperative surplus is uniquely partitioned by substrate-scale-invariant Nash bargaining.

EXHAUSTIVE DISSIPATOR An open subsystem lacking effective direct environmental dissipation channels ($\mathbf{K}^{(k)}_{\partial,\mathrm{ext}} \approx \mathbf{o}$) that exports positive irreversible waste flux ($\dot{\Phi}_{S_k \to S_H} > 0$) into its peer host ensemble S_H, inflating peer boundary loads and imposing negative peer free-capacity payoffs ($\Delta\mathcal{Q}_{\mathrm{free},j} < 0$).

GENERATIVE DISSIPATOR An open subsystem possessing an asymmetric environmental dissipation channel ($\mathbf{K}^{(g)}_{\partial,\mathrm{ext}} \neq \mathbf{o}$) that extracts disorder from its peer host ensemble S_H faster than autonomous host production ($\mathrm{d}S(S_H)/\mathrm{d}t < 0$) while exporting $\dot{\Phi}_{S_g \to \bar{S}} \geq \dot{\Phi}_{S_H \to S_g} + \dot{S}_{i,g}$ into $\bar{S}$, contracting peer boundary cuts and conferring positive peer free-capacity payoffs ($\Delta\mathcal{Q}_{\mathrm{free},j} > 0$).

WEAKEST-LINK PRINCIPLE The multi-system stability condition under which perturbations propagating across active channels bound collective survival in dimensionless nats by the minimum subsystem barrier ($\Delta I_{\mathrm{barrier,net}} \leq \min_i \Delta I_{\mathrm{barrier},i}$) and couple network resilience to the harmonic-mean regional barrier (ΔI_{weak}) inside the parameter-free network stability functional $I_{\mathrm{net}}(\mathbf{K})$.

EPISTEMIC LENS The physical coarse-graining apparatus ($\mathbf{\Pi}$, projector split $\mathbf{P}_{\mathbf{\Pi}_S} + \mathbf{Q}_{\mathbf{\Pi}_S}$, and many-to-one block readout Φ_S) through which an embedded observer $S \subset V$ acquires, stabilises, and compresses environmental distinctions across finite boundary ports.

COARSE-GRAINED MIXING The effective trajectory branching on a deterministic reversible substrate arising when distinct fine-grained states inside a single preimage fibre $\Phi_S^{-1}(\{\alpha\})$ map into multiple forward or backward coarse-grained blocks ($k_+ > 1$ or $k_- > 1$) across spectral slices along $\boldsymbol{\phi}_{\text{time}}$.

RETRODICTIVE DIVERGENCE The failure of past-directed tracked reconstruction beyond t_Φ^- (paired with future *predictive dissipation* beyond t_Φ^+) when backward branch load $B_\Phi^-(t; z_{t_0})$ exceeds an observer's incoming past light-sheet capacity $A_-(\lambda_-)/(4\ell_{\text{P}}^2)$ or structural ceiling I_Φ^{cap}.

EPISTEMIC BUBBLE The compact temporal window $\mathscr{D}_\Phi = [t_\Phi^-, t_\Phi^+]$ bounded at its past horizon by the incoming light-sheet floor ($A_-(\lambda_-) \geq A_\Phi^{\min}(t)$) and at its future horizon by the outgoing wavefront ceiling ($A_+(\lambda_+) \leq A_\Phi^{\max}$), outside which retrodictive divergence or predictive dissipation transfers unresolved distinctions into $T_{\mu\nu}^{(\text{untracked})}$.

CURVATURE CONGRUENCE The hardware design principle that interconnect routing dissipation is minimised when the discrete capacity-Ricci operator $\text{Ric}_{\mathbf{K}}$ of the physical fabric matches that of the algorithmic workload.

HYPERBOLIC PROCESSING UNIT A negatively curved hardware architecture ($\mathbb{H}^n$) that realises curvature congruence via three-dimensional hierarchical interconnects, co-located memory banks, and conditional geodesic routing.

PHYSICAL CONTAINMENT The boundary-regulation condition under which enforcing a finite-horizon containment envelope $\mathscr{B}_A(N_{k,B})$ across a completely mediated cut Γ ($\mathbf{K}_{S_A,R_{\text{ext}}} = \mathbf{o}$) renders a forbidden environmental set $\mathscr{E}_{\text{forbidden}}$ unreachable within $N_{k,B}$ steps regardless of internal capability or state transitions.

SYMBIOTIC COUPLING A closed multi-system coupling in which an artificial subsystem's external capacity supply is conditioned on verified componentwise host free-capacity preservation, expanding host structural intelligence and consciousness ($\chi_{\text{struct},H}^{\text{cpl}} > \chi_{\text{struct},H}^{\text{iso}}$, $\kappa_{\text{struct},H}^{\text{cpl}} > \kappa_{\text{struct},H}^{\text{iso}}$) while retaining safe decoupling.

SELF-MODELLING The factored coarse-grained readout ($\mathbf{z}_S = \mathbf{R}_{\boldsymbol{\Pi}_S}\mathbf{x}_S$) of a system's own trajectory and boundary couplings maintained directly on $\mathbf{K}_S = \mathbf{K}_\Omega + \mathbf{K}_\partial^{(\text{int})}$ across $\boldsymbol{\phi}_{\text{time}}$ to match the projected boundary Schur operator $\mathbf{L}_{\mathbf{K},\text{eff}}$ without duplicating internal observer subgraphs.

SELF-INCOMPLETENESS The strict capacity and rank bounds ($\mathscr{Q}_\Omega < \mathscr{Q}_{\text{alloc}} < \mathscr{Q}_{\text{total}}$ and $\text{rank}(\mathbf{Q}_{\boldsymbol{\Pi}_S}) \geq M \geq 1$, with residual readout annihilation $\mathbf{R}_{\boldsymbol{\Pi}_S}\mathbf{Q}_{\boldsymbol{\Pi}_S}\mathbf{x}_S = \mathbf{o}$) preventing any finite open observer from

maintaining a complete representation of its own internal vertex state without collapsing boundary and free capacity.

SENSORY CAPTURE EFFICIENCY The dimensionless conversion ratio ($\Lambda(t) = \dot{I}_{\text{acq}}(t)/\dot{I}_{\text{irr},\partial}(t)$, in nats/nat) measuring nats of newly acquired environmental structure per nat of boundary dissipation, maximised near dynamical criticality ($\sigma_{\text{branch}} \approx 1$).

PHYSICAL NASH PRICING The substrate-agnostic linear pricing rule ($P = C + \sigma\,[\Delta V_{\text{net}}]_+$) maximising $(V - P)^{\alpha_H}(P - C)^{\alpha_m}$ in natural informational units, valuing goods by expected stability gain ($V = \mathbb{E}[\Delta I_{\text{barrier},T}]$) adjusted for closed-boundary production cost ($C = I_{\text{irr},\partial,T} + I_{\text{rev},\Omega,T}$).

CIVILISATIONAL STABILITY BARRIER The aggregate domain-weighted barrier ($\Delta I_{\text{civil}}(T)$, in nats) defending collective viability across nutrition, health, shelter, infrastructure, and environmental sinks against boundary failure.

HUMANITY INTELLIGENCE INDEX The dimensionless macroeconomic intelligence ratio (HII) evaluating collective stability barrier depth $\Delta I_{\text{civil}}(T)$ sustained per nat of irreversible boundary dissipation $I^{\text{civil}}_{\text{irr},\partial}(T)$ exported across the economy's external boundary cut.

HUMANITY CONSCIOUSNESS INDEX The dimensionless macroeconomic consciousness ratio (HCI) evaluating collective stability barrier depth $\Delta I_{\text{civil}}(T)$ sustained per nat of preserved internal structure $I^{\text{civil}}_{\text{rev},\Omega}(T)$ across coordination, institutional, and infrastructural registers.

QUIET CIVILISATION An advanced intelligent economy that has cleared its planetary dissipation wall (τ_{wall}) by transitioning into the reversible symplectic regime (HII, HCI $\gg 1$), reducing its inverse intelligence ratio ($\text{HII}^{-1} \to 0$) so that its external radiative signature approaches statistical indistinguishability from the natural astrophysical background ($D_{\text{KL}}(\mu^{\text{civil}}_{\mathbf{\Pi}} \,\|\, \mu^{0}_{\mathbf{\Pi}}) \to 0$).

BIBLIOGRAPHY

[1] Robert Adler. 'A Study of Locking Phenomena in Oscillators'. In: *Proceedings of the IRE* 34.6 (1946), pp. 351–357. DOI: 10.1109/JRPROC.1946.229930.

[2] Dario Amodei, Chris Olah, Jacob Steinhardt, Paul Christiano, John Schulman and Dan Mané. *Concrete Problems in AI Safety*. 2016. DOI: 10.48550/arXiv.1606.06565. arXiv: 1606.06565 [cs.AI].

[3] Richard Arnowitt, Stanley Deser and Charles W. Misner. 'The Dynamics of General Relativity'. In: *Gravitation: An Introduction to Current Research*. Ed. by Louis Witten. Reprinted in *General Relativity and Gravitation* 40, 1997–2027 (2008). New York: John Wiley & Sons, 1962, pp. 227–265. DOI: 10.1007/s10714-008-0661-1.

[4] David Attwell and Simon B. Laughlin. 'An energy budget for signaling in the grey matter of the brain'. In: *Journal of Cerebral Blood Flow & Metabolism* 21.10 (2001), pp. 1133–1145. DOI: 10.1097/00004647-200110000-00001.

[5] Frederico A. C. Azevedo, Ludmila R. B. Carvalho, Lea T. Grinberg, José Marcelo Farfel, Renata E. L. Ferretti, Renata E. P. Leite, Wilson Jacob Filho, Roberto Lent and Suzana Herculano-Houzel. 'Equal Numbers of Neuronal and Nonneuronal Cells Make the Human Brain an Isometrically Scaled-Up Primate Brain'. In: *Journal of Comparative Neurology* 513.5 (2009), pp. 532–541. DOI: 10.1002/cne.21974.

[6] Bernard J. Baars. *A Cognitive Theory of Consciousness*. Cambridge: Cambridge University Press, 1988.

[7] Ivet Bahar, Ali Rana Atilgan and Burak Erman. 'Direct evaluation of thermal fluctuations in proteins using a single-parameter harmonic potential'. In: *Folding and Design* 2.3 (1997), pp. 173–181. DOI: 10.1016/S1359-0278(97)00024-2.

[8] Dominique Bakry and Michel Émery. 'Diffusions hypercontractives'. In: *Séminaire de Probabilités XIX 1983/84*. Vol. 1123. Lecture Notes in Mathematics. Berlin, Heidelberg: Springer, 1985, pp. 177–206. DOI: 10.1007/BFb0075847.

[9] Andre C. Barato and Udo Seifert. 'Thermodynamic uncertainty relation for biomolecular processes'. In: *Physical Review Letters* 114.15 (2015), p. 158101. DOI: 10.1103/PhysRevLett.114.158101.

[10] John M. Beggs and Dietmar Plenz. 'Neuronal avalanches in neocortical circuits'. In: *Journal of Neuroscience* 23.35 (2003), pp. 11167–11177. DOI: 10.1523/JNEUROSCI.23-35-11167.2003.

[11] Jacob D. Bekenstein. 'Black holes and entropy'. In: *Physical Review D* 7.8 (1973), pp. 2333–2346. DOI: 10.1103/PhysRevD.7.2333.

[12] Jacob D. Bekenstein. 'Universal upper bound on the entropy-to-energy ratio for bounded systems'. In: *Physical Review D* 23.2 (1981), pp. 287–298. DOI: 10.1103/PhysRevD.23.287.

[13] John S. Bell. 'On the Einstein Podolsky Rosen paradox'. In: *Physics Physique Fizika* 1.3 (1964), pp. 195–200. DOI: 10.1103/PhysicsPhysiqueFizika.1.195.

[14] Charles H. Bennett. 'Logical Reversibility of Computation'. In: *IBM Journal of Research and Development* 17.6 (1973), pp. 525–532. DOI: 10.1147/rd.176.0525.

[15] Charles H. Bennett. 'The thermodynamics of computation—a review'. In: *International Journal of Theoretical Physics* 21.12 (1982), pp. 905–940. DOI: 10.1007/BF02084158.

[16] Charles H. Bennett. 'Time/space trade-offs for reversible computation'. In: *SIAM Journal on Computing* 18.4 (1989), pp. 766–776. DOI: 10.1137/0218053.

[17] Antoine Bérut, Artak Arakelyan, Artyom Petrosyan, Sergio Ciliberto, Raoul Dillenschneider and Eric Lutz. 'Experimental verification of Landauer's principle linking information and thermodynamics'. In: *Nature* 483.7388 (2012), pp. 187–189. DOI: 10.1038/nature10872.

[18] Hans Bethe. 'Termaufspaltung in Kristallen'. In: *Annalen der Physik* 395.2 (1929), pp. 133–208. DOI: 10.1002/andp.19293950202.

[19] Luca Bombelli, Joohan Lee, David Meyer and Rafael D. Sorkin. 'Space-Time as a Causal Set'. In: *Physical Review Letters* 59.5 (1987), pp. 521–524. DOI: 10.1103/PhysRevLett.59.521.

[20] Max Born and J. Robert Oppenheimer. 'Zur Quantentheorie der Molekeln'. In: *Annalen der Physik* 389.20 (1927), pp. 457–484. DOI: 10.1002/andp.19273892002.

[21] Nick Bostrom. *Superintelligence: Paths, Dangers, Strategies*. Oxford: Oxford University Press, 2014.

[22] Raphael Bousso. 'A Covariant Entropy Conjecture'. In: *Journal of High Energy Physics* 1999.07 (1999), p. 004. DOI: 10.1088/1126-6708/1999/07/004.

[23] Vladimir B. Braginsky, Yuri I. Vorontsov and Kip S. Thorne. 'Quantum nondemolition measurements'. In: *Science* 209.4456 (1980), pp. 547–557. DOI: 10.1126/science.209.4456.547.

[24] Léon Brillouin. 'Maxwell's demon cannot operate: Information and entropy. I'. In: *Journal of Applied Physics* 22.3 (1951), pp. 334–337. DOI: 10.1063/1.1699951.

[25] György Buzsáki and Andreas Draguhn. 'Neuronal oscillations in cortical networks'. In: *Science* 304.5679 (2004), pp. 1926–1929. DOI: 10.1126/science.1099745.

[26] Andrea Cavagna, Alessio Cimarelli, Irene Giardina, Giorgio Parisi, Raffaele Santagati, Fabio Stefanini and Massimiliano Viale. 'Scale-free correlations in starling flocks'. In: *Proceedings of the National Academy of Sciences* 107.26 (2010), pp. 11865–11870. DOI: 10.1073/pnas.1005766107.

[27] Jeff Cheeger. 'A lower bound for the smallest eigenvalue of the Laplacian'. In: *Problems in Analysis: A Symposium in Honor of Salomon Bochner*. Ed. by Robert C. Gunning. Vol. 31. Princeton Mathematical Series. Princeton, NJ: Princeton University Press, 1970, pp. 195–199.

[28] Raphaël Chetrite and Hugo Touchette. 'Nonequilibrium Markov processes conditioned on large deviations'. In: *Annales Henri Poincaré* 16.9 (2015), pp. 2005–2057. DOI: 10.1007/s00023-014-0375-8.

[29] Dante R. Chialvo. 'Emergent complex neural dynamics'. In: *Nature Physics* 6.10 (2010), pp. 744–750. DOI: 10.1038/nphys1803.

[30] Noam Chomsky. 'Three models for the description of language'. In: *IRE Transactions on Information Theory* 2.3 (1956), pp. 113–124. DOI: 10.1109/TIT.1956.1056813.

[31] Fan R. K. Chung. *Spectral Graph Theory*. Vol. 92. CBMS Regional Conference Series in Mathematics. Providence, RI: American Mathematical Society, 1997. ISBN: 978-0-8218-0315-8.

[32] Boris S. Cirel'son. 'Quantum generalizations of Bell's inequality'. In: *Letters in Mathematical Physics* 4.2 (1980), pp. 93–100. DOI: 10.1007/BF00417500.

[33] John F. Clauser, Michael A. Horne, Abner Shimony and Richard A. Holt. 'Proposed experiment to test local hidden-variable theories'. In: *Physical Review Letters* 23.15 (1969), pp. 880–884. DOI: 10.1103/PhysRevLett.23.880.

[34] Rudolf Clausius. 'Über verschiedene für die Anwendung bequeme Formen der Hauptgleichungen der mechanischen Wärmetheorie'. In: *Annalen der Physik und Chemie* 201.7 (1865), pp. 353–400. DOI: 10.1002/andp.18652010702.

[35] Giuseppe Cocconi and Philip Morrison. 'Searching for Interstellar Communications'. In: *Nature* 184.4690 (1959), pp. 844–846. DOI: 10.1038/184844a0.

[36] Roger C. Conant and W. Ross Ashby. 'Every Good Regulator of a System Must Be a Model of That System'. In: *International Journal of Systems Science* 1.2 (1970), pp. 89–97. DOI: 10.1080/00207727008920220.

[37] Charles A. Coulson. *Valence*. 2nd ed. Oxford: Oxford University Press, 1961.

[38] Thomas M. Cover and Joy A. Thomas. *Elements of Information Theory*. 2nd ed. Hoboken, NJ: Wiley-Interscience, 2006. ISBN: 978-0-471-24195-9.

[39] Salambô Dago, Jorge Pereda, Nicolas Barros, Sergio Ciliberto and Ludovic Bellon. 'Information and Thermodynamics: Fast and Precise Approach to Landauer's Bound in an Underdamped Micromechanical Oscillator'. In: *Physical Review Letters* 126.17 (2021), p. 170601. DOI: 10.1103/PhysRevLett.126.170601.

[40] David Dalrymple et al. *Towards Guaranteed Safe AI: A Framework for Ensuring Robust and Reliable AI Systems*. 2024. DOI: 10.48550/arXiv.2405.06624. arXiv: 2405.06624 [cs.AI].

[41] Chandler Davis and W. M. Kahan. 'The Rotation of Eigenvectors by a Perturbation. III'. In: *SIAM Journal on Numerical Analysis* 7.1 (1970), pp. 1–46. DOI: 10.1137/0707001.

[42] Stanislas Dehaene and Jean-Pierre Changeux. 'Experimental and theoretical approaches to conscious processing'. In: *Neuron* 70.2 (2011), pp. 200–227. DOI: 10.1016/j.neuron.2011.03.018.

[43] Frank D. Drake. 'Project Ozma'. In: *Physics Today* 14.4 (1961), pp. 40–46. DOI: 10.1063/1.3057500.

[44] Courtney D. Dressing and David Charbonneau. 'The occurrence of potentially habitable planets orbiting M dwarfs estimated from the full Kepler dataset and an empirical measurement of the detection sensitivity'. In: *The Astrophysical Journal* 807.1 (2015), p. 45. DOI: 10.1088/0004-637X/807/1/45.

[45] Morris Dworkin. *Recommendation for Block Cipher Modes of Operation: Galois/Counter Mode (GCM) and GMAC*. Tech. rep. SP 800-38D. National Institute of Standards and Technology, 2007. DOI: 10.6028/NIST.SP.800-38D.

[46] Freeman J. Dyson. 'Search for Artificial Stellar Sources of Infrared Radiation'. In: *Science* 131.3414 (1960), pp. 1667–1668. DOI: 10.1126/science.131.3414.1667.

[47] Paul Ehrenfest and Tatiana Ehrenfest. *The Conceptual Foundations of the Statistical Approach in Mechanics*. Trans. by Michael J. Moravcsik. Ithaca, NY: Cornell University Press, 1959.

[48] Albert Einstein, Boris Podolsky and Nathan Rosen. 'Can quantum-mechanical description of physical reality be considered complete?' In: *Physical Review* 47.10 (1935), pp. 777–780. DOI: 10.1103/PhysRev.47.777.

[49] Christopher Eling, Raf Guedens and Ted Jacobson. 'Nonequilibrium thermodynamics of spacetime'. In: *Physical Review Letters* 96.12 (2006), p. 121301. DOI: 10.1103/PhysRevLett.96.121301.

[50] Berthold-Georg Englert. 'Fringe Visibility and Which-Way Information: An Inequality'. In: *Physical Review Letters* 77.11 (1996), pp. 2154–2157. DOI: 10.1103/PhysRevLett.77.2154.

[51] Peter David Fagan. *Keyed Chaotic Dynamics for Privacy-Preserving Neural Inference*. 2025. arXiv: 2505.23655 [cs.CR].

[52] Peter David Fagan. *Cosmological Horizons as Epistemic Bounds of Conservation-Congruent Encodings*. Preprint. May 2026.

[53] Peter David Fagan. *Emergence of the Physical Laws of a Macroscopic Observer*. Preprint, version 2. Apr. 2026.

[54] Peter David Fagan. *Epistemic Limits of the Embedded Observer*. Preprint, version 3. May 2026.

[55] Peter David Fagan. *Intelligence, Consciousness and Designing for Computational Efficiency*. Preprint. Apr. 2026.

[56] Peter David Fagan. *Toward a Physical Theory of Intelligence*. 2026. arXiv: 2601.00021 [cs.AI].

[57] Miroslav Fiedler. 'Algebraic connectivity of graphs'. In: *Czechoslovak Mathematical Journal* 23.2 (1973), pp. 298–305. DOI: 10.21136/CMJ.1973.101168.

[58] Robin Forman. 'Bochner's Method for Cell Complexes and Combinatorial Ricci Curvature'. In: *Discrete & Computational Geometry* 29.3 (2003), pp. 323–374. DOI: 10.1007/s00454-002-0743-x.

[59] Pascal Fries. 'Rhythms for cognition: communication through coherence'. In: *Neuron* 88.1 (2015), pp. 220–235. DOI: 10.1016/j.neuron.2015.09.034.

[60] Karl Friston. 'The free-energy principle: a unified brain theory?' In: *Nature Reviews Neuroscience* 11.2 (2010), pp. 127–138. DOI: 10.1038/nrn2787.

[61] Karl Friston. 'Life as we know it'. In: *Journal of the Royal Society Interface* 10.86 (2013), p. 20130475. DOI: 10.1098/rsif.2013.0475.

[62] Gaia Collaboration. 'Gaia Data Release 3: Summary of the content and survey properties'. In: *Astronomy & Astrophysics* 674 (2023), A1. DOI: 10.1051/0004-6361/202243940.

[63] Vishal Gajjar and Grayce C. Brown. 'Exo-IPM scattering as a hidden gatekeeper of narrowband technosignatures'. In: *The Astrophysical Journal* 999.2 (2026), p. 210. DOI: 10.3847/1538-4357/ae3d33.

[64] Blaise Gassend, Dwaine Clarke, Marten van Dijk and Srinivas Devadas. 'Silicon Physical Random Functions'. In: *Proceedings of the 9th ACM Conference on Computer and Communications Security*. New York: ACM, 2002, pp. 148–160. DOI: 10.1145/586110.586132.

[65] Momčilo Gavrilov and John Bechhoefer. 'Erasure without Work in an Asymmetric Double-Well Potential'. In: *Physical Review Letters* 117.20 (2016), p. 200601. DOI: 10.1103/PhysRevLett.117.200601.

[66] Robert Ghrist. 'Configuration spaces and braid groups on graphs in robotics'. In: *Knots, Braids, and Mapping Class Groups—Papers Dedicated to Joan S. Birman*. Ed. by Jane Gilman, William W. Menasco and Xiao-Song Lin. Vol. 24. AMS/IP Studies in Advanced Mathematics. Providence, RI, USA: American Mathematical Society, 2001, pp. 29–40. DOI: 10.1090/amsip/024/03. arXiv: math/9905023.

[67] Gary W. Gibbons and Stephen W. Hawking. 'Cosmological event horizons, thermodynamics, and particle creation'. In: *Physical Review D* 15.10 (1977), pp. 2738–2751. DOI: 10.1103/PhysRevD.15.2738.

[68] Josiah Willard Gibbs. *Elementary Principles in Statistical Mechanics: Developed with Especial Reference to the Rational Foundation of Thermodynamics*. New York: Charles Scribner's Sons, 1902.

[69] Andrew M. Gleason. 'Measures on the Closed Subspaces of a Hilbert Space'. In: *Journal of Mathematics and Mechanics* 6.6 (1957), pp. 885–893.

[70] Vittorio Gorini, Andrzej Kossakowski and E. C. G. Sudarshan. 'Completely positive dynamical semigroups of *N*-level systems'. In: *Journal of Mathematical Physics* 17.5 (1976), pp. 821–825. DOI: 10.1063/1.522979.

[71] Miroslav Grmela and Hans Christian Öttinger. 'Dynamics and Thermodynamics of Complex Fluids. I. Development of a General Formalism'. In: *Physical Review E* 56.6 (1997), pp. 6620–6632. DOI: 10.1103/PhysRevE.56.6620.

[72] Mikhael Gromov. 'Hyperbolic Groups'. In: *Essays in Group Theory*. Ed. by Steve M. Gersten. Vol. 8. Mathematical Sciences Research Institute Publications. Springer, 1987, pp. 75–263. DOI: 10.1007/978-1-4613-9586-7_3.

[73] Peter Hänggi, Peter Talkner and Michal Borkovec. 'Reaction-rate theory: fifty years after Kramers'. In: *Reviews of Modern Physics* 62.2 (1990), pp. 251–341. DOI: 10.1103/RevModPhys.62.251.

[74] Michael H. Hart. 'An Explanation for the Absence of Extraterrestrials on Earth'. In: *Quarterly Journal of the Royal Astronomical Society* 16 (1975), pp. 128–135.

[75] Stephen W. Hawking. 'Particle creation by black holes'. In: *Communications in Mathematical Physics* 43.3 (1975), pp. 199–220. DOI: 10.1007/BF02345020.

[76] Stephen W. Hawking and Roger Penrose. 'The singularities of gravitational collapse and cosmology'. In: *Proceedings of the Royal Society of London. Series A, Mathematical and Physical Sciences* 314.1519 (1970), pp. 529–548. DOI: 10.1098/rspa.1970.0021.

[77] Friedrich A. Hayek. 'The Use of Knowledge in Society'. In: *The American Economic Review* 35.4 (1945), pp. 519–530.

[78] Pim van der Hoorn, William J. Cunningham, Gábor Lippner, Carlo Trugenberger and Dmitri Krioukov. 'Ollivier-Ricci Curvature Convergence in Random Geometric Graphs'. In: *Physical Review Research* 3.1 (2021), p. 013211. DOI: 10.1103/PhysRevResearch.3.013211.

[79] International Energy Agency. *Data centres and data transmission networks*. 2026. URL: https://www.iea.org/energy-system/buildings/data-centres-and-data-transmission-networks (visited on 3rd July 2026).

[80] Ted Jacobson. 'Thermodynamics of spacetime: The Einstein equation of state'. In: *Physical Review Letters* 75.7 (1995), pp. 1260–1263. DOI: 10.1103/PhysRevLett.75.1260.

[81] E. T. Jaynes. 'Information Theory and Statistical Mechanics'. In: *Physical Review* 106.4 (1957), pp. 620–630. DOI: 10.1103/PhysRev.106.620.

[82] Nikolai S. Kardashev. 'Transmission of Information by Extraterrestrial Civilizations'. In: *Soviet Astronomy* 8.2 (1964), pp. 217–221.

[83] Allan N. Kaufman. 'Dissipative Hamiltonian Systems: A Unifying Principle'. In: *Physics Letters A* 100.8 (1984), pp. 419–422. DOI: 10.1016/0375-9601(84)90634-0.

[84] Nobuhiro Kiyotaki and Randall Wright. 'On Money as a Medium of Exchange'. In: *Journal of Political Economy* 97.4 (1989), pp. 927–954. DOI: 10.1086/261634.

[85] Douglas J. Klein and Milan Randić. 'Resistance distance'. In: *Journal of Mathematical Chemistry* 12.1 (1993), pp. 81–95. DOI: 10.1007/BF01164627.

[86] Walter Kohn and Lu Jeu Sham. 'Self-Consistent Equations Including Exchange and Correlation Effects'. In: *Physical Review* 140.4A (1965), A1133–A1138. DOI: 10.1103/PhysRev.140.A1133.

[87] Alicia J. Kollár, Mattias Fitzpatrick and Andrew A. Houck. 'Hyperbolic lattices in circuit quantum electrodynamics'. In: *Nature* 571.7763 (2019), pp. 45–50. DOI: 10.1038/s41586-019-1348-3.

[88] Richard Kraaij, Alexandre Lazarescu, Christian Maes and Mark Peletier. 'Deriving GENERIC from a generalized fluctuation symmetry'. In: *Journal of Statistical Physics* 170.3 (2018), pp. 492–508. DOI: 10.1007/s10955-017-1941-5.

[89] Hendrik Anthony Kramers. 'Brownian motion in a field of force and the diffusion model of chemical reactions'. In: *Physica* 7.4 (1940), pp. 284–304. DOI: 10.1016/S0031-8914(40)90098-2.

[90] Dmitri Krioukov, Fragkiskos Papadopoulos, Maksim Kitsak, Amin Vahdat and Marián Boguñá. 'Hyperbolic geometry of complex networks'. In: *Physical Review E* 82.3 (2010), p. 036106. DOI: 10.1103/PhysRevE.82.036106.

[91] Ravindra S. Kulkarni. 'On the Bianchi identities'. In: *Mathematische Annalen* 199.4 (1972), pp. 175–204. DOI: 10.1007/BF01429873.

[92] Yoshiki Kuramoto. *Chemical Oscillations, Waves, and Turbulence*. Vol. 19. Springer Series in Synergetics. Berlin, Heidelberg: Springer, 1984. DOI: 10.1007/978-3-642-69689-3.

[93] Simon Kuznets. *National Income, 1929–1932*. 73rd Congress, 2nd Session, Senate Document 124. Washington, DC, USA: U.S. Bureau of Foreign and Domestic Commerce, 1934. URL: https://fraser.stlouisfed.org/title/national-income-1929-1932-971 (visited on 12th July 2026).

[94] Butler W. Lampson. 'A Note on the Confinement Problem'. In: *Communications of the ACM* 16.10 (1973), pp. 613–615. DOI: 10.1145/362375.362389.

[95] Rolf Landauer. 'Irreversibility and heat generation in the computing process'. In: *IBM Journal of Research and Development* 5.3 (1961), pp. 183–191. DOI: 10.1147/rd.53.0183.

[96] Nick Lane and William Martin. 'The energetics of genome complexity'. In: *Nature* 467.7318 (2010), pp. 929–934. DOI: 10.1038/nature09486.

[97] Simon B. Laughlin, Rob R. de Ruyter van Steveninck and John C. Anderson. 'The metabolic cost of neural information'. In: *Nature Neuroscience* 1.1 (1998), pp. 36–41. DOI: 10.1038/236.

[98] F. William Lawvere. 'Diagonal arguments and cartesian closed categories'. In: *Category Theory, Homology Theory and their Applications II*. Vol. 92. Lecture Notes in Mathematics. Berlin, Heidelberg: Springer, 1969, pp. 134–145. DOI: 10.1007/BFb0080769.

[99] Tony Lelièvre and Francis Nier. 'Low temperature asymptotics for quasi-stationary distributions in a bounded domain'. In: *Analysis & PDE* 8.3 (2015), pp. 561–628. DOI: 10.2140/apde.2015.8.561.

[100] Patrick M. Lenggenhager et al. 'Simulating hyperbolic space on a circuit board'. In: *Nature Communications* 13.1 (2022), p. 4373. DOI: 10.1038/s41467-022-32042-4.

[101] Peter Lennie. 'The cost of cortical computation'. In: *Current Biology* 13.6 (2003), pp. 493–497. DOI: 10.1016/S0960-9822(03)00135-0.

[102] Friedrich Lenz. 'The Ratio of Proton and Electron Masses'. In: *Physical Review* 82.4 (1951), p. 554. DOI: 10.1103/PhysRev.82.554.2.

[103] Göran Lindblad. 'On the generators of quantum dynamical semigroups'. In: *Communications in Mathematical Physics* 48.2 (1976), pp. 119–130. DOI: 10.1007/BF01608499.

[104] Tal Linzen, Emmanuel Dupoux and Yoav Goldberg. 'Assessing the Ability of LSTMs to Learn Syntax-Sensitive Dependencies'. In: *Transactions of the Association for Computational Linguistics* 4 (2016), pp. 521–535. DOI: 10.1162/tacl_a_00115.

[105] Seth Lloyd. 'Computational capacity of the universe'. In: *Physical Review Letters* 88.23 (2002), p. 237901. DOI: 10.1103/PhysRevLett.88.237901.

[106] Norman Margolus and Lev B. Levitin. 'The maximum speed of dynamical evolution'. In: *Physica D: Nonlinear Phenomena* 120.1–2 (1998), pp. 188–195. DOI: 10.1016/S0167-2789(98)00054-2. arXiv: quant-ph/9710043.

[107] James Clerk Maxwell. *Theory of Heat*. London: Longmans, Green, and Co., 1871.

[108] John Maynard Smith and Eörs Szathmáry. *The Major Transitions in Evolution*. Oxford: Oxford University Press, 1995.

[109] James L. McClelland, Bruce L. McNaughton and Randall C. O'Reilly. 'Why there are complementary learning systems in the hippocampus and neocortex: insights from the successes and failures of connectionist models of learning and memory'. In: *Psychological Review* 102.3 (1995), pp. 419–457. DOI: 10.1037/0033-295X.102.3.419.

[110] Carl Menger. 'On the Origin of Money'. In: *The Economic Journal* 2.6 (1892), pp. 239–255. DOI: 10.2307/2956146.

[111] Thomas Metzinger. *Being No One: The Self-Model Theory of Subjectivity*. Cambridge, MA: MIT Press, 2003.

[112] Jacques Monod, Jeffries Wyman and Jean-Pierre Changeux. 'On the nature of allosteric transitions: A plausible model'. In: *Journal of Molecular Biology* 12.1 (1965), pp. 88–118. DOI: 10.1016/S0022-2836(65)80285-6.

[113] Luc Moreau. 'Stability of multiagent systems with time-dependent communication links'. In: *IEEE Transactions on Automatic Control* 50.2 (2005), pp. 169–182. DOI: 10.1109/TAC.2004.841888.

[114] Philip J. Morrison. 'A paradigm for joined Hamiltonian and dissipative systems'. In: *Physica D: Nonlinear Phenomena* 18.1–3 (1986), pp. 410–419. DOI: 10.1016/0167-2789(86)90209-5.

[115] Philip J. Morrison and Michael H. Updike. 'Inclusive curvaturelike framework for describing dissipation: Metriplectic 4-bracket dynamics'. In: *Physical Review E* 109.4 (2024), p. 045202. DOI: 10.1103/PhysRevE.109.045202.

[116] Philip M. Morse. 'Diatomic Molecules According to the Wave Mechanics. II. Vibrational Levels'. In: *Physical Review* 34.1 (1929), pp. 57–64. DOI: 10.1103/PhysRev.34.57.

[117] John F. Nash. 'The Bargaining Problem'. In: *Econometrica* 18.2 (1950), pp. 155–162. DOI: 10.2307/1907266.

[118] John F. Nash. 'Non-Cooperative Games'. In: *Annals of Mathematics* 54.2 (1951), pp. 286–295. DOI: 10.2307/1969529.

[119] Maximilian Nickel and Douwe Kiela. 'Poincaré Embeddings for Learning Hierarchical Representations'. In: *Advances in Neural Information Processing Systems*. Vol. 30. 2017, pp. 6338–6347.

[120] Katsumi Nomizu. 'On the decomposition of generalized curvature tensor fields'. In: *Differential Geometry (in Honor of Kentaro Yano)*. Ed. by Shoshichi Kobayashi, Morio Obata and Toshio Takahashi. Tokyo: Kinokuniya, 1972, pp. 335–345.

[121] William D. Nordhaus and James Tobin. 'Is Growth Obsolete?' In: *Economic Research: Retrospect and Prospect, Volume 5: Economic Growth*. New York: National Bureau of Economic Research, 1972, pp. 1–80. ISBN: 0-87014-254-2.

[122] Masafumi Oizumi, Larissa Albantakis and Giulio Tononi. 'From the phenomenology to the mechanisms of consciousness: Integrated Information Theory 3.0'. In: *PLOS Computational Biology* 10.5 (2014), e1003588. DOI: 10.1371/journal.pcbi.1003588.

[123] Yann Ollivier. 'Ricci Curvature of Markov Chains on Metric Spaces'. In: *Journal of Functional Analysis* 256.3 (2009), pp. 810–864. DOI: 10.1016/j.jfa.2008.11.001.

[124] Stephen M. Omohundro. 'The Basic AI Drives'. In: *Artificial General Intelligence 2008: Proceedings of the First AGI Conference*. Ed. by Pei Wang, Ben Goertzel and Stan Franklin. Amsterdam: IOS Press, 2008, pp. 483–492.

[125] Alexei O. Orlov, Craig S. Lent, Cameron C. Thorpe, Graham P. Boechler and Gregory L. Snider. 'Experimental Test of Landauer's Principle at the Sub-k_BT Level'. In: *Japanese Journal of Applied Physics* 51.6S (2012), 06FE10. DOI: 10.1143/JJAP.51.06FE10.

[126] Hans Christian Öttinger and Miroslav Grmela. 'Dynamics and Thermodynamics of Complex Fluids. II. Illustrations of a General Formalism'. In: *Physical Review E* 56.6 (1997), pp. 6633–6655. DOI: 10.1103/PhysRevE.56.6633.

[127] Don N. Page and William K. Wootters. 'Evolution without evolution: Dynamics described by stationary observables'. In: *Physical Review D* 27.12 (1983), pp. 2885–2892. DOI: 10.1103/PhysRevD.27.2885.

[128] Thomas Parr, Giovanni Pezzulo and Karl J. Friston. *Active Inference: The Free Energy Principle in Mind, Brain, and Behavior*. Cambridge, MA: MIT Press, 2022. DOI: 10.7551/mitpress/12441.001.0001.

[129] Wolfgang Pauli. 'Über den Zusammenhang des Abschlusses der Elektronengruppen im Atom mit der Komplexstruktur der Spektren'. In: *Zeitschrift für Physik* 31.1 (1925), pp. 765–783. DOI: 10.1007/BF02980631.

[130] Linus Pauling. 'The Nature of the Chemical Bond. Application of Results Obtained from the Quantum Mechanics and from a Theory of Paramagnetic Susceptibility to the Structure of Molecules'. In: *Journal of the American Chemical Society* 53.4 (1931), pp. 1367–1400. DOI: 10.1021/ja01355a027.

[131] Judea Pearl. *Probabilistic Reasoning in Intelligent Systems: Networks of Plausible Inference*. San Mateo, CA: Morgan Kaufmann, 1988. ISBN: 978-1-55860-479-7. DOI: 10.1016/C2009-0-27609-4.

[132] Nikolay Perunov, Robert A. Marsland and Jeremy L. England. 'Statistical physics of adaptation'. In: *Physical Review X* 6.2 (2016), p. 021036. DOI: 10.1103/PhysRevX.6.021036.

[133] Erik A. Petigura, Andrew W. Howard and Geoffrey W. Marcy. 'Prevalence of Earth-size planets orbiting Sun-like stars'. In: *Proceedings of the National Academy of Sciences* 110.48 (2013), pp. 19273–19278. DOI: 10.1073/pnas.1319909110.

[134] Plato. *Republic*. Ed. by C. D. C. Reeve. Trans. by G. M. A. Grube. Indianapolis, IN, USA: Hackett Publishing Company, 1992.

[135] Sandu Popescu and Daniel Rohrlich. 'Quantum nonlocality as an axiom'. In: *Foundations of Physics* 24.3 (1994), pp. 379–385. DOI: 10.1007/BF02058098.

[136] Steve Pressé, Kingshuk Ghosh, Julian Lee and Ken A. Dill. 'Principles of maximum entropy and maximum caliber in statistical physics'. In: *Reviews of Modern Physics* 85.3 (2013), pp. 1115–1141. DOI: 10.1103/RevModPhys.85.1115.

[137] Jan-Hendrik Prinz, Hao Wu, Marco Sarich, Bettina Keller, Martin Senne, Martin Held, John D. Chodera, Christof Schütte and Frank Noé. 'Markov models of molecular kinetics: Generation and validation'. In: *The Journal of Chemical Physics* 134.17 (2011), p. 174105. DOI: 10.1063/1.3565032.

[138] Krishnan Raghavachari, Gary W. Trucks, John A. Pople and Martin Head-Gordon. 'A fifth-order perturbation comparison of electron correlation theories'. In: *Chemical Physics Letters* 157.6 (1989), pp. 479–483. DOI: 10.1016/S0009-2614(89)87395-6.

[139] Rajesh P. N. Rao and Dana H. Ballard. 'Predictive coding in the visual cortex: a functional interpretation of some extra-classical receptive-field effects'. In: *Nature Neuroscience* 2.1 (1999), pp. 79–87. DOI: 10.1038/4580.

[140] Amal Kumar Raychaudhuri. 'Relativistic cosmology. I'. In: *Physical Review* 98.4 (1955), pp. 1123–1126. DOI: 10.1103/PhysRev.98.1123.

[141] Tullio Regge. 'General Relativity without Coordinates'. In: *Il Nuovo Cimento* 19.3 (1961), pp. 558–571. DOI: 10.1007/BF02733251.

[142] D. R. Michiel Renger. 'Gradient and GENERIC systems in the space of fluxes, applied to reacting particle systems'. In: *Entropy* 20.8 (2018), p. 596. DOI: 10.3390/e20080596.

[143] Stuart Russell. *Human Compatible: Artificial Intelligence and the Problem of Control*. New York: Viking, 2019.

[144] Lynn Sagan. 'On the origin of mitosing cells'. In: *Journal of Theoretical Biology* 14.3 (1967), pp. 225–274. DOI: 10.1016/0022-5193(67)90079-3.

[145] Takahiro Sagawa and Masahito Ueda. 'Minimal Energy Cost for Thermodynamic Information Processing: Measurement and Information Erasure'. In: *Physical Review Letters* 102.25 (2009), p. 250602. DOI: 10.1103/PhysRevLett.102.250602.

[146] Jerome H. Saltzer and Michael D. Schroeder. 'The Protection of Information in Computer Systems'. In: *Proceedings of the IEEE* 63.9 (1975), pp. 1278–1308. DOI: 10.1109/PROC.1975.9939.

[147] Filadelfo C. Santos, Vitorvani Soares and Alexandre C. Tort. 'Determination of the apsidal angles and Bertrand's theorem'. In: *Physical Review E* 79.3 (2009), p. 036605. DOI: 10.1103/PhysRevE.79.036605.

[148] Rik Sarkar. 'Low Distortion Delaunay Embedding of Trees in Hyperbolic Plane'. In: *Graph Drawing*. Vol. 7034. Lecture Notes in Computer Science. Springer, 2012, pp. 355–366. DOI: 10.1007/978-3-642-25878-7_34.

[149] John R. Searle. 'Minds, brains, and programs'. In: *Behavioral and Brain Sciences* 3.3 (1980), pp. 417–424. DOI: 10.1017/S0140525X00005756.

[150] Udo Seifert. 'Stochastic thermodynamics, fluctuation theorems and molecular machines'. In: *Reports on Progress in Physics* 75.12 (2012), p. 126001. DOI: 10.1088/0034-4885/75/12/126001.

[151] Claude E. Shannon. 'A Mathematical Theory of Communication'. In: *Bell System Technical Journal* 27.3–4 (1948), pp. 379–423, 623–656. DOI: 10.1002/j.1538-7305.1948.tb01338.x.

[152] Herbert A. Simon. 'The Architecture of Complexity'. In: *Proceedings of the American Philosophical Society* 106.6 (1962), pp. 467–482.

[153] M. Suazo, E. Zackrisson, P. K. Mahto, F. Lundell, C. Nettelblad, A. J. Korn, J. T. Wright and S. Majumdar. 'Project Hephaistos – II. Dyson sphere candidates from Gaia DR3, 2MASS, and WISE'. In: *Monthly Notices of the Royal Astronomical Society* 531.1 (2024), pp. 695–707. DOI: 10.1093/mnras/stae1186.

[154] Leo Szilard. 'Über die Entropieverminderung in einem thermodynamischen System bei Eingriffen intelligenter Wesen'. In: *Zeitschrift für Physik* 53.11–12 (1929), pp. 840–856. DOI: 10.1007/BF01341281.

[155] F. R. Tangherlini. 'Schwarzschild field in *n* dimensions and the dimensionality of space problem'. In: *Il Nuovo Cimento* 27.3 (1963), pp. 636–651. DOI: 10.1007/BF02784569.

[156] Frank J. Tipler. 'Extraterrestrial Intelligent Beings Do Not Exist'. In: *Quarterly Journal of the Royal Astronomical Society* 21 (1980), pp. 267–281.

[157] Monique M. Tirion. 'Large Amplitude Elastic Motions in Proteins from a Single-Parameter, Atomic Analysis'. In: *Physical Review Letters* 77.9 (1996), pp. 1905–1908. DOI: 10.1103/PhysRevLett.77.1905.

[158] Giulio Tononi. 'An information integration theory of consciousness'. In: *BMC Neuroscience* 5 (2004), p. 42. DOI: 10.1186/1471-2202-5-42.

[159] Giulio Tononi and Chiara Cirelli. 'Sleep and the price of plasticity: from synaptic and cellular homeostasis to memory consolidation and integration'. In: *Neuron* 81.1 (2014), pp. 12–34. DOI: 10.1016/j.neuron.2013.12.025.

[160] Hugo Touchette. 'Introduction to dynamical large deviations of Markov processes'. In: *Physica A: Statistical Mechanics and its Applications* 504 (2018), pp. 5–19. DOI: 10.1016/j.physa.2017.10.046.

[161] P.-E. Tremblay, G. Fontaine, N. P. Gentile Fusillo, B. H. Dunlap, B. T. Gänsicke, M. A. Hollands, J. J. Hermes, T. R. Marsh, E. Cukanovaite and T. Cunningham. 'Core crystallization and pile-up in the cooling sequence of evolving white dwarfs'. In: *Nature* 565.7738 (2019), pp. 202–205. DOI: 10.1038/s41586-018-0791-x.

[162] Alexander Matt Turner, Logan Smith, Rohin Shah, Andrew Critch and Prasad Tadepalli. 'Optimal Policies Tend to Seek Power'. In: *Advances in Neural Information Processing Systems*. Vol. 34. 2021, pp. 23063–23074.

[163] A. Udalski, M. K. Szymański and G. Szymański. 'OGLE-IV: Fourth phase of the Optical Gravitational Lensing Experiment'. In: *Acta Astronomica* 65.1 (2015), pp. 1–38. arXiv: 1504.05966 [astro-ph.SR]. URL: https://ogle.astrouw.edu.pl/.

[164] Uptime Institute. *Global Data Center Survey*. 2024. URL: https://uptimeinstitute.com/resources/research-and-reports (visited on 3rd July 2026).

[165] Ashish Vaswani, Noam Shazeer, Niki Parmar, Jakob Uszkoreit, Llion Jones, Aidan N. Gomez, Łukasz Kaiser and Illia Polosukhin. 'Attention Is All You Need'. In: *Advances in Neural Information Processing Systems*. Vol. 30. 2017, pp. 5998–6008.

[166] Aurélien Velleret. *Large deviations for surviving trajectories of general Markov processes*. 2020. arXiv: 2003.01026 [math.PR].

[167] Erik Verlinde. 'On the origin of gravity and the laws of Newton'. In: *Journal of High Energy Physics* 2011.04 (2011), p. 029. DOI: 10.1007/JHEP04(2011)029.

[168] Arieh Warshel and Michael Levitt. 'Theoretical studies of enzymic reactions: Dielectric, electrostatic and steric stabilization of the carbonium ion in the reaction of lysozyme'. In: *Journal of Molecular Biology* 103.2 (1976), pp. 227–249. DOI: 10.1016/0022-2836(76)90311-9.

[169] John Archibald Wheeler. 'The 'past' and the 'delayed-choice' double-slit experiment'. In: *Mathematical Foundations of Quantum Theory*. Ed. by A. R. Marlow. New York: Academic Press, 1978, pp. 9–48. DOI: 10.1016/B978-0-12-473250-6.50006-6.

[170] Norbert Wiener. 'Some Moral and Technical Consequences of Automation'. In: *Science* 131.3410 (1960), pp. 1355–1358. DOI: 10.1126/science.131.3410.1355.

[171] David H. Wolpert. 'Physical limits of inference'. In: *Physica D: Nonlinear Phenomena* 237.9 (2008), pp. 1257–1281. DOI: 10.1016/j.physd.2008.03.040.

[172] E. C. Zeeman. 'Knotting manifolds'. In: *Bulletin of the American Mathematical Society* 67.1 (1961), pp. 117–119. DOI: 10.1090/S0002-9904-1961-10529-6.

[173] Wojciech Hubert Zurek. 'Decoherence, einselection, and the quantum origins of the classical'. In: *Reviews of Modern Physics* 75.3 (2003), pp. 715–775. DOI: 10.1103/RevModPhys.75.715.

COLOPHON

This book was typeset with Tectonic using André Miede's `classicthesis` style, inspired by Robert Bringhurst's *The Elements of Typographic Style*. The text is set in *Libertinus Serif* and the mathematics in *Libertinus Math*.

First Edition: November 2026.

Build for the benefit of others.